

Volume 65 • Number 5 • October 2017

Acta Geophysica

PAN
POLISH ACADEMY OF SCIENCES




Institute of Geophysics
Polish Academy of Sciences



Springer

Statistical damage constitutive model for rocks subjected to cyclic stress and cyclic temperature

Shu-Wei Zhou^{1,2}  · Cai-Chu Xia^{1,3} · Hai-Bin Zhao⁴ · Song-Hua Mei⁴ · Yu Zhou¹

Received: 20 January 2017 / Accepted: 12 August 2017 / Published online: 21 August 2017
© Institute of Geophysics, Polish Academy of Sciences & Polish Academy of Sciences 2017

Abstract A constitutive model of rocks subjected to cyclic stress–temperature was proposed. Based on statistical damage theory, the damage constitutive model with Weibull distribution was extended. Influence of model parameters on the stress–strain curve for rock reloading after stress–temperature cycling was then discussed. The proposed model was initially validated by rock tests for cyclic stress–temperature and only cyclic stress. Finally, the total damage evolution induced by stress–temperature cycling and reloading after cycling was explored and discussed. The proposed constitutive model is reasonable and applicable, describing well the stress–strain relationship during stress–temperature cycles and providing a good fit to the test results. Elastic modulus in the reference state and the damage induced by cycling affect the shape of reloading stress–strain curve. Total damage induced by cycling and reloading after cycling exhibits three stages: initial slow increase, mid-term accelerated increase, and final slow increase.

Keywords Cyclic stress · Cyclic temperature · Constitutive model · Damage · Weibull distribution

Introduction

Rocks are subjected to simultaneous cyclic stress and temperature during rock engineering in cold regions and rock caverns for underground compressed air energy storage (CAES). Rock engineering in cold regions, particularly in slopes or tunnels, is subjected to cyclic diurnal temperature variation and cyclic seasonal temperature (Günzburger et al. 2005). Constraint conditions induce cyclic stress variations in rocks and adversely affect rock structure safety. Thus, the effects of cyclic stress and cyclic temperature on rocks warrant considerable investigation. On one hand, CAES is an energy storage and power generation technology with broad application prospects (Zhou et al. 2015a). On the other hand, frequent and rapid inflation and discharge of compressed air induce a significant temperature variation in CAES caverns. Moreover, varying air pressures act on the cavern surface simultaneously. Consequently, the rocks around the cavern are evidently influenced by cyclic stress and cyclic temperature in CAES engineering (Allen et al. 1982; Zhou et al. 2015a). Repeated stress and temperature influence the mechanical performance of rocks and thus the long-term stability of the corresponding engineering. Therefore, choosing a reasonable constitutive model is a key factor to predict engineering stability. However, only elastic models (Kim et al. 2012; Zhou et al. 2015a) and ideal elastoplastic models (Zimmels et al. 2002) were chosen as the constitutive models in the corresponding rock engineering during the past decades, particularly in lined rock caverns for underground CAES. These models differ from actual

✉ Cai-Chu Xia
tjxiaccb@126.com

¹ Department of Geotechnical Engineering, College of Civil Engineering, Tongji University, Shanghai 200092, People's Republic of China

² Institute of Structural Mechanics, Bauhaus-University Weimar, 99423 Weimar, Germany

³ College of Civil Engineering, Shaoxing University, Shaoxing 312000, People's Republic of China

⁴ Hunan Key Laboratory of Key Technology on Hydropower Development, Power China Zhongnan Engineering Corporation Limited, Changsha 410014, Hunan, People's Republic of China

engineering conditions. Thus, establishing a constitutive model for rocks subjected to both cyclic stress and temperature is urgently needed.

Such special constitutive models remain unreported in the literature during the past decades. Moreover, only a few researchers have worked on establishing constitutive models for rocks subjected only to cyclic stress. For example, Mo (1988) conducted cyclic loading tests on red sand stones and marbles, and proposed an endochronic constitutive model of rocks. However, the proposed model had complicated material functions, too many model parameters, and unclear physical implications. Wang et al. (2013, 2015) carried out triaxial cyclic loading tests for granitic rocks and proposed a fatigue constitutive model based on inner variables to describe the evolution of deformational modulus during stress cycles. The proposed model was disabled to completely describe the stress–strain relationship of rocks. White (2014) established a constitutive modeling framework for rough rock joints under cyclic loads. Souley et al. (1995) extended the constitutive model proposed by Saeb and Amadei (1992). The extended model was suitable for jointed rock mass subjected to cyclic loading. In addition, damage accumulates inside a rock when exposed to repeated stress and temperature effects (Song et al. 2013). Thus, rock damage theory can be applicable to research on constitutive models. Based on statistical mesoscopic damage mechanics, Xu et al. (2004) defined three damage stages during rock deformation. Li et al. (2012) established a damage-softening constitutive model of rocks on the basis of Weibull distribution and found that this model can describe well the stress–strain curve during rock failure. Other statistical damage models based on Weibull distribution were reported in Cao et al. (2007), Zhou et al. (2010) and Deng and Gu (2011). However, the proposed models were only aimed at monotonic loading and not cyclic loading. Li et al. (2001) established a damage model for jointed rock mass subjected to cyclic loading. Xiao et al. (2011) provided conclusions for the law of rock damage and several damage models. They also proposed an invested-S damage model and a damage model that represent the damage evolution of rocks as a logarithmic cycle function (Xiao et al. 2009, 2010). Qiu et al. (2014) proposed a model for the pre-peak unloading damage evolution of marble. However, the above-mentioned damage models focus only on cyclic stress and do not consider the influence of cyclic temperature. Therefore, the influence of both cyclic stress and cyclic temperature must be considered in establishing a constitutive model for rocks subjected to cyclic stress–temperature in accordance with damage theory or cyclic stress–temperature tests.

This study proposed a statistical damage constitutive model for rocks subjected to cyclic stress and cyclic

temperature in accordance with statistical damage theory. This model is an extension of the damage constitutive model of rocks based on Weibull distribution. The influence of model parameters on the stress–strain curves after stress–temperature cycling was analyzed. Cyclic uniaxial stress and cyclic temperature tests were then conducted to initially validate the proposed constitutive model. Finally, the evolution of the total damage induced by stress–temperature cycling and reloading after cycling was further discussed. The proposed model described well the stress–strain relationship of rocks during each stress–temperature cycle and proved good fits to the experimental results. The success in establishing such a constitutive model provides a new idea for studies on the mechanical performance of rocks subjected to both cyclic stress and cyclic temperature.

Constitutive model for rocks subjected to cyclic stress and cyclic temperature

According to the strain equivalence principle proposed by Lemaitre (1984), the induced strain of a damaged material subjected to stress σ is equal to the induced strain of the undamaged material subjected to the effective stress σ' . Thus, the following equation is obtained:

$$\varepsilon = \sigma/E' = \sigma'/E, \quad (1)$$

where ε is the strain, and E and E' are the Young's moduli of undamaged and damaged materials, respectively.

The Young's modulus of a dense undamaged rock is difficult to obtain, because most rocks have the initial defects. Zhang et al. (2003) defined the initial damage state of a rock as the reference damage state of the rock and then proposed an extended strain equivalence principle. Any two damage states (States A and B) are applied to explain the proposed principle when the rock is subjected to a load F and the resulting damage propagated. The effective stress of State A acting on State B can achieve an identical strain with that of State B acting on State A:

$$\varepsilon = \sigma_A/E_B = \sigma_B/E_A, \quad (2)$$

where σ_A and σ_B are effective stresses of States A and B, respectively, and E_A and E_B are the Young's moduli of States A and B, respectively. In addition, the effective stresses of States A and B satisfy the following equation:

$$\sigma_A A_A = \sigma_B A_B, \quad (3)$$

where A_A and A_B are the effective bearing areas of States A and B.

The rock is in the reference damage state before the cyclic stress and temperature effects are initiated because of its initial damage. This reference state can then be

regarded as State A. The state where the rock has been subjected to n cycles of stress and temperature effects is regarded as State B. Moreover, the damage factor of the rock after n cycles of stress and temperature is obtained in accordance with the equation defined by the following Lemaitre (1984):

$$D_n = 1 - A_n/A_0, \quad (4)$$

where A_0 and A_n are the bearing areas of the reference state and the state after the stress–temperature effects of n cycles. Thus, we can obtain the following equation based on the extended strain equivalence principle:

$$D_n = 1 - E_n/E_0, \quad (5)$$

where E_0 and E_n are the Young's moduli of the reference state and the state after the stress–temperature effects of n cycles. Equation (5) is used to determine the evolution of damage factor during stress–temperature effects and is similar to the expression used in the study on cyclic stress by Xiao et al. (2010).

The rock damage generated during loading is assumed to be isotropic in this study. The damage state of the rock after n cycles of stress–temperature is set as State A, and the total damage state induced by reloading after stress–temperature cycling is set as State B. Applying the extended strain equivalence principle again, we obtain the following constitutive model for rocks:

$$[\sigma] = [C]_n[\varepsilon](1 - D). \quad (6)$$

Equation (6) can also be rewritten as follows:

$$[\sigma^*] = [\sigma]/(1 - D) = [C]_n[\varepsilon], \quad (7)$$

where $[\sigma^*]$ is the matrix of effective stress, $[\sigma]$ is the matrix of nominal stress, D is the damage factor of the rock when reloading, and $[\varepsilon]$ is the matrix of strain. $[C]_n$ is the matrix of elasticity when reloading, which is also the matrix of elasticity of the rock material after n cycles of stress and temperature. $[C]_n$ can be easily obtained by Eq. (5). Thus, the determination of the damage factor D is a key to establish the constitutive model for rocks subjected to cyclic stress and cyclic temperature.

The statistical damage approach is a mesoscopic damage approach that has been developed in recent years (Wang et al. 2007). This approach is adopted in this study, and the strength of a mesoscopic element F^* is assumed to obey Weibull distribution, which has a probability density function as follows:

$$P[F^*] = \frac{m}{F_0} \left(\frac{F^*}{F_0}\right)^{m-1} \exp\left[-\left(\frac{F^*}{F_0}\right)^m\right], \quad (8)$$

where F^* is the variable of strength distribution; m and F_0 are parameters of Weibull distribution. F_0 has the same dimension as stress. F^* can be regarded as the stress level

and F_0 as the average of F^* (Wang et al. 2007). m is the shape parameter or the uniformity factor of material, which reflects the concentration degree of F^* . As shown in Fig. 1a, less m means higher uniformity.

The damage of the rock material results from the continuous failure of mesoscopic elements. Thus, damage factor D can be obtained using the failure probability of the mesoscopic elements of rock. The damage factor is expressed as follows:

$$D = \int_0^{F^*} p(F^*)dF^* = 1 - \exp\left[-\left(\frac{F^*}{F_0}\right)^m\right]. \quad (9)$$

Equation (9) is the damage evolution equation of mesoscopic elements based on the statistical damage constitutive model of rocks. Meanwhile, Fig. 1b shows the variations in damage factor D with F^*/F_0 for different m . The figure shows that damage factor D increases with the increase in F^*/F_0 . In addition, larger m means larger damage factor at the same stress level when $F^*/F_0 > 1$, that is, when the rock is at a relatively large stress level. Thus, a fully damaged state ($D = 1$) can be easily achieved when m has a large value.

As shown in Eq. (9), the strength of the mesoscopic elements of rock F^* must be determined to calculate the damage factor D . The previous studies used principal strains to describe the mesoscopic element strength of rocks. However, this treatment cannot reflect the influence of complicated stress state on the strength of mesoscopic element. Thus, Li et al. (2012) considered the rock failure mode and criterion, and proposed a new expression for the strength of rock mesoscopic elements. The present study also defines the strength of mesoscopic elements using the rock failure mode. In general, the rock failure criterion can be expressed as follows:

$$f([\sigma^*]) - k_0 = 0, \quad (10)$$

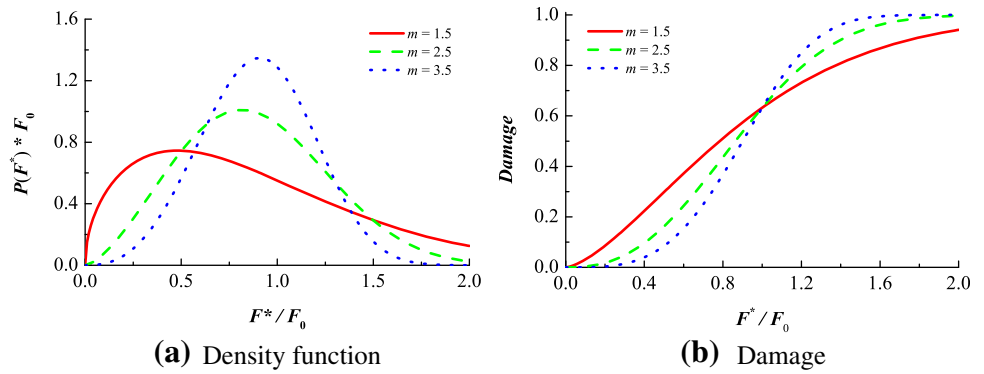
where k_0 is a constant related to the cohesion and internal frictional angle of a material. $F^* = f([\sigma^*])$ reflects the extent to which mesoscopic elements approach failure, and this equation can be used in Eq. (8) to define the strength of the mesoscopic element of rocks.

Thus, the strength of mesoscopic elements can be directly expressed depending on the failure mechanism and mode of the rock. The failure criteria of rocks involve the Drucker–Prager criterion and the Hoek–Brown criterion. In this case, F^* has different forms. The Mohr–Coulomb (M–C) form of the strength of mesoscopic element F^* is applied in the present study, because the widely used M–C criterion has a simple and suitable form for rock materials. The M–C criterion can be written as follows:

$$\sigma_1^* - \frac{1 + \sin \varphi}{1 - \sin \varphi} \sigma_3^* = \frac{2c \cos \varphi}{1 - \sin \varphi}, \quad (11)$$

where c and φ are the cohesion and the internal frictional angle of rocks. In accordance with Eq. (11), the basic form

Fig. 1 Density function and damage for different m



for the strength of the mesoscopic element is achieved as follows:

$$F^* = \sigma_1^* - \alpha\sigma_3^*, \tag{12}$$

where $\alpha = (1 + \sin \varphi)/(1 - \sin \varphi)$.

The three effective principal stresses of rocks (σ_1^* , σ_2^* , and σ_3^*) correspond to their nominal stresses (σ_1 , σ_2 , and σ_3). The three principal strains are ε_1 , ε_2 , and ε_3 . Based on Eq. (7), we obtain the following equations:

$$\sigma_i^* = \sigma_i/(1 - D), \tag{13}$$

with $i = 1, 2, 3$.

Applying the generalized Hooke’s law and considering the damage, we also obtain the following:

$$1 - D = \frac{\sigma_1 - \mu(\sigma_2 + \sigma_3)}{E_n \varepsilon_1}. \tag{14}$$

Thus, we use Eqs. (12)–(14) to express the strength of a mesoscopic element as follows:

$$F^* = \frac{(\sigma_1 - \alpha\sigma_3)E_n \varepsilon_1}{\sigma_1 - \mu(\sigma_2 + \sigma_3)}. \tag{15}$$

Equation (15) is simplified to $F^* = E_n \varepsilon_1$ when the rock is in the uniaxial state ($\sigma_2 = \sigma_3 = 0$). In this case, the strength form of a mesoscopic element using the stresses is equivalent to that using the principal strains.

Subsequently, the statistical damage constitutive model for the rock during loading after n cycles of stress–temperature based on Weibull distribution can be easily obtained as follows when the expression for F^* is determined:

$$\begin{aligned} \sigma_1 &= E_n \varepsilon_1 (1 - D) + \mu(\sigma_3 + \sigma_2) \\ &= E_0(1 - D_n) \varepsilon_1 \exp\left[-\left(\frac{F^*}{F_0}\right)^m\right] + \mu(\sigma_3 + \sigma_2), \end{aligned} \tag{16}$$

$$\begin{aligned} \sigma_2 &= E_n \varepsilon_2 (1 - D) + \mu(\sigma_1 + \sigma_3) \\ &= E_0(1 - D_n) \varepsilon_2 \exp\left[-\left(\frac{F^*}{F_0}\right)^m\right] + \mu(\sigma_1 + \sigma_3), \end{aligned} \tag{17}$$

$$\begin{aligned} \sigma_3 &= E_n \varepsilon_3 (1 - D) + \mu(\sigma_1 + \sigma_2) \\ &= E_0(1 - D_n) \varepsilon_3 \exp\left[-\left(\frac{F^*}{F_0}\right)^m\right] + \mu(\sigma_1 + \sigma_2). \end{aligned} \tag{18}$$

For the state of uniaxial stress, the above constitutive model for rocks subjected to cyclic stress and cyclic temperature can be rewritten as follows:

$$\sigma = E_0(1 - D_m) \varepsilon = E_0(1 - D_n) \exp[-(F^*/F_0)^m] \varepsilon, \tag{19}$$

where

$$D_m = D_n + D - DD_n. \tag{20}$$

Equation (19) uses the initial damage state of the rock as a reference state. The Young’s modulus E_0 in the reference state can be easily achieved; thus, testing the Young’s modulus of the rock in the ideal undamaged dense state can be avoided. Meanwhile, D_m in Eq. (20) can be regarded as the total damage. Equation (20) shows that the previous cyclic stress and temperature to which the rock is subjected and the damage induced by reloading after stress–temperature cycling exaggerate the total damage, which consequently shows significant nonlinear characteristics. Temperature causes uneven load among the mineral grains and the microcracks of the rock. Meanwhile, loading induces the sliding and dislocation of the rock grains. The load-induced damage couples and interacts with the temperature-induced damage, thereby resulting in variations in rock properties.

Determination of model parameters and development of constitutive subroutine

Determination of model parameters

The model parameters m and F_0 of the rock during reloading after several cycles of stress and temperature effects are determined depending on two cases: (i) the damage softening of the rock is considered; (ii) the loaded

stress does not increase to the failure stress (yield stress), and then, the rock is unloaded. In Case (i), the strain continues to increase, but the stress level decreases after the loading stress achieves a peak value.

For Case (i), the stresses at the peak point (σ_{1pe} , σ_{2pe} and σ_{3pe}) and the strain ε_{1pe} can be used to determine m and F_0 . At the peak point, the partial derivative of σ_1 with respect to ε_1 should be equal to zero. Thus, we obtain the following equation from Eq. (16):

$$\begin{aligned} \frac{\partial \sigma_1}{\partial \varepsilon_1} &= E_0(1 - D_n)\varepsilon_1 \exp\left[-\left(\frac{F^*}{F_0}\right)^m\right] \\ &+ E_0(1 - D_n)\varepsilon_1 \exp\left[-\left(\frac{F^*}{F_0}\right)^m\right](-m)\left(\frac{F^*}{F_0}\right)^{m-1} \frac{1}{F_0} \frac{\partial F^*}{\partial \varepsilon_1} = 0. \end{aligned} \quad (21)$$

Rearranging Eq. (21) gives:

$$1 + (-m)\left(\frac{F^*}{F_0}\right)^{m-1} \frac{1}{F_0} \frac{\partial F^*}{\partial \varepsilon_1} = 0. \quad (22)$$

The following equation can be easily achieved by Eq. (15):

$$\varepsilon_1 \frac{\partial F^*}{\partial \varepsilon_1} = F^*. \quad (23)$$

Therefore, based on Eqs. (15) and (16), we obtain the following equation:

$$1 - m\left(\frac{F^*}{F_0}\right)^m = 0. \quad (24)$$

Substituting Eq. (24) into Eqs. (14) and (15), we obtain that

$$\begin{cases} m = \frac{1}{-\ln(1 - D_{pe})}, \\ F_0 = \sqrt[m]{m} F_{pe}^* \end{cases} \quad (25)$$

where $D_{pe} = 1 - \frac{\sigma_{1pe} - \mu(\sigma_{2pe} + \sigma_{3pe})}{E_0(1 - D_n)\varepsilon_{1pe}}$; $F_{pe}^* = \frac{(\sigma_{1pe} - \alpha\sigma_{3pe})E_0(1 - D_n)\varepsilon_{1pe}}{\sigma_{1pe} - \mu(\sigma_{2pe} + \sigma_{3pe})}$.

Hence, m and F_0 can be calculated using Eq. (25) when the values of σ_{1pe} , σ_{2pe} , σ_{3pe} , and ε_{1pe} are at the peak points, and when the E_0 , D_n , c , and φ of the rock are known.

For Case (ii), the stress is not loaded to the failure value after n cycles of stress–temperature effects, and it is subsequently unloaded. Thus, a combination of the least-squares method and iterative methods can be used to determine the m and F_0 that fit the testing curves best. In addition, corresponding stress–temperature tests can be conducted to obtain the damage D_n induced by cyclic stress and cyclic temperature in accordance with Eq. (5).

Development of constitutive subroutine

The constitutive subroutine needs to be established before implementing the proposed statistical damage constitutive

model into numerical software. This subroutine can be helpful in the following analysis. The subsequent subsection shows how the user-defined constitutive subroutine for the proposed model is established. The established subroutine is applied to obtain some results about the stresses or strains when all the parameters are given.

Commercial software (e.g., ABAQUS or FLAC^{3D}) usually provides interfaces for users to accomplish their defined material models. In these user-defined subroutines, strain increment $\Delta\varepsilon_{ij}$ is usually taken as an input term, and its corresponding export is usually stress σ_{ij} . The user-defined subroutine for the proposed constitutive model in this study is constructed by applying the same approach as that used in the interfaces. First, the proposed statistical model is rewritten as the following incremental equation of $K - G$ form in accordance with Hooke's law:

$$\Delta\sigma_{ij} = K_d\Delta\varepsilon_{kk}\delta_{ij} + 2G_d\Delta e_{ij}, \quad (26)$$

where δ_{ij} is the Kronecker sign; $\delta_{ij} = 1$ when $i = j$, and $\delta_{ij} = 0$, when $i \neq j$; σ_{ij} and e_{ij} are the stress tensor and deviatoric strain tensor, respectively; ε_{kk} represents volume strain; Δ denotes the incremental variable; K_d ; and G_d are the degraded bulk modulus and shear modulus calculated using the damaged Young's modulus E_d and Poisson's ratio μ , respectively. In this study, we have the following relationship:

$$E_d = E_0(1 - D_n) \exp\left[-\left(\frac{F^*}{F_0}\right)^m\right]. \quad (27)$$

Then, the flow for the user-defined subroutine is developed through the following procedures:

1. The evolution of damage D_n and all the parameters necessary for calculation are obtained through laboratory tests.
2. Strain components ε_{ij} for given strain increments $\Delta\varepsilon_{ij}$ are calculated.
3. The current volume strain $\varepsilon_{kk} = \varepsilon_x + \varepsilon_y + \varepsilon_z$ is calculated.
4. The stress components σ_{ij} that can be approximately replaced by the stress component obtained in the former one-load step are evaluated.
5. The strength of mesoscopic element F^* and damage factor D are evaluated using the strain components ε_{ij} and the evaluated stress components σ_{ij} .
6. Let $D = 0$ if $D < 0$ and let $D = 1.0$ if $D > 1.0$. The corresponding degraded moduli E_d , K_d , and G_d are calculated.
7. The stress increments $\Delta\sigma_{ij}$ are calculated, and then, the total stress σ_{ij} are achieved.

The developed user-defined subroutine for the proposed constitutive model is established similar to the flowchart of

the constant stiffness method. The subroutine can achieve satisfactory results when $\Delta\varepsilon_{ij}$ is set to be small enough. The developed subroutine is applied to some typical strain paths, and the corresponding results show good fit to the well-known general results. This finding indicates the feasibility and validity of the developed subroutine, which indirectly reflects that the proposed constitutive model can be applicable in actual engineering.

Influence of model parameters

This study realized the proposed statistical damage constitutive model by the user-defined subroutine and then investigated the influence of model parameters on the stress–strain curves during reloading after stress–temperature cycling. Equations (15)–(18) show that the principal parameters that influence the stress–strain relationship for rock reloading after stress–temperature cycling are E_0 , D_n , F_0 , m , c , and φ . Taking the stress–strain in the direction of the first principal strain as an example, we considered $E_0 = 120$ GPa, $D_n = 0.2$, $F_0 = 350$ MPa, $m = 2$, $c = 1$ MPa, $\varphi = 30^\circ$, and $\sigma_3 = 0$ MPa as the reference parameters. The influence of the model parameters on the stress–strain curves was analyzed by changing one of the corresponding parameters and leaving the other parameters unchanged.

Figure 2 shows the stress–strain curves of the rocks as a function of the different model parameters. The Young's modulus of the rock in the reference elastic affects the shapes of the stress–strain curves (Fig. 2a). However, the peak stresses of the rocks remain almost unchanged and only slightly decrease with the decrease in the Young's modulus in the reference state. In addition, the softening behaviors are significantly affected by the Young's modulus in the reference state after the peak points. Figure 2b shows the influence of the damage induced by stress–temperature cycling on the stress–strain curves when reloading. The peak stresses of the reloading curves slightly decrease with the increase in the damage induced by stress–temperature cycling when the induced damage is relatively large and the other model parameters are unchanged. The strains at the peak points increase with the increase in the induced damage. Larger damage causes relatively more moderate variations in both the pre-peak and post-peak periods.

Figure 2c, d shows the influence of the model parameters F_0 and m_0 on the reloading stress–strain curves. Three conclusions can be obtained from the figures. First, the peak stresses of the stress–strain curves increase with the increase in F_0 and m ; however, the changes in F_0 and m do not change the linear deformation periods of the curves

before the peak points. Second, F_0 and m significantly affect the nonlinear parts of the curves, particularly the post-peak parts. Thus, these parameters alter the shapes of the curves. Third, the peak strains increase with the increase in F_0 and m . In addition, the value of m can be used to reflect the brittleness or ductility of the rock. Larger m means lower brittleness and higher ductility.

Figure 2e illustrates the influence of confining pressures on the stress–strain curves. The figure shows that the initial stress increases with an increase in confining pressure. The peak stresses and strains increase with an increase in confining pressure. This result shows good agreement with the results obtained from regular triaxial compression tests. Moreover, this result shows that the proposed constitutive model can completely reflect the influence of confining pressure on the mechanical properties of rocks.

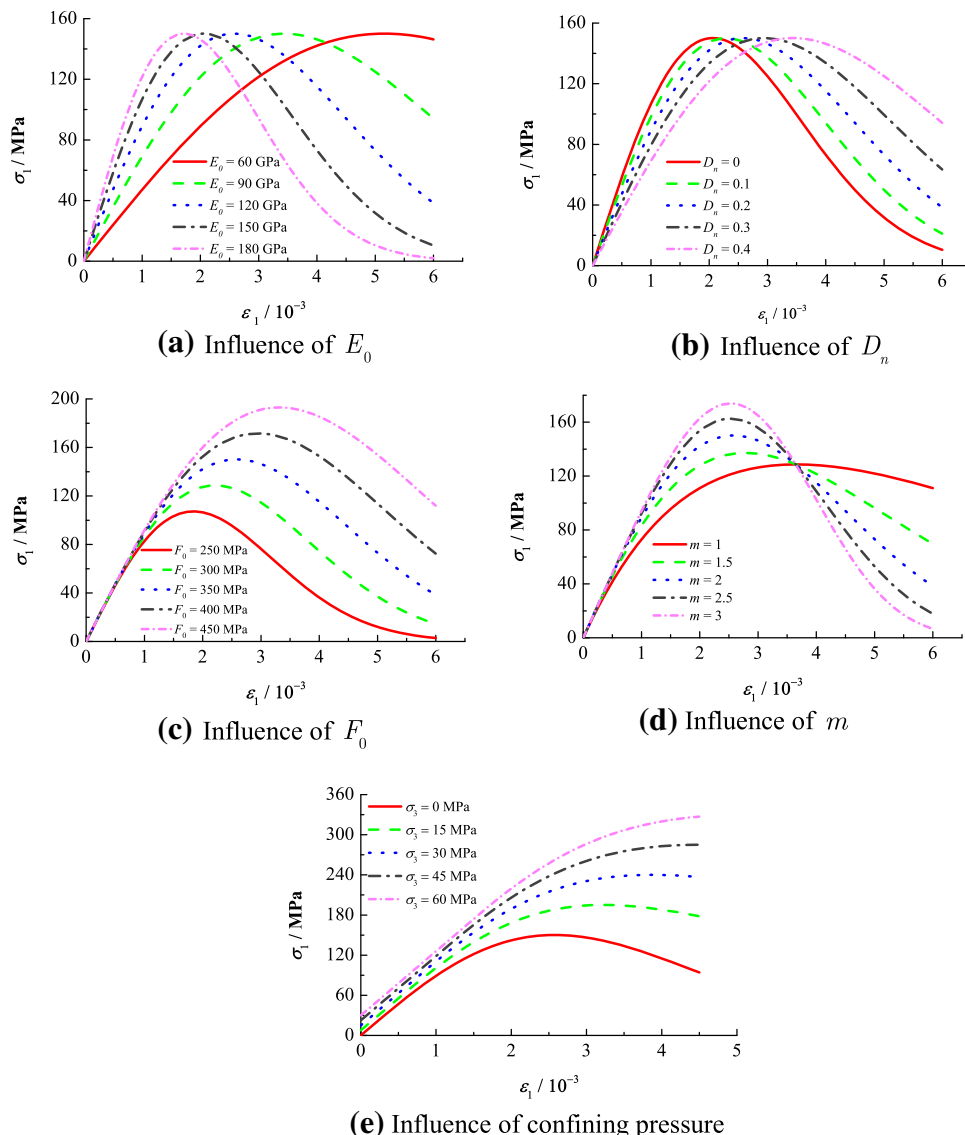
Validation of the proposed constitutive model

Cyclic uniaxial stress–temperature tests

Only a few researchers investigated the influence of cyclic temperature on the mechanical properties of rocks over the past years (Mahmutoglu 1998; Inada et al. 1997) and rock tests associated with the cyclic stress and temperature effects have rarely been reported in the literature. Thus, this study designed and conducted cyclic uniaxial stress–temperature tests to initially verify the proposed statistical damage constitutive model.

Rock preparation and test procedures were shown in Xia et al. (2015) and Zhou et al. (2015b). All the rock specimens were gray weathering basalt collected from Hanwula Wind Farm in Inner Mongolia, China. These specimens were made into cylinders of 25 mm in radius and 100 mm in height according to the Chinese Rock Mechanics Testing Standards (GB/T 50266–2013). In addition, the rock specimens all had end flatness within ± 0.05 mm. For a rock specimen, a complete stress–temperature cycle included one loading–unloading process and one heating–cooling process. The temperature of rock specimens fluctuated between the room temperature and 60 °C (90 °C, in some cases) and the stress threshold exerted on the samples were 45 and 55 MPa. In one cycle, the specimens were loaded to the prescribed stress threshold by an electronic universal testing machine and then unloaded to zero. The specimens were subsequently placed in an electronic blast heating furnace and heated to the prescribed temperature. After being kept at the prescribed temperature for 1 h, the specimens were taken out of the furnace to be cooled to room temperature. The uniaxial stress loading–unloading and heating–cooling processes were repeated to subject the specimens to the effects of cyclic stress and cyclic

Fig. 2 Influence of model parameters on the stress–strain curves



temperature. Both damage and hardening effects were observed in the test. Hence, all the rock specimens for test were named damaged and hardened ones. The readers can refer to Zhou et al. (2015b) for details about the test results. Zhou et al. (2015b) have shown the stress–strain curves of some typical damaged and hardened specimen. For a damaged specimen, obvious compaction stages are observed in a few of the initial cycles. However, the compaction stages become obscure as the cycle number is increased. The stress–strain curve moves toward the right as the cycle proceeds, which reflects specimen damage. The peak strain increases and the Young’s modulus decreases as the cycle increases.

For a hardened rock specimen, no obvious compaction stage is observed, and the stress–strain curves move toward the left as the cycle number increases. The peak strain decreases, and the Young’s modulus increases. The

specimen exhibits obvious hardening characteristics as the cycle number increases; this hardening characteristic is also called “negative damage” in this paper, because the calculated damage factors are negative.

Validation of the model by cyclic uniaxial stress–temperature tests

Evolution of D_n

The damage factor in the stress–temperature cycles is calculated using Eq. (5). The corresponding results show that the damage factor D_n for the damaged specimens satisfies the following equation (Zhou et al. 2015b):

$$D_n = \frac{D_n(\bar{\sigma}_{\max}^b - \bar{\sigma}_{\min}^b)n^{1-c}}{M[1 - (1 - D_n)^{1+b}]} + a_0\Delta T^* e^{-b_0/n}, \tag{28}$$

where σ_c is the uniaxial compressive strength of rock, $\bar{\sigma}_{\max} = \sigma_{\max}/\sigma_c$, and $\bar{\sigma}_{\min} = \sigma_{\min}/\sigma_c$. σ_{\max} and σ_{\min} are the maximum and minimum stresses of one cycle, respectively. ΔT^* is the relative temperature variation, which is calculated by the difference between the maximum and minimum temperatures in one cycle divided by the maximum temperature. The unit for the temperature is K. a_0 , b_0 , b , c , and M are parameters.

The hardened rock specimens suffer from “negative damage.” The “negative damage” here is adopted to show an increase in the Young’s modulus as a result of stress–temperature cycling. However, the damage factor calculated by Eq. (5) decreases with the increase in cycle number. Thus, Eq. (28) is unsuitable. The data analysis indicates that the damage factors of the hardened specimens satisfy the following equation (Zhou et al. 2015b):

$$D_n = a_0 \Delta T^* e^{-b_0/n} - c_0 (\delta \bar{\sigma}) e^{-d_0/n}, \quad (29)$$

where $\delta \bar{\sigma} = (\sigma_{\max} - \sigma_{\min})/\sigma_c$, and c_0 and d_0 are parameters.

The relationship between the damage of a hardened rock specimen and number of cycles can be observed in Eq. (29), the model parameters of which can be easily obtained by applying the least-squares method for explicit equations. However, the damage evolution model for a damage rock specimen is Eq. (28), which is an implicit equation. The model parameters for implicit equations are difficult to obtain by direct data fitting. A combination of the nonlinear least-squares method and a regular iterative method was used to obtain the parameters b , c , M , a_0 , and b_0 . The damage factor for the rock specimen was initially calculated using the Young’s modulus of the first cycle. n is the subsequent cycle number after the first cycle. Zhou et al. (2015b) have shown that Eqs. (28) and (29) match well the test results. Thus, Eqs. (28) and (29) are applied in the proposed constitutive model.

Damaged rock specimens

For the damaged rock specimens, the corresponding constitutive model is Eq. (19), and the damage evolution equation is Eq. (28). The parameters m and F_0 that fit the proposed constitutive model were obtained using the nonlinear curve fitting method. The fitting results show that m increases in the first few cycles and then decreases with the increase in cycle number. This result indicates that the brittleness of the rock in the first few stress–temperature cycles initially decreases and then increases. The reason for this situation is that the mesoscopic elements with low strength fail in the cycles and that the strength distribution of the mesoscopic elements becomes concentrated. In addition, F_0 initially increases in the first few cycles and

then decreases with the increase in cycle number. This result indicates that the total rock strength increases with the increase in cycle number in the first few cycles. However, it decreases as the cycle number increases. An analysis of the fitting results of the parameters shows that the relationship of m or F_0 with n satisfies the following equations:

$$m = An^2 + Bn + C, \quad (30)$$

$$F_0 = Fn^2 + Gn + H, \quad (31)$$

where A , B , C , F , G , and H are the parameters.

Figure 3 compares the stress–strain curves of the damaged specimens obtained by the proposed constitutive model and the test results. The figure indicates that the results given by the proposed model provide good a fit to the test results. Thus, the proposed constitutive model achieves the stress–strain characteristics or tendencies of the damaged rocks after they are subjected to cyclic stress and cyclic temperature. Moreover, Eqs. (30) and (31) reflect well the variations in Weibull parameters. Thus, the proposed constitutive model is applicable for the damaged rock specimens.

Hardened rock specimens

For the hardened rock specimens, the corresponding constitutive model is Eq. (19), and the damage evolution equation is Eq. (29). The parameters m and F_0 that fit the proposed constitutive model were also obtained using a nonlinear curve fitting method. The fitting results show that m decreases with the increase in cycle number and then stabilizes. This result indicates that the rock becomes brittle when exposed to the “hardening” effects of cyclic stress and cyclic temperature. The mesoscopic elements with low strength also fail in the cycles, and the distribution for the strength of the mesoscopic elements becomes concentrated. However, F_0 increases to a stable value with the increase in cycle number. This result indicates that the total rock strength increases with the increase in cycle number. However, the strength cannot be infinitely large. Thus, it has a limited upper bound. On the basis of the fitting results of the parameters, the relationship of m or F_0 with n satisfies the following equations:

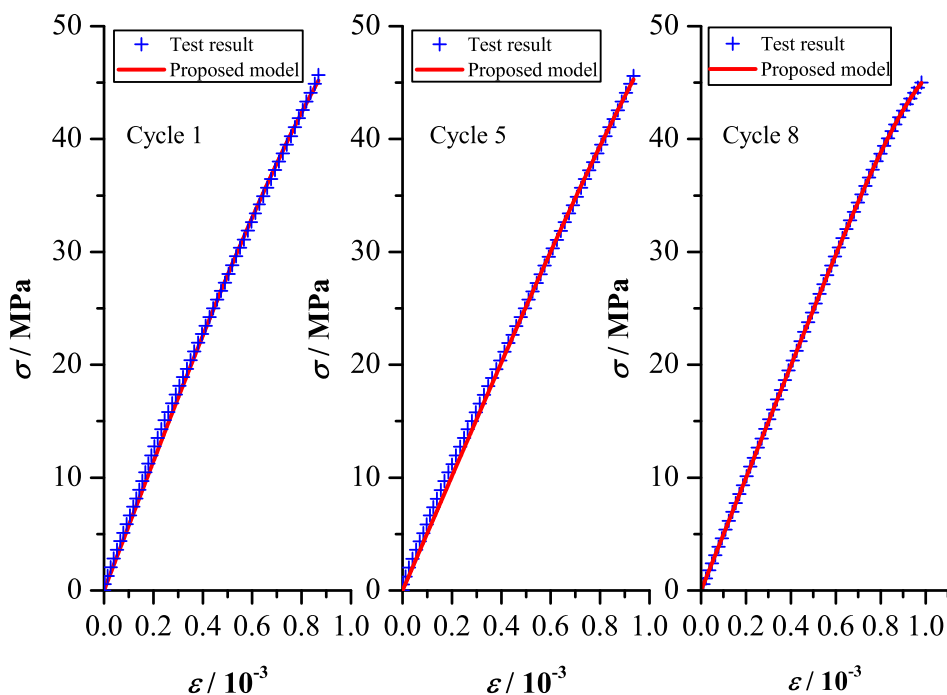
$$m = A_1 + B_1 \exp(-n/C_1), \quad (32)$$

$$F_0 = F_1 + G_1 \exp(-n/H_1), \quad (33)$$

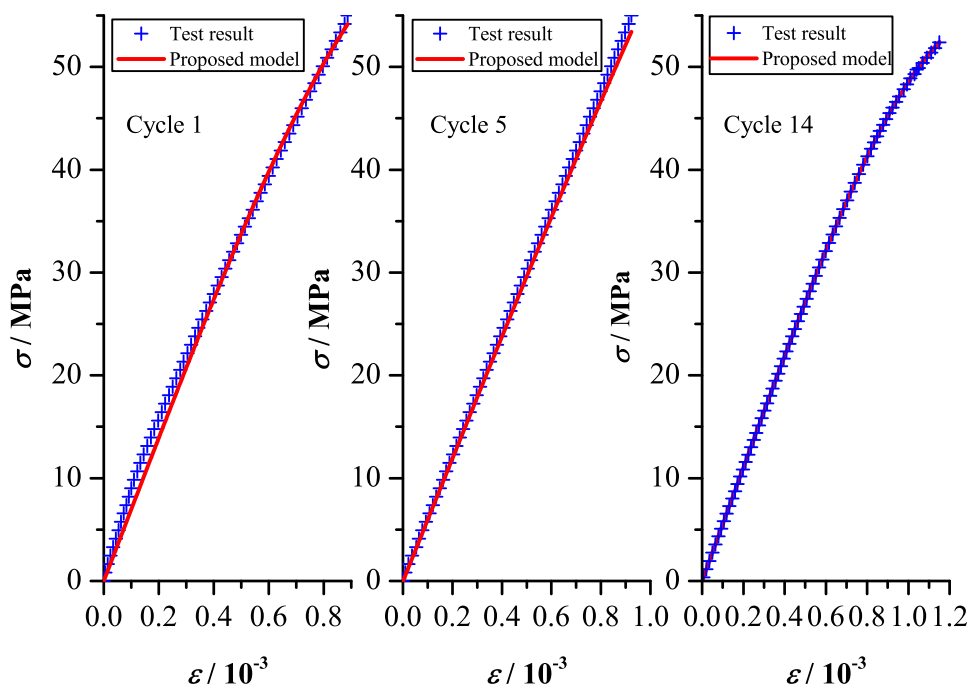
where A_1 , B_1 , C_1 , F_1 , G_1 , and H_1 are the parameters.

Figure 4 compares the stress–strain curves of the hardened specimens obtained by the proposed constitutive model and the test results. The figure indicates that the results given by the proposed model provide a good fit to the test results. Thus, the proposed constitutive model can

Fig. 3 Comparison of the fitting values and measured stress–strain curves for damaged rock specimens



(a) Sample T1S1-1: $A = 0.0928$, $B = -0.2013$, $C = 2.3571$,
 $F = -2.5437$ MPa, $G = 9.6845$ MPa, $H = 133.60$ MPa



(b) Sample T2S2-1: $A = 0.0082$, $B = -0.0734$, $C = 2.4620$,
 $F = -3.2906$ MPa, $G = 40.560$ MPa, $H = 140.25$ MPa

achieve the reloading stress–strain characteristics or tendencies of the hardened rocks after exposure to cyclic stress and cyclic temperature. Moreover, Eqs. (32) and (33)

can reflect the variations in Weibull parameters. Thus, the proposed constitutive model is applicable to the hardened rock specimens.

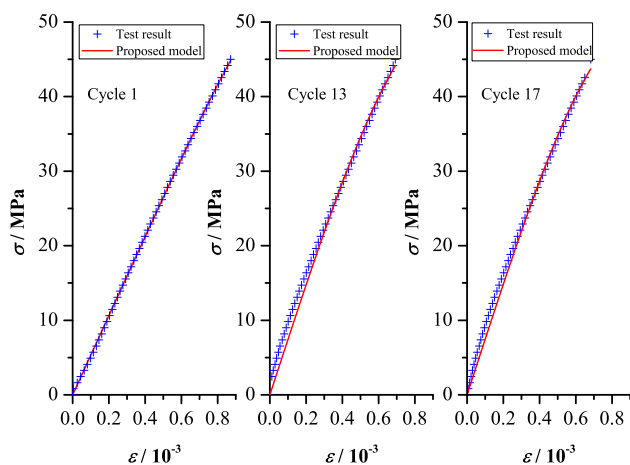


Fig. 4 Comparison of the fitting values and measured stress–strain curves for hardened rock specimens T2S1-1: $A_1 = 2.448$, $B_1 = 1.870$, $C_1 = 0.311$, $F_1 = 110.6$ MPa, $G_1 = -7.989$ MPa, and $H_1 = 3.042$

In summary, the stress–strain curves consistent with the actual rock test results can be obtained by the proposed constitutive model when the rocks are reloading after exposure to several stress–temperature cycles. This finding preliminarily verifies the accuracy and feasibility of the proposed model. The proposed constitutive model can provide a reference for studies on the stability of underground CAES and engineering in cold regions. The proposed model can also aid in further understanding the effects of cyclic stress and temperature on the mechanical properties of rocks.

Validation by test results for only cyclic stress

The proposed constitutive model for rocks subjected to cyclic stress and cyclic temperature can be degenerated into the model for only cyclic stress without consideration of temperature. Thus, the proposed constitutive model can also be validated by the rock tests for cyclic stress (cyclic loading).

Wang et al. (2015) proposed the equation for long-term Young’s modulus E_n for cyclic stress, described as follows:

$$E_n = M(\bar{\sigma}^{cr})^q \varepsilon_{1r}^l, \tag{34}$$

with $\bar{\sigma}^{cr} = (q_p - p_p \tan \beta)/(1 - \tan \beta/3)$, $p_p = (\sigma_{1p} + 2\sigma_3)/3$, and $q_p = \sigma_{1p} - \sigma_3$. M , n , q and l are all model parameters. ε_{1r} is the residual axial strain and σ_{1p} is the peak axial stress. $\bar{\sigma}^{cr}$ is an effective stress and β is the inclination angle of effective stress line that is related to internal friction angle of rock.

From Eq. (34), the following expression is deduced:

$$D_n = [E_0 - M(\bar{\sigma}^{cr})^q \varepsilon_{1r}^l]/E_0. \tag{35}$$

Applying Eq. (35) to Eq. (19), the constitutive model for only cyclic stress is obtained. The model now has five parameters, i.e., m , F_0 , M , q , and l . These parameters can also be obtained from the rock tests using the least-square method. We take the rock tests conducted by Zhang (2011) as an example to validate the proposed model, Eq. (19). After data fitting, the test results of Zhang (2011) show that m and F_0 satisfy the following equations:

$$\begin{cases} m = B_2 \ln(n) + C_2 \\ F_0 = D_2 \ln(n) + E_2 \end{cases}, \tag{36}$$

where B_2 , C_2 , D_2 , and E_2 are fitting parameters and n is the cycle number.

By substituting Eqs. (35) and (36) into (19), we finally have the equation for rocks subjected to only cyclic stress as follows:

$$\begin{aligned} \sigma_1 = & M(\bar{\sigma}^{cr})^q \varepsilon_{1r}^l \exp \left[- \left(\frac{F^*}{D_2 \ln(n) + E_2} \right)^{B_2 \ln(N) + C_2} \right] \\ & + 2\mu\sigma_3. \end{aligned} \tag{37}$$

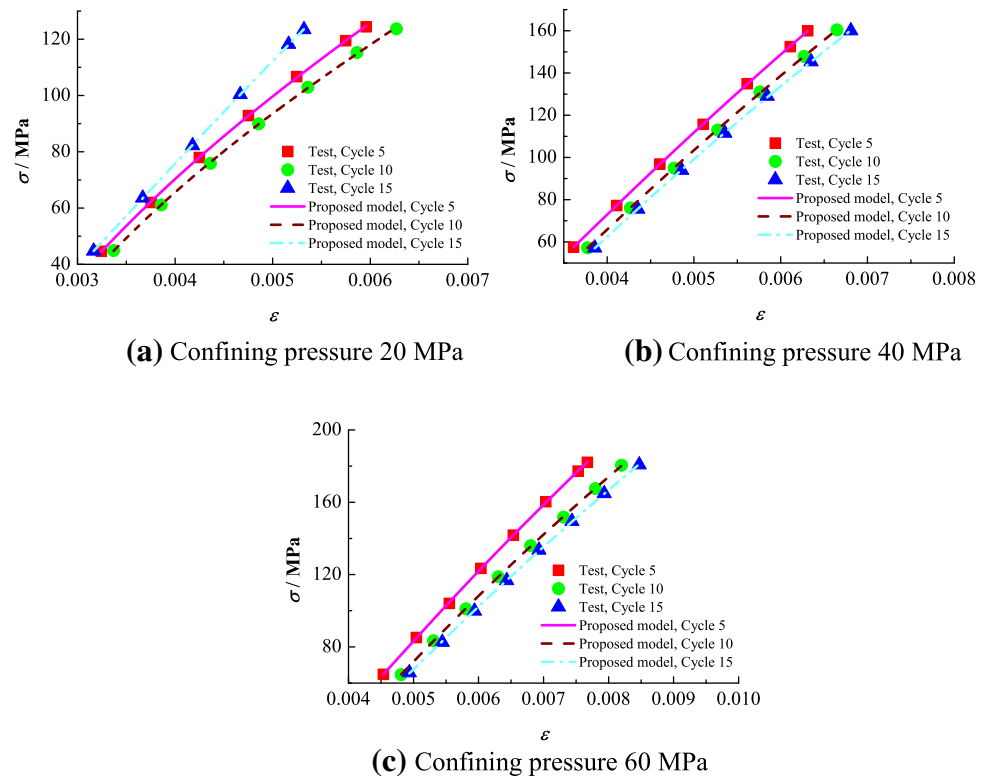
Zhang (2011) conducted triaxial compression tests of sandstone under cyclic loading. The triaxial compressive strength of sandstone was first measured. Then, 20 and 70% of the strength were taken as the lower and upper limits of the tests. Zhang (2011) also presented some fitting curves matching well the test results, from which the maximum axial strain, axial residual strain, initial modulus, and unloading modulus could be easily obtained. Applying Eq. (34) to fit the test results by Zhang (2011), the best fitting parameters are listed in Table 1.

The constitutive model for rocks subjected to cyclic stress focuses on description of the relationship of stress and strain in each cycle. Thus, comparisons of the fitting results and the proposed model for Cycle 5, Cycle 10, and Cycle 15 with the confining pressure of 20, 40, and 60 MPa were presented in Fig. 5. It can be easily seen that the proposed model matches well the test results. The fitting curves are basically consistent with the original test data, indicating that the proposed constitutive model can reproduce suitable stress–strain curves compared to actual rock test results under different confining pressures and cycle

Table 1 Fitting parameters from tests

Confining pressure (MPa)	M	q	l
20	0.991	0.815	-1.264
40	1.101	0.466	-1.468
60	0.983	0.878	-1.325

Fig. 5 Comparisons of test results and proposed model for only cyclic stress



numbers. The success in applying the proposed model to rock tests for cyclic stress implies indirectly that the proposed model is feasible.

Further discussion on the total damage induced by stress–temperature cycling and reloading after cycling

The total damage induced by stress–temperature cycling and reloading after cycling was further discussed in accordance with the uniaxial stress–temperature tests in “Validation of the proposed constitutive model” and the theoretical study on damage in “Constitutive model for rocks subjected to cyclic stress and cyclic temperature”. Considering that the damage characteristics of the damaged rock specimens became obvious in the stress–temperature cycles, we used samples T1S1-1 and T2S2-1 as examples to analyze the total damage evolution.

Figure 6 gives the theoretical curves for the total damage evolution when the specimens are reloading after suffering from stress–temperature cycles. These curves were calculated by Eqs. (20) and (28)–(30), and the parameters were obtained from the stress–temperature tests. The damage and weakening effects induced by cyclic stress and cyclic temperature on the damaged specimens increase with cycle number (Fig. 6). The variation in rock damage differs depending on the effects of cyclic stress and cyclic

temperature. The initial damages in the curves for the evolution of the total damage D_m gradually increase after stress–temperature cycling with respect to the absence of cyclic stress–temperature effects. Meanwhile, the incremental amplitude gradually decreases. The initial damage of the two damaged specimens in Fig. 6 is not more than 0.3, which indicates that the total damage of these two specimens is principally caused by the reloading after stress–temperature cycling. The total damage D_m of the damaged specimens increases with the increase in the strain after cycling at a constant number. The evolution for the total damage D_m exhibits three stages: the initial slow increase, mid-term accelerated increase, and the final slow increase stages. The evolution of D_m is consistent with loading of the rock. The initial stage during reloading of the rock after stress–temperature cycling is a damage-weakening stage. In this stage, the micropores and microcracks become gradually closed. The density and strength both increase. The rock is subsequently under the linear stage. The damage evolution of the rock starts and then stably extends with the continued deformation of the rock. The damage factor is subsequently increased and tends to be 1. This result is always accompanied by initiation, expansion, and convergence of the microcracks. Macrocracks also occur. Finally, the stress of the rock achieves a peak value, and the rock starts to fail.

Figure 6 shows that the steepness of the curve for total damage is reduced with the increase in cycle number in the

Fig. 6 Evolution curves for total damage factor D_m of damaged rock specimens

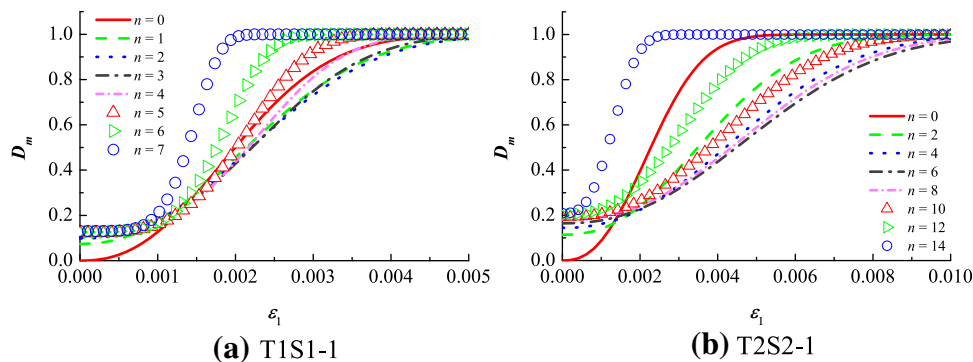
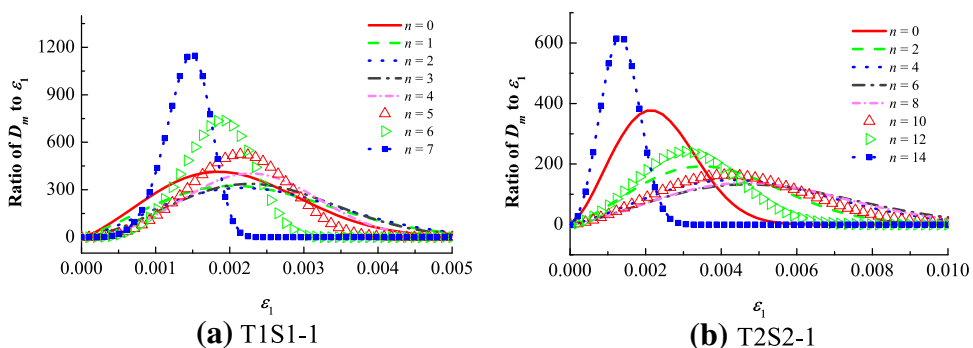


Fig. 7 Evolution curves for total damage ratios of damaged rock specimens



first few cycles. The strain span during the mid-term accelerated increase and final slow increase stages becomes larger as the number of cycles increases. However, the steepness of the total damage increases as the cycle number continues to increase. In addition, the strain range in the mid-term accelerated increase stage increases and then sharply decreases during the final slow increase stage. This result indicates that rock failure occurs when the rock is reloaded to a relatively small strain. In addition, the strains of the two damaged specimens in Fig. 6 are located in the interval of (0, 0.0015) during the tests (Zhou et al. 2015b). Thus, $D_m < 1$ and the rock specimens will not fail in the stress–temperature cycles, as shown in Zhou et al. 2015b.

Based on Eqs. (15) and (20), we obtain the following equation:

$$\frac{\partial D_m}{\partial \varepsilon_1} = \exp \left[- \left(\frac{F^*}{F_0} \right)^m \right] \left(\frac{F^*}{F_0} \right)^m \frac{m}{\varepsilon_1}. \tag{38}$$

If the cycle number of stress and temperature is fixed, then Eq. (38) can be regarded as the evolution rate of the total damage, which denotes the increasing rate of the total damage. Figure 7 shows the evolution curves for the total damage rate, which is calculated by Eqs. (28)–(30) and (38) using the measured data provided by the cyclic uniaxial stress–temperature tests. Figure 7 shows that the number of stress–temperature cycles exerts negligible effects on the evolution tendency of the total damage rate and affects only the value of the total damage rate. The

span of strain during which the damage rate is more than 0 increases in the first few cycles and then decreases as the number of stress–temperature cycles increases. However, the peak value of the total damage rate decreases in the first few cycles and then increases. The total damage rate increases as the rock strain increases when the number of stress–temperature cycles is fixed. By contrast, the total damage rate gradually decreases after reaching a peak value, which shows good agreement with the curves in Fig. 6. In addition, a large slope can be observed in the declining period of the total damage rate curve when the cycle number increases, which indicates increased rock brittleness.

Conclusion

This paper proposed a statistical damage constitutive model for rocks subjected to both cyclic stress and cyclic temperature in accordance with statistical damage theory. The proposed model can be regarded as an extension of the damage constitutive model of rock based on Weibull distribution. This paper also presented approaches to determine the model parameters and to develop a user-defined subroutine for the proposed constitutive model. The proposed model was accomplished to analyze the influence of model parameters on the stress–strain curves after stress–temperature cycling. Cyclic uniaxial stress and temperature

tests were conducted to initially validate the proposed constitutive model, which was also validated by rock tests for only cyclic stress. Finally, the evolution of the total damage induced by stress–temperature cycling and reloading after cycling was further discussed.

The proposed constitutive model has the following characteristics. (1) The cyclic effects of stress and temperature as well as the mechanical damage effect after stress–temperature cycling are considered. The coupled nonlinear characteristics of the damage induced by both cyclic stress and cyclic temperature are reflected in the proposed model. The correlation of the thermodynamic and mechanical performances is also reflected in the model. (2) The nonuniformity of the mesoscopic structures of rocks is completely considered. The damage evolution equation and damage propagation constitutive model are established considering the fact that the strength of the mesoscopic elements of rocks has a random distribution. The proposed constitutive model depicts the effects of the damage evolution on the macrobehavior of a material. (3) The constitutive model is not based on laboratory tests and thus has good applicability. Only rock parameters are required when applying the model, and these parameters can be easily obtained through laboratory tests.

The proposed constitutive model can describe the stress–strain relationship of rocks during each stress and temperature cycle. The proposed model provides a good fit to the test results, and a user-defined subroutine can also be developed to accomplish this model. These indicate that the proposed constitutive model is reasonable and applicable. For the proposed constitutive model and the damage induced by cyclic stress and cyclic stress, the following conclusions are obtained:

- Both the elastic modulus of the rock in the reference state and the damage induced by stress–temperature cycling affect the shape of the reloading stress–strain curve. However, the peak stress of the reloading curve is almost unchanged. It slightly decreases with the decrease in the initial elastic modulus and with the increase in the damage caused by stress–temperature cycling.
- The peak stress of the reloading curve increases with the increase in F_0 and m . These parameters obviously influence the nonlinear part of the stress–strain curve, particularly the post-peak curve. In addition, they change the shape of the stress–strain curve. m can be used to reflect the brittleness of the rock; larger m means less brittleness and higher ductility.
- The proposed constitutive model can reflect the influence of confining pressure on the stress–strain curves.
- The total damage D_m induced by stress–temperature cycling and by reloading after cycling exhibits three stages: the initial slow increase, mid-term accelerated increase, and the final slow increase stages. The total damage rate increases in the first few cycles and then decreases as the number of stress–temperature cycles increases.

The proposed constitutive model describes rock deformation under cyclic stress and cyclic temperature. However, the practical problems are complicated. Thus, the applicability and feasibility of the proposed model for different, complicated application environments or different rock types may need to be further explored. But for now, the test results in this study and the proposed constitutive model can provide a reference for studies on the mechanical properties of rocks exposed to cyclic stress and cyclic temperature, as well as for engineering studies on underground rock caverns for CAES.

Acknowledgements The financial supports provided by the Research Project of Power China Zhongnan Engineering Corporation Limited (No. GWKJ2012261), the National Natural Science Foundation of China (No. 51278378), and the Sino-German (CSC-DAAD) Postdoc Scholarship Program 2016 are gratefully acknowledged.

References

- Allen RD, Doherty TJ, Fossum AF (1982) Geotechnical issues and guidelines for storage of compressed air in excavated hard rock caverns. Pacific Northwest Laboratory, Springfield
- Cao WG, Li X, Zhao H (2007) Damage constitutive model for strain-softening rock based on normal distribution and its parameter determination. *J Cent South Univ Technol* 14:719–724. doi:10.1007/s11771-007-0137-6
- Deng J, Gu D (2011) On a statistical damage constitutive model for rock materials. *Comput Geosci* 37:122–128. doi:10.1016/j.cageo.2010.05.018
- Gunzburger Y, Merrien-Soukatchoffa V, Guglielmi Y (2005) Influence of daily surface temperature fluctuations on rock slope stability: case study of the Rochers de Valabres slope (France). *Int J Rock Mech Min Sci* 42:331–349. doi:10.1016/j.ijrmms.2004.11.003
- Inada Y, Kinoshita N, Ebisawa A, Gomi S (1997) Strength and deformation characteristics of rocks after undergoing thermal hysteresis of high and low temperatures. *Int J Rock Mech Min Sci* 34:3–4. doi:10.1016/S1365-1609(97)00048-8
- Kim HM, Rutqvist J, Ryu DW, Sunwoo C, Song WK (2012) Exploring the concept of compressed air energy storage (CAES) in lined rock caverns at shallow depth: a modeling study of air tightness and energy balance. *Appl Energ* 92:653–667. doi:10.1016/j.apenergy.2011.07.013
- Lemaitre J (1984) How to use damage mechanics. *Nucl Eng Des* 80:233–245. doi:10.1016/0029-5493(84)90169-9
- Li N, Chen W, Zhang P, Swoboda G (2001) The mechanical properties and a fatigue-damage model for jointed rock masses subjected to dynamic cyclical loading. *Int J Rock Mech Min Sci* 38:1071–1079. doi:10.1016/S1365-1609(01)00058-2

- Li X, Cao WG, Su YH (2012) A statistical damage constitutive model for softening behavior of rocks. *Eng Geol* 143–144:1–17. doi:[10.1016/j.enggeo.2012.05.005](https://doi.org/10.1016/j.enggeo.2012.05.005)
- Mahmutoglu Y (1998) Mechanical behavior of cyclically heated fine grained rock. *Rock Mech Rock Eng* 31:169–179. doi:[10.1007/s006030050017](https://doi.org/10.1007/s006030050017)
- Mo HH (1988) Investigation of cyclic loading tests and constitutive relation of rock. *Chin J Rock Mech Eng* 7:215–224 (in Chinese)
- Qiu SL, Feng XT, Xiao JQ, Zhang CQ (2014) An experimental study on the pre-peak unloading damage evolution of marble. *Rock Mech Rock Eng* 47:401–419. doi:[10.1007/s00603-013-0394-7](https://doi.org/10.1007/s00603-013-0394-7)
- Saeb S, Amadei B (1992) Modelling rock joints under shear and normal loading. *Int J Rock Mech Min Geomech Abstr* 29:267–278. doi:[10.1016/0148-9062\(92\)93660-C](https://doi.org/10.1016/0148-9062(92)93660-C)
- Song HP, Zhang H, Kang YL, Huang GY, Fu DH, Qu CY (2013) Damage evolution study of sandstone by cyclic uniaxial test and digital image correlation. *Tectonophysics* 608:1343–1348. doi:[10.1016/j.tecto.2013.06.007](https://doi.org/10.1016/j.tecto.2013.06.007)
- Souley M, Homand F, Amadei B (1995) An extension to the Saeb and Amadei constitutive model for rock joints to include cyclic loading paths. *Int J Rock Mech Min Sci Geomech Abstr* 32:101–109. doi:[10.1016/0148-9062\(94\)00039-6](https://doi.org/10.1016/0148-9062(94)00039-6)
- Wang ZL, Li YC, Wang JG (2007) A damage-softening statistical constitutive model considering rock residual strength. *Comput Geosci* 33:1–9. doi:[10.1016/j.cageo.2006.02.011](https://doi.org/10.1016/j.cageo.2006.02.011)
- Wang ZC, Li SC, Qiao LP, Zhao JG (2013) Fatigue behavior of granite subjected to cyclic loading under triaxial compression condition. *Rock Mech Rock Eng* 46:1603–1615. doi:[10.1007/s00603-013-0387-6](https://doi.org/10.1007/s00603-013-0387-6)
- Wang ZC, Li SC, Qiao LP, Zhang QS (2015) Finite element analysis of the hydro-mechanical behavior of an underground crude oil storage facility in granite subject to cyclic loading during operation. *Int J Rock Mech Min Sci* 73:70–81. doi:[10.1016/j.ijrmms.2014.09.018](https://doi.org/10.1016/j.ijrmms.2014.09.018)
- White JA (2014) Anisotropic damage of rock joints during cyclic loading: constitutive framework and numerical integration. *Int J Numer Anal Methods Geomech* 38:1036–1057. doi:[10.1002/nag.2247](https://doi.org/10.1002/nag.2247)
- Xia CC, Zhou SW, Zhang PY, Hu YS, Zhou Y (2015) Strength criterion for rocks subjected to cyclic stress and temperature variations. *J Geophys Eng* 47:753. doi:[10.1088/1742-2132/12/5/753](https://doi.org/10.1088/1742-2132/12/5/753)
- Xiao JQ, Ding DX, Xu G, Jiang FL (2009) Inverted S-shaped model for nonlinear fatigue damage of rock. *Int J Rock Mech Min Sci* 46:643–648. doi:[10.1016/j.ijrmms.2008.11.002](https://doi.org/10.1016/j.ijrmms.2008.11.002)
- Xiao JQ, Ding DX, Jiang FL, Xu G (2010) Fatigue damage variable and evolution of rock subjected to cyclic loading. *Int J Rock Mech Min Sci* 47:461–468. doi:[10.1016/j.ijrmms.2009.11.003](https://doi.org/10.1016/j.ijrmms.2009.11.003)
- Xiao JQ, Feng XT, Ding DX, Jiang FL (2011) Investigation and modeling on fatigue damage evolution of rock as a function of logarithmic cycle. *Int J Numer Anal Methods Geomech* 35:1127–1140. doi:[10.1002/nag.946](https://doi.org/10.1002/nag.946)
- Xu XH, Ma SP, Xia MF, Ke FJ, Bai YL (2004) Damage evaluation and damage localization of rock. *Theor Appl Fract Mech* 42:131–138. doi:[10.1016/j.tafmec.2004.08.002](https://doi.org/10.1016/j.tafmec.2004.08.002)
- Zhang Y (2011) Experimental research on characteristic of deformation and dissipated energy of rock under cyclic loading conditions. Chongqing University, Chongqing (in Chinese)
- Zhang QS, Yang GS, Ren JX (2003) New study of damage variable and constitutive model of rock. *Chin J Rock Mech Eng* 22:30–34 (in Chinese)
- Zhou JW, Xu WY, Yang XG (2010) A microcrack damage model for brittle rocks under uniaxial compression. *Mech Res Commun* 37:399–405. doi:[10.1016/j.mechrescom.2010.05.001](https://doi.org/10.1016/j.mechrescom.2010.05.001)
- Zhou SW, Xia CC, Du SG, Zhang PY, Zhou Y (2015a) An analytical solution for mechanical responses induced by temperature and air pressure in a lined rock cavern for underground compressed air energy storage. *Rock Mech Rock Eng* 48:749–770. doi:[10.1007/s00603-014-0570-4](https://doi.org/10.1007/s00603-014-0570-4)
- Zhou SW, Xia CC, Hu YS, Zhou Y, Zhang PY (2015b) Damage modeling of basaltic rock subjected to cyclic temperature and uniaxial stress. *Int J Rock Mech Min* 77:163–173. doi:[10.1016/j.ijrmms.2015.03.038](https://doi.org/10.1016/j.ijrmms.2015.03.038)
- Zimmels Y, Kirzhner F, Krasovitski B (2002) Design criteria for compressed air storage in hard rock. *Energ Environ* 13:851–872

A study and application of high-resolution methods for reef reservoir identification

Lili Yan¹ · Bingjie Cheng^{2,3} · Tianji Xu⁴ · Shuijian Wei⁵ · Zhongping Qian⁶

Received: 1 March 2017 / Accepted: 12 August 2017 / Published online: 11 September 2017
© Institute of Geophysics, Polish Academy of Sciences & Polish Academy of Sciences 2017

Abstract Reefs represent a special type of carbonate trap that plays a key role in the migration, accumulation, and formation of a reservoir. They have commonly been the targets of exploration and development. However, reefs have complex interior structures and easily grow as thin, interbedded geological frames with reef microfacies that include the cap, core, and base of the reef. Because of the inherent drawbacks of seismic signals, including their low frequencies and narrow bandwidths, it is difficult to accurately identify reef reservoirs. Fortunately, the seismic frequency, phase, energy, waveform and other dynamic and geometrical properties can be used to compensate for the energy, expand the frequency bandwidth, and decompose and reconstruct the wavelet to obtain high-resolution seismic data. These data can highlight certain seismic responses of reefs, including boundary reflections, dome-shaped reflections from the reef outline, strong reflections

from the reef cap, reflections from the reef bottom, and onlap reflections from the reef flanks. Some impedance response regularities, such as the lower impedance of the reef cap relative to the reef core and biotritus beach and the fluctuating impedance of the reef-flat complex, are observed by combining log data with geological and high-resolution seismic data for a reef reservoir inversion. These methods were applied to the Changxing Formation in the Yuanba Gas Field. Good prediction results were obtained with a high consistency between the log and seismic data in a comparative analysis with the original seismic data and well logs.

Keywords Organic reef · Seismic signal · Decomposition · Reconstruction · High resolution · Reservoir prediction

Introduction

Carbonate oil and gas reservoirs are widespread throughout China, with abundant resources and a great potential for prospecting and exploitation (Cai 2011). Reef and shoal facies reservoirs play crucial roles in the development of carbonate oil and gas reservoirs, of which reef flat facies reservoirs are a special type. For example, in the marine facies carbonate gas reservoirs of Northeast Sichuan, reef and reef flat facies reservoirs are the controlling factors of the spatial distribution, reserves, and capacity of natural gas (Ma et al. 2007; Bi et al. 2007). Such reservoirs are mainly composed of dissolved-pore dolomite, bioclastic dolomite, and reef dolomite, which are easy to develop into multiple types of pore-type, fracture pore-type, and fracture-type oil and gas reservoirs. In addition to difficulties in the prediction of reservoir characteristics, questions regarding whether there is a reservoir, whether it is thick or thin, and whether it

✉ Bingjie Cheng
chengbingjie09@cdut.cn

¹ College of Earth Science, State Key Laboratory of Oil and Gas Reservoir Geology and Exploitation, Chengdu University of Technology, Chengdu, China

² State Key Laboratory of Oil and Gas Reservoir Geology and Exploitation, Chengdu University of Technology, Chengdu, China

³ College of Geophysics, Chengdu University of Technology, Chengdu, China

⁴ Exploration & Production Institute, Southwest Oil & Gas Company, SINOPEC, Chengdu, China

⁵ Oil Exploration & Production Institute, SINOPEC, Beijing, China

⁶ Geophysical R&D Center, Bureau of Geophysical Prospecting, CNPC, Beijing, China

is economical must be solved first in order to effectively explore and develop such an oil and gas reservoir.

Generally, under the condition that a reef reservoir is irregularly distributed throughout space and is defined by strong anisotropy, a complex internal structure, and little contrast with the physical characteristics of the surrounding lithologies, its seismic reflections are described as a number of complicated features, including mounded, sagging, broken, random, and dim. The combination of deep reservoir burial depths, the low frequencies of seismic data and their consequent low resolution, and other adverse factors make it difficult to improve upon the precision of prediction for these types of reservoirs; thus, the key to resolving this problem is enhancing the quality of the seismic data. Accordingly, if the seismic resolution and signal-to-noise ratio can be effectively improved, the obstacles present in the high-precision prediction of reservoirs can be removed.

The processing of high-resolution seismic data remains one of the most ongoing problems in geophysical exploration. Several high-resolution processing methods have been developed both in China and abroad, including the full spectrum inversion method, which is one of the most efficient approaches for high-resolution processing. This method was initially proposed by Puryear and Castagna (2008) based on the parity-decomposition principle through which the odd and even numbers in a reflection coefficient sequence are decomposed, after which the LSCG (least-squared conjugate gradient) method is adopted to invert the reflection coefficients, including their polarity and magnitude. Chai (2012) also deduced a spectral inversion equation set and adopted an LSQR (least squares QR decomposition) method to solve the equation set, which highly improved the inversion accuracy and efficiency. Inverse Q filtering also serves as a common method for improving the seismic signal resolution and eliminating the amplitude decay and phase distortion effects caused during the seismic wave transmission process, thereby recovering the high-frequency component of the signal, upgrading the continuity, compensating for the energy loss, and improving upon the signal-to-noise ratio of the seismic data (Wang 2006; Yan et al. 2011). The newly developed band-broadening processing technology is used to improve seismic resolution, the premise of which is to maintain the relative amplitude in order to emphasize the enhancement of high-frequency and weak signals, and the seismic responses of thin reservoirs, and to employ corresponding prediction technologies to depict the features of thin formations. Such a technology is fundamentally capable of maintaining the signal-to-noise ratio of seismic data, the relative amplitude relationship and the time–frequency characteristics. Some examples of major band-broadening processing technologies include the high-frequency imaging technique (Countiss 2002; Gavin 2002), the frequency band

extension method (Li and Guo 2007), and the high-frequency extension (HFE) technique (Xie et al. 2012). Among these, the HFE technique views a seismic record as the projection of a reflection coefficient sequence at the low-frequency end of the frequency spectrum and subsequently back-projects the seismic record into higher frequency bands, thereby achieving a broadening of the frequency band and an improvement of the resolution. In addition, it also plays an important role with respect to the high-resolution processing and precise analysis of thin-interbedded coalbeds (Xu 2006), the complex high-resolution processing of gas reservoirs (Yuan et al. 2008), and the development of a dynamic analysis of thin-formation oil reservoirs (Sun et al. 2010). Multi-wavelet decomposition is another oil and gas reservoir detection technology that treats a seismic signal as a combination of harmonic waves by utilizing the original signal to establish a series of atomic function sets incorporating frequency, amplitude, and energy. Different attributes are used for the screening and optimization of the seismic data and the subsequent decomposition into a new seismic dataset that can highlight the oil and gas responsive characteristics of a target reservoir under geological constraints. Hence, this method is highly applicable in the precise analysis and characterisation of thin-formation oil and gas reservoirs (Sinha et al. 2005; Wang 2007, 2010; Gao et al. 2001).

As the objects of exploration are becoming more complex and are buried at increasingly greater depths, the high-resolution processing of seismic data continues to face greater challenges. The individual application of currently available conventional methods is unable to characterise thin-formation targets and perform the high-resolution processing required for deep formations. These tasks require the intensive testing and verification of several processing methods to select and combine different methods and obtain the optimal scheme for the high-resolution processing of target reflections. This paper has explored a set of high-resolution identification methods for the seismic data processing of reef reservoirs by examining earlier studies, tests, and combined applications, by performing energy compensation on seismic data in addition to wavelet decomposition and reconstruction, and by applying high-frequency expansion and precise analyses specific to carbonate reef reservoirs. The results of this study provide a favourable method to determine the spatial distribution and internal structure of a reef reservoir.

High-resolution identification methods for reef reservoirs based on seismic signals

A reef is a type of special carbonate trap with a complex interior structure, and it can easily grow into a thin, interbedded geological frame with reef microfacies, including the cap, core and base of a reef. The reef cap,

core, and base all exhibit modest thicknesses, and the reef cap can especially serve as a high-quality reservoir (such as in the Northeast Sichuan Yuanba Gas Field). Such reservoirs are capable of forming even thinner microfacies inside the reef body and developing thin, interbedded geological structures. On the basis of conventional seismic signals, it is relatively difficult to identify the internal structures of the reef body, describe the reservoir evolution, discriminate among the lithologies, and detect the oil- or gas-bearing possibilities. Therefore, it is necessary to conduct energy compensation, band broadening, wavelet decomposition, and wavelet reconstruction in addition to other specific processing steps based on the seismic frequency, phase, energy, waveform, and other dynamic and geometric features of the seismic data. These tasks serve to efficiently enhance the resolution of the seismic data, which is an important foundation for the high-precision prediction of a reef reservoir. The high-resolution processing scheme of seismic data for a reef reservoir are described hereinafter.

Energy compensation

It is well known that the high-frequency components of a seismic wave are absorbed, the frequency spectrum becomes narrow, and the phase of the wavelet becomes distorted due to earth filtering effects during the transmission of a seismic wave. In addition, all of these phenomena reduce the seismic resolution. To compensate for these absorption effects, an inverse Q filtering approach can be utilized, which may include a series expansion to approximate the high-frequency compensation, wavefield extrapolation or several other types of inverse Q filtering methods. A stable and full inverse Q filtering method can effectively compensate for the high-frequency components of seismic data, expand the frequency bandwidth, and increase the pre-stack or post-stack seismic resolution, thereby improving the seismic data quality. Based on the wavefield downward continuation principle, Wang (2002) proposed a stable and efficient inverse Q filtering method. After a seismic wave is transmitted a distance Δx , its plane wave component $U(x, \omega)$ can be expressed as

$$U(x + \Delta x, \omega) = U(x, \omega) \exp[-ik(\omega)\Delta x], \quad (1)$$

where i is an imaginary unit, ω is the angular frequency, and $k(\omega)$ is the wave number. After introducing the complex wave number, the Q effect of the Earth can be expressed as

$$k(\omega) = \left(1 - \frac{i}{2Q_r}\right) \frac{\omega}{v_r} \left(\frac{\omega}{\omega_h}\right)^{-\gamma} \quad (2)$$

in which

$$\gamma = \frac{1}{\pi Q_r}, \quad (3)$$

where Q_r and v_r are the Q value and phase velocity under a certain reference frequency, respectively, while ω_h is the harmonic parameter corresponding to the highest possible frequency within the exploration seismic frequency band (Kolsky 1953; Kjartansson 1979). After substituting a complex wave $k(\omega)$ into Eq. (1) and replacing the distance increment Δx with the corresponding travel time $\Delta \tau$, the inverse Q filtering approach can be expressed as

$$U(\tau + \Delta \tau, \omega) = U(\tau, \omega) \exp\left[\left(\frac{\omega}{\omega_h}\right)^{-\gamma} \frac{\omega \Delta \tau}{2Q_r}\right] \exp\left[i\left(\frac{\omega}{\omega_h}\right)^{-\gamma} \omega \Delta \tau\right] \quad (4)$$

In Eq. (4), the two exponential terms are the amplitude compensation operator for energy absorption and the phase correction operator for velocity frequency dispersion, respectively.

After inverse Q filtering, the amplitude attenuation and phase distortion caused by the attenuation of the Earth will be eliminated and the high-frequency components will be recovered. Consequently, the data continuity will be improved and the seismic resolution will be enhanced, and thus, the true characteristics of the subsurface media will be revealed.

Frequency band expansion

Under the convolution model, a seismic record $s(t)$ can be regarded as the convolution of the reflection coefficients $r(t)$ with a seismic wavelet $w(t)$, namely $s(t) = r(t) \times w(t)$. Among the available conventional deconvolution methods, which include sparse spiking deconvolution, spectrum broadening and spectral whitening, the spectrum broadening method is used to apply compression processing on $w(t)$ to enhance the resolution, but it is unable to effectively broaden the frequency band of the seismic data. This is because high-frequency noise will be amplified and the signal-to-noise ratio will be reduced after the amplitude spectrum within the effective frequency band is flattened (i.e., if the energy frequencies outside the effective frequency band are further enhanced). Therefore, the frequency expanding capability with the spectrum broadening technique is highly restricted.

The high-frequency seismic components recorded at the surface are much weaker than the low-frequency components due to strong absorption within the Earth during the propagation of a seismic wave. On the premise of protecting the low-frequency information and intensifying the high-frequency components of effective reflections, the seismic resolution can be enhanced by ensuring high data

fidelity. This is the foundation for seismic frequency band expansion.

For a given reflection series, the produced seismic records will provide different resolutions when convoluted separately with a low-frequency wavelet and a high-frequency wavelet. In the event that a seismic record $s(t)_{\text{Low}}$ formed by a low-frequency wavelet is converted into that formed by a high-frequency wavelet, the high-frequency components of the effective reflections in the seismic signal are enhanced and the resolution is improved. To implement this concept, the seismic record can be transformed into the frequency domain using a wavelet transform, a Fourier transform or another mathematical method. On the basis of a frequency spectrum analysis for $s(t)_{\text{Low}}$, a new type of convolution between the high-frequency wavelet and $r(t)$ can be established to form a different seismic record $S(t)$ for matching through a least squares method:

$$\sum_t (S(t) - s(t))^2 = E. \quad (5)$$

In Eq. (5), an error $E \approx 0$ indicates that $s(t)_{\text{Low}}$ is successfully transformed into a high-resolution seismic record formed by a high-frequency wavelet.

Wavelet decomposition and the reconstruction of seismic data

At present, the decomposition and reconstruction of seismic data (Thang and John 2000; Castagna et al. 2003; Liu and Marfurt 2005) can be performed by applying a short-time Fourier transform, a wavelet transform, an S -transform, a matching pursuit algorithm or another mathematical method. Among these techniques, the matching pursuit algorithm was developed in recent years using atomic decomposition theory.

As indicated by atomic decomposition theory, a seismic signal can be decomposed into a series of wavelet functions with various amplitudes, frequencies and other dynamical features, after which the original seismic signal is recovered through a simple linear stack of those wavelet functions. Assuming that N decompositions are applied to a seismic signal $f(t)$ by utilizing the wavelet function $M(t)$, then

$$f(t) = \sum_{n=0}^{N-1} A_n M_n(t) + E^{(N)}f \quad (6)$$

In Eq. (6), A_n is the amplitude of the n th wavelet function $M_n(t)$, and $E^{(N)}f$ is the residual error (when $n = 0$, $E^{(N)}f = f$).

During the wavelet decomposition, a Morlet wavelet is typically chosen as $M(t)$ in Eq. (6) because it can

effectively represent the attenuation and dispersion caused by earth absorption. Using Eq. (6) in the frequency or time domain, the seismic signal $f(t)$ can be iteratively decomposed into a wavelet function library composed of different Morlet wavelet functions. Then, different Morlet wavelet functions can be randomly selected from the library for a simple linear summation, and a new seismic signal $f'(t)$ can be constructed:

$$f'(t) = \sum_{m=0}^{M-1} A_m M_m(t), M \leq N. \quad (7)$$

If the number of iterations during the iterative decomposition process is sufficient to make the residual error $E^{(N)}f = 0$, then the sum of all of the wavelet functions in the library leads to $f'(t) = f(t)$, indicating that wavelet decomposition and the reconstruction of a seismic signal are performed with the highest possible precision. In the case when the residual error $E^{(N)}f$ generated during the wavelet decomposition process is ignored, $f'(t) \approx f(t)$ after linearly summing over all of the Morlet wavelet functions in the wavelet library. When conducting a wavelet decomposition for an actual seismic signal, the computational cost should be considered, as $E^{(N)}f$ is generally not expected to be zero to meet production demands (Xu et al. 2010).

Energy compensation, broadening the frequency band, and decomposing and reconstructing the wavelet from the seismic reflections of a reef reservoir can effectively intensify the low-frequency energies of seismic signals, raise the peak frequency, broaden the frequency band, and successfully extract the seismic responses features of the reef reservoir in different frequency bands. This can serve to highlight the frame of the reef body and its internal structure. Subsequently, in conjunction with logging and geological data, the seismic data can be used for further analyses of the sedimentary stages of the reef reservoir and its lithology and for predicting the reservoirs' spatial distribution.

The processes for the high-resolution identification of a reef reservoir based on seismic data are summarized in Fig. 1.

Application examples: high-resolution identification of reef reservoirs in a gas field

The reef reservoir located in the Changxing Formation of the Northeast Sichuan Yuanba Gas Field is a special carbonate reservoir. The spatial distributions of the natural gas, reserves, and production capacity of this field are controlled by the reef (Liu 2011; He et al. 2011; Chen 2011; Hu et al. 2010). However, the reef reservoir is influenced by complex and weak reflections from the inner

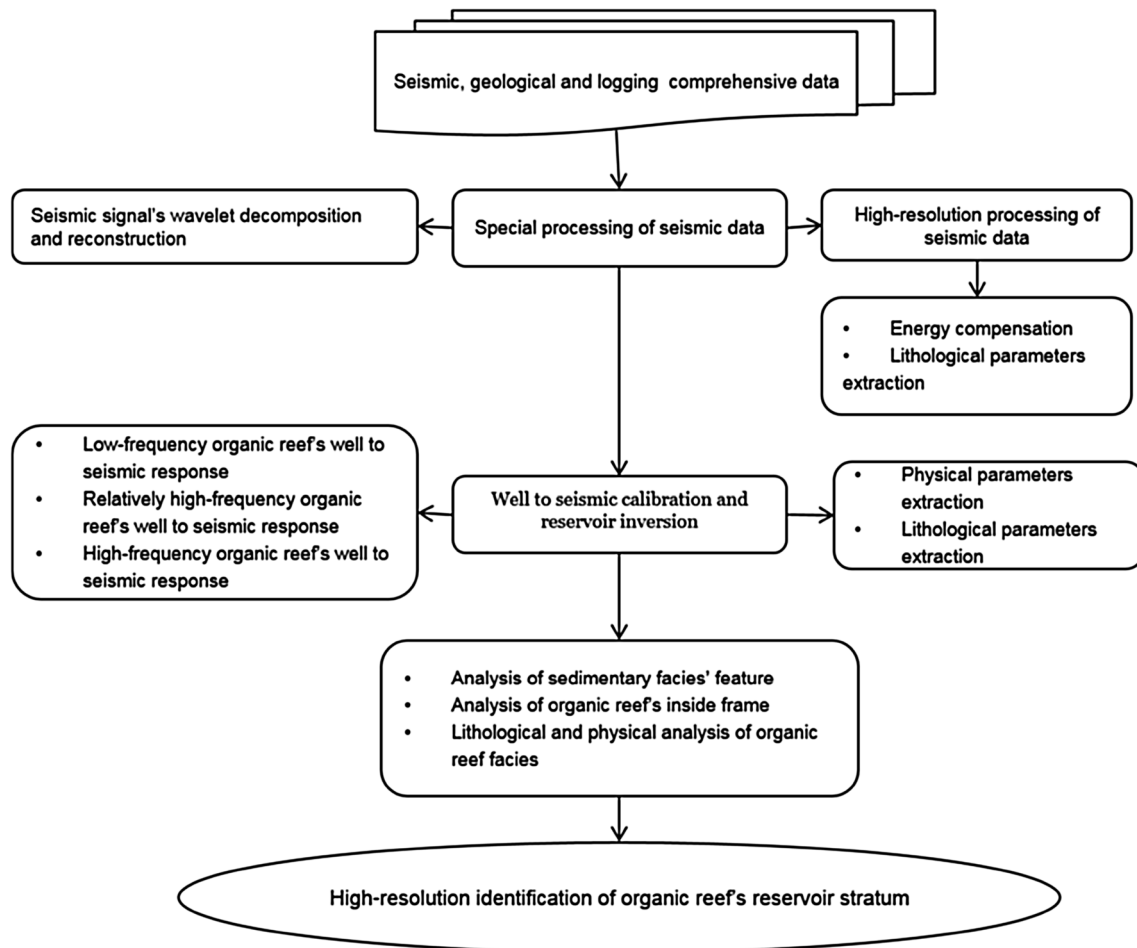


Fig. 1 Workflow for the high-resolution identification of reef reservoirs based on seismic data

reef body, and thus, the seismic resolution is very low. It is further complicated by the irregular reservoir spatial distribution, large burial depths, strong anisotropy, and small differences in the physical properties between the reservoir and the surrounding rocks. As a consequence, predictions of the reef reservoir characteristics and delineations of the internal structure for gas identification face great difficulties. For this reason, we conducted inverse Q filtering, frequency-broadening, and wavelet decomposition and reconstruction of the seismic data based on the above-mentioned methods. We subsequently explored valid approaches for the high-resolution identification of the reef on the basis of analysing the well-seismic response and impedance features of the reef reservoir so as to provide theoretical and methodological supports for an accurate description of complex oil and gas reef reservoirs.

Sedimentary facies characteristics

The Changxing Formation in the Yuanba region is a typical beach sedimentary facies that manifests shelf facies, slope

facies, and platform margin reef sedimentary facies as well as open platform facies from the southwest to the northeast. During the early Changxing age, the southwest part experienced open platform deposition while the northwest part received slope and shelf deposits with relatively placid depositional forms. Shortly thereafter, parts of the open platform generally developed into thin-formation bioclastic beaches and psammitic banks with deep overall water levels. Afterwards, reservoirs such as high-energy bioclastic beaches grew sporadically, but were confined to within certain topographic and high-energy regions. In the middle Changxing age, the southwest part gradually evolved into a platform margin and was accompanied by high-energy bioclastic beach deposits with large reef-beach thicknesses and an extensive range of distribution. In the late Changxing age, the differentiation among those depositional forms increased and reefs were generated along the shelf margin. Consequently, reefs in the Changxing Formation in the Yuanba Gas Field were mainly developed outside of the platform margin in a banded distribution, but each reef belt was not fully

connected. Meanwhile, following a continuous and alternating infill of bioclastic accretion and reef detritus, a shallow back-reef depositional environment was developed. In the upper Changxing Formation, reef and shallow back-reef microfacies are the most favourable reservoir facies belts.

Reservoir characteristics

The bank and reef sedimentary facies reservoir rock of the Changxing Formation is composed of dolomite and limestone, among which the physical reservoir properties of the dolomite are more effective than those of the limestone; therefore, bioclastic dolomite and fine-grained dolomite are considered supreme reservoir rocks. The reef-facies reservoir mainly consists of residual bioclastic dissolved-pore dolomite, bioclastic dissolved-pore dolomite, residual grained clastic dolomite, grey dolomite, bioclastic limestone, and reef limestone. The reef beach facies reservoir is mainly composed of grey dissolved-pore dolomite, grey dolomite, residual bioclastic dolomite, and grey bioclastic, sandy clastic and calcirudite limestones. Dissolved-pore dolomite is considered to exhibit good reservoir properties.

According to the core test statistics, the porosity of the Changxing Formation reef-facies reservoir is within 0.23–19.59% with an average of 4.06%, and it is dominated by 2–5% porosity (Fig. 2a). Meanwhile, its permeability is between 0.0028 and $1720.7187 \times 10^{-3} \mu\text{m}^2$ and its main peak value is between 0.01 and $0.1 \times 10^{-3} \mu\text{m}^2$. Samples with permeabilities of less than $0.1 \times 10^{-3} \mu\text{m}^2$ accounted for 39%, and samples with permeabilities between 0.1 and $10 \times 10^{-3} \mu\text{m}^2$ accounted for 44% (Fig. 2b). Most of the porosities of the limestone reservoir rocks are less than 5%, but their permeability is larger than 1 mD, which indicates that cracks and micro-cracks are the major reservoir spaces. Overall, the Changxing Formation reservoir is a pore-type and crack-pore type reservoir (Cheng et al. 2015).

Reef-facies reservoir identification

Reefs represent a special carbonate sedimentary body and generate unique seismic responses. The seismic records show dome-shaped reflections from the outside reef, strong reflections or draping structure reflections from the reef top, discontinuous chaotic or nearly blank reflections from the inner reef, low elevation reflections from the reef bottom, and onlap reflections from the wings of the reef. However, due to irregular or very weak reflections from within the internally broken reef body in the original seismic data, the growth stages and internal structures of the reef are difficult to analyse. For this reason, we adopted wavelet decomposition and reconstruction technology to decompose the original seismic data for reconstruction and processing in order to comprehend the regularity of the reef seismic frequency response and further understand reef reservoirs.

Taking the seismic data from well YB103H (with a natural gas open-flow capacity of 7.516 million cubic m/day) in the Yuanba Gas Field as the example, Fig. 3 presents the following from left to right: the logging curve, original seismic data, 25 Hz reconstructed seismic data and 45 Hz reconstructed seismic data. The first set of reflection peaks above the blue stratum curve T-cx-5 \times corresponds to the top boundary of the reef, T-cx-3 \times corresponds to the basal boundary of the reef, and T-cx-down is the basal boundary of the Changxing Formation. The red arrow denotes a mudstone overlying the reef top. In the original seismic data, the reef contour is reflected clearly while the reef crest beneath the overlying mudstone cap rock and the inner reef body are shown as disordered and composite reflections, which introduce difficulties into the reef reservoir prediction and recognition. After the wavelet decomposition and screening of the original seismic data, the overlying mudstone cap rock and the reef body contours are all depicted explicitly in the 25 Hz reconstructed seismic data. Moreover, the reef contour is depicted with

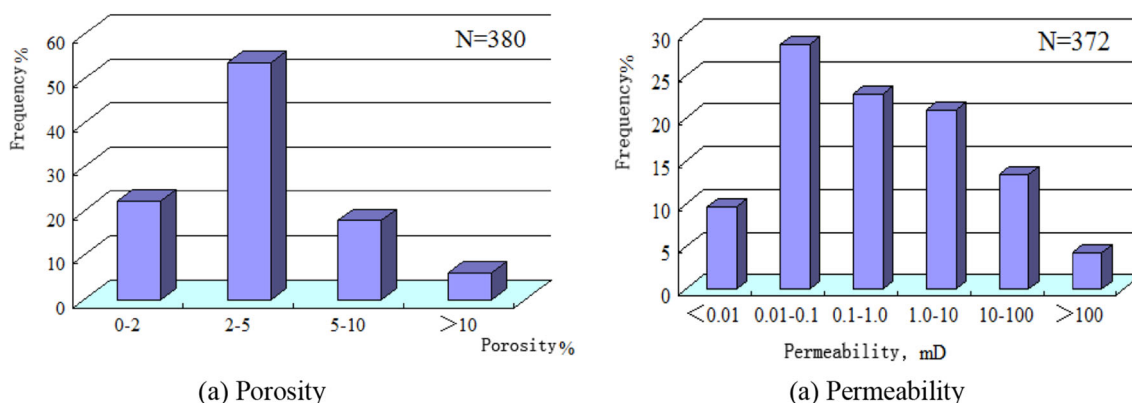
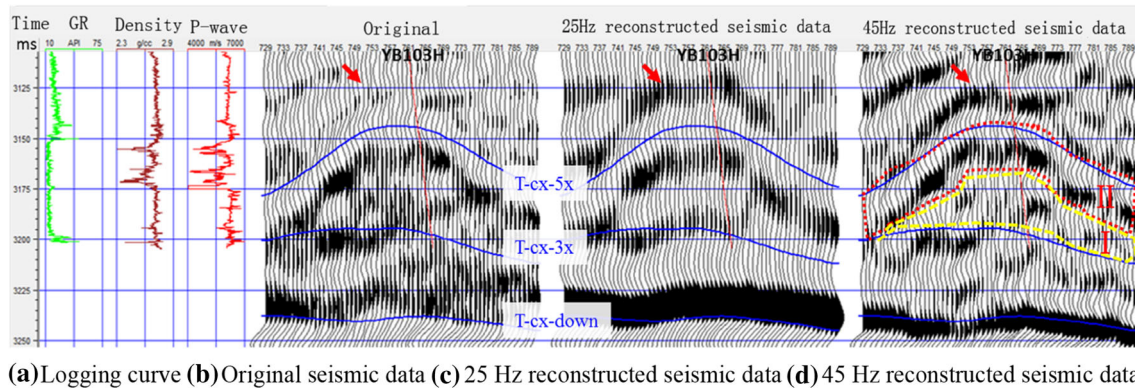


Fig. 2 Histogram of the distribution of physical properties of the reef reservoir in the Changxing Formation of the Yuanba Gas Field



(a) Logging curve (b) Original seismic data (c) 25 Hz reconstructed seismic data (d) 45 Hz reconstructed seismic data

Fig. 3 Comparison between the original and reconstructed seismic data with well-seismic calibration in well YB103H in the Yuanba Gas Field

clear reflection features in the 45-Hz reconstructed seismic data, and the internal evolutionary character of the reef body is comparatively developed and clearly demonstrates layers of evolution related to the reef base-core-reef cap and the reef core-reef cap in the reef body (parts I and II in Fig. 3d, respectively, which correspond to yellow and red boxes). It is clear that reconstructed seismic data are more favourable for reef reservoir prediction as it helps to integrate well and seismic information and improve the accuracy of reef recognition.

Figure 4 shows a comparison between the calibration of well YB103H in the Yuanba Gas Field YB103H with the original seismic data and the processed high-resolution seismic data. As shown in Fig. 4, the reef reflections in the original seismic data are complex and cannot be clearly seen, and the reef responses are invisible in the logging data (e.g., the sonic impedance, density and velocity). Therefore, it is very difficult to identify the internal structures of the reef reservoir from either the seismic data or logging data. Meanwhile, reflections from the cap, core, and base of the reef body can be clearly seen in the high-resolution seismic data, and thus, the surrounding and internal structures of the reef and the growth stages (first stage: reef base-reef core-reef cap; second stage: reef core-reef cap) of the reef can be easily identified.

Seismic impedance is a key parameter for identifying oil and gas reservoirs. In most cases, it can reveal the reservoir lithology, physical properties, and fluid distribution. Joint well-seismic studies indicate that the high-quality reservoirs in the Changxing Formation of the Yuanba Gas Field mainly exhibit low impedance responses. The white rectangular frame of Fig. 5 shows the acoustic impedance of the reef reservoir. Figure 5a illustrates that the rocks surrounding the reef body exhibit higher acoustic impedances, and the state of internal development of the reef is difficult to identify due to the low resolution, especially with regard to accurately estimating the thickness of the high-quality reservoir. Meanwhile, Fig. 5b, which is based on a high-

resolution seismic data inversion, clearly describes the inner details of the reef body and highlights impedance differences between the reef cap (low impedance), reef core (medium impedance), and reef base (relatively low impedance) as sedimentary microfacies that are all extremely favourable for predicting the spatial distribution of the high-quality reservoir.

Figure 6 illustrates the acoustic impedance of the T-cx-5 \times layer and the along-strata state of reef development. Likewise, Fig. 6a shows that the along-strata reef developmental state cannot be delineated due to a limited seismic resolution. In contrast, the reef (blue dotted box), the bioclastic beach (black dotted box), the reef-bank complex (blue solid box) and other natural gas reservoir bodies are identified precisely by utilizing the impedance differences demonstrated in Fig. 6b in conjunction with geological constraints. These three kinds of geological bodies are delineated effectively as different acoustic impedance features; among them, the margin of the reef body has a high impedance, while the inner parts of the reef exhibit low-impedance features, thereby manifesting specially as a high impedance boundary encompassing low impedance on the plane. In the Changxing Formation of the Yuanba Gas Field, the bioclastic beach is also a favourable reservoir that has a relatively high impedance along the T-cx-5 \times stratum, while the complex acoustic impedance response of the reef-bank ranges between the reef and bioclastic beach to manifest high and low impedances that frequently fluctuate as complex responses on the plane.

Reservoirs in the Changxing Formation of the Yuanba Gas Field are very tight and demonstrate relatively high porosities and well-developed cracks, which are favourable for the reserve and transport natural gas and serve as critical factors in controlling the spatial distribution, reserve volume and output of the reservoir. According to a comparative analysis of the original seismic data with 25 and 45 Hz reconstructed seismic data and high-resolution seismic data, the reconstructed and high-resolution seismic

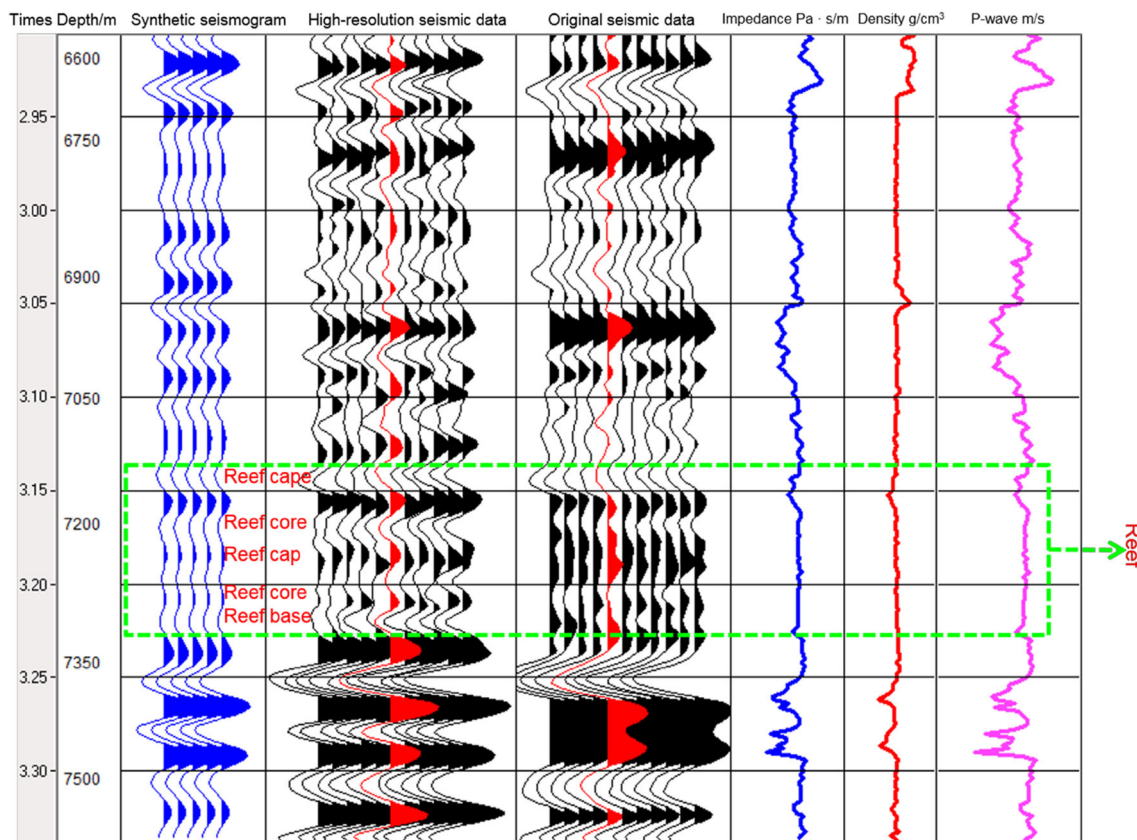


Fig. 4 Comparison between the original and reconstructed seismic data with well-seismic calibration in Well YB103H in the Yuanba Gas Field

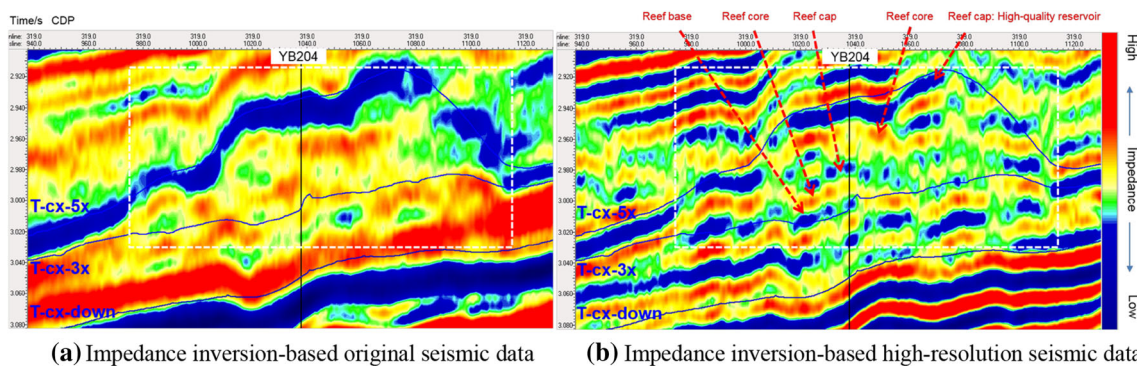


Fig. 5 Profile comparison of acoustic impedances within the Yuanba Gas Field Well YB204 and a high-resolution identification of the reef. These results indicate the difficulty in identifying the internal structure of an organic reef with low-resolution seismic data. High-resolution impedance values can provide a clear description of the

internal details of a reef and highlight the impedance differences between the sedimentary microfacies of the reef cap (low impedance), reef core (medium impedance) and reef base in order to accurately forecast the spatial arrangement of high-quality reservoirs

data can effectively highlight the seismic reflection features of high-quality reef reservoirs. Taking advantage of the variations in the acoustic impedances inverted from the high-resolution seismic data, we can predict the differences in the physical properties between the internal reef body microfacies as well as those among the reef and bioclastic beach, reef-bank complex, tide ditch and other geological bodies. After an integration with the well-seismic response

and abnormal geophysical parameters, we can perform further analyses and obtain an understanding of the spatial distribution, internal structures and evolutionary stages of high-quality reef reservoirs, which also enables us to precisely predict natural gas-rich regions. Overall, the results of the application of this technique to well YB103H, well YB204 and the T-cx-5× strata are consistent with drilling results, and they have proven that the method described in

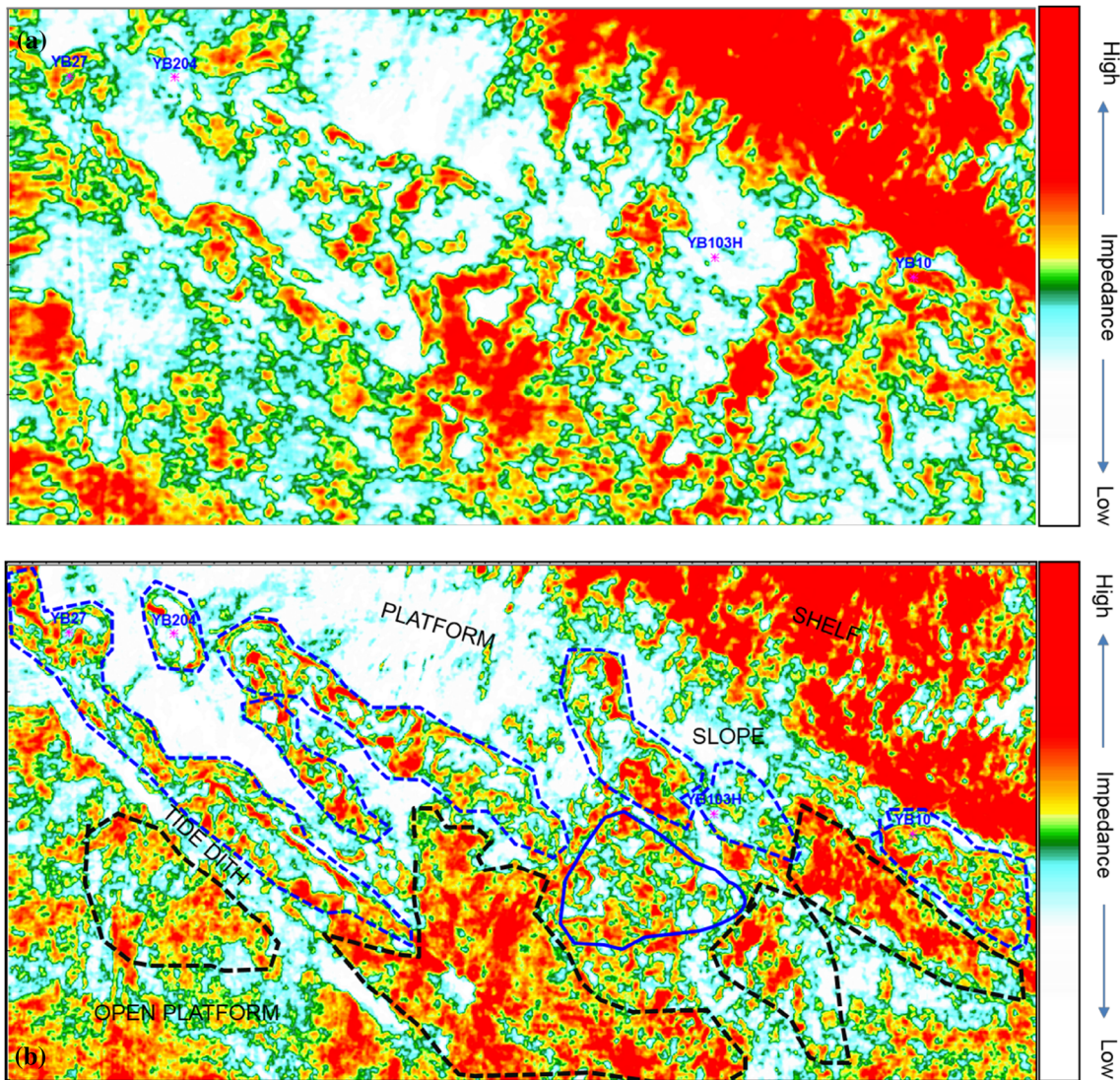


Fig. 6 Comparison of the acoustic impedance of the T-cx-5x stratum in the Yuanba Gas Field and the high-resolution reef identification. **a** The inverted acoustic impedance of the target stratum based on the original seismic data. **b** The inverted acoustic impedance of the target stratum based on the high-resolution seismic data. Figure 6 indicates

that it is difficult to identify the developmental features of different layers within the organic reef due to resolution limitations. However, by combining geological constraints with high-resolution impedance differences, it is possible to accurately recognize the natural gas reservoirs of the organic reef, biotritus beach and reef flat

this paper can provide a significant foundation for the successful exploration and development of reef reservoirs.

Conclusion

The following have been proven from this study on a method for the high-resolution identification of reef reservoirs and the effectiveness of its practical application in the Yuanba Gas Field:

- (1) Reefs represent a type of special carbonate reservoir body with complex internal structures composed of a reef cap, core, base and other reef body microfacies

that are small in thickness. They easily grow into thin, interbedded geological frames. The peak frequency of a conventional seismic signal is low with a narrow frequency bandwidth, which makes it impossible to be used for the identification of thin, interbedded strata. The seismic reflections representative of a reef are mounded, concave downward, broken, irregular and weak, among other highly complicated reflection characteristics. These features highly affect the ability to conduct an identification of the reservoir internal structure, a description of the evolutionary phases, a discrimination of the lithologies, and a determination of the reservoir oil–gas bearing possibility.

- (2) On the basis of a comprehensive analysis of the frequency, phase, energy, waveform and other dynamic and geometrical features of a conventional seismic signal, this paper has developed a special method involving target energy compensation frequency band expansion, wavelet decomposition and reconstruction and other special processing steps following the combination of the seismic response features of the reef. This method effectively improves the resolution of the seismic data as an important foundation for achieving a high-precision prediction of reef reservoirs.
- (3) An application of the method to the reef reservoir of the Changxing Formation in the Yuanba Gas Field shows that reconstructed seismic data in different frequency bands can highlight the reef top and the overlying mudstone cap rock, the reef contour and the drape structures of the reef, while high-resolution seismic data are able to highlight the interior details of the reef body to identify the reef outlines and precisely delineating high-quality reservoirs. High-resolution acoustic impedance variations reflect the physical property differences between the internal microfacies of the reef body as well as reef and bioclastic beach, reef-bank complex, tide ditch and other geological bodies. When combined with well-seismic response data and other abnormal geophysical parameters, it is possible to identify high-quality reef reservoirs with high resolution.


Acknowledgements The research is sponsored by the National Natural Science Foundation of China (No. 41574099) and the national key science and technology special projects (No. 2016ZX05002004-005).

References

- Bi CC, Li LX, Mei Y, Zhang YC, He C (2007) Geological control factors of Changxing organic reef distribution and seismic prediction techniques, East Sichuan Basin. *Nat Gas Geosci* 18(4):2–7. doi:10.3969/j.issn.1672-1926.2007.04.005 (in Chinese)
- Cai XY (2011) The subtly method of reservoir and exploration effects on the organic reef-beach body of Changxing Formation, Yuanba Area, Northeastern Sichuan. *Eng Sci* 13:28–33. doi:10.3969/j.issn.1009-1742.2011.10.004 (in Chinese)
- Castagna JP, Sun SJ, Siegfried RW (2003) Instantaneous spectral analysis: detection of low-frequency shadows associated with hydrocarbons. *Lead Edge* 22(2):120–127. doi:10.1190/1.1559038
- Chai XT (2012) Research for spectrum inversion method based on LSQR algorithm. *Geophys Prospect Petrol* 51(1):11–18. doi:10.3663/j.issn.1000-1441.2012.01.002 (in Chinese)
- Chen Y (2011) Prediction on reef reservoir in Changxing group of Yuanba area, Northeast Sichuan Basin. *Geophys Prospect Petrol* 50(2):173–180 (in Chinese)
- Cheng BJ, Xu TJ, Robbins B, Shen ZM (2015) Reef reservoir identification by wavelet decomposition and reconstruction: a case study from Yuanba Gas Field in China. *Acta Geophys* 63(4):1025–1043. doi:10.1515/acgeo-2015-0028
- Countiss ML (2002) Frequency-enhanced imaging of stratigraphically complex, thin-bed reservoirs: a case study from south marsh island block 128 Field. *Lead Edge* 21(9):826–836. doi:10.1190/1.1508943
- Gao JH, Wu RS, and Wang BJ (2001) A new type of analyzing wavelet and its applications for extraction of instantaneous spectrum bandwidth. In: 71th Annual international meeting, SEG, Expanded Abstracts, pp 1937–1940. doi:10.1190/1.1816515
- Gavin HJ (2002) A new technology for high frequency imaging using seismic data comes to the North Sea. *First Break* 20(11):695–698
- He J, Wu SH, Cai K (2011) Seismic prediction for Northeast Sichuan Yuanba region Changxing Formation's bank and reef sedimentary facies. *Neijiang Technol* 32(11):125–126. doi:10.3969/j.issn.1006-1436.2011.11.105 (in Chinese)
- Hu WG, Pu Y, Yi XL, Xiao W, You SK, Zhao ZN (2010) A tentative discussion on the recognition of bioherm in Yuanba area Eastern Sichuan province. *Geophy Geochem Explor* 34(5):635–642 (in Chinese)
- Kjartansson E (1979) Constant Q-wave propagation and attenuation. *J Geophys Res Part B Solid Earth* 84(B9):4737–4748. doi:10.1029/JB084iB09p04737
- Kolsky H (1953) *Stress waves in solids*. Oxford University Press, London, pp 81–83
- Li ZS, Guo XB (2007) Predicting the distribution of thin bed reservoirs by broad frequency band seismic. *Appl Geophys* 4(2):118–126. doi:10.1007/s11770-007-0017-8
- Liu H (2011) Seismic identification characteristics for Northeast Sichuan Yuanba region Changxing Formation's bank and reef sedimentary facies. *Sci Technol West China* 10(31):37–38. doi:10.3969/j.issn.1671-6396.2011.31.018 (in Chinese)
- Liu JL, Marfurt KJ (2005) Matching pursuit decomposition using Morlet wavelets. In: 75th Annual international meeting, SEG, Expanded Abstracts, pp 786–789. doi:10.1190/1.2148276
- Ma YS, Mon CL, Tan QY, Yu Q, Wang RH (2007) Reef-bank features and their constraint to reservoirs of natural gas, from Permian Changxing Formation to Triassic Feixianguan formation in Daxian-Xuanhan area of Sichuan province, South China. *Earth Sci Front* 14(1):182–192. doi:10.1016/S1872-5791(07)60007-4
- Puryear CI, Castagna JP (2008) Layer-thickness determination and stratigraphic interpretation using spectral inversion: theory and application. *Geophysics* 73(2):37–48. doi:10.1190/1.2838274
- Sinha S, Routh PS, Anno PD, Castagna JP (2005) Spectral decomposition of seismic data with continuous-wavelet transformation. *Geophysics* 70(6):19–25. doi:10.1190/1.2127113
- Sun XP, Zhang Y, Zhang YQ, Zhou C (2010) Frequency-broadening processing technology's application in the thin-formation oil reservoir's development dynamic analysis. *Oil Geophys Prospect* 45(5):695–699 (in Chinese)
- Thang N, John C (2000) Matching pursuit of two-dimensional seismic data and Its filtering application. In: 70th Annual international meeting, SEG, Expanded Abstracts, pp 2067–2069
- Wang YH (2002) A stable and efficient approach of inverse Q filtering. *Geophysics* 67(3):657–663. doi:10.1190/1.1468627
- Wang YH (2006) Inverse Q-filter for seismic resolution enhancement. *Geophysics* 71(3):V51–V60. doi:10.1190/1.2192912

- Wang YH (2007) Seismic time-frequency spectral decomposition by matching pursuit. *Geophysics* 72(1):13–20. doi:[10.1190/1.2387109](https://doi.org/10.1190/1.2387109)
- Wang YH (2010) Multichannel matching pursuit for seismic trace decomposition. *Geophysics* 75(4):61–66. doi:[10.1190/1.3462015](https://doi.org/10.1190/1.3462015)
- Xie YJ, Zheng JM, Liu G (2012) Application of high-frequency expanding technique in improving resolution of seismic data. *Recent Dev World Seismol* 399(3):28–33. doi:[10.3969/j.issn.0235-4975.03.006](https://doi.org/10.3969/j.issn.0235-4975.03.006) (in Chinese)
- Xu YH (2006) Application of optimized high-frequency expanding technique in coalfield exploration. *Coal Geol China* 18(2):52–54 (in Chinese)
- Xu TJ, Shen ZM, Wen XK (2010) Research and application of multi-wavelet decomposition and reconstructing technology. *J Chengdu Univ Technol (Sci Technol Ed)* 37(6):660–665. doi:[10.3969/j.issn.1671-9727.2010.06.011](https://doi.org/10.3969/j.issn.1671-9727.2010.06.011) (in Chinese)
- Yan HY, Zhao Y, Zhao QH, Li XX, Jiang NS (2011) A kind of method for improving inverse Q filtering's VSP Resolution. *Oil Geophys Prospect* 46(6):873–880 (in Chinese)
- Yuan HJ, Wu SG, Wang JB, Dong N, Zhou XY, Liu JZ, Xia HM, Xiao HM, She G, Yu WQ (2008) Frequency-broadening processing technology's application in the development of Daniudi gas field exploration. *Oil Geophys Prospect* 43(1):69–75. doi:[10.3321/j.issn:1000-7210.2008.01.012](https://doi.org/10.3321/j.issn:1000-7210.2008.01.012) (in Chinese)

Seismic activity prediction using computational intelligence techniques in northern Pakistan

Khawaja M. Asim¹  · Muhammad Awais¹ · F. Martínez-Álvarez² · Talat Iqbal¹

Received: 10 April 2017 / Accepted: 2 September 2017 / Published online: 14 September 2017
© Institute of Geophysics, Polish Academy of Sciences & Polish Academy of Sciences 2017

Abstract Earthquake prediction study is carried out for the region of northern Pakistan. The prediction methodology includes interdisciplinary interaction of seismology and computational intelligence. Eight seismic parameters are computed based upon the past earthquakes. Predictive ability of these eight seismic parameters is evaluated in terms of information gain, which leads to the selection of six parameters to be used in prediction. Multiple computationally intelligent models have been developed for earthquake prediction using selected seismic parameters. These models include feed-forward neural network, recurrent neural network, random forest, multi layer perceptron, radial basis neural network, and support vector machine. The performance of every prediction model is evaluated and McNemar's statistical test is applied to observe the statistical significance of computational methodologies. Feed-forward neural network shows statistically significant predictions along with accuracy of 75% and positive predictive value of 78% in context of northern Pakistan.

Keywords Earthquake prediction · Computational intelligence · Seismic activity · Seismic precursors

Introduction

Earthquakes have been one of the highly feared natural catastrophic events. Recently, the forecasting of different geological and environmental disasters, such as volcanoes (Houlié et al. 2006), hurricanes (Yan et al. 2015), great tsunamis (Ramar and Mirnalinee 2012), and thunderstorms (Anad et al. 2011) has been consigned from multiple aspects. The occurrence of earthquakes, and especially major events that caused casualties, massive damage to economy, and disappearance of societies in a flash from the face of the earth, has been documented throughout the historical times. These destructive earthquakes accelerate the need to understand them in depth regarding their phenomena that might lead us to predict them. Prediction of an earthquake means to foretell about exact magnitude, location, and time of occurrence earthquake. Unavailability of such a prediction model makes this field of research challenging. Earthquake prediction holds great potential for saving lives, reducing property damage and enhancing the safety of critical facilities. Research on forecasting of earthquakes has been earnestly committed from the last few decennium. However, due to the highly non-linear earthquake generation phenomenon, it has not been possible to precisely find out the location, magnitude, and time of impending event. Sometimes, earth projects some precursory signals before occurrence of destructive earthquakes, but often, we are unable to sensitise such subtle phenomena. Most of earthquake prediction research is based upon retrospective study of presupposed precursory phenomena for major earthquakes. Such phenomena

✉ Khawaja M. Asim
asim.khawaja@ncp.edu.pk

Muhammad Awais
emawais@gmail.com

F. Martínez-Álvarez
fmaralv@upo.es

Talat Iqbal
talat.iqbal@ncp.edu.pk

¹ Centre for Earthquake Studies, National Centre for Physics, Islamabad, Pakistan

² Department of Computer Science, Pablo de Olavide University, Seville, Spain

include variations in sub-soil radon gas (Jilani et al. 2017; Barkat et al. 2017; Awais et al. 2017), vertical electric field, total electron content of ionosphere (Pulinets and Ouzounov 2011), and so forth. Earthquake predictions are time dependent, so it can be divided into time-based categories: long term (tens of years), intermediate term (few years), and short term (days to weeks) and immediate (hours) prediction (Keilis-Borok and Soloviev 2003).

The Computational Intelligence (CI) and Machine Learning (ML) techniques have a vast history of successful applications in many fields, such as signal processing (Graves et al. 2013), computer vision (Murtza et al. 2017), wind power prediction (Arshad et al. 2014), medical (Hassan et al. 2015), and finance (Idris et al. 2012), which are highly non-linear and complicated problems. Such techniques have also been used for prediction of earthquakes in the last decade (Panakkat and Adeli 2007; Adeli and Panakkat 2009; Alarifi et al. 2012; Ikram and Qamar 2015; Asencio-Cortés et al. 2015a; Last et al. 2016; Asim et al. 2017). The CI-based classification and prediction models take features (in this case seismic parameters) with respect to corresponding targets (earthquakes). An intelligent model is generated on the basis of available dataset, capable of predicting target earthquakes through seismic parameters.

Earthquakes are recorded by modern instruments and a catalog is prepared which contains information about date, origin time, hypocentral location, and magnitude of earthquakes. In this particular study, earthquake prediction is carried out for northern Pakistan, based upon seismic precursors calculated using earthquake catalog. Initially, eight precursors are computed based upon important seismological facts. These seismic parameters are meant to represent the internal seismic state of the region. Every region may possess different seismic properties; therefore, it is not necessary that every precursor holds the same information about seismic state. Feature selection is carried out on the basis of mutual information gain, which leads to the final selection of six parameters. The selected six parameters are used in combination with computationally intelligent techniques to obtain earthquake predictions. The predictions are generated for 1 month; therefore, it lies in the category of short-term earthquake prediction.

The rest of the manuscript is structured as follows. “[Related works](#)” reviews the latest and most relevant studies related to this work. Tectonics of northern Pakistan is described in “[Tectonics of northern Pakistan](#)”. Earthquake prediction methodology is detailed in “[Earthquake prediction methodology](#)”, including seismic feature calculation, selection, and feed-forward neural networks. The results achieved through different CI-based techniques are reported in “[Results and discussion](#)”. Finally, the

conclusion is drawn along with suggestions for future work in “[Conclusions](#)”.

Related works

Foremost, we consider the general outline of the contemporary research work related to the earthquake prediction. Algorithm M8 aims to forecast the earthquake of magnitude 8.0 and above tested successfully at the different regions of the globe along with increased efficiency of intermediate term earthquake forecasting. It analyzes the earthquake catalog and gives the alarming area in circular region for the next 5 years (Keilis-Borok and Kossobokov 1990; Kossobokov 1997). There are several studies conducted based on this algorithm and its advanced stabilized version, i.e., M8S algorithm to forecast the seismic events of magnitude 5.5 and above (Kossobokov et al. 2002).

A model for forecasting earthquakes introduced by Petersen et al. (2007) is based on the distribution of rare events, i.e., Poisson distribution. This approach gives the likelihood for the occurrence of event in terms of time-independent and dependent Poissonian probabilities at several faults of California (Helmstetter et al. 2007). It is noted that this model is mainly used as a good precursor for larger earthquakes, seismic mitigation, and hazard preparedness studies.

Kagan et al. (2007) proposed the model based only on the earthquake catalog with observed regular occurrence of events. It does not take into account the geological, geomorphological, and tectonic settings of the region. The work is mainly based on the database containing earthquakes of intermediate level magnitude, i.e., 5.0. The zone for the aftershock activity signalized pertinent measure of rupture length for recent earthquakes.

Panakkat and Adeli (2007) proposed a significant approach for earthquake prediction using seismicity indicators. These indicators represent the underlying seismic state of the region and are calculated from temporal distribution of earthquakes. These eight seismic parameters are fed to Artificial Neural Networks (ANN) for generating prediction models. Southern California and San Francisco bay regions were considered for prediction studies. Following this research, Adeli and Panakkat (2009) used the same seismic features as an input to the Probabilistic Neural Network (PNN) for earthquake prediction of the same regions.

Martínez-Álvarez et al. (2013) and Reyes et al. (2013) proposed seven mathematically calculated seismic features using earthquake catalog. The suggested parameters are the realization of Bath’s law (Bath 1965) and Omori’s law (Utsu et al. 1995). Earthquake predictions were performed for Chile and Iberian Peninsula using ANN in combination

with seismic features. The horizon of prediction for Chile and Iberian Peninsula is kept to 5 and 7 days, respectively.

Ikram and Qamar (2015) presented an automated methodology for worldwide prediction of earthquakes. This technique includes the splitting of whole globe into four quadrants. The seismic activity patterns are considered for forming predicate logic and associations rules. These rules are fed to the expert system to make it capable of predicting earthquakes. The predictions are carried out for the time span of 24 h in each quadrant of globe on the basis of seismic activity patterns.

Asim et al. (2017) considered Hindukush region for earthquake prediction studies. Catalog-based seismic features have been computed on monthly basis. These features are used in combination with different machine learning techniques to predict magnitude of 5.5 and above. Asim et al. (2016) also performed prediction study for the similar region using tree-based ensemble methodologies with prediction horizon of 15 days. ANNs have also been used to predict medium–large earthquakes in Japan (Asencio-Cortés et al. 2015b). In particular, the authors examined a circular area, centered in Tokyo, with a radius of 200 km. The test set was year 2015 and the temporal prediction horizon was set to 7 days.

Seismicity indicator-based Earthquake Early Warning System (EEWS) capable of forecasting major earthquakes for horizon period of weeks is proposed by Rafiei and Adeli (2017). The EEWS employs classification algorithms of Neural Dynamic Classification (NDC), PNN, enhanced PNN, and Support Vector Machine (SVM) for earthquake forecasting. The EEWS also provides the location of earthquake using optimization algorithm of Neural Dynamic Optimization (NDO). Wang et al. (2017) suggested that the historic earthquake data of multiple locations should be considered for making successful earthquake prediction. A deep learning technique known as long short-term memory networks is employed to model the spatio-temporal relationship among earthquakes in different locations.

Tectonics of northern Pakistan

Study area has been selected owing to the fact that it has high rate of seismicity due to its location at the north-western boundary of the Indian Plate (Ali et al. 2009; Rehman et al. 2017). Indian Plate is thrusting at the rate of about 20 mm/year under Eurasian Plate since Eocene time on the northwestern and northern edges (Jouanne et al. 2014). The formation of the high mountain ranges of the Himalaya is resulted by thick sheets of sediments that have been thrusting over the Eurasian shield (Kemal 1992). In this region, transpression is also operative along with

compressional regime (Sercombe et al. 1998; Pêcher et al. 2008). The Himalayas in northern Pakistan can be divided into four major subdivisions. Hindukush and Karakoram ranges lie in the north of the Main Karakoram Thrust (MKT). North of Main Mantle Thrust (MMT) and South of MKT lie the Kohistan block. The Lesser Himalayas of India that include low ranges of Swat, Hazara, and Kashmir lie between the MMT and the Main Boundary Thrust (MBT). The marginal foreland fold-and-Thrust belt of Indo-Pakistan subcontinent is represented by Potwar Plateau, Salt Range Thrust (SRT) bounds Potwar Plateau from south (Kazmi and Jan 1997). Figure 1 shows the overall tectonic setting of northern Pakistan.

Earthquake prediction methodology

Figure 2 reveals the brief overview of the methodology employed for generating earthquake prediction model. The seismic features considered in this study are based on earthquake catalog. Seismic feature computation is followed by selection of the informative features. CI-based prediction models are generated using selected seismic features and their subsequent earthquakes. These models are further tested over unseen data and results are evaluated. McNemar's test highlights the statistical significance of predictions obtained through every CI model. The catalog for this region is obtained from US Geological Survey starting from January 1, 1976 to December, 2013. Cut-off magnitude (M_c) for this catalog is found to be 4.0. M_c refers to the earthquake magnitude, below which seismic events are missing from catalogs due to instrumentation limitations. There are different methods available in the literature for finding M_c (Florido et al. 2015).

Seismic feature calculation

The study of features and their calculations is motivated by the work of Panakkat and Adeli (2007) and Adeli and Panakkat (2009). Eight seismic features have been calculated using catalog for earthquake prediction. These seismic indicators are calculated using the past 100 events before every month. These features are then exploited for making earthquake predictions for subsequent month. The parameters express seismic facts of Gutenberg–Richter law, seismic energy release, and foreshock frequency in numeric form. Thus, feature vector consisting of eight parameters represents internal geological state of the region before every upcoming month. Gutenberg–Richter law states that the number of cumulative seismic events increase exponentially with the decreasing magnitudes (Gutenberg and Richter 1954). Figure 3 demonstrates the frequency–magnitude relationship for available catalog of

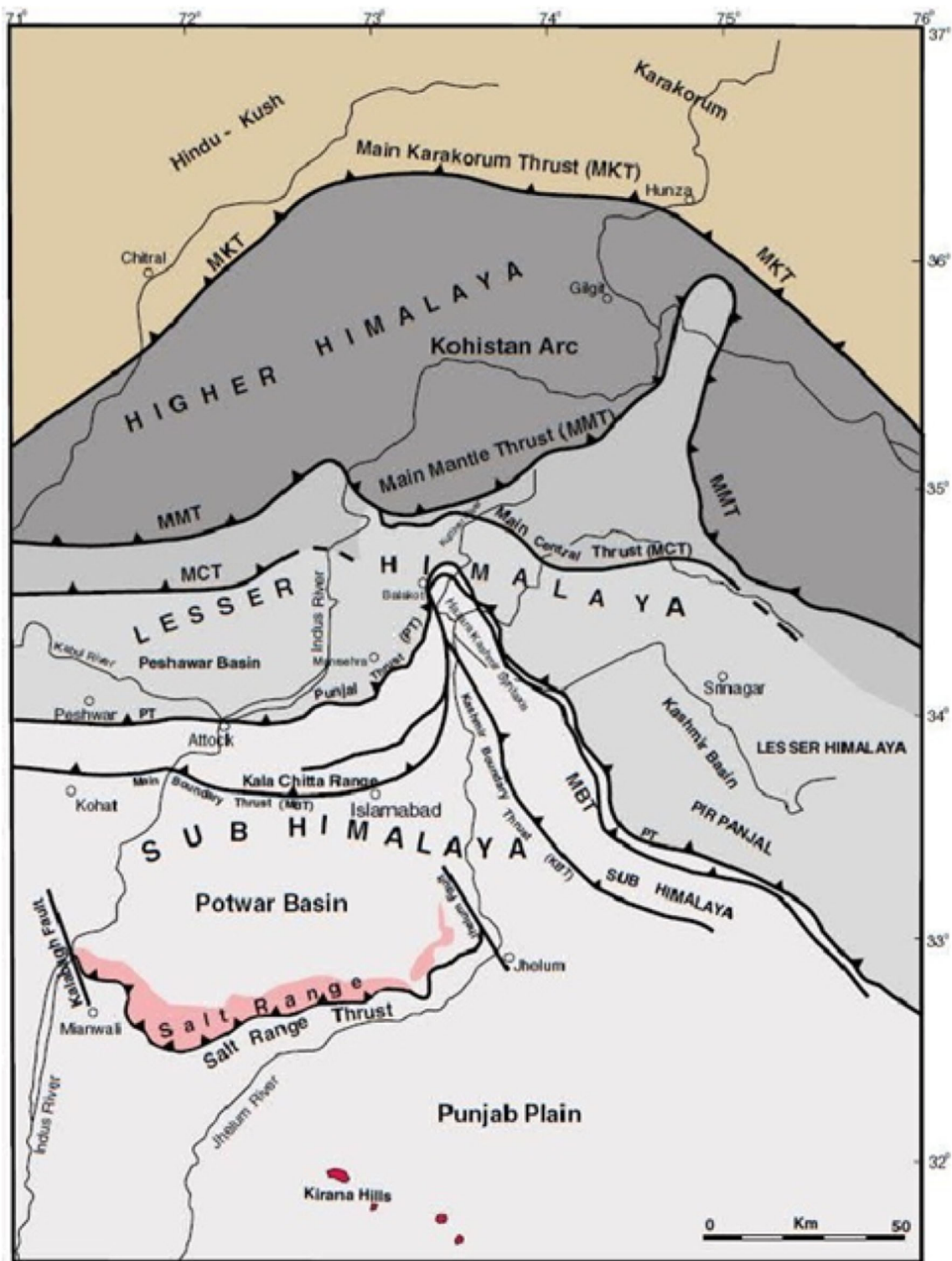
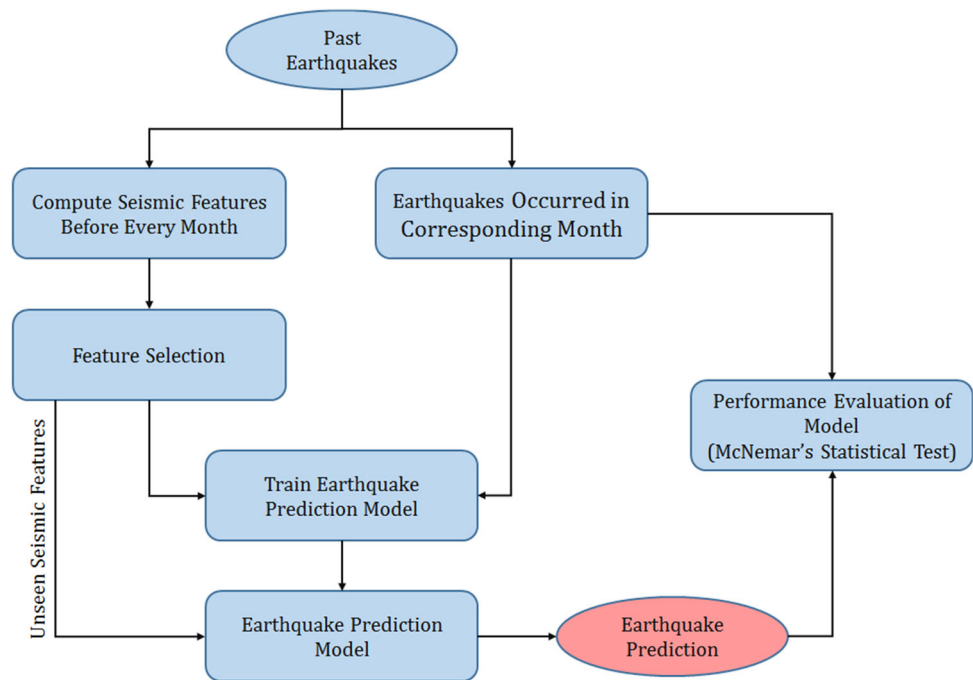


Fig. 1 Generalized tectonic map of northern Pakistan showing subdivisions of the Himalayan mountains (Kazmi et al. 1982)

the northern Pakistan. The frequency of earthquakes and their relationship with magnitudes is represented in the following equation:

$$\log N = a - bM \quad (1)$$

where a and b are constants relating to y -intercept and slope of the log-curve, respectively. This slope (b value) is considered as an important seismic feature. It is used vastly by numerous researchers for the seismic analysis of the

Fig. 2 Flowchart of earthquake prediction methodology

region and earthquake prediction (Morales-Esteban et al. 2013; Reyes et al. 2013).

a and b values in the Gutenberg–Richter inverse power law form a regression line which is capable of estimating the frequency of future earthquakes. Sum of mean square deviation from the regression line of Gutenberg–Richter law (η) is considered to be an important seismic parameter. Equation (2) represents the difference between the actually occurred seismic events and those estimated by Gutenberg–Richter law. η shows the capability of a and b in terms of estimation of future earthquakes:

$$\eta = \frac{\sum (\log N_i - (a - bM_i))^2}{n - 1} \quad (2)$$

where N_i is the number of events of magnitude M_i and greater, while $n = 100$ is the total number of seismic events employed for calculation of parameters.

Gutenberg–Richter regression line can estimate the maximum expected earthquake magnitude in the previous n events using two-point line formula, as shown in Eq. 3. The difference between actual maximum occurred event and maximum expected event is also considered as a seismic precursor (M_{def}).

$$M_{\text{max,expected}} = \frac{a}{b}. \quad (3)$$

Seismic energy releases from every fault in the form of small seismic events on regular basis (Morales-Esteban et al. 2012). If seismic energy release stops for a longer period, it starts accumulating in the fault and the state is known as seismic quiescence. The accumulating energy

may release in the form of a major earthquake; therefore, it is also considered as a worthy seismic precursor. Square root of seismic energy release is calculated using the following equation:

$$dE^{\frac{1}{2}} = \frac{\sum (10^{11.8+1.5M})^{\frac{1}{2}}}{T}. \quad (4)$$

Average magnitude of the last n seismic events (M_{mean}) is also taken as a seismic precursor. It shows that whether the overall magnitude of seismic activity has increased or decreased. Formula for mean magnitude is given in the following equation:

$$M_{\text{mean}} = \frac{\sum_i M}{n}. \quad (5)$$

Sometimes, small earthquakes are observed before a major earthquake, called foreshocks. Frequency of foreshocks is another important seismic precursor. This precursor is expressed in terms of time elapsed in days (T) during the last n seismic events:

$$T = t_n - t_1. \quad (6)$$

Smaller value of T leads to the greater foreshock frequency and vice versa.

Another seismic precursor considered in this study is the mean time between characteristic events (μ) among the last n events. For example, the seismic events of magnitude between 4.5 and 5 are considered as a single earthquake magnitude, known as characteristic event. It can be calculated using Eq. 7. The duration between characteristic events (c) should be same ideally. The deviation from

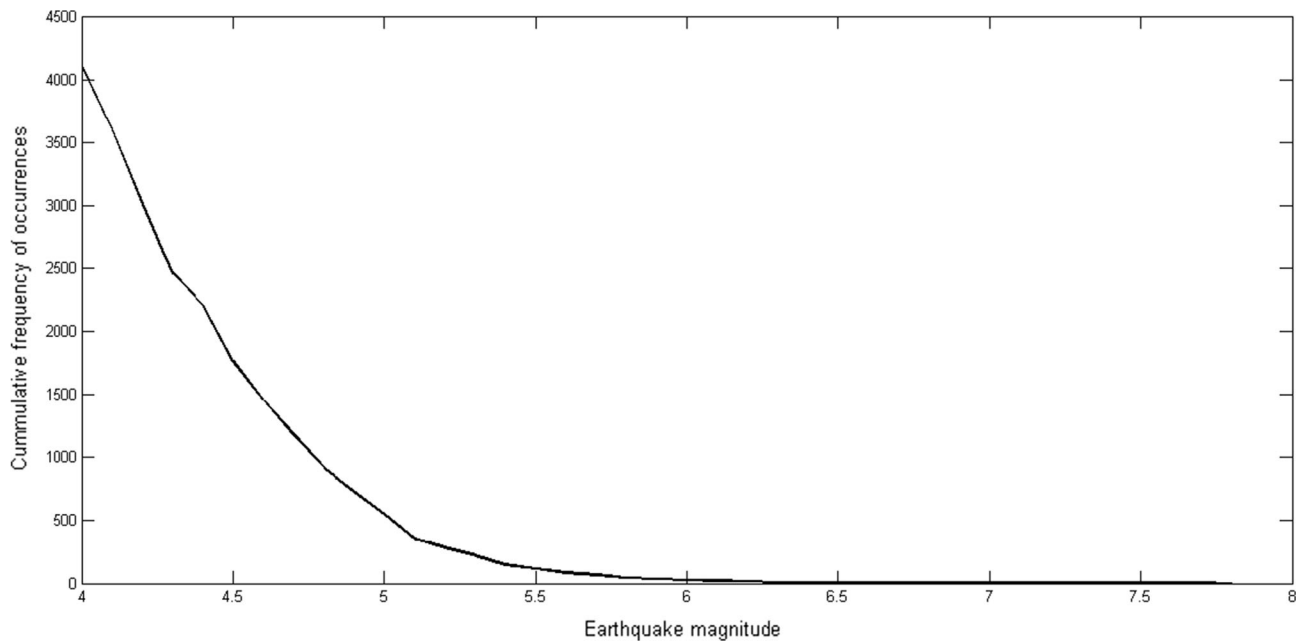


Fig. 3 Frequency–magnitude distribution of earthquake occurrences for northern Pakistan

mean time between characteristic events is calculated using Eq. 8, where σ_t is the standard deviation of observed time.

$$\mu = \frac{t_{i\text{characteristic}}}{n_{\text{characteristic}}} \quad (7)$$

$$c = \frac{\sigma_t}{\mu} \quad (8)$$

Figure 4 visualizes the structure of data set obtained for developing earthquake prediction models. Every instance corresponds to a feature vector of eight seismic parameters preceding every upcoming month. Earthquake corresponding to every feature vector is in the form of yes/no. Seismic activity is treated as a binary classification problem, as explained in “[Feed-forward neural network](#)”.

Feature selection

Seismic regions may show different behavior and properties from each other. It is, therefore, evident that every seismic feature may possess different information content. The eight seismic features are already calculated for northern Pakistan, but only selected seismic indicators are employed for developing earthquake prediction models. Information gain of every feature is calculated to realize their usefulness. Table 1 shows the normalized gain of every feature scaled between [0 1]. Normalized gain value of 1 corresponds to the maximum useful feature, while 0 relates to the features with negligible information content.

It can be observed that every seismic feature useful for other regions, such as Hindukush (Asim et al. 2016), Southern California, and San Francisco (Adeli and Panakkat 2009) regions, may not be equally useful for earthquake prediction in context of northern Pakistan. Therefore, the features with zero information gain are left out and only six seismic features with non-zero information gain are passed to computational intelligence techniques. Information gain of features is computed using WEKA data-mining tool (Hall et al. 2009).

Feed-forward neural network

In this study, multiple CI techniques are employed for creating earthquake prediction models, namely, Random Forest (RF), Recurrent Neural Network (RNN), Multi-layer Perceptron (MLP), Radial Basis Function (RBF), Support Vector Machine (SVM), and Feed-Forward Neural Network (FFNN). The reason for explaining only FFNN in detail is that it performed better for seismic activity prediction of northern Pakistan than other mentioned techniques. However, the introduction and implementation of other CI techniques are summarized in “[Results and discussion](#)”.

Artificial Neural Networks (ANNs) are a subfield of CI and have been used vastly in different fields for classification, regression, and decision purposes. ANN is a computational architecture which comprises of many sensory units called neurons. It is organized in a layer format, i.e., input layer, hidden layers, and output layer. Each layer

Fig. 4 Visualization of earthquake prediction data set

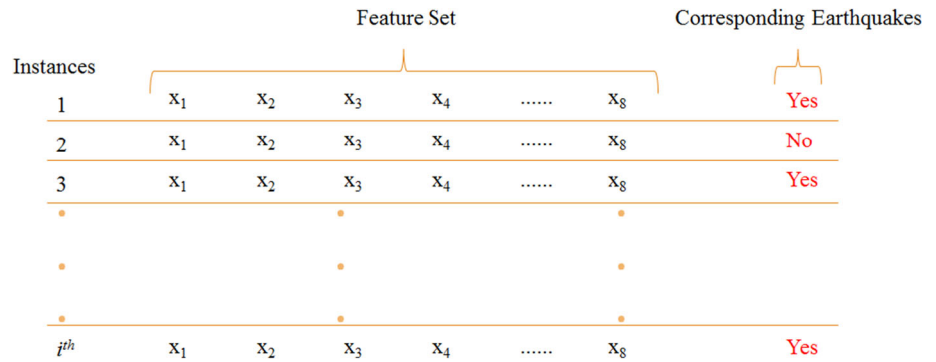


Table 1 Normalized information gain for every feature

Feature	Normalized info. gain
T	1.0
dE	0.81
μ	0.51
b	0.43
c	0.33
M_{mean}	0.30
M_{def}	0
η	0

consists of neurons which are connected to the neurons of the next layer. Feature vectors are passed to ANN through input layer, which communicates to the hidden layer via weighted synaptic connections. The real processing is concluded as weighted connections which can adapt conferring to the needs of system input patterns. The hidden layers are linked with outer layer, where final result is yielded (Fausett 1994).

A neural network is characterized by its topology and learning paradigm. In this study, FFNN has been applied to predict earthquake magnitude for the region of interest. In this topology of ANN, neurons in each layer are connected to all the neurons of the next layer through weighted connections. These weights are either inhibitory or excitatory and learning of ANN takes place through weights update. Since the neurons in this topology of ANN do not contain any loop back or self-connection, so these are not capable of storing current state. The signal can only propagate in forward direction.

Training of a neural network is basically iterative updating of synaptic weights and it employs supervised learning technique. Supervised learning means that seismic feature vector is provided as an input and actual earthquake in the subsequent month is provided as corresponding target output, for learning of model. There are different learning paradigms and the method used in this study is Levenberg–Marquardt Back Propagation (LMBP). During learning of model, features at input layer are forwarded to the next layer through weighted connections. The processed data

ultimately reach to the output neuron, where error is calculated between the outputs of network and actual targets. The error is then propagated in backward direction and weights of layers are updated accordingly. This procedure is termed back-propagation learning methodology. The learning stops when there are no changes recorded in the weight update process. In LMBP algorithm, the errors are minimized using Levenberg Marquardt algorithm, initially proposed by Levenberg (1944).

There are six input seismic features, and therefore, six input neurons are used in this ANN architecture. Each of these neurons is connected to all the neurons in first hidden layer which in turn are connected to all the neurons of the second hidden layer. The number of neurons in each hidden layer is selected to be 11 empirically. The second hidden layer leads to the single output neurons. Figure 5 shows the overall structure and layout of FFNN model developed in this work. Transfer function at each layer also determines the behavior of neural network. The transfer functions used for hidden layer 1 and hidden layer 2 is tan-sigmoid and log-sigmoid, as shown in Eqs. 9 and 10, respectively. The transfer function of output layer is also selected to be tan-sigmoid.

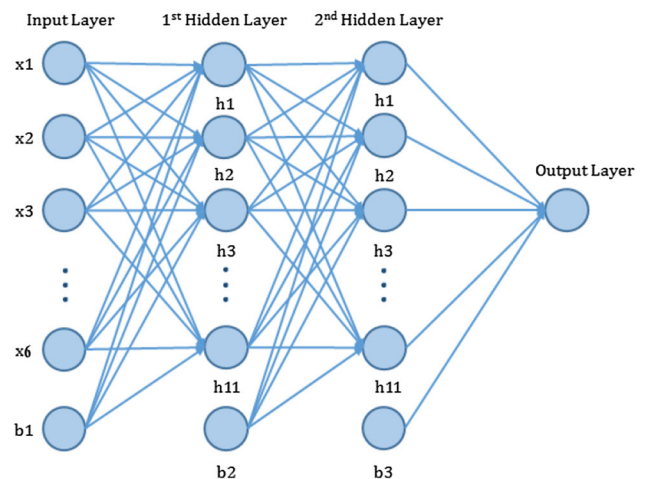


Fig. 5 Structure of FFNN employed for seismic activity prediction of northern Pakistan

$$T_1(n) = \tanh(cn) = \frac{e^{cn} - e^{-cn}}{e^{cn} + e^{-cn}} \quad (9)$$

$$T_2(n) = \frac{1}{1 + e^{-cn}}. \quad (10)$$

The number of unknown weights, w or synaptic connections in this architecture of neural network is given in the following equation:

$$w = (I + 1)H_1 + (H_1 + 1)H_2 + (H_2 + 1)O \quad (11)$$

where I is the number of input neurons, O is the output neuron, while H_1 and H_2 show the neurons in hidden layer 1 and hidden layer 2 of ANN.

Earthquake prediction task is treated as a binary classification problem and setup is arranged to predict earthquakes of magnitude M_w 5.0 and above. There are total 364 feature vectors out of which 70% are used for training of ANN which account to almost 255 instances and the rest of 109 instances are used for testing purposes. Corresponding to every training vector, maximum earthquake magnitude that actually occurred in the subsequent month is selected as a target magnitude, which is further converted to binary class by applying threshold. During training of a supervised learning model, both inputs and target outputs are provided. Once a model is trained, it can be tested over unseen data from the past by passing just feature vectors. The results obtained for training and testing data are further discussed according to the performance evaluation criteria, as given in “[Performance evaluation parameters](#)”.

Results and discussion

The prediction model needs to be backed by certain performance evaluation criteria. This section describes the parameters used to assess the performance of the all the prediction methodologies. Later, the results are discussed and comparison of FFNN is drawn with the results of other CI techniques.

Performance evaluation parameters

Basic performance measures for binary classification problems are True Positive (TP), False Positive (FP), True Negative (TN), and False Negative (FN). In addition, there are some other evaluation criteria which are derived from these four measures and represent overall proficiency of the prediction algorithm. These evaluation criteria consist of Sensitivity (S_n), Specificity (S_p), Positive Predictive Value (PPV), Negative Predictive Value (NPV), accuracy, R score, and Matthew’s Correlation Coefficient (MCC).

S_n represents the rate of actual positives predicted by algorithm and is calculated using Eq. 12. S_p means the rate

of actual negative predictions of algorithm and is calculated using Eq. 13. PPV and NPV account for the ratio of actual positives among all positive predictions and ratio of actual negatives among all the negative predictions, as shown in Eqs. 14 and 15, respectively. Thus, for a reliable algorithm generating least false alarms, these value must be high:

$$S_n = \frac{TP}{TP + FN} \quad (12)$$

$$S_p = \frac{TN}{TN + FP} \quad (13)$$

$$PPV = \frac{TP}{TP + FP} \quad (14)$$

$$NPV = \frac{TN}{TN + FN}. \quad (15)$$

Accuracy is general evaluation criterion and used in many performance evaluations. It accounts for all the actual predictions of algorithm, irrespective of positive or negative predictions. It is calculated using the following equation:

$$Accuracy = \frac{TP + TN}{TP + FP + TN + FN}. \quad (16)$$

When the available data set is highly unbalanced, which means that one of the two classes is in abundance, then value of accuracy does not represent the actual strength of prediction algorithm. For example, if there is a data set containing 100 instances out of which 90 instances actually belong to class 1 while remaining belongs to class 2. The available prediction algorithm is incapable of classifying these instances and ends up predicting class 1 for every instance. In such a case, the accuracy will be 90%, but it does not represent the true worth of the prediction algorithm. Therefore, some other performance measures are also considered, such as MCC and R score, which give the balanced measure of TP, FP, TN, and FN.

MCC was proposed by a biochemist (Matthews 1975). It is calculated using Eq. 17. Hanssen–Kuipers discriminant (R score or True skill statistics) is also used for evaluation of prediction algorithms and calculated using Eq. 18:

$$MCC = \frac{TP \times TN - FP \times FN}{\text{sqrt}((TN + FN)(TP + FP)(TP + FN)(TN + FP))} \quad (17)$$

$$R = \frac{TP \times TN - FP \times FN}{(TP + FN)(FP + TN)}. \quad (18)$$

The value of MCC and R score varies between -1 and $+1$. The value $+1$ represents the perfect prediction model, -1 expresses total disagreement between predicted values and actual values and 0 represents random behavior of the prediction technique. The values ranging from 0.01 to 0.19

Table 2 Training results for ANN for northern Pakistan

Parameter	Value
TP	54
FP	18
TN	134
FN	49
S_n	0.52
S_p	0.88
PPV	0.75
NPV	0.73
Accuracy	0.74
R score	0.40
MCC	0.44

Table 3 Testing results of earthquake prediction for northern Pakistan

Parameter	Value
TP	21
FP	6
TN	56
FN	26
S_n	0.44
S_p	0.90
PPV	0.77
NPV	0.68
Accuracy	0.70
R score	0.35
MCC	0.40

represent negligible relationship between features and outputs and the values between 0.20 to 0.29 show weak positive relationship. Moderate relationship is shown onwards from 0.3 to 0.39 and it gets stronger with increasing value (Matthews 1975).

Training of ANN

Supervised learning techniques are used for the training of ANN, using 255 training instances along with the target class, as mentioned in “[Feed-forward neural network](#)”. The network adapts itself to the corresponding inputs and outputs by changing synaptic weights. After completion of training, the network is presented with the same set of feature vectors used for training and the results predicted by network is given in Table 2.

Testing of ANN

After training of ANN, six seismic precursor-based feature vectors for upcoming months are used to obtain predictions on unseen data. These prediction results are then compared to the actual earthquake occurrences and prediction model is evaluated on the basis of criteria, as given in Eqs. 12–18. The results of earthquake prediction on unseen data is listed in Table 3.

Feed-forward NN gives meaningful and promising results for earthquake prediction. Five other earthquake prediction models in addition to FFNN have also been applied separately to the same data set for generating predictions. The results of all the techniques are evaluated and compared through the aforementioned criteria. The setup arranged for their application is mentioned below:

- Multi-Layer Perceptron (MLP) (Haykin 1998): MLP is an ANN-based prediction model. The values of momentum and learning rate for setting up MLP is kept to 0.4 and 0.5, respectively.
- Radial Basis Function (RBF) (Broomhead and Lowe 1988): RBF is another ANN-based prediction model. The value of minimum clusters is kept to 2 and minimum standard deviation has been set to 0.5.
- Random Forest (RF) (Ho 1998): RF is a tree-based classifier. It is basically a multitude of different decision trees. It takes seismic features from top and passes them to bottom through intermediate branches. The lowest layer of trees leads to the decision about earthquake prediction. The number of trees employed to generate the random forest are selected to be 10.
- Recurrent Neural Network (RNN) (Williams and Zipser 1989): RNN is also a different type of ANN, which has the capability to retain memory of the previous step. The network topology consists of two hidden layers containing seven neurons in each layer. The transfer function used for hidden layer 1 and hidden layer 2 are tan-sigmoid and log-sigmoid, respectively, as given in Eqs. 9 and 10.
- Support Vectors Machine (SVM) (Cristianini and Shawe-Taylor 2000): SVM is a classifier that discriminates between earthquake and non-earthquake through drawing hyperplane in feature space. For applying SVM on data set Gaussian radial basis kernel function is selected with spread of 4.4.

MLP and RBF are implemented using WEKA data mining. Similarly, RF, RNN and SVM have been implemented in MATLAB. The setup parameters for every classifier are selected on the basis of experimentation. Every classifier is evaluated on different combinations of setup parameters during training. The performance for all the combinations is recorded, and in the end, the parameters with best performance are chosen. For example, SVM is trained for different values of Gaussian spread, ranging from 0.1 to 10, with step increment of 0.1. The best training performance of SVM is noted with the Gaussian spread of 4.4, which is, therefore, retained as the finalized parameter for classifier.

Results generated by each of applied technique are presented in Table 4 and a comparison is drawn with the results of FFNN. It is demonstrated that FFNN outperforms other applied classification models for northern Pakistan region. RNN is found to be showing the second best results for earthquake prediction in terms of PPV, R score, and MCC.

Considering the fact that there exists no robust earthquake prediction tool, the results generated by FFNN are quite encouraging over unseen dataset. A major issue in earthquake prediction problem is the false alarm (FP) generation, which is highly undesired. The results show that FFNN-based model is capable of predicting earthquakes with accuracy of 70%, with a very low false alarm ratio. Positive predictive ratio of 78% shows that out of 100 predictions, 78 are found to be true, and therefore, false alarm tendency of the algorithm is just 22%, which is noteworthy for this field of research. Furthermore, 0.40 value of MCC shows that an acceptable relationship exists between the parameters and earthquake occurrences. The results obtained through other models, given in Table 4, are also meaningful, thus motivating the researchers to explore earthquake prediction ideas through merging of seismology with computational intelligence and data-mining techniques.

McNemar's statistical test

McNemar's statistical test is performed on prediction results to validate the performance of the aforementioned models. The results obtained through all the techniques are compared with actual earthquake occurrences and significance values (p value) are calculated. The p value shows whether there exists a notable difference in the results of

Table 4 Comparison of different models for earthquake prediction in terms of the performance evaluation parameters

Parameter	MLP	RBF	RF	RNN	SVM	FFNN
TP	25	21	21	19	29	21
FP	14	16	14	7	24	6
TN	48	46	48	55	38	56
FN	22	26	26	28	18	26
S_n	0.53	0.44	0.44	0.40	0.62	0.45
S_p	0.77	0.74	0.77	0.88	0.61	0.90
PPV	0.64	0.56	0.60	0.73	0.55	0.78
NPV	0.68	0.63	0.64	0.66	0.68	0.68
Accuracy	0.66	0.61	0.63	0.68	0.61	0.70
R score	0.30	0.18	0.22	0.30	0.23	0.35
MCC	0.31	0.19	0.23	0.33	0.23	0.40

Table 5 McNemar's test statistics for prediction models compared with other classifiers

Prediction models	Significance (p)
MLP	0.2430
RBF	0.1641
RF	0.0807
RNN	0.005
SVM	0.4408
FFNN	0.005

two techniques or not. If the statistical significance level, i.e., p value is less than 0.05, then results are statistically significant and the proportion of "Yes" responses for one technique is significantly similar to the actual results. Alternatively, if p value is greater than 0.05, then results are not statistically significant. Table 5 lists the p values obtained for earthquake predictions of the applied computational intelligence models as compared to the actual earthquake occurrences.

Differences in the performance of MLP, RBF, RF, RNN, FFNN, and SVM over actual results can be assessed through confusion matrices. The p value for MLP is 0.2430, showing that there is significant difference in the earthquake predictions of MLP and actual occurrences. The p value for RBF is 0.1641, representing that there is significant difference in the performance of RBF and actual results. The p value for RF is 0.0807, showing that it is better than MLP and RBF. However, there is still a significant difference in the predictions of RF and actual earthquake occurrences. The p value for RNN is 0.005 representing that the results obtained through this model are nearer to the actual results. The p value for SVM is 0.4408, which shows that it is the least performing prediction model. The p value for FFNN is 0.005 proving that its results are closer to the actual earthquake occurrences.

McNemar's test validates that FFNN and RNN are statistically significant as compared to other applied techniques. Both RNN- and FFNN-based predictions are leading to the p value of 0.005 when compared with actual results. FFNN is ahead of RNN in terms of PPV and MCC. Therefore, it is concluded that FFNN-based model is better suited for earthquake prediction for northern Pakistan region.

Conclusions

This study has explored the suitability of using different computational intelligence techniques to predict earthquakes in northern Pakistan. Thus, the application of six different models has been studied, showing overall

satisfactory results. From all of them, feed-forward neural network highlighted, with particularly few false positives, reached to the accuracy of 75%. Future works are directed towards the joint use of several machine learning algorithms to obtain better results: ad hoc ensembles are expected to perform better. In addition, adapting neural networks to be used in imbalanced data sets is proposed to predict magnitude for large earthquakes.

Acknowledgements The authors would like to thank friends and colleagues for nice suggestions, in particular, Mr. Iqbal Murtza for his valuable remarks and guidance. Spanish Ministry of Science and Technology, Junta de Andalucía and University Pablo de Olavide under projects TIN2011-28956-C02, P12-TIC-1728 and APPB813097 are also acknowledged.

References

- Adeli H, Panakkat A (2009) A probabilistic neural network for earthquake magnitude prediction. *Neural Netw* 22:1018–1024
- Alarifi ASN, Alarifi NSN, Al-Humidan S (2012) Earthquakes magnitude prediction using artificial neural network in northern Red Sea area. *J King Saud Univ Sci* 24:301–313
- Ali Z, Qaisar M, Mahmood T, Shah MA, Iqbal T, Serva L, Michetti AM, Burton PW (2009) The Muzaffarabad, Pakistan, earthquake of 8 October 2005: surface faulting, environmental effects and macroseismic intensity. *Geol Soc Lond Spec Publ* 316(1):155–172
- Anad M, Dash A, Kumar MSJ, Kesarkar A (2011) Prediction and classification of thunderstorms using artificial neural network. *Int J Eng Sci Technol* 3(5):4031–4035
- Arshad J, Zameer A, Khan A (2014) Wind power prediction using genetic programming based ensemble of artificial neural networks (GPeANN). In: Proceedings of the 12th international conference on frontiers of information technology. FIT '14, pp 257–262
- Asencio-Cortés G, Martínez-Álvarez F, Morales-Esteban A, Reyes J, Troncoso A (2015a) Improving earthquake prediction with principal component analysis: application to Chile. In: Hybrid artificial intelligent systems: 10th international conference, HAIS 2015, Bilbao, Spain, June 22–24, 2015, Proceedings. Springer International Publishing, pp 393–404
- Asencio-Cortés G, Martínez-Álvarez F, Troncoso A, Morales-Esteban A (2015b) Medium-large earthquake magnitude prediction in Tokyo with artificial neural networks. *Neural Comput Appl* 28:1043–1055
- Asim KM, Idris A, Martínez-Álvarez F, Iqbal T (2016) Short term earthquake prediction in Hindukush region using tree based ensemble learning. In: 2016 International conference on frontiers of information technology (FIT), pp 365–370. doi:10.1109/FIT.2016.073
- Asim K, Martínez-Álvarez F, Basit A, Iqbal T (2017) Earthquake magnitude prediction in Hindukush region using machine learning techniques. *Nat Hazards* 85(1):471–486
- Awais M, Barkat A, Ali A, Rehman K, Ali Zafar W, Iqbal T (2017) Satellite thermal IR and atmospheric radon anomalies associated with Haripur earthquake (Oct 2010; M_w 5.2), Pakistan. *Adv Space Res*. doi:10.1016/j.asr.2017.08.034
- Barkat A, Ali A, Siddique N, Alam A, Wasim M, Iqbal T (2017) Radon as an earthquake precursor in and around northern Pakistan: a case study. *Geochem J* 51(4):337–346
- Bath M (1965) Lateral inhomogeneities in the upper mantle. *Tectonophysics* 2:483–514
- Broomhead DS, Lowe D (1988) Radial basis functions, multi-variable functional interpolation and adaptive networks. Technical report, DTIC Document
- Cristianini N, Shawe-Taylor J (2000) An introduction to support vector machines and other kernel-based learning methods. Cambridge University Press, Cambridge
- Fausett L (1994) Fundamentals of neural networks: architectures, algorithms, and applications. Prentice-Hall Inc, Upper Saddle River
- Florido E, Martínez-Álvarez F, Morales-Esteban A, Reyes J, Aznarte JL (2015) Detecting precursory patterns to enhance earthquake prediction in Chile. *Comput Geosci* 76:112–120
- Graves A, Mohamed AR, Hinton G (2013) Speech recognition with deep recurrent neural networks. In: 2013 IEEE international conference on acoustics, speech and signal processing, pp 6645–6649. doi:10.1109/ICASSP.2013.6638947
- Gutenberg B, Richter CF (1954) Seismicity of the Earth. Princeton University, Princeton
- Hall M, Frank E, Holmes G, Pfahringer B, Reutemann P, Witten IH (2009) The WEKA data mining software: an update. *ACM SIGKDD Explor Newsl* 11(1):10–18
- Hassan A, Riaz F, Basit A (2015) A robust classification model with voting based feature selection for diagnosis of epilepsy. In: 2015 IEEE 28th Canadian conference on electrical and computer engineering (CCECE), pp 176–179. doi:10.1109/CCECE.2015.7129181
- Haykin S (1998) Neural networks: a comprehensive foundation, 2nd edn. Prentice Hall PTR, Upper Saddle River, NJ, USA
- Helmstetter A, Kagan YY, Jackson DD (2007) High-resolution time-independent grid-based forecast for $M = 5$ earthquakes in California. *Seismol Res Lett* 78(1):78–86
- Ho TK (1998) The random subspace method for constructing decision forests. *IEEE Trans Pattern Anal Mach Intell* 20(8):832–844
- Houlié N, Komorowski JC, de Michele M, Kasereka M, Ciraba H (2006) Early detection of eruptive dykes revealed by normalized difference vegetation index (NDVI) on Mt. Etna and Mt. Nyiragongo. *Earth Planet Sci Lett* 246(3–4):231–240
- Idris A, Rizwan M, Khan A (2012) Churn prediction in telecom using Random Forest and PSO based data balancing in combination with various feature selection strategies. *Comput Electr Eng* 38:1808–1819
- Ikram A, Qamar U (2015) Developing an expert system based on association rules and predicate logic for earthquake prediction. *Knowl Based Syst* 75:87–103
- Jilani Z, Mehmood T, Alam A, Awais M, Iqbal T (2017) Monitoring and descriptive analysis of radon in relation to seismic activity of Northern Pakistan. *J Environ Radioact* 172:43–51
- Jouanne F, Awan A, Pêcher A, Kausar A, Mugnier J, Khan I, Khan N, Van Melle J (2014) Present-day deformation of northern Pakistan from Salt Ranges to Karakorum Ranges. *J Geophys Res Solid Earth* 119(3):2487–2503
- Kagan YY, Jackson DD, Rong Y (2007) A testable five-year forecast of moderate and large earthquakes in southern California based on smoothed seismicity. *Seismol Res Lett* 78(1):94–98
- Kazmi AH, Jan MQ (1997) Geology and tectonics of Pakistan. Graphic Publishers, Karachi
- Kazmi AH, Rana RA, Asrarullah, (1982) Tectonic map of Pakistan. Government of Pakistan, Ministry of Petroleum and Natural Resources
- Keilis-Borok V, Kossobokov V (1990) Premonitory activation of earthquake flow: algorithm M8. *Phys Earth Planet Inter* 61:73–83
- Keilis-Borok V, Soloviev AA (2003) Nonlinear dynamics of the lithosphere and earthquake prediction. Springer Science & Business Media, Dordrecht

- Kemal A (1992) Geology and new trends for hydrocarbon exploration in Pakistan. In: Proceedings of international petroleum seminar, 22–24 November 1991, Islamabad, pp 16–57
- Kossobokov V (1997) User manual for M8 algorithms for earthquake statistics and prediction. IASPEI Softw Libr 6:1–33
- Kossobokov V, Romashkova L, Panza G, Peresan A (2002) Stabilizing intermediate-term medium-range earthquake predictions. *J Seismol Earthq Eng* 4:11–19
- Last M, Rabinowitz N, Leonard G (2016) Predicting the maximum earthquake magnitude from seismic data in Israel and its neighboring countries. *PLoS One* 11(1):e0146101
- Levenberg K (1944) A method for the solution of certain non-linear problems in least squares. *Q Appl Math* 2:164–168
- Martínez-Álvarez F, Reyes J, Morales-Esteban A, Rubio-Escudero C (2013) Determining the best set of seismicity indicators to predict earthquakes. Two case studies: Chile and the Iberian Peninsula. *Knowl Based Syst* 50:198–210
- Matthews BW (1975) Comparison of the predicted and observed secondary structure of T4 phage lysozyme. *Biochim Biophys Acta Protein Struct* 405:442–451
- Morales-Esteban A, de Justo JL, Martínez-Álvarez F, Azañón JM (2012) Probabilistic method to select calculation accelerograms based on uniform seismic hazard acceleration response spectra. *Soil Dyn Earthq Eng* 43:174–185
- Morales-Esteban A, Martínez-Álvarez F, Reyes J (2013) Earthquake prediction in seismogenic areas of the Iberian Peninsula based on computational intelligence. *Tectonophysics* 593:121–134
- Murtza I, Abdullah D, Khan A, Arif M, Mirza SM (2017) Cortex-inspired multilayer hierarchy based object detection system using PHOG descriptors and ensemble classification. *Vis Comput* 33(1):99–112
- Panakkat A, Adeli H (2007) Neural network models for earthquake magnitude prediction using multiple seismicity indicators. *Int J Neural Syst* 17(1):13–33
- Pécher A, Seeber L, Guillot S, Jouanne F, Kausar A, Latif M, Majid A, Mahéo G, Mugnier JL, Rolland Y, van der Beek P, Van Melle J (2008) Stress field evolution in the northwest Himalayan syntaxis, northern Pakistan. *Tectonics* 27(6):n/a–n/a. doi:10.1029/2007TC002252
- Petersen MD, Cao T, Campbell KW, Frankel AD (2007) Time-independent and time-dependent seismic hazard assessment for the state of California: uniform California earthquake rupture forecast model 1.0. *Seismol Res Lett* 78(1):99–109
- Pulinets S, Ouzounov D (2011) Lithosphere–Atmosphere–Ionosphere Coupling (LAIC) model—an unified concept for earthquake precursors validation. *J Asian Earth Sci* 41(4):371–382
- Rafiei MH, Adeli H (2017) NEEWS: a novel earthquake early warning model using neural dynamic classification and neural dynamic optimization. *Soil Dyn Earthq Eng* 100:417–427
- Ramar K, Mirmalinee TT (2012) An ontological representation for tsunami early warning system. In: IEEE-international conference on advances in engineering, science and management (ICAESM -2012), pp 93–98
- Rehman K, Ali W, Ali A, Barkat A (2017) Shallow and intermediate depth earthquakes in the Hindu Kush region across the Afghan-Pakistan border. *J Asian Earth Sci*. doi:10.1016/j.jseas.2017.09.005
- Reyes J, Morales-Esteban A, Martínez-Álvarez F (2013) Neural networks to predict earthquakes in Chile. *Appl Soft Comput* 13(2):1314–1328
- Sercombe WJ, Pivnik DA, Wilson WP, Albertin ML, Beck RA, Stratton MA (1998) Wrench faulting in the northern Pakistan foreland. *AAPG Bull* 82(11):2003–2030
- Utsu T, Ogata Y, Matsu'ura RS (1995) The centenary of the Omori formula for a decay law of aftershock activity. *J Phys Earth* 43:1–33
- Wang Q, Guo Y, Yu L, Li P (2017) Earthquake prediction based on spatio-temporal data mining: an LSTM network approach. *IEEE Trans Emerg Top Comput PP(99):1–1*. doi:10.1109/TETC.2017.2699169
- Williams RJ, Zipser D (1989) A learning algorithm for continually running fully recurrent neural networks. *Neural Comput* 1(2):270–280
- Yan T, Pietrafesa LJ, Dickey DA, Gayes PT, Bao S (2015) Seasonal prediction of landfalling hurricanes along Eastern Seaboard of the United States. *Int J Climatol* 35(9):2647–2653

Validation of recent geopotential models in Tierra Del Fuego

Maria Eugenia Gomez^{1,2} · Raul Perdomo^{1,2} · Daniel Del Cogliano^{1,2}

Received: 28 December 2016 / Accepted: 13 September 2017 / Published online: 22 September 2017
© Institute of Geophysics, Polish Academy of Sciences & Polish Academy of Sciences 2017

Abstract This work presents a validation study of global geopotential models (GGM) in the region of Fagnano Lake, located in the southern Andes. This is an excellent area for this type of validation because it is surrounded by the Andes Mountains, and there is no terrestrial gravity or GNSS/levelling data. However, there are mean lake level (MLL) observations, and its surface is assumed to be almost equipotential. Furthermore, in this article, we propose improved geoid solutions through the Residual Terrain Modelling (RTM) approach. Using a global geopotential model, the results achieved allow us to conclude that it is possible to use this technique to extend an existing geoid model to those regions that lack any information (neither gravimetric nor GNSS/levelling observations). As GGMs have evolved, our results have improved progressively. While the validation of EGM2008 with MLL data shows a standard deviation of 35 cm, GOCO05C shows a deviation of 13 cm, similar to the results obtained on land.

Keywords Global geopotential models · RTM data · Tierra del Fuego · GOCE · EGM2008

Introduction

With the advent of the GOCE (Gravity field and steady-state Ocean Circulation Explorer) and GRACE (Gravity Recovery and Climate Experiment) dedicated gravity

satellite missions, global geopotential models (GGMs) started to be regularly produced. Some are satellite-only models, like GO_CONS_GCF_2_TIM_R5 (Brockmann et al. 2014), GOCO05s (Mayer-Gürr, T. and the GOCO Team 2015), and EIGEN-6S4v2 (Förste et al. 2016), with a spherical harmonic expansion of the gravity field up to degree 180–200. There are also combined models that use satellite data in combination with terrestrial data. Some notable examples include EGM96 (Lemoine et al. 1998), EGM2008 (Pavlis et al. 2012), the EIGEN family (Förste et al. 2013, 2014, among others), and the most recent GOCO05C (Fecher et al. 2017).

The availability of so many GGMs often presents a challenge to the user regarding which model to use. Therefore, the regional validation of GGMs plays an important role, since their performance is not homogeneous over the entire planet. Erol (2012) indicates that this is a way to provide reliable information on the GGMs' performance and their adjustment to the local gravity field.

The error of the GGMs can be divided into two types: commission and omission errors (Jekely 2009). The former is related to the quality of the spherical harmonic coefficient determination, which depends on the quality of the input data. The latter is caused by the truncation of the spherical harmonics' expansion up to a maximum degree. This truncation is related to data distribution which has a limited spatial resolution (Torge and Müller 2012). The quality and distribution of the data sets used in a GGM solution (especially terrestrial gravity) constrain the accuracy of any gravity field functional computed via a spherical harmonic synthesis.

GGMs are commonly examined according to different methods: through their coefficients and formal error degree variances, comparison against a reference GGM, and by means of external data such as GNSS/levelling (Tsoulis

✉ Maria Eugenia Gomez
eugegomez80@gmail.com

¹ Facultad de Ciencias Astronómicas y Geofísicas, Universidad Nacional de la Plata, La Plata, Argentina

² Consejo Nacional de Investigaciones Científicas y Técnicas, Buenos Aires, Argentina

and Patlakis 2013; Ustun and Abbak 2010; Vergos et al. 2006).

When the evaluation of GGMs comprises observed data such as GNSS/levelling, it is necessary to take into account that they contain the full gravity spectrum, while GGM geoid heights or height anomalies contain the gravity spectrum up to a certain degree and order.

This paper presents a case study of a small region, located in the southern part of Tierra del Fuego Island, which is notable for the absence of terrestrial data included in any GGM. Since mean lake level (MLL) data exists for the region, it constitutes a valuable test area for the evaluation of GGMs. This information was derived from GPS buoys and simultaneous pressure tide gauge observations (Del Cogliano et al. 2007) on the Fagnano Lake, which are not included as input data in any GGM. Therefore, they can be considered as independent data. In addition, there is no terrestrial gravity data available for the lake surroundings because this region is part of the southern Andes, and it is characterised by the absence of roads and on-land access. Thus, as explained in Gomez et al. (2013) these MLL measurements represent the only geodetic information available to validate GGMs in the southern part of Tierra del Fuego.

The aim of this work is to validate and examine some of the latest combined GGMs to reveal their improvements in the modelling of the gravitational field. The selected models are: EGM2008, EIGEN6C4, GECO, GGM05c, and GOCO05C.

The comparisons will be made against the height anomalies derived from GNSS/levelling points and the previously mentioned MLL data.

Previous validations of the GOCO05C yielded the following RMS between geoid heights derived from the model and GNSS/levelling data for Australia, Germany, Brazil, and the USA: 24, 4, 30, and 58 cm, respectively (Fecher et al. 2017). Similar results have been obtained when evaluating EGM2008 and EIGEN6C4 in the countries mentioned above, except for the USA, which shows an RMS of 24.5 cm (Förste et al. 2014).

In the case of Argentina, the validation of EGM2008 on GNSS/levelling points indicates an RMS of 31 cm, while EIGEN6C4 yields 28 cm, when the 2016 levelling network adjustment is considered (Piñon 2016).

For previous GGMs, including EGM2008, 15–10 cm RMS were obtained when evaluating on GNSS/levelling points located in the Argentine portion of Tierra del Fuego (Tocho 2012; Gomez et al. 2014).

The omission error can be estimated by a high degree GGM like EGM2008, or by the combination of a GGM with Residual Terrain Modelling (RTM) data to take into account the short frequency of the Earth's gravity field spectrum (Hirt et al. 2010). Improvements are not expected

in all the tested cases since, according to Ferreira et al. (2013), GGMs do not always show a significant improvement at the shortest wavelengths of the gravity field. They depend not only on the local gravity data considered to develop the GGMs, but also on the capability of the digital terrain model (DTM) to represent the topographic structures.

EGM2008 is commonly used to estimate the omission error (Hirt et al. 2010; Alothman et al. 2016; Ferreira et al. 2013; Godah et al. 2015; Bomfin et al. 2013; among others). But, as established in Yi and Rummel (2013), it will not show a good performance in those areas where the surface gravity data available for the development of EGM2008 were poor or fill-in data. This is the case for the southern part of Tierra del Fuego.

In this study, the omission error will be determined in three different ways: using EGM2008 at the short wavelengths, by extending the spectral content of EGM2008 with RTM data, and by computing the omission error from RTM data only.

DATA and methodology

MLL data

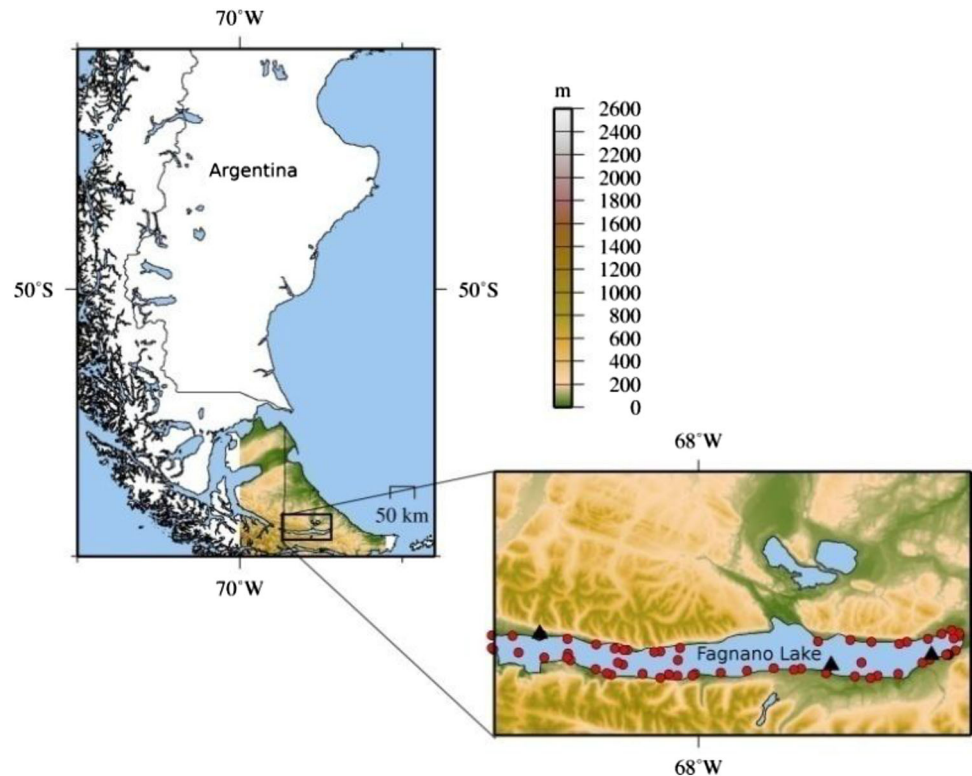
Fagnano Lake is located in the south-western part of Tierra del Fuego, the southernmost province of Argentina. It has an east–west extension of 100 km (Fig. 1), is 7 km wide, and has a maximum depth of 206 m (Lodolo et al. 2007). It is surrounded by mountains whose heights vary from 200 to 1000 m.

After two campaigns of GPS buoy observations, together with the information provided by three tide gauges on the lake bed (Richter et al. 2010), Del Cogliano et al. (2007) determined the MLL. This surface, which approximates an equipotential surface, was tied to the vertical datum of Tierra del Fuego through GPS/levelling points as explained in Del Cogliano et al. (2007) and Gomez et al. (2013). The accuracy of these 81 MLL observations was estimated at 5 cm RMS for one buoy position, and 2 cm RMS for the entire profile.

The uncertainty of the MLL observations depends not only on the uncertainties of the GPS buoys and tide gauge observations, but also on spatio-temporal lake level variations. The tide gauge measurements were used to reduce the instantaneous buoy observations to the mean lake level. The MLL accounts for the major driving mechanisms like the response to atmospheric forcing, seiches, water volume fluctuations, and lake tides, among others (Richter et al. 2010; Del Cogliano et al. 2007).

As noted in the paragraphs above, MLL observations are derived directly from GPS observations which were

Fig. 1 The study region, located in southern Argentina. The enclosed rectangle shows the area and topography surrounding Fagnano Lake. Additionally, it shows the distribution of MLL observations (red dots) and tide gauges (black triangles). The topography surrounding the lake is represented by SRTM digital terrain model (Farr et al. 2007)



processed following the IERS Convention 2003 (McCarthy and Petit 2004). Therefore, they are expressed in a tide-free system (Richter, pers. comm.).

GNSS/levelling

GPS coordinates of 67 levelling marks were determined during several field campaigns in the Argentine part of Tierra del Fuego Island. The accuracy of the ellipsoidal heights is 3 cm.

Regarding the height system, all levelling data located in this part of Tierra del Fuego references the Ushuaia tide gauge. The accuracy of the levelling information (in millimetres), is in agreement with the levelling specifications of $3 \text{ mm } \sqrt{k}$, where k is the length of the levelled line in km. In the case of Tierra del Fuego, this implies an accuracy of about 1 cm, whereas in other regions it is close to mm accuracy (IGN 2016) since the levelling lines constitute closed circuits.

This information allows the determination of the geoid or quasigeoid with an accuracy of about 3 cm. In this study, no distinction was made between geoid height and height anomalies because, as established in Gomez et al. (2014), the difference between these gravity field functionals is less than 2 cm in the study region. Moreover, this difference was insignificant when compared to the discrepancies between GGMs and GNSS/levelling or MLL data in the Fagnano Lake area.

Concerning the tide system, GNSS/levelling results refer to a tide-free system.

Global geopotential models

As established by Pavlis (2010), GGMs are mathematical approximations to the external gravitational potential of an attracting body, which in this case is the Earth.

The disturbing gravitational potential, T , written in spherical harmonics, can be developed up to a certain maximum degree (N_{max}) as expressed in Eq. 1 (Heiskanen and Moritz 1967; Torge 2001):

$$T(r, \lambda, \varphi) = \frac{GM}{r} \sum_{n=2}^{N_{max}} \left(\frac{R}{r}\right)^n \sum_{m=0}^n P_n^m(\sin(\varphi)) (\bar{C}_{nm}^T \cos(m\lambda) + \bar{S}_{nm}^T \sin(m\lambda)), \tag{1}$$

where GM and R are the geocentric gravitational constant and the mean equatorial radius of the Earth, respectively.

$P_n^m \sin(\varphi)$ denotes the fully normalised associated Legendre functions. \bar{C}_{nm}^T and \bar{S}_{nm}^T are the residual harmonic coefficients derived from the difference between the actual and normal gravity field. Finally, (r, λ, ϕ) represent the spherical geocentric coordinates of the specific point where the disturbing potential is computed.

The zero and first-degree term are assumed to be zero because it is considered that the mass of the Earth and the

mass of the reference ellipsoid coincide. The implications of this assumption will be discussed later.

Table 1 provides a list of the models used in this work, and their main characteristics. At the time this work started, the selection was made because it was considered that they represented the latest combined models which involve GOCE data, thus allowing the investigation of the evolution of these GGMs in regions like the southern Andes. Although they are all combined models, they differ in the solution combination technique, as well as in the satellite and the terrestrial data included. EGM2008 (Pavlis et al. 2012) was used because it can be considered to be a classical geopotential model, and the first GGM that reached a global resolution of 9 km. It has full resolution to degree and order 2159 of the spherical harmonic expansion and provides additional coefficients to degree 2190 and order 2159 (Hirt et al. 2010; Pavlis et al. 2012). This resolution depends on the availability of accurate topographic data.

As seen in Table 1, with the exception of EGM2008, the models include GOCE data. They differ in the number of days of GOCE and GRACE data considered, as well as the altimetry and terrestrial data used.

GOCO05C is one of the latest combined models based on almost 4 years of GOCE, as well as GRACE, data and a grid of DTU13 gravity anomalies (Andersen et al. 2014) whose spatial resolution is $15' \times 15'$. It is independent of EGM2008, while EIGEN6C4 and GECO include EGM2008 information to reach their maximum degree of the spherical harmonic expansion.

GGM05C includes DTU13 terrestrial gravity anomalies in addition to the GOCE and GRACE data listed in Table 1. It combines surface gravity information with GGM05G to obtain the GGM05C solution (Ries et al. 2016).

EIGEN6C4 is a combined GGM up to degree 2190. It includes LAGEOS data, as well as 10 years of GRACE data. It also contains GOCE-SGG information. A grid of DTU10 global gravity anomalies plus EGM2008 from degree 370 onwards allows the model to reach its maximum degree.

Finally, GECO integrates the GOCE TIM R5 and EGM2008 information (Gilardoni et al. 2016).

Except GOCO05C, all of the listed GGMs are expressed in the tide-free system, as far as the permanent tide is concerned. Here, the GOCO05C model was also used in the tide-free version. The conversion can be done by means of the correction given by Smith (1998), which only affects the C20 coefficient. The ICGEM web service provides geoid heights in the three possible tide systems: tide-free, zero-tide, and mean-tide.

The analysis of GGMs can be divided into two parts: a global and a regional spectral analysis.

Global analysis

A global analysis of the behaviour of the GGMS can be done considering the degree and error degree variances of each model, which are derived from the coefficients (\bar{C}_{nm}^T and \bar{S}_{nm}^T) in Eq. (1), and their variances ($\sigma_{\bar{C}_{nm}}^2$ and $\sigma_{\bar{S}_{nm}}^2$), respectively.

According to Rapp (1986), “the signal degree variances represent the amount of the signal contained in each degree or up to a specific degree (if computed cumulatively), while the error degree variances represent the total error power of the model at a given degree”. The latter represent the formal errors (Hirt et al. 2015).

Signal degree variances (DV) and error degree variances (EDV) per degree (n), in the geoid heights were computed based on the following formulas (Eq. (2), (3); Tsoulis and Patlakis 2013):

$$DV(n) = R^2 \sum_{m=0}^n \left(\bar{C}_{nm}^{T^2} + \bar{S}_{nm}^{T^2} \right) \quad (2)$$

$$EDV(n) = R^2 \sum_{m=0}^n \left(\sigma_{\bar{C}_{nm}}^2 + \sigma_{\bar{S}_{nm}}^2 \right) \quad (3)$$

where R is the mean Earth radius.

It is also possible to compare two GGMs using one of them as a reference. This allows the improvement evaluation in the GGM geoid heights to be compared to the geoid heights computed from the reference GGM. For the present case, EGM2008 is the reference GGM used to investigate the contribution that GOCE and new terrestrial data provide to the newest GGMs. This comparison is based on the gain determination (Eq. 4) as explained in Sneeuw (2000).

Table 1 List of the five GGMs used and their data classification according to the ICGEM web page: S (satellite gravity), G (terrestrial gravity), and A (altimetry) data

Model	Year	N_{\max}	Data	References
EGM2008	2012	2190	S(Grace), G, A	Pavlis et al. (2012)
EIGEN6C4	2014	2190	S(Goce, Grace, Lageos), G, A	Förste et al. (2014)
GECO	2015	2190	S(Goce), EGM2008	Gilardoni et al. (2016)
GGM05C	2016	360	S(Grace, Goce), G, A	Ries et al. (2016)
GOCO05C	2016	720	S(Grace, Goce, SLR), G, A	Fecher et al. (2017)

$$\text{Gain}(n) = \frac{\text{EDV}(n)^{\text{ref}}}{\text{EDV}(n)^{\text{new}}} \quad (4)$$

where $\text{EDV}(n)^{\text{ref}}$ and $\text{EDV}(n)^{\text{new}}$ are the error degree variances of the reference model and the new model, respectively; both computed per degree n .

Regional analysis

The regional analysis can be done through the comparisons of GNSS/levelling results with geoid heights (N) or height anomalies (ζ) computed from a GGM up to a particular expansion degree. However, GNSS/levelling height anomalies contain the full gravity spectrum, whereas the GGMs include only the gravity spectrum expanded up to its maximum degree (N_{max}). To overcome this situation, Gruber et al. (2011) suggested subtracting the high-frequency components from the GNSS/levelling results before comparing them with GGMs' height anomalies or geoid undulations.

The high frequencies can be removed by means of a long wavelength GGM like EGM2008. For example, consider a GGM, different from EGM2008, with a maximum degree of expansion up to N_{max} . The comparison of these GGM height anomalies with GNSS/levelling data can be made in the following way:

$$D\zeta = \zeta_{\text{GNSS/levelling}} - \left(\zeta_{\text{egm2008}} \Big|_{(N_{\text{max}}+1)}^{2190} \right) - \zeta_{\text{GGM}} \Big|_0^{N_{\text{max}}} \quad (5)$$

Applying Eq. (5) gives GNSS/levelling results in a similar (not equal) frequency band up to N_{max} , like the considered GGM. Of course, this mechanism does not remove the highest frequencies beyond degree 2159. It must be taken into account that although the EGM2008 spherical harmonics are developed up to 2190, it has full resolution up to degree and order 2159.

In Eq. (5) it is seen that EGM2008 is used to estimate the short wavelength part of the height anomalies. Thus, it is used to estimate the omission error of the GGM. In this work, the methodology proposed by Hirt et al. (2010) was applied. However, as mentioned in the introduction, EGM2008 does not include observed gravity data in the south-west of Tierra del Fuego Island. Therefore, the omission error was also determined by considering the RTM effect on height anomalies.

RTM height anomalies

Short wavelength effects can be taken into account by means of an RTM reduction (Forsberg 1984). According to Hirt (2013), this technique is capable of modelling the major part of the omission error at shorter scales than $5'$.

The RTM approach implies a density reference model which has crustal density up to the height of the reference surface. A DTM representing the Earth's topography is referred to that reference surface. This leads to a residual topography which accounts for the high frequency of the gravity field spectrum if the reference surface has the same wavelength as the GGM used (Forsberg 1984; Forsberg and Tscherning 1981; Rizos and Willis 2011).

SRTM3 (Farr et al. 2007) completed with the Fagnano Lake bathymetry (Lodolo et al. 2007) and SRTM30 plus were used to represent the topography. The mean reference surface was obtained by smoothing this combined model, in agreement with the maximum degree used for each GGM. The smoothing was performed by the SELECT routine (in mode 3) of the GRAVSOFT package (Forsberg 2003) which allows the generation of a mean height grid surface from a dense DTM. For example, when working with a maximum degree of 360, the mean reference surface should have a wavelength of around 100 km (Forsberg 1984).

Although DTM2006 (Pavlis 2007) was considered, it was not employed in this study because it does not include information about the bathymetry of the lake, and it has a lower resolution than the combined DTM.

RTM effects on height anomalies were estimated by a prism-integration method where each elevation z_{RTM} represented the difference between z_{SRTM} and the mean reference surface. These differences were arranged in such a way that they could be interpreted as a grid of rectangular prisms. The gravitational potential of each prism (V^{P}) with corner coordinates (x_1, y_1, z_1) and (x_2, y_2, z_2) reads:

$$V^{\text{P}}(x, y, z) = G\rho_0 \left[|x| \ln(z+r) + yz \ln(x+r) - \frac{x^2}{2} \tan^{-1} \left(\frac{yz}{xr} \right) - \frac{y^2}{2} \tan^{-1} \left(\frac{zx}{yr} \right) - \frac{z^2}{2} \tan^{-1} \left(\frac{xy}{zr} \right) \right] \Big|_{x_1, y_1, z_1}^{x_2, y_2, z_2} \quad (6)$$

Equation (6) was proposed by Nagy et al. (2000) and it assumes prisms of constant density ρ_0 , which in this case is 2.67 g cm^{-3} on land, and 1.00 g cm^{-3} on the lake.

Applying a variant of Bruns formula, the RTM effect on height anomalies can be written as (Heiskanen and Moritz 1967, p. 293):

$$\zeta_{\text{RTM}} = \frac{V_{\text{RTM}}}{\gamma_Q}, \quad (7)$$

where V_{RTM} is the sum of the prism gravitational contribution at the computation point represented by Eq. (6), and γ_Q is the normal gravity on point Q located on the telluroid (Heiskanen and Moritz 1967; Torge 2001, p. 257). This effect was computed by means of the TC routine (Forsberg 1984) which was modified to account for the density of the lake.

As established in Forsberg (1984), the gravitational formulas for the rectangular prisms are computationally slow and numerically unstable at large distances because they involve small differences between large numbers, which correspond to the corners of the prisms. Therefore, approximate formulas are needed at larger distances. Such formulas are based on an expansion of the prism field in spherical harmonics, which provide the simple expansion given by McMillan (1958):

$$V^P = G\rho\Delta x\Delta y\Delta z \left\{ \frac{1}{r} + \frac{1}{24\gamma^5} [(2\Delta x^2 - \Delta y^2 - \Delta z^2)x^2 + (-\Delta x^2 + 2\Delta y^2 - \Delta z^2)y^2 + (-\Delta x^2 - \Delta y^2 - 2\Delta z^2)z^2 + \frac{1}{288r^9}(\alpha x^4 + \beta y^4 + \dots) + \dots] \right\} \quad (8)$$

$$\Delta x = x_2 - x_1, \Delta y = y_2 - y_1, \Delta z = z_2 - z_1$$

α , β , and γ depend on the distance between the mass element and its distance to the computation point P .

In the innermost zone, around the computation point, the DTM is densified using bicubic spline interpolation. This gives place to a “finer” (a greater number) set of prisms that are used to minimise the usual large effects of the inner zone (Forsberg 1984).

Results and discussion

Global analysis

From the global spectral analysis of the square root of DV per degree, it can be seen that all GGMs retained full power almost up to their maximum (Fig. 2a). In fact, many of the GGMs did not show visible differences when inspecting the power spectra up to the maximum degree of each model. This was the case for GECO, EIGEN6C4, and EGM2008, because the first two GGMs are not independent from EGM2008, as mentioned in the previous sections. Figure 2a, shows enlarged sections at those degrees where GGM05c, GOCO05c, and the remaining models reach their maximum degree of the spherical harmonic expansion. When the EDV were considered (Fig. 2b), and EGM2008 was used as the reference GGM, the error in all of the remaining models was less than that of EGM2008 up to $n = 200$. This is because the GOCE models are more accurate than EGM2008 in the medium frequencies up to degree 200. The error increased or remained equal beyond degree 230/240, except for EIGEN6C4. The abrupt reduction of its formal error from degree 370 onwards is due to the extension of this GGM with the DTU12 global grid of gravity anomalies (Andersen et al. 2009).

EIGEN6C4 and GOCO05C showed similar behaviour in the error per degree up to approximately degree 220. According to Fig. 2b, the EDV of all models differed in the low frequencies of the spectrum, which indicates that this difference is due to the satellite data. This result is confirmed in Fig. 3. It shows the gain of the GGMs with respect to EGM2008. It can be seen that GOCE and GRACE data contributed to the long wavelengths, except for degrees higher than 240 where there was no gain with respect to EGM2008. It remained equal to 1 or less, even for GOCO05C. A different situation is seen for EIGEN6C4, which showed an improvement by a factor of 10 when compared to EGM2008 for degrees higher than 360. This is related to the gravity anomaly data mentioned above.

A comparison between EGM2008 and EGM96 (Le-moine et al. 1998) is also included to display a typical case of significant improvement. All other models, however, are evaluated with respect to EGM2008.

Regional analysis

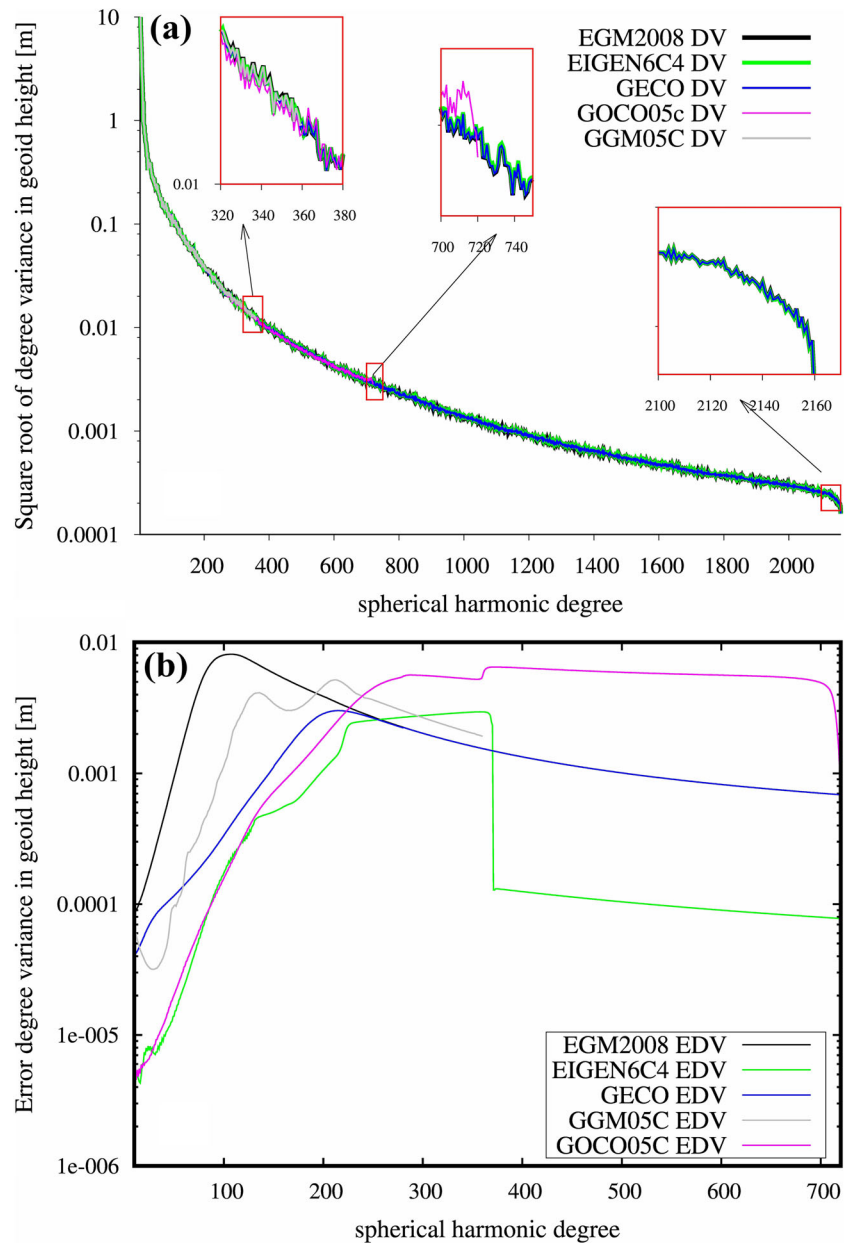
The evaluation of the aforementioned GGMs on GNSS/levelling points, located in the Argentine part of Tierra del Fuego Island, gave the statistics shown in Table 2. The standard deviations are mostly in agreement with the accuracy published for these GGMs (see introduction section). This was an expected result because the GNSS/levelling points are located in areas with observed gravity information which has been provided to several agencies involved in global geopotential modelling. However, evaluating the GGMs using MLL data on Fagnano Lake lead to a different result (Table 3). This behaviour is explained by the presence of mountains and steep topographic gradients. In this region, the statistics were quite different, around 0.30 m in standard deviation for most of the models (EGM2008, GECO, and EIGEN6C4).

A bias correction was applied to all comparisons between observations and GGM solutions to avoid any offset caused by datum discrepancies between the local vertical datum and the geoid models (Sansò and Sideris 2013).

As established in Hirt et al. (2010) this bias correction eliminated the impact of the neglected zero and first-degree terms, and it is consistent with those studies that use standard deviation to evaluate the performance of GGMs.

Figures 4 and 5 show the RMS per degree after the evaluation of the five GGMs used for Fagnano Lake, and for the rest of the island, respectively. This computation was performed by applying Eq. (5), i.e., the high frequencies were removed using EGM2008 from degree $N_{\max} + 1$ up to 2190, being N_{\max} : 10, 20, 30... and so on, before comparing with each GGM. This was done in

Fig. 2 **a** DV of the selected GGMs. To appreciate the differences, the inset boxes show enlarged sections at those degrees where the models reach their maximum degree of the spherical harmonic expansion; **b** EDV of the GGMs



steps of 10 degrees of spherical harmonic expansion, and MLL data were used for the comparison within the lake area (Fig. 4). The RMS increased from degree 200 to remain constant from degree 400 onwards.

In the case of GOCO05C, the RMS decreased from degree 200–720. For degree 720 it had the same accuracy as if the effect of the high frequencies had not been removed with the EGM2008 model.

This behaviour was different when evaluating the GGMs in regions covered by gravity data (Fig. 5). The difference in RMS also became evident. The removal of the high-frequency signal from GNSS/levelling data made the result better than or equal to those shown in Table 2.

According to Figs. 4 and 5, GOCO05C showed identical behaviour to the remaining models at the lowest frequencies. But major differences appeared above approximately degree 400. It was the only model that showed the same accuracy in the lake area and on land. This is confirmed by the statistics shown in Tables 2 and 3. This fact can be attributed to some improvement in the gravimetric information contained in this GGM which was not included in previous models.

Local improvement of GGMs

The aim of this section is to show the computed differences in height anomalies between MLL data and GGMs

Fig. 3 Gain of GGMs w.r.t. EGM2008 per degree

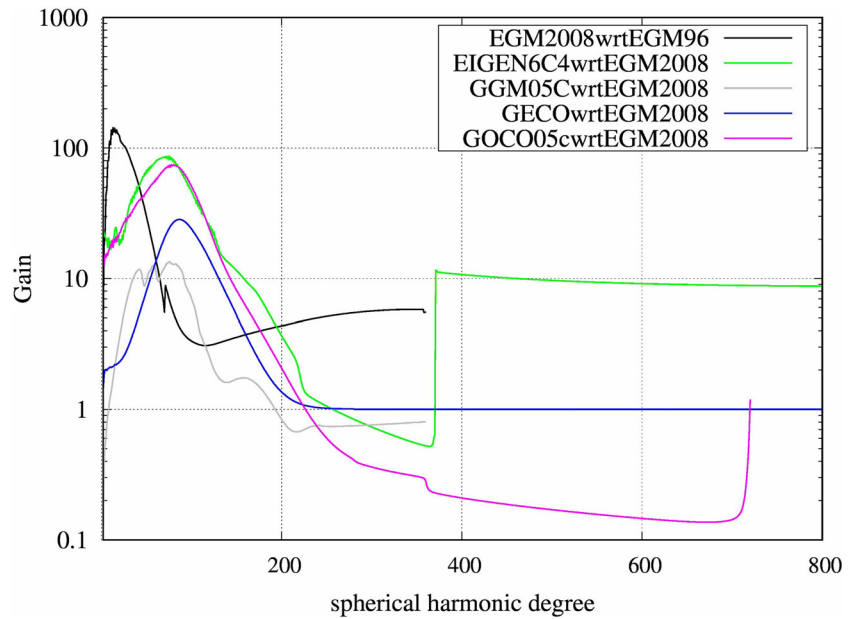


Table 2 Evaluation of the GGMs selected on 67 GNSS/levelling points located in the Argentine part of Tierra del Fuego, after removing bias

Model (N_{max})	SD [m]	Max [m]	Min [m]
EGM2008(2190)	0.11	0.22	-0.25
EIGEN6C4(2190)	0.12	0.24	-0.24
GECO(2190)	0.10	0.18	-0.17
GGM05c(360)	0.16	0.41	-0.27
GOCO05C(720)	0.10	0.20	-0.26

The evaluation does not include Fagnano Lake MLL observations

Table 3 Evaluation of the GGMs on 81 MLL observations, after removing bias

Model (N_{max})	SD [m]	Max [m]	Min [m]
EGM2008(2190)	0.35	0.49	-0.8
EIGEN6C4(2190)	0.27	0.38	-0.71
GECO(2190)	0.30	0.46	-0.68
GGM05C(360)	0.15	0.34	-0.5
GOCO05C (720)	0.13	0.25	-0.38

augmented with RTM data as well as EGM2008 + RTM solutions.

Height anomalies derived from GGMs were estimated at different degrees of expansion (N_{max}):360, 720, 1080, and 2190. Table 4 shows the differences:

$$D_{\zeta_{MLL}}^r = \begin{cases} \zeta_{MLL} - (\zeta_{GGMi}|_2^{N_{max}} + \zeta_{RTM}(N_{max} + 1)) \\ \zeta_{MLL} - (\zeta_{GGMi}|_2^{N_{max}} + \zeta_{egm2008}|_{(N_{max}+1)}^{2190} + \zeta_{RTM}(2160)) \end{cases} \tag{9}$$

with GGM_i being each of the five GGMs up to different degree N_{max} . In the case of EGM2008, just the first option of Eq. (9) was applied.

The solutions listed in Table 4 were examined, along with their gain, with respect to the EGM2008 (2190) solution. The gain shown in Table 4, was determined using a variant of Eq. (4) regarding the standard deviation (STD) of each solution, such that:

$$Gain = \frac{STD(DN_{egm2008(2190)})}{STD_{GGMi}(DN_{MLL})} \tag{10}$$

with $DN_{egm2008(2190)}$ being the difference between MLL observations and the EGM2008 (2190) solution for height anomalies.

For some of these solutions, the omission error was modelled through the RTM approach, while in other cases this result was combined with EGM2008 to complete the estimation. The starting point was degree 360, because it is the minimum degree of a combined model like GGM05C. Degree 720 corresponds to the maximum wavelength of “fill-in” data in EGM2008 for areas without observed gravity data. This “fill-in” data were generated using RTM gravity anomalies obtained from DTM2006 and a satellite-only model (Pavlis 2007).

As seen in table, there was an improvement with respect to the EGM2008 (2190) solution, especially when it was augmented with RTM data. As expected, based on the results presented in Table 4, GOCO05C (720) was the best GGM, even without any RTM improvement. According to Fecher et al. (2017), GOCE data produced a visible impact, even for higher degrees, in areas where “fill-in” data had been applied. However, the improvement was related to the

Fig. 4 RMS of the differences between geoid heights derived from GGMs and MLL observations on Fagnano Lake, after applying Eq. (5). The spatial distribution of the MLL data (red dots) is shown on the right

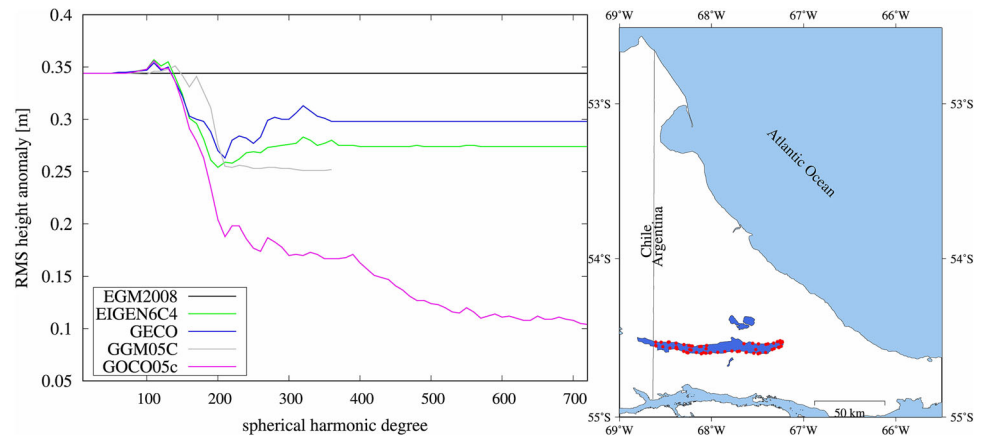
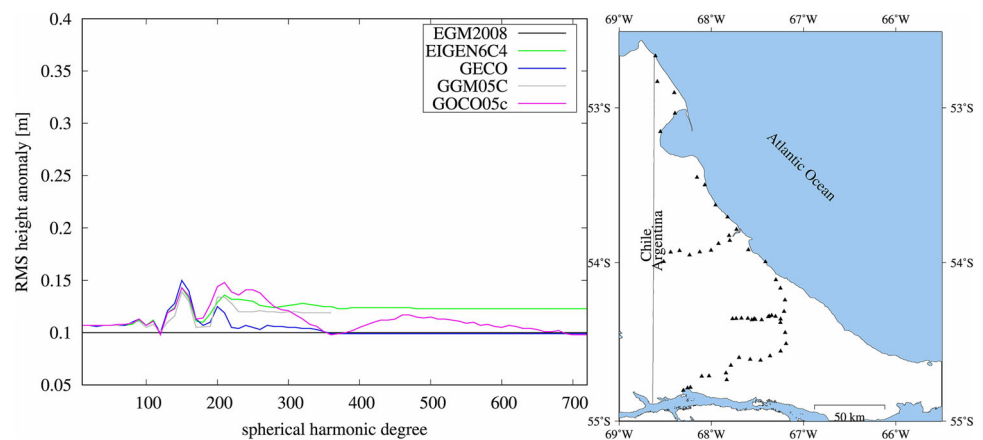


Fig. 5 RMS of the differences between GGMs and observations on GPS/levelling points over areas covered by gravity data, after applying Eq. (5). The spatial distribution of the GPS/levelling data (black triangles) is shown on the right



incorporation of new terrestrial information made by some agencies.

Differences between observed height anomalies and those derived from the GGMs up to their maximum degree are plotted in Fig. 6. To appreciate the contribution of RTM information, Fig. 7 depicts the difference between observed height anomalies and the best solution provided by each GGM after augmenting them with RTM data (according to Table 4).

Figure 6 shows that the discrepancies between GGMs and MLL data increased progressively to the west. There are two main reasons that explain this situation: the west side of the Fagnano Lake is close to the Andes Mountains, and it is characterised by steep topographic gradients. Secondly, most of the GGMs do not include observed gravity anomalies of this region as input data.

Figure 7 shows that the selected solutions produced better behaviour than EGM2008 (2190) when compared to the observations, not only in the western part of the lake but also in the east. Figure 7 also shows that a low standard deviation does not always imply a significant improvement in the western part, which is the most critical region.

Even after improvements have been made, the discrepancies in the western part of the lake were still greater than

on the eastern side. This is because the observed gravity information included into the GGMs is from the north and east side of Tierra del Fuego Island (Pacino and Tocho 2009; Pavlis et al. 2012).

According to Fig. 7, GGM05C (360) and GOCO05C (720), improved by applying RTM corrections, yielded the best results. This is consistent with the values given in Table 4 when adding the omission error. These models are two of the latest combined models. They have the advantage of including GOCE data as well as new terrestrial information. As mentioned before, these two facts are responsible for the global and local improvement of GGMs.

Conclusion

The numerical results obtained at the beginning of Sect. 3 allow the conclusion to be drawn that the gain of the newest GGMs with respect to EGM2008 takes place in the lowest degrees of the spherical harmonic expansion. This situation can be explained by the inclusion of GOCE data in the most recent GGMs.

Table 4 Statistics of the differences between observations and the solutions considered, together with their gain with respect to EGM2008 (2190)

Model (N_{\max})	Omission error	STD	Max.	Min.	Gain
EGM(2190)	–	0.35	0.49	–0.8	–
EGM2008(2190)	RTM(2160)	0.3	0.43	–0.73	1.17
EGM2008(1080)	–	0.39	0.51	–0.86	0.9
EGM2008(1080)	RTM(1081)	0.36	0.8	–0.55	0.97
EGM2008(720)	–	0.34	0.48	–0.8	1.03
EGM2008(720)	RTM(721)	0.32	0.47	–0.77	1.09
EGM2008(360)	–	0.2	0.31	–0.63	1.84
EGM2008(360)	RTM(361) ^a	0.2	0.3	–0.59	1.84
EIGEN6C4(2190)	–	0.27	0.38	–0.71	1.3
EIGEN6C4(2190)	RTM(2160)	0.23	0.34	–0.63	1.52
EIGEN6C4(1080)	–	0.31	0.4	–0.77	1.13
EIGEN6C4(1080)	RTM(1081)	0.28	0.36	–0.71	1.25
EIGEN6C4(1080)	EGM(2190-1081) + RTM(2160)	0.23	0.33	–0.64	1.52
EIGEN6C4(720)	–	0.31	0.39	–0.72	1.13
EIGEN6C4(720)	RTM(721)	0.28	0.37	–0.69	1.25
EIGEN6C4(720)	EGM(2190-721) + RTM(2160)	0.23	0.32	–0.64	1.52
EIGEN6C4(360)	–	0.16	0.34	–0.54	2.19
EIGEN6C4(360)	RTM(361) ^a	0.15	0.34	–0.53	2.33
EIGEN6C4(360)	EGM(2190-361) + RTM(2160)	0.24	0.34	–0.64	1.46
GECO(2190)	–	0.3	0.46	–0.68	1.17
GECO(2190)	RTM(2160)	0.16	0.41	–0.62	2.19
GECO(1080)	–	0.34	0.48	–0.74	1.03
GECO(1080)	RTM(1081)	0.31	0.43	–0.69	1.13
GECO(1080)	EGM(2190-1081) + RTM(2160)	0.25	0.4	–0.625	1.4
GECO(720)	–	0.33	0.46	–0.71	1.06
GECO(720)	RTM(721)	0.31	0.44	–0.68	1.13
GECO(720)	EGM(2190-721) + RTM(2160)	0.25	0.4	–0.625	1.4
GECO(360)	–	0.16	0.28	–0.52	2.33
GECO(360)	RTM(361) ^a	0.15	0.28	–0.51	2.33
GECO(360)	EGM(2190-361) + RTM(2160)	0.25	0.4	–0.625	1.4
GGM05c(360)	–	0.15	0.34	–0.5	2.33
GGM05c(360)	RTM(361) ^a	0.14	0.33	–0.49	2.5
GGM05c(360)	EGM(361-2190) + RTM(2160)	0.21	0.29	–0.63	1.67
GOCO05C(720)	–	0.13	0.25	–0.38	2.69
GOCO05C(720)	RTM(720)	0.11	0.23	–0.35	3.18
GOCO05C(720)	EGM(721-2190) + RTM(2160) ^a	0.1	0.19	–0.3	3.5
GOCO05C(360)	–	0.13	0.31	–0.29	2.69
GOCO05C(360)	RTM(360)	0.12	0.31	–0.28	2.92
GOCO05C(360)	EGM(360-2190) + RTM(2160)	0.17	0.3	–0.44	2.06

The gain was obtained applying Eq. (10)

^aIndicate the best solutions, plotted in Fig. 7

It can also be appreciated that, as the GGMs evolve, their solutions are increasingly approaching the observed values. This is related to the newest gravimetric missions, better combination techniques, and new terrestrial data.

RTM height anomalies were estimated in the area of Fagnano Lake to better estimate the omission error of GGMs in that region. As seen in this work, the RTM

technique has served to estimate omission errors from approximately 360 degrees onwards, but it does not make a significant contribution at higher degrees for most of the GGMs.

According to the statistics shown in Table 4 and the shape of the solutions depicted in Fig. 7, the best solution

Fig. 6 Differences in geoid height between GGMs and MLL data

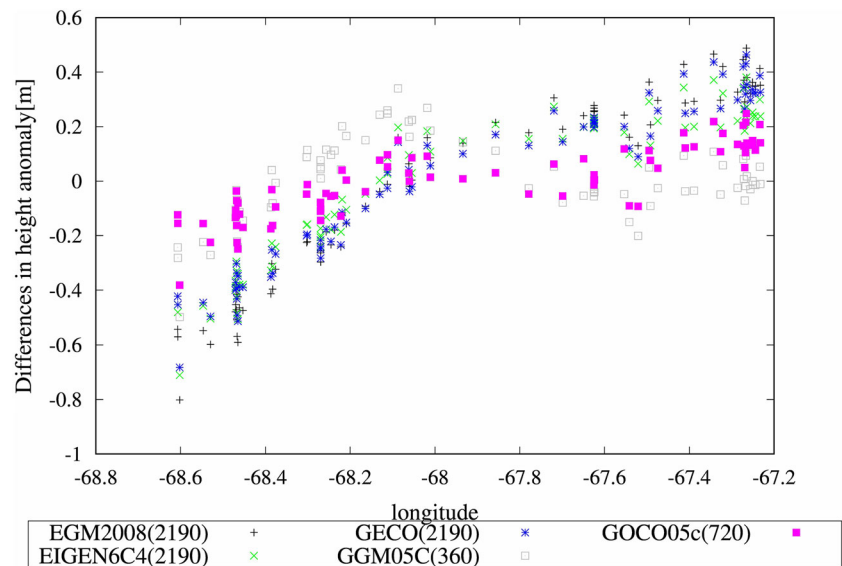
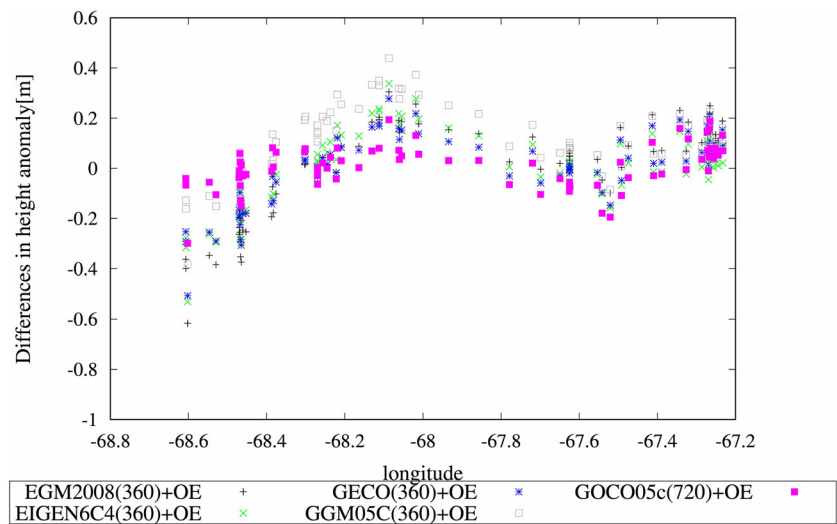


Fig. 7 Differences between the best solutions obtained with each model and MLL observations. The omission errors (OE) are indicated in Table 4 with (asterisk) for each GGM



is obtained by adding RTM height anomalies to GOCO05C.

EGM2008 does not include observed terrestrial gravity information in the western part of the Fuegian Andes, and this becomes evident in the evaluation of that model in the area of the Fagnano Lake. It has also been confirmed that the model improves when applying RTM anomalies obtained from the SRTM3 digital elevation model.

The results obtained here suggest that existing geoid models can be extended to the south-western areas of Tierra del Fuego Island by means of a better estimation of the omission error of GGMs.

Acknowledgements We thank Dr. Lodolo and his team for providing us with the bathymetry data for Fagnano Lake. We are also grateful to Andreas Richter for the revision of our document, to Dr Franz Barthelmes for his suggestions regarding the proper evaluation of global

geopotential models, and to the team of Estacion Astronómica de Río Grande (EARG) for their support in the field activities.

We also thank the reviewers and editor for their valuable comments and suggestions.

References

- Alothman A, Godah W, Elsaka B (2016) Gravity field anomalies from recent GOCE satellite-based geopotential models and terrestrial gravity data: a comparative study over Saudi Arabia. *S Arab J Geosci* 9(5):1–12. doi:[10.1007/s12517-016-2393-y](https://doi.org/10.1007/s12517-016-2393-y)
- Andersen OB, Knudsen P, Berry P (2009) DNSCO8 mean sea surface and mean dynamic topography models. *J Geophys Res.* doi:[10.1029/2008JC005179](https://doi.org/10.1029/2008JC005179)
- Andersen OB, Knudsen P, Kenyon SC, Holmes S (2014), Global and arctic marine gravity field from recent satellite altimetry (DTU13). In: 76th EAGE Conference and Exhibition 2014. Extended abstract. doi:[10.3997/2214-4609.20140897](https://doi.org/10.3997/2214-4609.20140897). Accessed 1 Mar 2017

- Bomfin EP, Braitenberg C, Molina EC (2013) Mutual evaluation of global gravity models (EGM2008 and GOCE) and terrestrial data in Amazon Basin, Brazil. *Geophys J Int* 195(2):870–882. doi:10.1093/gji/ggt283
- Brockmann JM, Zehentner N, Höck E, Pail R, Loth I, Mayer-Gürr T, Schuh W-D (2014) EGM_TIM_RL05: an independent geoid with centimeter accuracy purely based on the GOCE mission. *Geophys Res Lett* 41:8089–8099. doi:10.1002/2014GL061904
- Del Cogliano D, Dietrich R, Richter A, Perdomo R, Hormaechea JL, Liebsch G, Fritsche M (2007) Regional geoid determination in Tierra del Fuego including GPS/levelling. *Geol Acta* 5(4):315–322
- Erol B (2012) Spectral evaluation of Earth geopotential models and an experiment on its regional improvement for geoid modeling. *J Earth Syst Sci* 121(3):823–835
- Farr TG, Rosen PA, Caro E, Crippen R, Duren R, Hensley S, Kobrick M, Paller M, Rodriguez E, Roth L, Seal D, Shaffer S, Shimada J, Umland J, Werner M, Oskin M, Burbank D, Alsdorf D (2007) The Shuttle radar topography mission. *Rev Geophys*. doi:10.1029/2005RG000183
- Fecher T, Pail R, Gruber T, The GOCO Consortium (2017) GOCO05c: a new combined gravity field model based on full normal equations and regionally varying weighting. *Surv Geophys* 38(3):571–590. doi:10.1007/s10712-016-9406-y
- Ferreira VG, Zhang Y, Freitas SRC (2013) Validation of GOCE gravity field models using GPS-leveling data and EGM08: a case study in Brazil. *J Geod Sci* 3(3):209–218. doi:10.2478/jogs-2013-0027
- Forsberg R (1984) A study of terrain reductions, density anomalies and geophysical inversion methods in gravity field modelling. The Ohio State University, Reports of the Department of Geodetic Science and Surveying, vol 355, p 116–126
- Forsberg R (2003) An overview manual for the GRAVSOFIT Geodetic Gravity Field Modelling Programs. Danish National Space Center. http://cct.gfz.ku.dk/publ_cct/cct1792.pdf. Accessed 25 May 2017
- Forsberg R, Tscherning CC (1981) The use of height data in gravity field approximation by collocation. *J Geophys Res* 86(B9):7843–7854
- Förste C, Bruinsma S, Abrykosov O, Flechtner F et al (2013) EIGEN-6C3stat—the newest high resolution global combined gravity field model based on the 4th release of the GOCE direct approach. IAG scientific assembly, 1–6 September, Postdam, Germany. http://icgem.gfz-potsdam.de/tom_longtime. Accessed 25 May 2017
- Förste C, Bruinsma SL, Abrikosov O, Lemoine JM, Schaller T, Götze J, Ebbing J, Marty JC, Flechtner F, Balmino G, Biancale R (2014) EIGEN-6C4 The latest combined global gravity field model including GOCE data up to degree and order 2190 of GFZ Potsdam and GRGS Toulouse. 5th GOCE User Workshop, Paris. http://icgem.gfz-potsdam.de/tom_longtime. Accessed 25 May 2017
- Förste C, Bruinsma SL, Rudenko S, Abrikosov O, Lemoine J-M, Marty J-C, Neumayer KH, Biancale R (2016) EIGEN-6S4 a time-variable satellite-only gravity field model to d/o 300 based on LAGEOS, GRACE and GOCE data from the collaboration of GFZ Potsdam and GRGS Toulouse (version 2). GFZ Data Services. <http://doi.org/10.5880/icgem.2016.008>. http://icgem.gfz-potsdam.de/tom_longtime. Accessed 25 May 2017
- Gilardoni M, Reguzzoni M, Sampietro D (2016) GECHO: a global gravity model by locally combining GOCE data and EGM2008. *Stud Geophys Geod* 60(2):228–247. doi:10.1007/s11200-015-1114-4
- Godah W, Krynski J, Szelachowska M (2015) On the accuracy assessment of the consecutive releases of GOCE-based GGMs over the area of Poland, Assessment of GOCE geopotential models. Special Issue Newton's Bull 5:49–62
- Gomez ME, Del Cogliano D, Perdomo R (2013) Geoid modelling in the area of Fagnano Lake, Tierra del Fuego (Argentina): insights from mean lake-level observations and reduced gravity data. *Acta Geod Geophys Hu* 48(2):139–147. doi:10.1007/s40328-012-0009-x
- Gomez ME, Del Cogliano D, Perdomo R, Hormaechea JL (2014) A new combined quasigeoid model in Tierra del Fuego. *Geol Acta* 12(3):219–226. doi:10.1344/GeologicaActa2014.12.3.4
- Gruber T, Visser PNAM, Ackermann CH, Hosse M (2011) Validation of GOCE gravity field models by means of orbit residuals and geoid comparisons. *J Geod* 85:845–860. doi:10.1007/s00190-011-0486-7
- Heiskanen WA, Moritz H (1967) Physical geodesy. Freeman and Company, San Francisco
- Hirt C (2013) RTM gravity forward-modeling using topography/bathymetry data to improve high-degree global geopotential models in the coastal zone. *Mar Geod* 36(2):183–202
- Hirt C, Featherstone WE, Marti U (2010) Combining EGM2008 and SRTM/DTM2006.0 residual terrain model data to improve quasigeoid computations in mountainous areas devoid of gravity data. *J Geod* 84:557–567. doi:10.1007/s00190-010-0395-1
- Hirt C, Rexer M, Claessens S (2015) Topographic evaluation of fifth-generation GOCE gravity field models—globally and regionally. *Newton's Bull* 5:163–186
- IGN (2016) Red de Nivelación Argentina. <http://www.ign.gob.ar/NuestrasActividades/Geodesia/Nivelacion/Introduccion>. Accessed 25 May 2017
- Jekely C (2009) Omission error, data requirements, and the fractal dimension of the geoid. In: Sneew et al. (eds) VII Hotine-Marussi Symposium on Mathematical Geodesy. Proceedings of the symposium in Rome, vol 137, 6–10 June 2009. Springer, Berlin. doi:10.1007/978-3-642-22078-4
- Lemoine FG, Kenyon SC, Factor JK, Trimmer RG, Pavlis NK, Chinn DS, Cox CM, Klosko SM, Luthcke SB, Torrence MH, Wang YM, Williamson RG, Pavlis EC, Rapp RH, Olson TR (1998) The development of the joint NASA/GSFC and the national imagery and mapping agency (NIMA) geopotential model EGM96. NASA Goddard Space Flight Center, Greenbelt
- Lodolo E, Lipai H, Tassone A, Zanolla C, Menichetti M, Hormaechea JL (2007) Gravity map of the Isla Grande de Tierra del Fuego, and morphology of Lago Fagnano. *Geol Acta* 5(4):307–314
- Mayer-Gürr T, The GOCO Team (2015) The combined satellite gravity field model GOCO05s. EGU2015-12364, EGU general assembly, Vienna, Austria. https://www.researchgate.net/publication/277325861_The_new_combined_satellite_only_model_GOCO05s. Accessed 25 May 2017
- McCarthy D, Petit G (eds) (2004) IERS conventions (2003). IERS technical note No. 32, IERS conventions centre
- McMillan WD (1958) The theory of potential. Theoretical mechanics, vol 2. Dover, New York
- Nagy D, Papp G, Benedek J (2000) The gravitational potential and its derivatives for the prism. *J Geod* 74(7/8):552–560
- Pacino C, Tocho C (2009) Validation of EGM2008 over Argentina. SIRGAS report
- Pavlis N (2010) Global gravitational modelling & development and applications of geopotential models. In: Guarracino Tochoand (ed) The determination and use of the geoid. Lecture and Seminar notes, International IGes Geoid School, La Plata
- Pavlis NK, Factor JK, Holmes SA (2007) Terrain-related gravimetric quantities computed for the next EGM. In: Proceedings of the 1st International Symposium of the International Gravity Field Service, vol 18. Harita Dergisi, Istanbul, p 318–323
- Pavlis NK, Holmes SA, Kenyon SC, Factor JK (2012) The development and evaluation of the Earth gravitational model

- 2008 (EGM2008). *J Geophys Res* 117(B04406):1–38. doi:[10.1029/2011JB008916](https://doi.org/10.1029/2011JB008916)
- Piñon DA (2016) Development of a precise gravimetric geoid model for Argentina. Masters thesis, School of Mathematical and Geospatial Sciences. College of Science Engineering and Health RMIT University
- Rapp RH (1986) Global geopotential solutions, in *Lect. Notes in Earth science, mathematical and numerical techniques in physical geodesy*, vol 7. Springer, Berlin, p 365–415. doi:[10.1007/BFb0010136](https://doi.org/10.1007/BFb0010136)
- Richter A, Hormaechea JL, Dietrich R, Perdomo R, Fritsche M, Del Cogliano D, Liebsch G, Mendoza L (2010) Lake-level variations of Lago Fagnano, Tierra del Fuego: observations, modelling and interpretation. *J Limnol* 69(1):29–41
- Ries J, Bettadpur S, Eanes R, Kang Z, Ko U, McCullough C, Nagel P, Pie N, Poole S, Richter T, Save H, Tapley B (2016) The combined gravity model GGM05C. GFZ Data Serv. doi:[10.5880/icgem.2016.002](https://doi.org/10.5880/icgem.2016.002)
- Rizos C, Willis P (eds) (2011) *Earth on the edge: science for a sustainable planet*. In: *Proceedings of the IAG general assembly*, Melbourne, Australia
- Sansò F, Sideris M (eds) (2013) *Geoid determination. Theory and Methods*. *Lecture notes in earth system sciences*. Springer, Berlin
- Smith DA (1998) There is no such thing as “The” EGM96 geoid: subtle points on the use of a global geopotential model. *IGeS Bull* 8:17–28
- Sneeuw N (2000) A semi-analytical approach to gravity field analysis from satellite observations. Ph.D. thesis. Institut für Astronomische und Physikalische Geodäsie
- Tocho C (2012) *Geoidegravimetrico para la República Argentina*. Ph.D thesis. National University of La Plata, La Plata
- Torge W (2001) *Geodesy*, 3rd edn. Walter de Gruyter, Berlin
- Torge W, Müller J (2012) *Geodesy*, 4th edn. De Gruyter, Berlin. ISBN 978-3-11-020718-7
- Tsoulis D, Patlakis K (2013) A spectral assessment review of current satellite only and combined Earth gravity models. *Rev Gephys* 51:186–243
- Ustun A, Abbak RA (2010) On global and regional spectral evaluation of global geopotential models. *J Geophys Eng* 7(4):369–379
- Vergos GS, Tziavos IN, Sideris MG (2006) On the validation of CHAMP- and GRACE-type EGMs and the construction of a combined model. *GeodCartogr* 55(3):115–131
- Yi W, Rummel R (2013) A comparison of GOCE gravitational models with EGM2008. *J Geodyn* 73:14–22. doi:[10.1016/j.jog.2013.10.004](https://doi.org/10.1016/j.jog.2013.10.004)

Theoretical derivation of basic mechanical property required for triggering mine-pillar rockburst

Houxu Huang¹ · Jie Li¹ · Haiming Jiang¹

Received: 29 December 2016 / Accepted: 30 August 2017 / Published online: 7 September 2017
© Institute of Geophysics, Polish Academy of Sciences & Polish Academy of Sciences 2017

Abstract Rockburst is divided into two types, one is strain-type resulting from rock damage and another is sliding-type resulting from fault slip events. Triggering mine pillar rockburst mainly consists of two steps: the occurrence of shear-band and the application of disturbance. In this paper, mechanical model of mine pillar subjected to uniaxial compression is established. By simplifying the complete stress–strain curve and the crack propagation behaviour, based on the derived energy expressions corresponding to different crack propagation stages, the type of rockburst that the disturbance-induced pillar instability belongs to is defined. Next, by establishing the model of mine pillar with one inclined shear-band and by simplifying the stress evolution on the band, based on the necessary physical characteristics for triggering dynamic events, the basic mechanical property of mine pillar required for triggering instability is derived. It shows that the post-peak modulus greater than or equal to the pre-peak modulus is the basic mechanical property required for triggering mine pillar instability. Finally, by conducting laboratory experiments, the proposed model is verified. The requirement that the post-peak modulus is greater than or equal to the pre-peak modulus may be the reason why triggered mine pillar rockburst is not often observed.

Keywords Rockburst · Mine pillar · Equivalent-average · Disturbance · Basic mechanical property

Introduction

Rockburst is a transition process from one equilibrium to another, accompanied with dramatic release of residual energy in the form of stress wave (Tan 1987; Ryder 1988; Linkov 1992; Salamon 1993; Qian 2014). Therefore, rockburst leads to serious threat to both the staff life and the engineering safety. Until now, much attention has been paid to the study of rockburst (Tan 1987; Li et al. 2007a; Stacey 2013; Jiang et al. 2014; Qian 2014; Wang et al. 2016). Researchers, such as Tan (1987), Ryder (1988), Linkov (1992), Salamon (1993), Stacey (2013), divided the rockburst into two types: the strain-type rockburst resulting from rock damage and the sliding-type rockburst resulting from fault slip events. Compared with strain-type rockburst, the sliding-type rockburst can often be triggered by disturbance: however, study towards the sliding-type rockburst is inadequate and its mechanism is still unclear (Qian 2014). Therefore, study on sliding-type rockburst is meaningful and necessary.

Large numbers of mine pillars, which are subjected to long-term static load, are reserved in the gob to help support the gravity of overlying strata and to help maintain the surface stability. In situ observations show that disturbances induced by mining or blasting often lead to sudden instability of mine pillar (i.e., the rockburst) (Tan 1987). The instability of mine pillar may result in surface subsidence and threaten seriously both the staff life and engineering safety. Therefore, the analysis of mine pillar instability is necessary and important. Based on the catastrophic theory, the effects of pillar stiffness and pillar size on pillar instability are analyzed and the critical stress corresponding to pillar instability is deduced (Wang et al. 2006; Wang and Miao 2006; Li and Cao 2006; Lu et al. 2015). The essence of catastrophic theory is to establish the

✉ Houxu Huang
wuhanhp14315@163.com

¹ State Key Laboratory of Disaster Prevention and Mitigation of Explosion and Impact, PLA University of Science and Technology, Nanjing, China

system's potential energy equation and then obtain the critical values by taking the derivative of the potential energy equation. The catastrophic theory, although helpful for understanding the phenomenon of instability, as a mathematical method, cannot reveal the effects of static load and dynamic load on pillar instability.

Numerical simulations show that long-term static load leads to the emergence of shear-band on mine pillar and the instability is the result of excessive sliding on the band (Wang et al. 2003). Therefore, the instability of mine pillar is only attributed to long-term static load, the effect of dynamic load on instability is not considered. Lu et al. (2015) realized the effect of dynamic load on mine pillar; through numerical simulation, he showed that dynamic load can obviously affect the stress evolution and leads to the increase of surface subsidence. Li et al. (2007a) conducted experiment on mine pillar that is simultaneously subjected to dynamic and static loads. The results show that dynamic load will increase the plastic deformation and the increase of static load can obviously increase the effects of dynamic load. Therefore, Li et al. (2007b) predicted that the instability of single pillar may lead to the instability of group pillars and result in catastrophic events. Although it has contributed greatly to our understanding of the mine pillar instability, the conclusions drawn from the numerical simulation are mainly based on the analyses of the simulation results, such as the stress and strain contours; thus, it is phenomenological and its reference value for practical engineering is limited.

In fact, the effects of static load and dynamic load on the instability of mine pillar are different (Landau and Lifshitz 2013; Qian 2014; Wang et al. 2016). Long-term static load leads to the decrease of pillar strength (Yang et al. 2015), and consequently the pillar may reach its critical state. Compared with the static load, the dynamic load often acts as a trigger. The common feature of triggering dynamic events such as earthquake and rockburst is believed to be that the long-term static load results in large amounts of energy stored in the system. However, the dynamic load often leads to part of the stored energy release and compared with the released energy, the energy applied by the dynamic load is tiny and negligible (Tan 1987; Hill et al. 1993; Xia et al. 2004; Johnson and Jia 2005; Qian 2014).

Tan (1987), based on the failure mechanism of brittle rocks and the statistical results of practical engineering, pointed out that the rocks can transform from stability to instability while affected by disturbance induced by mining or blasting. Therefore, he stressed that attention should be paid to the triggering effects of dynamic load on the occurrence of rock burst. Interestingly, analyses of two earthquakes in the northern Italy show that both the two events are triggered by disturbance caused by the release of

high-stressed carbon dioxide (Johnson and Jia 2005). Johnson and Jia (2005) also emphasized the important effects of dynamic disturbance on triggering instability. He stressed that a weak zone or low-friction zone exists in the system and the stress state in the zones reach the critical state are the basic premises for triggering dynamic events. These conclusions which are drawn from the study of earthquake provide a valuable reference for us to study the instability of mine pillar with shear-band.

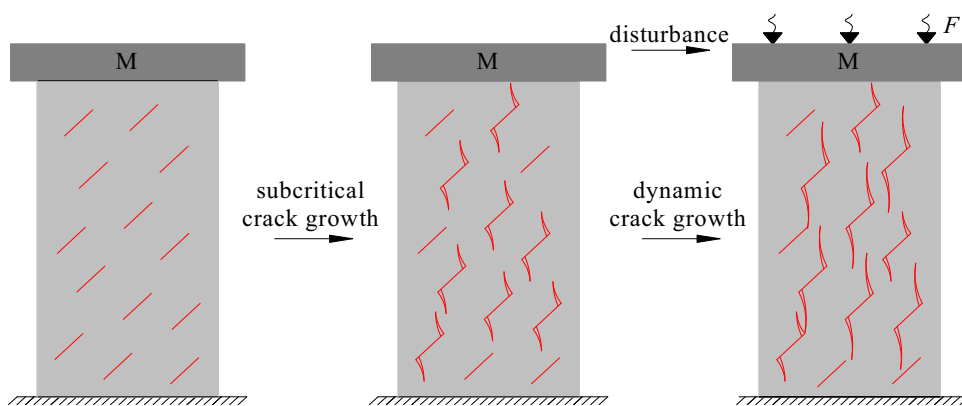
As aforementioned, when investigating the mechanism of rockburst, attention is mainly paid to the effects of loads. However, the required mechanical property of mine pillar, to some extent, is often ignored and thus leads to lack of study. In fact, whether the rockburst could be triggered or not is not only related to the load conditions, but also has direct relation with the mechanical property of the mine pillar itself. Johnson and Jia (2005), although they have presented the premises closely related to the system itself, have raised the question whether we can derive the basic mechanical property of system required for triggering mine pillar rockburst.

In this paper, different from the aforementioned studies, our attentions are mainly paid to the system itself; we will try to derive the mechanical property required for triggering mine pillar rockburst from the theoretical point of view. Thus, the following analyses are organized as follows: In the first section we will try to analyze the type that the triggered mine pillar rockburst belongs to; in the second section, we will deduce the basic mechanical property required for triggering mine pillar rockburst.

Premises of mechanical property for triggering mine pillar rockburst

In fact, special conditions are required for triggering mine pillar rockburst; therefore, in this section, we will try to answer what type of rockburst does the triggered mine pillar rockburst belongs to. As shown in Fig. 1, the failure of pillar is assumed to be the results of growth of large numbers of micro-cracks. When subjected to long-term static load, M_g , even the stress intensity factor at crack tips, is less than the fracture toughness; the cracks will still undergo subcritical growth (Atkinson 1992; Hoek and Martin 2014; Zhou et al. 2014). After a long period of growth, at the end of the subcritical growth stage, the crack length will increase to the critical length l_c from the initial length l_0 . When the critical length is reached, the cracks will enter into the unstable dynamic growth stage (Hori and Nemat-Nasser 1985). If a dynamic disturbance, F , is suddenly applied to the pillar at special moment, for that the crack growth is an energy-driven process; therefore, the energy provided by the disturbance may further increase

Fig. 1 Possible failure model of pillar subjected to static load and dynamic disturbance



the crack growth rate and decrease the time taken for the pillar failure. Next, based on the fracture mechanics and some necessary assumptions, we will try to analyze the aforementioned processes theoretically.

As shown in Fig. 2, the crack growth state can be estimated through the corresponding relations between crack growth and the stress–strain state (Cai et al. 2004; Cai 2010; Hoek and Martin 2014). As shown in Fig. 2, from the view of fracture mechanics, the failure of rock which is caused by the crack growth can be divided into three typical stages: (1) crack closure stage, in which the rock volume slightly decreases and the corresponding initial stress is denoted by σ_{cc} ; (2) stable crack growth stage, in which the crack increases slowly to the critical length l_c and the corresponding initial stress is denoted by σ_{ci} , where

$\sigma_{ci} = k_1 \sigma_c = (0.4 - 0.6) \sigma_c$, σ_c is the compressive strength; (3) unstable crack growth till compressive strength reached: in this stage, rock damage occurs and rock modulus decreases slightly; the initial stress of this stage is σ_{cd} , where $\sigma_{cd} = k_2 \sigma_c = (0.7 - 0.9) \sigma_c$.

The behavior of single crack is complex enough and to simultaneously describe the behavior of a set of cracks is almost impossible. Therefore, in this paper, we will try to analyze the rock failure based on the simplified stress–strain curve and the corresponding energy state.

In order to simplify the analyses, the rock modulus corresponding to the simplified stress–strain curve in Fig. 2 is divided into three stages: (1) rock modulus E_0 , the stress increase from 0 to σ_{cd} and there is no rock damage in this stage; (2) rock modulus E_1 (where $E_1 < E_0$), the stress is

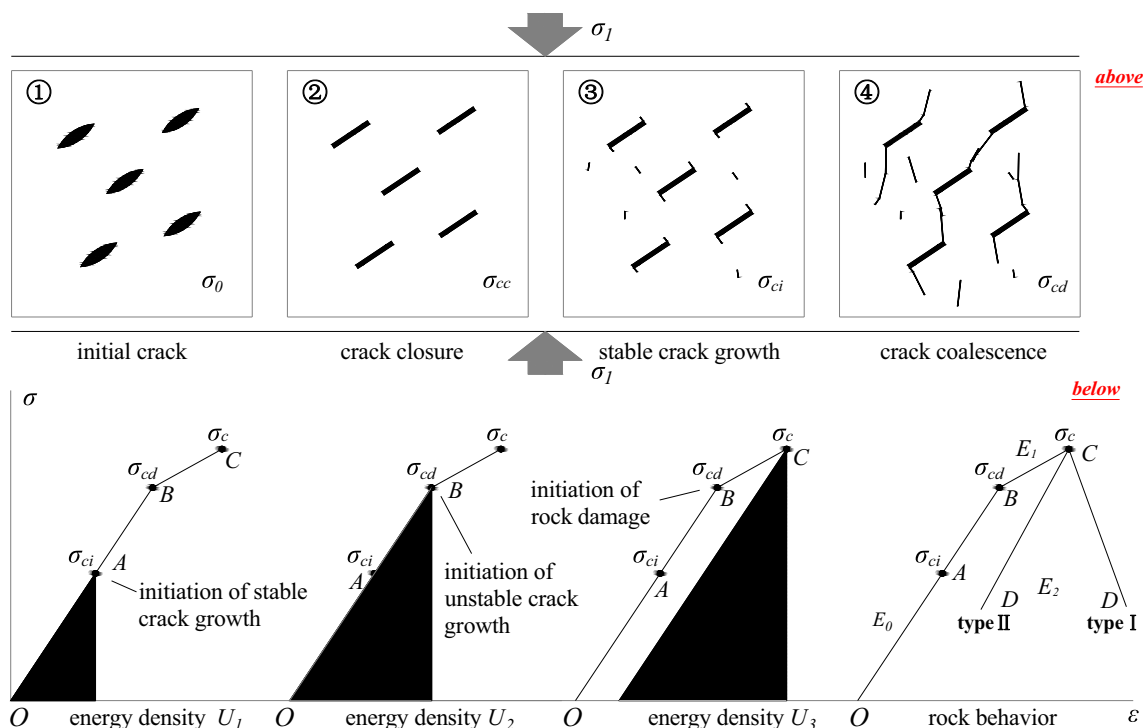


Fig. 2 Relationship between crack behavior (above) and energy density (below)

greater than σ_{cd} but less than the compressive strength, σ_c , and rock damage occurs; (3) rock modulus E_2 : the stress exceeds the compressive strength, σ_c and the rock enters into the post-peak stage. Based on whether the rock will undergo gradual weakening or sudden failure in the post-peak stage, the rock behavior can be divided into two types (Cook 1965), of which, type I refers to the rock that undergoes gradual weakening in the post-peak stage and type II refers to the rock that does not belong to type I.

Take the plane strain model as an example, the energy density of the rock corresponding to the crack initiation, rock damage emergence and the compressive strength is reached can be expressed as U_1 , U_2 and U_3 , respectively

$$\begin{cases} U_1 = \frac{(1 - \nu^2) \cdot \sigma_{ci}^2}{2E_0} \\ U_2 = \frac{(1 - \nu^2) \cdot \sigma_{cd}^2}{2E_0} \\ U_3 = \frac{(1 - \nu^2) \cdot \sigma_c^2}{2E_1} \end{cases} \quad (1)$$

In this paper, the rock is assumed to consist of rock matrix and cracks. There is no crack propagation before crack initiation stress, σ_{ci} is reached, therefore, the energy exerted by the compression is assumed to be completely absorbed by the rock matrix. The crack will undergo stable growth when the stress is larger than σ_{ci} but less than σ_{cd} . Assume that the crack number in per unit volume is N_0 , the initial crack length and critical crack length are denoted by l_0 and l_c , respectively. The crack will enter into the unstable dynamic growth stage while the crack length is greater than l_c . If we denote the energy increase of rock caused by the growth of crack of unit length as Ω_e , then, the equilibrium equation of energy in pre-peak stage can be expressed as (Klein and Reuschle 2004)

$$W_S = W_Y + W_C \quad (2)$$

Based on Eq. (1), the expressions in Eq. (2) are as follows:

$$\begin{cases} W_S = \frac{(1 - \nu^2) \cdot \sigma^2 \cdot V}{2E_b} \\ W_Y = \frac{(1 - \nu^2) \cdot \sigma^2 \cdot V}{2E_m} \\ W_C = N_0 \cdot V \cdot (l - l_0) \cdot \Omega_e \end{cases}, \quad (3)$$

where $V = Lh$ is the pillar volume in plain model; W_S , W_Y and W_C are the energy absorbed by the rock, the rock matrix and the cracks when the stress is σ ($\sigma \leq \sigma_c$); l is crack length corresponding to σ ; E_m denotes the modulus of rock matrix, E_b is the equivalent pre-peak modulus of rock, E_1 is rock modulus in pre-peak stage after damage emergence; E_0 is rock modulus in pre-peak stage before damage emergence, where $E_m \geq E_0 > E_b > E_1$.

The rock is assumed to be still in equilibrium when the stress increases from σ_{ci} to σ ($\sigma_{ci} \leq \sigma \leq \sigma_{cd}$); the energy absorbed by the rock mass W_{S1} and rock matrix W_{Y1} is

$$\begin{cases} W_{S1} = \frac{(1 - \nu^2) \cdot (\sigma^2 - \sigma_{ci}^2) \cdot V}{2E_0} \\ W_{Y1} = \frac{(1 - \nu^2) \cdot (\sigma^2 - \sigma_{ci}^2) \cdot V}{2E_m} \end{cases} \quad (4)$$

Therefore, the energy, W_{C1} , consumed by the crack growth during this period is

$$W_{C1} = W_{S1} - W_{Y1} = \frac{(1 - \nu^2) \cdot (\sigma^2 - \sigma_{ci}^2) \cdot V}{2} \left(\frac{1}{E_0} - \frac{1}{E_m} \right). \quad (5)$$

While σ reaches σ_{cd} , Eq. (5) can be expressed as

$$W_{C1} = \frac{(1 - \nu^2) \cdot (k_2^2 - k_1^2) \cdot \sigma_c^2 \cdot Lh}{2} \left(\frac{1}{E_0} - \frac{1}{E_m} \right). \quad (6)$$

Based on Eqs. (6), (3), the energy, Ω_e , consumed by the increase of crack of unit length is

$$\Omega_e = \frac{(1 - \nu^2) \cdot (k_2^2 - k_1^2) \cdot \sigma_c^2}{2N_0(l_c - l_0)} \left(\frac{1}{E_0} - \frac{1}{E_m} \right). \quad (7)$$

If σ is greater than σ_{cd} , the cracks enter into the unstable dynamic growth stage and macro cracks start to occur. Based on Eq. (4), W_{S2} absorbed by the rock and W_{Y2} absorbed by the rock matrix from the occurrence of rock damage to the compressive strength σ_c is reached and can be expressed as

$$\begin{cases} W_{S2} = \frac{(1 - \nu^2) \cdot (\sigma_c^2 - \sigma_{cd}^2) \cdot V}{2E_1} \\ W_{Y2} = \frac{(1 - \nu^2) \cdot (\sigma_c^2 - \sigma_{cd}^2) \cdot V}{2E_m} \end{cases} \quad (8)$$

Based on Eq. (8), the total energy, W_{C2} , consumed by the cracks during the unstable crack growth stage is

$$W_{C2} = W_{S2} - W_{Y2} = \frac{(1 - \nu^2) \cdot (1 - k_2^2) \cdot \sigma_c^2 \cdot Lh}{2} \left(\frac{1}{E_1} - \frac{1}{E_m} \right). \quad (9)$$

Therefore, the increase of the crack length, l_d , during the unstable crack growth stage is

$$l_d = \frac{W_{C2}}{N_0 \cdot \Omega_e \cdot Lh}. \quad (10)$$

Substituting Eqs. (7) and (9) into Eq. (10), we have

$$l_d = \frac{(1 - k_2^2)(l_c - l_0)}{k_2^2 - k_1^2}. \quad (11)$$

Therefore, the total increase of single crack, l_{tot} during the whole crack growth stage (including stable and unstable crack growth stages) is

$$l_{\text{tot}} = (l_c - l_0) + l_d = \frac{(1 - k_1^2)(l_c - l_0)}{k_2^2 - k_1^2}. \quad (12)$$

The energy, W_{Ct} , consumed by the cracks during the whole crack growth stage (including stable and unstable crack growth stages), is

$$W_{\text{Ct}} = W_{\text{C1}} + W_{\text{C2}} = \frac{(1 - \nu^2) \cdot (1 - k_1^2) \cdot \sigma_c^2 \cdot Lh}{2} \left(\frac{1}{E_0} + \frac{1}{E_1} - \frac{2}{E_m} \right). \quad (13)$$

During the whole crack growth stage, the stress intensity factor is a variable; in order to simplify the analyses, we introduce the concept of equivalent stress intensity factor and denote it as K_i . Therefore, the equivalent stress intensity factor, K_i , in pre-peak stage can be obtained based on energy equilibrium and has the following form:

$$K_i = \sqrt{\frac{W_{\text{Ct}}}{\left[\frac{2(1-\nu^2)}{E_m} \right] \cdot l_{\text{tot}} \cdot N_0 \cdot Lh}} = \frac{\sigma_c}{2} \sqrt{\frac{(k_2^2 - k_1^2)}{N_0 \cdot (l_c - l_0)} \left(\frac{E_m}{E_0} + \frac{E_m}{E_1} - 2 \right)}. \quad (14)$$

Since the stress intensity factor at any moment of the pre-peak stage can be expressed based on K_i , the introduction of equivalent stress intensity factor is helpful for simplifying our following analyses. Based on the above analyses, the disturbance is assumed to be applied to the pillar at the moment that σ_c is reached, i.e., the moment that the pillar is in the critical state. Assume that the stress intensity factor, K_{it} , at the moment the stress reaches the compressive strength, σ_c , can be expressed as

$$K_{\text{it}} = \eta K_i = \eta \cdot \frac{\sigma_c}{2} \sqrt{\frac{(k_2^2 - k_1^2)}{N_0 \cdot (l_c - l_0)} \left(\frac{E_m}{E_0} + \frac{E_m}{E_1} - 2 \right)}, \quad (15)$$

where $\eta > 0$: while subjected to uniaxial compression, the crack propagation mode is mainly tension and expansion; therefore, the fracture toughness, K_{IC} has the following form:

$$K_{\text{IC}} = \sigma_t \sqrt{\pi l}. \quad (16)$$

Kachanov (1986) and Cotterell and Rice (1980) argued that the crack propagation mode in rock is not single, and may simultaneously include three modes. Therefore, the effective fracture toughness, K can be expressed as (Hoek and Martin 2014)

$$K = \kappa K_{\text{IC}}. \quad (17)$$

While based on maximum stress criterion, $\kappa = \sqrt{3}/2$; while based on maximum strain criterion, $\kappa = \sqrt{3(1-\nu)/(2+2\nu-\nu^2)}$; while based on maximum

energy release rate criterion, $\kappa = 1$. Therefore, when σ reaches σ_c , i.e., the total length of single one crack is $l_0 + l_{\text{tot}}$; the maximum fracture toughness K_{max} can be expressed as

$$K_{\text{max}} = \kappa \sigma_t \sqrt{\pi(l_0 + l_{\text{tot}})}. \quad (18)$$

Substituting Eq. (12) into Eq. (18), we obtain the maximum fracture toughness: K_{max}

$$K_{\text{max}} = \kappa \sigma_t \sqrt{\pi \frac{(1 - k_1^2) l_c - (1 - k_2^2) l_0}{(k_2^2 - k_1^2)}}. \quad (19)$$

Assume that a disturbance whose equivalent static stress can be denoted by $\Delta\sigma$ ($\Delta\sigma \rightarrow 0$) is applied to the pillar at the moment that the compressive strength, σ_c is reached (as aforementioned, the rock is in critical state when σ_c is reached), and then the stress of the pillar reaches $\sigma_c + \Delta\sigma$. At this moment, the energy increase in the rock and the energy consumed by the cracks corresponding to the stress increase from σ_c to $\sigma_c + \Delta\sigma$ are tiny enough and negligible. However, if there exists the relationship, $K_{\text{it}} \geq K_{\text{max}}$, the crack growth will continue; thus, the weak disturbance may trigger the instability of pillar.

As the stress increases from σ_c to $\sigma_c + \Delta\sigma$, although the increase of crack length can be ignored, it should be noted that the pillar will enter into the post-peak stage and the rock modulus will be the post-peak modulus. Hence, the modulus, E_1 in Eq. (15) should be replaced by E_2 , and the stress intensity factor, K_{ite} , corresponding to stress $\sigma_c + \Delta\sigma$, will be

$$K_{\text{ite}} = \eta \frac{\sigma_c}{2} \cdot \sqrt{\frac{(k_2^2 - k_1^2)}{N_0 \cdot (l_c - l_0)} \left(\frac{E_m}{E_0} + \frac{E_m}{|E_1|} - 2 \right)}. \quad (20)$$

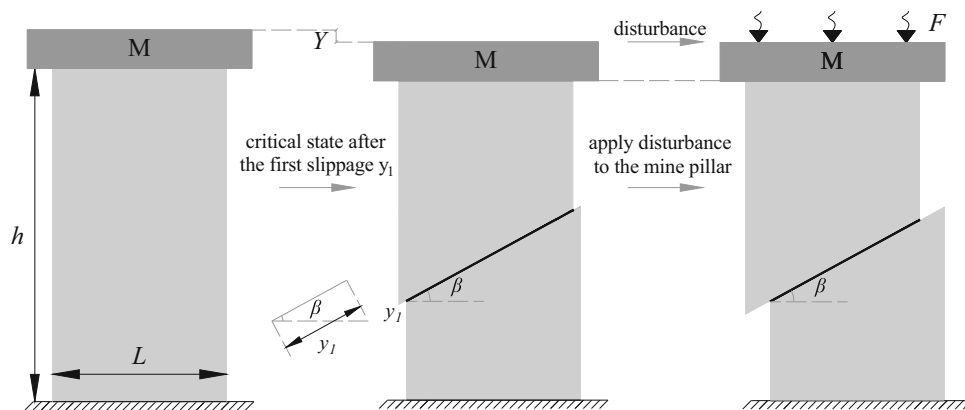
Comparing Eq. (15) with Eq. (20), we can see that if the stress increases from σ_c to $\sigma_c + \Delta\sigma$, E_1 will be replaced by $|E_2|$; thus, the changes of stress intensity factor may be obvious. In order to simplify the analysis, before the occurrence of rock damage, the modulus of rock matrix can be approximated by the rock modulus; hence, we use E_0 to replace E_m . Therefore, based on the relationship $K_{\text{ite}} \geq K_{\text{max}}$ and Eqs. (19), (20), the condition required for triggering pillar instability with weak disturbance is

$$\frac{E_0}{|E_2|} = \left(\frac{2\kappa\sqrt{\pi}}{\eta} \right)^2 \left(\frac{\sigma_t}{\sigma_c} \right)^2 \frac{[(1 - k_1^2) l_c - (1 - k_2^2) l_0] (l_c - l_0) \cdot N_0}{(k_2^2 - k_1^2)^2} + 1, \quad (21)$$

where E_0 is the rock modulus before damage emergence.

According to the existing studies (Qian 2014; Wang et al. 2016), the essence of triggering instability is maintaining the self-sustained failure with energy released by the system itself. The role of weak disturbance is a trigger, which will induce the system's energy release and energy

Fig. 3 Sliding-type instability of pillar (slippage y_1 corresponding to A_1 in Fig. 5)



transformation. The requirement for this characteristics is the rock’s post-peak modulus, which is greater than zero (Tarasov and Potvin 2013); thus, $|E_2| = E_2$. Let us denote the equivalent pre-peak modulus of rock as E_b , and there will be $E_b/E_2 \leq E_0/E_2$. In order to further simplify Eq. (21), we introduce δ to represent the maximum open of the crack during the stable crack growth stage. The crack open, δ , the critical crack length, l_c , and the increase of crack length, $(l_c - l_0)$, will have the same order of magnitude; thus

$$\frac{E_b}{E_2} \leq \frac{E_0}{E_2} \leq \left(\frac{2\kappa\sqrt{\pi}}{\eta}\right)^2 \left(\frac{\sigma_t}{\sigma_c}\right)^2 \left\{ \frac{l_c}{\delta} \cdot \frac{\Delta V}{(k_2^2 - k_1^2)} \right\} + 1, \quad (22)$$

where $l_c/\delta \sim (10 \sim 100)$, $\Delta V \sim (10^{-5} \sim 10^{-4})$ is the volume increase during the stable crack growth stage, which is tiny enough when compared with $(k_2^2 - k_1^2) \approx 0.4$. Equation (22) also shows that the introduction of κ and η , namely, although the stress intensity factor and the fracture toughness are neither uncertain, the final conclusion is unchanged. Therefore, the mechanical property required for triggering mine pillar instability is

$$E_2 \geq E_b. \quad (23)$$

Equation (23) shows that, if the pillar instability can be triggered by weak disturbance, it is required that the post-peak modulus is greater than or equal to the pre-peak modulus.

Based on large numbers of experimental studies, Tarasov and Potvin (2013) have drawn the conclusion that if the post-peak modulus is greater than or equal to the pre-peak modulus, the rock is super-brittle and it can undergo self-sustained failure under uniaxial compression. In fact, as aforementioned, the essence of triggering instability is the self-sustained failure triggered by weak disturbance, and the effects of weak disturbance help transforming the system’s potential energy into kinetic energy (Wang et al. 2015, 2016). It is shown that our conclusion derived

theoretically, which is denoted by Eq. (23), is the same with the conclusions proposed by Tarasov and Potvin.

Interestingly, the experimental study of Tarasov and Potvin (2013) also showed that the phenomenon corresponding to the mechanical property that the post-peak modulus is greater than zero is the occurrence of shear-band when subjected to uniaxial compression, and the final failure of these rocks is the result of excessive sliding along the shear-band. Therefore, the triggered instability of mine pillar can belong to sliding-type. Hence, our following analyses of pillar instability triggered by weak disturbance will start from the establishment of a pillar with an inclined shear-band and the assumption that the stress state on the shear-band is in its critical state.

In fact, the studies of large numbers of earthquake and sudden dynamic events all show that when investigating these problems, more attention should be paid to the shear-band, the weaker zone and the fault (Lastakowski et al. 2015; Johnson and Jia 2005; Gomberg et al. 2001). This really provides valuable references for us to study the induced mine pillar instability which is caused by excessive sliding on shear-band in the following section.

Triggering instability of mine pillar with single shear-band

As shown in Fig. 3, the mine pillar is in unit thickness, with its height and width shown in h and L ; when subjected to long-term static load, a shear-band with its dip angle in β occurs. Assume that the stress state on the shear-band is in critical state and the pillar will undergo sliding-type instability when triggered by weak disturbance. Johnson and Jia (2005) pointed out that three conditions are simultaneously required for triggering dynamic events: (1) a weaker zone in the system; in this paper, the shear-band is the weaker zone in pillar; (2) stress state in weaker zone reaches the critical state; in this paper, it is assumed that the shear-band is in its critical state; (3) the order of strain

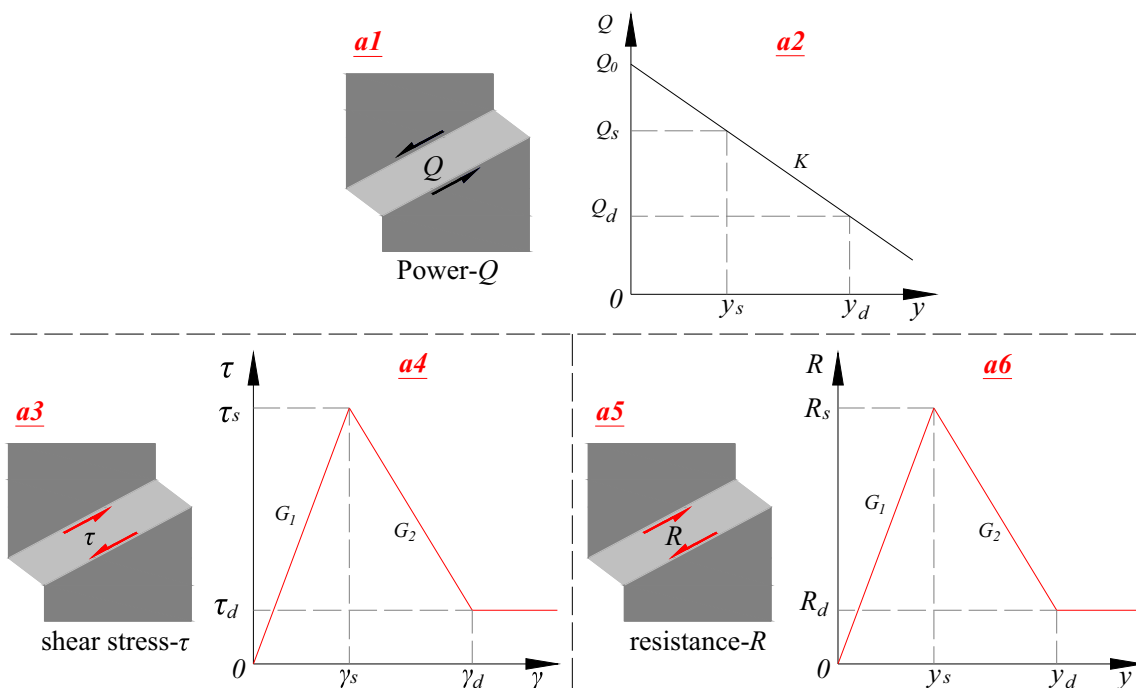


Fig. 4 Evolution of R and Q on the shear-band

induced by disturbance is greater than 10^{-6} , which is mainly due to that the transition from static friction to dynamic friction requires a certain amount of cumulative displacement.

As shown in Fig. 3, the total axial deformation of pillar consists of the roof displacement, Y , the elastic deformation of pillar, y_e and the axial component of sliding, y

$$Y = y_e + y \sin \beta. \tag{24}$$

The occurrence of shear-band in pillar takes very long time; thus, the thermal effects in this process is negligible. Assume that the energy consumed by the shear-band is only related to sliding and the energy consumed is stored as potential energy on shear-band. Therefore, the total potential energy of the pillar consists of the gravity potential, the energy consumed by the shear-band and the elastic potential energy:

$$W = M_g(h - Y) + \frac{LU(y)}{\cos \beta} + \frac{1}{2} \frac{E}{1 - \nu^2} \left(\frac{y_e}{h}\right)^2 Lh, \tag{25}$$

where M_g is the roof gravity, ν is Poisson's ratio, $E/(1 - \nu^2)$ is modulus of plane model, y_e/h is the axial elastic strain of pillar, Lh is the pillar volume in plane model.

In practical engineering, the total roof displacement can be obtained by monitoring and it can be regarded as a known quantity here; thus, the total potential energy will be function of variables, y_e and y . Simplifying Eq. (25) as an expression containing single one variable and based on the

minimum potential energy principle, let $\partial W/\partial y = 0$; then we have

$$U'(y) = \frac{E}{1 - \nu^2} \frac{Y - y \sin \beta}{h} \sin \beta \cos \beta = -\frac{\lambda}{h} y + \frac{\lambda}{h \sin \beta} Y, \tag{26}$$

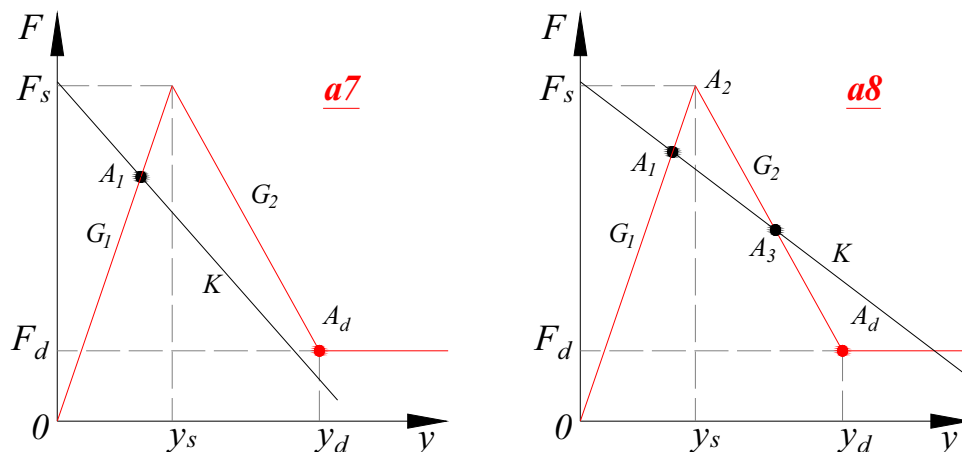
where $\lambda = \frac{E}{1 - \nu^2} \sin^2 \beta \cos \beta > 0$; $U'(y) = \partial U(y)/\partial y$ represents the shear stress on shear-band; for that the area of shear-band in plane model is $L/\cos \beta$, which has the same expression as the length of shear-band. Therefore, based on Eq. (26), the force, Q , which drives the pillar sliding, can be expressed as

$$Q = Ky + Q_0, \tag{27}$$

where $K = -\lambda L/h \cos \beta < 0$, $Q_0 = \lambda LY/h \sin \beta \cos \beta$; when $y = 0$, Q_0 can be also expressed as $Q_0 = (M_g \sin \beta)L/h$. The direction of Q is shown in Fig. 4a1; the decrease of Q with the increase of y is shown in Fig. 4a2.

The force, R , which resists the pillar sliding, is determined by the shear stress, τ . Figure 4a3 shows the direction of τ , and Fig. 4a4 shows the relationship between τ and the shear strain, γ . τ increases from 0 to τ_s with the increase of γ from 0 to γ_s , and then decreases to τ_d with γ increasing from γ_s to γ_d . The shear-stress is assumed to be unchanged when the shear strain is greater than γ_d . According to $\tau = G\gamma$, we can deduce that $\tau(L/\cos \beta) = G\gamma(L/\cos \beta)$; thus, $R = Gy$ (as shown in Fig. 4a5, a6). Where

Fig. 5 Relationship between R and Q on the shear-band



$R_s = \tau_s(L/\cos \beta)$, $R_d = \tau_d(L/\cos \beta)$; G_1 and G_2 are the pre-peak and post-peak shear moduli, respectively.

In fact, special conditions are required for triggering sliding-type mine pillar instability. The typical relationships between R and Q are shown in Fig. 5. Pillar instability is assumed to occur when the sliding is greater than y_d .

As shown in Fig. 5, intersection A_1 denotes that Q and R are equal for the first time; in this case, the stress state on shear-band is in critical state, which is the beginning of triggering pillar instability. As shown in Fig. 5a7, there is no intersection besides A_1 ; in this case, from A_1 to A_d , R is always greater than Q , and thus, the pillar is stable. However, as shown in Fig. 5a8, besides A_1 , there is another intersection, A_3 , which is located in the post-peak stage; in this case, the pillar may undergo self-sustained failure with appropriate energy inputted (the inputted energy is consumed by sliding from A_1 to A_3 , and it can be approximately estimated by the area $A_1A_2A_3$ as shown in Fig. 5a8). For that R is greater than Q from A_1 to A_3 , while less than Q from A_3 to A_d ; thus, when A_3 is exceeded, self-sustained sliding will occur, i.e., mine pillar instability can be induced by disturbance. Next, we will try to derive the conditions corresponding to the aforementioned two cases.

As shown in Fig. 5a6, the expression of R is

$$R(y) \begin{cases} G_1 y & 0 \leq y < y_s \\ -G_2(y - y_s) + R_s & y_s \leq y < y_d, \\ R_d & y \geq y_d \end{cases} \quad (28)$$

Based on the aforementioned statements and $|K| = G_1$, the conditions corresponding to the state of pillar can be expressed as

$$\begin{cases} G_1 \leq G_2 & \text{unstable, can be triggered} \\ G_1 > G_2 & \text{stable, can not be triggered} \end{cases} \quad (29)$$

As aforementioned, let us denote the pre-peak and post-peak moduli as E_b and E_2 , respectively, and then Eq. (29) can be further simplified as

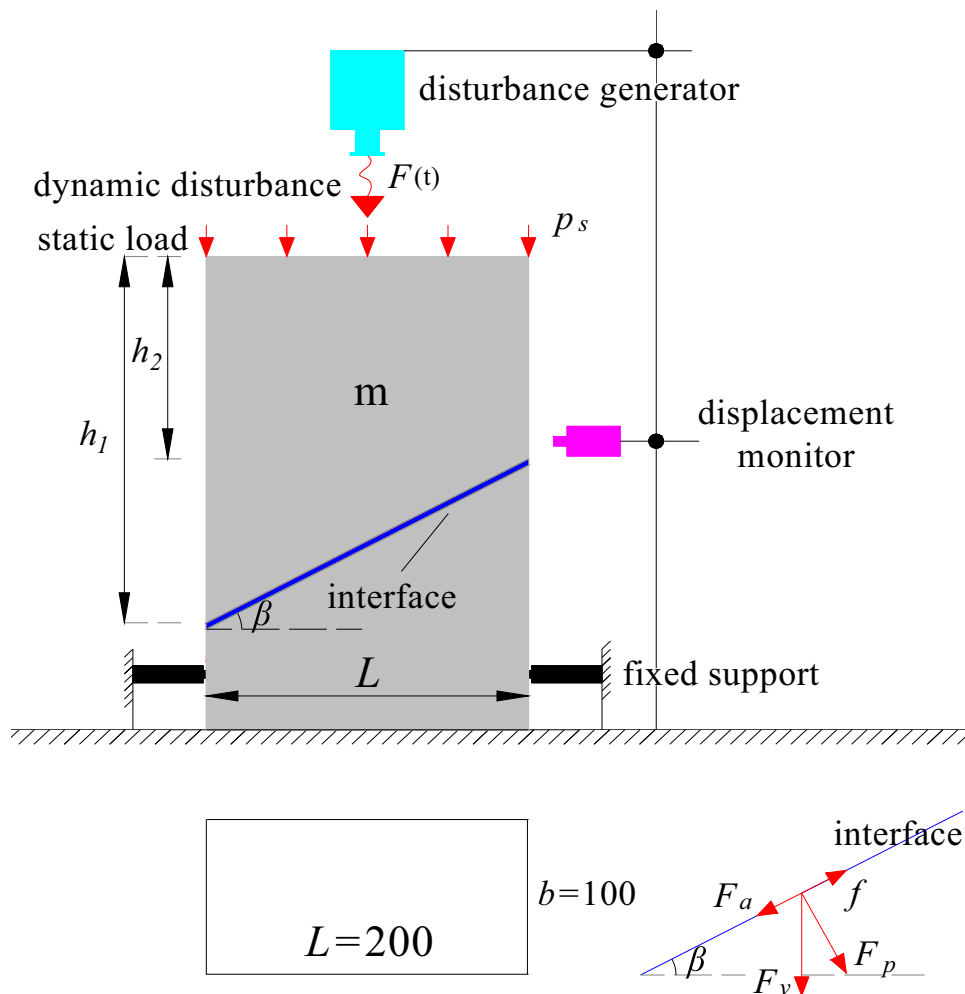
$$\begin{cases} E_b \leq E_2 & \text{unstable, can be triggered} \\ E_b > E_2 & \text{stable, can not be triggered} \end{cases} \quad (30)$$

Interestingly, the mechanical property required for triggering mine pillar instability derived based on the above two models in Sects. “Premises of mechanical property for triggering mine pillar rockburst” and “Triggering instability of mine pillar with single shear-band” are the same. Considering that the occurrence of shear-band (corresponding to the occurrence of weak zone) is the premise of triggering instability, and the pillar with stress state on shear-band in its critical state is the beginning of triggering instability (corresponding to stress state on weak zone is in critical state). Therefore, the post-peak modulus greater than or equal to the pre-peak modulus is the basic mechanical property required for triggering mine pillar instability.

Verification of proposed model

In order to verify the model proposed in this manuscript, experiments are conducted, and the schematic diagram of the experiment is shown in Fig. 6. The disturbance-induced instability is studied in incoherent, frictional interfaces held together by uniaxial compression, p_s . The interface, which represents the shear-band in our experiment, is inclined at an angle, β to the horizontal direction. The super-brittle quartzite specimen, with Young’s modulus $E = 55.7$ GPa, Poisson’s ration $\nu = 0.15$ and density $\rho = 2680$ kg/m³ is adopted in our experiment. The carefully prepared interfaces has a measured static friction coefficient $\mu_s = 0.6$,

Fig. 6 Diagram of triggering sliding instability of mine pillar with external disturbance



which is estimated by finding critical angle for triggering dynamic instability, and the dynamic coefficient is estimated to be $\mu_d = 0.2$. The sizes of the quartzite specimen are $L \times b = 200 \text{ mm} \times 100 \text{ mm}$, $h_1 = 400 \text{ mm}$, $h_2 = 350 \text{ mm}$; therefore, $\beta \approx 14^\circ$. The mass of the block above the interface is $m = 20.1 \text{ kg}$. If β is too large, the static balance is difficult to maintain, and if β is too small, the instability would not be triggered. The critical angle for triggering instability is estimated to be $\beta = 10^\circ - 15^\circ$. The stresses tangential to and perpendicular to the interface, as shown in the lower part of Fig. 6, are denoted by f , F_a and F_p , respectively.

$$\begin{cases} f = \mu F_p \\ F_a = \Sigma F \cdot \sin \beta \\ F_p = \Sigma F \cdot \cos \beta \end{cases} \quad (31)$$

where $\Sigma F = M_g + p_s b L$.

The disturbance force, $F(t)$, is applied by the generator as shown in Fig. 6; the energy of disturbance is calculated by dealing the force–time curve with MATLAB software, and the (cumulative horizontal) displacement of the above

block is monitored by the displacement monitor. With a given inclined angle β , the critical displacement before instability is determined by both the disturbance energy and the compression, p_s .

Figure 7 reflects two phenomena: (1) with a given disturbance energy, the displacement will increase with the compression, where p_s is increased; (2) under the same compression, the larger the disturbance energy, the larger the cumulative displacement: however, the smaller the critical displacement for instability. In order to see the second phenomenon clearly, we conducted another experiment with smaller disturbance energy. As shown in Fig. 8, the relations among the compression, the disturbance energy and the displacement reflected by the above two figures are the same.

In fact, it is not difficult to understand the first phenomenon, but the second one is really confusing. Because based on Eq. (31), the larger the compression, p_s , the larger the friction, f will be, thus; more energy will be consumed in the same sliding distance. It is obvious that the second phenomenon reflected in the above figures is inconsistent

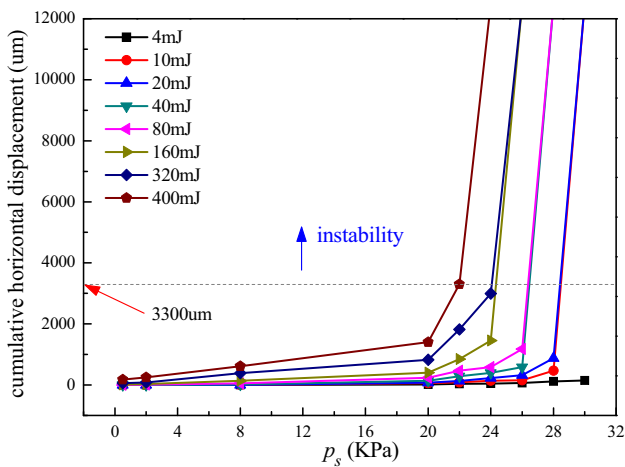


Fig. 7 Curves of horizontal displacement

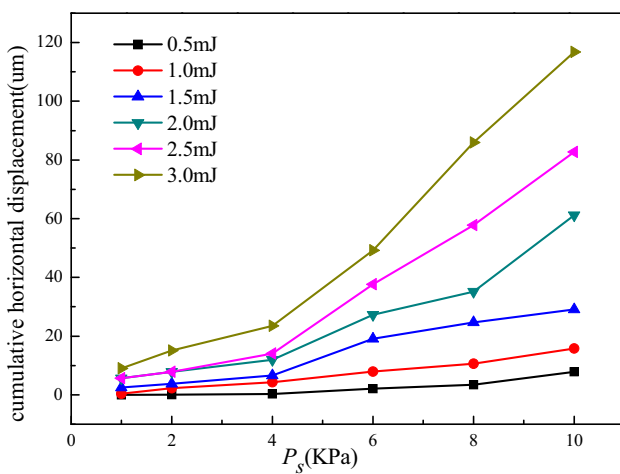


Fig. 8 Curves of horizontal displacement with low disturbance energy and low compression

with the analysis based on Eq. (31); thus, we can guess that the application of disturbance will obviously influence the evolution of normal stress on the interface, we can also guess that the disturbance will induce rebound in the normal direction of the shear-band. Larger p_s will result in larger amount of elastic energy stored in the shear-band and thus, the larger the disturbance-induced rebound may be. However, they are just preliminary guesses; the systematic study of the mechanism underlying the above phenomena is outside the scope of this manuscript and we will try to present it in another manuscript in the future.

Conclusions

In this paper, two plane models are established, of which, one is the mine pillar with large numbers of cracks, and another is the mine pillar with single shear-band. With

appropriate assumptions, the basic mechanical property required for triggering mine pillar instability is separately derived based on the above two models. Based on our analyses, the following conclusions are drawn:

- (1) When attributing the instability of mine pillar to the induced unstable crack growth, if the post-peak modulus is greater than or equal to the pre-peak modulus, the instability can be triggered if a weak disturbance is applied to the pillar in its critical state.
- (2) If the post-peak modulus is larger than or equal to the pre-peak modulus, the disturbance-induced sliding on shear-band can cause the instability of mine pillar.
- (3) The pillar instability that can be triggered by weak disturbance belongs to sliding-type rockburst.
- (4) Considering the whole processes of triggering mine pillar instability are (1) the occurrences of shear-band under long-term static load; (2) stress state on shear-band reaches its critical state; (3) an appropriate disturbance is applied to the pillar; (4) mine pillar instability occurs. Therefore, the post-peak modulus is greater than or equal to the pre-peak modulus, which is the decisive mechanical property controlling the aforementioned instability processes.
- (5) The mine pillar instability can be triggered only if the post-peak modulus is greater than or equal to the pre-peak modulus, which may be the reason why the triggered mine pillar rockburst is not often observed.
- (6) More efforts are still required to further investigate the mechanism underlying triggered mine pillar instability, especially the stresses evolution on shear-band while the pillar is simultaneously subjected to static load and dynamic disturbance.

Acknowledgements The authors would like to acknowledge the financial support from the National Natural Science Foundation of China (Grant nos. 51527810, 51679249), which is greatly appreciated by the authors.

Compliance with ethical standards

Conflict of interest On behalf of all authors, the corresponding author states that there is no conflict of interest.

References

- Atkinson BK (1992) Fracture mechanics of rock. Seismological Press, Beijing
- Cai M (2010) Practical estimates of tensile strength and Hoek-Brown strength parameter m_i of brittle rocks. *Rock Mech Rock Eng* 43:167–184
- Cai M, Kaiser PK, Tasaka Y, Maejima T, Morioka H, Minami M (2004) Generalized crack initiation and crack damage stress

- thresholds of brittle rock masses near underground excavations. *Int J Rock Mech Min Sci* 41:833–847
- Cook NGW (1965) A note on rockburst considered as a problem of stability. *J S Afr Inst Min Metall* 65:437–445
- Cotterell B, Rice JR (1980) Slightly curved or kinked cracks. *Int J Fract* 16(2):155–169
- Gomberg J, Reasenber PA et al (2001) Earthquake triggering by seismic waves following the Landers and Hector Mine earthquake. *Nature* 411:462–466
- Hill DP, Reasenber PA et al (1993) Seismicity remotely triggered by the magnitude 7.3 landers, california, earthquake. *Science* 260:1617–1623
- Hoek E, Martin CD (2014) Fracture initiation and propagation in intact rock—a review. *J Rock Mech Geotech Eng* 6:287–300
- Horii H, Nemat-Nasser S (1985) Compression-induced microcrack growth in brittle solids: axial splitting and shear failure. *J Geophys Res* 90:3105–3125
- Jiang YD, Pan YS, Jiang FX, Dou LM, Ju Y (2014) State of the art review on mechanism and prevention of coal bumps in china. *J China Coal Soc* 39(2):205–213
- Johnson PA, Jia XP (2005) Nonlinear dynamics, granular media and dynamic earthquake triggering. *Nature* 437:871–874
- Kachanov LM (1986) Introduction to the continuum damage mechanics. Springer, Dordrecht
- Klein E, Reuschle T (2004) A pore crack model for the mechanical behaviour of porous granular rocks in the brittle deformation regime. *Int J Rock Mech Min Sci* 41:975–986
- Landau LD, Lifshitz EM (2013) Fluid mechanics, Volume 6 of Course of Theoretical Physics, 5th edn. Higher Education Press, Beijing
- Lastakowski H, Geminard JC, Vidal V (2015) Granular friction: triggering large events with small vibrations. *Sci Rep* 5:1–5
- Li JT, Cao P (2006) Analysis of pillar stability in hard rock mass by longitudinal splitting based on catastrophe theory. *J Cent South Univ (Sci Tech)* 37(2):371–375
- Li T, Cai MF, Cai M (2007a) A review of mining-induced seismicity in China. *Int J Rock Mech Min Sci* 44:1149–1171
- Li XB, Li DY, Guo L, Ye ZY (2007b) Study on mechanical response of highly-stressed pillars in deep mining under dynamic disturbance. *Chin J Rock Mech Eng* 26(5):922–928
- Linkov AV (1992) Dynamic phenomena in mines and the problem of stability. University of Minnesota, Minnesota
- Lu HJ, Liang P, Gan DQ, Sun GP (2015) Stress evolution and surface subsidence laws of hard rock pillars under dynamic disturbance. *Metal Mine* 7:6–10
- Qian QH (2014) Definition, mechanism, classification and quantitative forecast model for rockburst and pressure bump. *Rock Soil Mech* 35(1):1–6
- Ryder JA (1988) Excess shear stress in the assessment of geologically hazardous situations. *J S Afr Inst Min Metall* 88:27–39
- Salamon MDG (1993) Keynote address: Some applications of geomechanical modelling in rockburst and related research// Rockburst and seismicity in mines. A.A. Balkema, Rotterdam
- Stacey TR (2013) Dynamic rock failure and its containment. In: Proceedings of the first international conference on rock dynamic and applications. CRC Press, Lausanne, p 57–70
- Tan TK (1987) Rockburst, case records, theory and control. *Chin J Rock Mech Eng* 6(1):1–18
- Tarasov B, Potvin Y (2013) Universal criteria for rock brittleness estimation under triaxial compression. *Int J Rock Mech Min Sci* 59:57–69
- Wang LG, Miao XX (2006) Study of mechanism of destabilization of the mine pillar based on a cusp catastrophic model. *J Min Saf Eng* 23(2):137–140
- Wang XB, Pan YS, Ren WJ (2003) Instability criterion of shear failure for rock specimen based on gradient-dependent plasticity. *Chin J Rock Mech Eng* 22(5):747–750
- Wang SY, Lam KC, Au SK, Tang CA, Zhu WC, Yang TH (2006) Analytical and numerical study on the pillar rockburst mechanism. *Rock Mech Rock Eng* 39(5):445–467
- Wang MY, Li J, Li KR (2015) A nonlinear mechanical energy theory in deep rock mass engineering and its application. *Chin J Rock Mech Eng* 34(4):659–667
- Wang MY, Li J, Ma LJ, Huang HX (2016) Study on the characteristic energy factor of the deep rock mass under weak disturbance. *Rock Mech Rock Eng* 49(8):3165–3173
- Xia KW, Rosakis AJ, Kanamori H (2004) Laboratory earthquake: the sub-Rayleigh-to-supershear rupture transition. *Science* 303:1859–1861
- Yang YJ, Xing LY, Zhang YQ, Ma DP (2015) Analysis of long-term stability of gypsum pillars based on creep tests. *Chn J Rock Mech Eng* 34(10):2106–2113
- Zhou XP, Shou YD, Qian QH, Yu MH (2014) Three-dimensional nonlinear strength criterion for rock-like materials based on the micromechanical method. *Int J Rock Mech Min Sci* 72:54–60

Splitter plate as a flow-altering pier scour countermeasure

Shivakumar Khaple¹ · Prashanth Reddy Hanmaiahgari¹ · Roberto Gaudio² · Subhasish Dey^{1,3,4} 

Received: 5 April 2017 / Accepted: 7 September 2017 / Published online: 18 September 2017
© Institute of Geophysics, Polish Academy of Sciences & Polish Academy of Sciences 2017

Abstract Results of an experimental study on the countermeasure of scour depth at circular piers are presented. Experiments were conducted for pier scour with and without a splitter plate under a steady, uniform clear-water flow condition. The results of pier scour without splitter plate were used as a reference. Different combinations of lengths and thicknesses of splitter plates were tested attaching each of them to a pier at the upstream vertical plane of symmetry. Two different median sediment sizes ($d_{50} = 0.96$ and 1.8 mm) were considered as bed sediment. The experimental results show that the scour depth consistently decreases with an increase in splitter plate length, while the scour depth remains independent of splitter plate thickness. In addition, temporal evolution of scour depth at piers with and without a splitter plate is observed. The best combination is found to be with a splitter plate thickness of

$b/5$ and a length of $2b$. Here, b denotes the pier diameter. An empirical formula for the estimation of equilibrium scour depth at piers with splitter plates is obtained from a multiple linear regression analysis of the experimental data. The flow fields for various combinations of circular piers with and without splitter plate including plain bed and equilibrium scour conditions were measured by using an acoustic Doppler velocimeter. The turbulent flow fields for various configurations are investigated by plotting the velocity vectors and the turbulent kinetic energy contours on vertical and horizontal planes. The splitter plate attached to the pier deflects the approach flow and thus weakens the strength of the downflow and the horseshoe vortex, being instrumental in reducing the equilibrium scour depth at piers. The proposed method of pier scour countermeasure is easy to install and cost effective as well.

✉ Subhasish Dey
sdey@iitkgp.ac.in

Shivakumar Khaple
shivabku@gmail.com

Prashanth Reddy Hanmaiahgari
hpr@civil.iitkgp.ernet.in

Roberto Gaudio
gaudio@unica.it

¹ Department of Civil Engineering, Indian Institute of Technology Kharagpur, Kharagpur, West Bengal, India

² Dipartimento di Ingegneria Civile, Università della Calabria, Rende, CS, Italy

³ Physics and Applied Mathematics Unit, Indian Statistical Institute Kolkata, Kolkata, West Bengal, India

⁴ Department of Hydraulic Engineering, State Key Laboratory of Hydro-Science and Engineering, Tsinghua University, Beijing, China

Keywords Scour · Erosion · Scour countermeasure · Bridge piers · Sediment transport · Pier protection · Splitter plate

List of symbols

B	Channel width
B	Pier diameter
C_{sp}	Coefficient of splitter plate
d_s	Maximum scour depth
$d_{s,o}$	Observed scour depth
$d_{s,c}$	Computed scour depth
d_{s0}	Scour depth at unprotected pier
d_{sp}	Scour depth at protected pier
d_{su}	Maximum scour depth at unprotected pier
d_{16}	16% finer sediment size
d_{50}	Median sediment size
d_{84}	84% finer sediment size
F	Flow Froude number

g	Gravitational acceleration
h	Approaching flow depth
k	Turbulent kinetic energy
K_e	Equivalent roughness height
l_p	Splitter plate length
R_e	Equivalent Reynolds number
r_{ds}	Percentage reduction of scour depth
s	Relative sediment density
t	Time
t_p	Thickness of splitter plate
U	Approaching flow velocity
U_c	Critical flow velocity
U_{*c}	Critical shear flow velocity
u	Instantaneous streamwise velocity component
u'	Fluctuations of u
v	Instantaneous spanwise velocity component
v'	Fluctuations of v
w	Instantaneous vertical velocity component
w'	Fluctuations of w
x	Streamwise distance from the flume inlet
\hat{x}	Non-dimensional streamwise distance ($= x/b$)
z	Vertical distance from the bed
\hat{z}	Non-dimensional vertical distance ($= z/b$)
Δ	Relative submerged density ($= s - 1$)
σ_g	Geometric standard deviation of sediment size

Introduction

The topic of local scour has a wide practical importance from the viewpoint of the stability of river and marine structures, such as bridges, coastal structures, storm-surge barriers, offshore platforms, subsea templates etc., as excessive scour causes the failure of structures (Dey et al. 2006). Estimation of scour at bridge piers poses a challenging problem to the hydraulic engineers, in particular. When river flows across a bridge pier, flow separation takes place around the pier. The upstream boundary layer undergoes a three-dimensional separation and forms a system of horseshoe vortex and a downflow close to the pier. As a result, scour occurs at piers owing to the removal of bed sediments (Dey et al. 1995). It is therefore utmost important to find an effective pier scour countermeasure, which is easy to install and cost effective as well.

Various researchers extensively studied to propose different effective pier scour countermeasures for the safety of bridges. Countermeasures for controlling scour at piers can be divided into two categories: bed-armoring countermeasure and flow-altering countermeasure. Flow-altering countermeasures include sacrificial piles arranged in a triangular pattern upstream of piers (Chabert and Engeldinger 1956; Melville and Hadfield 1999), a collar placed around the pier (Chiew 1992; Zarrati et al. 2004; Jahangirzadeh et al.

2014), combined system of slot and bed sill (Grimaldi et al. 2009), submerged vanes (Odgaard and Mosconi 1987; Lauchlan 1999; Ouyang and Lin 2016), rectangular slots through piers (Chiew 1992; Kumar et al. 1999), and triple rectangular plates (Arabani and Hajikandi 2015). A detailed review on flow-altering countermeasures was compiled by Tafarajnoruz et al. (2010). However, most of the available scour countermeasures are expensive and time consuming.

The full-depth splitter plate can be included among the flow-altering countermeasures to protect bridge piers from scour. Very few researchers (say Dey et al. 2006) studied a splitter plate attached to the nose of the pier up to the flow depth to control the scour depth at a circular pier. Downflow, horseshoe vortex, and wake vortices behind the pier are the primary agents causing the scour at piers. When a splitter plate is attached to the pier, it deflects the streamlines and decreases the erosive strength of the downflow and the horseshoe vortex. In addition, length and thickness influence the effectiveness of the splitter plate. Parker et al. (1998) reported that the splitter plate is an important factor to modify the flow pattern around the pier, which in turn affects the scour hole dimensions.

The present study investigates the efficiency of splitter plates, in terms of reduction of equilibrium scour depth at a circular pier, under clear-water condition. The temporal evolution of the scour depth at the pier with a splitter plate is also studied. An empirical formula for the estimation of equilibrium scour depth at piers with splitter plates is obtained using a multiple linear regression analysis. Finally, the turbulent flow field around the pier, with and without splitter plate for plane bed and equilibrium scour hole, is analyzed to identify the reasons behind the scour reduction in presence of a splitter plate.

Experimental methodology and procedure

Experiments were carried out in a 0.91 m wide, 0.70 m deep, and 15.5 m long rectangular flume with a longitudinal slope of 0.02%, located in the Hydraulic and Water Resources Engineering Laboratory of the Department of Civil Engineering, at the Indian Institute of Technology Kharagpur, India. Figure 1 shows the schematic of the experimental setup. An acrylic circular pier model of diameter b was embedded vertically in the sediment bed at the middle of a 2.5 m long, 0.91 m wide, and 0.3 m deep sediment recess box, which was filled with uniform sediment. In this study, two different pier sizes ($b = 6$ and 8.2 cm) and two median sediment sizes ($d_{50} = 0.96$ and 1.8 mm) were used in the experiments. The geometric standard deviation of the particle size distribution, $\sigma_g = (d_{84}/d_{16})^{0.5}$, was 1.21 and 1.18 for the sediment sizes $d_{50} = 0.96$ and 1.8 mm, respectively (d_{84}

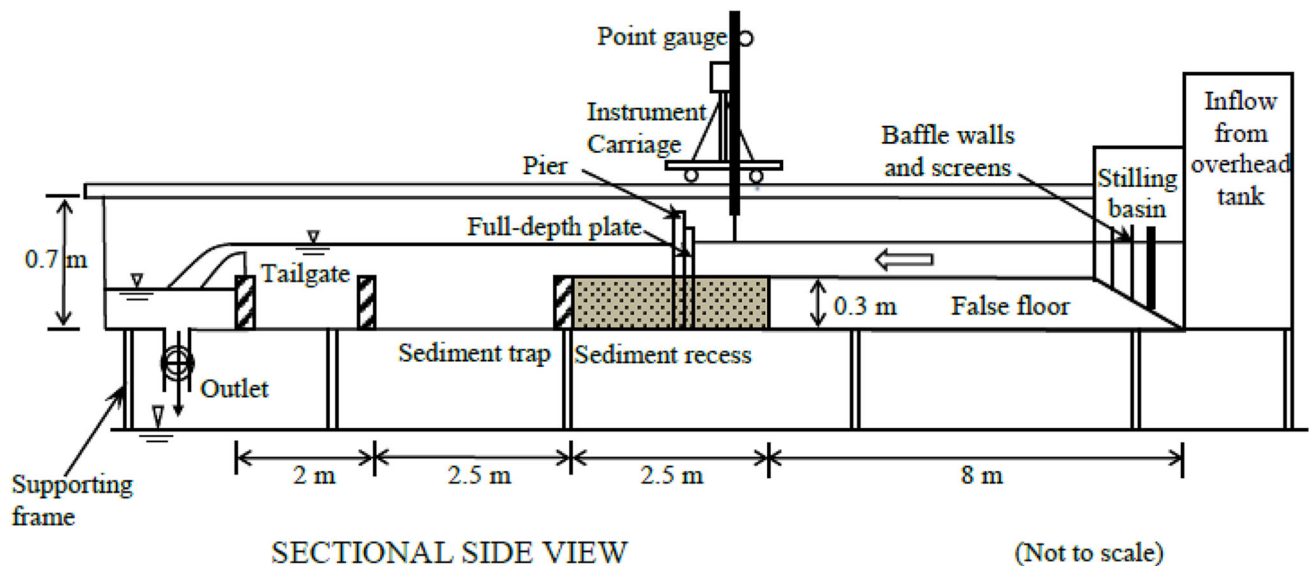


Fig. 1 Schematic diagram of the flume with a pier model

and d_{16} being the sediment size for which 84 and 16%, respectively, by weight of the sediment is finer). The computed σ_g values of the two sediment beds are less than 1.4, which is the upper limit for uniformly graded sediment (Dey et al. 1995).

The test section was taken at 8.5 m downstream of the flume inlet to allow formation of fully developed turbulent flow at the test section. In order to maintain the same level as that of the sediment recess, the full length of the flume floor was constructed at an elevation of 0.3 m from the flume bottom (Fig. 1). To create a fully developed turbulent flow, the same uniform sediment as that in the sediment recess was glued over the full length of the flume during the experiments. The side walls of the test section were made of 4.5 m long transparent glass panels, to visualize the scouring process and related hydrodynamic phenomena. The flume was connected to a re-circulating water supply system in the laboratory. A 2.5 m long, 0.91 m wide, and 0.3 m deep sediment trap was constructed to collect the scoured sediments, at the downstream end of the sediment recess box. A calibrated V-notch weir, through which flow enters the flume, was

used to measure the flow discharge. The flow depth in the flume was adjusted by using a tailgate. A Vernier point gauge with an accuracy of ± 0.1 mm was used to measure the water surface level and the scour depth.

All the experiments were conducted with an accurately leveled sediment bed at the beginning of the experiments. Experiments were carried out with a steady, uniform flow and clear-water condition for a period of 24 h, at the end of which an equilibrium scour was attained.

In these experiments, the lengths and thickness splitter plates were varied. Five different lengths l_p ($l_p/b = 0, 0.5, 1.0, 1.5, 2.0, 2.5$) and two plate thicknesses t_p ($t_p/b = 1/12$ and $1/5$) were used. Table 1 presents the various hydraulic conditions and dimensionless groups pertaining to the experiments.

To obtain the equilibrium scour depth in clear-water conditions, utmost care has been taken to perform the experiments. The flow intensity was maintained as $U/U_c = 0.9$ (clear-water condition) in all the tests, where U is the approach flow velocity and U_c is the critical value for the inception of sediment motion. The critical shear velocities U_{*c} for sediments used in this study were

Table 1 Experimental conditions and dimensionless groups

Test series	b (cm)	d_{50} (mm)	h (cm)	U (m/s)	U_c (m/s)	U_{*c} (m/s)	U/U_c	B/d_{50}	B/b	B/h	F	h/d_{50}	R_p
I	6.0	0.96	15.0	0.343	0.381	0.0203	0.9	62.5	15.2	6.07	0.282	156.25	20580
II	8.2	0.96	20.5	0.359	0.398	0.0203	0.9	85.4	11.1	4.44	0.253	213.5	29438
III	6.0	1.80	15.0	0.467	0.518	0.0305	0.9	33.3	15.2	6.07	0.385	83.30	28020
IV	8.2	1.80	20.5	0.490	0.544	0.0305	0.9	45.5	11.1	4.44	0.345	113.8	40180

b pier diameter, d_{50} median sediment size, h flow depth, U approach flow velocity, U_c critical velocity, U_{*c} critical shear velocity, B flume width, F Froude number $[=U/(gh)^{0.5}]$, R_p pier Reynolds number $(=Ub/\nu)$ and ν coefficient of kinematic viscosity

determined using the Shields diagram as furnished in Table 1. Critical velocity U_c in each experiment was calculated using the logarithmic average velocity equation for a rough bed as follows (Lauchlan and Melville 2001; Dey and Barbhuiya 2005; Khaple et al. 2017):

$$\frac{U_c}{U_{*c}} = 5.75 \log\left(\frac{h}{k_e}\right) + 6, \quad (1)$$

where h is the flow depth and k_e is the equivalent roughness height ($= 2d_{50}$).

Time variation of scour depths during the experimental run at different times and the equilibrium scour depth were measured at the upstream base of the pier with the help of a Vernier point gauge.

The efficiency of the proposed flow-altering counter-measure was calculated in terms of percentage reduction of scour depth (r_{ds}) at the upstream base of the pier and is given as follows:

$$r_{ds} = \frac{d_{s0} - d_{sp}}{d_{s0}} \times 100, \quad (2)$$

Table 2 Experimental data of unprotected pier

Run	b (cm)	h (cm)	U/U_c	h/b	d_{50} (mm)	d_s (cm)
A01	6.0	15.0	0.9	2.5	0.96	9.0
A02	8.2	20.5	0.9	2.5	0.96	11.8
B01	6.0	15.0	0.9	2.5	1.80	9.4
B02	8.2	20.5	0.9	2.5	1.80	12.5

b pier diameter, h flow depth, U approach flow velocity, U_c critical velocity, d_{50} median sediment size and d_s equilibrium scour depth

In Eq. (2), d_{s0} and d_{sp} denote the maximum equilibrium scour depths measured at unprotected pier and pier protected with a splitter plate, respectively.

Experimental program

Experiments were performed in two phases. In the first phase, a pier without splitter plate was used to study undisturbed scour. In the second phase, a pier with a splitter plate was used to study the scour depth reduction. In the first phase, experiment with single unprotected pier was continued until the equilibrium scour depth was reached. Equilibrium scour depth was achieved when the rate of change of scour depth was less than or equal to 0.05 times the pier diameter in the last 24 h (Melville and Chiew 1999). Therefore, to ensure the equilibrium scour depth, a minimum duration of each experimental was run for 24 h. A total of 44 experiments were conducted in this study, out of which, four runs were performed in the first phase and 40 runs were carried out in the second phase.

Scour at circular piers without splitter plate

A total of four experiments were carried out to determine the equilibrium scour depth at two circular piers with different diameters ($b = 6$ and 8.2 cm) for two different median sediment sizes ($d_{50} = 0.96$ and 1.8 mm). The flow depths in these experiments are 15 and 20.5 cm, corresponding to $b = 6$ and 8.2 cm, respectively, to neglect the flow shallowness effect, i.e., $h/b \geq 2.5$ (Ettema 1980). The main objective of the tests was to determine the equilibrium scour depth at an unprotected pier, which could be compared those at piers with splitter plates. Table 2 presents the various hydraulic conditions and dimensionless groups pertaining to the experiments of phase 1. In addition, equilibrium scour depths measured in these

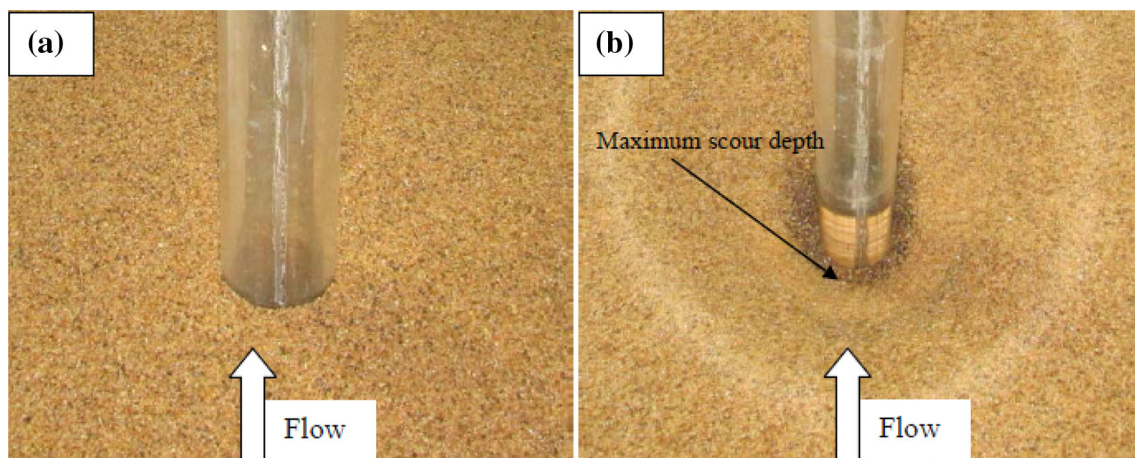


Fig. 2 Photographs of an unprotected circular pier: **a** before experiment and **b** after experiment

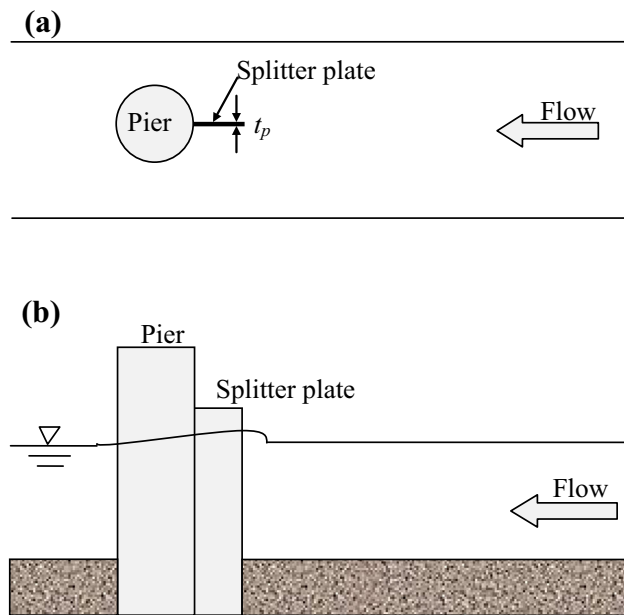


Fig. 3 Splitter plate attached to the pier upstream face along the vertical plane of symmetry: **a** plan view, and **b** elevation view

experiments are also given in Table 2. It is observed that the maximum scour depth occurs at the upstream base of the pier with respect to time (Fig. 2).

Scour at circular piers with splitter plates

Further, 40 experiments were performed by testing five different lengths of splitter plates (i.e., $l_p = 0.5b, b, 1.5b, 2b,$ and $2.5b$) and two different thicknesses of plates (i.e., $t_p = b/12$ and $b/5$). In addition, two different median sediment sizes ($d_{50} = 0.96$ and 1.8 mm) were used. Schematic of a pier with a splitter plate (plan and elevation views) is shown in Fig. 3a, b. In all the tests, the splitter plate was attached to the upstream face of the pier along the vertical plane of symmetry, as shown in Fig. 3b. The experimental data obtained from these tests are presented in Table 3. Experimental runs with median sediment size $d_{50} = 0.96$ mm were denoted by series A, which includes runs A1–A20; analogously, experiments with median sediment size $d_{50} = 1.8$ mm were denoted by series B, which includes runs B1–B20.

To study the time variation of scour depth, scour depth measurements were taken using a Vernier point gauge at different time intervals during 24 h. Equilibrium scour depth measurement was considered as maximum scour depth measured at the end of the experiment. As usual the occurrence of location of the maximum scour depth is at the upstream base of piers.

A four-receiver downlooking acoustic Doppler velocimeter (ADV) probe, named *Vectrino plus* (manufactured by Nortek), functioning with an acoustic

frequency of 10 MHz was used to capture the instantaneous flow velocity components. Data acquisition was done with a sampling rate of 100 Hz. The cylindrical sampling volume had a 6 mm diameter and an adjustable height of 1–4 mm. As the measuring location was 5 cm below the probe, there was no significant influence of the *Vectrino* probe on the measuring location; however, the data acquisition was not possible within 5 cm from the free surface of the flow. The duration of sampling was 300 s, that ensured to achieve a time-independent averaged velocity and turbulent kinetic energy (Dey and Das 2012). The signal captured by the *Vectrino* in the near-bed flow zone contained spikes due to the interaction between incident and reflected pulses. Therefore, the raw data were filtered by a spike removal algorithm, known as *acceleration thresholding method*, which could detect and replace the spikes in two phases (Goring and Nikora 2002). The threshold values (± 1.5) for despiking were determined by trial and error until the velocity power spectra corresponded to the Kolmogorov “ $-5/3$ scaling-law” within the inertial subrange (Kolmogorov 1941).

Results and discussion

Time variation of scour depth at circular piers without splitter plate

Scour depth d_s as a function of time at a circular pier without splitter plate is presented in Fig. 4. It is observed that the rate of scour depth decreases with time. Figure 4 demonstrates that smaller the pier size ($b = 6$ cm), lower the scour depth, whereas higher scour depth occurs at a larger pier size ($b = 8.2$ cm). The rate of increase of scour depth for different bed sediments ($d_{50} = 0.96$ and 1.8 mm) is the same during the initial development of scour hole; however, it is different in the long-term phase. The reason might be that as the scour hole deepens, the removal of sediment particles from the scour hole becomes more difficult.

Time variation of scour depth at circular piers with splitter plates

The comparisons of the time variation of scour depth (d_s) in test series A with respect to that of the unprotected piers are shown in Figs. 5 and 6 for pier sizes $b = 6$ and 8.2 cm, respectively. In all the runs, d_s was measured at the point represented in Fig. 3a at different time intervals. Twenty tests were conducted for each sediment size (that is altogether 40 experiments were conducted for both the sediment sizes). Duration of each run was always considered as 24 h, during which the equilibrium scour depth was

Table 3 Experimental data for splitter plate attached to a pier in uniform sediments

<i>b</i> (cm)	<i>t_p</i> (cm)	<i>l_p</i> (cm)	<i>h</i> (cm)	Series A <i>d</i> ₅₀ = 0.96 mm		Series B <i>d</i> ₅₀ = 1.8 mm		<i>r_{ds}</i> (%)	
				Run	<i>d_s</i> (cm)	Run	<i>d_s</i> (cm)	Series A <i>d</i> ₅₀ = 0.96 mm	Series B <i>d</i> ₅₀ = 1.8 mm
6	0.5	3.0	15.0	A1	8.1	B1	8.5	10.00	9.60
6	0.5	6.0	15.0	A2	7.4	B2	7.7	17.77	18.10
6	0.5	9.0	15.0	A3	6.9	B3	6.9	23.33	26.60
6	0.5	12.0	15.0	A4	5.9	B4	6.0	34.44	36.20
6	0.5	15.0	15.0	A5	6.1	B5	6.2	32.22	34.04
6	1.2	3.0	15.0	A6	8.0	B6	8.3	11.11	11.70
6	1.2	6.0	15.0	A7	7.1	B7	7.5	21.11	20.20
6	1.2	9.0	15.0	A8	6.3	B8	6.8	30.00	27.60
6	1.2	12.0	15.0	A9	5.8	B9	5.8	35.55	38.30
6	1.2	15.0	15.0	A10	5.9	B10	6.1	34.44	35.11
8.2	0.7	4.1	20.5	A11	9.9	B11	10.5	16.10	16.00
8.2	0.7	8.2	20.5	A12	8.5	B12	9.2	27.96	26.40
8.2	0.7	12.3	20.5	A13	7.9	B13	8.4	33.05	32.80
8.2	0.7	16.4	20.5	A14	7.4	B14	7.4	37.30	40.80
8.2	0.7	20.5	20.5	A15	7.6	B15	7.5	35.59	40.00
8.2	1.6	4.1	20.5	A16	10.5	B16	10.4	11.01	16.80
8.2	1.6	8.2	20.5	A17	8.4	B17	9.1	28.81	27.20
8.2	1.6	12.3	20.5	A18	7.8	B18	8.2	34.00	34.40
8.2	1.6	16.4	20.5	A19	6.9	B19	7.2	41.50	42.40
8.2	1.6	20.5	20.5	A20	7.2	B20	7.4	38.98	40.80

b pier diameter, *t_p* thickness of splitter plate, *l_p* splitter plate length, *h* flow depth, *d*₅₀ median sediment size, *d_s* equilibrium scour depth and *r_{ds}* percentage reduction of scour depth

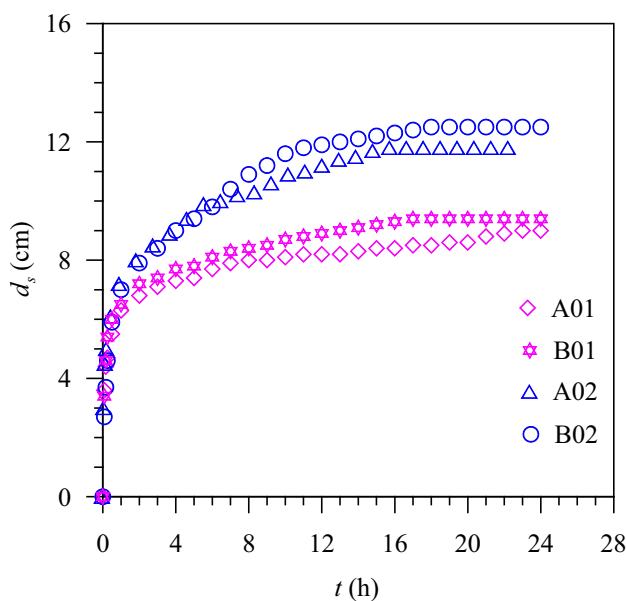


Fig. 4 Scour depth as a function of time at unprotected circular piers

achieved (Melville and Chiew 1999). Table 3 gives the details of the experimental runs in which splitter plates of varied dimensions are attached to piers in different

sediment beds. Figures 5 and 6 show the comparison of the time variation of the scour depth between the tests of series A and unprotected piers (tests A01 and A02) for two different pier sizes, *b* = 6 and 8.2 cm, respectively. Figures 5 and 6 present the time variation of scour depth for two different thicknesses and five different lengths of splitter plates. It is clear from Figs. 5 and 6 that the use of a splitter plate produces a significant decrease of the equilibrium scour depth at a pier with reference to an unprotected pier. As the length of the splitter plate increases, the rate of scour depth development decreases and finally attains a minimum scour depth as compared to that of the unprotected pier. This phenomenon was observed in both the sediment piers in the similar way. In addition, irrespective of an increase in the thickness of the plate (*t_p* = *b*/5 and *b*/12), time variation of scour depth was almost the same.

Figures 7 and 8 show the comparison of the time variation of scour depths in experiments of series A (*d*₅₀ = 0.96 mm) with the corresponding tests of series B (*d*₅₀ = 1.8 mm). The time variation of scour depths at pier diameters *b* = 6 cm (tests A1–A10, B1–B10) and 8.2 cm (tests A11–A20, B11–B20) are presented in Figs. 7 and 8, respectively. In these figures, the general trend of the evolution of scour depth at a pier with a splitter plate is the

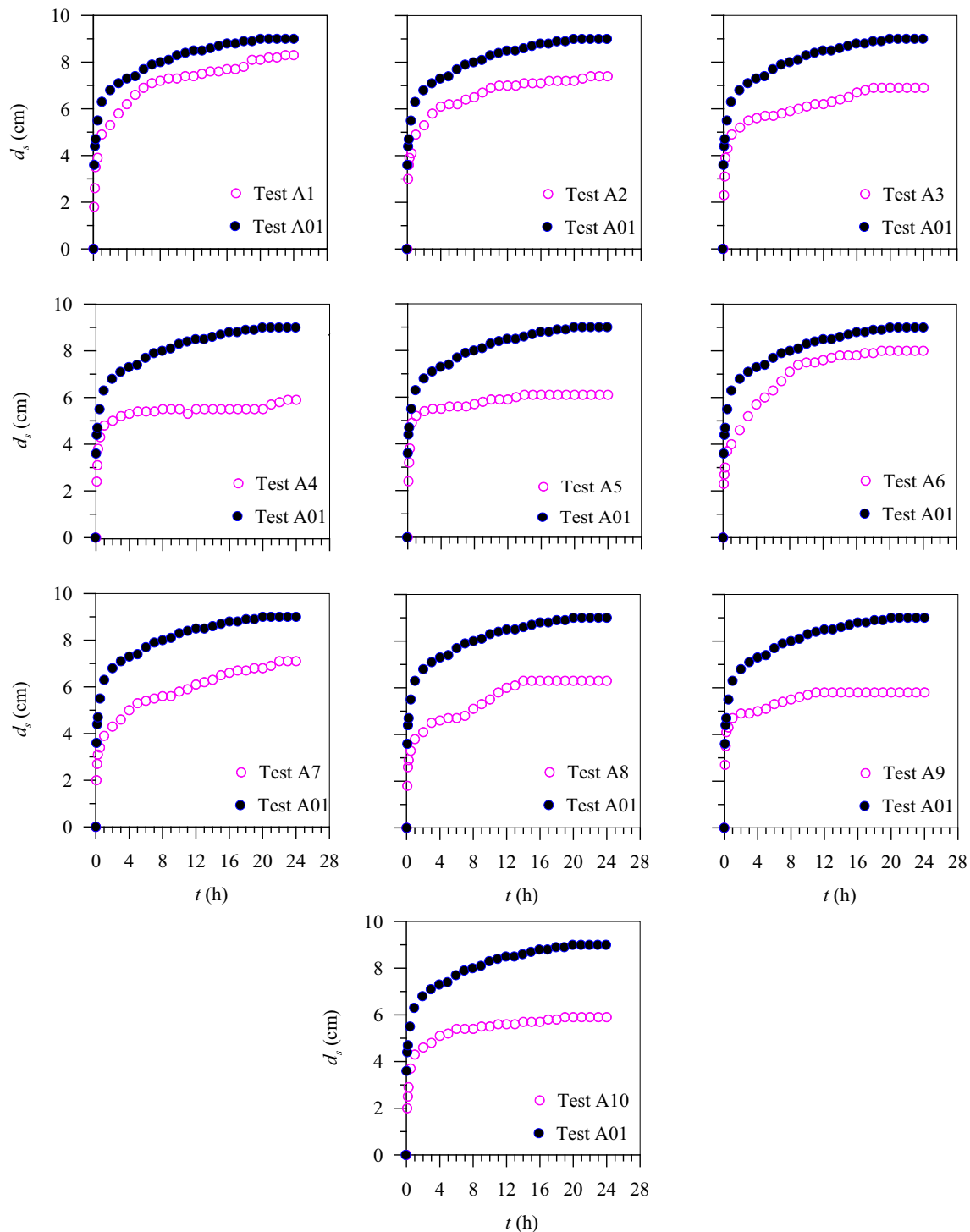


Fig. 5 Comparison of the time variation of scour depths in tests of series A with splitter plates (A1–A10) with respect to the corresponding test with unprotected piers, A01 ($b = 6$ cm, $d_{50} = 0.96$ mm): tests A1 and A01, ..., tests A10 and A01

same as that of the unprotected pier. It is observed that the maximum percentage reduction was about 42.4% for the best configuration of $l_p = 2b$ and $t_p = b/5$. The general profile of time variation of scour depth at a pier with a splitter plate is found to be similar in the experiments for

two different sediment sizes, i.e., $d_{50} = 0.96$ and 1.8 mm, as well as for two pier sizes, namely $b = 6$ and 8.2 cm. In addition, for a given pier size, it is found that the rate of increase of scour depth is initially high for the finer sediment size $d_{50} = 0.96$ mm as compared to the coarser

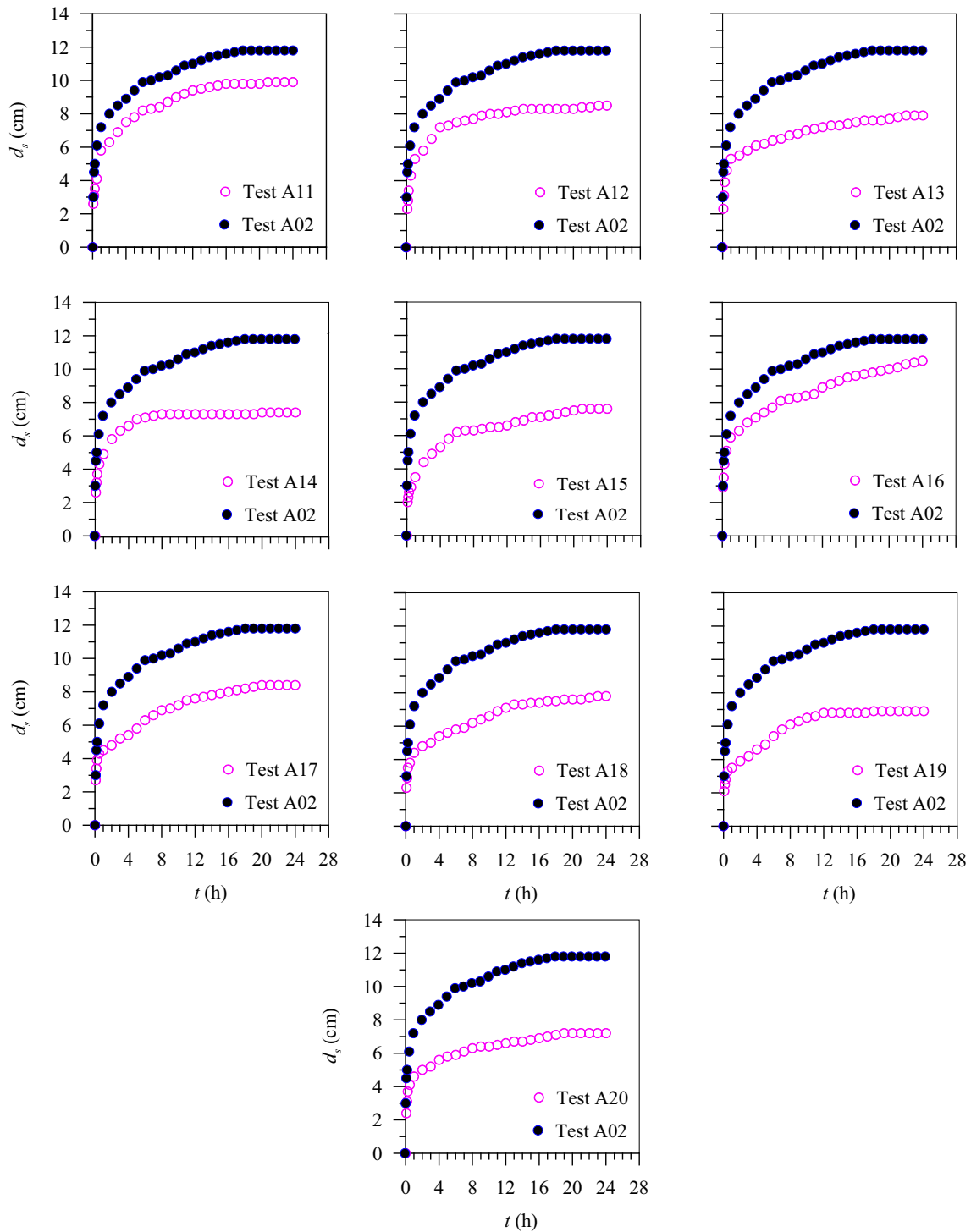


Fig. 6 Comparison of the time variation of scour depths in tests of series A with splitter plates (A11–A20) with respect to the corresponding test with unprotected piers, A02 ($b = 8.2$ cm, $d_{50} = 0.96$ mm): tests A11 and A02, ..., tests A20 and A02

sediment size $d_{50} = 1.8$ mm. Interestingly, the final equilibrium scour depth is approximately the same for both the sediment sizes and two pier sizes, as shown in Figs. 7 and 8, respectively.

Equilibrium scour depths at circular piers with splitter plates

Figure 9 shows a comparison between equilibrium scour holes developed at piers with and without splitter plate.

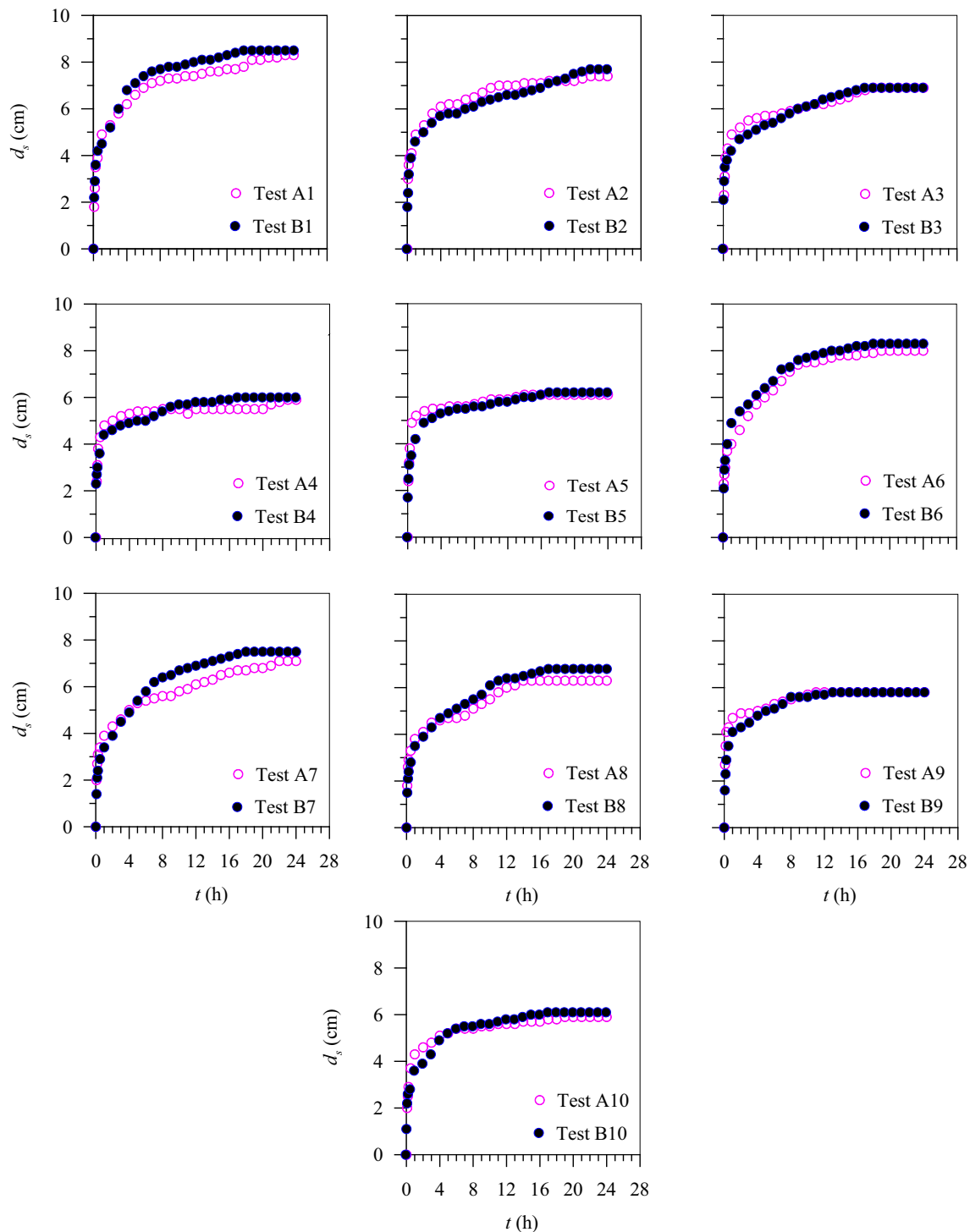


Fig. 7 Comparison of the time variation of scour depths in corresponding tests of series A ($d_{50} = 0.96$ mm) and B ($d_{50} = 1.8$ mm) with splitter plates (A1–A10, B1–B10; $b = 6$ cm): tests A1 and B1, tests A10 and B10

Figure 9a illustrates a scour hole at a pier without a splitter plate, whereas Fig. 9b–f represents the scour holes at piers with the different lengths of the splitter plates in an increasing order. It is obvious that the shape of scour holes varies with an increase in length of a splitter plate for an

identical flow condition. Figure 9b–f also demonstrates the reduction of scour depth at the upstream base of piers and area of scour hole with an increase in the length of the splitter plates. Further, it is observed that when the splitter plate lengths are equal to $2b$ and $2.5b$, an additional scour

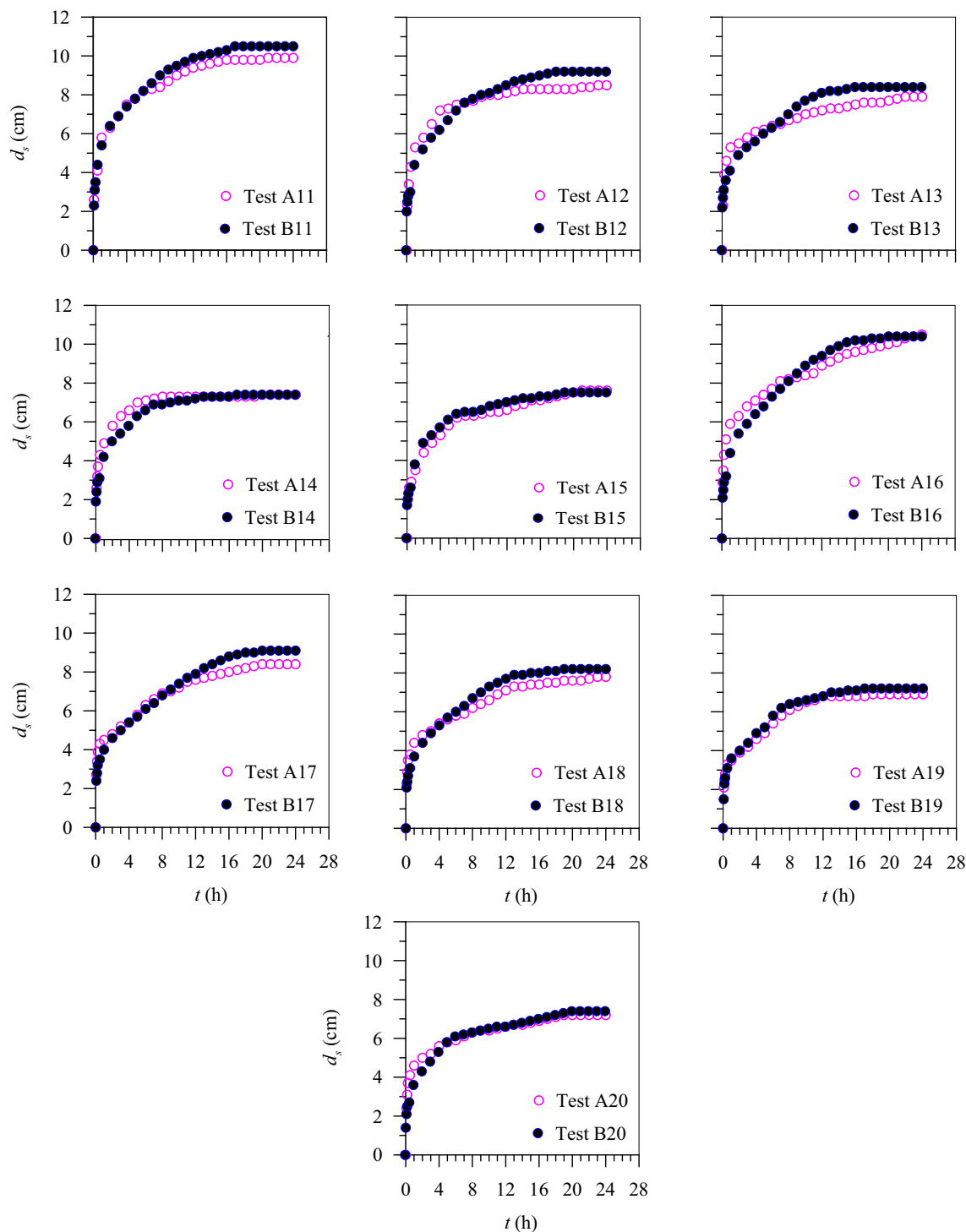


Fig. 8 Comparison of the time variation of scour depths in corresponding tests of series A ($d_{50} = 0.96$ mm) and B ($d_{50} = 1.8$ mm) with splitter plates (A11–A20, B11–B20; $b = 8.2$ cm): tests A11 and B11, tests A20 and B20

hole was produced at the upstream edge of the plate (Fig. 9e–f).

Analysis of the present experimental data reveals that, with an increase in length and thickness of the splitter plate, equilibrium scour depth decreases, as shown in

Fig. 10, and the percentage of scour reduction increases, as shown in Table 3. However, there is no reduction in equilibrium scour depth with further increase in length of a splitter plate beyond $2b$. In fact, the splitter plate attached to the pier is found reducing the magnitude of the approach

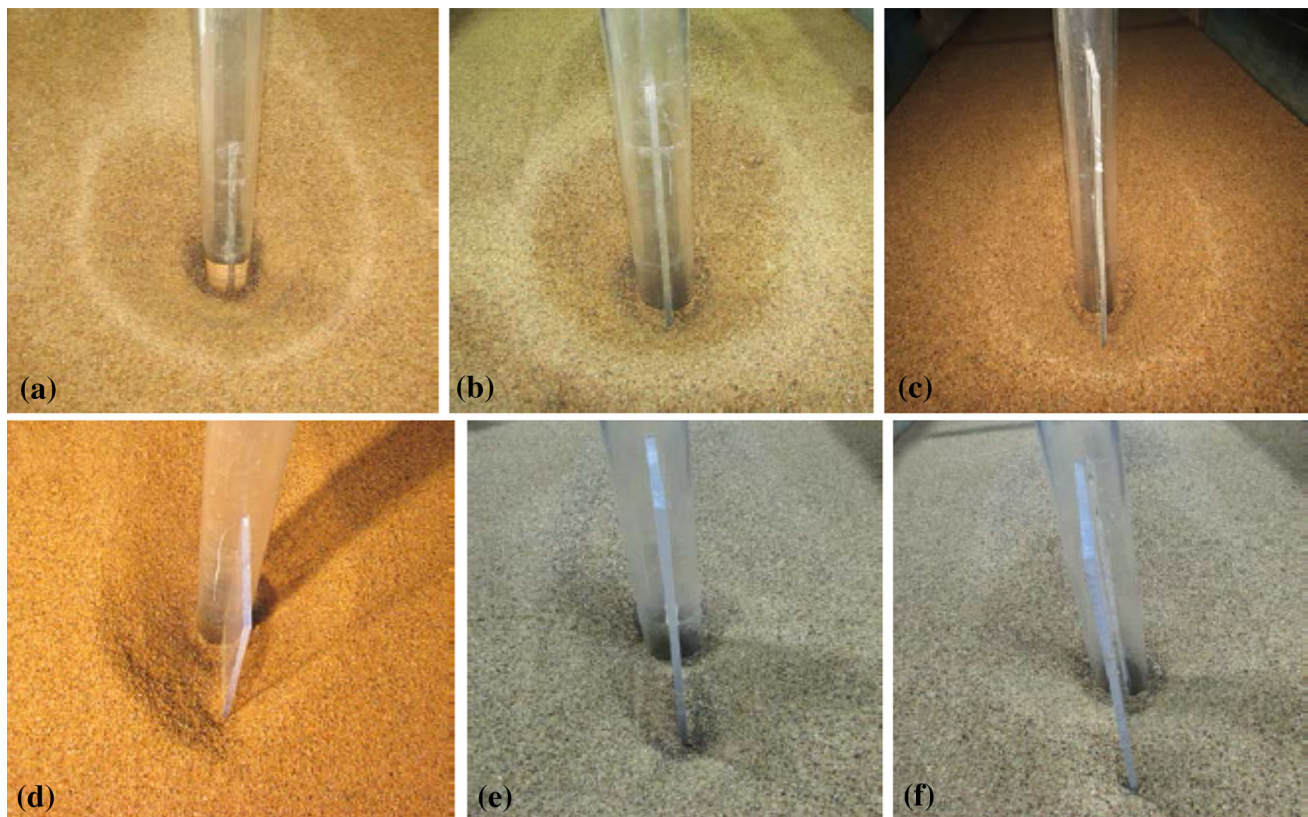


Fig. 9 Photographs showing the equilibrium scour hole with a maximum scour depth located upstream of circular piers in some tests of series A ($d_{50} = 0.96$ mm): **a** test A01, **b** test A1, **c** test A2, **d** test A3, **e** test A4, **f** test A5

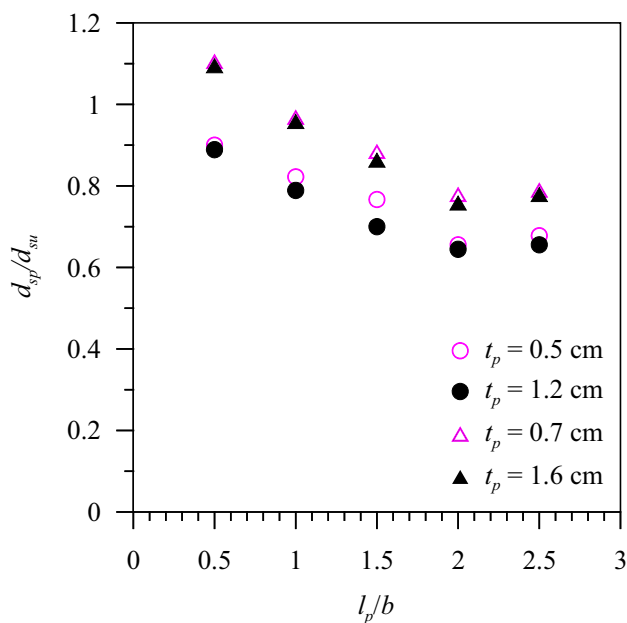


Fig. 10 Comparison of dimensionless maximum scour depth in the corresponding tests with splitter plate with median sediment size $d_{50} = 0.96$ mm for plate thicknesses of: 0.5 cm, 1.2 cm ($b = 6$ cm) and 0.7 cm, 1.6 cm ($b = 8.2$ cm)

flow and deflecting it as well, which in turn forms weak vortices close to the countermeasure. This causes weakening of horseshoe vortex formed around the pier aided by the splitter plate, resulting in a decrease in equilibrium scour depth.

The major controlling dimensions of splitter plate are its length (l_p), thickness (t_p), and height (h_p). To study the effect of the length, it was varied from $0.5b$ to $2.5b$, i.e., $l_p = 0.5b$, b , $1.5b$, $2b$, and $2.5b$ by keeping the other dimensions constant. The effect of splitter plate length on scour depth was studied with different pier diameters ($b = 6$ and 8.2 cm), sediment sizes and thicknesses of splitter plate in order to arrive at consistent conclusions. In all the experiments the flow depth was maintained constant as $h/b = 2.5$ to have flow depth independency of scour depth (Ettema 1980). Figures 10 and 11 show that, as the plate length increases, the scour depth decreases. In these figures, protected scour depth (d_{sp}) and length of the plates are normalized by the unprotected pier scour depth (d_{su}) and pier diameter, respectively. An important finding obtained from this analysis is that the limiting length of splitter plate is $2b$. Length of splitter plate more than $2b$ did not help any further reduction in scour depth, but has an adverse effect to increase scour depth, as shown in Figs. 10

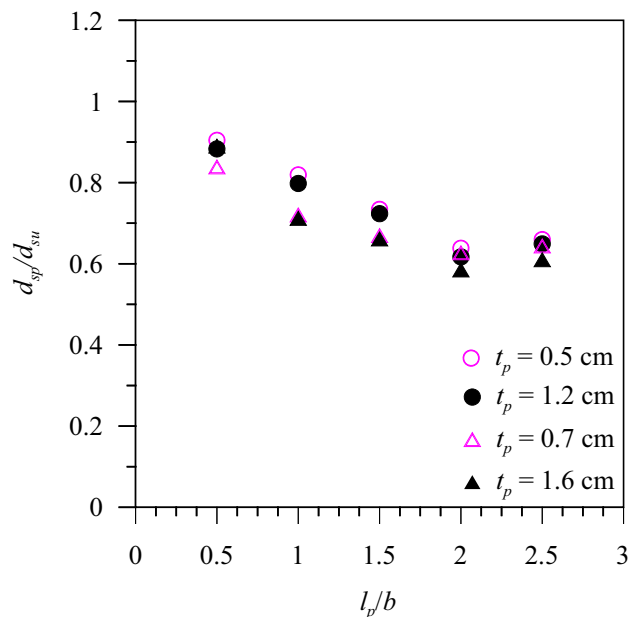


Fig. 11 Comparison of dimensionless maximum scour depth in the corresponding tests with splitter plate with median sediment size, $d_{50} = 1.8$ mm for plate thicknesses of: 0.5, 1.2 cm ($b = 6$ cm) and 0.7, 1.6 cm ($b = 8.2$ cm)

and 11. Therefore, the optimum length of splitter plate is identified as $2b$. Analysis of the velocity field indicates that, if the plate length equals $2b$, the approach flow upstream of the pier is split into two parts and deflected, reducing the strength of the downflow and the horseshoe vortex in the scour hole (see the following section), and hence, resulting in minimum scour depth. The findings obtained for the optimum length of splitter plate are consistent for different pier diameters (i.e., $b = 6$ and 8.2 cm), median sediment sizes ($d_{50} = 0.96$ and 1.8 mm) and plate thicknesses (i.e., $t_p = b/5$ and $b/12$). Further, effects of plate thickness on the equilibrium scour depth are also investigated in this study for different pier diameters and median sediment sizes. It is observed that the percentage reduction of scour depth is negligible with an increase in thickness of a splitter plate, as shown in Figs. 10 and 11. From the viewpoint of a structural issue, it is convenient to recommend a $b/5$ thick splitter plate. Therefore, the best configuration of splitter plate length and thickness is $2b$ and $b/5$, respectively, with a maximum scour depth reduction of 42.4%. Finally, the experimental findings are summarized in Table 3. It may be noted from Table 3 that the percentage reduction of scour depth for different pier sizes ($b = 6$ and 8.2 cm) is almost similar for different splitter plate lengths and thicknesses. In addition, a minimum reduction of scour depth is found to be of 10% for $l_p = 0.5b$.

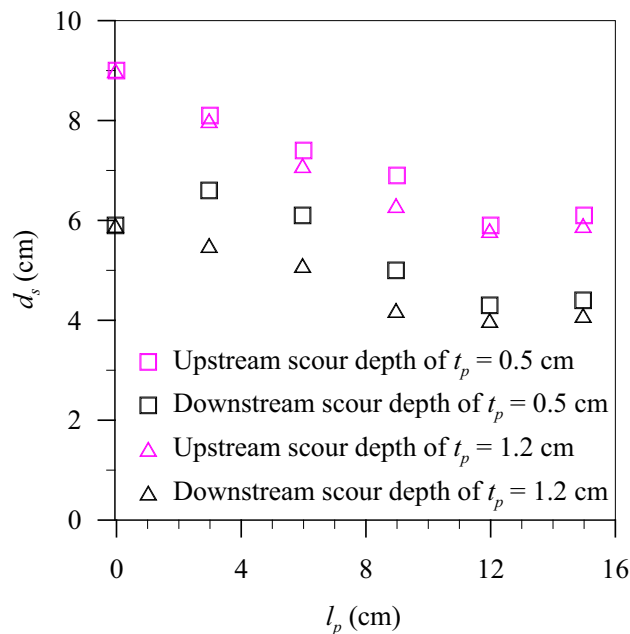


Fig. 12 Equilibrium scour depths at upstream and downstream of a pier ($b = 6$ cm) for different lengths of splitter plates and plate thicknesses of: $t_p = 0.5$ and 1.2 cm

Scour depth variations at upstream and downstream of piers

Figure 12 illustrates the variations of scour depths at upstream and downstream of the pier ($b = 6$ cm) for two different plate thicknesses of varying splitter plate lengths. In Fig. 12, upstream and downstream scour depths for the thicknesses of the splitter plates $t_p = 0.5$ and 1.2 cm, respectively, are shown. In addition, in Fig. 12, plate length equaling zero corresponds to the unprotected pier. It is observed that the scour depths at the upstream and downstream of a pier decrease with an increase in plate length, and the maximum percentage of reduction in scour depth was recorded as 35% for $l_p = 2b$, irrespective of the plate thickness. In addition, it is apparent in Fig. 12 that scour depth at the upstream of the pier is approximately 1.64 times of the scour depth at the downstream of the pier for the plate thickness $t_p = 0.5$ cm. Similarly, in Fig. 12, the scour depth at the upstream of pier is found to be 2.08 times the scour depth at the downstream of pier for the plate thickness $t_p = 1.2$ cm. Therefore, it is inferred that with an increase in the thickness of the plate, the ratio of the scour depths at upstream and downstream of pier increases.

Formulation for equilibrium scour depth at a pier with a splitter plate

The design of a bridge pier foundation requires an accurate estimation of maximum scour depth at a pier. To develop an empirical formula for the prediction of the maximum scour depth at a bridge pier is highly challenging, because of the three-dimensional characteristics of the flow field around a pier. In such a situation, regression modeling is widely adopted to develop an empirical model using the experimental data. From the analysis of experimental data and reviewing the literature, scour depth d_s is found to be a function of several parameters, such as pier diameter b , length of splitter plate l_p , flow depth h and sediment size d_{50} . Therefore, a multiple linear regression method was adopted to develop the design formula, noting that the scour depth is independent of splitter plate thickness for $t_p = b/5$ and $b/12$. Using the dimensional analysis, the independent non-dimensional groups identified are normalized splitter plate length l_p/b and normalized sediment size depth d_{50}/b . The non-dimensional scour depth d_s/b is considered as a dependent variable. The independent non-dimensional variables are called as the independent scour depth predictor variables. A regression analysis of experimental data (Table 3) yields the following equation of non-dimensional equilibrium scour depth at a circular pier attached with a splitter plate:

$$\frac{d_{s,c}}{b} = C_{sp} \left(\frac{l_p}{b} \right)^{-0.22} \left(\frac{d_{50}}{b} \right)^{0.13}, \quad (3)$$

where $d_{s,c}$ is the computed scour depth and C_{sp} is the coefficient of splitter plate.

Figure 13 shows the comparison of observed scour depths $d_{s,o}/b$ with computed ones $d_{s,c}/b$ from Eq. (3). The coefficient of splitter plate is 1.88. The regression coefficient between the experimentally obtained and the computed scour depths is 0.93, indicating that Eq. (3) agrees satisfactorily with the experimental data. For a conservative design purpose, the coefficient in Eq. (3) should be 2.16 which represents the envelope line +15% in Fig. 13.

Flow field

The components of the flow field around an unprotected pier are the downflow, horseshoe vortex, wake vortices and bow wave, as shown schematically in Fig. 14a, b, where d_s is the equilibrium scour depth and h is the flow depth (Dey et al. 1995).

In contrast, the schematic flow field around the pier in the presence of a splitter plate is presented in Fig. 15. The splitter plate is extended over the entire flow depth. The affected components, i.e., weakened downflow, weak horseshoe

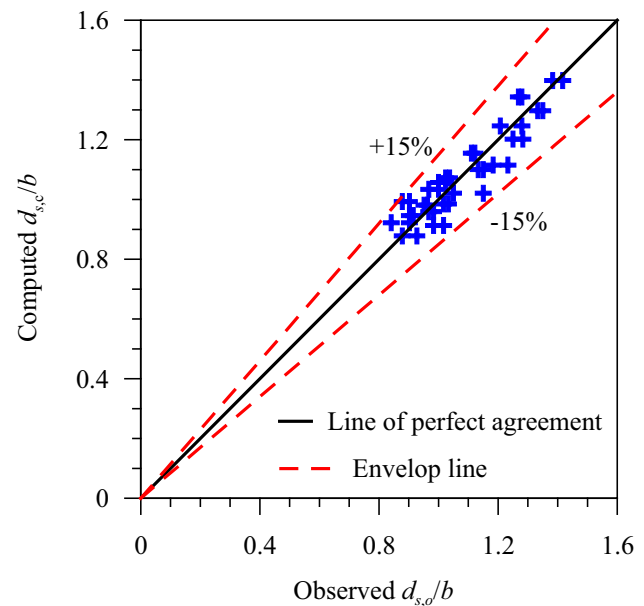


Fig. 13 Computed versus observed scour depths at piers with splitter plates

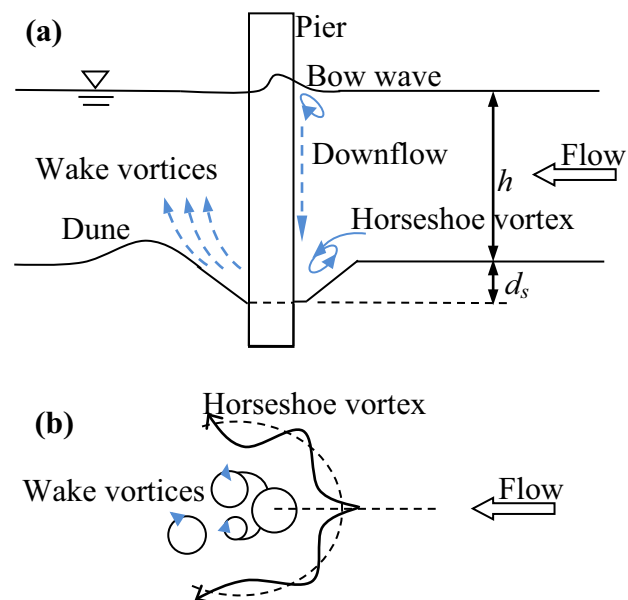


Fig. 14 Schematic of a scour hole and the components of the flow field around a circular pier: **a** elevation view and **b** plan view

vortex, and weak wake vortices (Fig. 15) in the presence of a splitter plate are explained clearly in this paper. It was found that minimum scour depth occurs for splitter plate length $l_p = 2b$ and thickness $t_p = b/5$ and therefore subsequently this optimum configuration is chosen to study the flow field.

In the presence of a splitter plate at the upstream face of the pier, the separation of boundary layer of divided approach flow develops the horseshoe vortex (Fig. 15) on both sides of the splitter plate. The split horseshoe vortex at

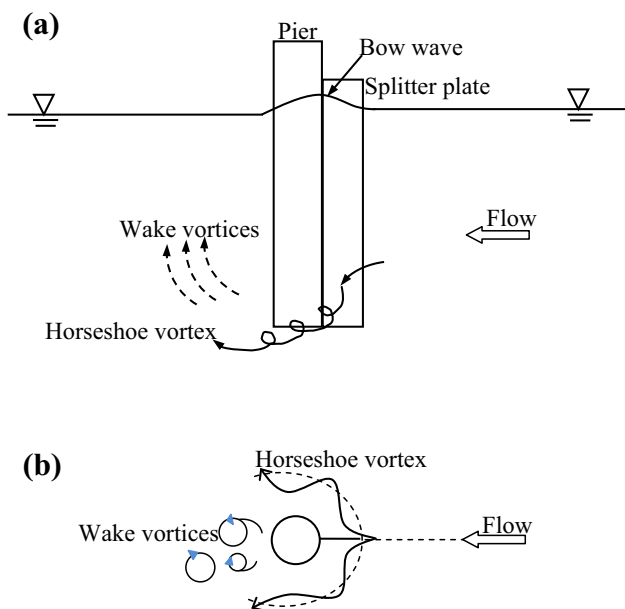


Fig. 15 Schematic of flow field around a circular pier with a splitter plate

a pier with a splitter plate is weaker than that at an unprotected pier (in the case of the pier without a splitter plate).

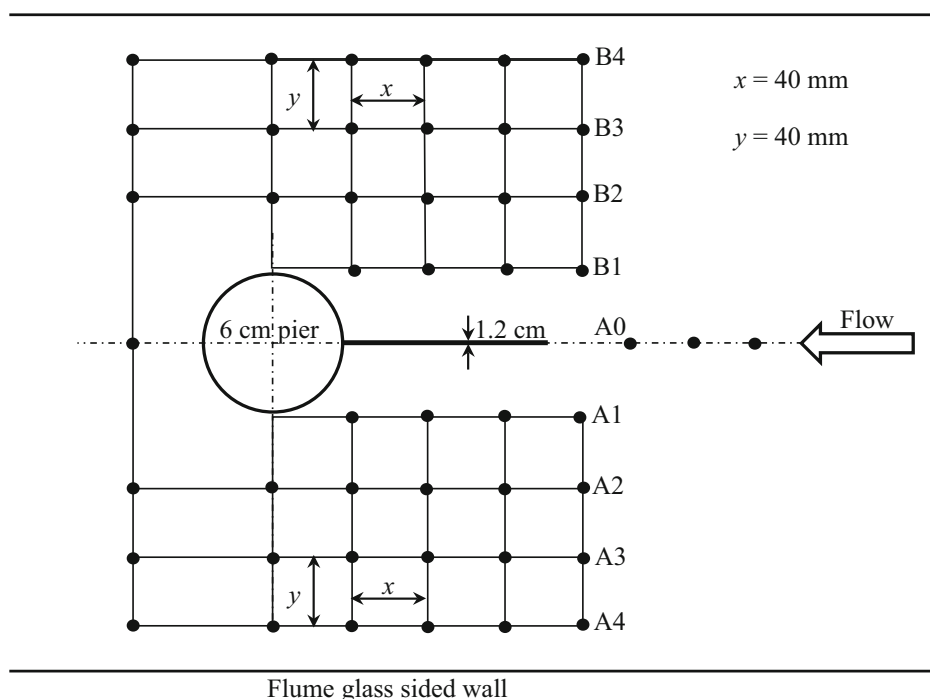
In order to identify the effects of the splitter plate on the vortex flow field in an equilibrium scour condition, the flow field is analyzed in four configurations: (1) unprotected pier (without a splitter plate) on a plane bed; (2) pier with a splitter plate on a plane bed; (3) unprotected pier in an equilibrium

scour hole, and (4) pier with a splitter plate in an equilibrium scour hole. Nortek Vectrino plus acoustic Doppler velocimeter (ADV) was used to measure the instantaneous flow velocities. To study the flow field in each configuration, 48 measuring locations were chosen in a grid pattern, as shown in Fig. 16. To generalize the findings of the study, figures are presented in non-dimensional form. In Cartesian coordinates, streamwise length x and vertical length z are normalized by the pier diameter b . The scaled variables are represented as $\hat{x} = x/b$ (non-dimensional streamwise distance) and $\hat{z} = z/b$ (non-dimensional vertical distance), as used in Figs. 17, 18, 19 and 20.

Velocity vectors in vertical plane of a pier with and without a splitter plate

Flow field at an unprotected pier on a plane bed The time-averaged velocity vector plots for an unprotected pier on a plane bed, with magnitude $(u^2 + w^2)^{0.5}$ and direction $\arctan(w/u)$, where u and w are the time-averaged streamwise and vertical velocity components, respectively, are shown in Fig. 17. The vector plots are drawn at sections A0 and A1, as shown in Fig. 17. The vector plots represent the characteristics of the flow at the upstream face of the pier and by the side of it. In Fig. 17, the approaching flow has a maximum velocity at the free surface and decreases to zero at the bed, owing to the decrease in the stagnation pressure along the upstream face of the pier; the magnitudes of approaching flow diminishes towards the pier and the flow bends down.

Fig. 16 Sketch of the ADV reading locations with a splitter plate attached to the pier



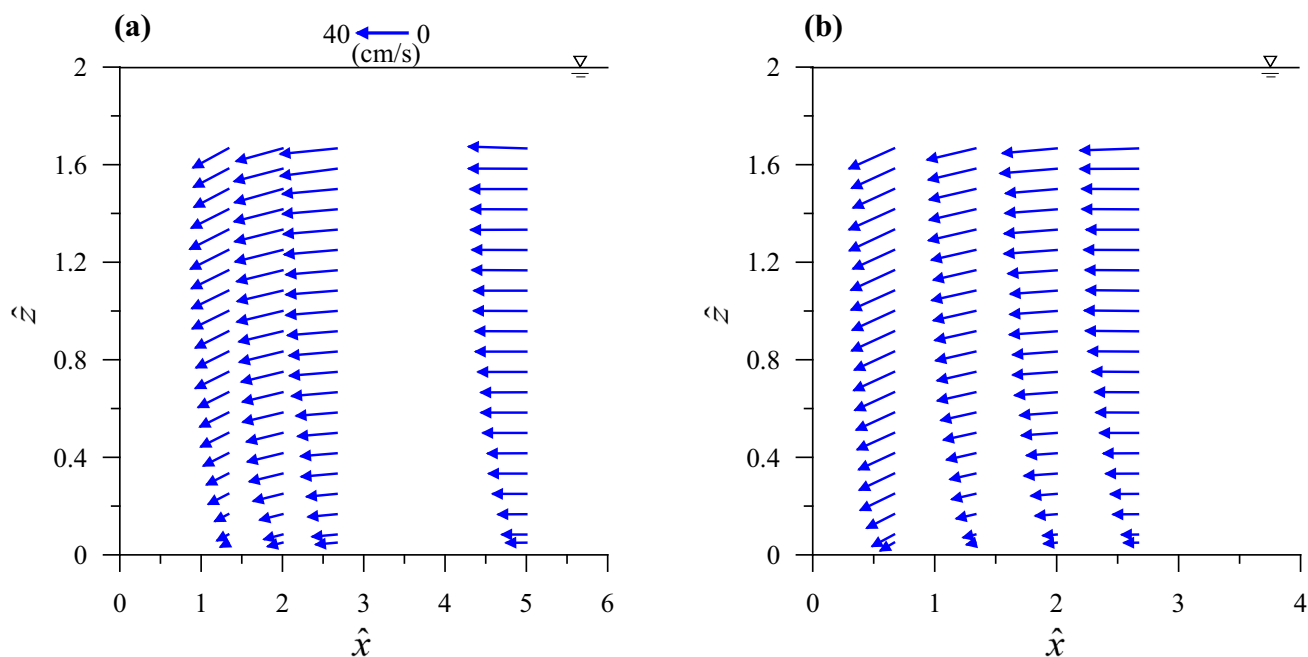


Fig. 17 Normalized velocity vectors in the vertical plane for the unprotected pier ($b = 6$ cm) on a plane bed ($d_{50} = 1.8$ mm): **a** section A0 and **b** section A1

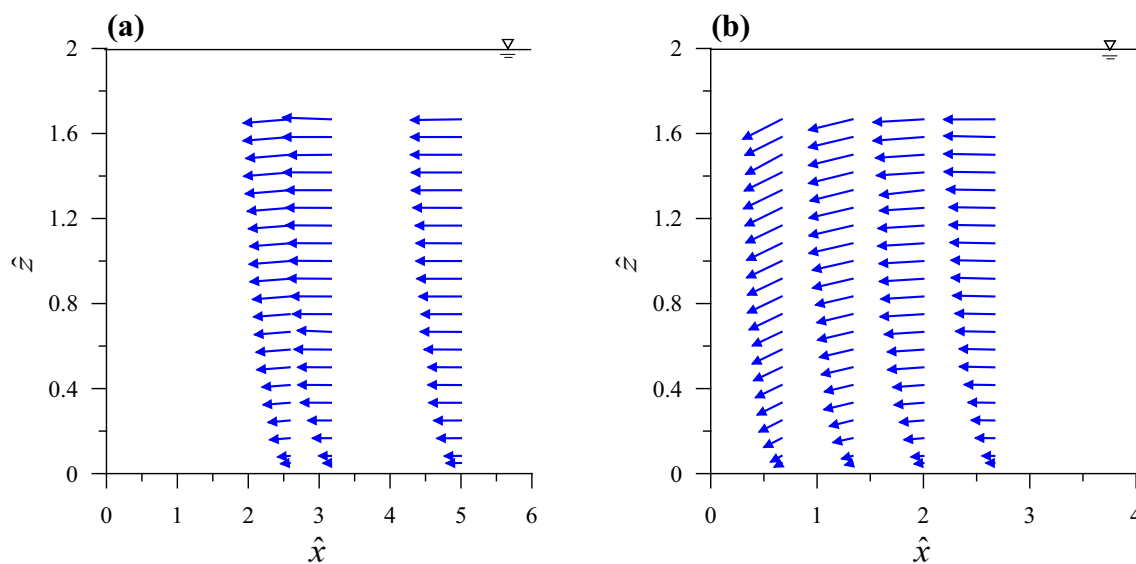


Fig. 18 Normalized velocity vectors in the vertical plane for the pier with a splitter plate ($b = 6$ cm, $l_p = 2b$ and $t_p = b/5$) on a plane bed ($d_{50} = 1.8$ mm): **a** section A0 and **b** section A1

Flow field at a pier with a splitter plate on a plane bed Similarly, the vector plots represent the characteristics of the flow at the upstream face of the pier with a splitter plate on a plane bed and by side of it. The presence of a splitter plate on the upstream face of the pier separates the approaching flow and therefore reduces the strength of the downflow. In fact, the downflow is not present along the vertical plane at the nose of the splitter plate (section

A1) (Fig. 18a), and this could be an important factor for decreasing the scour depth. However, by the pier side (section A1) (Fig. 18b), a downflow still exists.

Flow field at an unprotected pier with an equilibrium scour hole Figure 19a shows the time-averaged velocity vectors in the upstream vertical plane of symmetry (section A0) at an unprotected pier with an equilibrium scour hole.

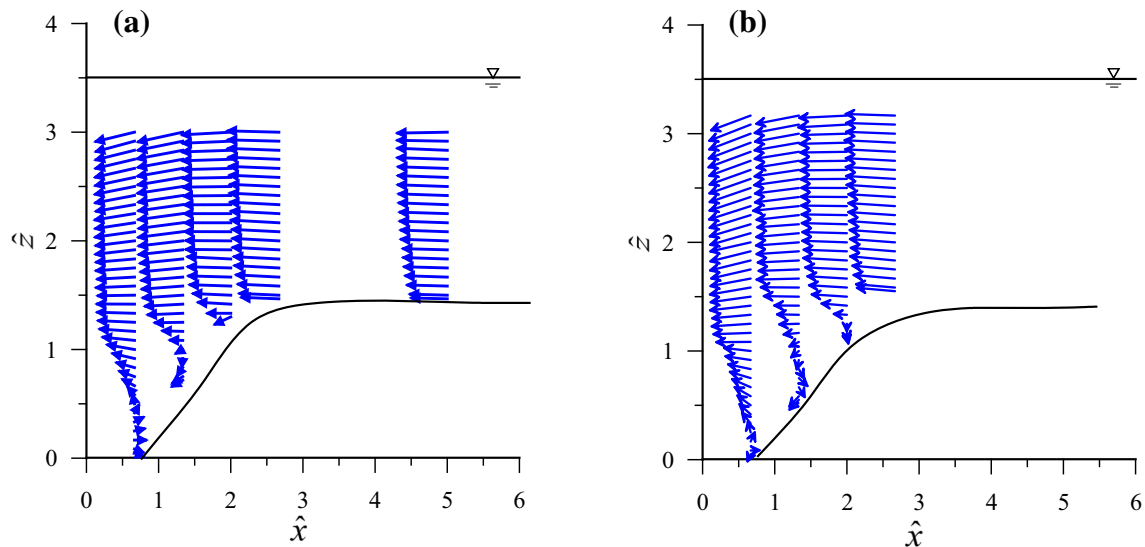


Fig. 19 Normalized velocity vectors in the vertical plane for the unprotected pier ($b = 6$ cm) in an equilibrium scour hole ($d_{50} = 1.8$ mm): **a** section A0 and **b** section A1

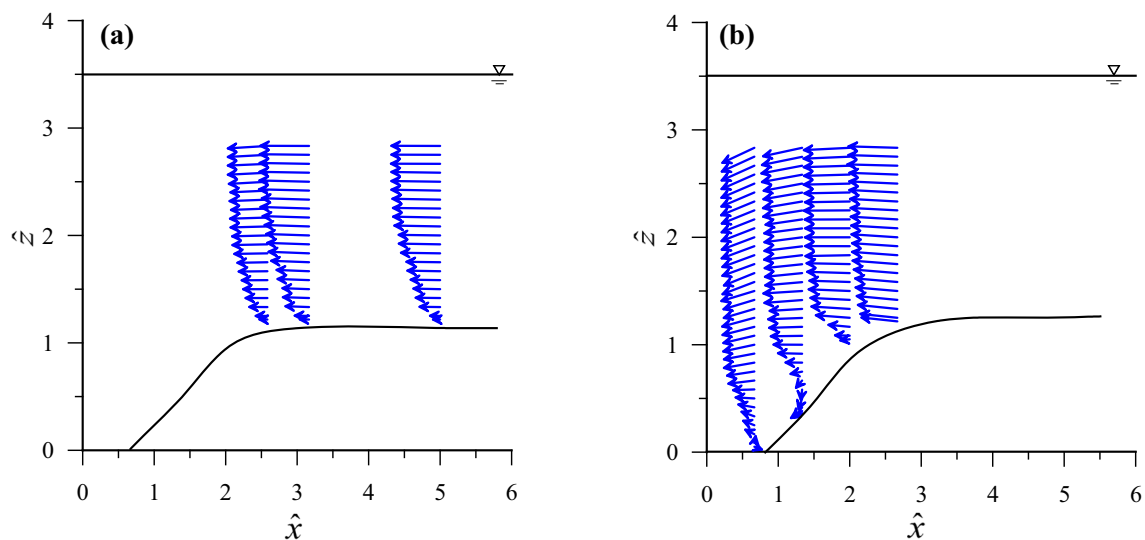


Fig. 20 Normalized velocity vectors in the vertical plane for the pier with a splitter plate ($b = 6$ cm, $l_p = 2b$ and $t_p = b/5$) in an equilibrium scour hole ($d_{50} = 1.8$ mm): **a** section A0 and **b** section A1

The vector plots are also shown at section A1 (Fig. 19b). The flow field provides an understanding on the horseshoe vortex within the equilibrium scour hole. In Fig. 19a, the magnitude of the approaching flow diminishes towards the pier and the flow bends down to form a horseshoe vortex at the lower portion of the pier in the scour hole. A close observation of the velocity vector field reveals that a vertical flow prevails near the scoured bed. Owing to the flow expansion in the scour hole, the average velocity in the equilibrium scour hole decreases and is less than the

approach flow velocity. In Fig. 19a, the magnitude of the approaching flow diminishes towards the nose of the pier; however, reduction is less in approaching flow velocity at the side of the pier, as shown in Fig. 19b.

Flow field at a pier with a splitter plate in an equilibrium scour hole Figure 20a, b shows the time-averaged velocity vectors at a pier with a splitter plate in an equilibrium scour hole at sections A0 and A1. Figure 20a shows a reduction in approach flow velocity and no downward flow at the nose of

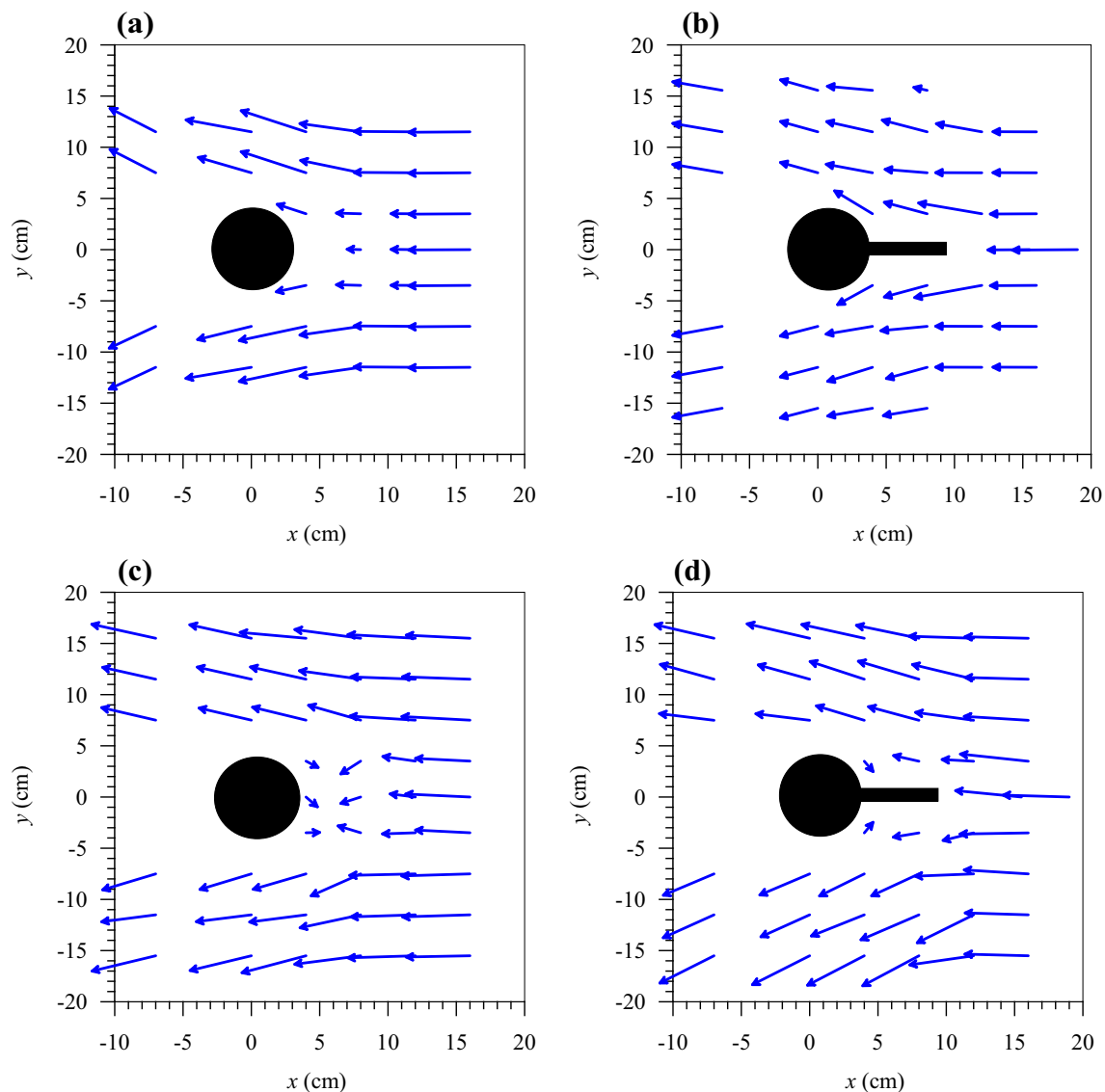


Fig. 21 Depth-averaged velocity vectors for the configurations: **a** unprotected pier ($b = 6$ cm) on a plane bed ($d_{50} = 1.8$ mm); **b** pier with a splitter plate ($b = 6$ cm, $l_p = 2b$ and $t_p = b/5$) on a plane bed ($d_{50} = 1.8$ mm); **c** unprotected pier ($b = 6$ cm) with an

equilibrium scour hole ($d_{50} = 1.8$ mm) and **d** pier with a splitter plate ($b = 6$ cm, $l_p = 2b$ and $t_p = b/5$) with an equilibrium scour hole ($d_{50} = 1.8$ mm)

the splitter plate, resulting in a reduced scour depth. However, flow field by the pier side is not affected by the presence of the splitter plate and shows a weak vertical flow near the bed in the equilibrium scour hole (Fig. 20b).

Depth-averaged velocity vectors on the horizontal plane

The depth-averaged velocity vectors are plotted on the horizontal plane for four experimental configurations (Fig. 21a–d). In Fig. 21a, the velocity vectors show the fluid motion around an unprotected pier on a plane bed having a stagnation effect at the immediate upstream of the

pier. In Fig. 21b, the velocity vectors display the deflected approaching flow by the splitter plate attached to a pier on a plane bed indicating a flow splitting. On the other hand, in Fig. 21c, the velocity vectors exhibit a horseshoe vortex, in the equilibrium scour hole, upstream of the unprotected pier. In Fig. 21d, the velocity vectors clearly demonstrate that a pier with a splitter plate splits the approaching flow to weaken the strength of the horseshoe vortex, causing a reduction of scour depth. In essence, owing to the split approaching flow and the flow retardation by the side of the splitter plate attached to the pier, the maximum scour depth reduction is found to be 43%.

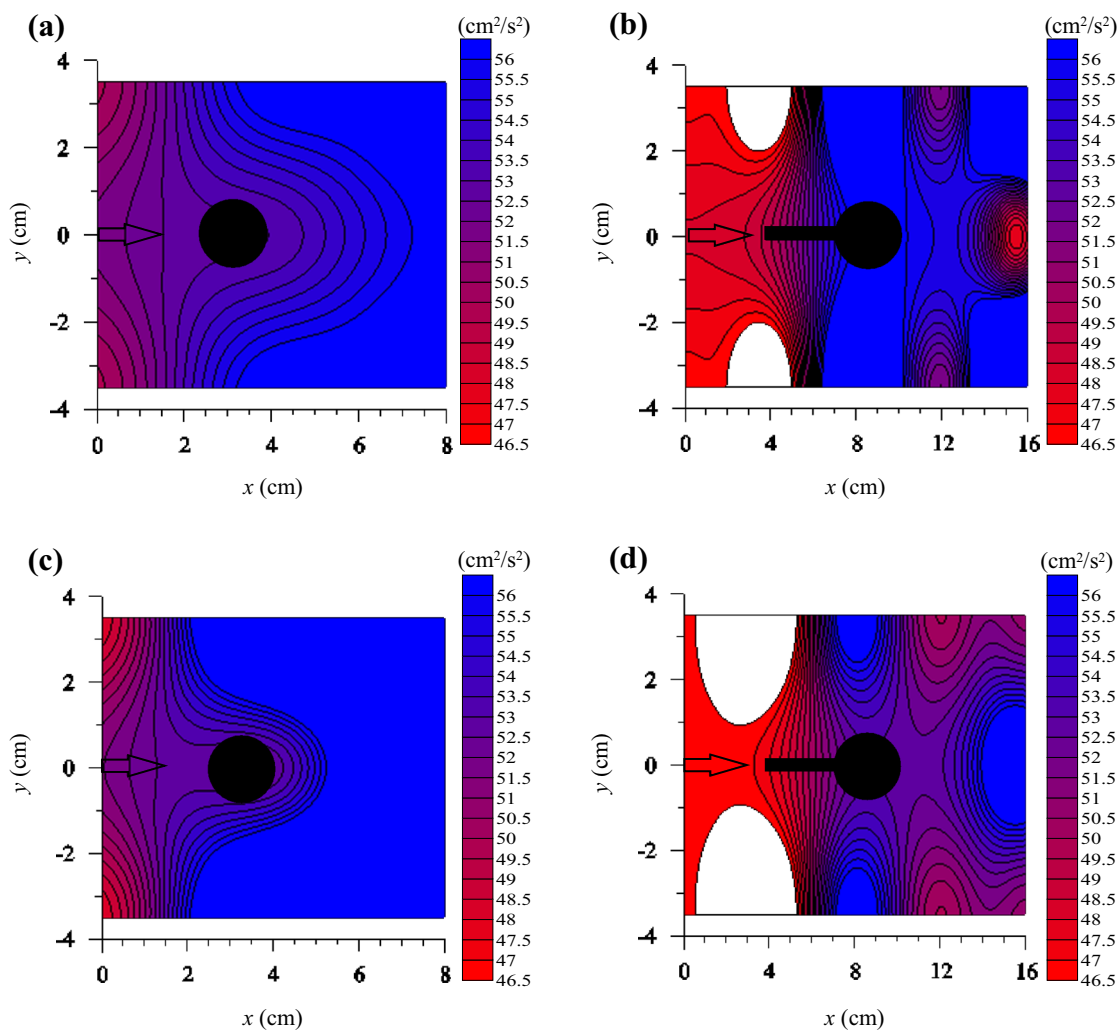


Fig. 22 Contours of TKE k on the horizontal plane for the configurations: **a** unprotected pier ($b = 6$ cm) on a plane bed ($d_{50} = 1.8$ mm); **b** pier with a splitter plate ($b = 6$ cm, $l_p = 2b$ and $t_p = b/5$) on a plane bed ($d_{50} = 1.8$ mm); **c** unprotected pier

($b = 6$ cm) with an equilibrium scour hole ($d_{50} = 1.8$ mm) and **d** pier with a splitter plate ($b = 6$ cm, $l_p = 2b$ and $t_p = b/5$) with an equilibrium scour hole ($d_{50} = 1.8$ mm)

Turbulent kinetic energy (TKE)

Turbulent kinetic energy (TKE) k is computed as $0.5(\overline{u'u'} + \overline{v'v'} + \overline{w'w'})$, where u' , v' and w' are the fluctuations of instantaneous velocity components in streamwise, lateral and vertical directions, respectively. Cartesian coordinates x , y and z in streamwise, lateral, and vertical directions, respectively, are used to represent the TKE fields, as shown in Fig. 22a–d. The contours of TKE in the xy -plane at $z = 0.5$ cm above the bed, as shown in Fig. 22a–d, represent the characteristics of the TKE around the circular pier with and without splitter plate on a plane bed and in an equilibrium scour hole.

The contours for an unprotected pier on a plane bed show an increase in TKE towards and around the pier indicating

higher turbulence fluctuations, that increase the scour potential (Fig. 22a). On the contrary, for a pier with a splitter plate, Fig. 22b exhibits a clear indication of the reduction of TKE at the immediate upstream of the pier, suggesting a lesser scour potential as compared to the case of an unprotected pier. Further, having compared the TKE contours for an unprotected pier (Fig. 22c) and a pier with a splitter plate (Fig. 22d) in an equilibrium scour hole, a substantial reduction of TKE at the immediate upstream of the pier is apparent for the latter case as compared to the former one. In essence, the TKE contours clearly suggest a reduction of TKE values in presence of a splitter plate attached to a pier. This further substantiates the cause of reduction of scour by the splitter plate in terms of TKE values.

Conclusions

In this experimental study, a full-depth splitter plate attached to the upstream face of a circular pier along the vertical plane of symmetry has been proved to be an effective pier scour flow-altering countermeasure.

With an increase in splitter plate length, the equilibrium scour depth decreases irrespective of sediment median sizes and pier diameters, while equilibrium scour depth remains invariant of splitter plate thickness. The minimum value of the equilibrium scour depth at a circular pier with full-depth splitter plate occurs at a splitter plate length of $2b$ and splitter plate thickness of $b/5$, which is considered as the best configuration for the design. The maximum reduction in the equilibrium scour depth at the pier with the splitter plate was observed as 42.4%. Using the experimental data, a multiple linear regression analysis was carried out to obtain the maximum scour depth formula at a circular pier with a splitter plate. In the present experiments, the turbulent flow field around the bridge pier in the presence of a splitter plate with optimum configuration is compared with that of a pier without a splitter plate. Piers embedded in a plane bed and with an equilibrium scour hole were tested to identify the reasons for reduction of scour depth. The velocity vectors show reduced velocities and the formation of a weak horseshoe vortex within the equilibrium scour hole as compared to that on a plane bed. The maximum downflow was observed at the nose of the pier for plane bed; however, for same plane bed condition, downflow is very weak in the case of pier with a splitter plate. Therefore, it is concluded that the splitter plate almost eliminates downflow at the nose of the pier. The most important observation is that the splitter plate in the best configuration splits and deflects the flow at the upstream of the pier, reducing the strength of the downflow and the horseshoe vortex, and hence reducing the equilibrium scour depth. Further, the TKE contours show a reduction of TKE values in presence of a splitter plate attached to a pier, suggesting a reduced scour potential.

Compliance with ethical standards

Conflict of interest On behalf of all the authors, the corresponding author states that there is no conflict of interest.

References

- Arabani AP, Hajikandi H (2015) Reduction of local scour around a bridge pier using triple rectangular plates. *Curr World Environ* 10(1):47–55. doi:[10.12944/CWE.10.Special-Issue1.08](https://doi.org/10.12944/CWE.10.Special-Issue1.08)
- Chabert J, Engeldinger P (1956) Etude des affouillements autour des piles de ponts. Serie A, Laboratoire National d'Hydraulique, Chatou, France (in French)
- Chiew Y (1992) Scour protection at bridge piers. *J Hydraul Eng* 118(9):1260–1269
- Dey S, Barbhuiya AK (2005) Time variation of scour at abutments. *J Hydraul Eng* 131(1):11–23
- Dey S, Das R (2012) Gravel-bed hydrodynamics: double-averaging approach. *J Hydraul Eng* 138(8):707–725. doi:[10.1061/\(ASCE\)HY.1943-7900.0000554](https://doi.org/10.1061/(ASCE)HY.1943-7900.0000554)
- Dey S, Bose SK, Sastry GLN (1995) Clear water scour at circular piers: a model. *J Hydraul Eng* 121(12):869–876. doi:[10.1061/\(ASCE\)0733-9429](https://doi.org/10.1061/(ASCE)0733-9429)
- Dey S, Sumer BM, Fredsoe J (2006) Control of scour at vertical circular piles under waves and current. *J Hydraul Eng* 132(3):270–279. doi:[10.1061/\(ASCE\)0733-9429](https://doi.org/10.1061/(ASCE)0733-9429)
- Ettema R (1980) Scour at bridge piers. Ph.D. Thesis, Department of Civil Engineering, University of Auckland, Auckland, New Zealand
- Goring DG, Nikora VI (2002) Despiking acoustic Doppler velocimeter data. *J Hydraul Eng* 128(1):117–126
- Grimaldi C, Gaudio R, Calomino F, Cardoso AH (2009) Countermeasures against Local Scouring at Bridge Piers: Slot and Combined System of Slot and Bed Sill. *J Hydraul Eng* 135(5):425–431
- Jahangirzadeh A, Basser H, Akib S, Karami H, Naji S, Shamshirband S (2014) Experimental and numerical investigation of the effect of different shapes of collars on the reduction of scour around a single bridge pier. *PLoS ONE* 9(6):98592. doi:[10.1371/journal.pone.0098592](https://doi.org/10.1371/journal.pone.0098592)
- Khaple S, Hanmaiahgari PR, Gaudio R, Dey S (2017) Interference of an upstream pier on local scour at downstream piers. *Acta Geophys* 65(1):29–46. doi:[10.1007/s11600-017-0004-2](https://doi.org/10.1007/s11600-017-0004-2)
- Kolmogorov A (1941) The local structure of turbulence in incompressible viscous fluid for very large Reynolds' numbers. *Dokl Akad Nauk SSSR* 30:301–305
- Kumar V, Raju KGR, Vittal N (1999) Reduction of local scour around bridge piers using slots and collars. *J Hydraul Eng* 125(12):1302–1305. doi:[10.1061/\(ASCE\)0733-9429](https://doi.org/10.1061/(ASCE)0733-9429)
- Lauchlan CS (1999) Pier scour countermeasures. PhD thesis, The University of Auckland, Auckland, New Zealand
- Lauchlan CS, Melville BW (2001) Riprap protection at bridge piers. *J Hydraul Eng* 127(5):412–418. doi:[10.1061/\(ASCE\)0733-9429](https://doi.org/10.1061/(ASCE)0733-9429)
- Melville BW, Chiew YM (1999) Time scale for local scour at bridge piers. *J Hydraul Eng* 125(1):59–65. doi:[10.1061/\(ASCE\)0733-9429](https://doi.org/10.1061/(ASCE)0733-9429)
- Melville BW, Hadfield AC (1999) Use of sacrificial piles as pier scour countermeasures. *J Hydraul Eng* 125(11):1221–1224. doi:[10.1061/\(ASCE\)0733-9429](https://doi.org/10.1061/(ASCE)0733-9429)
- Odgaard AJ, Mosconi CE (1987) Streambank protection by submerged vanes. *J Hydraul Eng* 113(4):520–536. doi:[10.1061/\(ASCE\)0733-9429](https://doi.org/10.1061/(ASCE)0733-9429)
- Ouyang HT, Lin CP (2016) Characteristics of interactions among a row of submerged vanes in various shapes. *J. Hydro-Environ Res* 13:14–25. doi:[10.1016/j.jher.2016.05.003](https://doi.org/10.1016/j.jher.2016.05.003)
- Parker G, Toro-Escobar C, Voigt RL Jr (1998) Countermeasures to protect bridge piers from scour. St. Anthony Falls Laboratory, Minneapolis
- Tafarojnoruz A, Gaudio R, Dey S (2010) Flow-altering countermeasures against scour at bridge piers: a review. *J Hydraul Res* 48(4):441–452. doi:[10.1080/00221686](https://doi.org/10.1080/00221686)
- Zarrati AR, Gholami H, Mashahir MB (2004) Application of collar to control scouring around rectangular bridge piers. *J Hydraul Res* 42(1):97–103. doi:[10.1080/00221686](https://doi.org/10.1080/00221686)

The nonlinear oil–water two-phase flow behavior for a horizontal well in triple media carbonate reservoir

Yong Wang^{1,2} · Zhengwu Tao³ · Liang Chen⁴ · Xin Ma⁵

Received: 18 May 2017 / Accepted: 13 September 2017 / Published online: 18 September 2017
© Institute of Geophysics, Polish Academy of Sciences & Polish Academy of Sciences 2017

Abstract Carbonate reservoir is one of the important reservoirs in the world. Because of the characteristics of carbonate reservoir, horizontal well has become a key technology for efficiently developing carbonate reservoir. Establishing corresponding mathematical models and analyzing transient pressure behaviors of this type of well-reservoir configuration can provide a better understanding of fluid flow patterns in formation as well as estimations of important parameters. A mathematical model for a oil–water two-phase flow horizontal well in triple media carbonate reservoir by conceptualizing vugs as spherical shapes are presented in this article. A semi-analytical solution is obtained in the Laplace domain using source function theory, Laplace transformation, and superposition principle. Analysis of transient pressure responses indicates that seven characteristic flow periods of horizontal well in triple media carbonate reservoir can be identified. Parametric analysis shows that water saturation of matrix, vug and fracture system, horizontal section length, and horizontal well position can significantly influence the transient

pressure responses of horizontal well in triple media carbonate reservoir. The model presented in this article can be applied to obtain important parameters pertinent to reservoir by type curve matching.

Keywords Oil–water two-phase flow · Horizontal well · Mathematical model · Transient pressure analysis · Triple media carbonate reservoir

List of symbols

α_m	Shape factor between matrix system and fracture system, $1/m^2$
B_o	Oil volume factor, dimensionless
B_w	Water volume factor, dimensionless
c_v	Compressibility of vug system, $1/Pa$
c_{Lo}	Compressibility of oil, $1/Pa$
c_{Lw}	Compressibility of water, $1/Pa$
c_{mt}	Total compressibility of oil–water two-phase flow in matrix system, $1/Pa$
c_{ft}	Total compressibility of oil–water two-phase flow in fracture system, $1/Pa$
c_{vt}	Total compressibility of oil–water two-phase flow in vug system, $1/Pa$
f_w	Water cut of well, dimensionless
ϕ	Porosity, dimensionless
$K_0(x)$	Modified Bessel function of second kind, zero order
k	Permeability, m^2
k_{fh}	Horizontal permeability of fracture system, m^2

✉ Yong Wang
ywangsc@qq.com

¹ School of Sciences, Southwest Petroleum University, Chengdu, Sichuan 610500, China

² State Key Laboratory of Oil and Gas Reservoir Geology and Exploitation, Southwest Petroleum University, Chengdu, Sichuan 610500, China

³ Research Institute of Exploration and Development, Tarim Oilfield Company, PetroChina, Korla, Xinjiang 84100, China

⁴ PetroChina Xinjiang Oilfield Company, Karamay 834000, China

⁵ School of Science, Southwest University of Science and Technology, Mianyang 621010, China

k_{fv}	Vertical permeability of fracture system, m^2
k_{fro}	Oil relative permeability of fracture system, dimensionless
k_{frw}	Water relative permeability of fracture system, dimensionless
k_{mro}	Oil relative permeability of matrix system, dimensionless
k_{mrw}	Water relative permeability of matrix system, dimensionless
k_{vro}	Oil relative permeability of vug system, dimensionless
k_{vrw}	Water relative permeability of vug system, dimensionless
h	Formation thickness, m
u	Laplace transformation variable
μ_o	Oil viscosity, Pa·s
μ_w	Water viscosity, Pa·s
ω_j	Capacitance coefficient, dimensionless
p_i	Initial pressure of reservoir, Pa
q_{sc}	Oil production rate of fractured vertical well, m^3/s
q_{vo}	Outflow oil volume in unit time from the unit volume vug, $m^3/(m^3 \cdot s)$
q_{vw}	Outflow water volume in unit time from the unit volume vug, $m^3/(m^3 \cdot s)$
$\Omega_0 = 1 + \frac{B_w f_w}{B_o(1-f_w)}$	Dimensionless
$\Omega_1 = \frac{\mu_o}{k_{fro}} \left(\frac{k_{fro}}{\mu_o} + \frac{k_{frw}}{\mu_w} \right)$	Dimensionless
$\Omega_2 = \frac{\mu_o}{k_{fro}} \left(\frac{k_{mro}}{\mu_o} + \frac{k_{mrw}}{\mu_w} \right)$	Dimensionless
$\Omega_3 = \frac{\mu_o}{k_{fro}} \left(\frac{k_{vro}}{\mu_o} + \frac{k_{vrw}}{\mu_w} \right)$	Dimensionless
r_w	Radius of well, m
r_l	Radius of vug, m
S_{fo}	Oil saturation of fracture, dimensionless
S_{fw}	Water saturation of fracture, dimensionless
S_{vo}	Oil saturation of vug, dimensionless
S_{vw}	Water saturation of vug, dimensionless
x_f	Half-length of the fracture, m

Subscripts

D	Dimensionless
m	Matrix
f	Fracture
v	Vug

Superscripts

- Laplace transform

Introduction

Carbonate reservoirs have complex structures, and challenged research community, such as petroleum engineers, geologists, fluid mechanics, and water resource researches (Gua and Chalaturnyk 2010; Jazayeri Noushabadi et al. 2011; Popov et al. 2009). Each reservoir is composed of different combinations of matrix, fracture, and vug systems, and thus, it has various properties of porosity, permeability, and fluid transport behavior. The flow problem of fluids through a reservoir is a complicated inverse problem. Therefore, a task for researchers is to establish various test models for the industry to evaluate the properties of these reservoirs.

The flow problem for vertical well production in carbonate reservoirs is well known. Bourdet and Gringarten (1980) used type curve analysis to analyze fissure volume and block size in fractured reservoirs. Camacho-Velázquez et al. (2005) studied an oil transient flow modeling in naturally fractured-vuggy reservoirs and analyzed its pressure transient behaviors. Corbett et al. (2010) studied the numerical well test modeling of fractured carbonate reservoirs, and discovered that numerical well testing has its limitations. Izadi and Yildiz (2007) examined transient flow in discretely fractured porous media, and Jalali and Ershaghi (1987) investigated pressure transient analysis of heterogeneous naturally fractured reservoirs. In addition, Leveinen (2000) established a composite model with fractional flow for well test analysis in fractured reservoirs, Wu et al. (2004, 2007, 2011) investigated a triple-continuum pressure transient model for a naturally fractured-vuggy reservoir, and Pulido et al. (2006) established a well-test pressure theory of analysis for naturally fractured reservoirs, considering transient interporosity matrix, micro fractures, vugs, and fractures flow, Cai and Jia (2007) investigated dynamic analysis for pressure in limit conductivity vertical fracture wells of triple-porosity reservoir, Nie et al. (2011, 2012) investigated a flow model for triple-porosity carbonate reservoirs by conceptualizing vugs as spherical shapes, Wang et al. (2013) studied pressure transient analysis of horizontal wells with positive/negative skin in triple-porosity reservoirs, Jiang et al. (2014) studied rate transient analysis for multistage fractured horizontal well in tight oil reservoirs considering stimulated reservoir volume, Su et al. (2015) investigated performance analysis of a composite dual-porosity model in multi-scale fractured shale reservoir, Zhang et al. (2015a, b) investigated triple-continuum modeling of shale gas reservoirs considering the effect of kerogen, Guo et al. (2015) investigated transient

pressure behavior for a horizontal well with multiple finite-conductivity fractures in tight reservoirs, Zhang et al. (2015a, b) studied the production performance of multi-stage fractured horizontal well in shale gas reservoir, Wu et al. (2016) investigated a practical method for production data analysis from multistage fractured horizontal wells in shale gas reservoirs, Wei et al. (2016) studied pressure transient analysis for finite-conductivity multi-staged fractured horizontal well in fractured-vug carbonate reservoirs, Wu et al. (2017) investigated numerical analysis for promoting uniform development of simultaneous multiple-fracture propagation in horizontal wells, Ma and Liu (2016), and Ma et al. (2017) studied the oil production using the novel multivariate nonlinear model based on Arps decline model and kernel method, and Wang and Yi (2017) investigated transient pressure behavior of a fractured vertical well with a finite-conductivity fracture in triple media carbonate reservoir.

However, to the best of our knowledge, little has been done on modeling the nonlinear oil–water two-phase flow behavior for a horizontal well in triple media carbonate reservoir by conceptualizing vugs as spherical shapes. The main purpose of this article is to study the nonlinear oil–water two-phase flow behavior for a horizontal well in triple media carbonate reservoir.

The outline of this article is as follows. In Sect. 2, a physical model is introduced, which is of horizontal well in triple media carbonate reservoir by conceptualizing vugs as spherical shapes. In Sect. 3, some key source functions are obtained. In Sect. 4, a mathematic model is developed, which is of the horizontal well in triple media carbonate reservoir. In Sect. 5, we selected a set of the oil and water relative permeability for the matrix, fracture, and vug systems, respectively, which can provide the necessary base data for the theoretical analysis and calculation of oil–water two-phase well test. In Sect. 6, pressure behavior analyses are done. Section 7 gives some conclusions.

Physical model of a horizontal well in triple media carbonate reservoir

The practical reservoir may be triple media for most carbonate reservoirs, and the fractured-vuggy triple media reservoir scheme and its flow scheme are shown in Figs. 1 and 2.

Physical model assumptions are as follows:

1. A horizontal well production at constant rate in fractured-vuggy triple media reservoir, and the upper and lower boundaries of the reservoir are both closed, while the external boundary of the reservoir is infinite.

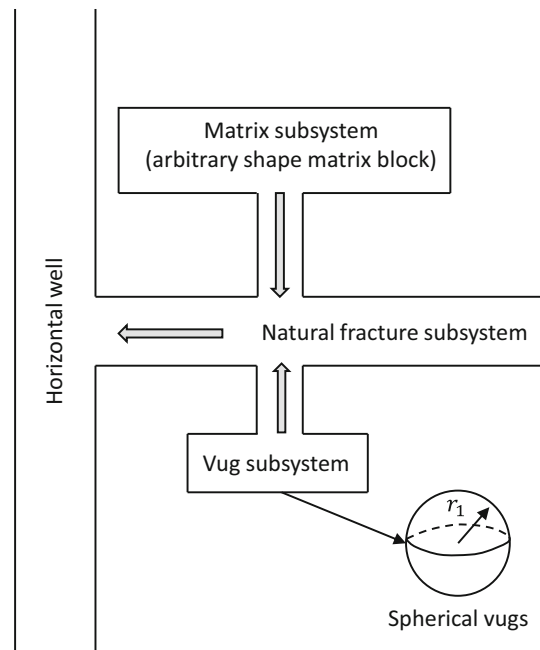


Fig. 1 Triple media carbonate reservoir flow scheme

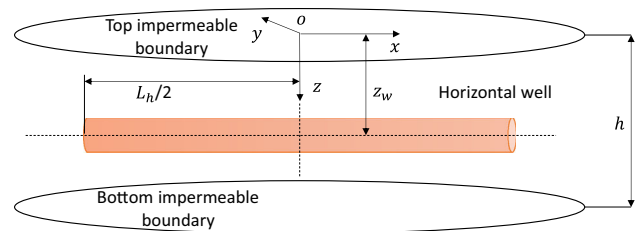


Fig. 2 Schematic of a horizontal well in triple media carbonate reservoir

2. Oil–water two-phase flow with constant oil and water saturation at a certain moment in the early production period.
3. The shape of all the vugs is spherical, the radius of the vugs is equal and equals to r_1 , the distribution of pressure in the vug is spherically symmetric, and the shape of matrix block is arbitrary; both vug and matrix connect individually to fractures.
4. The fracture subsystem is the main flow pathway, and the interporosity flow between matrix and vug subsystems is ignored; the interporosity flow manner of matrix to fracture is pseudo-steady, and the interporosity flow manner of vug to fracture is unsteady.
5. Total compressibility is a constant.
6. Fluid flow in reservoir is isothermal and Darcy flow, and the gravity and capillary effect are ignored.
7. At the initial time, pressure is uniformly distributed in reservoir, equals to the initial pressure p_i .

Basic solutions of governing flow equations in triple media carbonate reservoir

The governing equations in triple media carbonate reservoir

By Darcy’s law, the oil flow velocity at spherical surface of vug is

$$v_o = -\frac{k_v k_{vro}}{\mu_o} \left(\frac{\partial p_v}{\partial r_v} \right) \Big|_{r_v=r_1} \tag{1}$$

The water flow velocity at spherical surface of vug is

$$v_w = -\frac{k_v k_{vrw}}{\mu_w} \left(\frac{\partial p_v}{\partial r_v} \right) \Big|_{r_v=r_1} \tag{2}$$

Because the outflow oil and water volume in unit time from the unit volume vug is q_{vo} and q_{vw} , the velocity at the spherical surface equals the result that the surface area of a spherical vug divides the outflow volume of fluid from a vug in unit time, that is

$$v_o = \frac{1}{3} r_1 q_{vo} \tag{3}$$

and

$$v_w = \frac{1}{3} r_1 q_{vw} \tag{4}$$

Combining Eqs. (1)–(4), the connecting condition of interporosity flow between vug and fracture can be obtained from the following equation:

$$q_{vo} = -\frac{3 k_v k_{vro}}{r_1 \mu_o} \left(\frac{\partial p_v}{\partial r_v} \right) \Big|_{r_v=r_1} \tag{5}$$

and

$$q_{vw} = -\frac{3 k_v k_{vrw}}{r_1 \mu_w} \left(\frac{\partial p_v}{\partial r_v} \right) \Big|_{r_v=r_1} \tag{6}$$

where r_1 is the radius of vug; v_o is the oil flow velocity, m/s; v_w is the water flow velocity, m/s; q_{vo} is the outflow oil volume in unit time from the unit volume vug, $m^3/(m^3 \cdot s)$; q_{vw} is the outflow water volume in unit time from the unit volume vug, $m^3/(m^3 \cdot s)$.

The oil flow governing differential equations of vug system in radial spherical coordinate system is as follows:

$$\frac{k_v k_{vro}}{\mu_o} \frac{\partial^2 p_v}{\partial r_v^2} + \frac{k_v k_{vro}}{\mu_o} \frac{2}{r_v} \frac{\partial p_v}{\partial r_v} = S_{vo} \phi_v c_{vto} \frac{\partial p_v}{\partial t} \quad (0 < r_v < r_1). \tag{7}$$

The water flow governing differential equations of vug system in radial spherical coordinate system is as follows:

$$\frac{k_v k_{vrw}}{\mu_w} \frac{\partial^2 p_v}{\partial r_v^2} + \frac{k_v k_{vrw}}{\mu_w} \frac{2}{r_v} \frac{\partial p_v}{\partial r_v} = S_{vw} \phi_v c_{vtw} \frac{\partial p_v}{\partial t} \quad (0 < r_v < r_1). \tag{8}$$

Combining Eqs. (7) and (8), we have

$$\begin{aligned} &k_v \left(\frac{k_{vro}}{\mu_o} + \frac{k_{vrw}}{\mu_w} \right) \frac{\partial^2 p_v}{\partial r_v^2} + k_v \left(\frac{k_{vro}}{\mu_o} + \frac{k_{vrw}}{\mu_w} \right) \frac{2}{r_v} \frac{\partial p_v}{\partial r_v} \\ &= \phi_v c_{vt} \frac{\partial p_v}{\partial t} \quad (0 < r_v < r_1), \end{aligned} \tag{9}$$

where $c_{vt} = c_v + S_{vo} c_{Lo} + S_{vw} c_{Lw}$ is the compressibility of oil–water two-phase flow in vug system, $1/Pa$.

Initial conditions:

$$p_v|_{t=0} = p_i. \tag{10}$$

At the center point of vugs:

$$\left. \frac{\partial p_v}{\partial r_v} \right|_{r_v=0} = 0. \tag{11}$$

At the spherical surface of vugs, the vugs pressure is equal to the fracture pressure:

$$p_v(r_v, t)|_{r_v=r_1} = p_f. \tag{12}$$

The oil flow governing differential equation of fracture system in Cartesian coordinate system is as follows:

$$\begin{aligned} &\frac{\partial}{\partial x} \left(\frac{k_{fh} k_{fro}}{\mu_o} \frac{\partial p_f}{\partial x} \right) + \frac{\partial}{\partial y} \left(\frac{k_{fh} k_{fro}}{\mu_o} \frac{\partial p_f}{\partial y} \right) + \frac{\partial}{\partial z} \left(\frac{k_{fv} k_{fro}}{\mu_o} \frac{\partial p_f}{\partial z} \right) \\ &+ \alpha_m \frac{k_m k_{mro}}{\mu_o} (p_m - p_f) + q_{vo} = S_{fo} \phi_f c_{fto} \frac{\partial p_f}{\partial t}. \end{aligned} \tag{13}$$

The water flow governing differential equation of fracture system in Cartesian coordinate system is as follows:

$$\begin{aligned} &\frac{\partial}{\partial x} \left(\frac{k_{fh} k_{frw}}{\mu_w} \frac{\partial p_f}{\partial x} \right) + \frac{\partial}{\partial y} \left(\frac{k_{fh} k_{frw}}{\mu_w} \frac{\partial p_f}{\partial y} \right) + \frac{\partial}{\partial z} \left(\frac{k_{fv} k_{frw}}{\mu_w} \frac{\partial p_f}{\partial z} \right) \\ &+ \alpha_m \frac{k_m k_{mrw}}{\mu_w} (p_m - p_f) + q_{vw} = S_{fw} \phi_f c_{ftw} \frac{\partial p_f}{\partial t} \end{aligned} \tag{14}$$

Combining Eqs. (13) and (14), we have

$$\begin{aligned} &k_{fh} \left(\frac{k_{fro}}{\mu_o} + \frac{k_{frw}}{\mu_w} \right) \frac{\partial^2 p_f}{\partial x^2} + k_{fh} \left(\frac{k_{fro}}{\mu_o} + \frac{k_{frw}}{\mu_w} \right) \frac{\partial^2 p_f}{\partial y^2} \\ &+ k_{fv} \left(\frac{k_{fro}}{\mu_o} + \frac{k_{frw}}{\mu_w} \right) \frac{\partial^2 p_f}{\partial z^2} + \alpha_m k_m \left(\frac{k_{mro}}{\mu_o} + \frac{k_{mrw}}{\mu_w} \right) (p_m - p_f) \\ &+ q_{vo} + q_{vw} = (S_{fo} c_{fto} + S_{fw} c_{ftw}) \phi_f \frac{\partial p_f}{\partial t}. \end{aligned} \tag{15}$$

The oil flow governing differential equation of matrix system is as follows:

$$\alpha_m \frac{k_m k_{mro}}{\mu_o} (p_m - p_f) + S_{mo} \phi_m c_{mto} \frac{\partial p_m}{\partial t} = 0. \tag{16}$$

The water flow governing differential equation of matrix system is as follows:

$$\alpha_m \frac{k_m k_{mrw}}{\mu_w} (p_m - p_f) + S_{mw} \phi_m c_{mtw} \frac{\partial p_m}{\partial t} = 0. \tag{17}$$

Combining Eqs. (16) and (17), we have

$$\alpha_m k_m \left(\frac{k_{mro}}{\mu_o} + \frac{k_{mrw}}{\mu_w} \right) (p_m - p_f) + \phi_m c_{mt} \frac{\partial p_m}{\partial t} = 0. \tag{18}$$

Initial condition:

$$p_f|_{t=0} = p_m|_{t=0} = p_i. \tag{19}$$

External boundary condition:

$$\lim_{r_f \rightarrow \infty} p_f = p_i \text{ (infinite)}. \tag{20}$$

Cube geometric shape factor (Warren and Root 1963; Al-Ghamdi and Ershaghi 1996):

$$\alpha_m = 16/L^2. \tag{21}$$

Spherical geometric shape factor (De Swaan 1976; Rangel-German and Kovscek 2005):

$$\alpha_v = 15/r_1^2. \tag{22}$$

Interporosity flow factor of vug subsystem to fracture subsystem is as follows

$$\lambda_v = \alpha_v r_w^2 \frac{k_v}{k_f} = 15 \left(\frac{r_w}{r_1} \right)^2 \frac{k_v}{k_f}. \tag{23}$$

Interporosity flow factor of matrix subsystem to fracture subsystem is as follows:

$$\lambda_m = 16 \left(\frac{r_w}{L} \right)^2 \frac{k_m}{k_f}. \tag{24}$$

Capacitance coefficient:

$$\omega_j = \phi_j c_{jt} / (\phi_f c_{ft} + \phi_m c_{mt} + \phi_v c_{vt}), \quad (j = f, m, v). \tag{25}$$

The dimensionless governing equations in triple media carbonate reservoir

For simplification, the mathematical model is derived and solved in dimensionless form. Table 1 lists some dimensionless variables used in the mathematical model presented in this article. The dimensionless models are as follows:

The governing differential equations of vug system in radial spherical coordinate system are as follows:

$$\frac{\partial^2 p_{vD}}{\partial r_{vD}^2} + \frac{2}{r_{vD}} \frac{\partial p_{vD}}{\partial r_{vD}} = \frac{15\omega_v}{\Omega_3 \lambda_v} \frac{\partial p_{vD}}{\partial t_D} \quad (0 < r_{vD} < 1), \tag{26}$$

Table 1 Definitions of dimensionless variables

Dimensionless pressure	$p_{jD} = 2\pi k_f h (p_i - p_j) / (q_{sc} B_o \mu_o), \quad (j = f, m, v)$
Dimensionless radius of fracture system	$r_{fD} = r_f / r_w$
Dimensionless radius of vug system	$r_{vD} = r_v / r_1$
Dimensionless wellbore storage coefficient	$C_D = C / [2\pi h r_w^2 (\phi_f c_{ft} + \phi_m c_{mt} + \phi_v c_{vt})]$
Dimensionless time	$t_D = k_{fh} k_{fro} t / [\mu_o r_w^2 (\phi_f c_{ft} + \phi_m c_{mt} + \phi_v c_{vt})]$
Dimensionless horizontal section length in a horizontal well	$L_{hD} = \frac{L_h}{r_w}$
Dimensionless formation thickness	$h_D = \frac{h}{r_w} \sqrt{\frac{k_{fh}}{k_{fv}}}$
Dimensionless horizontal well position	$z_{wD} = \frac{z_w}{r_w} \sqrt{\frac{k_{fh}}{k_{fv}}}$

where $\Omega_3 = \frac{\mu_o}{k_{fro}} \left(\frac{k_{vro}}{\mu_o} + \frac{k_{vrw}}{\mu_w} \right)$.

Initial conditions:

$$p_{vD}|_{t_D=0} = 0. \tag{27}$$

At the center point of vugs:

$$\left. \frac{\partial p_{vD}}{\partial r_{vD}} \right|_{r_{vD}=0} = 0. \tag{28}$$

At the spherical surface of vugs, the vugs' pressure is equal to the fracture pressure:

$$p_{vD}(r_{vD}, t_D)|_{r_{vD}=1} = p_{fD}. \tag{29}$$

The governing differential equations of fracture system in radial cylindrical system are as follows:

$$\Omega_1 \frac{\partial^2 p_{fD}}{\partial r_{fD}^2} + \Omega_1 \frac{2}{r_{fD}} \frac{\partial p_{fD}}{\partial r_{fD}} + \Omega_2 \lambda_m (p_{mD} - p_{fD}) - \Omega_3 \frac{\lambda_v}{5} \left(\frac{\partial p_{vD}}{\partial r_{vD}} \right) \Big|_{r_{vD}=1} = \omega_f \frac{\partial p_{fD}}{\partial t_D}, \tag{30}$$

where $\Omega_1 = \frac{\mu_o}{k_{fro}} \left(\frac{k_{fro}}{\mu_o} + \frac{k_{frw}}{\mu_w} \right)$, $\Omega_2 = \frac{\mu_o}{k_{fro}} \left(\frac{k_{mro}}{\mu_o} + \frac{k_{mrw}}{\mu_w} \right)$, and $\Omega_3 = \frac{\mu_o}{k_{fro}} \left(\frac{k_{vro}}{\mu_o} + \frac{k_{vrw}}{\mu_w} \right)$, and

The matrix system:

$$\Omega_2 \lambda_m (p_{fD} - p_{mD}) = \omega_m \frac{\partial p_{mD}}{\partial t_D}. \tag{31}$$

Initial condition:

$$p_{fD}|_{t_D=0} = 0. \tag{32}$$

External boundary condition:

$$\lim_{r_{fD} \rightarrow \infty} p_{fD} = 0 \text{ (infinite)}. \tag{33}$$

Laplace transformation of dimensionless governing equations

Introduce the Laplace transformation based on t_D , that is

$$L[p_D(r_D, t_D)] = \bar{p}_D(r_D, u) = \int_0^\infty p_D(r_D, t_D)e^{-ut_D} dt_D, \quad (34)$$

where p_D is the dimensionless pressure in real space; \bar{p}_D is the dimensionless pressure in Laplace space; t_D is the dimensionless time in real space; u is the Laplace transformation variable.

Now making the Laplace transformation to Eqs. (26)–(33), then they become as follows.

The governing differential equations of vug system in radial spherical coordinate system are as follows:

$$\frac{\partial^2 \bar{p}_{vD}}{\partial r_{vD}^2} + \frac{2}{r_{vD}} \frac{\partial \bar{p}_{vD}}{\partial r_{vD}} = \frac{15u\omega_v}{\Omega_3 \lambda_v} \bar{p}_{vD} \quad (0 < r_{vD} < 1). \quad (35)$$

Initial conditions:

$$\bar{p}_{vD}|_{t_D=0} = 0. \quad (36)$$

At the center point of vugs:

$$\left. \frac{\partial \bar{p}_{vD}}{\partial r_{vD}} \right|_{r_{vD}=0} = 0. \quad (37)$$

At the spherical surface of vugs, the vugs' pressure is equal to the fracture pressure:

$$\bar{p}_{vD}(r_{vD}, t_D)|_{r_{vD}=1} = \bar{p}_{fD}. \quad (38)$$

The governing differential equations of fracture system in radial cylindrical system are as follows:

$$\begin{aligned} \Omega_1 \frac{\partial^2 \bar{p}_{fD}}{\partial r_{fD}^2} + \Omega_1 \frac{2}{r_{fD}} \frac{\partial \bar{p}_{fD}}{\partial r_{fD}} + \Omega_2 \lambda_m (\bar{p}_{mD} - \bar{p}_{fD}) \\ - \Omega_3 \frac{\lambda_v}{5} \left(\frac{\partial \bar{p}_{vD}}{\partial r_{vD}} \right) \Big|_{r_{vD}=1} = u\omega_f \bar{p}_{fD}. \end{aligned} \quad (39)$$

The matrix system:

$$\Omega_2 \lambda_m (\bar{p}_{fD} - \bar{p}_{mD}) = u\omega_m \bar{p}_{mD}. \quad (40)$$

Initial condition:

$$\bar{p}_{fD}|_{t_D=0} = 0. \quad (41)$$

External boundary condition:

$$\lim_{r_{fD} \rightarrow \infty} \bar{p}_{fD} = 0 \text{ (infinite)}. \quad (42)$$

The general solution of Eq. (35) is as follows:

$$\bar{p}_{vD} = (A_v e^{\sigma_v r_{vD}} + B_v e^{-\sigma_v r_{vD}}) / r_{vD} \quad (43)$$

$$\sigma_v = \sqrt{15u\omega_v / \Omega_3 \lambda_v}. \quad (44)$$

Substitute Eq. (43) into Eqs. (36) and (37), we then obtain

$$A_v = \frac{1}{e^{\sigma_v} - e^{-\sigma_v}} \bar{p}_{fD} \quad (45)$$

$$B_v = -\frac{1}{e^{\sigma_v} - e^{-\sigma_v}} \bar{p}_{fD}. \quad (46)$$

Then, the solution of Eq. (35) in Laplace space is as follows:

$$\bar{p}_{vD} = \frac{\bar{p}_{fD}}{r_{vD}} \frac{e^{\sigma_v r_{vD}} - e^{-\sigma_v r_{vD}}}{e^{\sigma_v} - e^{-\sigma_v}}. \quad (47)$$

Through the derivative calculation to r_{vD} of Eq. (47), we have

$$\left. \frac{d\bar{p}_{vD}}{dr_{vD}} \right|_{r_{vD}=1} = [\sigma_v \text{cth}(\sigma_v) - 1] \bar{p}_{fD}, \quad (48)$$

where hyperbolic cotangent function $\text{cth}(\sigma_v) = (e^{\sigma_v} + e^{-\sigma_v}) / (e^{\sigma_v} - e^{-\sigma_v})$.

Substitute Eqs. (40) and (48) into Eq. (39), the governing equation of fracture system in radial spherical coordinate system is as follows:

$$\frac{\partial^2 \bar{p}_{fD}}{\partial r_{fD}^2} + \frac{2}{r_{fD}} \frac{\partial \bar{p}_{fD}}{\partial r_{fD}} = f(u) \bar{p}_{fD} \quad (49)$$

$$f(u) = \frac{\Omega_2}{\Omega_1} \frac{u\omega_m \lambda_m}{u\omega_m + \Omega_2 \lambda_m} + \frac{\Omega_3}{\Omega_1} \frac{\lambda_v}{5} [\sigma_v \text{cth}(\sigma_v) - 1] + \frac{u\omega_f}{\Omega_1}. \quad (50)$$

Point-source function in triple media carbonate reservoir

The boundary condition at the surface of a vanishingly small sphere corresponding to the instantaneous withdrawal of an amount of oil fluid \tilde{q}_o and water fluid \tilde{q}_w at $t = 0$ can be expressed by the following:

$$\lim_{\xi_D \rightarrow 0^+} \left[4\pi r_w r_{fD}^2 k_f \frac{k_{fro}}{\mu_o} \frac{\partial \Delta p_f}{\partial r_{fD}} \right] \Big|_{r_{fD}=\xi_D} = -B_o \tilde{q}_o \delta(t) \quad (51)$$

and

$$\lim_{\xi_D \rightarrow 0^+} \left[4\pi r_w r_{fD}^2 k_f \frac{k_{frw}}{\mu_w} \frac{\partial \Delta p_f}{\partial r_{fD}} \right] \Big|_{r_{fD}=\xi_D} = -B_w \tilde{q}_w \delta(t), \quad (52)$$

where $\delta(t)$ is the Dirac Delta function.

Combining Eqs. (51) and (52), we have

$$\begin{aligned} \lim_{\xi_D \rightarrow 0^+} \left[4\pi r_w r_{fD}^2 k_f \left(\frac{k_{fro}}{\mu_o} + \frac{k_{frw}}{\mu_w} \right) \frac{\partial \Delta p_f}{\partial r_{fD}} \right] \Big|_{r_{fD}=\xi_D} \\ = -(B_o \tilde{q}_o + B_w \tilde{q}_w) \delta(t). \end{aligned} \quad (53)$$

Because it assumes that only natural fracturing systems in the carbonate reservoir are connected to the wellbore, the water cut of well can be expressed by the following:

$$f_w = \frac{\tilde{q}_w}{\tilde{q}_o + \tilde{q}_w}. \tag{54}$$

Substitute Eqs. (54) into Eq. (53), we get

$$\lim_{\xi_D \rightarrow 0^+} \left[4\pi r_w r_{fD}^2 \frac{k_f k_{fro}}{\mu_o} \frac{\partial \Delta p_f}{\partial r_{fD}} \right]_{r_{fD}=\xi_D} = -\frac{\Omega_0 B_o \tilde{q}_o \delta(t)}{\Omega_1}, \tag{55}$$

where $\Omega_0 = 1 + \frac{B_w f_w}{B_o(1-f_w)}$ and $\Omega_1 = \frac{\mu_o}{k_{fro}} \left(\frac{k_{fro}}{\mu_o} + \frac{k_{frw}}{\mu_w} \right)$.

Taking Laplace transformation for t with Eq. (55) and setting the source strength to unity, and then combining with Eq. (49), the instantaneous point-source solution can be obtained (Raghavan 1993; Ozkan and Raghavan 1992). Using the image-well technique and the superposition method, the continuous point-source solution in laterally infinite triple media carbonate reservoir with impermeable top and bottom boundaries in Laplace domain is given as follows:

$$\Delta \bar{p}_f = \frac{\Omega_0 \tilde{q}_o B_o \mu_o}{2\pi \Omega_1 k_f k_{fro} r_w u h_D} \left[K_0(r_{fD} \sqrt{f(u)}) + 2 \sum_{n=1}^{\infty} K_0 \left(r_{fD} \sqrt{f(u) + \frac{n^2 \pi^2}{h_D^2}} \right) \cos n\pi \frac{z_D}{h_D} \cos n\pi \frac{z_{wD}}{h_D} \right], \tag{56}$$

where $K_0(x)$ is the modified Bessel function of second kind, zero order.

Flow model of horizontal well in triple media carbonate reservoir

According to the superposition principle, we can get the pressure response in triple media carbonate reservoir caused by horizontal well by integrating the point-source solution obtained in the previous section along the horizontal well, that is

$$\Delta \bar{p}_f = \frac{\Omega_0 \tilde{q} B_o \mu_o}{2\pi \Omega_1 k_f k_{fro} r_w u h_D} \int_{-L_h/2}^{L_h/2} \left[K_0(r_{fD} \sqrt{f(u)}) + 2 \sum_{n=1}^{\infty} K_0 \left(r_{fD} \sqrt{f(u) + \frac{n^2 \pi^2}{h_D^2}} \right) \cos n\pi \frac{z_D}{h_D} \cos n\pi \frac{z_{wD}}{h_D} \right] dx_w, \tag{57}$$

where $\Omega_0 = 1 + \frac{B_w f_w}{B_o(1-f_w)}$, $\Omega_1 = \frac{\mu_o}{k_{fro}} \left(\frac{k_{fro}}{\mu_o} + \frac{k_{frw}}{\mu_w} \right)$, and $r_{fD} = \sqrt{(x_D - x_{wD})^2 + (y_D - y_{wD})^2}$.

For a horizontal well, the assumption of constant flow rate can yield the following equation:

$$q_{sc} = \tilde{q} L_h. \tag{58}$$

Combining Eqs. (57) and (58), we have

$$\Delta \bar{p}_f = \frac{\Omega_0 q_{sc} B_o \mu_o}{2\pi \Omega_1 k_f k_{fro} r_w u h_D L_h} \int_{-L_h/2}^{L_h/2} \left[K_0(r_{fD} \sqrt{f(u)}) + 2 \sum_{n=1}^{\infty} K_0 \left(r_{fD} \sqrt{f(u) + \frac{n^2 \pi^2}{h_D^2}} \right) \cos n\pi \frac{z_D}{h_D} \cos n\pi \frac{z_{wD}}{h_D} \right] dx_w. \tag{59}$$

Substitute $r_{fD} = \sqrt{(x_D - x_{wD})^2 + (y_D - y_{wD})^2}$ into Eq. (59) and together with $y_{wD} = 0$, then we can get the dimensionless as follows:

$$\bar{p}_{fD} = \frac{\Omega_0}{u \Omega_1 L_{hD}} \int_{-L_{hD}/2}^{L_{hD}/2} \left[K_0(\sqrt{(x_D - x_{wD})^2 + y_D^2} \sqrt{f(u)}) + 2 \sum_{n=1}^{\infty} K_0 \left(\sqrt{(x_D - x_{wD})^2 + y_D^2} \sqrt{f(u) + \frac{n^2 \pi^2}{h_D^2}} \right) \times \cos n\pi \frac{z_D}{h_D} \cos n\pi \frac{z_{wD}}{h_D} \right] dx_{wD}. \tag{60}$$

According to Ozkan’s conclusion (Ozkan 1988), the equivalent pressure point for the horizontal well bottom pressure in the top-bottomed reservoir is as follows:

$$\begin{cases} x_D = \frac{0.732L_{hD}}{2} \\ y_D = 0 \\ z_D = z_{wD} + 1 \end{cases}. \tag{61}$$

Substitute Eq. (61) into Eq. (60), we can get the bottom hole pressure of the horizontal well in triple media carbonate reservoir:

$$\bar{p}_{wD} = \frac{\Omega_0}{u \Omega_1 L_{hD}} \int_{-L_{hD}/2}^{L_{hD}/2} \left[K_0 \left(\left| \frac{0.732L_{hD}}{2} - x_{wD} \right| \sqrt{f(u)} \right) + 2 \sum_{n=1}^{\infty} K_0 \left(\left| \frac{0.732L_{hD}}{2} - x_{wD} \right| \sqrt{f(u) + \frac{n^2 \pi^2}{h_D^2}} \right) \times \cos n\pi \frac{z_{wD} + 1}{h_D} \cos n\pi \frac{z_{wD}}{h_D} \right] dx_{wD}. \tag{62}$$

Following Van-Everdingen (1953) and Kucuk and Ayestaran (1985), the wellbore storage (C_D) and skin (S) can be incorporated in the above solution by the following:

$$\bar{p}_{wD} = \frac{u \bar{p}_{wD}^* + S}{u + C_D u^2 (u \bar{p}_{wD}^* + S)}, \tag{63}$$

where the dimensionless pressure solution \bar{p}_{wD}^* at the bottom hole of a horizontal well without considering the wellbore storage and skin can be obtained from the solution of Eq. (62).

With the numerical inversion algorithm proposed by Stehfest (1970), we can get the real dimensionless bottom hole pressure of the horizontal well, p_{wD} , in real-time space with consideration the wellbore storage and skin in the triple media carbonate reservoir. Subsequently, the transient pressure behavior of a horizontal well will be analyzed, and the type curves will also be shown.

Oil and water relative permeability of triple media carbonate reservoir

According to the research results of the oil and water relative permeability for the matrix, fracture, and vug systems of the triple media carbonate reservoir (Lian et al. 2011, 2013), we selected a set of the oil and water relative permeability for the matrix, fracture, and vug systems, respectively, which can provide the necessary base data for the theoretical analysis and calculation of oil–water two-phase well test. The detailed data are shown in Tables 2, 3, 4 and Figs. 3, 4, 5. The field measured oil and water

Table 2 Oil and water relative permeability of matrix system (Lian et al. 2011)

S_{mw}	K_{mrw}	K_{mro}
20	0	0.4095
25	0.005	0.387
30	0.01	0.32535
35	0.02	0.27
40	0.03	0.2214
45	0.045	0.1764
50	0.06	0.1368
55	0.082	0.10125
60	0.11	0.0693
65	0.143	0.04185
70	0.18	0.0189
75	0.23	0

Table 3 Oil and water relative permeability of fracture system (Lian et al. 2011)

S_{fw}	K_{frw}	K_{fro}
0	0	1
10	0.036	0.882
20	0.09	0.819
30	0.189	0.729
40	0.315	0.585
50	0.423	0.468
60	0.54	0.333
70	0.675	0.207
80	0.747	0.099
90	0.819	0.036
100	1	0

Table 4 Oil and water relative permeability of vug system (Li et al. 2013)

S_{vw}	K_{vrw}	K_{vro}
0	0	1
8	0.025	0.95
18	0.05	0.9
28	0.065	0.75
55	0.15	0.45
70	0.38	0.19
78	0.55	0.16
83	0.67	0

relative permeability data should be used when the results of this article are applied to the field.

Pressure behavior analyses

Flowing periods

Figure 6 shows the whole transient flow process of a horizontal well in triple media carbonate reservoir; it can be divided into seven flow stages:

Stage 1: The pure wellbore storage stage; the pressure and pressure derivative assume unit slope;

Stage 2: The skin effect stage; the shape of the derivative curve is just like a ‘hump’ due to the wellbore storage effect and the skin effect;

Stage 3: Early, or first, radial flow regime (Fig. 7a). Slope of the pressure derivative curve is zero. Duration of the regime is very short, because formation thickness is usually less than 100 m. Radial flow regime will stop when pressure wave spreads to the closed boundary on top or bottom. This regime would be hardly observed for a small thickness.

Stage 4: Linear flow regime (see Fig. 7b). The pressure derivative curve is a line with a slope of 0.5.

Stage 5: The interporosity flow stage of the vug system to fracture system; because the permeability of vug is better than that of the matrix, the interporosity flow of the vug system to fracture system takes place first, and the pressure derivative is V-shaped, which is the reflection of the interporosity flow of vug to fracture;

Stage 6: The interporosity flow stage of the matrix system to fracture system; the interporosity flow of the vug system to fracture system has already been completed, and in this stage, the manner of pseudo-steady interporosity flow of matrix system to fracture system takes place;

Stage 7: The whole radial flow stage of fracture system, vug system, and matrix system (see Fig. 7c); the interporosity flow of matrix to fracture has already been completed, and the pressures between matrix and vug and fracture have come up to a state of dynamic balance.

Fig. 3 Oil and water relative permeability of matrix system (Lian et al. 2011)

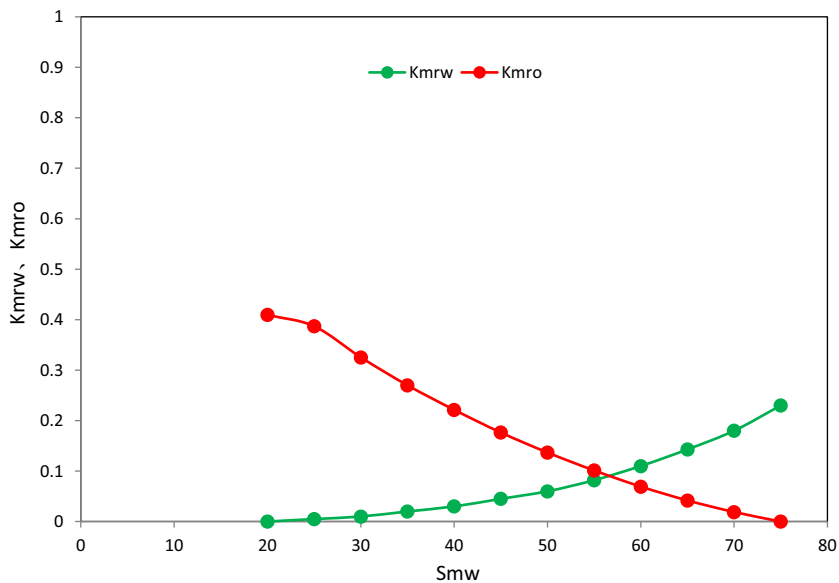


Fig. 4 Oil and water relative permeability of fracture system (Lian et al. 2011)

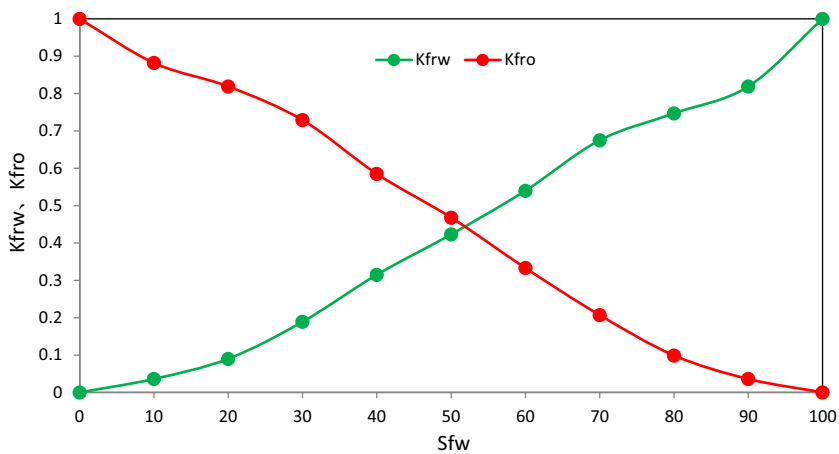
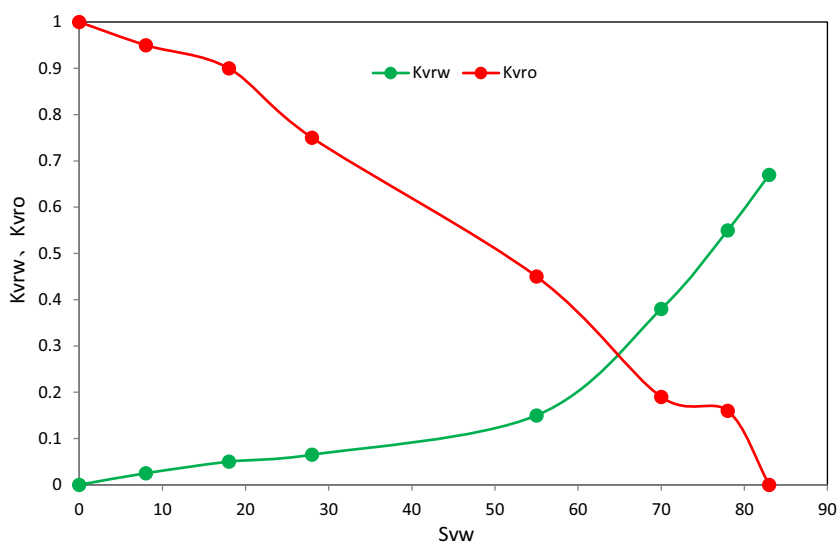


Fig. 5 Oil and water relative permeability of vug system (Li et al. 2013)



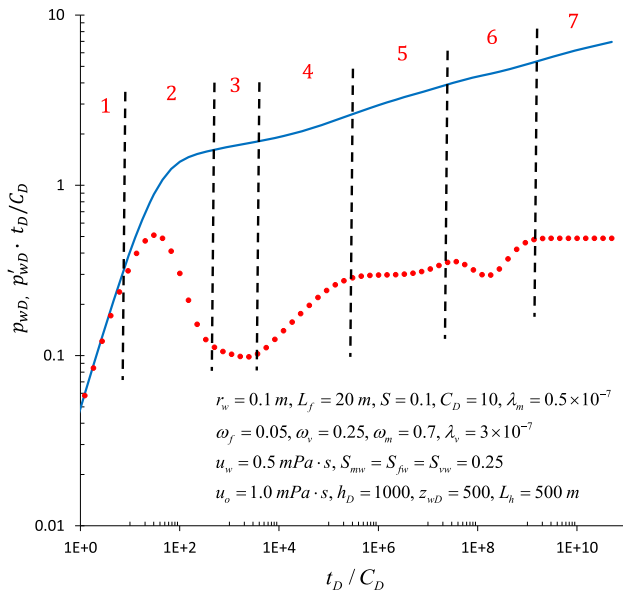


Fig. 6 Dimensionless pressure and pressure derivative responses of a horizontal well in triple media carbonate reservoir

Effect of water saturation of matrix system

Figure 8 shows the effect of water saturation of matrix system on pressure and pressure derivative of a horizontal well in triple media carbonate reservoir. It can be seen that the parameter S_{mw} represents the starting time of interporosity flow of matrix subsystem to fracture subsystem; the time of interporosity will be earlier if the parameter S_{mw} is smaller, since the flow resistance of oil phase in the matrix is also smaller.

Effect of water saturation of vug system

Figure 9 shows the effect of water saturation of vug system on pressure and pressure derivative of a horizontal well in triple

Fig. 7 a Early radial flow. b Linear flow. c Late pseudo-radial flow

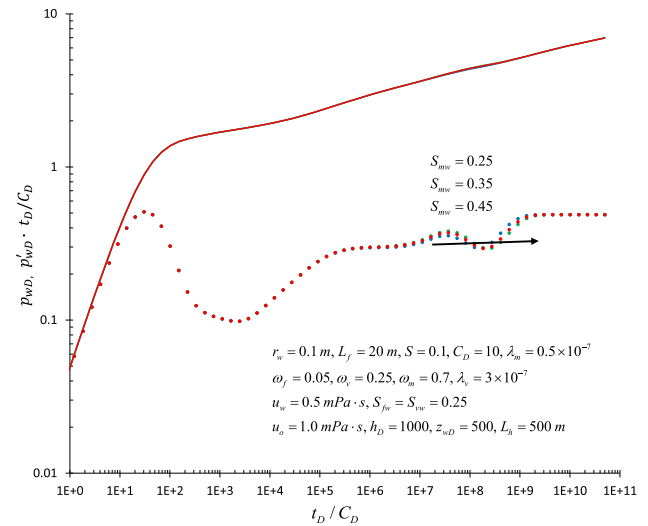
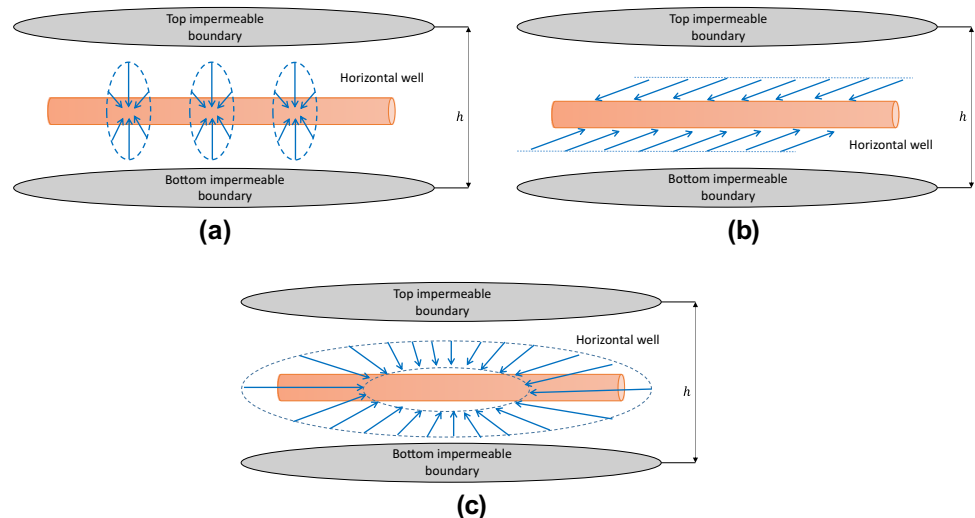


Fig. 8 Effect of water saturation of matrix system on pressure transient responses

media carbonate reservoir. It can be seen that the parameter S_{vw} represents the starting time of interporosity flow of vug subsystem to fracture subsystem; the time of interporosity will be earlier if the parameter S_{vw} is smaller, since the flow resistance of oil phase in the matrix is also smaller.

Effect of water saturation of fracture system

Figure 10 shows the effect of water saturation of fracture system on pressure and pressure derivative of a horizontal well in triple media carbonate reservoir. Figure 1 indicates that only the fracture system supplies fluid to the wellbore in the model of this article. Hence, the pressure and pressure derivative will be smaller if the parameter S_{fw} is smaller, since the flow resistance of oil phase in the fracture is also smaller.

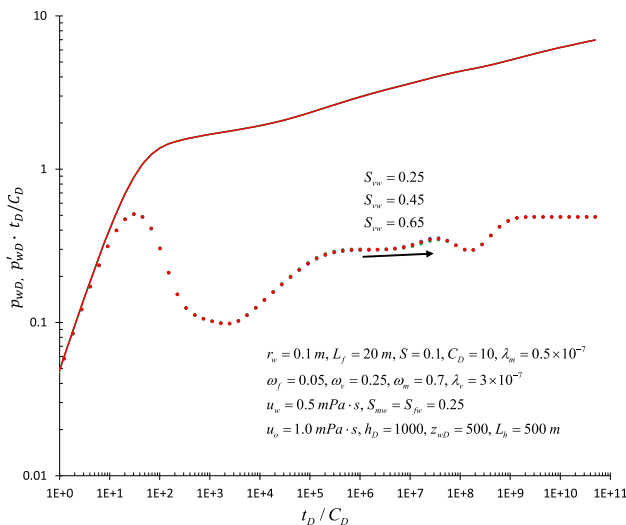


Fig. 9 Effect of water saturation of vug system on pressure transient responses

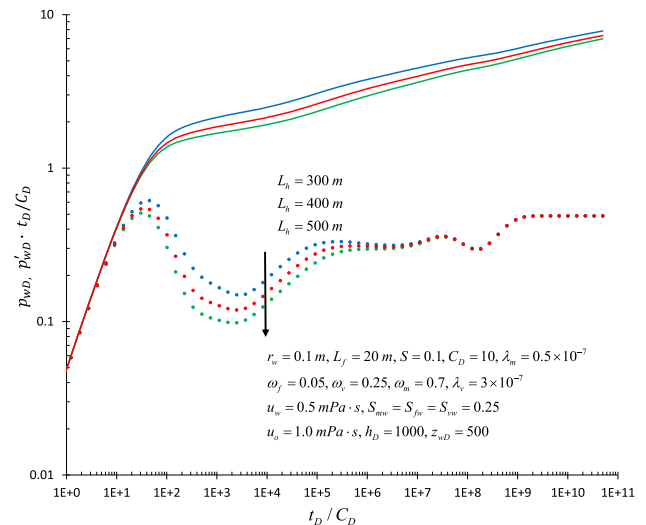


Fig. 11 Effect of horizontal section length in a horizontal well on pressure transient responses

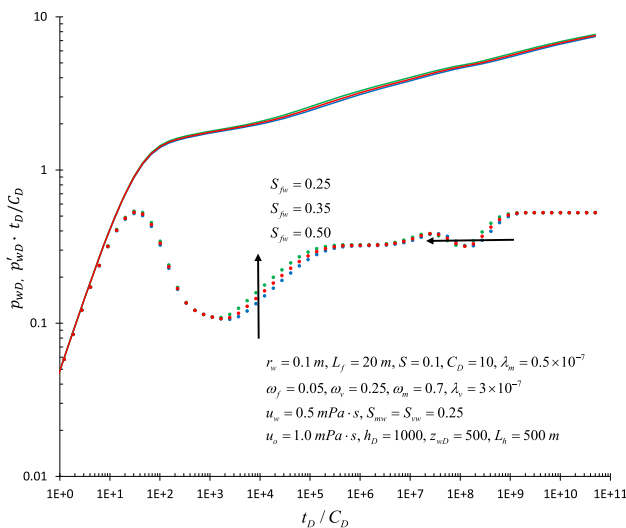


Fig. 10 Effect of water saturation of fracture system on pressure transient responses

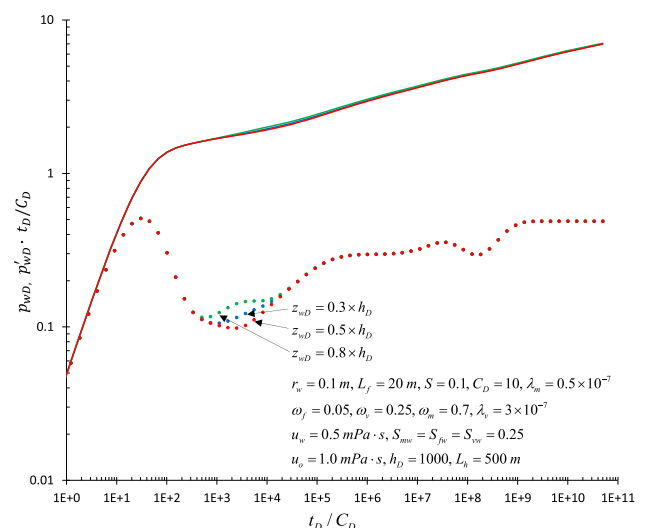


Fig. 12 Effect of horizontal section length in a horizontal well on pressure transient responses

Effect of horizontal section length in a horizontal well

Figure 11 shows the effect of horizontal section length in a horizontal well on pressure and pressure derivative of a horizontal well in triple media carbonate reservoir. It can be seen that the pressure and pressure derivative of the early radial flow and the linear flow stage will be smaller if the horizontal section length in a horizontal well is longer.

Effect of horizontal well position

Figure 12 shows the effect of horizontal well position on pressure and pressure derivative of a horizontal well in

triple media carbonate reservoir. It can be seen that the pressure and pressure derivative of the early radial flow and the linear flow stage will be smaller if the horizontal well position is closer to the middle of the reservoir.

Conclusions

The main purpose of this work is to provide a mathematical model to analyze oil–water two-phase flow transient pressure for a horizontal well in triple media carbonate reservoir. The following conclusions can be obtained

1. A solution is obtained in the Laplace space. With the Stehfest numerical inversion algorithm, transient pressure in the real-time space can be obtained.
2. Seven flow periods can be identified for a horizontal well in triple media carbonate reservoir.
3. Parametric analysis indicates that parameters pertinent to horizontal well, such as water saturation of matrix, vug, and fracture system, horizontal section length, and horizontal well position, have obvious influence on dimensionless pressure and pressure derivative curves of a horizontal well in triple media carbonate reservoir.
4. The model can be applied to interpret actual transient pressure responses for horizontal well in triple media carbonate reservoir.
5. Comparing the method of this paper with the well-known commercial software Saphir (Ecrin v4.12.03), developed by the French company Kappa, we can see that the software Saphir did not contain the oil–water two-phase well test model of triple media carbonate reservoir; hence, our model is new, and our method improved the current well test interpretation theory. The method of this paper may be used if the sort of field well test data is like Fig. 6.

Acknowledgements This work was supported by the scientific research starting project of SWPU (No. 2014QHZ031).

Compliance with ethical standards


Conflict of interest The authors declare that there is no conflict of interests regarding the publication of this paper.

References

- Al-Ghamdi A, Ershaghi I (1996) Pressure transient analysis of dually fractured reservoirs. *SPEJ* 1(1):93–100 (**SPE 26959-PA**)
- Bourdet D, Gringarten AC (1980) Determination of fissure volume and block size in fractured reservoirs by type-curve analysis. In: *SPE 9293-MS*. Presented at the 55th annual fall technical conference and exhibition held in Dallas, Texas, 21–24 September. doi:10.2118/9293-MS
- Cai M, Jia Y (2007) Dynamic analysis for pressure in limit conductivity vertical fracture wells of triple-porosity reservoir. *Well Test.* 16(5):12–15
- Camacho-Velázquez R, Vásquez-Cruz M, Castrejón-Aivar R (2005) Pressure transient and decline curve behaviors in naturally fractured vuggy carbonate reservoirs. *SPE Reserv Eval Eng* 8(2):95–112 (**SPE 77689-PA**)
- Corbett PWM, Geiger S, Borges L, Garayev M, Gonzalez J, Camilo V (2010) Limitations in the numerical well test modelling of fractured carbonate rocks. *SPE 130252-MS*. In: presented at Europec/EAGE, Barcelona, June
- De Swaan O (1976) Analytical solutions for determining naturally fractured reservoir properties by well testing. *SPE J* 16(3):117–122 (**SPE 5346-PA**)
- Gua F, Chalaturnyk R (2010) Permeability and porosity models considering anisotropy and discontinuity of coalbeds and application in coupled simulation. *J Petroleum Sci Eng* 73(4):113–131
- Guo JJ, Wang HT, Zhang LH (2015) Transient pressure behavior for a horizontal well with multiple finite-conductivity fractures in tight reservoirs. *J Geophys Eng* 12(4):638–656
- Izadi M, Yildiz T (2007) Transient flow in discretely fractured porous media. In: *SPE 108190-MS*. Paper Presented at the Rocky Mountain oil & gastech technology symposium held in Denver, Colorado, 16–18 April
- Jalali Y, Ershaghi I (1987) Pressure transient analysis of heterogeneous naturally fractured reservoirs. In: *SPE 16341-MS*. Paper Presented at the SPE California Regional Meeting held in Ventura, California, 8–10 April
- Jazayeri Noushabadi MR, Jourde H, Massonnat G (2011) Influence of the observation scale on permeability estimation at local and regional scales through well tests in a fractured and karstic aquifer (Lez aquifer, Southern France). *J Hydrol* 403(3–4):321–336
- Jiang R, Xu J, Sun Z et al (2014) Rate transient analysis for multistage fractured horizontal well in tight oil reservoirs considering stimulated reservoir volume. *Math Probl Eng* 2014:1–11
- Kucuk F, Ayestaran L (1985) Analysis of simultaneously measured pressure and sandface flow rate in transient well testing (includes associated papers 13 937 and 14 693). *J Pet Technol* 37:323–334
- Leveinen J (2000) Composite model with fractional flow dimensions for well test analysis in fractured rocks. *J Hydrol* 234(3–4):116–141
- Li AF, Sun Q, Zhang D et al (2013) Oil-water relative permeability and its influencing factors in single fracture-vuggy. *J China Univ Pet* 37(3):98–102
- Lian PQ, Cheng LS, Liu LF (2011) The relative permeability curve of fractured carbonate reservoirs. *Acta Petrolei Sin* 32(6):1026–1030
- Ma X, Liu Z (2016) Predicting the oil production using the novel multivariate nonlinear model based on Arps decline model and kernel method. *Neural Comput Appl* 2016:1–13
- Ma X, Hu Y, Liu Z (2017) A novel kernel regularized nonhomogeneous grey model and its applications. *Commun Nonlinear Sci Numer Simul* 48:51–62
- Nie R, Meng Y, Yang Z, Guo J, Jia Y (2011) New flow model for the triple media carbonate reservoir. *Int J Comput Fluid Dyn.* 25(2):95–103
- Nie RS, Meng YF, Jia YL, Shang JL, Wang Y, Li JG (2012) Unsteady inter-porosity flow modeling for a multiple media reservoir. *Acta Geophys* 60(1):232–259
- Ozkan E (1988) Performance of horizontal wells. Doctoral dissertation of Tulsa, University of Tulsa, pp 119–120
- Ozkan E, Raghavan R (1992) New solutions for well-test-analysis problems: part I-analytical solutions. *Int J Rock Mech Min Sci Geomech Abstr* 29:A159–A160
- Popov P, Qin G, Bi L, Efendiev Y, Kang Z, Li J (2009) Multiphysics and multiscale methods for modeling fluid flow through naturally fractured carbonate Karst reservoirs. *SPE Reserv Eval Eng* 12(2):218–231 (**SPE 105378-PA**)
- Pulido H, Samaniego F, Rivera J (2006) On a well-test pressure theory of analysis for naturally fractured reservoirs, considering transient inter-porosity matrix, microfractures, vugs, and fractures flow. In: *SPE 104076-MS*. Paper presented at the first international oil conference and exhibition held in Mexico, 31 August
- Raghavan R (1993) *Well test analysis*. Prentice-Hall Inc., PTR, Englewood Cliffs, pp 23–25
- Rangel-German ER, Kovscek AR (2005) Matrixfracture shape factors and multiphase-flow properties of fractured porous media. In: *SPE 95105-MS*, presented at the SPE Latin American and

- Caribbean Petroleum Engineering Conference, 20–23 June, Rio de Janeiro, Brazil
- Stehfest H (1970) Algorithm 368: numerical inversion of Laplace transforms Commun. ACM 13:47–49
- Su Y, Zhang Q, Wang W et al (2015) Performance analysis of a composite dual-porosity model in multi-scale fractured shale reservoir. *J Nat Gas Sci Eng* 26:1107–1118
- Van-Everdingen AF (1953) The skin effect and its influence on the productive capacity of a well. *J Pet Technol* 5:171–176
- Wang Y, Yi Y (2017) Transient pressure behavior of a fractured vertical well with a finite-conductivity fracture in triple media carbonate reservoir. *J Porous Media* 20(8):1–16
- Wang HT, Zhang LH, Guo JJ (2013) A new rod source model for pressure transient analysis of horizontal wells with positive/negative skin in triple-porosity reservoirs. *J Petrol Sci Eng* 108:52–63
- Warren JE, Root PJ (1963) The behavior of naturally fractured reservoirs. SPE 426-PA. *SPE J* 3(3):245–255
- Wei M, Duan Y, Zhou X et al (2016) Pressure transient analysis for finite conductivity multi-staged fractured horizontal well in fractured-vuggy carbonate reservoirs. *Int J Oil Gas Coal Eng* 4(1–1):1–7
- Wu YS, Liu HH, Bodvarsson GS (2004) A triple-continuum approach for modeling flow and transport processes. *J Contam Hydrol* 73:145–179
- Wu YS, Ehlig-Economides C, Qin G, Kang Z, Zhang W, Ajayi B, Tao Q (2007) A triple continuum pressure transient model for a naturally fractured vuggy reservoir. In: SPE 110044-MS. Paper presented at the SPE annual technical conference and exhibition held in Anaheim, California, USA, 11–14, November
- Wu YS, Di Y, Kang ZJ, Fakcharoenphol P (2011) A multiple-continuum model for simulating single-phase and multiphase flow in naturally fractured vuggy reservoirs. *J Pet Sci Eng* 78(1):13–22
- Wu YH, Cheng LS, Huang SJ et al (2016) A practical method for production data analysis from multistage fractured horizontal wells in shale gas reservoirs. *Fuel* 186:821–829
- Wu K, Olson J, Balhoff MT et al (2017) Numerical analysis for promoting uniform development of simultaneous multiple-fracture propagation in horizontal wells. *SPE Prod Oper* 32:41–50
- Zhang DL, Zhang LH, Guo JJ et al (2015a) Research on the production performance of multistage fractured horizontal well in shale gas reservoir. *J Nat Gas Sci Eng* 26:279–289
- Zhang M, Yao J, Sun H et al (2015b) Triple-continuum modeling of shale gas reservoirs considering the effect of kerogen. *J Nat Gas Sci Eng* 24:252–263

DHI evaluation by combining rock physics simulation and statistical techniques for fluid identification of Cambrian-to-Cretaceous clastic reservoirs in Pakistan

Nisar Ahmed¹  · Pervez Khalid¹ · Hafiz Muhammad Bilal Shafi¹ · Patrick Connolly²

Received: 26 May 2017 / Accepted: 10 August 2017 / Published online: 20 August 2017
© Institute of Geophysics, Polish Academy of Sciences & Polish Academy of Sciences 2017

Abstract The use of seismic direct hydrocarbon indicators is very common in exploration and reservoir development to minimise exploration risk and to optimise the location of production wells. DHIs can be enhanced using AVO methods to calculate seismic attributes that approximate relative elastic properties. In this study, we analyse the sensitivity to pore fluid changes of a range of elastic properties by combining rock physics studies and statistical techniques and determine which provide the best basis for DHIs. Gassmann fluid substitution is applied to the well log data and various elastic properties are evaluated by measuring the degree of separation that they achieve between gas sands and wet sands. The method has been applied successfully to well log data from proven reservoirs in three different siliciclastic environments of Cambrian, Jurassic, and Cretaceous ages. We have quantified the sensitivity of various elastic properties such as acoustic and extended elastic (EEI) impedances, elastic moduli (K_{sat} and $K_{\text{sat}}-\mu$), lambda-mu-rho method

($\lambda\rho$ and $\mu\rho$), P-to-S-wave velocity ratio (V_p/V_s), and Poisson's ratio (σ) at fully gas/water saturation scenarios. The results are strongly dependent on the local geological settings and our modeling demonstrates that for Cambrian and Cretaceous reservoirs, $K_{\text{sat}}-\mu$, EEI, V_p/V_s , and σ are more sensitive to pore fluids (gas/water). For the Jurassic reservoir, the sensitivity of all elastic and seismic properties to pore fluid reduces due to high overburden pressure and the resultant low porosity. Fluid indicators are evaluated using two metrics: a fluid indicator coefficient based on a Gaussian model and an overlap coefficient which makes no assumptions about a distribution model. This study will provide a potential way to identify gas sand zones in future exploration.

Keywords Statistical rock physics · Extended elastic impedance · Probability density function · 1D marginal distribution · Histogram · Chi angle

Introduction

Statistical rock physics analysis is normally employed to combine physical equations and statistical methods in reservoir characterization studies constrained by seismic data. One of the aims of statistics combined with rock physics is to map and predict the heterogeneities and complexities in petrophysical measurements and seismic attributes due to reservoir fluids. Therefore, the utilization of statistics in rock physics is getting to be more and more recurrent (Avseth et al. 2005; Tarantola 2005; Doyen 2007; Grana and Rossa 2010; Connolly and Hughes 2014; Grana 2014; Baddari et al. 2016). The uncertainties caused by the natural heterogeneities arising in real data can be estimating by building

✉ Nisar Ahmed
ahmedseis23@gmail.com

Pervez Khalid
pervez.geo@pu.edu.pk

Hafiz Muhammad Bilal Shafi
bilal907ahmed@yahoo.com

Patrick Connolly
patrick.connolly.451@gmail.com

¹ Institute of Geology, University of the Punjab, Lahore 54590, Pakistan

² Patrick Connolly Associates Ltd., 9 Pump Lane, Ascot, Berkshire SL5 7RW, UK

probabilistic frameworks around the theoretical or empirical relationships between reservoir and elastic properties. Grana et al. (2015) used statistical methods for facies classification by plotting Gaussian likelihoods (1D marginal distribution) and 2D confidence intervals (2D joint distributions) for various lithologies such as shale, limestone, and sandstone. Connolly (1999) exhibits the litho-fluid discrimination at shale/brine sand and shale/oil sand interfaces by portraying Gaussian probability function for acoustic (AI) and elastic (EI) impedances for shale, brine, and oil sands. These methods show that probability density functions of hydrocarbon and brine sand facies can help to define the direct hydrocarbon indicators sensitivity to pore fluids.

The use of direct hydrocarbon indicators (DHIs) from seismic data is very common in hydrocarbon prospecting and exploration strategies. Many seismic attributes have been proposed to enhance DHIs, most based on AVO behaviour (Aki and Richards 1980). These includes lambda–mu–rho (LMR) method (Goodway et al. 1997), pore space modulus (Hedlin 2000), difference in bulk (K_{sat}) and shear (μ) modulus (Batzle et al. 2001), elastic impedance (Connolly 1999) later modified as extended elastic impedance (Whitcombe et al. 2002), generalized fluid term (Russell et al. 2003), Poisson impedance (Quakenbush et al. 2006), and P-wave attenuation and dispersion (Khalid and Ahmed 2016). However, their discrimination strength varies reservoir to reservoir depending on local geological settings and control to the field data (Castagna and Smith 1994; Ahmed et al. 2015). Dillon et al. (2003) defined the fluid indicator coefficient (FIC) as the difference in mean values of attributes related to each pore fluid divided by the standard deviation of hydrocarbons saturated attribute. Higher FIC value is representative of better litho-fluid discrimination and has edge of taking into consideration as universally (best indicator) for all fluid-saturated rocks (Ahmed et al. 2016).

The objective of this work is to find the best direct hydrocarbon indicators (DHIs) for three siliciclastic reservoirs: the Khewra sandstone (Cambrian), the Datta Formation (Jurassic), and the Lower Goru Formation (Cretaceous), all onshore Pakistan. The fluid substitution analysis is performed using the well data and considers two different pore fluids, gas, and brine. In the current study, we first have applied Gassmann fluid substitution (1951) and then compute probability density functions (pdfs) of the different rock physics properties to determine the optimum fluid indicators. Histograms of data sets superimposed by probability density functions are also displayed to verify the effectiveness of Gaussians models. We calculate the fluid indicator coefficients (FICs) to quantify the

results. FICs and overlap coefficients are used also to find the best chi angles for extended elastic impedance for each reservoir.

Geological descriptions of reservoir rocks

The total sedimentary basinal area of Pakistan is about 827,000 km² and of which 10–20% has been explored. Up to June 2009, 221 out of 742 drilled exploration wells were hydrocarbon discoveries and 934 million barrels oil and 54 trillion cubic feet of gas have been exploited so far (Hydrocarbon Development Institute of Pakistan 2008; Pakistan Petroleum Information Service 2009).

Tectonically Pakistan is divided into three main basins: Baluchistan, Pishin, and Indus Basins, of which the Indus Basin is the largest and the only hydrocarbon producing basin in Pakistan. The Indus basin is subdivided into Upper (Kohat and Potwar sub Basins) and Lower (Central and Southern) Indus Basins (Kadri 1995). The Lower Indus Basin has the highest rate of discoveries in a succession of reservoir rock in small tilted fault blocks (Jamil et al. 2012).

For our current study, the Cambrian Khewra sandstone and the Jurassic Datta Formation are located in the Upper Indus Basin, while the Cretaceous Lower Goru Formation is from the Lower Indus Basin Pakistan (Fig. 1).

The Cambrian Khewra sandstone is an assemblage of thick clastic sediments well exposed in the Salt Range, Potwar area (sub-Basin in Upper Indus Basin). The Salt Range and its adjacent areas show the continental system tract and Baqri and Baloch (1991) has inferred deltaic environment of deposition for the Khewra sandstone. The Khewra Sandstone is proven reservoir in the Upper Indus Basin and has produced hydrocarbons at different fields as Rajian, Chak Naurang, and Adhi fields. The Khewra sandstone is also well developed in Punjab Platform (PPF) and encountered in different wells such as Bijnot-1 with average porosity 15%, Fort Abbas-1 (porosity about 14%), Suji-1 (porosity is about 10%), and with 6% porosity in Bahawalpur East 1 (Raza et al. 2008). However, no hydrocarbon discovery has been made in the southeastern part of PPF, and therefore, the reservoir characteristics have not been studied in detail.

The Lower Jurassic Datta Formation constitutes a significant reservoir horizon in the western Potwar and Kohat sub-Basin, where it is encountered in several oil–gas wells at the depth of more than 4 km (Kadri 1995; Shams et al. 2005). It shows a prograding deltaic facies sequence, and on the basis of proportion of sandstone detrital minerals, Datta Formation has been classified as quartzarenites. The

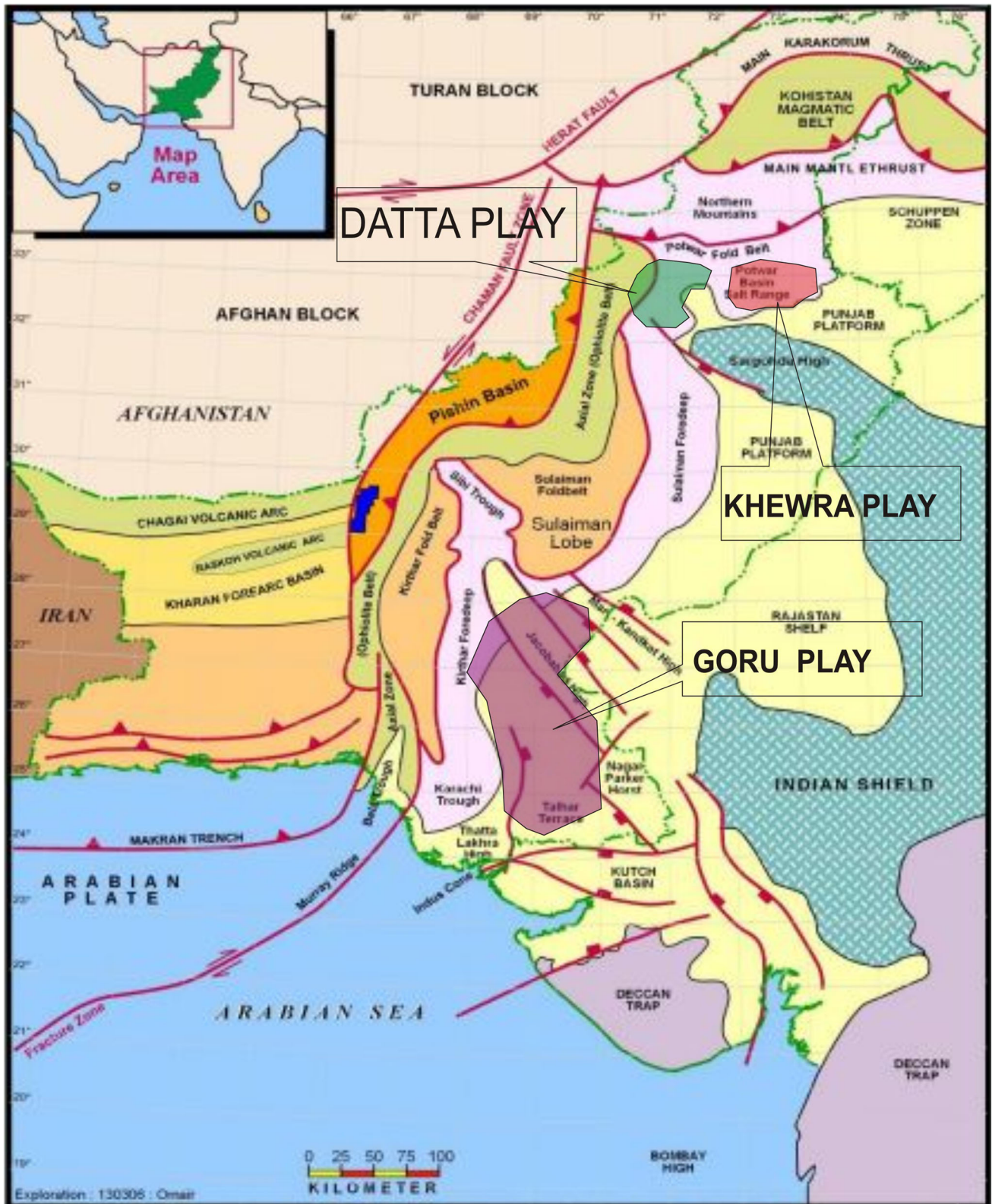


Fig. 1 Tectonic map of Pakistan. The distribution of reservoir rock in the Upper and Lower Indus Basin is also highlighted

Datta Formation is principally comprised of fine-to-coarse-grained sand particles interstratified with shales. Therefore, it has both source and reservoir rock potential. In Dhulian, the Meyal, and Toot fields located in the Potwar Plateau, Datta Formation has produced more than 15 hundred million barrels of oil, while the successful exploratory wells of Chanda and Mela fields in Datta sands in Kohat sub-Basin have made it more significant (Zaidi et al. 2013).

Clastic sediments of the Lower Goru Formation of Early Cretaceous are high-volume producers of oil, gas, and condensate in different parts of the Lower Indus Basin (Fig. 1). The Lower Goru Formation is a major plays that has contributed almost 14% of total oil and gas discoveries (Hussain et al. 2017). The Lower Indus Basin has a high success rates from a series of discoveries in comparatively small faulted blocks in the Lower Goru Formation. Recently, efforts are being made to target the stratigraphic traps in the Lower Goru Formation with some marginal success in the Lower Indus Basin. The sands of Lower Goru are primarily deposited in (lower shoreface to inner shelf settings) shallow marine environment and, therefore, have excellent reservoir characteristics (Baig et al. 2016).

Methods and theory

In this section, the mathematical theory of rock physics model and statistical algorithm to compute probability density function is described. The rock physics model permits us to calculate the elastic properties and seismic velocities from material properties such as mineralogical composition, porosity, fluid saturations and types, etc. derived from well logs by petrophysical evaluation. The effect of reservoir fluids on elastic parameters (elastic moduli) is determined by applying fluid substitution. Once we have calculated the elastic properties, seismic velocities, and density as a function of pore fluid types using fluid substitution modeling, the probability density function of the fluid indicators is estimated. The quantitative methodological framework consists of three parts: (1) petrophysical evaluation of reservoir zones; (2) fluid substitution workflow and numerical formulation of computed fluid indicators; and (3) probability density function (pdf) and calculation of fluid indicator coefficients.

Petrophysical characterization of reservoir rocks at Cambrian, Jurassic, and Cretaceous stages has been performed using available wireline log measurements of three different wells drilled in these three successions. The input wireline logs data used for present work consist of caliper, natural gamma ray (GR), density (RHOB), sonic transit

time (DT), latero log shallow (LLS) and deep (LLD), spontaneous potential (SP), neutron porosity (NPHI), etc. along with temperature data, geological formation tops, and mud filtrate resistivities. Using numerical formulas described below, the derived logs of shale volume (V_{sh}) P-wave velocity (V_p), S-wave velocity (V_s), porosity (ϕ), and water saturation (S_w) are computed. These input log measurements and derived logs are presented in results (Fig. 3).

Natural gamma ray measurements are used to identify and quantify shale volume. First, using GR measurements, linear gamma ray index (I_{GR}) is estimated, and then, substituting linear gamma ray index further into non-linear shale volume presented by Clavier et al. (1984), shale volume is estimated. These formulas are given below:

$$I_{GR} = \frac{GR_{log} - GR_{min}}{GR_{max} - GR_{min}} \quad (1)$$

$$V_{sh} = 1.7 - (3.38 - (I_{GR} + 0.7)^2)^{0.5}, \quad (2)$$

where GR_{log} , GR_{min} , and GR_{max} are gamma ray log, gamma ray minimum, and maximum values in the zone of interest, respectively.

P-wave velocity log (V_p) is derived using sonic transit time (Δt) into the relation specified below:

$$V_p \text{ (ft/s)} = \frac{1}{\Delta t \times 10^{-6}}. \quad (3)$$

The shear wave logs are not available for these wells, and therefore, various researchers (Krief et al. 1990; Gholami et al. 2014) defined algorithm to predict V_s . S-wave velocity is measured from P-wave velocity using Castagna's equation (Castagna et al. 1985):

$$V_p = 1.16V_s + 1.36. \quad (4)$$

Porosity (ϕ) log is computed by averaging density and neutron log derived porosities (Schlumberger 1997) and water saturation is estimated using the formulas given by Archie's approach (Archie 1942) and Indonesian equation (Poupon and Levieux 1971) used for clean (Eq. 5) and shaly sands (Eq. 6), respectively:

$$S_w = \sqrt{\frac{0.62}{\phi^{2.15}} \times \frac{R_w}{R_t}}, \quad (5)$$

and

$$\frac{1}{R_t} = \frac{S_w^2}{F \cdot R_w} + 2\sqrt{\frac{V_{sh}^2 - V_{sh}}{FR_w R_{sh}}} S_w^2 \frac{V_{sh}^{2-V_{cl}} S_w^2}{R_{sh}}, \quad (6)$$

where S_w , R_t , R_{sh} , and R_w are water saturation, observed total resistivity, shale resistivity, and formation water resistivity, respectively. Archie unites formation resistivity

factor (F) with the resistivity index ($R_i = R_w/R_t$). The formation resistivity factor given by Humble’s formula ($F = 0.62/\phi^{2.15}$) is the best average for sandstone reservoirs (Rider 2002).

Fluid substitution is an essential step in seismic attributes analysis and it allows us to understand how porous rock behaves seismically when its pore fluid changes. Gassmann’s equation (1951) gives a very simple relation to model pore fluid type and saturation effect on saturated bulk modulus (K_{sat}). Equations (7a) and (8) present the convenient form of Gassmann’s relations:

$$K_{sat} = K_d - \Delta K_d \tag{7a}$$

$$\Delta K_d = \frac{K_o \left(1 - \frac{K_d}{K_o}\right)^2}{1 - \phi - \frac{K_d}{K_o} + \phi \frac{K_o}{K_f}}, \tag{7b}$$

and

$$\mu_{sat} = \mu_d = \mu, \tag{8}$$

where K_d , K_o , and K_f are bulk moduli of dry rock, matrix, and fluids, respectively, and ϕ is the effective porosity of reservoir rock. μ_d and μ_{sat} are the dry and saturated rock shear moduli, respectively, and are not affected by pore fluid. ΔK_d represents the increment of bulk modulus due to fluid saturation. The bulk moduli of dry rock, matrix, and fluids are computed using the set of equations discussed by Batzle and Wang (1992) and Kumar (2006), while the effective porosity is estimated from well logs such as density and neutron. By performing the fluid substitution modeling at reservoir zones defined by well logs, two sets of saturated bulk modulus and effective density (ρ) at two different scenarios (when fully saturated either with water or gas) are calculated. This may further be used to calculate the seismic velocities of P (V_P)- and S (V_S)-wave velocities which are directly linked with bulk and shear modulus, respectively, and given by the following relations as

$$V_P = \left(\frac{K_{sat} + 4/3\mu}{\rho}\right)^{\frac{1}{2}} \tag{9}$$

and

$$V_S = \left(\frac{\mu}{\rho}\right)^{\frac{1}{2}}, \tag{10}$$

where the effective density (ρ) is the function of porosity (ϕ), matrix density (ρ_o), and fluid density (ρ_f) and is $\rho = \phi \rho_f + (1 - \phi) \rho_o$.

Using the seismic velocities and saturated bulk modulus, other rock physics properties such as acoustic impedance

($V_P \times \rho$), Poisson’s ratio ($(V_P^2 - 2V_S^2)/2(V_P^2 - V_S^2)$), and lambda ($K_{sat} - 2\mu/3$) are estimated.

Elastic impedance (EI), introduced by Connolly (1999), is the generalization of AI for non-zero incident angle and is given by the equation below:

$$EI = \left(V_P(V_P^{\tan^2 \theta} V_S^{-8K \sin^2 \theta}) \rho^{(1-4K \sin^2 \theta)}\right), \tag{11}$$

where K is a constant equal to the average value of V_S^2/V_P^2 . The original EI formula (Eq. 11) had dimensions, and hence average values, that changed with angle (theta). This problem was subsequently fixed by Whitcombe (2002) in his short note ‘Elastic Impedance Normalization’. He introduced normalisation constants, so average EI values remained the same as AI. The extended elastic impedance (EEI) equation published by Whitcombe et al. (2002) also includes normalisation constants and is given as

$$EEI(\chi) = V_{Po} \rho_o \times \left[\left(\frac{V_P}{V_{Po}}\right)^{(\cos \chi + \sin \chi)} \left(\frac{V_S}{V_{So}}\right)^{(-8K \sin \chi)} \left(\frac{\rho}{\rho_o}\right)^{(\cos \chi - 4K \sin \chi)} \right], \tag{12}$$

where V_{Po} , V_{So} , and ρ_o are the constants introduced to keep the dimensionality the same as AI and are set as the average values of P-wave velocity, S-wave velocity, and effective density of reservoir zone, respectively. We have calculated an average value of K from the normalisation constants and used single value instead of the variable K . The variable angle is now replaced with chi angle (χ) which varies between -90° and $+90^\circ$ and defined as the rotation angle in intercept–gradient space.

The normal distribution also called Gaussian distribution is an extremely important continuous probability distribution very frequently used in theory and practice. If x is the random variable, the equation of the probability density function (pdf) of Gaussian distribution is given as

$$f(x) = \frac{1}{s\sqrt{2\pi}} e^{-\frac{1}{2s^2}(x-a)^2}. \tag{13a}$$

Here, $f(x)$ is the probability density function, which gives the height of the curve at point ‘ x ’ (random variable) and a is the mean of distribution and both can take on any finite value such as $-\infty < x < \infty$. Whereas s and s^2 are the standard deviation and variance, respectively, and both must have some positive values.

To get the easier form of Gaussian distribution equation, it can be first rearranged as

$$f(x) = \frac{1}{\sqrt{2\pi}s^2} e^{-\frac{1}{2}\left(\frac{x-a}{s}\right)^2}. \tag{13b}$$

Table 1 Average of numerical values of several petrophysical properties at gross thickness levels for three sandstone reservoirs

	Khewra sandstone (Cambrian)	Datta formation (Jurassic)	Lower Goru formation (Cretaceous)
Depth (m)	2650	4735	2924.5
Reservoir thickness (m)	30	25	12
Effective porosity	0.16	0.12	0.10
Archie S_w (%)	25.09	34.73	58.09
Indonesian S_w (%)	22.09	19.99	45.89
Shale volume (%)	29	21	23

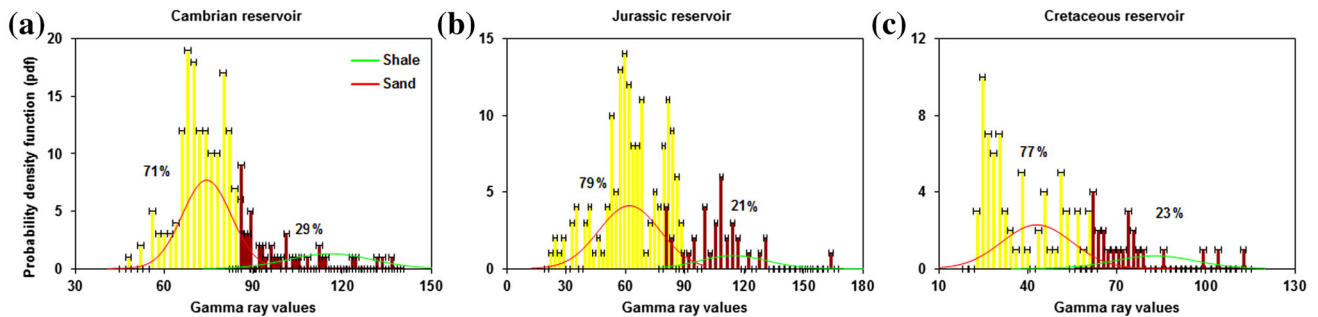


Fig. 2 Histograms with Gaussian distribution curves of gamma ray values overlaid for **a** Cambrian succession, **b** Jurassic sand, and **c** Cretaceous sandstone. The shale cut-off line for each reservoir is different and the value of shale volume varies from 21 to 29%. Shale

has higher values on gamma ray logs and lies within 70–170 API. Gaussian likelihoods functions for each facies (sand/shale) have been computed separately

This can be rearranged as

$$f(x) = \frac{1}{\sqrt{2\pi s^2}} \left(e^{\left(\frac{x-a}{s}\right)^2} \right)^{-\frac{1}{2}} \tag{13c}$$

If we consider z equal to how many standard deviations away from mean $(x - a)/s$, then the equation of the probability density function (pdf) of Gaussian distribution can be written in simplified form as

$$f(x) = \frac{1}{\sqrt{2\pi s^2 e^{-z^2}}} \tag{13d}$$

The variance (s^2) is the average of the squared deviation from mean and is calculated using following relation:

$$s^2 = \frac{\sum (x_i - a)^2}{n - 1} \tag{13e}$$

Here, x is random variable with subscript i (may be 1, 2, 3, and so on), a is the mean of all available data points (random variables), and $n - 1$ is sample size (n is total number random variables).

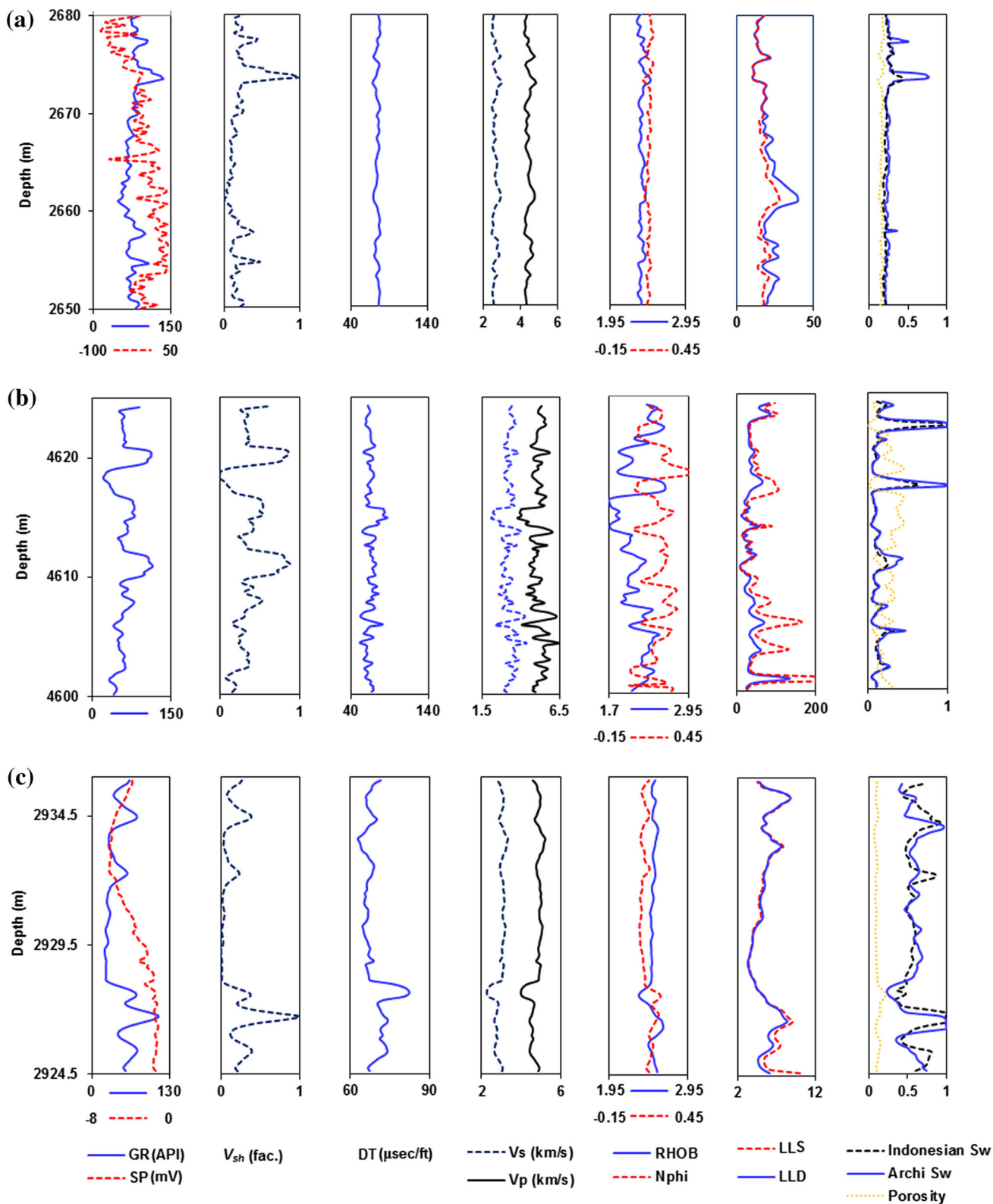
To quantify the sensitivity of each property to pore fluids, we have calculated fluid indicator coefficients (FICs). FIC is the difference between the average of the elastic property of the fully brine-saturated zone (M_{brine}) and of the fully gas-saturated zone (M_{gas}) divided by the

Fig. 3 Basic log measurements including gamma ray (GR), spontaneous potential (SP), sonic transit time (DT), density (RHOB), neutron (NPHI), latero log shallow (LLS), and petrophysically derived logs such as shale volume (V_{sh}), P- and S-wave velocities, effective porosity, and water saturation (S_w) curves are shown. These curves are computed in the reservoir zone of the entire three cases under study **a** Cambrian succession, **b** Jurassic sand, and **c** Cretaceous sandstone. All the three reservoirs mainly composed of sandstones (shale volume varies between 21 and 29%), reasonably good effective porosity (about 10–16%) and high hydrocarbon saturation (55–78%). The water saturation is computed by both Archie and Indonesian equations

standard deviation (s) of the gas-saturated zone (Dillon et al. 2003):

$$FIC = \frac{Mean_{brine} - Mean_{gas}}{s_{gas}} \tag{14}$$

The fluid indicator coefficient assumes that elastic properties for the two pore fluids are normally distributed. To test this assumption, we also measure the overlap coefficients (or Szymkiewicz–Simpson coefficient) which describes the overlap between two probability distributions without requirement of a normal distribution. Suppose X and Y are two data sets (brine sand facies and gas sand facies), then overlap coefficient is defined by dividing the



size of intersection to the smaller of the size of two data sets as

$$\text{Overlap } (X, Y) = \frac{|X \cap Y|}{\min(|X|, |Y|)}. \quad (15)$$

The intersection can be found by taking the minimum of the two sets for each histogram bin then summing that over all bins and then dividing that by the total number of samples for one of the sets (sets are both the same size in this case). The Szymkiewicz–Simpson coefficient will equal to one if X is a subset of Y .

Statistical classification of facies and reservoir fluids (gas/water)

The above-described methodology is applied to the input well log data and the results are discussed under different sections.

Facies classification and petrophysical evaluation

One of the essential steps in reservoir characterization is lithologically based facies classification to recognize the principal rock types at well locations. In the absence of depositional and sedimentological models, core analysis, and outcrop studies, the well log curves (gamma ray and spontaneous potential) are generally used to define lithologic facies (Grana et al. 2015). Rocks with clayey minerals have high values of gamma ray log as compared to clastic and carbonate rocks. The reservoir units comprise of shale and sandstone (intercalation), and therefore, gamma ray logs for each reservoir can be used to quantify the shale, as described in Table 1 and Fig. 2. All three reservoir rocks are mainly composed of sandstone with small amount of clays. Histograms and the overlying frequency (Gaussian) distribution curves for shale and sand (yellow) zones are plotted in Fig. 2.

Qualitative and quantitative evaluation of the well logs is performed and presented in Fig. 3 and Table 1. Figure 3a–c describes the input log measurements including gamma ray, sonic, density, spontaneous potential, laterolog shallow and deep, neutron porosity and derived curves of shale volume, effective porosity, and water/hydrocarbons saturation curves Cambrian, Jurassic, and Cretaceous reservoirs, respectively. The saturation of water in reservoir rock is an important parameter that is used for the evaluation of oil and gas reservoirs and many relations are available to compute it from well logs (Malureanu et al. 2016). Both the Archie (Archie 1942) and Indonesian

(Poupon and Levaux 1971) equations are used to estimate the water saturation for the Cambrian succession (Fig. 3a), Jurassic sandstone (Fig. 3b), and the Cretaceous reservoir (Fig. 3c). From Fig. 3 and Table 1, it is clear that the Archie equation overestimates the water saturation in shaley sandstones. The amount of water saturation (S_w) rises, where the shale proportion increases, because as shale volume increases, the true formation resistivity drops and S_w gets larger. Numerical values of petrophysical parameters such as effective porosity, permeability, shale volume, and water saturations for Cambrian-to-Cretaceous reservoir are given in Table 1.

Direct hydrocarbon indicators

In this section, the performance of various elastic properties that may be used as the basis for direct hydrocarbon indicators involved in exploration geophysics is examined. Using Gassmann's equation and fluid substitution algorithm described above, the behaviours log curves of different fluid indicators are calculated at two scenarios: 100% brine and 100% gas saturations are shown in Fig. 4a–c. We analyse the effectiveness of the following DHIs: EEI, AI, K_{sat} , $K_{sat}-\mu$, $\lambda\rho$, $\mu\rho$, V_p/V_s , and σ for Cambrian (Fig. 4a), Jurassic (Fig. 4b), and Cretaceous (Fig. 4c) reservoirs. Seismic AVO methods can be used to estimate relative attributes proportional to each of these with the exception of $K_{sat}-\mu$ which would require a full inversion method to estimate absolute values of K_{sat} and μ . Most of these elastic property curves show good separation for Cambrian and Cretaceous sandstones. The probability density functions derived from these are generated and discussed next.

Extended elastic and acoustic impedances

We first compare the effect of fluid substitution on acoustic and extended elastic impedances. When using EEI for fluid identification, it important to select the best chi angle. Earlier publications have used correlation coefficient to optimise chi angle (χ); however, in the current work, we have selected the best EEI angles using the fluid indicator coefficient and the overlap coefficient as described above. The results of this analysis, which are discussed in more detail below, show that a chi angle of 26° is optimal for the Cambrian reservoirs and 25° for the Jurassic and Cretaceous reservoirs. The histograms of data points overlying with Gaussian frequency curves for all three reservoir sands for gas- and brine-saturated facies are plotted in

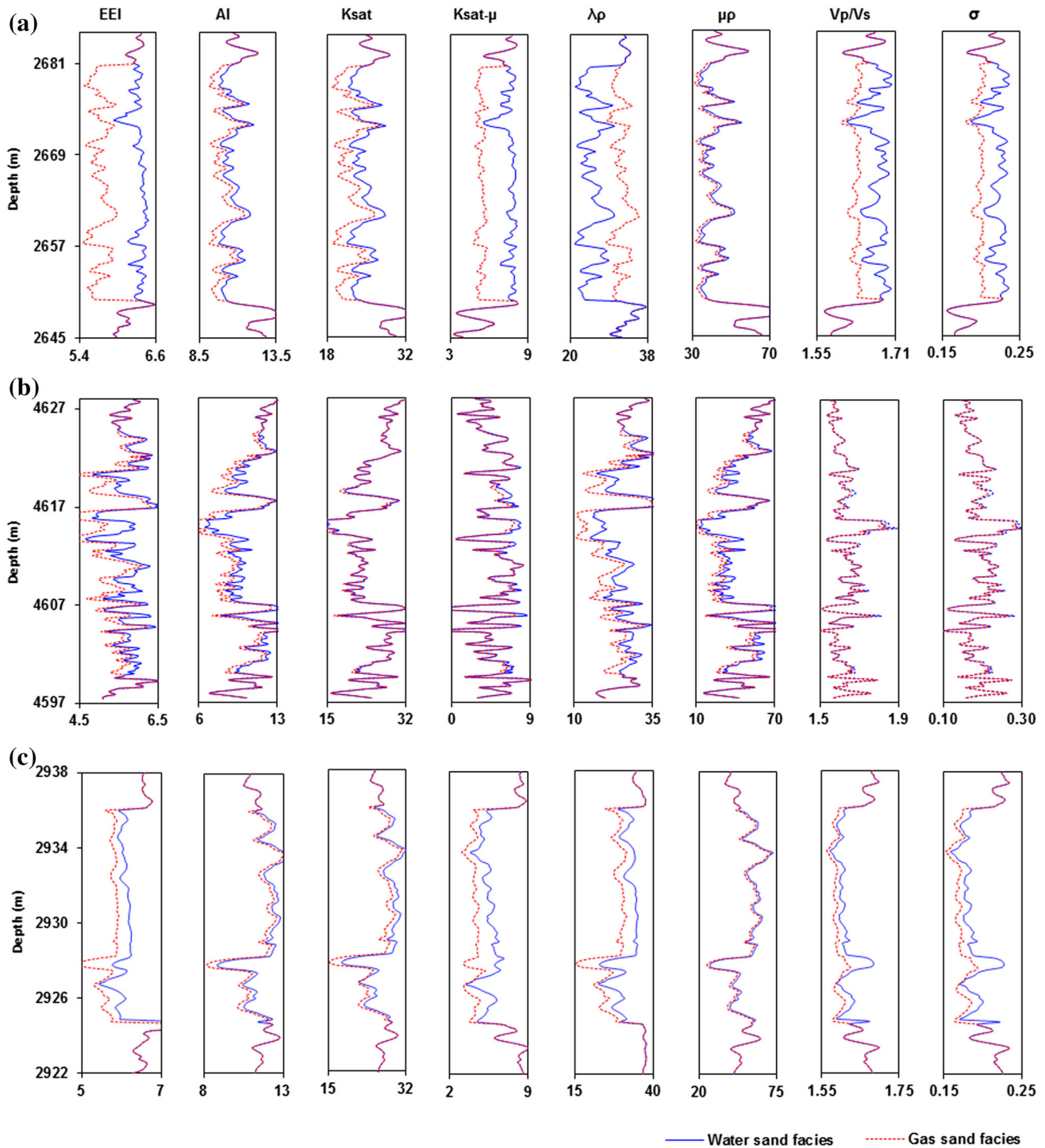


Fig. 4 Derived direct hydrocarbon indicator curves of extended elastic (EEI) and acoustic (AI) impedances, elastic moduli (K_{sat} , $K_{sat}-\mu$, $\lambda\rho$, and $\mu\rho$), and P-to-S-wave velocity ratio (V_P/V_S) and Poisson's ratio (σ) computed after performing fluid replacement modeling at

reservoir zone of Cambrian (a), Jurassic (b), and Cretaceous (c). These DHIs are computed at two different saturation levels of 100% gas and 100% brine

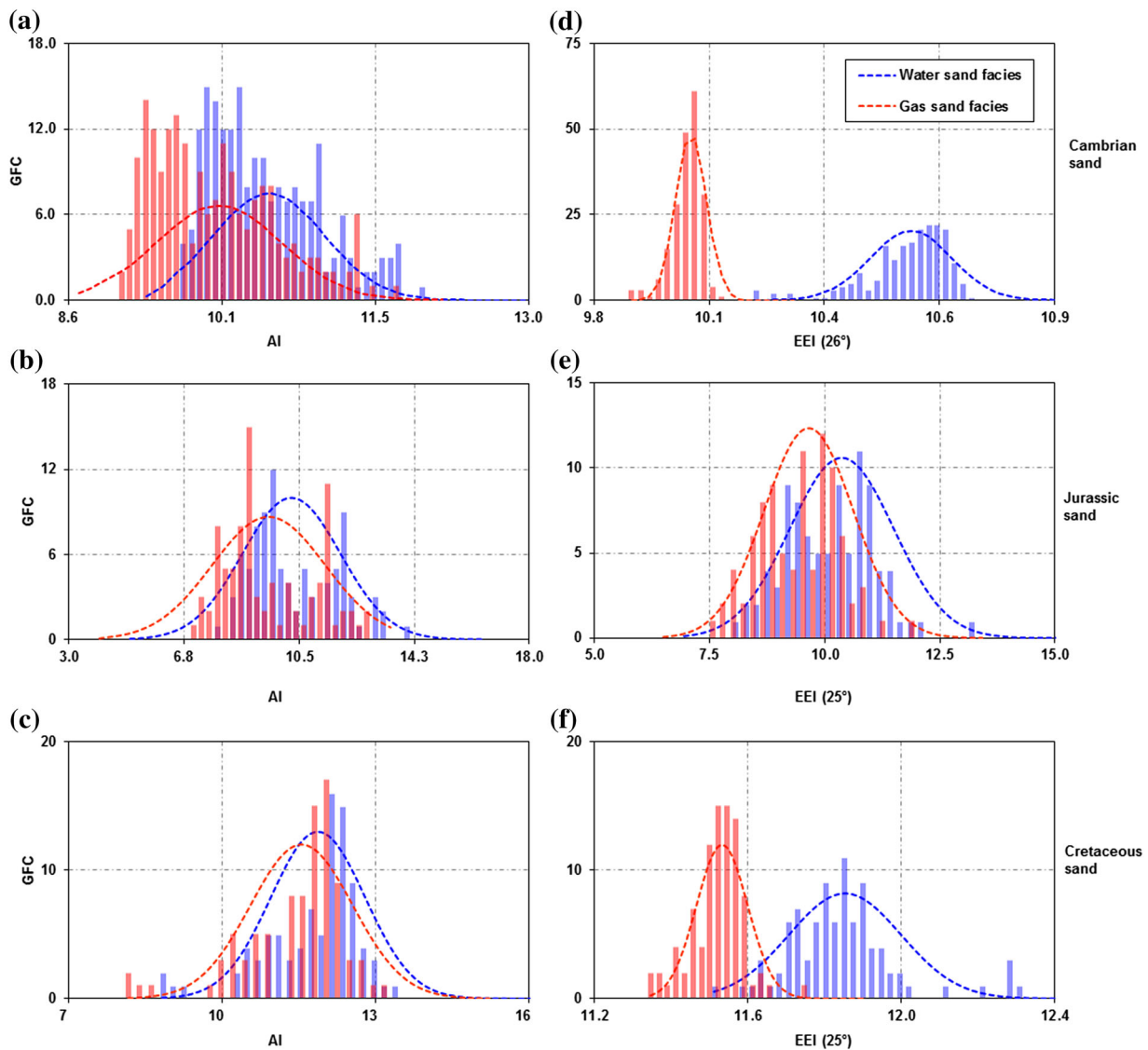


Fig. 5 Gaussian frequency curves (GFCs) and underlying histograms of acoustic (a–c) and extended elastic impedances (d–f) are plotted for Cambrian, Jurassic, and Cretaceous sands by assuming gas/water fluids. Strong overlapping of gas and brine sand GFCs (pdfs) indicates that is not a good discriminator. EEI provides maximum

differentiation between pore fluids as compared to acoustic impedance. Probability density functions and underlying data frequencies for EEIs are plotted at different chi angles for all cases. The best values of chi angles are selected after testing range of values

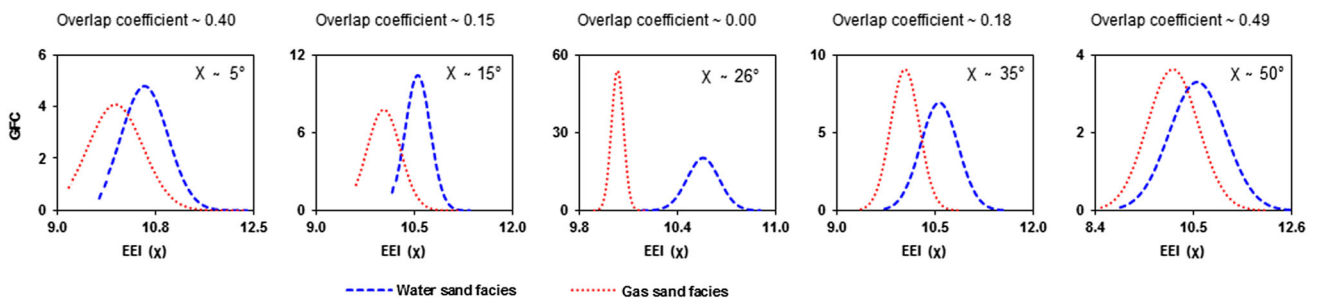


Fig. 6 Gaussian functions of extended elastic impedance for brine and gas populations at different chi angles (χ) are plotted. After testing range of values of chi angles, the best chi angle for Cambrian sand ($\chi \sim 26^\circ$) is defined, and at $\chi \sim 26^\circ$, extended elastic

impedance shows complete separation between brine and gas facies. The overlap coefficient for EEI at each chi angle is also given and has zero values at $\chi \sim 26^\circ$

Fig. 5. There is less area of overlap between gas- and water-saturated sand facies for EEI than AI. It clearly indicates that in all three cases, the extended elastic impedance is more sensitive to pore fluid types and changing saturations. However, the ability to separate the gas–water sand facies varies for each geological setting because of variations of reservoir porosity, mineralogical composition, compaction, etc. From Fig. 5a–f, it is clear that EEI is always better than AI in all three reservoirs Cambrian, Jurassic, and Cretaceous sands. The Gaussian

function and histograms for extended elastic impedance are computed and plotted at chi angle 26° (for Cambrian sand) and 25° (for Jurassic and Cretaceous sands), as shown in Fig. 5d–f.

An example of how chi angle works to describe the best option to separate fluids is shown in Fig. 6 for Cambrian case. At $\chi \sim 26^\circ$, Gaussian models have almost overlap coefficients equal to zero indicating the best option for Cambrian sand. The best options verified by plotting chi angles against fluid indicator coefficients and overlap

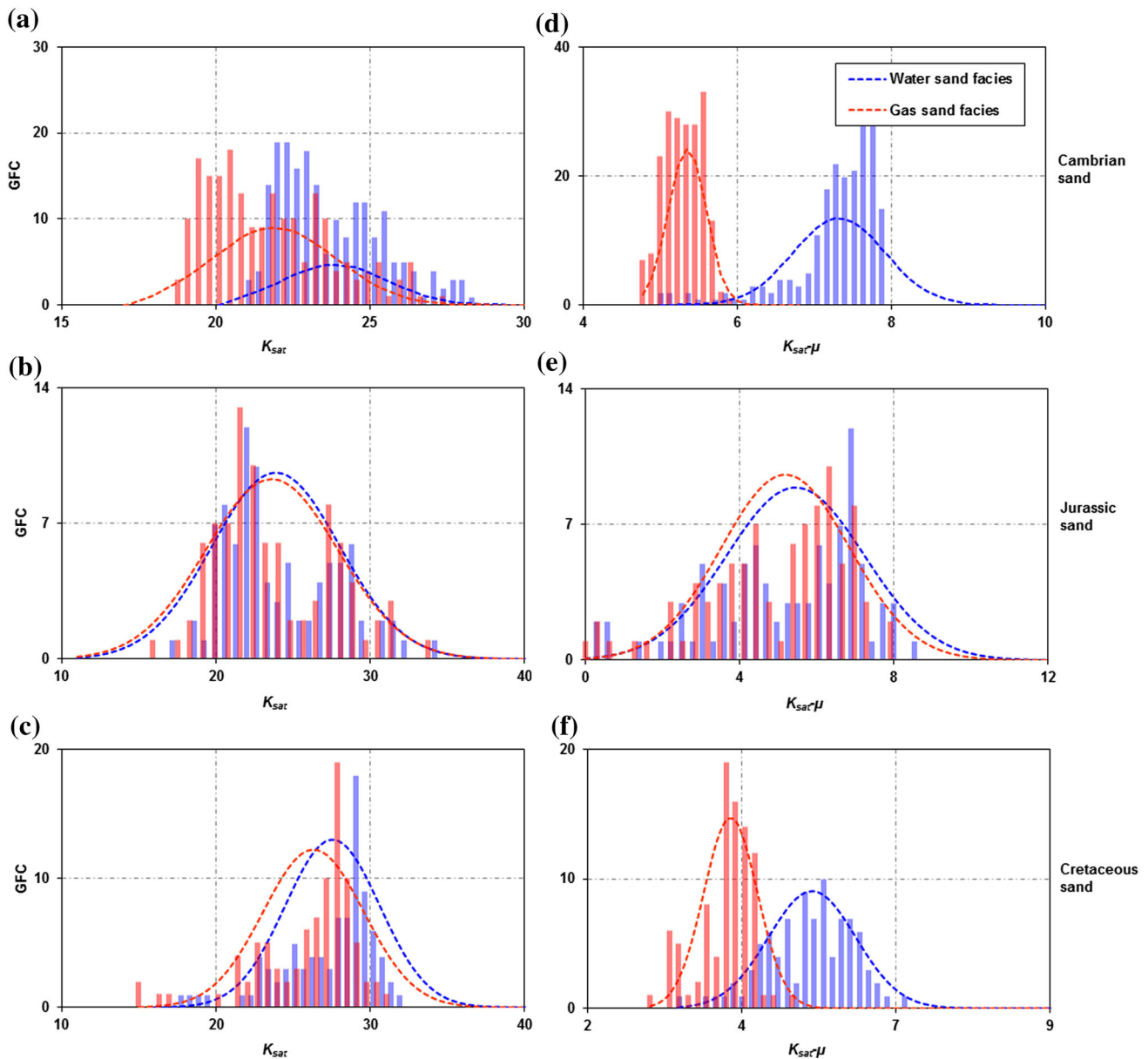


Fig. 7 1D state-conditional GFCs and underlying histograms of saturated bulk modulus (a–c) and difference in saturated bulk modulus and shear modulus (d–f) assuming that the three reservoirs are either saturated with gas (red) or water (blue). Both attributes do

not give good separation for Jurassic sandstone and show strong overlapping of GFCs. $K_{\text{sat}}-\mu$ gives very good results in case of Cambrian and Cretaceous sands

coefficients (a discussion has been made in the last section of paper).

Elastic moduli

Numerous combinations of rock properties such as elastic properties and their combinations with effective density and shear modulus subtracted from saturated bulk modulus are tested. The bulk volume deformation yielded by the passage of a compressional wave causes a change in

volume of pore that results in a pressure rise of reservoir fluids (gas/water). This may stiffen the reservoir rock and cause a variation in the saturated bulk modulus. In Fig. 7, Gaussian frequency curves and histograms of data sets of saturated bulk modulus (K_{sat}) and $K_{\text{sat}}-\mu$ (also called Batzle indicator, as given by Batzle et al. 2001) for the Cambrian, Jurassic, and Cretaceous reservoirs are plotted. Sensitivity of K_{sat} to pore fluids (Fig. 7a–c) is moderate for the Cambrian sands and weak in the other two cases. Differing pore fluids has no effect on shear deformation; however,

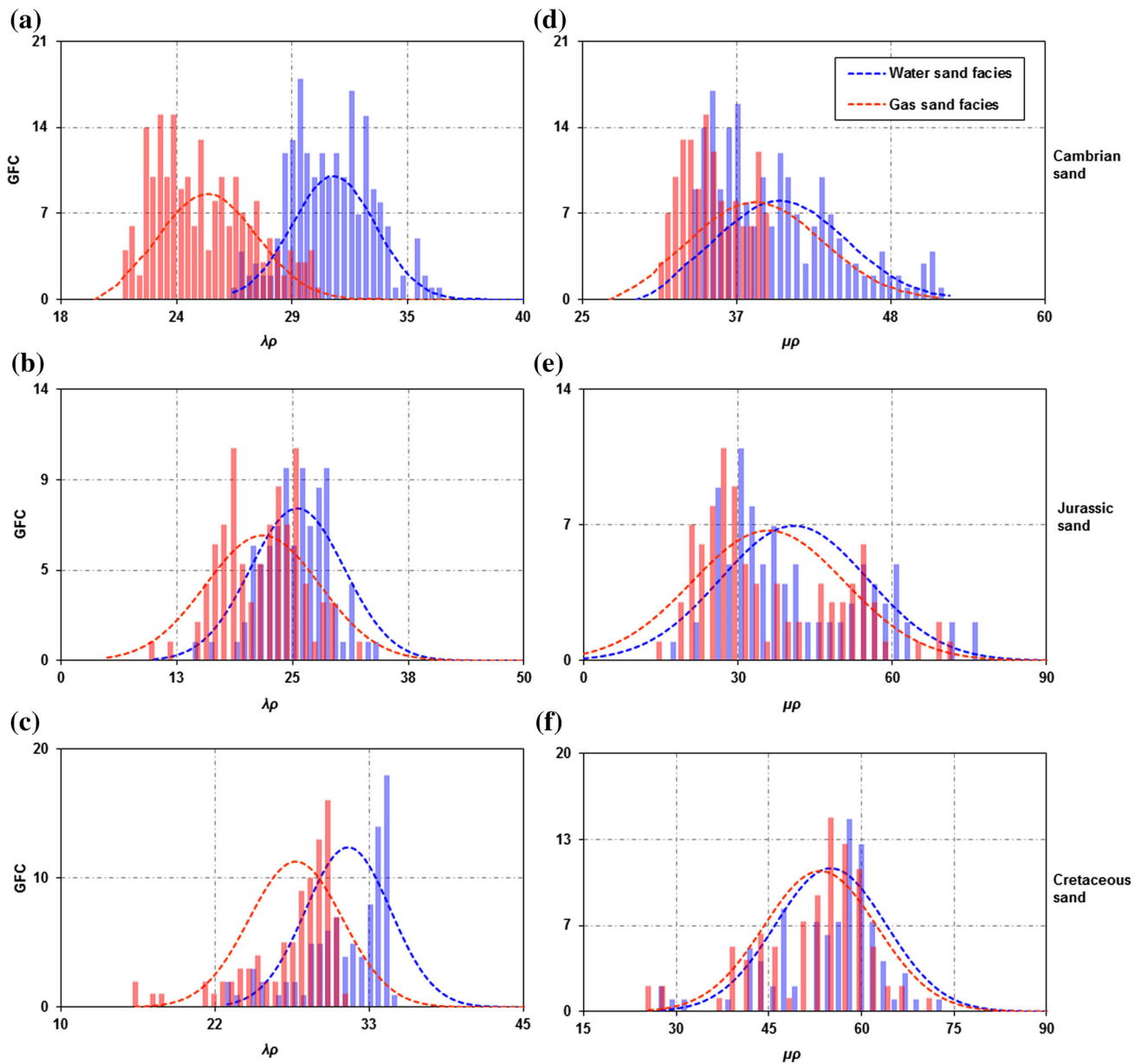


Fig. 8 Probability distribution curves and histograms of data points of $\lambda\rho$ (a–c) and $\mu\rho$ (d–f) values for wet (blue) and gas (red) sands for three different reservoirs which have geological ages from Cambrian

to Cretaceous are shown. Gaussian curves show strong overlapping for $\mu\rho$ data points, while $\lambda\rho$ is a good gas indicator which specially shows excellent discrimination in Cambrian reservoirs

when shear modulus is subtracted from saturated bulk modulus ($K_{\text{sat}}-\mu$), its pore fluid discrimination strength is increased (Fig. 7d–f). $K_{\text{sat}}-\mu$ is an excellent fluid discrimination indicator for the Cambrian sand and also works well for Cretaceous reservoirs. GFCs and histograms of both elastic properties (K_{sat} and $K_{\text{sat}}-\mu$) strongly overlap in case of Jurassic sandstone (Fig. 7b, e) and, therefore, do not work as fluid indicators. From Fig. 7, it is clearly visualized that there are some cases, where the data are a bit skewed and the Gaussian model may not be the best, but

overall data fit Gaussian model and it is a reasonable approach.

The so-called lambda–mu–rho method (Goodway et al. 1997) has been used extensively for fluid and lithology discrimination. Figure 8 shows the Gaussian frequency curves for the product of density with lambda ($\lambda\rho$) and with shear modulus ($\mu\rho$). From Fig. 8a–c, it can be inferred that $\lambda\rho$ is an excellent gas indicator for Cambrian succession and works to some extent for the Jurassic and Cretaceous sands, although there is strong overlapping of Gaussian

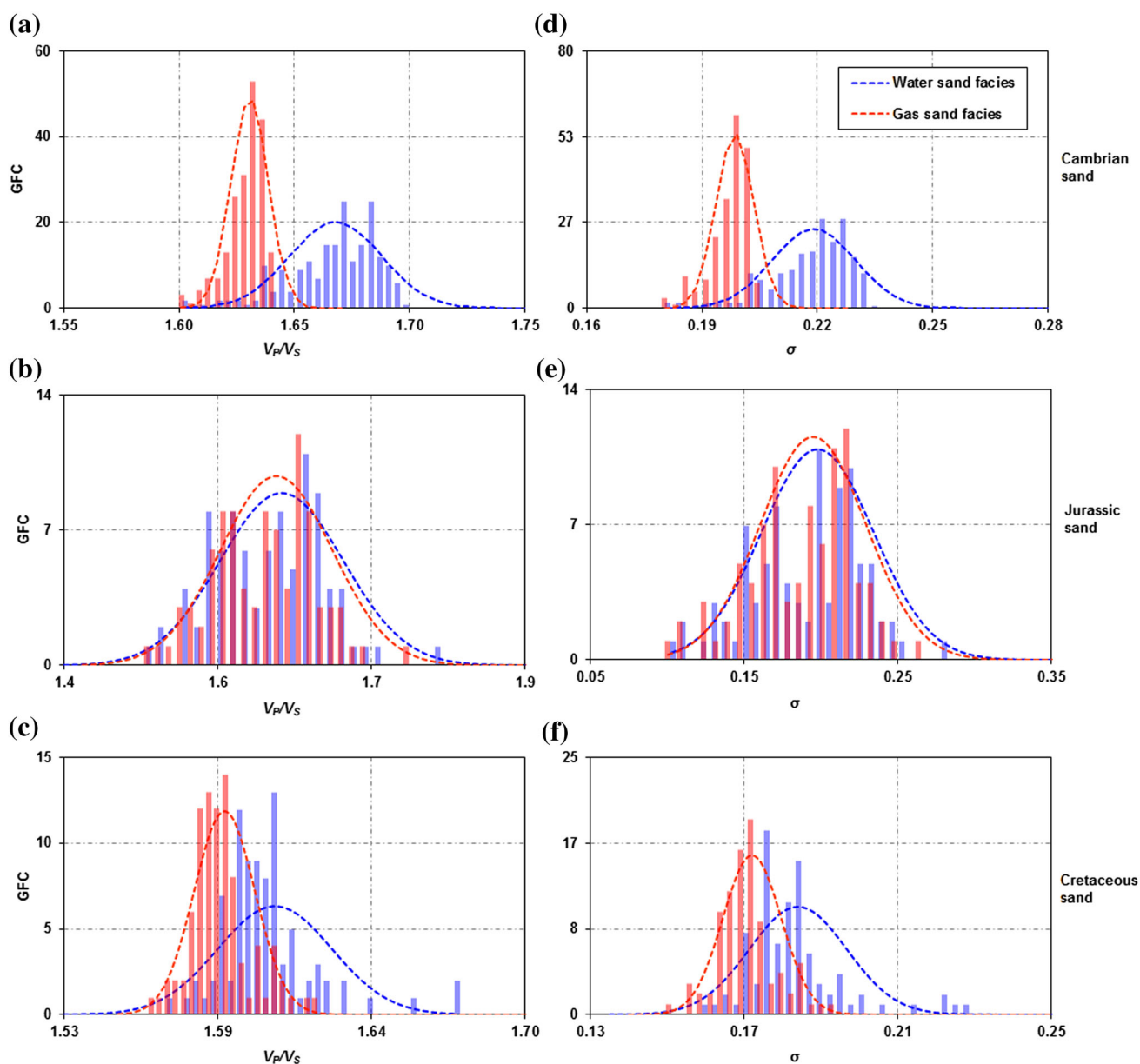


Fig. 9 Gaussian likelihoods of P-to-S-wave velocities (V_p/V_s) and Poisson's ratio (σ) for brine (blue) and gas (red) saturated and underlying histograms of data sets of Cambrian, Jurassic, and

Cretaceous sand plays are plotted. Strong overlapping clouds of 1D marginal distribution (b, e) show poor separation of gas anomalies

distributions and histograms of data points for the wet and gas sands (Fig. 8d–f). Shear modulus within the product of $\mu\rho$ does not change with fluid saturation and the GFCs only change due to the change in density.

P-to-S-wave velocities and Poisson's ratio

P-to-S-wave velocities ratio (V_P/V_S) and Poisson's ratio (σ) are often considered as helpful tools to distinguish gas-related anomalies. For an isotropic medium, σ is directly related to V_P/V_S and shows very similar trends. In Fig. 9, Gaussian frequency curves for both velocity ratio and Poisson's ratio of gas and wet zones are plotted and show very similar trend in all three reservoir plays. Both indicators also have very similar sensitivity to fluid discrimination as diagnosed graphically (Fig. 9) and numerically (Table 2). The small overlapping of Gaussian distribution curves for V_P/V_S and σ shows that they have a good chance of distinguishing wet sandstones and gas sandstones in Cambrian (Fig. 9a, d) and Cretaceous sand plays (Fig. 9c, f). However, in case of Jurassic reservoir (Fig. 9b, e), both these seismic parameters have poor chance to separate the gas sand zones as probability distribution curves strongly overlapped. However, V_P/V_S is more sensitive to fluid content than σ for all three reservoirs modeled in this study.

Fluid indicator coefficients and overlap coefficients

Fluid indicator coefficients help to analyse the sensitivity for each fluid term to discriminate reservoir fluids (gas/brine) quantitatively. These fluid indicator coefficients for Cambrian-to-Cretaceous sandstones are plotted in Fig. 10a–c and their numerical values for each property are summarized in Table 2. It can be observed that FIC values of each fluid strongly depend on local geological settings and, therefore, vary in all three reservoirs. In the case of the Cambrian sand (Fig. 10a; Table 2), $K_{\text{sat}}-\mu$, V_P/V_S , σ , and EEI (χ) have much higher FICs than all other fluid indicators which imply that these ones can easily be utilized to distinguish gas zones. Among the four seismic and elastic properties, EEI (χ) is most sensitive to pore fluid types. For Jurassic sand, except EEI (χ), all other rock physics indicators have very poor sensitivity to pore fluid content and have lower FICs values, as described in Fig. 10b and Table 2. The reason behind lower FICs may be that the Jurassic reservoir lies at the depth of 4735 m and formation pressure is 56.20 MPa. At lower pressure (higher porosity), we can have a good chance to identify and differentiate the gas-saturated sandstones. The values of FICs for Jurassic sand vary between 0.06 and 1.49 and EEI (χ) and $\lambda\rho$ have relatively higher values, as shown in Table 2. The performance of DHIs in Cretaceous sand is demonstrated in Fig. 10c and Table 2. Note that acoustic and elastic

Table 2 Numerical values of means, standard deviations, and fluid indicator coefficients (FICs) for each hydrocarbon indicator calculated at in-situ conditions are given. The fluid indicators are evaluated for three different reservoirs of Cambrian, Jurassic, and Cretaceous sandstones. Higher the values of fluid coefficients indicate better discrimination

	V_P/V_S	K_{sat}	σ	$\mu\rho$	$\lambda\rho$	$K_{\text{sat}}-\mu$	AI	EEI (χ)
Khewra sandstone (Cambrian)								
Mean water	1.66	23.86	0.21	39.93	30.96	7.32	10.51	10.55
Standard deviation water	0.02	1.70	0.01	4.96	1.98	0.59	0.53	0.098
Mean gas	1.63	21.88	0.19	38.07	24.98	5.35	10.04	10.03
Standard deviation gas	0.01	1.99	0.005	5.02	2.31	0.25	0.60	0.036
FICs	4.58	0.99	4.18	0.37	2.59	8.01	0.79	14.21
Datta sandstone (Jurassic)								
Mean water	1.63	23.87	0.19	41.13	25.37	5.34	10.25	10.27
Standard deviation water	0.07	4.13	0.04	14.83	5.03	2.02	1.59	0.45
Mean gas	1.63	23.60	0.19	36.10	21.64	5.08	9.51	9.53
Standard deviation gas	0.06	4.28	0.03	15.26	6.11	1.91	1.84	0.48
FICs	0.09	0.06	0.08	0.32	0.61	0.13	0.40	1.49
Lower Goru (Cretaceous)								
Mean water	1.60	27.53	0.18	54.94	31.68	5.39	11.86	11.55
Standard deviation water	0.02	3.06	0.01	8.96	3.20	0.66	0.92	0.146
Mean gas	1.59	26.30	0.17	53.32	27.76	4.16	11.55	11.53
Standard deviation gas	0.01	3.25	0.01	9.16	3.53	0.41	1.00	0.066
FICs	1.66	0.37	1.58	0.18	1.11	3.03	0.32	4.80

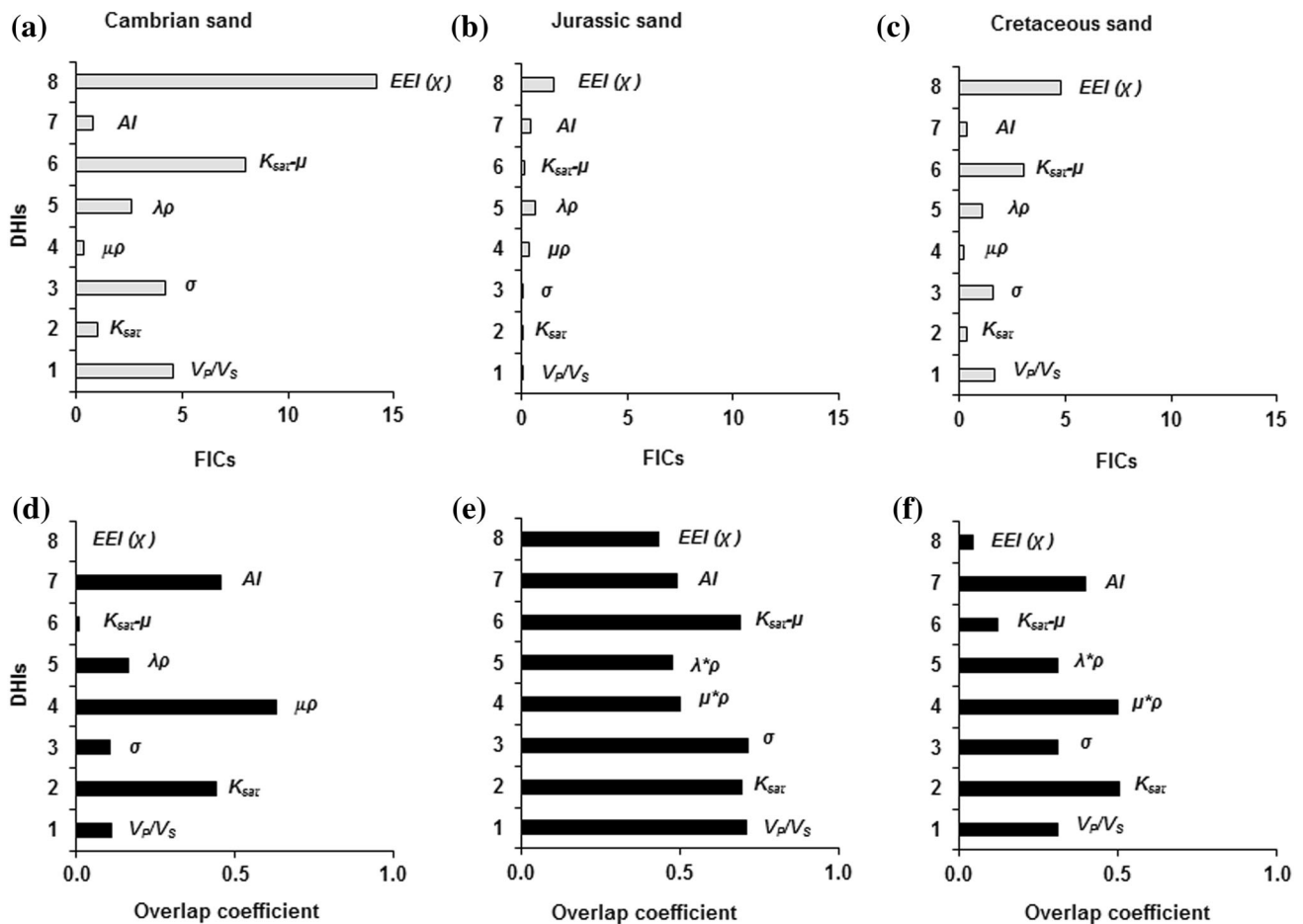


Fig. 10 FIC values of different attributes (a–c) for three reservoirs at the same scale are plotted. Most of the fluid indicators have very low values of fluid coefficients for Jurassic sands indicating that are less sensitive to pore fluids (b). Higher the values of fluid coefficients

mean excellent distinguisher of hydrocarbons facies. The overlap coefficients of brine and gas-saturated data sets for each attribute of three reservoirs are computed (d–f). The fluid indicators having higher FICs values show lower overlap coefficients

Table 3 Overlap coefficients (Szymkiewicz–Simpson coefficient) are given for each attribute of three reservoirs. Higher overlap coefficient values of fluid indicators indicate that both water and gas facies have less chance to distinguish

Overlap coefficients	V_p/V_s	K_{sat}	σ	$\mu\rho$	$\lambda\rho$	$K_{sat}-\mu$	AI	EEI (χ)
Cambrian sand	0.11	0.44	0.10	0.63	0.16	0.02	0.45	0.00
Jurassic sand	0.70	0.69	0.71	0.50	0.47	0.69	0.48	0.45
Cretaceous sand	0.31	0.51	0.31	0.50	0.31	0.12	0.40	0.05

properties EEI (χ) and $K_{sat}-\mu$ yielded excellent results to discriminate the gas sand zone from water-saturated zone. Some other properties such as V_p/V_s and σ are obviously more diagnostic than remaining.

As the name suggests, the overlap coefficients measure the degree of overlap between two populations or probability distributions. A smaller overlap coefficient for the two populations (wet sand and gas sand) indicates good separation and vice versa. The overlap coefficients for each property computed at two saturation limits for all the three clastic reservoirs are plotted in Fig. 10d (Cambrian sand),

Fig. 10e (Jurassic sand), and Fig. 10f (Cretaceous sand) and their numerical values are given in Table 3. The overlap coefficient analysis and the FIC analysis are in good agreement.

Chi angle (χ) versus fluid indicator coefficients and overlap coefficients

Extended elastic impedance is a function of chi, the rotation angle in intercept–gradient space. The value of chi must be optimised for whatever purpose EEI is being used

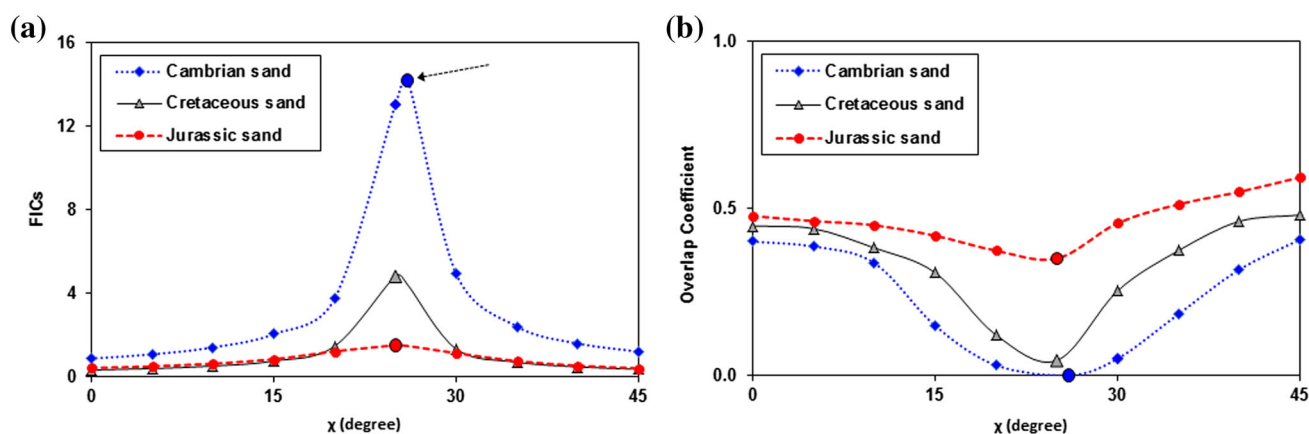


Fig. 11 **a** FICs are computed against a range of chi angles for three cases and plotted to select the best option. For Cambrian, Jurassic, and Cretaceous sands, the higher FICs are against 26°, 25°, and 25° chi

angles, respectively. **b** Best chi angle option does not change when it is plotted against overlap coefficients. At 26°, 25°, and 25° chi angles, the overlap coefficients have lower values

in the case of fluid discrimination. In this study, we optimised chi by measuring the FICs and the overlap coefficients for a range of chi values. FIC values and overlap coefficients for chi angles from 0°–45° are shown in Fig. 11a, b, respectively. The optimum angles exhibit a high FIC and a low overlap coefficient and both are in good agreement.

Conclusions

Quantitative analysis of three siliciclastic reservoirs has demonstrated that acoustic and elastic property reservoir rocks are strongly affected by pore fluid types. However, the sensitivity of the properties varies with the nature of the reservoir depending on various reservoir properties. Fluid indicator coefficients (FICs) and overlap coefficients provide an effective way of determining the degree of sensitivity for a range of elastic properties. Relative changes in elastic properties can be estimated using AVO techniques, and hence, an analysis of FICs and overlap coefficients will show which of these will be most useful as DHIs and will indicate the potential quality of the DHIs for different reservoirs. We have also demonstrated that fluid indicator and overlap coefficients can be used to optimise the extended elastic impedance chi angle for fluid discrimination.

In all cases, the optimised EEI proved to be most sensitive to changes in pore fluid, but the sensitivity varied considerably between the three reservoirs. The high porosity, shallow Khewra sandstone of Cambrian age, was most sensitive and the deeper, lower porosity Jurassic Datta sand the least sensitive. This study can suggest optimal ways to identify gas sand zones when exploration is carried in the future for the Cambrian, Jurassic, and Cretaceous reservoirs.

Acknowledgements The authors would like to acknowledge to Directorate General Petroleum Concessions (DGPC) for providing data to complete the present work. The Institute of Geology, University of the Punjab is also acknowledged for facilitating me in the compilation of this work. This research paper is from the Ph.D. work of Mr. Nisar Ahmed, Lecturer, Institute of Geology, University of the Punjab.

References

- Ahmed N, Khalid P, Ghazi S, Anwar AW (2015) AVO forward modeling and attributes analysis for fluid's identification: a case study. *Acta Geod Geophys* 50(4):377–390. doi:[10.1007/s40328-014-0097-x](https://doi.org/10.1007/s40328-014-0097-x)
- Ahmed N, Khalid P, Ali T, Ahmad SR, Akhtar S (2016) Differentiation of pore fluids using amplitude versus offset attributes in clastic reservoirs, Middle Indus Basin, Pakistan. *Arab J Sci Eng* 41(6):2315–2323. doi:[10.1007/s13369-015-1992-3](https://doi.org/10.1007/s13369-015-1992-3)
- Aki K, Richards PG (1980) *Quantitative seismology: theory and methods*. W. H. Freeman, San Francisco
- Archie GE (1942) The electrical resistivity log as an aid in determining some reservoir characteristics. *Trans Am Inst Mech Eng* 146(1):54–62
- Avseth P, Mukerji T, Mavko G (2005) *Quantitative seismic interpretation*. Cambridge University Press, Cambridge
- Baddari K, Bellalem F, Baddari I, Makdeche S (2016) Some probabilistic and statistical properties of the seismic regime of Zemmouri (Algeria) seismoactive zone. *Acta Geophys* 64(5):1275–1310. doi:[10.1515/acgeo-2016-0049](https://doi.org/10.1515/acgeo-2016-0049)
- Baig MO, Harris NB, Ahmed H, Baig MOA (2016) Controls on reservoir diagenesis in the Lower Goru Sandstone Formation, Lower Indus Basin, Pakistan. *J Petrol Geol* 39(1):29–48. doi:[10.1111/jpg.12626](https://doi.org/10.1111/jpg.12626)
- Baqri SRH, Baloch MQ (1991) Sedimentological studies and palaeo environments of Khewra Sandstone with reference to its hydrocarbon potential. *Pak J Pet Technol Altern Fuels* 1:23–38
- Batzle ML, Wang Z (1992) Seismic properties of pore fluids. *Geophysics* 57(11):1396–1408. doi:[10.1190/1.1443207](https://doi.org/10.1190/1.1443207)
- Batzle ML, Han DH, Hofmann R (2001) Optimal hydrocarbon indicators. In: 71th SEG international exposition and annual meeting 2001, September 9–14, 2001, San Antonio. doi:[10.1190/1.1816446](https://doi.org/10.1190/1.1816446)

- Castagna JP, Batzle ML, Eastwood RL (1985) Relationships between compressional and shear-wave velocities in clastic silicate rocks. *Geophysics* 50(4):551–570. doi:[10.1190/1.1441933](https://doi.org/10.1190/1.1441933)
- Castagna JP, Smith SW (1994) Comparison of AVO indicators: a modeling study. *Geophysics* 59(12):1849–1855. doi:[10.1190/1.1443572](https://doi.org/10.1190/1.1443572)
- Clavier C, Coates G, Dumanoir J (1984) The theoretical and experimental basis for the ‘dual water’ model for the interpretation of shaly sands. *Soc Pet Eng J* 24(2):153–168. doi:[10.2118/6859-PA](https://doi.org/10.2118/6859-PA)
- Connolly P (1999) Elastic impedance. *Lead Edge* 18(4):438–452. doi:[10.1190/1.1438307](https://doi.org/10.1190/1.1438307)
- Connolly P, Hughes M (2014) The application of very large numbers of pseudo-wells for reservoir characterization. Society of Petroleum Engineers 2014, SPE-171879-MS, November 10–13, 2014, Abu Dhabi. doi:[10.2118/171879-MS](https://doi.org/10.2118/171879-MS)
- Dillon L, Schwedersky G, Vasquez G, Velloso R, Nunes C (2003) A multiscale DHI elastic attributes evaluation. *Lead Edge* 22(10):1024–1029. doi:[10.1190/1.1623644](https://doi.org/10.1190/1.1623644)
- Doyen P (2007) Seismic reservoir characterization. EAGE, Netherlands
- Gassmann F (1951) Über die elastizität poröser medien. *Verteljahrsschrift der Naturforschenden Gesellschaft in Zurich* 96:1–23
- Gholami R, Moradzadeh A, Rasouli V, Hanachi J (2014) Shear wave velocity prediction using seismic attributes and well log data. *Acta Geophys* 62(4):818–848. doi:[10.2478/s11600-013-0200-7](https://doi.org/10.2478/s11600-013-0200-7)
- Goodway W, Chen T, Downton J (1997) Improved AVO fluid detection and lithology discrimination using Lamé petrophysical Parameters; “Lambda-Rho”, “Mu-Rho”, and “Lambda/Mu fluid stack”, from P and S inversions. In: 67th SEG annual international meeting 1997, November 2–7, 1997, Dallas. doi:[10.1190/1.1885795](https://doi.org/10.1190/1.1885795)
- Grana D (2014) Probabilistic approach to rock physics modeling. *Geophysics* 79(2):D123–D143. doi:[10.1190/GEO2013-0333.1](https://doi.org/10.1190/GEO2013-0333.1)
- Grana D, Rossa ED (2010) Probabilistic petrophysical-properties estimation integrating statistical rock physics with seismic inversion. *Geophysics* 75(3):O21–O37. doi:[10.1190/1.3386676](https://doi.org/10.1190/1.3386676)
- Grana D, Schlanser K, Campbell-Stone E (2015) Petroelastic and geomechanical classification of lithologic facies in the Marcellus Shale. *Interpretation* 3(1):SA51–SA63. doi:[10.1190/INT-2014-0047.1](https://doi.org/10.1190/INT-2014-0047.1)
- Hedlin K (2000) Pore space modulus and extraction using AVO. In: 70th SEG annual international meeting 2000, August 6–1, 2000, Calgary. doi:[10.1190/1.1815749](https://doi.org/10.1190/1.1815749)
- Hussain M, Ahmed N, Chun WY, Khalid P, Mahmood A, Ahmad SR, Rasool U (2017) Reservoir characterization of basal sand zone of lower Goru formation by petrophysical studies of geophysical logs. *J Geol Soc India* 89(3):331–338. doi:[10.1007/s12594-017-0614-y](https://doi.org/10.1007/s12594-017-0614-y)
- Hydrocarbon Development Institute of Pakistan (2008) Energy Year Book, 2008. Ministry of Petroleum and Natural Resources, Pakistan
- Jamil A, Waheed A, Sheikh RA (2012) Pakistan’s major petroleum plays: an overview of dwindling reserves. Search and Discovery article #10399 (2012), PAPG/SPE Annual Technical Conference 2009, December 03–05, 2012, Islamabad
- Kadri IB (1995) Petroleum geology of Pakistan. Pakistan Petroleum Ltd, Karachi
- Khalid P, Ahmed N (2016) Modulus defect, velocity dispersion and attenuation in partially-saturated reservoirs of Jurassic sandstone, Indus Basin, Pakistan. *Stud Geophys Geod* 60(1):112–129. doi:[10.1007/s11200-015-0804-2](https://doi.org/10.1007/s11200-015-0804-2)
- Krief M, Garat J, Stellingwerff J, Ventre J (1990) A petrophysical interpretation using the velocities of P and S waves (full-waveform sonic). *Log Analyst* 31(8):355–369
- Kumar D (2006) A Tutorial on Gassmann fluid substitution: formulation, algorithm and matlab code. *Geohorizons* 11(1):4–12
- Malureanu I, Boaca T, Daniela-Doina N (2016) New relations of water saturation’s Calculus from well logs. *Acta Geophys* 64(5):1542–1562. doi:[10.1515/acgeo-2016-0063](https://doi.org/10.1515/acgeo-2016-0063)
- Pakistan Petroleum Information Service (2009) Upstream Petroleum activities. Ministry of Petroleum and Natural Resources
- Poupon A, Levieux J (1971) Evaluation of water saturation in shaly formations. Society of Professional Well Log Analysts 12th annual logging symposium transactions, Paper O
- Quakenbush M, Shang B, Tuttle C (2006) Poisson impedance. *Lead Edge* 25(2):128–138. doi:[10.1190/1.2172301](https://doi.org/10.1190/1.2172301)
- Raza HA, Ahmad W, Ali SM, Mujtaba M, Alam S, Shafeeq M, Iqbal M, Noor I, Riaz N (2008) Hydrocarbon prospects of Punjab Platform Pakistan, with special reference to Bikaner-Nagaur Basin of India, Pakistan. *J Hydrocarbon Res* 18(6):1–33
- Rider MH (2002) The geological interpretation of well logs. Rider French Consulting Ltd, Sutherland
- Russell B, Hedlin K, Hilterman F, Lines L (2003) Fluid-property discrimination with AVO: a Biot–Gassmann perspective. *Geophysics* 68(1):29–39. doi:[10.1190/1.1543192](https://doi.org/10.1190/1.1543192)
- Schlumberger (1997) Log interpretation charts. Schlumberger well services, Houston
- Shams O, Qureshi AW, Abbasi IA (2005) Lithofacies, sand-bodies geometry and depositional setting of the Datta Formation in Surghar Range, North Pakistan. In: Annual technical conference 2005, November 21–23, 2005, Islamabad
- Tarantola A (2005) Inverse problem theory. SIAM, Paris, France
- Whitcombe DN (2002) Elastic impedance normalization. *Geophysics* 67(1):60–62. doi:[10.1190/1.1451331](https://doi.org/10.1190/1.1451331)
- Whitcombe DN, Connolly PA, Reagan RL, Redshaw TC (2002) Extended elastic impedance for fluid and lithology prediction. *Geophysics* 67(1):63–67. doi:[10.1190/1.1451337](https://doi.org/10.1190/1.1451337)
- Zaidi SNA, Brohi IA, Ramzan K, Ahmed N, Mehmood F, Brohi AU (2013) Distribution and hydrocarbon potential of Datta Sands in Upper Indus Basin, Pakistan. *Sindh Univ Res J* 45(2):325–332

A method of directly extracting multiwave angle-domain common-image gathers

Jianguang Han¹ · Yun Wang²

Received: 6 August 2017 / Accepted: 18 August 2017 / Published online: 28 August 2017
© Institute of Geophysics, Polish Academy of Sciences & Polish Academy of Sciences 2017

Abstract Angle-domain common-image gathers (ADCIGs) can provide an effective way for migration velocity analysis and amplitude versus angle analysis in oil–gas seismic exploration. On the basis of multi-component Gaussian beam prestack depth migration (GB-PSDM), an alternative method of directly extracting multiwave ADCIGs is presented in this paper. We first introduce multi-component GB-PSDM, where a wavefield separation is proceeded to obtain the separated PP- and PS-wave seismic records before migration imaging for multiwave seismic data. Then, the principle of extracting PP- and PS-ADCIGs using GB-PSDM is presented. The propagation angle can be obtained using the real-value travel time of Gaussian beam in the course of GB-PSDM, which can be used to calculate the incidence and reflection angles. Two kinds of ADCIGs can be extracted for the PS-wave, one of which is P-wave incidence ADCIGs and the other one is S-wave reflection ADCIGs. In this paper, we use the incident angle to plot the ADCIGs for both PP- and PS-waves. Finally, tests of synthetic examples show that the method introduced here is accurate and effective.

Keywords Angle-domain common-image gathers · Multiwave · Gaussian beam · Incidence angle

Introduction

Common-image gathers (CIGs) are usually used in migration velocity analysis (MVA) of seismic exploration as connection between migration and velocity updates (Zhang and McMechan 2011). Traditionally, MVA studies employ offset-domain common-image gathers (ODCIG). However, the artifacts existing in ODCIGs caused by multipathing will affect the accuracy of the MVA (Nolan and Symes 1996), which can be solved effectively in angle-domain common-image gathers (ADCIGs). Comparing with conventional ODCIGs, the ADCIGs are less affected from multiple paths, because the subsurface angle is used as index rather than the offset.

The ADCIGs are an effective MVA tool (Sava and Biondi 2004). The traveltimes errors caused by velocity model can be clearly reflected in the moveout of ADCIGs (Yan and Xie 2012). The ADCIGs are flat and positioned at the right depth with correct velocity model. In contrast, the ADCIGs display residual curvature and inconsistent angle-domain reflectivity with an incorrect migration velocity model. The correct migration velocity model can be estimated from curvature information on the ADCIGs. In addition, we can extract amplitude versus angle (AVA) information from the angle-domain imaging, which can provide an effective way for reservoir interpretation.

ADCIGs have been extracted using Kirchhoff methods and wave-equation methods. Kirchhoff-based ADCIGs methods are widely studied and implemented with good results (Audebert et al. 2002, 2003; Baina et al. 2002; Brandsberg-Dahl et al. 2003; Koren et al. 2008; Rousseau et al. 2000, 2001; Sollid and Ursin 2003; Xu et al. 2001). Meanwhile, many wave-equation techniques either for shot-geophone migration or for shot-profile migration have been used to extract the ADCIGs (Biondi and Symes 2004;

✉ Jianguang Han
hanjianguang613@163.com

¹ Institute of Geology, Chinese Academy of Geological Sciences, Beijing 100037, China

² School of Geophysics and Information Technology, China University of Geosciences, Beijing 100083, China

de Bruin et al. 1990; Jin et al. 2002; Mosher and Foster 2000; Prucha et al. 1999; Rickett and Sava 2002; Sava and Fomel 2003; Sava and Vlad 2011; Xu et al. 2011; Zhang et al. 2010; Zhang and McMechan 2011). With the development of the multi-component seismic technology, some studies about the extraction method of ADCIGs for converted wave are presented. Sava and Fomel (2005, 2006) proposed an extraction method of pseudo ADCIGs for converted wave, which is not real incident angle. Rosales et al. (2008) presented an extraction method of PS-ADCIGs through transforming ODCIGs into ADCIGs using wavefield downward-continuation migration. Du et al. (2010) obtained the time-shift PP- and PS-ADCIGs and analyzed the advantage of the ADCIGs using elastic wave Kirchhoff migration method.

However, for research methods of extracting ADCIGs mentioned above, artifact problem exists in Kirchhoff-based ADCIGs due to asymptotic assumptions of Kirchhoff migration method, and wave-equation based ADCIGs methods are very time consuming. Gaussian beam migration (Gray 2005; Hale 1992a, b; Han et al. 2013, 2014; Hill 1990, 2001; Nowack et al. 2010; Popov et al. 2010), as an effective depth migration imaging technique, has an imaging accuracy comparable to wave-equation migration. Meanwhile, it continues to have the flexibility and high calculation efficiency of Kirchhoff migration, and can effectively solve for multi-valued traveltimes problem.

Based on the study of multi-component Gaussian beam prestack depth migration (GB-PSDM), a method of directly extracting multiwave ADCIGs is presented in this paper. The purpose of this study is to provide an effective alternative method for extracting PP- and PS-ADCIGs. We first introduce the multi-component GB-PSDM method. Then, the principle of extracting PP- and PS-ADCIGs using GB-PSDM is presented. Finally, synthetic examples are tested to verify that our multiwave ADCIGs method is accurate and effective.

Multi-component Gaussian beam migration

We first make a wavefield separation to obtain the separated PP- and PS-wave seismograms from multi-component seismic data, and then common shot gathers GB-PSDM imaging for PP- and PS-waves are performed using cross-correlation imaging condition. The image is formed by cross-correlating the downward-continued wavefields in terms of Gaussian beams from source and beam center points, as shown in Fig. 1.

In 2D isotropic medium, the PP- and PS-wave GB-PSDM formulas can be written as (Han et al. 2013):

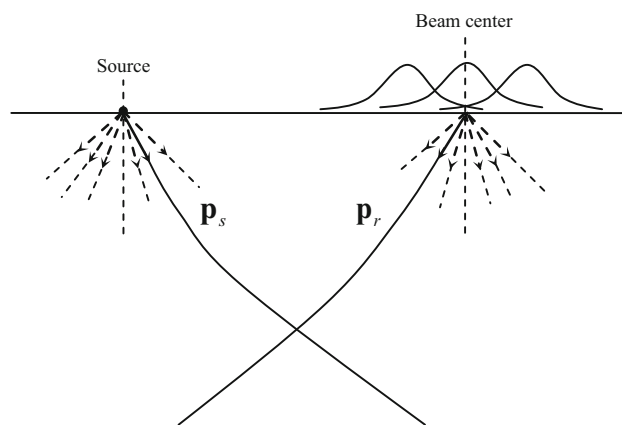


Fig. 1 Schematic diagram of GB-PSDM

$$I^{PP}(\mathbf{x}) = C^{PP} \int dx_s \sum_{L_r} \int d\omega D^{PP}(\mathbf{L}_r, \mathbf{p}_r^P, \omega) \int dp_{sx}^P \int dp_{rx}^P A_{x_s}^P(\mathbf{x}, \mathbf{p}_s^P) A_{L_r}^P(\mathbf{x}, \mathbf{p}_r^P) \times \exp\left\{-i\omega \left[T_{x_s}^P(\mathbf{x}, \mathbf{p}_s^P) + T_{L_r}^P(\mathbf{x}, \mathbf{p}_r^P)\right]\right\}, \quad (1)$$

$$I^{PS}(\mathbf{x}) = C^{PS} \int dx_s \sum_{L_r} \int d\omega D^{PS}(\mathbf{L}_r, \mathbf{p}_r^S, \omega) \int dp_{sx}^P \int dp_{rx}^S A_{x_s}^P(\mathbf{x}, \mathbf{p}_s^P) A_{L_r}^S(\mathbf{x}, \mathbf{p}_r^S) \times \exp\left\{-i\omega \left[T_{x_s}^P(\mathbf{x}, \mathbf{p}_s^P) + T_{L_r}^S(\mathbf{x}, \mathbf{p}_r^S)\right]\right\}, \quad (2)$$

where $\mathbf{x}_s = (x_s, 0)$ is the source location, and $\mathbf{L}_r = (L_r, 0)$ denotes the beam center location. $I^{PP}(\mathbf{x})$ and $I^{PS}(\mathbf{x})$ are migration imaging values of PP- and PS-wave. C^{PP} and C^{PS} are corresponding constants. $\mathbf{p}_s = (p_{sx}, p_{sz})$ and $\mathbf{p}_r = (p_{rx}, p_{rz})$ are the source and receiver ray parameter vectors, respectively. For the PP-wave image, the Gaussian beams employ the P-wave velocity to calculate the complex amplitude $A_{x_s}^P(\mathbf{x}, \mathbf{p}_s^P)$ and $A_{L_r}^P(\mathbf{x}, \mathbf{p}_r^P)$ and the complex traveltimes $T_{x_s}^P(\mathbf{x}, \mathbf{p}_s^P)$ and $T_{L_r}^P(\mathbf{x}, \mathbf{p}_r^P)$. For the PS-wave image, the complex amplitude $A_{x_s}^P(\mathbf{x}, \mathbf{p}_s^P)$ and the complex traveltimes $T_{x_s}^P(\mathbf{x}, \mathbf{p}_s^P)$ of Gaussian beams come from the source are

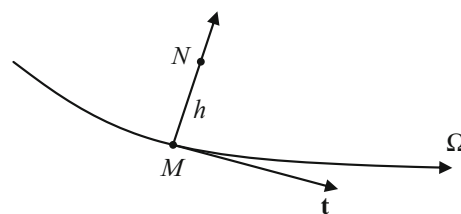


Fig. 2 Ray-centered coordinates

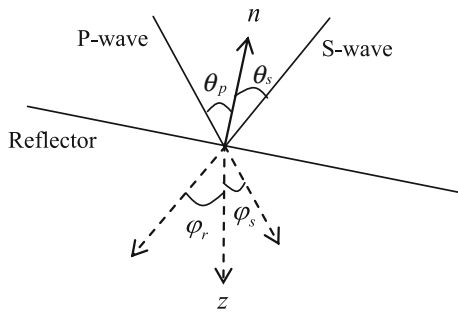


Fig. 3 Schematic of converted PS-wave reflection

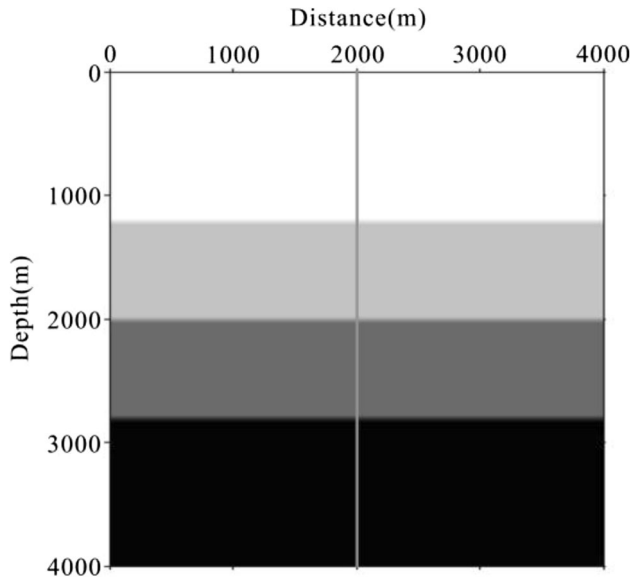


Fig. 4 Horizontal layer model

calculated with P-wave, while S-wave is employed to calculate the complex amplitude $A_{L_r}^S(\mathbf{x}, \mathbf{p}_r^S)$ and the complex traveltimes $T_{L_r}^S(\mathbf{x}, \mathbf{p}_r^S)$ from the beam center points. $D^{PP}(\mathbf{L}_r, \mathbf{p}_r^P, \omega)$ and $D^{PS}(\mathbf{L}_r, \mathbf{p}_r^S, \omega)$ are the local plane wave

components of PP- and PS-waves, respectively. In addition, the PS-wave has polarity reversal problem, which has been corrected in the process of GB-PSDM according to polarity characteristics of PS-wave (Rosales and Rickett 2001).

The principle of extracting PP- and PS-ADCIGs

The subsurface angle information can be obtained in the process of GB-PSDM, which can be used to extract ADCIGs directly. Because the traveltime and amplitude of Gaussian beam slow change in a wavelength range, the real-value travel time of Gaussian beams can be directly used to calculate the propagation angle.

In 2D ray-centered coordinates (Fig. 2), the real-value travel time $T(N)$ of Gaussian beam can be expressed as:

$$T(N) = T(M) + \frac{1}{2} \text{Re} \left[\frac{\mathbf{p}(M)}{\mathbf{q}(M)} \right] h^2, \tag{3}$$

where $T(M)$ denotes the travel time at the point M . $\mathbf{p}(M)$ and $\mathbf{q}(M)$ are obtained by solving dynamic ray tracing equation (Červeny 2007). h is the perpendicular distance from point N to the central ray Ω .

Converting the expression (3) to Cartesian coordinate system and taking the derivative with respect to x , we can get the following expression as:

$$\frac{\partial T(N)}{\partial x} = \frac{\partial T(M)}{\partial x} + \text{Re} \left[\frac{\mathbf{p}(M)}{\mathbf{q}(M)} \right] (x - x_M). \tag{4}$$

Because $p_x(N) = \frac{\partial T(N)}{\partial x}$, $p_x(M) = \frac{\partial T(M)}{\partial x}$, Eq. (4) can be rewritten as:

$$p_x(N) = p_x(M) + (x - x_M) \text{Re} \left[\frac{\mathbf{p}(M)}{\mathbf{q}(M)} \right], \tag{5}$$

where p_x is the horizontal component of slowness vector. Similarly, taking the derivative with respect to z , the corresponding vertical component p_z can be written as:

Fig. 5 The separated a PP-wave and b PS-wave single shot seismic records

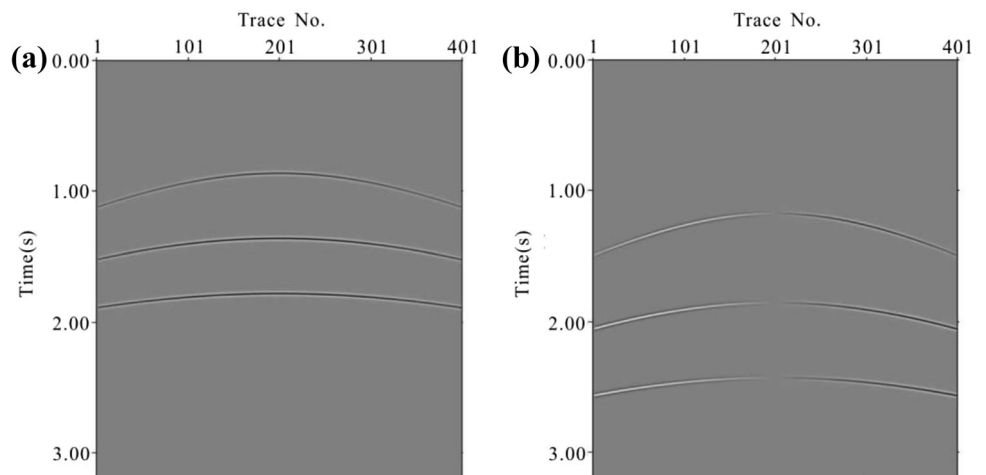


Fig. 6 **a** PP-ADCIGs and **b** PS-ADCIGs with correct migration velocities; **c** PP-ADCIGs and **d** PS-ADCIGs with 10% higher velocities; **e** PP-ADCIGs and **f** PS-ADCIGs with 10% lower velocities. The angle range is -50° to 50°

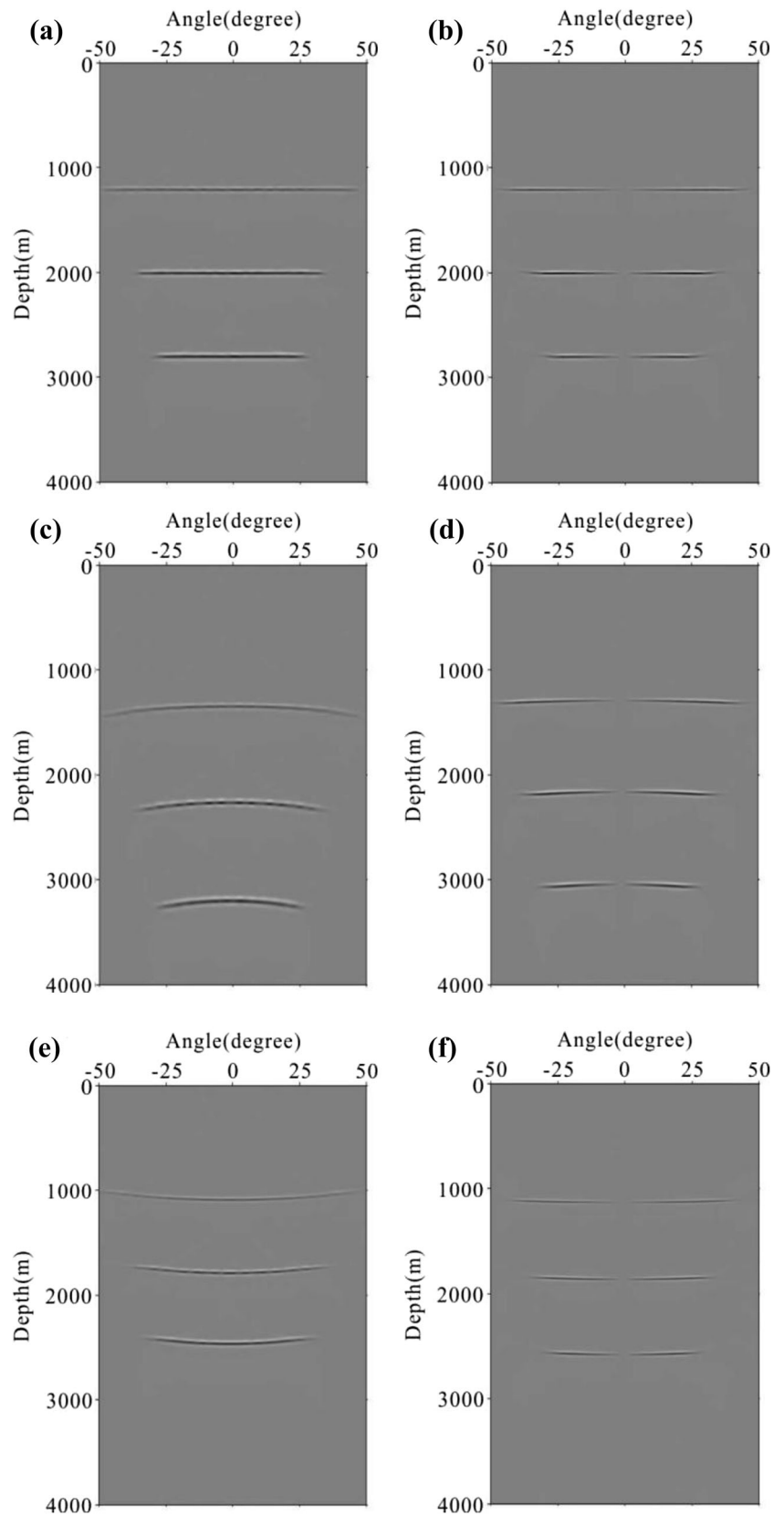
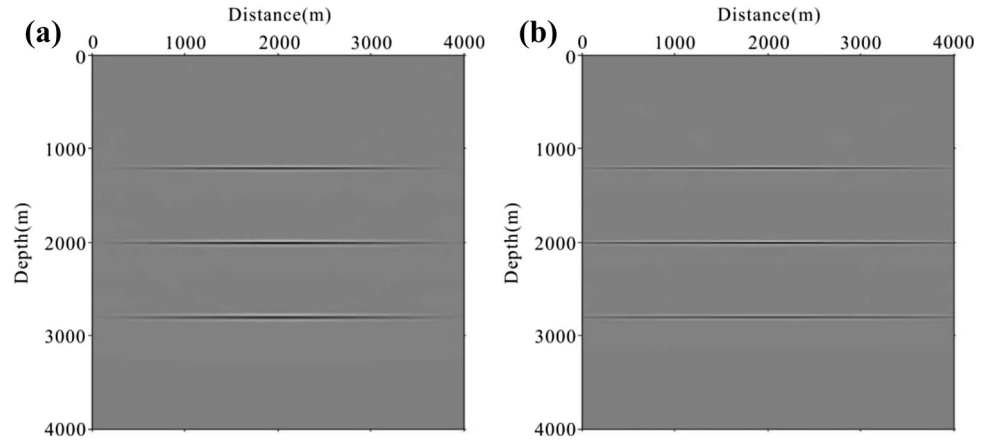


Fig. 7 The final **a** PP- and **b** PS-wave GB-PSDM imaging results with stacking in the angle domain



$$p_z(N) = p_z(M) + (z - z_M) \text{Re} \left[\frac{\mathbf{p}(M)}{\mathbf{q}(M)} \right]. \tag{6}$$

According to Eqs. (5) and (6), the propagation angle at the point N can be calculated as follows:

$$\text{Angle} = \begin{cases} -\pi + \arctan \left[\frac{p_x(N)}{p_z(N)} \right] & p_x(N) < 0, p_z(N) < 0 \\ \pi + \arctan \left[\frac{p_x(N)}{p_z(N)} \right] & p_x(N) > 0, p_z(N) < 0 \\ \arctan \left[\frac{p_x(N)}{p_z(N)} \right] & p_z(N) > 0 \end{cases} \tag{7}$$

The incidence and reflection angles are equal for the PP-wave. After we calculate the source and receiver wavefield propagation angles φ_s and φ_r , respectively, the incidence angle γ can be expressed as:

$$\gamma = \frac{\varphi_s - \varphi_r}{2}. \tag{8}$$

Now we can extract the PP-wave ADCIGs with the incidence angle calculated from GB-PSDM.

For the PS-wave, we can obtain two kinds of ADCIGs, one of which is P-wave incidence ADCIGs and the other one is S-wave reflection ADCIGs.

As shown in Fig. 3, the angles φ_s and φ_r denote the source and receiver wavefield propagation angles obtained by Gaussian beam migration method, where the former is computed from P-wave, and the latter is computed from S-wave. n denotes the direction normal to the geological interface. θ_p and θ_s are P-wave incidence and S-wave reflection angles, which are not equal for the PS-wave. Assume that angle is positive in a counterclockwise direction, we can describe the relational expression as follows:

$$\theta_p - \theta_s = \varphi_s - \varphi_r. \tag{9}$$

We define φ denotes the aperture angle, therefore

$$\varphi = \varphi_s - \varphi_r. \tag{10}$$

Snell's law in the imaging point can be expressed as:

$$\frac{\sin \theta_p}{V_p} = \frac{-\sin \theta_s}{V_s}. \tag{11}$$

Inserting Eqs. (9) and (10) into Eq. (11), after simple trigonometric manipulations, we can obtain the final two expressions for the incidence and reflection angles as follows:

$$\tan \theta_p = \frac{\sin \varphi}{\frac{V_s}{V_p} + \cos \varphi}, \tag{12}$$

and

$$\tan \theta_s = \frac{-\sin \varphi}{\frac{V_s}{V_p} + \cos \varphi}. \tag{13}$$

Expressions (12) and (13) clearly show that the incidence and reflection angles are nonlinear with the aperture angle, and then the PS-ADCIGs corresponding to the incidence and reflection angles can be extracted. In this

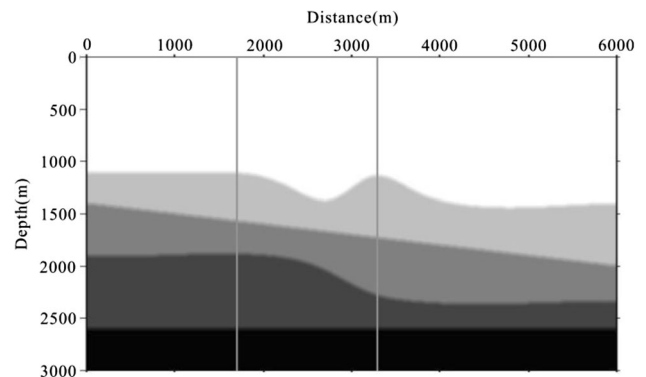


Fig. 8 Curved interface model. The P-wave velocities are $\alpha_1 = 2500$ m/s, $\alpha_2 = 3000$ m/s, $\alpha_3 = 3500$ m/s, $\alpha_4 = 4000$ m/s, $\alpha_5 = 4500$ m/s, and S-wave velocities are $\beta_1 = 1440$ m/s, $\beta_2 = 1700$ m/s, $\beta_3 = 2000$ m/s, $\beta_4 = 2300$ m/s, $\beta_5 = 2600$ m/s from top to bottom of the model, respectively

paper, we use the incident angle to plot the ADCIGs for both PP- and PS-waves.

Synthetic examples

Horizontal layer model

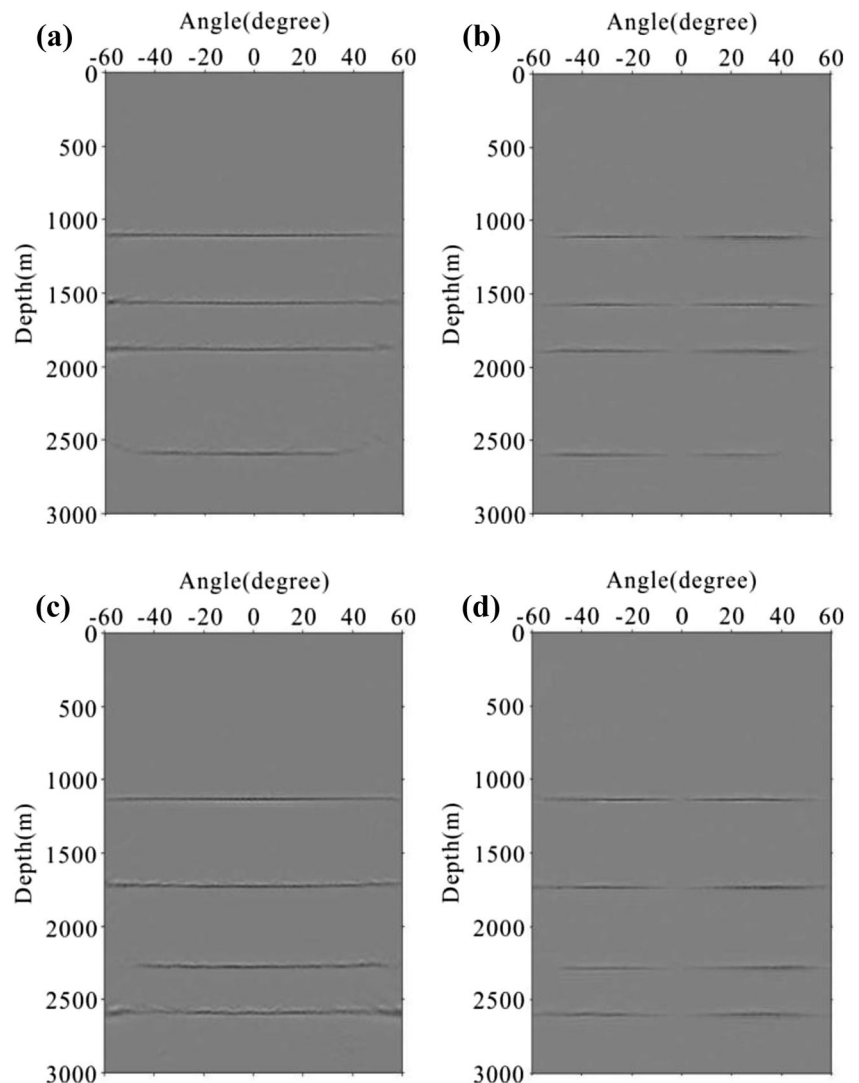
First of all, we build a horizontal layer model to test the accuracy of our directly extracting multiwave ADCIGs method, as shown in Fig. 4. The mesh size of the model is 401×401 and the grid spacing is 10 m. The P-wave velocities are $\alpha_1 = 2800$ m/s, $\alpha_2 = 3200$ m/s, $\alpha_3 = 3800$ m/s, $\alpha_4 = 4500$ m/s, and S-wave velocities are $\beta_1 = 1600$ m/s, $\beta_2 = 1850$ m/s, $\beta_3 = 2200$ m/s, $\beta_4 = 2600$ m/s from top to bottom of the model. The multi-component seismic dataset are calculated by the elastic finite-difference method. We set 51 shots for this model with sampling interval of 40 m. Each shot has 401 receivers with spacing of 10 m. Figure 5a, b are

the separated PP- and PS-wave single shot seismograms after wavefield separation. The polarity reversal is obvious for the PS-wave. Figure 6 displays PP- and PS-ADCIGs located at 2000 m (the vertical line in Fig. 4) with different migration velocities, where the angle range is -50° to 50° and we have corrected the polarity of PS-wave. Evidently, the ADCIGs are flat with correct migration velocities, as shown in Fig. 6a, b. In contrast, the ADCIGs are curve down with 10% higher velocities (Fig. 6c, d) and curve up with 10% lower velocities (Fig. 6e, f). Figure 7a, b are final PP- and PS-wave GB-PSDM imaging results of stacking in the corresponding PP- and PS-ADCIGs with the correct migration velocities, where both PP- and PS-wave images are accurate for this horizontal layer model.

Curved interface model

Next, we test our techniques on a curved interface model, as shown in Fig. 8. The model contains five layers, and the

Fig. 9 Extracting multiwave ADCIGs test on curved interface model. **a** PP-ADCIGs at location 1700 m, **b** PS-ADCIGs at location 1700 m, **c** PP-ADCIGs at location 3300 m, **d** PS-ADCIGs at location 3300 m



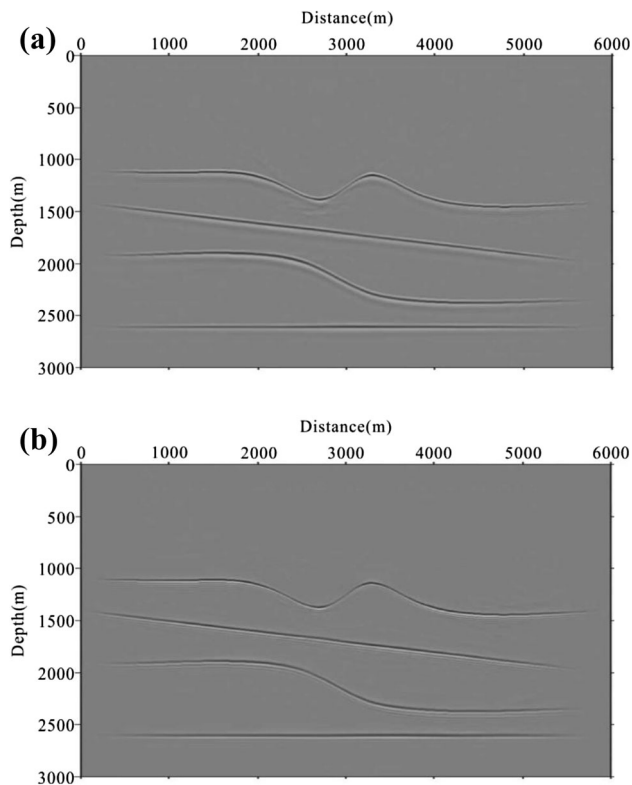
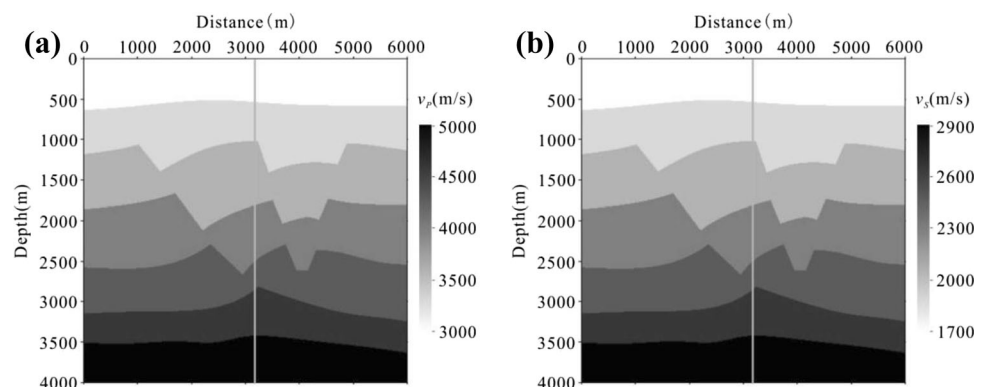


Fig. 10 The final **a** PP- and **b** PS-wave GB-PSDM imaging results with stacking in the angle domain

first and third reflectors are curved. The multi-component seismic dataset are calculated by the elastic finite-difference method. We set 51 shots for this model with sampling interval of 100 m. Each shot has 601 receivers with spacing of 10 m. The PP- and PS-ADCIGs are extracted at locations 1700 m and 3300 m in the model. Figure 9a, b are PP- and PS-ADCIGs at location 1700 m, and Fig. 9c, d are PP- and PS-ADCIGs at location 3300 m. The angle range is -60° to 60° , and we have corrected the polarity of PS-wave. Because the correct velocity model is used, the ADCIGs are flat and the depth position is correct. The final PP- and PS-wave GB-PSDM imaging results with stacking in the angle domain are shown in Fig. 10a, b, where good

Fig. 11 The fault model with velocities: **a** P-wave, **b** S-wave



migration images are obtained. These observations verify that the proposed directly extracting multiwave ADCIGs method is effective.

Fault model

In the end, a fault model with complex fault and sag structures is built to further test the directly extracting multiwave ADCIGs method. Figure 11a, b display the P- and S-wave velocities. The synthetic multi-component seismic dataset are calculated by the elastic finite-difference method, where we set 116 shots for this complex fault model with spacing of 40 m, and each shot has 341 receivers with sampling interval of 10 m. The PP- and PS-ADCIGs located at 3200 m are extracted with correct migration velocities, as shown in Fig. 12a, b. The angle range is -60° to 60° , and we have corrected the polarity of PS-wave. Both PP- ADCIGs and PS-ADCIGs are flat and positioned at the right depth. Figure 13a, b show final PP- and PS-wave GB-PSDM imaging results with stacking in the angle domain, where the complex fault structures are accurately imaged in both PP- and PS-wave migration sections. The test of this model further demonstrates the accuracy of the proposed extracting multiwave ADCIGs method for complex geological structures.

Conclusions

On the basis of multi-component GB-PSDM, we present a new directly extracting PP- and PS-ADCIGs method. Because the traveltimes and amplitude of Gaussian beam slow change in a wavelength range, the propagation angle can be obtained using the real-value traveltimes of Gaussian beam, which can be used to calculate the incidence and reflection angles. For the PP-wave, the incidence and reflection angles are equal, and then the PP-wave ADCIGs with the incidence angle can be extracted. In contrast, two kinds of ADCIGs can be obtained for the PS-wave: the first one is P-wave incidence ADCIGs and the other one is

Fig. 12 Extracting multiwave ADCIGs test on fault model with **a** PP-ADCIGs and **b** PS-ADCIGs at location 3200 m. The angle range is -60° to 60°

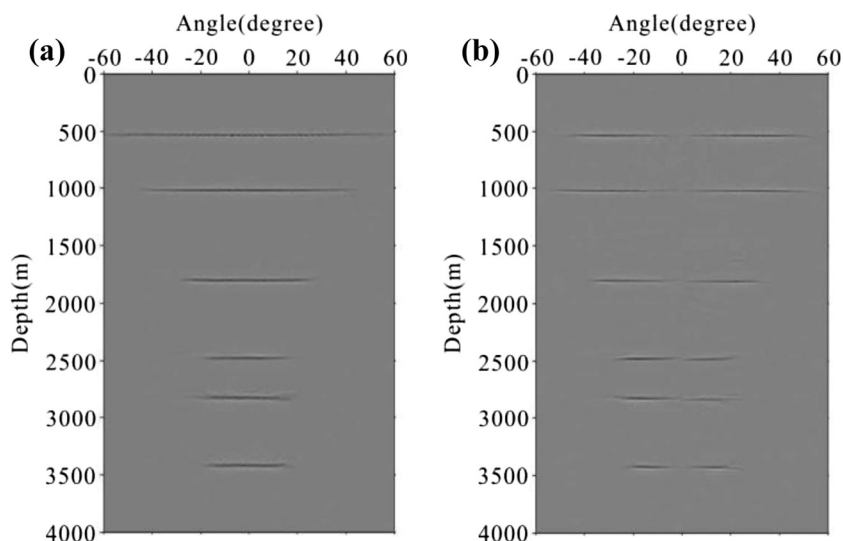
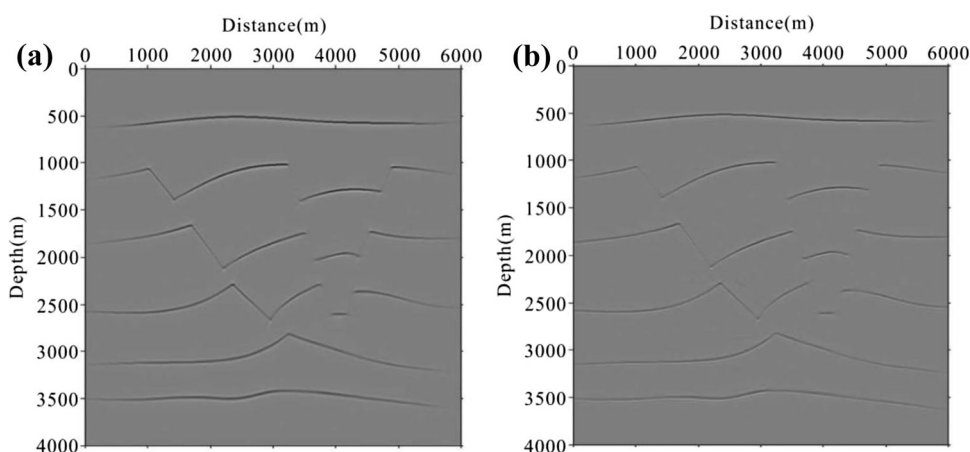


Fig. 13 The final **a** PP- and **b** PS-wave GB-PSDM imaging results with stacking in the angle domain



S-wave reflection ADCIGs, which have the attributes needed for both P- and S-wave MVA. The Gaussian beam migration is an effective migration imaging technique and it can solve multi-valued traveltimes. Therefore, the proposed directly extracting multiwave ADCIGs method based on GB-PSDM can effectively eliminate artifacts in ADCIGs owing to the multi-valued traveltimes. Tests of synthetic examples show that the multiwave ADCIGs method introduced here is accurate and effective.

Acknowledgements The research is supported by the Fundamental Research Funds for Central Public Welfare Research Institutes, CAGS (no. J1620) and China Postdoctoral Science Foundation (no. 2016M591250).

References

- Audebert F, Froidevaux P, Rakotoarisoa H, Svay-Lucas J (2002) Insight into migration in the angle domain: 72nd Annual International Meeting, SEG, Expanded Abstracts, pp 1188–1191
- Audebert F, Nicoletis L, Froidevaux P, Rakotoarisoa H (2003) True amplitude migration in the angle domain by regularization of illumination. In: 73rd Annual International Meeting, SEG, Expanded Abstracts, pp 921–924
- Baina R, Thierry P, Calandra H (2002) 3D preserved-amplitude prestack depth migration and amplitude versus angle relevance. *Lead Edge* 21:1237–1241. doi:[10.1190/1.1536141](https://doi.org/10.1190/1.1536141)
- Biondi B, Symes W (2004) Angle-domain common-image gathers for migration velocity analysis by wavefield continuation imaging. *Geophysics* 69:1283–1298. doi:[10.1190/1.1801945](https://doi.org/10.1190/1.1801945)
- Brandsberg-Dahl S, De Hoop MV, Ursin B (2003) Focusing in dip and AVA compensation on scattering-angle/azimuth common-image gathers. *Geophysics* 68:232–254. doi:[10.1190/1.1543210](https://doi.org/10.1190/1.1543210)
- Červený V (2007) A note on dynamic ray tracing in ray-centered coordinates in anisotropic inhomogeneous media. *Stud Geophys Geod* 51:411–422
- de Bruin C, Wapenaar C, Berkhout A (1990) Angle-dependent reflectivity by means of prestack migration. *Geophysics* 55:1223–1234
- Du QZ, Li F, Sun JM (2010) Time-shift angle domain common image gathers for multi-wave. In: 80th Annual International Meeting, SEG, Expanded Abstracts
- Gray SH (2005) Gaussian beam migration of common-shot records. *Geophysics* 70:S71–S77. doi:[10.1190/1.1988186](https://doi.org/10.1190/1.1988186)

- Hale D (1992a) Migration by the Kirchhoff, slant stack and Gaussian beam methods. Colorado School of Mines Center for Wave Phenomena Report 121
- Hale D (1992b) Computational aspects of Gaussian beam migration. Colorado School of Mines Center for Wave Phenomena Report 139
- Han JG, Wang Y, Lu J (2013) Multi-component Gaussian beam prestack depth migration. *J Geophys Eng* 10:055008. doi:[10.1088/1742-2132/10/5/055008](https://doi.org/10.1088/1742-2132/10/5/055008)
- Han JG, Wang Y, Han N, Xing ZT, Lu J (2014) Multiwave velocity analysis based on Gaussian beam prestack depth migration. *Appl Geophys* 11:186–196. doi:[10.1007/s11770-014-0431-7](https://doi.org/10.1007/s11770-014-0431-7)
- Hill NR (1990) Gaussian beam migration. *Geophysics* 55:1416–1428. doi:[10.1190/1.1442788](https://doi.org/10.1190/1.1442788)
- Hill NR (2001) Prestack Gaussian-beam depth migration. *Geophysics* 66:1240–1250. doi:[10.1190/1.1487071](https://doi.org/10.1190/1.1487071)
- Jin SW, Mosher CC, Wu RS (2002) Offset-domain pseudoscreen prestack depth migration. *Geophysics* 67:1895–1902. doi:[10.1190/1.1527089](https://doi.org/10.1190/1.1527089)
- Koren Z, Ravve I, Ragoza E, Bartana A, Kosloff D (2008) Full-azimuth angle domain imaging. 78th Annual International Meeting, SEG, Expanded Abstracts, pp 2221–2225
- Mosher C, Foster D (2000), Common-angle imaging conditions for prestack depth migration. In: 70th Annual International Meeting, SEG, Expanded Abstracts, pp 830–833
- Nolan CJ, Symes WW (1996) Imaging and coherency in complex structure. In: 66th Annual International Meeting, SEG, Expanded Abstracts, pp 359–363
- Nowack RL, Chen WP, Tseng TL (2010) Application of Gaussian-beam migration to multiscale imaging of the lithosphere beneath the Hi-CLIMB array in Tibet. *Bull Seismol Soc Am* 100:1743–1754
- Popov MM, Semtchenok NM, Popov PM, Verdel AR (2010) Depth migration by the Gaussian beam summation method. *Geophysics* 75:S81–S93. doi:[10.1190/1.3361651](https://doi.org/10.1190/1.3361651)
- Prucha M, Biondi B, Symes W (1999) Angle-domain common-image gathers by wave-equation migration. In: 69th Annual International Meeting, SEG, Expanded Abstracts, pp 824–827
- Rickett JE, Sava PC (2002) Offset and angle-domain common image-point gathers for shot-profile migration. *Geophysics* 67:883–889. doi:[10.1190/1.1484531](https://doi.org/10.1190/1.1484531)
- Rosales D, Rickett J (2001) PS-wave polarity reversal in angle domain common-image gathers. Stanford Exploration Project Report 108
- Rosales DA, Fomel S, Fomel BL, Sava PC (2008) Wave-equation angle-domain common-image gathers for converted waves. *Geophysics* 73:S17–S26. doi:[10.1190/1.2821193](https://doi.org/10.1190/1.2821193)
- Rousseau V, Nicoletis L, Svay-Lucas J, Rakotoarisoa H (2000) 3D true amplitude migration by regularization in the angle domain. In: 62nd Meeting, European Association of Geoscientists and Engineers, Session: B0013
- Rousseau V, Nicoletis L, Rakotoarisoa H (2001) Antialiased 3D true amplitude common diffraction angle migration by regularization in the dip domain. In: 63rd Meeting, European Association of Geoscientists and Engineers, Session: P080
- Sava P, Biondi B (2004) Wave-equation migration velocity analysis: I-theory. *Geophys Prospect* 52:593–606
- Sava P, Fomel S (2003) Angle-domain common-image gathers by wavefield continuation methods. *Geophysics* 68:1065–1074. doi:[10.1190/1.1581078](https://doi.org/10.1190/1.1581078)
- Sava P, Fomel S, 2005, Wave-equation common-angle gathers for converted waves. In: 75th Annual International Meeting, SEG, Expanded Abstracts, pp 947–950
- Sava P, Fomel S (2006) Time-shift imaging condition for converted waves. In: 76th Annual International Meeting, SEG, Expanded Abstracts, pp 2460–2464
- Sava P, Vlad I (2011) Wide-azimuth angle gathers for wave-equation migration. *Geophysics* 76:S131–S141. doi:[10.1190/1.3560519](https://doi.org/10.1190/1.3560519)
- Sollid A, Ursin B (2003) Scattering-angle migration of ocean-bottom seismic data in weakly anisotropic media. *Geophysics* 68:641–655. doi:[10.1190/1.1567234](https://doi.org/10.1190/1.1567234)
- Xu S, Chauris H, Noble M (2001) Common-angle migration: a strategy of imaging complex media. *Geophysics* 66:1877–1894. doi:[10.1190/1.1487131](https://doi.org/10.1190/1.1487131)
- Xu S, Zhang Y, Tang B (2011) 3D common-image gathers from reverse time migration. *Geophysics* 76:S77–S92. doi:[10.1190/1.3536527](https://doi.org/10.1190/1.3536527)
- Yan R, Xie XB (2012) An angle-domain imaging condition for elastic reverse time migration and its application to angle gather extraction. *Geophysics* 77:S105–S115. doi:[10.1190/GEO2011-0455.1](https://doi.org/10.1190/GEO2011-0455.1)
- Zhang QS, McMechan GA (2011) Direct vector-field method to obtain angle-domain common-image gathers from isotropic acoustic and elastic reverse time migration. *Geophysics* 76:WB135–WB149. doi:[10.1190/GEO2010-0314.1](https://doi.org/10.1190/GEO2010-0314.1)
- Zhang Y, Xu S, Tang B, Bai B, Huang Y, Huang T (2010) Angle gathers from reverse-time migration. *Lead Edge* 29:1364–1371. doi:[10.1190/1.3517308](https://doi.org/10.1190/1.3517308)

Micro-seismic monitoring after the shipwreck of the Costa Concordia at Giglio Island (Italy)

Andrea Fiaschi¹ · Luca Matassoni¹  · Alessia Lotti² · Gilberto Saccorotti³

Received: 3 March 2017 / Accepted: 18 August 2017 / Published online: 24 August 2017
© Institute of Geophysics, Polish Academy of Sciences & Polish Academy of Sciences 2017

Abstract A micro-seismic network was used for monitoring the wreck of the Costa Concordia cruise ship, wrecked and run agrounded along the Giglio Island coasts during the night of 13 January 2012, until its removal. The seismic traces were processed by means of real-time and “a posteriori” procedures to detect transients that could be ascribed to wreck movements on the sea bed to integrate this information in an early warning system for assessing the wreck stability. After a first discrimination of the transients using amplitude criteria we proceeded to the localization of the detected signals to focus the attention only on the transients originated in the shipwreck resting area. The results showed that most of the events localized on the wreck were likely related to human work activities or sudden internal brittle failure but not to displacements on the seafloor. Instead, the displacements are associated to the impact on the vessel of great sea storms which approach were well correlated with the increasing seismic noise at low frequency. The carried out procedures based on this unique dataset represent an opportunity to test

seismic monitoring techniques also in not usual engineering context to support emergency management activities.

Keywords Seismic monitoring · Costa Concordia · Giglio Island · Wreck displacement · Seismic noise

Introduction

On 13 January 2012 at about 9:45 p.m., the Costa Concordia cruise ship (114,500 GT, Gross Tonnage) struck a submerged rock in the Tyrrhenian Sea just off the eastern shore of Isola del Giglio, offshore the western coast of Italy (Fig. 1). This tore a 50 m gash on the port side of her hull, which caused rapid flooding of the engine room. While seawater was flooding in and listing, the vessel underwent a starboard rotation, and finally grounded on the granitic seabed (depth of about 25 m) in front of Gabbianara Spit, some 500 m north of the village of Giglio Porto (Fig. 1). Of the 3229 passengers and 1023 crew known to have been aboard, 32 died (Alexander 2012; Schröder-Hinricks et al. 2012).

The initial impact of the ship on the underwater rocks was also recorded by a permanent seismic station on the mainland (MAON, Monte Argentario; Mucciarelli 2012) that is part of the seismic monitoring system of the National Institute of Geophysics and Volcanology (INGV).

During the following days, several institutions participated to the deployment of a complex monitoring system under the coordination of the national Department for Civil Protection (DPC). That system was aimed at controlling the wreck stability on the seafloor, to ensure safety to the search-and-rescue and fuel removal operations (Manconi et al. 2013; Raspini et al. 2014). All the monitoring data were daily collected in a joint report used for supporting the emergency management services.

✉ Luca Matassoni
l.matassoni@pratoricerche.it

Andrea Fiaschi
a.fiaschi@pratoricerche.it

Alessia Lotti
alessia.lotti.17@gmail.com

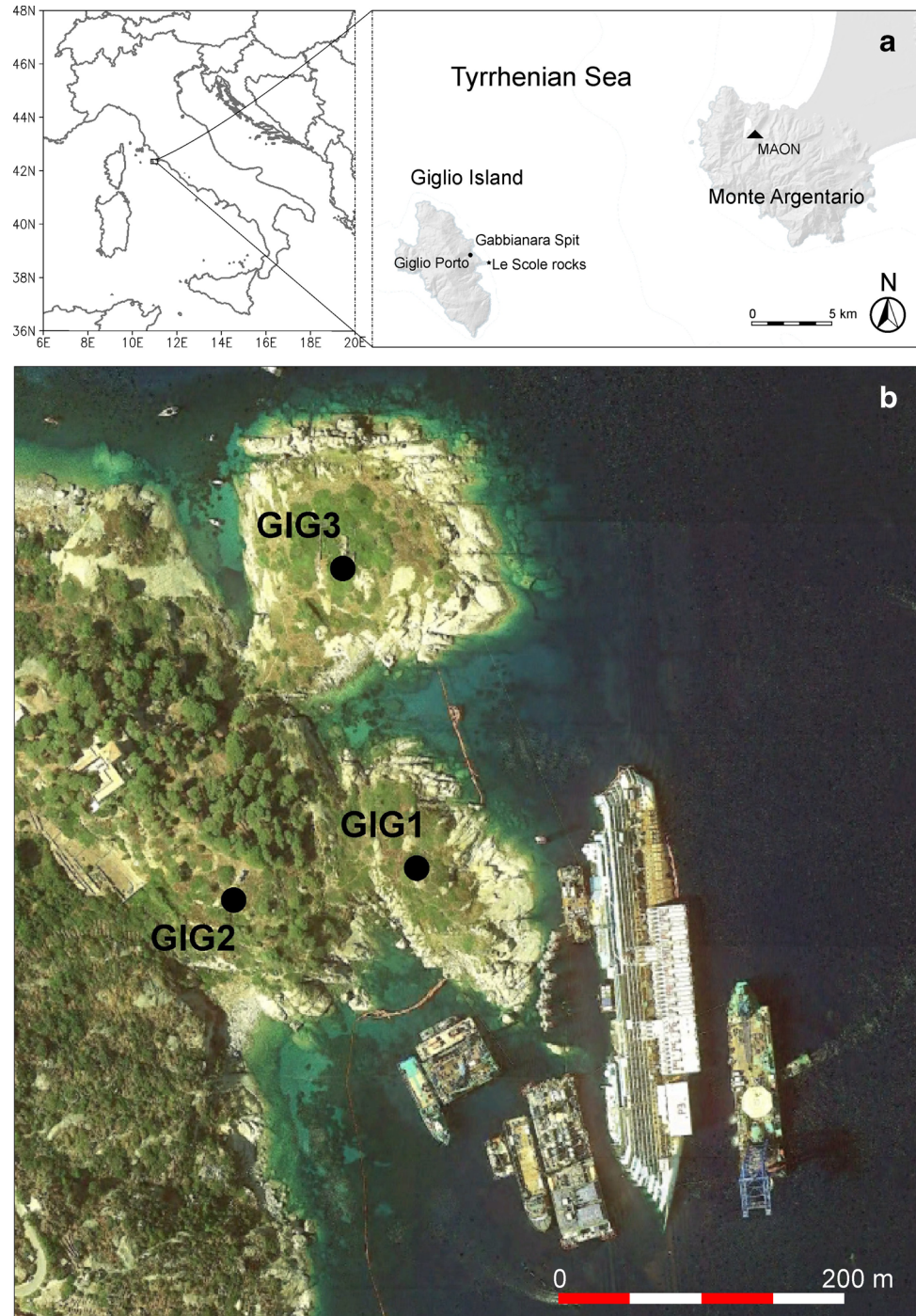
Gilberto Saccorotti
saccorotti@pi.ingv.it

¹ Fondazione Parsec, Via Galcianese 20/H, Prato, Italy

² Dipartimento di Scienze della Terra, Università di Firenze,
Via La Pira 4, Florence, Italy

³ Istituto Nazionale di Geofisica e Vulcanologia-Sezione di
Pisa, Via della Faggiola 32, Pisa, Italy

Fig. 1 Location of Giglio Island with respect to Italy (**a**) and position of the three seismic stations used for this study on a Google Earth © image acquired on the 2013, March during the wreck removal operations (**b**)



A description of the monitoring systems and their data can be found in Ciampalini et al. (2016), Broussolle et al. (2014), Raspini et al. (2014) and Manconi et al. (2013). Additional, independent works include those from Serafino et al. (2013) and Gómez-Enri et al. (2013), while a comprehensive environmental risk assessment study was conducted by Regoli et al. (2014).

Data from a robotized, total station measuring the 3D position of 12 targets positioned onboard showed

significant displacements of the wreck during the first weeks after the sinking. Although first interpretations assumed the prevalence of internal strains (Manconi et al. 2013), subsequent analyses indicated a general movement of the wreck away from the shore (Broussolle et al. 2014) due to a roto-translation on the sea bed with negligible internal deformation (Raspini et al. 2014). During the early phases of the monitoring, the maximum velocity of displacement at the bow of the ship was recorded between 31

January and 1 February 2012 (3.8 mm/h; Raspini et al. 2014). A major displacement episode also occurred by the end of October 2013 as a result of a violent sea storm (displacement >1 m with average velocity of 73 mm/h, not discussed in the above referenced papers).

The monitoring system worked until the early 2014 after the parbuckling salvage operation.

This unusual and complex scenario suggested to adopt a wide range of monitoring instruments and techniques, to detect signals related to possible wreck displacement over a wide frequency band. Following the raising attention of the scientific community on the use of seismic techniques for environmental monitoring (e.g., Battaglia and Aki 2003; Burtin et al. 2016; Coviello et al. 2015; Larose et al. 2015; Latorre et al. 2014; Manconi et al. 2016; Schmandt et al. 2017; Tang et al. 2015), a tri-partite seismic array was rapidly deployed as a part of this effort. Seismic monitoring aimed at the analysis of ground motion for the early detection of transient signals, rather than changes in the amplitude and spectral content of the background noise, possibly related to wreck movements. The assessment of eventual displacement of the vessel due to earthquakes was also carried out. In this paper we summarize methods, procedures and results from the seismological monitoring of the Concordia wreck.

Instruments and data acquisition

The micro-seismic monitoring began on the 19th of January 2012 under a cooperative effort jointly carried out by Parsec foundation (former Prato Ricerche) and INGV. Initially, we installed two local-recording mobile seismometers on the cliff overlooking the wreck. At the same time we carried out the installation of three seismic stations (GIG1, GIG2 and GIG3; Fig. 1b) in continuous data acquisition and transmission using the Universal Mobile Telecommunications System (UMTS) network.

The continuous data recording from the micro-seismic network began on January 25, 2012, and continued until the end of January, 2014 (Table 1). For the three stations, the completeness of the recorded data set amounts to about 96% of the whole recording period.

Table 1 reports the technical characteristics, location and working intervals of the three seismic stations.

The three instruments were deployed on the cliff overlooking the wreck, at distances from the hull ranging from 100 m (GIG1) to 230 m (GIG3). Each station was equipped with a Guralp CMG 40T/30s seismic sensor (a Lenartz Le3D-1s was initially installed at GIG2). Sensors were positioned at the bottom of ~50 cm deep holes dug in the granitic rock; we used cases in polyurethane foam to

protect the sensors and to ensure appropriate thermal insulation and protection from dust and weathering.

Prior to installation, we conducted a “huddle test” to verify the mutual similarity of the instrumental responses of the different instruments.

The suitability of the different installations was verified using power spectra density representations (Peterson 1993) and horizontal to vertical spectral ratio (HVSr) analysis (Nakamura 1989) to assess site noise level and site amplification effects, respectively.

All the stations were equipped with a 24-bit digitizer Taurus by Nanometrics.

The power supply at GIG1 and GIG3 was ensured by solar panels (200 W), while GIG2 was connected directly to the national electrical grid (220–240 V) by a 12 V transformer. Each station was equipped with a 12 V/60 Ah buffer battery to ensure the necessary continuity of power supply.

The data transmission from the digitizer to the processing centre in Prato was performed by UMTS telemetry via TCP/IP protocol with dynamic Domain Name System (DNS). Stations were also equipped with an internal 10 GB storage system to prevent loss of data due to possible interruptions in data transmission.

Digitizer, UMTS router and battery were placed near the sensor and protected from weathering.

Data were acquired by NAQS Server 2.1 software (Nanometrics Acquisition System) and stored in a circular ring buffer of 24 h. The NAQS software, in addition to receiving data from the stations, also verifies the completeness of the data received, in case requesting missing packet.

The continuous data streams on the ring buffer were then loaded by the SeisComp3 system (<https://www.seiscomp3.org>; accessed 15 February 2017), and stored as day-long, miniSEED data files. We also used an instance of the Earthworm server (<http://www.earthwormcentral.org/>, last accessed 15 February 2017) for data visualization and quality control. At the same time, the miniSEED data streams were also converted to the SAC format (Helffrich et al. 2013) for the real-time data analysis.

Data analysis

Acquired data were analyzed using both on- and off-line procedures based on several Matlab software scripts developed on purpose.

A first procedure was dedicated to the location of transient signals using travel-times differences at the array's stations. Every 10 min, the continuous data stream from the SeisComp archive was analysed using a triggering

Table 1 Station description by location coordinates, installed equipments and period of recording

Station name	Latitude (°N)	Longitude (°E)	Sensor	Digitizer	Data transmission	Sample frequency (Hz)	Start recording (UTC)	End recording (UTC)
GIG1	42.365966	10.919854	Guralp CMG 40T/30s	Nanometrics Taurus	UMTS	100	20/01/12	31/01/2014
GIG2	42.365868	10.918384	Lennartz Le3D-1s Guralp CMG 40T/30s	Nanometrics Taurus	UMTS	100	21/01/12 08/03/2012	08/03/2012 31/01/2014
GIG3	42.365966	10.919854	Guralp CMG 40T/30s	Nanometrics Taurus	UMTS	100	25/01/12	31/01/2014

procedure based on a simple amplitude threshold applied to the 2–20 Hz band-pass filtered signals. In that procedure, an event was declared whenever the vertical component of ground velocity exceeded by a factor 8 the mean amplitude (calculated over a 10-s long window) at the three stations, within a 0.5 s long time interval. These amplitude threshold and time window length were selected after calibration using the recordings from artificial explosions fired during the early stages of salvage operations (see Fig. 2).

Every time an event was declared, the delay times among independent station pairs were calculated using cross-correlation (Gibbons and Ringdal 2006; Gibbons et al. 2007; Saccorotti and Del Pezzo 2000; Shapiro et al. 2006). We then discretised the plane surrounding the wreck using a regular grid of nodes equally spaced by 5 m along the EW and NS directions. For each grid node, we calculated the theoretical travel times to individual stations using a homogeneous Earth model with constant velocity equal to 2.7 km/s. The probability for an event to be located at the grid node positioned at x is then expressed as:

$$P(x) = \text{Exp} \left[-0.5 \times \left(\frac{\sum_1^N \Delta t_i^{\text{obs}} - \Delta t_i^{\text{cal}}(x)}{\sigma} \right)^2 \right],$$

where Δt_i^{obs} are the delay times evaluated between the $N = 3$ possible independent station pairs for the triggered transient; $\Delta t_i^{\text{cal}}(x)$ are the theoretical delay times between the $N = 3$ possible independent station pairs for the grid node located at x ; σ is an error term, including both the experimental uncertainties and those associated with the adopted model (i.e., homogeneous velocity structure and source at the sea level).

Figure 2 illustrates the location procedure; the probability of source location is mapped as a function of the two UTM geographic coordinates, and compared to the position of the wreck. Integration of the $P(x)$ function over the grid nodes contained within the wreck's boundaries (gray region in Fig. 2b) provides the probability of the source to be located within or in close proximity of the ship.

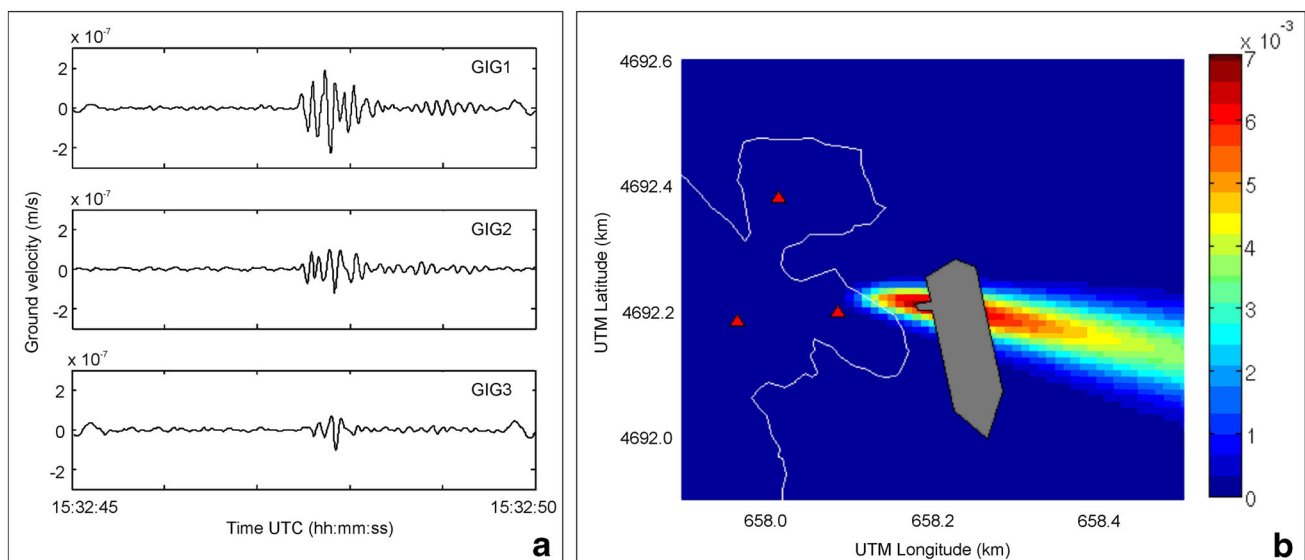


Fig. 2 Locator procedure results for the explosion on the January 26: vertical component of seismic traces recorded at the three stations (a) and horizontal representation of the function of localization probability density (b)

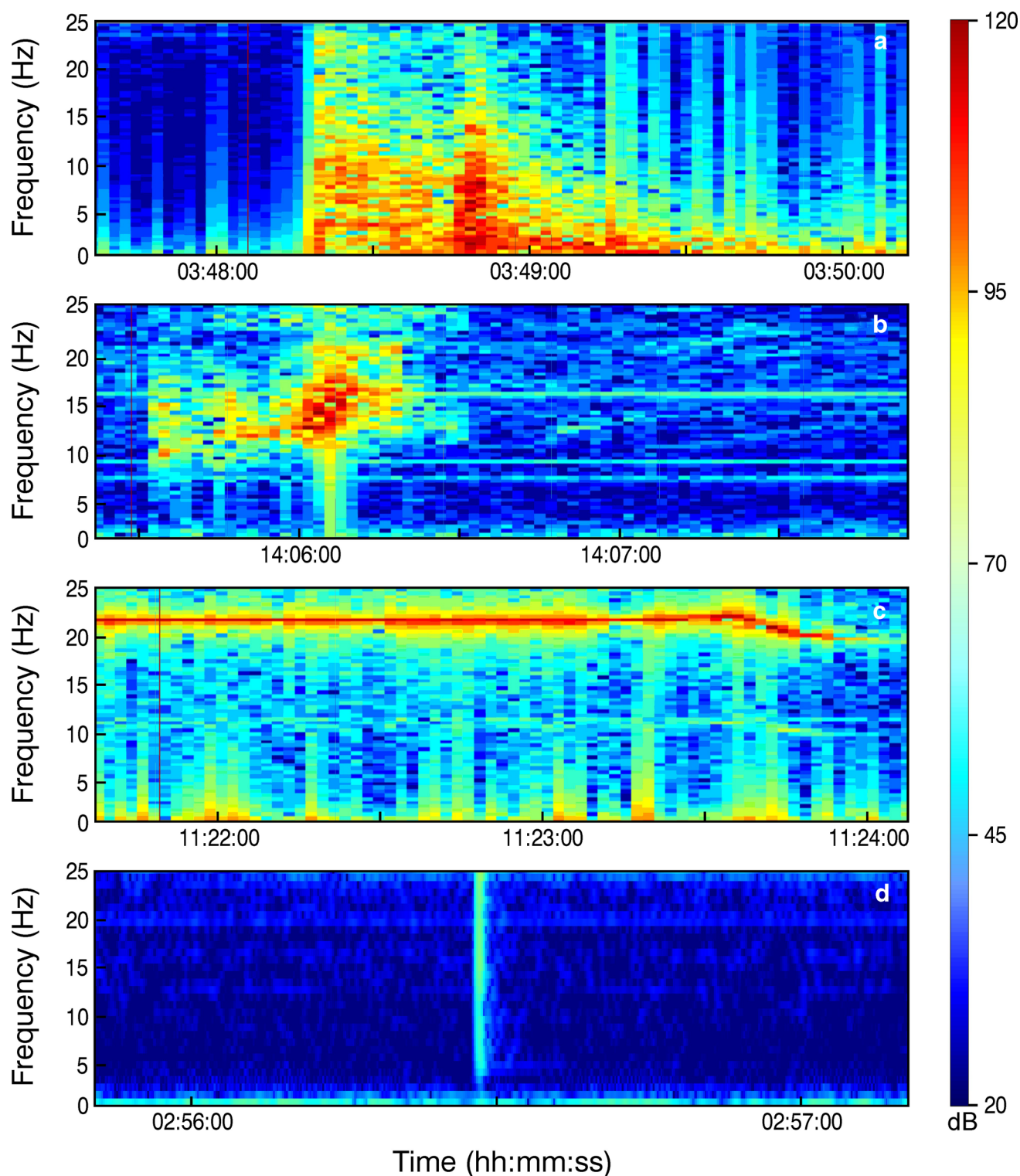


Fig. 3 Spectrograms for different, specific sources: a magnitude = 4.6 earthquake at 3:48:39 on 4 April 2012 with epicentre in the western Mediterranean (a), ferry boat mooring to Giglio Porto (b), helicopter flying at low altitude (c); transient localized on the wreck (d)

Every 24 h we also conducted additional, a posteriori analyses whose results were then summarised by daily and weekly reports transmitted to the Civil Protection authorities. These analysis included: (1) spectrogram of the three

component of ground motion at reference station GIG2, and (2), the root mean square (RMS) of the continuous data streams for two different frequency ranges (0.1–2 Hz and 2–40 Hz). These two particular frequency ranges were,

respectively, taken as representative of the sea climate condition (e.g., Longuet-Higgins 1950) and other local, natural or artificial disturbances.

Results and discussion

The recorded seismograms included a variety of sources, of both natural and artificial origin; this represented a further challenge for the discrimination of signals possibly related to the wreck displacement (Fig. 3).

During the whole monitoring period, the location procedure recognized more than 9000 micro-events originating on or nearby the wreck (Fig. 4a). The daily number of detections was generally higher during the removal and salvage

operations. Moreover, the occurrence of seismic transients was not directly related to the main displacement episodes of the wreck as recorded by other monitoring systems (see Fig. 5a); this suggests that movements were too slow to produce a significant energy release over the seismic frequency band. Therefore, seismic events detected by the automatic location procedure were most likely associated with causes such as (1) the sudden opening of internal, small fractures or cracks in the vessel structure; (2) transient disturbances associated with the human activities on and around the wreck, and (3) waves breaking at the wreck walls and adjacent cliffs. RMS amplitude of noise at low frequencies (0.1–2 Hz) is a parameter of significant interest (Fig. 4b). For that particular frequency band, the amplitude of seismic noise is directly related to sea climate and wave height

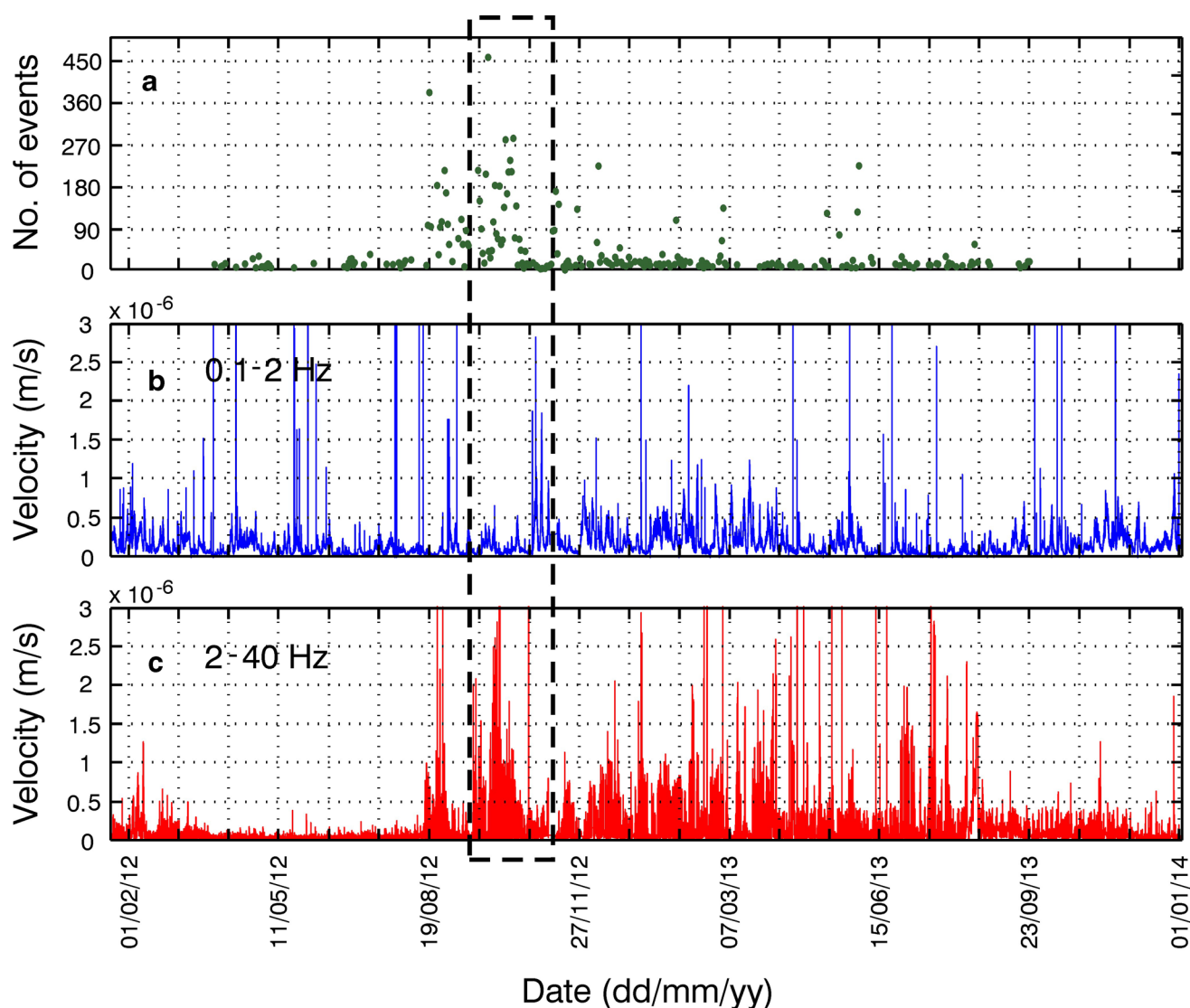


Fig. 4 Daily number of micro-events originating on or nearby the wreck (a) and RMS amplitude calculated from seismic noise recorded at GIG1 (vertical component) for low (b) and high (c) frequency

bands for the whole monitoring period. The velocity limited at 3×10^{-6} m/s to improve reading of the graphic. Days within the dashed box were detailed in Fig. 5

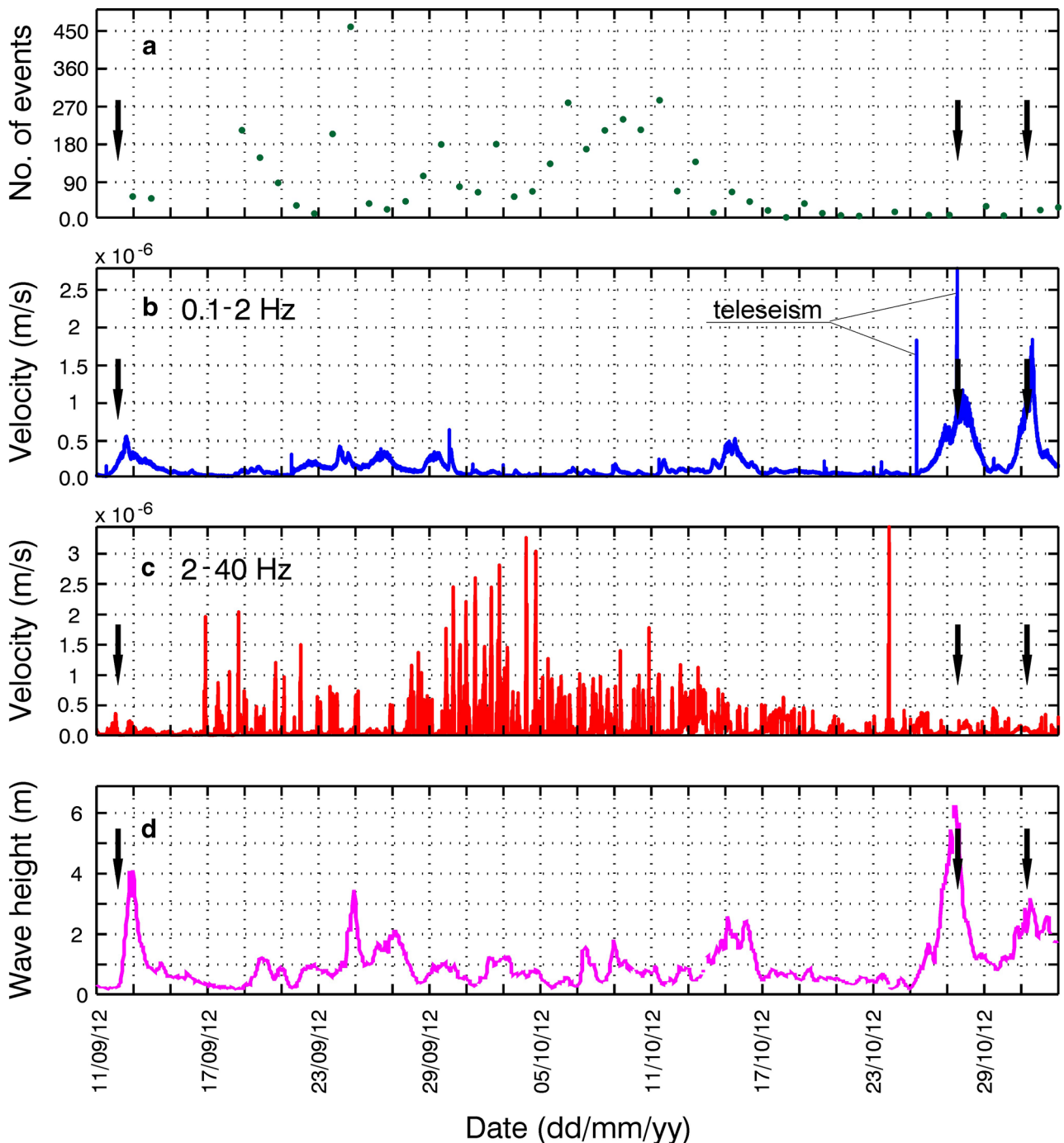


Fig. 5 Daily number of micro-events originating on or nearby the wreck (**a**) and RMS amplitude calculated from seismic noise recorded at GIG1 (*vertical* component) for low (**b**) and high (**c**) frequency bands for the period between 11 September–2 November 2012. **d** Sea

wave height recorded at the Gorgona Island waverider buoy station for the same time interval. *Black arrows* point out the days of the main wreck displacements recorded by the robotized total station

(Ferretti et al. 2013); this parameter thus evidences approximating sea storms, that in turn anticipate/match the wreck displacements as measured with geodetic (Manconi et al. 2013) and interferometric techniques.

This is well illustrated by Fig. 5, which shows the time behaviour of the monitored parameters encompassing three

displacement episodes occurred on 11–12 September (~ 1 cm), 26–29 October (~ 12 cm) and 31 October–2 November (>1 m). For all the three cases, the amplitude of the low-frequency microseism (Fig. 5b) exhibits a positive trend which is well correlated with the sea wave height increase (Fig. 5d) as recorded by the Gorgona Island

waverider buoy station (9.9560°E, 43.5683°N; Regional Hydrological Sector of Tuscany, data available at <http://www.cfr.toscana.it/index.php?IDS=42&IDSS=282>, accessed 15 February 2017). The Gorgona waverider buoy was selected because the nearest buoy of Castiglione della Pescaia (10.9468°E, 42.7282°N) did not work continuously in the considered period.

Noise increase at high frequencies (2–40 Hz) is most likely related to the drilling activities carried out to anchor the wreck to the rocky seabed (Fig. 5c), suspended as sea conditions get worse. Figure 5b also shows the occurrence of significant, low-frequency ground shaking associated with two major earthquakes at teleseismic distance. In particular, the second earthquake preceded by a few hours the displacement episode on October 26–29.

During the monitoring period, we also recorded many seismic events (more than 100), with magnitudes between 3 and 6 and epicentral distances ranging between 60 and 400 km. The closest one was recorded on the 21 November 2012, less than 10 km NE of the wreck (10.90°E–42.42°N, $M = 1.6$) while the strongest one occurred on the 5 May 2012 in Northern Italy (11.24°E–44.90°N, $M = 6.1$; data from EIDA, European-Mediterranean Seismological Centre, available at <http://www.emsc-csem.org/Earthquake/?filter=yes>, accessed 15 February 2017).

The ground displacement beneath the wreck associated with transiting seismic waves from earthquake sources were assessed by integration of observed broadband velocities recorded at GIG1. For all the recorded earthquake signals, such displacements resulted to be quite negligible, never exceeding 1 mm over the 1–30 Hz frequency band.

Conclusion

Overall, the results from the seismic monitoring are summarised as follows:

1. Before and during the anchor operations, the main wreck displacements are well correlated to wave height, as also highlighted by Manconi et al. (2013). This suggests that the movements of the wreck on the seafloor are a consequence of the impact of energetic sea waves on the vessel. On the other hand, the amplitude of seismic noise over the 0.1–2 Hz frequency band provides a direct measure of sea climate and wave height; retrospectively, the amplitude of the low-frequency ground vibrations could, therefore, be used for a short-term prediction of wreck displacements.
2. In general, ground shaking from earthquakes at a variety of epicentral distances did not affect the overall

stability of the wreck; a single exception is that of the teleseismic event on October 25, 2012 (Fig. 5b), which preceded by a few hours a significant (>10 cm) displacement episode. Such earthquake, however, occurred concurrently to a major sea storm, as indicated by wave-height and low-frequency seismic amplitude data. Therefore, although the transit of energetic teleseismic waves cannot be ruled out as the cause of the observed wreck displacement, wave impact on the vessel still remains the preferred causative phenomenon.

3. The amplitude of background seismic noise over the high (2–40 Hz) frequency band is mostly related to human activities at and around the wreck. Interestingly, the amplitude of such signals are somehow anti-correlated with those of the low-frequency ones, indicating a decrease/suspension of human interventions as the sea conditions get worse.
4. The automatic location procedure evidenced the vigorous occurrence of high-frequency micro-seismic transients occurring within or in close proximity of the vessel. These events are not directly correlated to the main displacement episodes of the wreck, indicating that these latter ones occurred over time scales (minutes to hours) well beyond the sensitivity band of our seismometers.

Given the nature of the problem, precise distance-measuring devices (e.g., total stations) demonstrate to be much more effective than seismic surveillance for detecting ship displacements and/or deformations. Nonetheless, the high-sensitivity, real-time monitoring system here presented may result of interest for other applications (e.g., land- or rock-slide monitoring), which require the rapid and automatic assessment of a large number of seismic transient signals.

Acknowledgements The seismic monitoring activities have been developed in the framework of the contracts between Dipartimento di Scienze della Terra-Università di Firenze (UNIFI-DST) and Prato Ricerche (now Fondazione Parsec) in application of the agreement “Monitoring of the vessel deformations and displacements of Costa Concordia (Giglio Island)” between UNIFI-DST and Dipartimento di Protezione Civile (DPC). We thank two anonymous reviewers for their suggestions which much improved this work.

Compliance with ethical standards

Conflict of interest On behalf of all authors, the corresponding author states that there is no conflict of interest.

References

- Alexander DE (2012) The ‘Titanic Syndrome’: risk and crisis management on the Costa Concordia. *J Homel Secur Emerg Manag.* doi:10.1515/1547-7355.1998

- Battaglia J, Aki K (2003) Location of seismic events and eruptive fissures on the Piton de la Fournaise volcano using seismic amplitudes. *J Geophys Res* 108(B8):2364. doi:[10.1029/2002JB002193](https://doi.org/10.1029/2002JB002193)
- Broussolle J, Kyovtorov V, Basso M, Ferraro di Silvi e Castiglione G, Figueiredo Morgado J, Giuliani R, Oliveri F, Sammartini PF, Tarchi D (2014) MELISSA, a new class of ground based InSAR system. An example of application in support to the Costa Concordia. *J Photogramm Remote Sens* 91:50–58. doi:[10.1016/j.isprsjprs.2014.02.003](https://doi.org/10.1016/j.isprsjprs.2014.02.003)
- Burtin A, Hovius N, Turowski JM (2016) Seismic monitoring of torrential and fluvial processes. *Earth Surf Dyn* 4(2):285–307. doi:[10.5194/esurf-4-285-2016](https://doi.org/10.5194/esurf-4-285-2016)
- Ciampalini A, Raspini F, Bianchini S, Tarchi D, Vespe M, Moretti S, Casagli N (2016) The Costa Concordia last cruise: the first application of high frequency monitoring based on COSMO-SkyMed constellation for wreck removal. *J Photogramm Remote Sens* 112:37–49. doi:[10.1016/j.isprsjprs.2015.12.001](https://doi.org/10.1016/j.isprsjprs.2015.12.001)
- Coviello V, Chiarle M, Arattano M, Pogliotti P, Morra di Cella U (2015) Monitoring rock wall temperatures and microseismic activity for slope stability investigation at J.A. Carrel hut, Matterhorn. In: Lollino G, Manconi A, Clague J, Shan W, Chiarle M (eds) *Engineering geology for society and territory*, vol 1. Springer, Cham, pp 305–309. doi:[10.1007/978-3-319-09300-0_57](https://doi.org/10.1007/978-3-319-09300-0_57)
- Ferretti G, Zunino A, Scafidi D, Barani S, Spallarossa D (2013) On microseisms recorded near the Ligurian coast (Italy) and their relationship with sea wave height. *Geophys J Int* 194(1):524–533. doi:[10.1093/gji/ggt114](https://doi.org/10.1093/gji/ggt114)
- Gibbons SJ, Ringdal F (2006) The detection of low magnitude seismic events using array-based waveform correlation. *Geophys J Int* 165(1):149–166. doi:[10.1111/j.1365-246X.2006.02865.x](https://doi.org/10.1111/j.1365-246X.2006.02865.x)
- Gibbons SJ, Sørensen MB, Harris DB, Ringdal F (2007) The detection and location of low magnitude earthquakes in northern Norway using multi-channel waveform correlation at regional distances. *Phys Earth Planet Inter* 160(3–4):285–309. doi:[10.1016/j.pepi.2006.11.008](https://doi.org/10.1016/j.pepi.2006.11.008)
- Gómez-Enrí J, Scozzari A, Soldovieri F, Vignudelli S (2013) ENVISAT radar altimetry for coastal and inland waters: case-study of the Costa Concordia ship to understand non-water targets using a tomographic technique. *Int Water Technol J* 3(2):60–69
- Helfrich G, Wookey J, Bastow I (2013) *The seismic analysis code: a primer and user's guide*. Cambridge University Press, Cambridge
- Larose E, Carrière S, Voisin C, Bottelin P, Baillet L, Guéguen P, Walter F, Jongmans D, Guillier B, Garambois S, Gimbert F, Massey C (2015) Environmental seismology: what can we learn on earth surface processes with ambient noise? *J Appl Geophys* 116:62–74. doi:[10.1016/j.jappgeo.2015.02.001](https://doi.org/10.1016/j.jappgeo.2015.02.001)
- Latorre D, Amato A, Cattaneo M, Carannante S, Michelini A (2014) Man-induced low-frequency seismic events in Italy. *Geophys Res Lett* 41(23):8261–8268. doi:[10.1002/2014GL062044](https://doi.org/10.1002/2014GL062044)
- Longuet-Higgins MS (1950) A theory of the origin of microseisms. *Philos Trans R Soc A* 243(857):1–35. doi:[10.1098/rsta.1950.0012](https://doi.org/10.1098/rsta.1950.0012)
- Manconi A, Allasia P, Giordan D, Baldo M, Lollino G (2013) Monitoring the stability of infrastructures in an emergency scenario: the “Costa Concordia” vessel wreck. In: Wu F, Qi S (eds) *Global view of engineering and the environment*. CRC Press, London, pp 587–591
- Manconi A, Picozzi M, Coviello V, De Santis F, Elia L (2016) Real-time detection, location, and characterization of rockslides using broadband regional seismic networks. *Geophys Res Lett* 43(13):6960–6967. doi:[10.1002/2016GL069572](https://doi.org/10.1002/2016GL069572)
- Mucciarelli M (2012) The seismic wake of Costa Concordia. *Seismol Res Lett* 83(4):636–638. doi:[10.1785/0220120020](https://doi.org/10.1785/0220120020)
- Nakamura Y (1989) A method for dynamic characteristics estimation of subsurface using microtremor on the ground surface. *Quart Rep Railw Tech Res Inst* 30(1):25–33
- Peterson J (1993) Observation and modeling of seismic background noise. *US Geol Surv Tech Rep* 93–322:1–95
- Raspini F, Moretti S, Fumagalli A, Rucci A, Novali F, Ferretti A, Prati C, Casagli N (2014) The COSMO-SkyMed constellation monitors the Costa Concordia wreck. *Remote Sens* 6:3988–4002. doi:[10.3390/rs6053988](https://doi.org/10.3390/rs6053988)
- Regoli F, Pellegrini D, Cicero AM, Nigro M, Benedetti M, Gorbi S, Fattorini D, d’Errico G, Di Carlo M, Nardi A, Gaion A, Scuderi A, Giuliani S, Romanelli G, Berto D, Trabucco B, Guidi P, Bernardeschi M, Scarcelli V, Frenzilli G (2014) A multidisciplinary weight of evidence approach for environmental risk assessment at the Costa Concordia wreck: integrative indices from mussel watch. *Mar Environ Res* 96:92–104. doi:[10.1016/j.marenvres.2013.09.016](https://doi.org/10.1016/j.marenvres.2013.09.016)
- Saccorotti G, Del Pezzo E (2000) A probabilistic approach to the inversion of data from a seismic array and its application to volcanic signals. *Geophys J Int* 143(1):249–261. doi:[10.1046/j.1365-246x.2000.00252.x](https://doi.org/10.1046/j.1365-246x.2000.00252.x)
- Schmandt B, Gaeuman D, Stewart R, Hansen SM, Tsai VC, Smith J (2017) Seismic array constraints on reach-scale bedload transport. *Geology*. doi:[10.1130/G38639.1](https://doi.org/10.1130/G38639.1)
- Schröder-Hinricks J, Hollnagel E, Baldauf M (2012) From Titanic to Costa Concordia—a century of lessons not learned. *WMU J Marit Aff* 11(2):151–167. doi:[10.1007/s13437-012-0032-3](https://doi.org/10.1007/s13437-012-0032-3)
- Serafino F, Ludeno G, Lugni C, Natale A, Arturi D, Brandini C, Soldovieri F (2013) Diffracted waves from the aground Costa Concordia cruise and detected by the Remoceano system. In: *IEEE international geoscience and remote sensing symposium (IGARSS)*. doi:[10.1109/IGARSS.2013.6723101](https://doi.org/10.1109/IGARSS.2013.6723101)
- Shapiro NM, Ritzwoller MH, Bensen GD (2006) Source location of the 26 sec microseism from cross-correlations of ambient seismic noise. *Geophys Res Lett* 33(18):L18310. doi:[10.1029/2006GL027010](https://doi.org/10.1029/2006GL027010)
- Tang C, Li L, Xu N, Ma K (2015) Microseismic monitoring and numerical simulation on the stability of high-steep rock slopes in hydropower engineering. *J Rock Mech Geotech Eng* 7(5):493–508. doi:[10.1016/j.jrmge.2015.06.010](https://doi.org/10.1016/j.jrmge.2015.06.010)

A seismic interpolation and denoising method with curvelet transform matching filter

Hongyuan Yang^{1,2} · Yun Long^{1,2} · Jun Lin^{1,2} · Fengjiao Zhang³ · Zubin Chen^{1,2}

Received: 29 December 2016 / Accepted: 19 August 2017 / Published online: 4 September 2017
© Institute of Geophysics, Polish Academy of Sciences & Polish Academy of Sciences 2017

Abstract A new seismic interpolation and denoising method with a curvelet transform matching filter, employing the fast iterative shrinkage thresholding algorithm (FISTA), is proposed. The approach treats the matching filter, seismic interpolation, and denoising all as the same inverse problem using an inversion iteration algorithm. The curvelet transform has a high sparseness and is useful for separating signal from noise, meaning that it can accurately solve the matching problem using FISTA. When applying the new method to a synthetic noisy data sets and a data sets with missing traces, the optimum matching result is obtained, noise is greatly suppressed, missing seismic data are filled by interpolation, and the waveform is highly consistent. We then verified the method by applying it to real data, yielding satisfactory results. The results show that the method can reconstruct missing traces in the case of low SNR (signal-to-noise ratio). The above three problems can be simultaneously solved via FISTA algorithm, and it will not only increase the processing efficiency but also improve SNR of the seismic data.

Keywords Interpolation · Denoising · Sparse constrained inversion · Matching filter · Curvelet transform · FISTA

Introduction

Seismic data acquired by various sources can be improved by the use of a matched filter (MF), but they may still be of poor quality with a low signal-to-noise ratio (SNR) and low resolution even after MF. Delamination may not be clearly observed after the MF of old and new seismic data, which makes it difficult to ensure the accuracy of wave impedance inversion and to extract seismic attribute parameters (Yuan et al. 2015). An event recorded from spliced seismic data from different blocks may not be continuous and might have low SNR. Furthermore, working conditions or field conditions may cause parts of seismic traces to be missing, making it challenging to match seismic data (Shi et al. 2005; Shen et al. 2013). Such problems limit the resolution and SNR of seismic data.

In response to the above issues, Wiener (1949) proposed a least-squares MF method for seismic data to improve data quality. Robinson (1957) proposed predictive deconvolution theory that yields a profile with higher time resolution, based on the Wiener theory. Berkhout (1977) proposed least squares filtering and wavelet deconvolution to produce zero-phase seismic wavelets of a desirable bandwidth. Given the improvements in computing power and the ensuing wide application of mathematic analyses, Wallace (1992) proposed a solution to achieve high resolution by network match filtering. Based on the minimum energy error of Wiener filtering, Cheng et al. (2004) proposed a fine-scale wavelet MF method and applied it to time-lapse seismic data (Jin et al. 2005). In data processing, it is common that vibrator data and the explosive source were collected together. Because the source wave group characteristics, energy, phase, and amplitude, are inconsistent, Wu et al. (2006) proposed a comprehensive pre-stack series matching filter method. In addition, Norman

✉ Yun Long
longy@jlu.edu.cn

¹ College of Instrumentation and Electrical Engineering, Jilin University, Changchun, China

² Key Laboratory of Geo-exploration Instruments, Ministry of Education of China (Jilin University), Changchun, China

³ College of Geo-Exploration Science and Technology, Jilin University, Changchun, China

and Townsley (2006) performed pre-interpretation amplitude and phase analysis using an iterative matching filter. More recently, Herrmann et al. (2008, 2009) proposed curvelet MF and used this approach to separate ground rolls. Wang et al. (2011) proposed a pseudo multichannel matching filter, and applied this approach to seismic processing to remove the non-reservoir difference (Zhang et al. 2014). Long et al. (2012) proposed optimal norm wavelet domain MF to improve the MF accuracy and suppress random noise. Wang et al. (2015) applied the least-squares MF method to mixed-phase deconvolution, in which the frequency-dependent wavelet is estimated using the ant colony optimization algorithm. Through application to real data, the authors observed that deconvolution using an optimum mixed-phase wavelet provides more details than that by the optimum constant-phase wavelet.

In this paper, we propose an MF method to interpolate seismic traces and simultaneously reduce noise in the curvelet domain. Seismic data can be affected by many factors (e.g., missing seismic traces, inadequate sampling, and low SNR) that limit the MF precision. We use MF based on the fast iterative shrinkage thresholding algorithm (FISTA) in the curvelet domain to attenuate noise. The results include a high-precision waveform and amplitude, and phase consistency. Using the FISTA, we deal simultaneously with MF, the interpolation of missing traces, and the suppression of random noise. Both the SNR and the processing efficiency are greatly improved by using the proposed method, which maintains the seismic amplitude and phase information. We then validate the method by processing real data.

Theory

Discrete curvelet transform

On the basis of the first-generation curvelet transform, Candès and Demanet (2003, 2004) and Candès et al. (2006) proposed an easily understood second-generation curvelet transform algorithm. For the sparse discrete curvelet transform, a pair of window functions should be defined: one radial $W(r)$ and one angular $V(t)$. In addition, $r \in (0.5, 2)$ and $t \in [-1, 1]$. The functions should satisfy the following conditions:

$$\sum_{j=-\infty}^{\infty} W^2(2^j r) = 1, r \in (3/4, 3/2), \quad (1)$$

$$\sum_{j=-\infty}^{\infty} V^2(t - l) = 1, t \in (-1/2, 1/2). \quad (2)$$

For every $j \geq j_0$, the frequency window definition U_j in the frequency domain is

$$U_j(r, \theta) = 2^{-3j/4} W(2^{-j} r) V\left(\frac{2^{j/2} \theta}{2\pi}\right), \quad (3)$$

where $[j/2]$ is the integer part of $j/2$. The supported area of U_j is a wedge area limited by W and V , which has scale-dependent window widths applied in each direction. Assuming that atom $\hat{\varphi}_j(\omega) = U_j(\omega)$, if φ_j is known at scale j , then the curvelet in other 2^{-j} scales can be obtained by rotating and translating φ_j . The setting interval sequence of rotation angle is $\theta_l = 2\pi \cdot 2^{-[j/2]} \cdot l$, where l is non-negative integers, and $0 \leq \theta < 2\pi$; the translation parameters are $k = (k_1, k_2) \in \mathbb{Z}^2$.

Based on the above concepts, the curvelet at scale 2^{-j} , direction θ , and translation parameters k_1, k_2 is defined as follows:

$$\varphi_{j,l,k}(x) = \varphi_j\left(R_{\theta_l}\left(x - x_k^{(j,l)}\right)\right), \quad (4)$$

with $x_k^{(j,l)} = R_{\theta_l}^{-1}(k_1 \cdot 2^{-j}, k_2 \cdot 2^{-j/2})$. R_{θ_l} and θ_l are gained by rotation. Curvelet transform can be represented as follows:

$$c(j, l, k) = \langle f, \varphi_{j,l,k} \rangle = \int_{\mathbb{R}^2} f(x) \overline{\varphi_{j,l,k}(x)} dx. \quad (5)$$

Given that $f[t_1, t_2], 0 \leq t_1, t_2 \leq n$, is the input signal in Cartesian coordinates, the discrete form of curvelet transform is

$$c^D[j, l, k] = \sum_{0 \leq t_1, t_2 \leq n} f[t_1, t_2] \overline{\varphi_{j,l,k}^D[t_1, t_2]}, \quad (6)$$

where $\overline{\varphi_{j,l,k}^D[t_1, t_2]}$ is the digital curvelet waveform. There is no specific expression for this waveform, because the curvelet transform is implemented in the frequency domain.

As illustrated in Fig. 1a, we use two types of windows to obtain the curvelet grids. Certain frequency bands are represented scales by square-shaped concentric annuli. A set of angular wedges composes an inner partitioning of each scale. The number of wedges doubles each second scale, making curvelets from higher scales more directional. The tiling of discrete curvelet transform shows a highly anisotropic elements at fine scales that obey the paramount parabolic scaling principle width/length².

The shade region (Fig. 1a) represents one typical tapered shape window (Herrmann et al. 2008). We can get a series of six scales curvelet coefficients using curvelet transform for a zero matrix of size (512, 512). The curvelet coefficient with a scale of 5, direction of 1, and position of (66, 23) is set to 1. Figure 1b shows the curvelet coefficient in the frequency-wavenumber domain. Figure 1c can be obtained using inverse curvelet transform for the curvelet coefficient in time-space domain.

Compared with wavelet transform and ridgelet transform, curvelet transform can better solve the problem of the

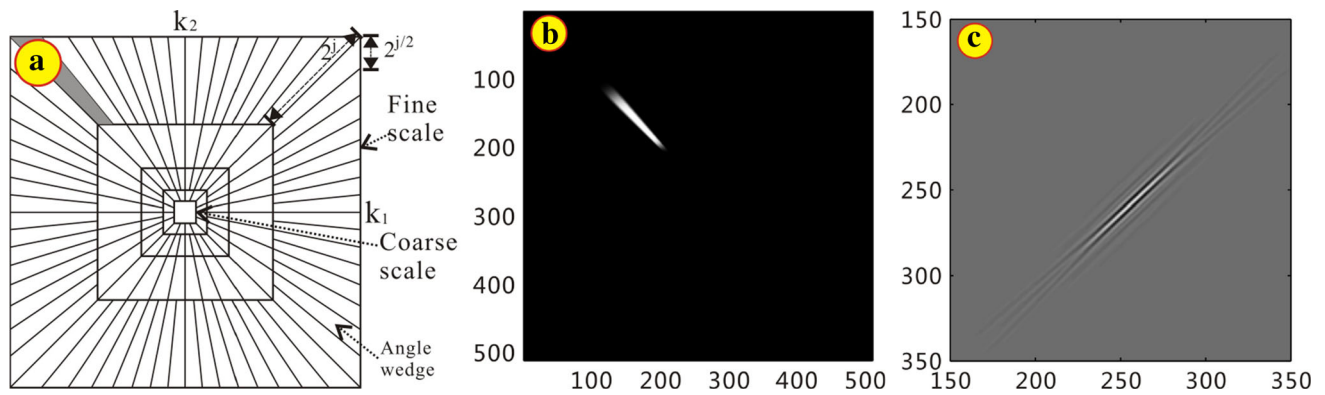


Fig. 1 **a** Partitioning of the 2D frequency plane-curvelet grid. **b** Example of curvelet in the frequency-wavenumber domain for scale = 5, direction = 1. **c** Corresponding curvelet in time-space domain

characteristics of higher dimensions and can theoretically achieve the optimal expression of a singularity characteristics curve. Therefore, given its advantages of multi-scale and multi-directional analysis, which enable the processing of optimal local decomposition to seismic data, the curvelet transform has been applied in seismic data processing (Douma and de Hoop 2007; Herrmann et al. 2008). Hennenfent et al. (2011) presented two real data examples of coherent and random noise attenuation in curvelet domain. The curvelet-based approach produces satisfactory results. Górszczyk et al. (2014) introduced scale and angle dependent weighting of curvelet coefficients, which suppressed the random noise and preserved the signal energy. Górszczyk et al. (2015a, b) developed an efficient workflow of denoising 3D post-stack seismic data using 2D DCT (discrete curvelet transform) and shown its benefits on three different 3D seismic volumes from different hardrock environments. Shi and Milkereit (2015) use the curvelet transform to reduce artificial noise on seismic images.

The curvelet transform has a better performance in describing edges and other point singularities than the traditional methods. It is a multi-scale transform and can achieve a precise reconstruction with very few coefficients. Furthermore, the curvelet transform has an appreciable advantage as it has direction parameters. It could also handle anisotropy problem. As a result, it has a sparser representation than the traditional method with the second-order continuous and differentiable piecewise smooth functions.

Curvelet transform can be used to obtain a better sparseness than the wavelet transform. We can deal with three things at the same time using FISTA method; they are matching filtering, missing traces interpolation, and random noise suppression. Figure 2 shows reconstruction errors for synthetic data set 1 (see below) using wavelet and curvelet transform with different sparseness percentages. Based on Fig. 2, we conclude that the curvelet transform has minimum reconstruction errors and is more suitable here than the wavelet transform.

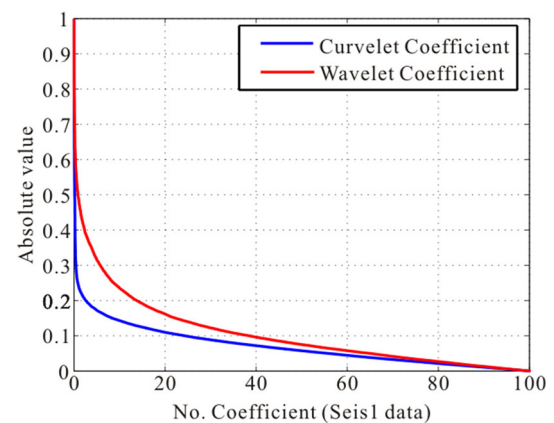


Fig. 2 Comparison of reconstruction error in curvelet and wavelet domain, the horizontal axis stands for the percentage of preserved coefficients, and the vertical axis stands for the normalized coefficients reconstruction error

Matched filtering and interpolation principle in the curvelet domain

Matching filter, noise suppression, and interpolation can be all described by one equation as a linear inversion problem, as shown in the following equation:

$$\mathbf{Ax} = \mathbf{b} + \mathbf{n}. \quad (7)$$

The physical meanings of \mathbf{A} and \mathbf{b} in the above three conditions are listed in Table 1. When we solve the matching filter problem during data reconstruction in $t-x$ space, \mathbf{A} is the inverse matching operator, which is approximately known; x is a model vector, which is the matching data; and \mathbf{b} is the observed data (i.e., reference data). In the process of random noise suppression, \mathbf{A} is expressed as an operator matrix of random noise, x is data without random noise, and \mathbf{b} is the seismic record with random noise. When interpolating for missing seismic traces, \mathbf{A} is the operator for missing seismic data traces, x is the complete set of data, and \mathbf{b} is the seismic records with

Table 1 Physical meaning of **A** and **b** in Eq. (7)

	Matched filtering	Random noise suppression	Missing traces interpolation
A	Matched filtering operator matrix	Matrix with random noise	Factor matrix in missing traces
b	Reference seismic data	Data with random noise	Data containing missing traces

missing traces. In the following three cases, n is random noise. In this paper, all the problems, matching filter, interpolation, and noise suppression can be simultaneously performed. In the end, we can get the perfect results.

There are usually multiple solutions to linear inverse problems. The non-uniqueness arises owing to the influence of exploration conditions and noise. Therefore, to reduce the multiple solutions, we need to constrain solutions by introducing a regularization method (Scales and Gersztenkorn 1988; Chen et al. 1998; Malioutov et al. 2005a, b; van den Berg and Friedlander 2008; Gill et al. 2011; Aster et al. 2012; Yuan and Wang 2013; Yuan et al. 2015). The optimal matching is an unsolved problem from the perspective of information theory. Chen (1993) proved that using a sparse reconstruction model provides good results under certain conditions. Sparse constraint inversion (Daubechies et al. 2004; Malioutov et al. 2005a, b; Wright et al. 2009; Beck and Teboulle 2009a, b) is a regularization inversion method that was developed alongside compress sensing, and has been widely applied to seismic data processing (Yuan et al. 2012; Yuan and Wang 2013) and other problems.

In many applications, it is often the case that **A** is ill-conditioned, and in these cases, the least squares (LS) solution generally has large amount of calculation and is meaningless. A popular approach to solve Eq. (7) is the L1 regularization. We can solve Eq. (7) by minimizing misfit **J**:

$$\mathbf{J} = \|\mathbf{D}\mathbf{m} - \mathbf{b}\|_2^2 + \lambda \|\mathbf{m}\|_1. \quad (8)$$

In Eq. (8), **m** is the vector/matrix coefficients of x in curvelet domain; $\mathbf{D} = \mathbf{AR}$, where **R** represents the inverse transformation. That is to say: $x = \mathbf{Rm}$. Curvelets are able to provide sparse representation of the seismic data. The regularization parameter λ is used to balance the trade-off between the L2 norm of the data misfit and the L1 norm of the solution. Clearly, if λ is too large, a very sparse solution would be obtained, but the data may not be properly fit. Conversely, if λ is too small, the noisy data would be overfit and the solution becomes unstable. It is important to select an appropriate value of λ . In general, the parameter λ depends on the noise level of the data. Various methods has been developed that can be used to estimate λ . We construct the L-curve of the data for choosing the parameter λ . It also known as Pareto curve which has a negative slope

$$\lambda = \frac{\|(\mathbf{AR})^T r\|_\infty}{\|r\|_2}$$

with the residual r given by $\mathbf{ARm} - \mathbf{b}$. The shape of the Pareto curve should resemble ‘L’ letter closely and the value of λ that locates at the corner is the optimum λ , because it minimizes the L1-norm, while the L2-norm of the errors $\|\mathbf{ARm} - \mathbf{b}\|_2^2$ remains less or equal than the noise level.

Equation (8) has the sparse coefficient that is to be solved in the curvelet domain; it can be re-written as follows using **AR** in place of **D**:

$$\mathbf{J} = \|\mathbf{ARm} - \mathbf{b}\|_2^2 + \lambda \|\mathbf{m}\|_1. \quad (9)$$

The right side in Eq. (9) consists two parts. The first item $\|\mathbf{ARm} - \mathbf{b}\|_2^2$ is a data item, also known as fidelity item, which reflects the error between approximate solution and the measured data. Its role is to retain the original data characteristics in the MF and ensure the authenticity of the solution. The second term $\lambda \|\mathbf{m}\|_1$ is a smoothing item (regularization item). In Eq. (9), the sparse domain is a curvelet, so **R** represents the inverse curvelet transform. In this condition, **m** is the curvelet coefficient of matching traces with random noise and missing traces (or solely random noise) in curvelet domain, **b** is the reference seismic data with random noise and missing traces (or solely random noise), and **A** is the matching filter operator matrix. FISTA (Daubechies et al. 2004; Beck and Teboulle 2009a, b; Zhang et al. 2011) is adopted to solve Eq. (8). This algorithm can solve linear inversion problems effectively due to its fast convergence rate, meaning that it requires relatively few iterations. The pseudo code of FISTA, which defines the soft-threshold iteration equation to calculate \mathbf{m}_k in Eq. (8), is as follows:

$$\mathbf{m}_k = \text{soft} \left(\left(\mathbf{m}_k + \frac{t_k - 1}{t_{k+1}} (\mathbf{m}_k - \mathbf{m}_{k-1}) \right) + \frac{1}{\alpha} \mathbf{D}^H \mathbf{b} - \mathbf{D} \left(\mathbf{m}_{k-1} + \frac{t_k - 2}{t_k} (\mathbf{m}_{k-1} - \mathbf{m}_{k-2}) \right), \frac{\lambda}{2\alpha} \right). \quad (10)$$

The iteration step-size α controls the convergence speed. To ensure iterative convergence in the FISTA algorithm, $\alpha \geq \max \text{eig}((\mathbf{AR})^H(\mathbf{AR}))$ need to be established. In other words, α must be greater than the maximum eigenvalue of $(\mathbf{AR})^H(\mathbf{AR})$. This ensures the convergence of the algorithm. $\mathbf{D} \in \mathbb{R}^{m \times n}$ is forward process function. \mathbf{D}^H is adjoint matrix/operator. **A** is the matching filter operator matrix. **R** represents the inverse curvelet transform. In addition, t_k is a parameter that is updated with the iteration

as defined by the following equation, which represents the number of iterations:

$$t_{k+1} = \frac{1 + \sqrt{1+4t_k^2}}{2}. \tag{11}$$

Initialization, $t_1 = 1$. The term $\text{soft}(x,t)$, which is the soft threshold when the input x is a complex number, $x = ze^{i\omega}$, can be expressed as follows:

$$\text{soft}(x,t) = \begin{cases} (Z - t)e^{i\omega}, & \text{if } z > t \\ 0, & \text{if } z \leq t \end{cases} \tag{12}$$

Signal-to-noise definition

To evaluate the accuracy of data processing of the new method, we will introduce the signal-to-noise ratio (SNR) (Liu and Li 1997). The seismic data $a_{i,j}$ (M is the sample numbers, N is the trace number; $i = 1, \dots, M, j = 1, \dots, N$) are composed of valid signal and the noise that is randomly distributed and uncorrelated. Based on this assumption, we can obtain seismic data:

$$a_{i,j} = s_i + n_{i,j}, \tag{13}$$

where s_i is the amplitude of valid signal, and $n_{i,j}$ is the amplitude of noise. Therefore, the whole energy of seismic data is as follows:

$$E_s = N \sum_{i=1}^M s_i^2 = \frac{1}{N} \sum_{i=1}^M \left(\sum_{j=1}^N a_{i,j} \right)^2. \tag{14}$$

The whole energy of noise is as follows:

$$E_N = \sum_{i=1}^M \sum_{j=1}^N a_{i,j}^2 - E_s. \tag{15}$$

We can ultimately obtain SNR equation:

$$\begin{aligned} \text{SNR} &= 10 \times \log_{10} \left(\frac{E_s}{E_N} \right) \\ &= 10 \times \log_{10} \left(\frac{\sum_{i=1}^M \left(\sum_{j=1}^N a_{i,j} \right)^2}{N \sum_{i=1}^M \sum_{j=1}^N a_{i,j}^2 - \sum_{i=1}^M \left(\sum_{j=1}^N a_{i,j} \right)^2} \right). \end{aligned} \tag{16}$$

Example

In this section, two examples of synthetic data are employed to demonstrate the performance of the proposed MF method. Figure 3 presents block diagram of the general MF workflow used for seismic data. We verify the advantage of the new method by comparing the waveform coherency between reference data and MF

results. The phase spectra and amplitude spectra is very important not only in MF but also other case (time-frequency analysis). What we are concerned is the capability of the optimized MF, and the consistency between the MF results and reference seismic data waveform, phase, and amplitude will also be discussed. In addition, field data are used to verify the new MF method in a real-life case.

Synthetic data

Wedge convolution models constructed using different types of seismic wavelet can represent seismic records from different sources or periods. The methods used to distinguish layers and wedges are different for different wavelets. Here, we construct convolution models using two different types of wavelet. To test the validity of this method, we construct a model using a wedge and a thin layer to simulate real experimental conditions. We select low resolution seismic records as matching seismic data, and high resolution seismic records as reference seismic data. The seismic resolution includes the vertical and lateral resolution. The vertical resolution refers to the ability to distinguish the thickness of two adjacent reflective interfaces corresponding to the formation. The lateral

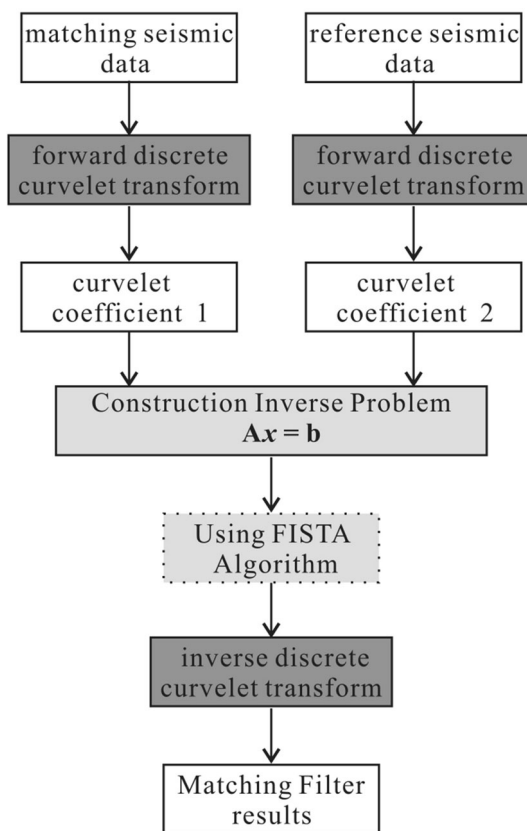


Fig. 3 Simplified block diagram of the matching filter workflow

resolution is the ability to distinguish the boundaries of two adjacent reflectors corresponding to the boundaries of the geological body. This paper refers to the vertical resolution. In different types of wavelet which have the same frequency, zero phase wavelet has higher vertical resolution. The high resolution refers to the ability to distinguish wedge. In other words, the thin layers are easy to distinguish.

The model includes 45 traces and the time interval of sampling is 2 ms. The lengths of the zero phase and minimum phase wavelets are 140 ms. The model thickness is 240 m (400 ms in the seismic stack section). Given that noise is unavoidable in actual seismic exploration, we use a noisy synthetic data set with a minimum phase wavelet (data set 1). Its time domain waveform is given in Fig. 4a and its SNR is -7.45 dB. Its norm is 12.9388, and standard deviation is 0.6304. The convolution model is simulated using a minimum phase seismic wavelet, and it has low resolution and low SNR. Figure 4e shows the frequency-wavenumber spectrum of data set 1. The spectra are obtained from analysis of a convolution model of the minimum phase seismic wavelet, with the main frequency band being $10\sim 80$ Hz (Fig. 5a, blue line). Because of the impact of the seismic wavelet type, the ability to distinguish wedges and thin layers is greatly reduced, which

hinders subsequent processing and interpretation. As the model is small, here, we use 32 angular windows at the third scale to decompose data set 1. We use forward and inverse DCT “via Wrapping” implementation according to the paper of Candès et al. 2006 (www.curvelet.org). We take a convolution model obtained from a minimum phase wavelet as the matching seismic data.

The synthetic seismic data sets 1 and 2 adopt the same reflection coefficient. We obtain the data set 2 using a zero phase wavelet convoluted in the same place, and add an amount of Gaussian noise. In addition, its SNR is 1.09 dB (Fig. 4b). Its norm is 10.0647, and standard deviation is 0.5058. The convolution model is simulated using a zero phase wavelet, and it has high resolution and high SNR. Figure 4f shows the frequency-wavenumber spectrum of data set 2. The amplitude spectral analysis reveals that the main frequency energy of seismic traces is concentrated within about $10\sim 80$ Hz (Fig. 5a, green line). We take synthetic data set 2 as the reference seismic data, as its high resolution, high SNR, and zero phase wavelet mean that the wedge and thin layer are easily distinguished. This is convenient for subsequent processing and interpretation of seismic data.

Figure 4c is seismic profiles that show the MF results after applying the new method. The time resolution and SNR is improved. Figure 4g shows the frequency-

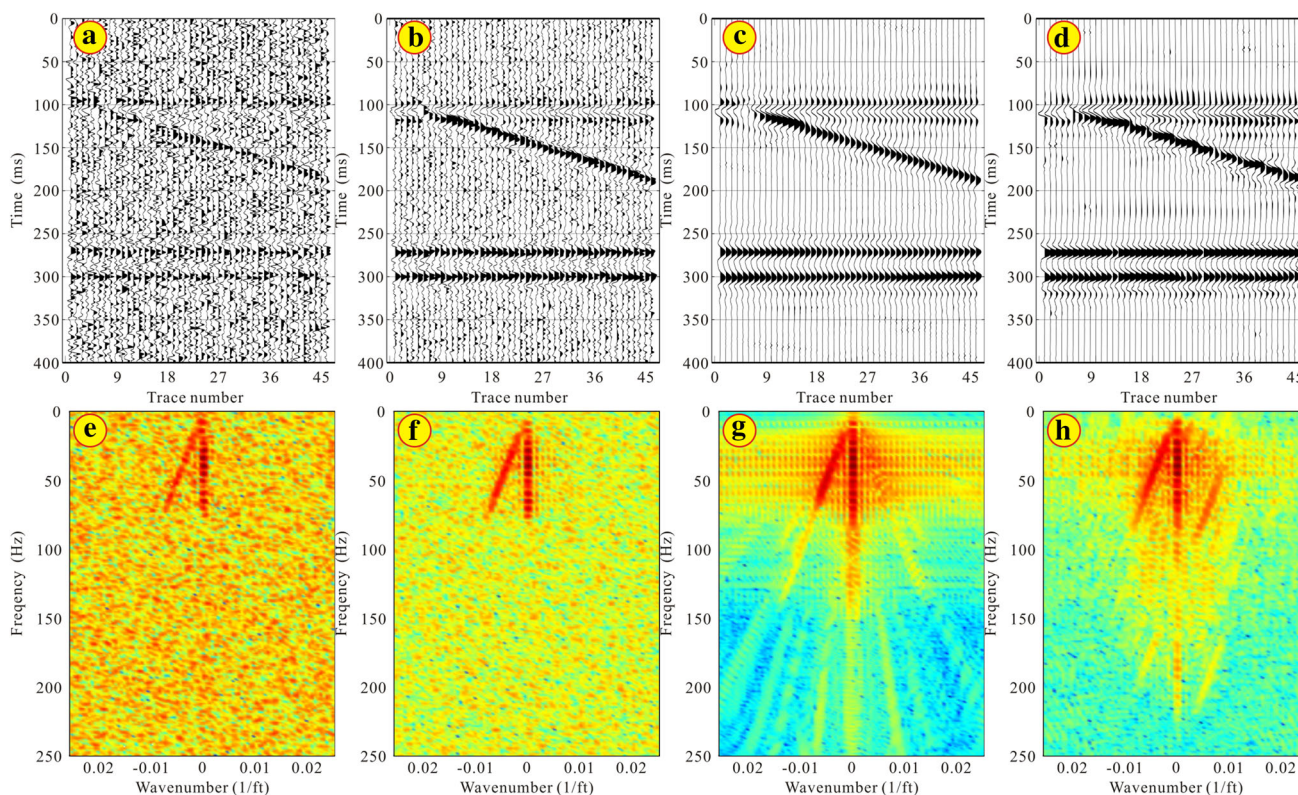


Fig. 4 **a** Synthetic data set 1. **b** Synthetic data set 2. **c** MF results in the curvelet domain. **d** MF results in the wavelet domain. **e** FK spectrum of synthetic data set 1. **f** FK spectrum of synthetic data set 2. **g** FK spectrum of MF results (c). **h** FK spectrum of MF results (d)

wavenumber spectrum. The waveform is similar to that of synthetic data set 2; SNR reaches 14 dB. The amplitude and phase spectra are also highly consistent between the MF results and reference seismic data set 2 (Fig. 5a, b, red line), which shows that the proposed method maintains amplitude and phase information. The noise in the seismic data is reduced and the clarity of the thin layer and wedge is improved. Figure 5c shows residuals between reference data and MF result data in curvelet domain. Satisfying MF results are obtained using the new method.

The result of applying FISTA and MF of the wavelet domain is shown in Fig. 4d. Figure 4h shows the frequency wavenumber spectrum. The SNR reaches 10 dB. Compared with MF results in the curvelet domain, MF results in the wavelet have lower SNR and lower waveform

similarity. The amplitude and phase (Fig. 5a, b, purple line) spectra are also low consistent between the MF results and reference seismic data set 2. From the FK spectrum of the matching traces (Fig. 4a), it can be concluded that the random noise is widely distributed and the noise energy is very large. From the FK spectrum of the reference traces (Fig. 4b), it can be concluded that the noise energy is small. We can get the MF results using the new method, and random noise distribution is less in FK spectrum. The advantage of obtaining MF results using the new method is that the random noise is less. Compared with the FK spectra obtained using the two methods, the new one has less random noise and richer frequency band.

The new method removes noise and yields good results from MF. We also compare the SNR data using four

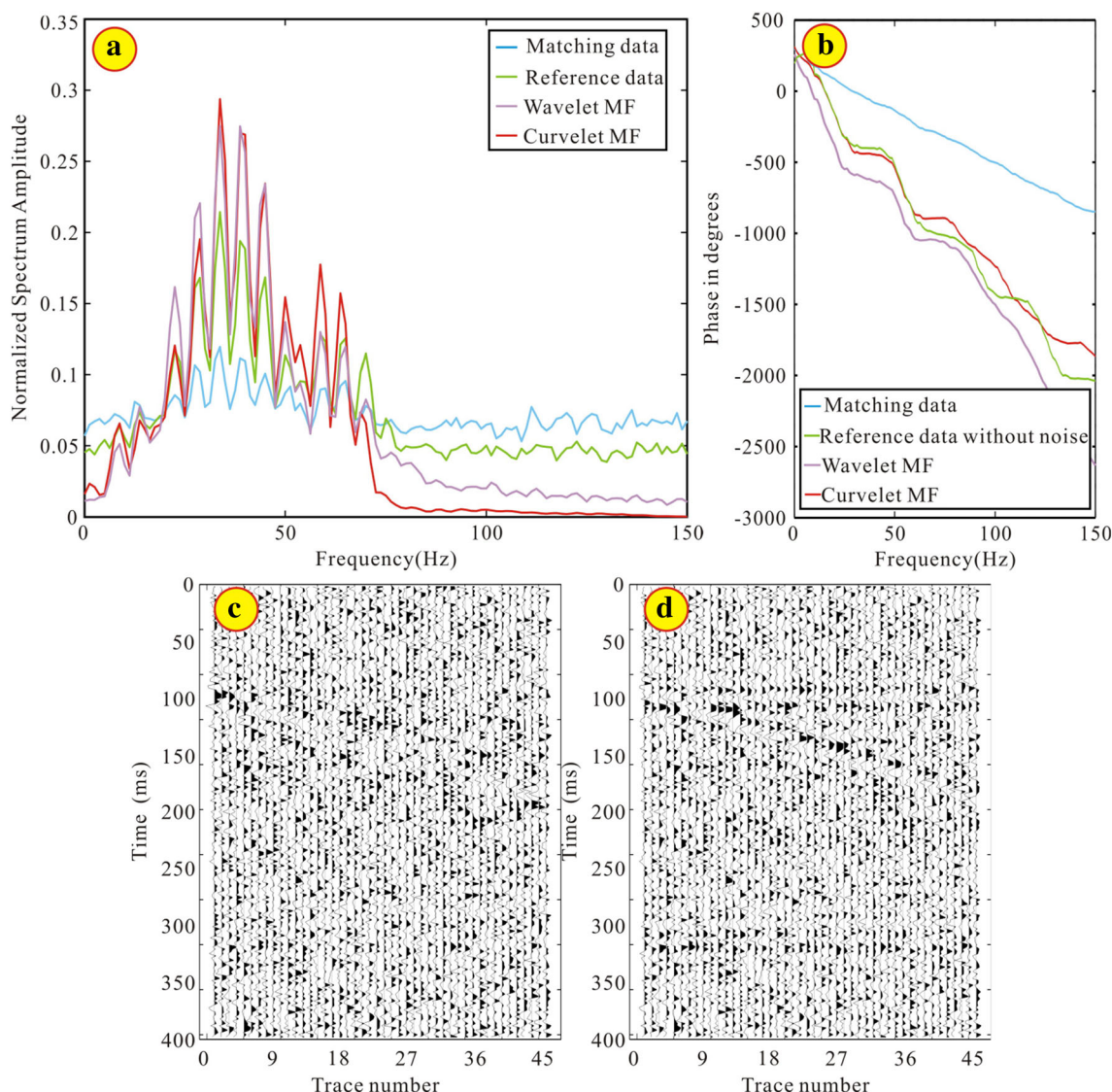


Fig. 5 Compared with the amplitude spectra **a** and phase spectra **b**. **c** Residual displays MF results (Fig. 4c) to the reference data (Fig. 4b) in curvelet domain. **d** Residual displays MF results (Fig. 4d) to the reference data (Fig. 4b) in wavelet domain

different MF methods (Table 2). The analysis employed two types of processing method (MF in Wavelet domain and MF in curvelet domain). We use two MF methods to make comparisons and analysis (MF in wavelet domain and MF in curvelet domain). Both methods use the same number of iterations in FISTA. Therefore, the new method not only improves SNR, but also yields excellent MF results. For the data that we mention in Table 2, we use a zero phase wavelet synthetic data set with different amount of Gaussian noise as the reference data.

Given the likelihood of missing traces in actual seismic data, traces are randomly removed from the synthetic seismic data set mentioned above to provide a more realistic situation. For synthetic data set 1, 40% of traces were randomly removed to yield synthetic data set 3 (Fig. 6a), which has an SNR of -7.45 dB. Figure 6e shows the frequency-wavenumber spectra of data set 3. This data set is used as matching seismic data.

Applying a similar 40% random loss to simulation data set 2 gives synthetic data set 4 (Fig. 6b), which has a SNR of 1.09 dB. Figure 6f shows the frequency-wavenumber spectra of data set 4, after frequency-wavenumber analysis. This data set is used as reference seismic data owing to its high SNR and high time resolution.

Curvelet matching and interpolation of missing data yield the result, as shown in Fig. 6c. It also shows the accompanying frequency-wavenumber spectra (Fig. 6g). The MF results are obtained using FISTA and MF in the curvelet domain. The restored waveform (Fig. 6c), amplitude spectrum, and phase spectrum (Fig. 7a, b) are consistent with the equivalent features with the reference data. The SNR is 12 dB. Therefore, we obtained good results in terms of suppressing noise and interpolating missing data. Figure 7c shows residuals between reference data (Fig. 6b) and MF results (Fig. 6c) in curvelet domain. The proposed method proved to be the sparse-constrained matching filter in the curvelet domain.

The MF in the wavelet domain obtains the result shown in Fig. 6d, which also shows the accompanying frequency-wavenumber spectra (Fig. 6h). The SNR is 8 dB. Compared with MF results in the wavelet domain, MF results in the curvelet domain have higher SNR, waveform similarity. The amplitude and phase (Fig. 7a, b) spectra are also low consistent between the MF results and reference seismic data set 4. From the FK spectrum of the matching traces (Fig. 6a), it can be concluded that the random noise is widely distributed and the noise energy is very large. From the FK spectrum of the reference traces (Fig. 6b), it can be concluded that the noise energy is small. We can get the MF results using the new method, and random noise distribution is less in FK spectrum (Fig. 6c). Compared with the FK spectra obtained using the two methods, the random noise distribution of the FK spectrum using the

Table 2 Comparison of SNR data obtained using four different MF methods

Matching data		Reference data		Wiener filter (dB)	Pseudomultichannel (dB)	Wavelet (dB)	Curvelet (dB)
SNR (dB)	Noise parameters	SNR (dB)	Noise parameters				
	Standard deviation	Norm	Standard deviation	Norm			
-7.45	$\sigma_{M1} = 0.6304$	$\ N_{M1}\ = 12.9388$	$\sigma_{R1} = 0.5058$	$\ N_{R1}\ = 10.0647$	-0.83	2.54	4.72
-6.34	$\sigma_{M2} = 0.5528$	$\ N_{M2}\ = 10.9009$	$\sigma_{R2} = 0.3350$	$\ N_{R2}\ = 6.7803$	1.41	5.68	9.10
-5.21	$\sigma_{M3} = 0.4960$	$\ N_{M3}\ = 10.1981$	$\sigma_{R3} = 0.2345$	$\ N_{R3}\ = 4.8340$	3.28	7.44	12.18
-3.15	$\sigma_{M4} = 0.3868$	$\ N_{M4}\ = 8.0830$	$\sigma_{R4} = 0.1668$	$\ N_{R4}\ = 3.5087$	4.59	7.68	13.12
2.35	$\sigma_{M5} = 0.2015$	$\ N_{M5}\ = 4.1851$	$\sigma_{R5} = 0.1052$	$\ N_{R5}\ = 2.1706$	8.66	8.68	15.98
8.07	$\sigma_{M6} = 0.1062$	$\ N_{M6}\ = 2.1649$	$\sigma_{R6} = 0.0748$	$\ N_{R6}\ = 1.4840$	13.52	16.96	19.16

The unit for SNR is dB. The matching data, reference data, wiener filter, pseudo multichannel, wavelet, and curvelet show SNR in dB. The terms ‘wavelet’ and ‘curvelet’ represent the wavelet transform and curvelet transform used in the MF method, respectively

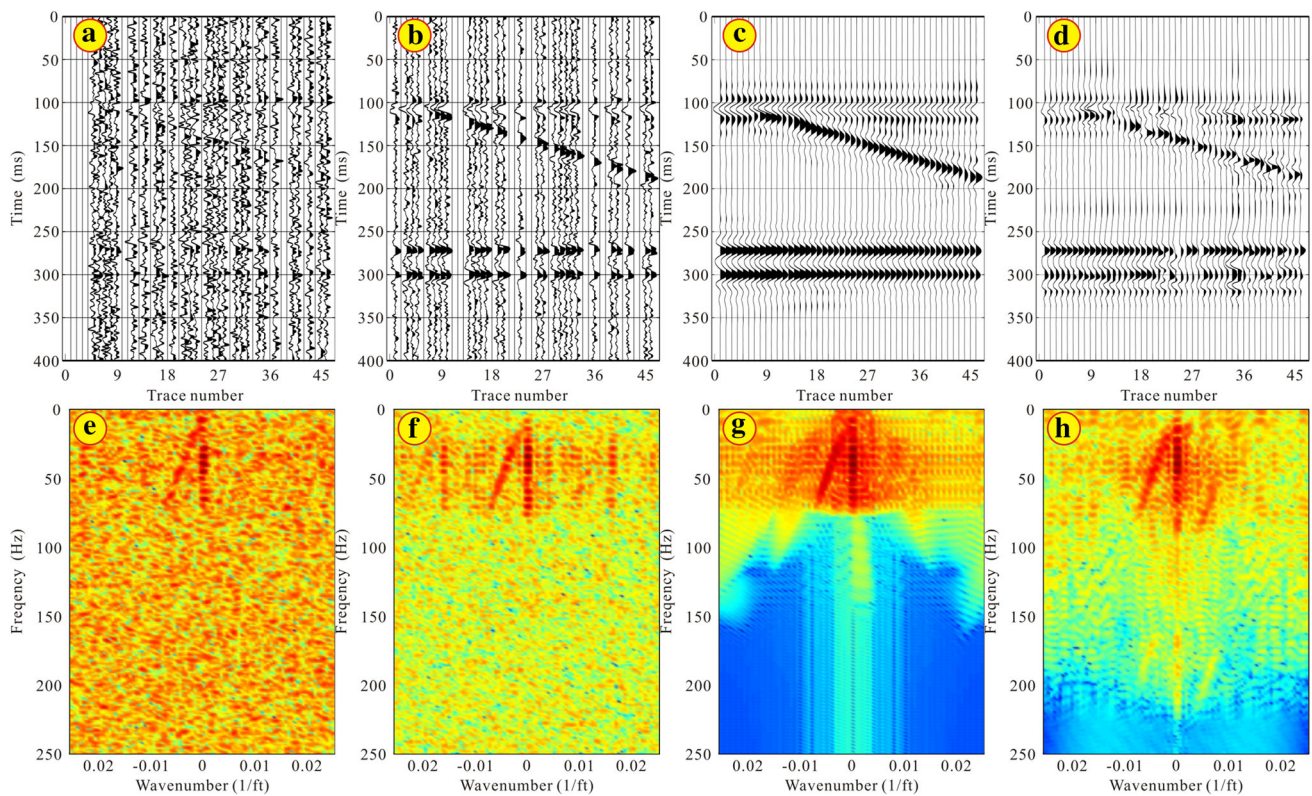


Fig. 6 **a** Synthetic data set 3. **b** Synthetic data set 4. **c** MF results in the curvelet domain. **d** MF results in the wavelet domain. **e** FK spectrum of synthetic data set 3. **f** FK spectrum of synthetic data set 4. **g** FK spectrum of MF results (c). **h** FK spectrum of MF results (d)

new method is less and the frequency band is richer. The new method has less false information than the traditional method in FK spectrum.

We assess the validity of the proposed method using different percentages of missing traces with a certain amount of noise as reference data, and synthetic data set 3 as match data. The goal is to verify the influence of the algorithm with different loss effects on the MF result. We tested the data set listed in Table 3 and then compared the MF results for different missing traces with two reference data having fixed SNR. We compare the impact of the reference data with different attributes (i.e., amount of noise and percentage of missing traces in the reference data) on the MF results. The percentage of missing reference data has a strong influence on the MF results, which shows that the MF results are strongly affected by the random loss of reference seismic data. The SNR of reference seismic data has a little effect on the MF results. Although missing traces have a strong influence on the SNR of MF results, the results are still satisfactory. The consistency of the waveform and SNR enables us to evaluate the MF results and verify whether the outcome is acceptable. In this study, we consider MF results to be acceptable if two conditions are met: the waveform semblance coefficient exceeds 0.85 and the SNR of the MF

results exceeds 4.5 dB. The matching of seismic data determines the value of α in Eq. (10). The value of α has a little influence on the iteration results, meaning that the match trace has a little effect on the MF results. In other words, the attributes of the matching data (i.e., the amount of noise and the percentage of missing traces in the matching data) have a little effect on the quality of the MF results. For the data that we list in Table 3, we add Gaussian noise to a zero phase wavelet synthetic data set to obtain a noise data set. Then, we randomly delete some traces of the noise data set to get the reference data.

Real data example

Post-stack data

We choose post-stack seismic data collected from the same area in 1997 and 2005 to assess the proposed method using field data. There are 70 traces and the trace spacing is 12.5 m. The sampling time interval is 2 ms and the target time depth is from 500 to 1000 ms. Figure 8a shows seismic data 1 collected in the region in 1997. The data show relatively poor event continuity and some traces are missing. Consequently, further interpretation and processing would be difficult. Figure 8b shows seismic data 2 from the same region

Fig. 7 Compared with the amplitude spectra **a** and phase spectra **b**. **c** Residual displays MF results Fig. 6c to the reference data in Fig. 6b in curvelet domain. **d** Residual displays MF results Fig. 6d to the reference data in Fig. 6b in wavelet domain

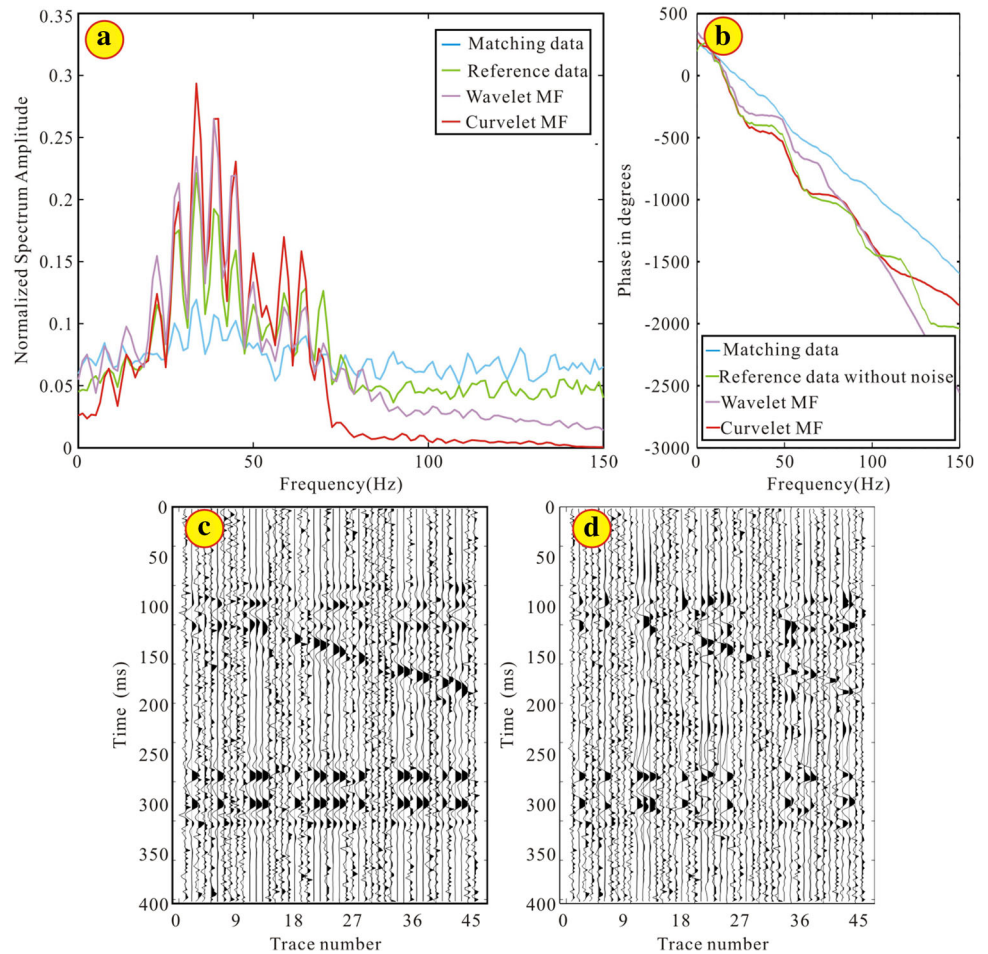


Table 3 Comparison of MF results obtained using different percentages of missing traces with two fixed SNR

Random loss of reference data (percent)	SNR of reference data (dB)	Noise parameters		MF results (dB)	Waveform semblance coefficient
		Standard deviation	Norm		
80%	3.63	$\sigma_{R1} = 0.1850$	$\ N_{R1}\ = 3.8618$	2.26	0.77
	-3.33	$\sigma_{R2} = 0.4099$	$\ N_{R2}\ = 8.4106$	1.96	0.74
75%	3.63	$\sigma_{R1} = 0.1850$	$\ N_{R1}\ = 3.8618$	4.02	0.83
	-3.33	$\sigma_{R2} = 0.4099$	$\ N_{R2}\ = 8.4106$	3.93	0.83
70%	3.63	$\sigma_{R1} = 0.1850$	$\ N_{R1}\ = 3.8618$	5.60	0.88
	-3.33	$\sigma_{R2} = 0.4099$	$\ N_{R2}\ = 8.4106$	5.44	0.86
60%	3.63	$\sigma_{R1} = 0.1850$	$\ N_{R1}\ = 3.8618$	6.67	0.91
	-3.33	$\sigma_{R2} = 0.4099$	$\ N_{R2}\ = 8.4106$	5.92	0.88
40%	3.63	$\sigma_{R1} = 0.1850$	$\ N_{R1}\ = 3.8618$	8.43	0.94
	-3.33	$\sigma_{R2} = 0.4099$	$\ N_{R2}\ = 8.4106$	8.40	0.93

The ‘MF results’ represent the SNR after using FISTA and MF in the curvelet domain. The ‘Random loss of reference data’ shows the percentage of missing traces. The ‘SNR of reference data’ and ‘MF results’ show SNR in dB. The waveform semblance coefficient is obtained from the MF results and the reference data

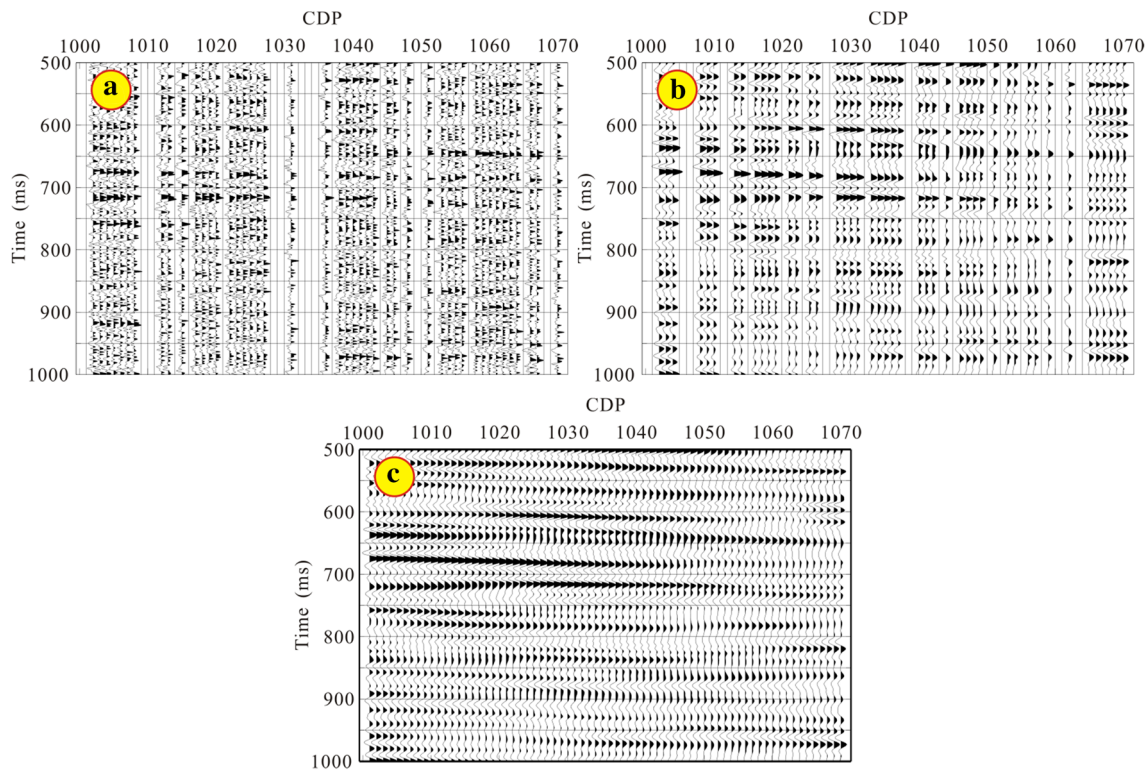


Fig. 8 Seismic data from a given region collected in **a** 1997 and **b** 2005. **c** MF results obtained using FISTA and MF in the curvelet domain

collected in 2005. While some traces are missing, this set shows better event continuity, which makes it convenient for subsequent processing and interpretation.

We processed the data collected in different years using the new methods to verify the effect of interpolation and MF in the curvelet domain. We use 32 angular windows at fourth scale to decompose the data, which mitigates the effect of noise and effectively separates the signals. The result of MF is shown in Fig. 8c. Figure 9c is the residual record of results from MF results (Fig. 8c) and reference data from Fig. 8b. Satisfactory results are obtained by processing the practical data by interpolation and matching in the curvelet domain. Our method performs well in maintaining the waveforms of the field data, thus greatly improving the quality of the seismic data. The compared amplitude spectrum and phase spectrum (Fig. 9a, b) are consistent with the reference data. We obtained satisfying results in terms of interpolating missing data and suppressing noise.

Pre-stack data

Here, we demonstrate the application of the new method to a real pre-stack data acquired in a same area. We choose pre-stack seismic data acquired in 2006 and 2009 to assess the proposed method. There are 41 traces and the trace spacing is 12.5 m. The sampling time interval is 1 ms. Seismic data 3 (Fig. 10a) acquired in 2006, which were

randomly removed 40% traces. This data set is used as matching seismic data. Applying a similar 40% random loss to data acquired in 2009 gives seismic data 4 (Fig. 10b). This data set is used as reference seismic data.

The MF results are obtained using FISTA and MF in the curvelet domain. Curvelet matching and interpolation of missing data yield the result shown in Fig. 10c. Our method performs well in maintaining the waveforms of the pre-stack data. The residual displays MF results to the reference data in Fig. 11c. Figure 11a shows the amplitude spectra of different seismic data. Therefore, we obtained satisfying results in terms of suppressing noise and interpolating missing data in pre-stack data. However, it is difficult to maintain the consistent of phase information (Fig. 11b) between the MF results and reference data when processing pre-stack data. Other linear noise is introduced as the MF results of regular noise.

Conclusion

A match filter is used within many important areas such as splicing seismic data, 4-D seismic monitoring, and so on. The traditional MF method is subject to many restrictions and is usually difficult to overcome the impact of noise and missing data. Based on the traditional MF, we propose the curvelet domain L1 norm optimal MF. The MF, missing

Fig. 9 Compared with the amplitude spectra **a** and phase spectra **b**. **c** Residual displays MF results Fig. 8b to the reference dat

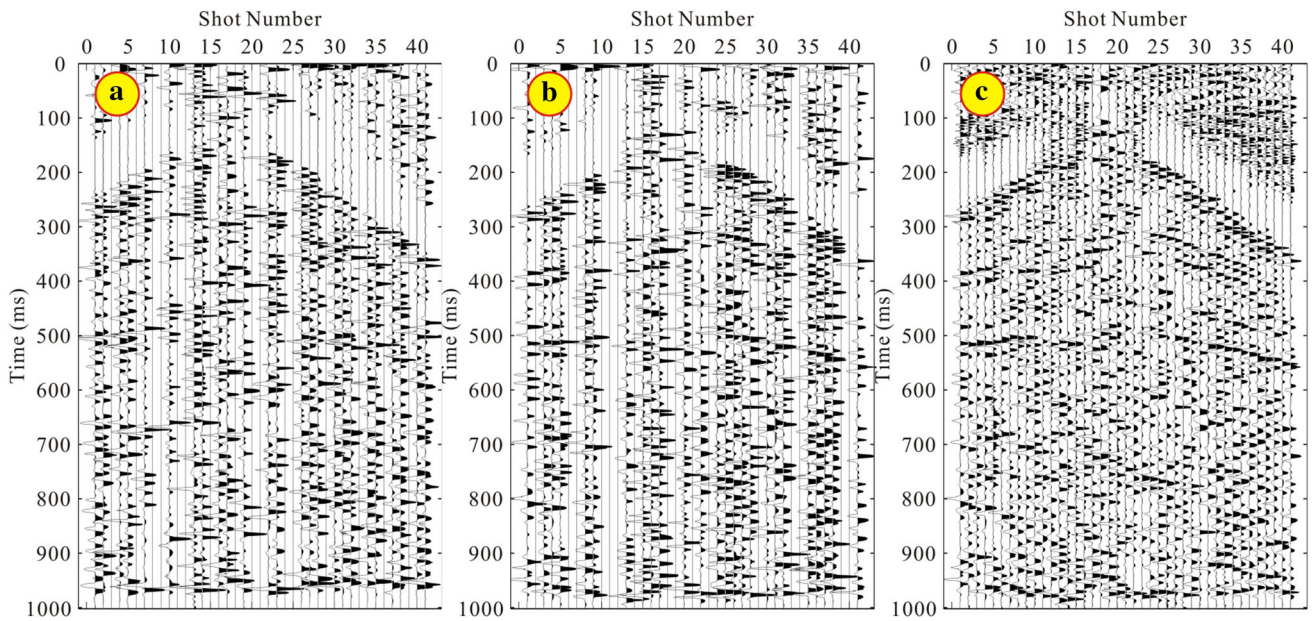
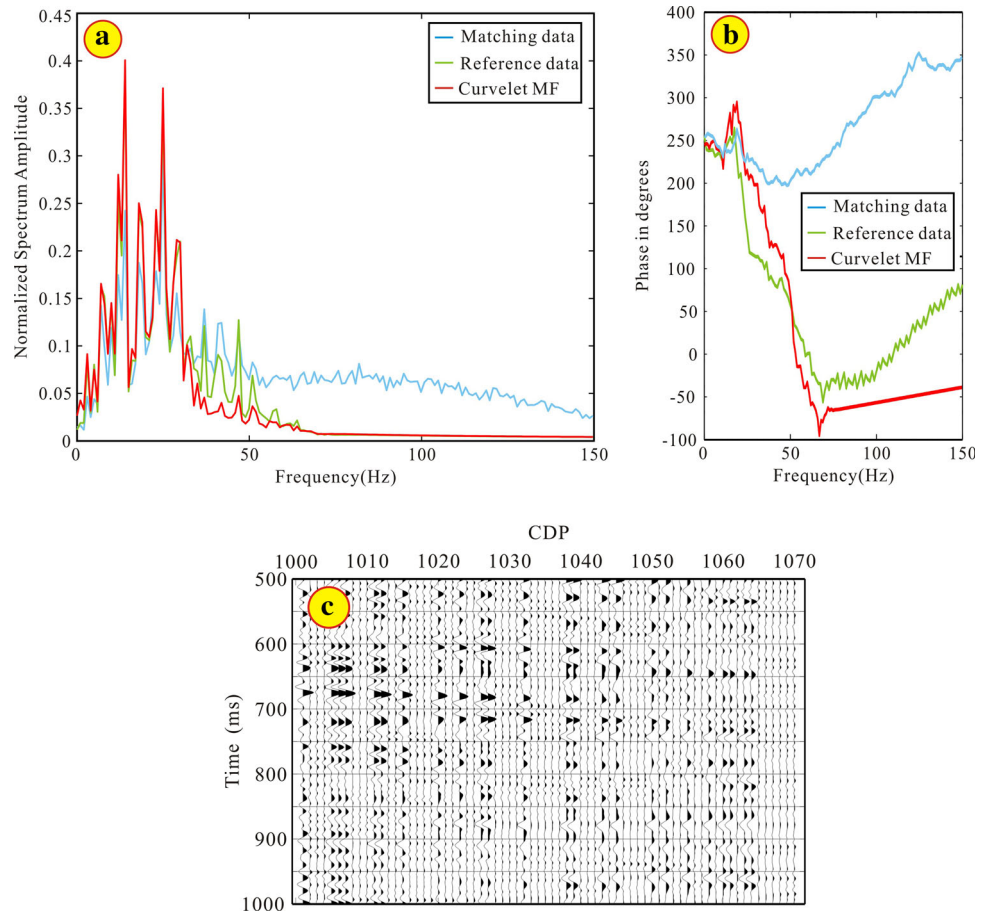
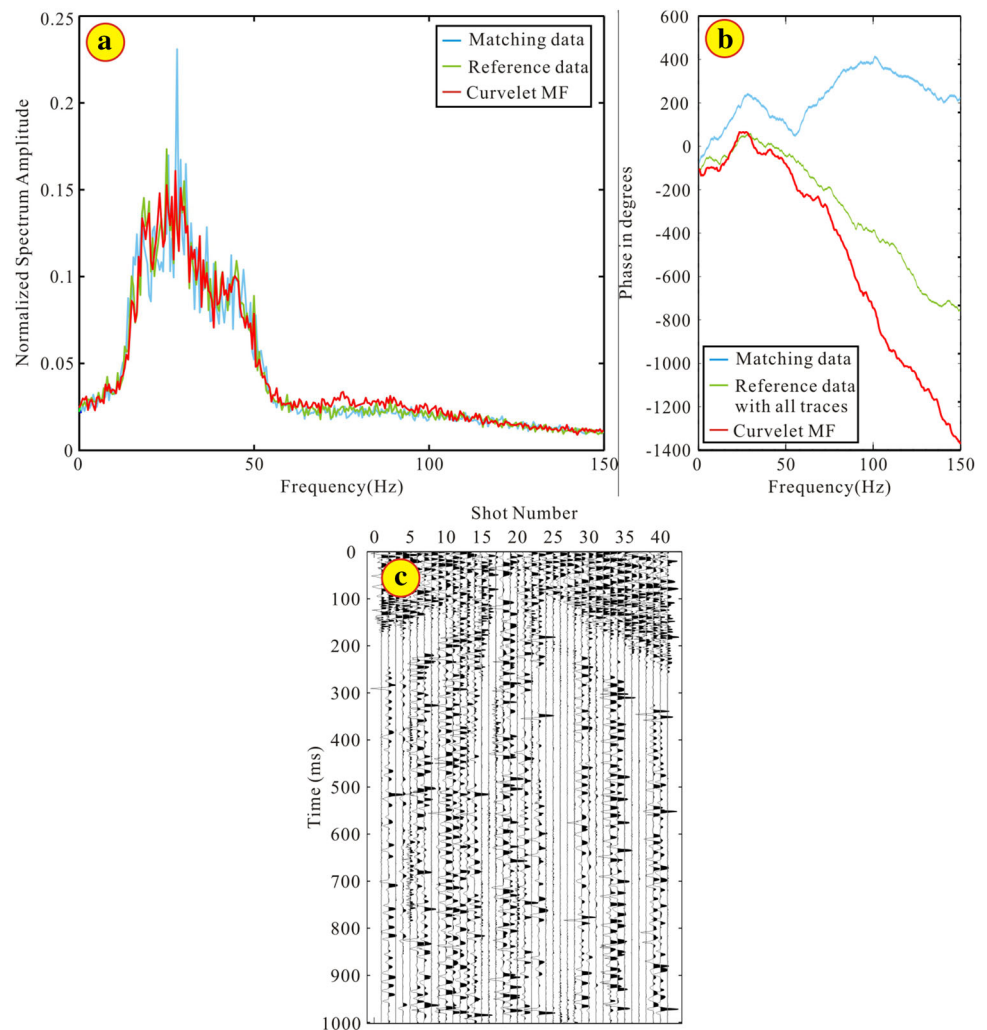


Fig. 10 Seismic data from a given region collected in **a** 2006 and **b** 2009. **c** MF results in the curvelet domain

Fig. 11 Comparing the amplitude spectra **a** and phase spectra **b**. **c** Residual displays MF results Fig. 10b to the reference data in Fig. 10c



trace and random noise problems can be simultaneously solved via FISTA algorithm, and it will increase the efficiency in seismic data processing and improve the SNR.

Compared with the L1 norm optimal match filter in the wavelet domain, the new method improves the SNR and interpolates missing seismic data. We tackle these three inversion problems simultaneously using the FISTA in the curvelet domain. Our results indicate that the method not only performs optimal matching, it also removes random noise and interpolates missing seismic data. Examples using both simulated and real data revealed that the method can achieve the desired results while greatly improving efficiency and increasing the SNR.

However, the new method also has some defects, such as seriously affected by coherent noise, the amount of missing traces. If the missing trace is large and the SNR is very low, it will seriously affect the MF results. Especially when it happens in the reference trace, we are supposed to interpolate the data and attenuate the noise. Then, we can make up a MF.

We verified that L1 optical norm matching with a signal extracted from the curvelet domain can suppress noise and interpolate missing data through an analysis of simulation data. The seismic data obtained using the proposed method are more analogical, and better maintain the amplitude and phase spectrum between the MF results and reference seismic data.

Finally, we verified the feasibility of the method by applying it to real data. Our method represents a new way of solving the matching problem (i.e., combining the optical norm and curvelet decomposition) and it achieves good results. The new method comprising a synthetic model and field data processing, which contains noise and 40% missing traces (Figs. 6a, 8a), yields satisfactory results after 300 iterations. The noise level has a little effect on the matching results. If the amount of missing seismic data exceeds 70%, the matching results are seriously impaired.

Acknowledgements The research is sponsored by the Natural Science Foundation of China (No. 41404097, 41404092), Science and Technology Development Project of Jilin Province (No.

20150520071JH), China Postdoctoral Science Foundation (No. 2015M571366), and SinoProbe-Deep Exploration in China (SinoProbe-09-04).

References

- Aster RC, Borchers B, Thurber CH (2012) *Parameter estimation and inverse problems*, 2nd edn. Academic Press, Cambridge
- Beck A, Teboulle M (2009a) A fast iterative shrinkage-thresholding algorithm for linear inverse problems. *SIAM J Imag Sci* 2:183–202
- Beck A, Teboulle M (2009) A fast iterative shrinkage-thresholding algorithm with application to wavelet-based image deblurring. In: *IEEE international conference on acoustics, speech and signal processing*, pp 693–696
- Berkhout AJ (1977) Least-squares inverse filtering and wavelet deconvolution. *Geophysics* 42:1369–1383
- Candès EJ, Demanet L (2003) Curvelets and Fourier integral operators. *CR Math* 336:395–398
- Candès EJ, Donoho DL (2004) New tight frames of curvelets and optimal representations of objects with C^2 singularities. *Commun Pure Appl Math* 57:219–266
- Candès EJ, Demanet L, Donoho DL, Ying LX (2006) Fast discrete curvelet transforms. *Multiscale Model Simul* 5:861–899
- Chen QS (1993) *Digital signal processing of principia mathematica*. Petroleum Industry Press, Beijing
- Chen SS, Donoho DL, Saunders MA (1998) Atomic decomposition by basis pursuit. *SIAM J Sci Comput* 20:33–61
- Cheng JX, Zhu LH, Yang CC, Chen J (2004) Putting 3-D seismic data together based on wavelet transform. *Oil Geophys Prospect* 39:406–408
- Daubechies I, Defrise M, De Mol C (2004) An iterative thresholding algorithm for linear inverse problems with a sparsity constraint. *Commun Pure Appl Math* 57:1413–1457
- Douma H, de Hoop M (2007) Leading-order seismic imaging using curvelets. *Geophysics* 72:S231–S248
- Gill PR, Wang A, Molnar A (2011) The in-crowd algorithm for fast basis pursuit denoising. *IEEE Trans Signal Process* 59:4595–4605
- Górszczyk A, Adamczyk A, Malinowski M (2014) Application of curvelet denoising to 2D and 3D seismic data—practical considerations. *J Appl Geophys* 105:78–94
- Górszczyk A, Cyz M, Malinowski M (2015a) Improving depth imaging of legacy seismic data using curvelet-based gather conditioning: a case study from Central Poland. *J Appl Geophys* 117:73–80
- Górszczyk A, Malinowski M, Bellefleur G (2015b) Enhancing 3D post-stack seismic data acquired in hardrock environment using 2D curvelet transform. *Geophys Prospect* 63:903–918
- Hennenfent G, Cole J, Kustowski B (2011) Interpretative noise attenuation in the curvelet domain. In: *81th Annual international meeting, SEG, expanded abstracts*, pp 3566–3570
- Herrmann FJ (2009) Curvelet-domain matched filtering. In: *79th Annual international meeting, SEG, expanded abstracts*, pp 3643–3649
- Herrmann FJ, Wang DL, Hennenfent G, Moghaddam PP (2008) Curvelet-based seismic data processing: a multiscale and non-linear approach. *Geophysics* 73:A1–A5
- Jin L, Chen XH, Li JY (2005) A new method for time-lapse seismic matching filter based on error criteria and cyclic iteration. *Chin J Geophys* 48:698–703
- Liu Y, Li CC (1997) Some methods for estimating the signal/noise ratio of seismic data. *Oil Geophys Prospect* 32:257–262
- Long Y, Han LG, Han L, Tan CQ (2012) L1 norm optimal solution match processing in the wavelet domain. *Appl Geophys* 9:451–458
- Malioutov DM, Cetin M, Willsky AS (2005a) Homotopy continuation for sparse signal representation. *IEEE Int Conf Acoust Speech Signal Process* 5:733–736
- Malioutov DM, Cetin M, Willsky AS (2005b) A sparse signal reconstruction perspective for source localization with sensor arrays. *IEEE Trans Signal Process* 53:3010–3022
- Norman K, Townsley J (2006) Using an interactive match filter to advance interpretation. In: *76th 85th Annual international meeting, SEG, expanded abstracts*, pp 1068–1072
- Robinson EA (1957) Predictive decomposition of seismic traces. *Geophysics* 22:767–778
- Scales JA, Gersztenkorn A (1988) Robust methods in inverse theory. *Inverse Prob* 4:1071–1091
- Shen HL, Tian G, Shi ZJ (2013) Partial frequency band match filtering based on high sensitivity data: method and applications. *Appl Geophys* 10:15–24
- Shi D, Milkereit B (2015) Migration-induced noise reduction using fast discrete curvelet transform. In: *85th Annual International Meeting, SEG, expanded abstracts*, pp 2001–2006
- Shi ZJ, Tian G, Dong SX, He HY, Wang ZJ (2005) Matching filtering of geophone coupling for high-frequencies of seismic data in desert area. *Oil Geophys Prospect* 44:261–263
- van den Berg E, Friedlander MP (2008) Probing the Pareto Frontier for basis pursuit solutions. *SIAM J Sci Comput* 31:890–912
- Wallace R, Gray FD (1992) Network match filters: a least-squares technique for minimizing seismic mis-ties. In: *62th Annual international meeting, SEG, expanded abstracts*, pp 1112–1115
- Wang YB, Zhu ZY, Jiang XD (2011) A pseudo-multichannel matching filter application to time-lapse seismic matching processing. In: *Shenzhen 2011 international geophysical conference technical program expanded abstracts*, pp 1803–1807
- Wang SX, Yuan SY, Ma M, Zhang R, Luo CM (2015) Wavelet phase estimation using ant colony optimization algorithm. *J Appl Geophys* 122:159–166
- Wiener N (1949) *Extrapolation, interpolation, and smoothing of stationary time series, with engineering applications*. Technology Press of the Massachusetts Institute of Technology, Cambridge
- Wright S, Nowak RD, Figueiredo MAT (2009) Sparse reconstruction by separable approximation. *IEEE Trans Signal Process* 57:2479–2493
- Wu DL, Jiang Y, Chen ZM (2006) Application of cascade matched filtering in mixed source data processing. *Geophysl Prospect Pet* 45:611–614
- Yuan SY, Wang SX (2013) Spectral sparse Bayesian learning reflectivity inversion. *Geophys Prospect* 61:735–746
- Yuan SY, Wang SX, Li GF (2012) Random noise reduction using Bayesian inversion. *J Geophys Eng* 9:60–68
- Yuan SY, Wang SX, Luo CM, He YX (2015) Simultaneous multitrace impedance inversion with transform-domain sparsity promotion. *Geophysics* 80:R71–R80
- Zhang LL, Wang HX, Xu YB, Wang D (2011) A fast iterative shrinkage-thresholding algorithm for electrical resistance tomography. *WSEAS Trans Circuits Syst* 10:393–402
- Zhang M, Wang YH, Li ZC, Yu HC, Ge DM (2014) Prestack cross-equalization based on pseudo-multichannel matching filter in time-lapse seismic. In: *84th Annual international meeting, SEG, expanded abstracts*, pp 4940–4944

Combined high-resolution aeromagnetic and radiometric mapping of uranium mineralization and tectonic settings in Northeastern Nigeria

A. A. Adepelumi¹ · A. H. Falade¹

Received: 18 April 2017 / Accepted: 24 August 2017 / Published online: 4 September 2017
© Institute of Geophysics, Polish Academy of Sciences & Polish Academy of Sciences 2017

Abstract Geological lineaments, depths to the basement, uranium concentrations, and remobilization in parts of the Upper Benue Trough, covering about $55 \times 55 \text{ km}^2$ (longitudes $11^\circ 30' - 12^\circ 00' \text{E}$ and $10^\circ 30' - 10^\circ 30' \text{N}$), Northeastern Nigeria were investigated using integrated High-Resolution Aeromagnetic Data (HRAD) and radiometric data. This was with a view to identifying the potential zones of uranium occurrence in the area. The HRAD was processed to accentuate anomalies of interest and depths estimate of 150–1941 m were obtained from source parameter imaging technique. The results from the superposition of the horizontal gradient magnitude, analytical signal amplitude, first vertical derivative, and 3D Euler solutions of the HRAD revealed that the study area was dissected by linear structures that trend ENE–WSW, NE–SW, E–W, NNE–SSW, WNW–ESE, and NW–SE; among which the ENE–WSW and NE–SW trends dominated. Analyses of radiometric data showed that uranium ores in the study area were possibly remobilized epigenetically from the granitic rocks, and were later deposited into sedimentary rocks (Bima formation). Burashika group (Bongna hills) and Wawa area of the study area showed vein-type deposits, while the anatectic migmatite in the northeastern region and the uranium rich Bima formation showed both fault/fracture and contact types of deposition. It was also observed the northwesterly and southeasterly, dominant dip direction, dipping faults dip in the same direction as the paleocurrent direction (direction of depositions of sediments), and trend in a direction perpendicular

to the hypothetical direction of uranium deposition. The study concluded that the studied area is dissected by several linear structures and the studied area possibly contains deposits of uranium ore, which are likely to be found in: the Bima Sandstones of Wade, Shinga, Bima hill, Wuyo, Teli, Bryel, Dali, Barkan, Gasi, Kunkun, Boragara, Deba, and Gberundi localities; the anatectic migmatite at Kubuku, Whada, and Hyama; and the Bongna hills and agglomerates around Burashika, Kawaba, and Galu.

Keywords Uranium · Radiometric · Aeromagnetic · Sandstone · Fault · Vein deposit

Introduction

Epileptic power supply has been of constant increase in Nigeria due to consistent increase in energy demand. In 2001, electricity generation went down from the installed capacity of about 5600 MW to an average of about 1750 MW, as compared to a load demand of 6000 MW (Sambo 2008). In addition, energy demand was projected to rise from 5746 MW in 2005 to 297,900 MW in the year 2030, which translates to construction of 11,686 MW every year to meet this demand (Sambo 2008). To meet this demand, nuclear energy is consistently being mentioned in government circles, but it is not optimistic at present. However, it may be adopted in the near future.

Uranium, being the principal fuel for world's nuclear plants, has become a valuable source of energy in many countries (Tauchid 1993). It is a very dense (19 g cm^{-3}) radioactive metallic element with an abundance of energy. Economical deposition of uranium can be found in a variety of rocks and the solubility of uranium in water has

✉ A. A. Adepelumi
aadelu@oauife.edu.ng; adelu@gmail.com

¹ Geology Department, Obafemi Awolowo University, Ile-Ife, Nigeria

enhanced its deposition and also accounts for its presence in surface water, ground water, and sea. In Nigeria, significant uranium occurrence was noted during the 1976–1983 search period. The ignimbrite field in Niger was observed, and the significant radiometric anomaly was shown with an unidentified source (Bowden et al. 1981). Further search that was conducted in Zona, Northeastern Nigeria, between years 1995 and 2000 revealed the Precambrian basement/Cretaceous sediment unconformity uraniumiferous anomaly in the area (Suh et al. 1998). Other radiometric anomalies were seen in Mika and Ghumchi, with their sources traced to granitic bodies (Maurin and Lancelot 1990; Funtua and Okujeni 1996; Suh and Dada 1998). This uranium anomaly revealed in Zona is arguably the most significant sandstone hosted Uranium deposition in Northeastern Nigeria (Suh et al. 1998). The host rocks are fluvial arkosic sandstones (Bima sandstone formation) interbedded in places with silty lenses and mudstones and occupying a more or less N 65 E trending structural basin (Suh et al. 1998).

Hence, the Upper Benue Trough of the Northeastern Nigeria has been chosen for this study to provide geophysical evidence of the deposition of uranium, analyse the tectonic settings, and map other areas suitable for uranium deposition in the area. Airborne magnetic and radiometric geophysical surveying methods, being the most commonly used methods for uranium exploration, will be adopted in this study.

Aeromagnetic survey technique is a powerful tool in delineating the regional geology (lithology and structure) of buried basement terrains (Gaafar and Aboelkhair 2014). This technique is used for detecting variation in geomagnetic field caused by changes in magnetic susceptibility of subsurface rocks due to changes in the percentage of grains of magnetic minerals forming these rocks. Variation in susceptibility assists in distinguishing various rock types; application of mathematical expressions on this helps in delineating some geological structures.

Airborne radiometric method has become a useful method, all over the world, in quest for uranium mineralization (Telford et al. 1990). The method utilizes a gamma ray spectrometer which measures the radioactivity emanating from the natural decay of elements such as potassium, uranium, and thorium from the earth surface. This tool, with shallow depth of penetration, has the special quality of distinguishing these decay elements from one another based on their energy level. Geological mapping and search for other mineral resources such as heavy minerals, beach sands, and phosphates can also be done using radiometric method (Foote and Humphrey 1976; Saunders and Potts 1976).

Geology of the study area

As shown in Fig. 1, the study area falls within the basement complex and sedimentary terrain of Nigeria. The basement complex terrain encompasses the Precambrian age rocks, which were classified, according to Carter et al. (1963), into Older granites and Burashika groups. The older granites are said to have emanated from the remnants of an ancient sedimentary series which have now transformed entirely into anatectic migmatites and granites (Carter et al. 1963). The older granites are distinguished into three phases; these are the basic and intermediate plutonic rocks, fine-grained granites (which form the earliest intrusions of the older granite orogeny), and syntectonic granites. The formation of Burashika group began, in the course of granitic dyke intrusion, after a considerable interval of the closure of the older granite orogeny. The formation led to magmatic activities which involved the intrusion of lavas and granites into the older granite. Sequential deposition of a great thickness of continental and marine sands and clays which are of Cretaceous-to-Paleocene age preceded after the formation of the Precambrian rocks.

This sequence of deposition forms the sedimentary terrain through which Bima sandstone, which unconformably overlaid the Precambrian rocks, formed the first set of the deposition. Upper Benue Trough is demarcated from Chad Basin by Zambuk Ridge. This area is entirely filled with Cretaceous right from the first formation on the crystalline basement, Bima formation, to the last formation and its lithostratigraphy is subdivided into two arms: the Gongola arm and the Yola arm. The Gongola arm of Upper Benue Trough is made up of five stratigraphic units which include the Bima sandstone at the bottom, Yolde formation, Pindiga formation, Gombe sandstone, and Keri–Keri formation, while that of Yola Arm include the Bima formation, Yolde formation, Dukul formation, Jessu formation, Sekule formation, Numanha formation, and the youngest, Lamja formation (Carter et al. 1963; Obaje 2009; Odebode 2010; Nwajide 2013).

Series of tectonic activities such as folds and fractures occurred in this area which led to the intrusion of volcanic plugs. The tertiary volcanic rocks that intruded these rocks are widely distributed across the study area; these rocks are grouped into three by Benkhelil (1986): basalt, phonolite, and trachyte. Earth movement of the late Cretaceous determined the structures of this area, but this ceased before the tertiary. The Paleocene and Younger strata are flat lying and unaffected by folding and faulting. Various fault trends are also present, but the dominant direction lies between NNE and ENE (Carter et al. 1963).

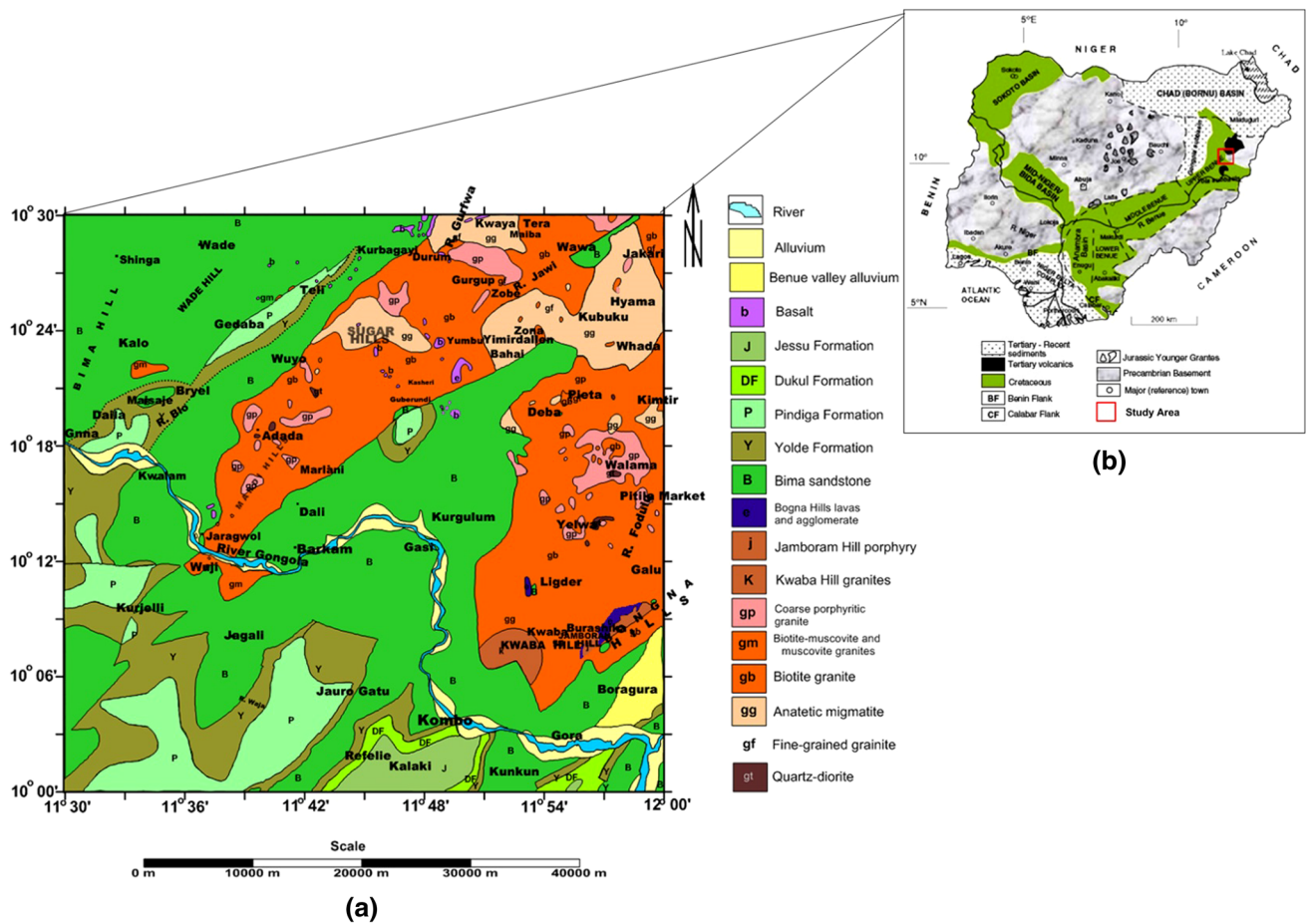


Fig. 1 **a** Geological map of the study area (modified from Carter et al. 1963); **b** Geological map of Nigeria showing the study area (modified from Obaje 2009)

Methodology

High-Resolution Aeromagnetic Data (HRAD) and airborne radiometric data (equivalent uranium and thorium data) of part of Northeastern Nigeria were acquired from the Nigeria Geological Survey Agency (NGSA). The data covered an area of about $55 \times 55 \text{ km}^2$ (bounded by latitudes $10^{\circ}00' - 10^{\circ}30' \text{N}$ and longitudes $11^{\circ}30' - 12^{\circ}00' \text{E}$). The aeromagnetic and radiometric surveys were carried out between 2003 and 2009 by Fugro Airborne Surveys for the NGSA. The data were recorded at an interval of 0.1 s ($\sim 7.5 \text{ m}$) for magnetic measurements and 1.0 s ($\sim 75 \text{ m}$) for radiometric measurements. The airborne surveys were flown in the NW–SE direction perpendicular to the major geological trends in the area, with flight line spacing of 500 m, terrain clearance of 80 m, and tie line spacing of 2000 m in NE–SW direction. Based on the very short recording interval, lower survey flight height (80 m), and narrower flight line spacing, the resolution of the anomalies is immensely higher than the conventional high-altitude airborne surveys. All essential data corrections, including the

removal of IGRF values, were done by Fugro Airborne Surveys.

The acquired magnetic and radiometric data were gridded at 100 m grid spacing, using minimum curvature technique, to produce the Total Anomaly Field (TAF) map and equivalent thorium and uranium maps. The 100 m grid spacing, which is one-fifth of the survey flight line spacing, was used to avoid short-wavelength errors which may appear as lines perpendicular to the survey flight line (Anudu et al. 2014). The chosen grid cell size also satisfies the opinion of Dentith (2011) that grid spacing should be between one-third and one-fifth of the survey flight line. The maps were processed using the Oasis Montaj software. The TAF map (Fig. 2) was reduced to the equator (Fig. 3a), using magnetic inclination (-2.33778°) and declination (-0.95732°) of the centre point of the study area, so that anomalies observed would be directly positioned on their respective causative source bodies. Unwanted signals which include the regional fields were removed by upward continuing the Reduced-to-Equator (RTE) map to a height of 2 km, where the resulted map

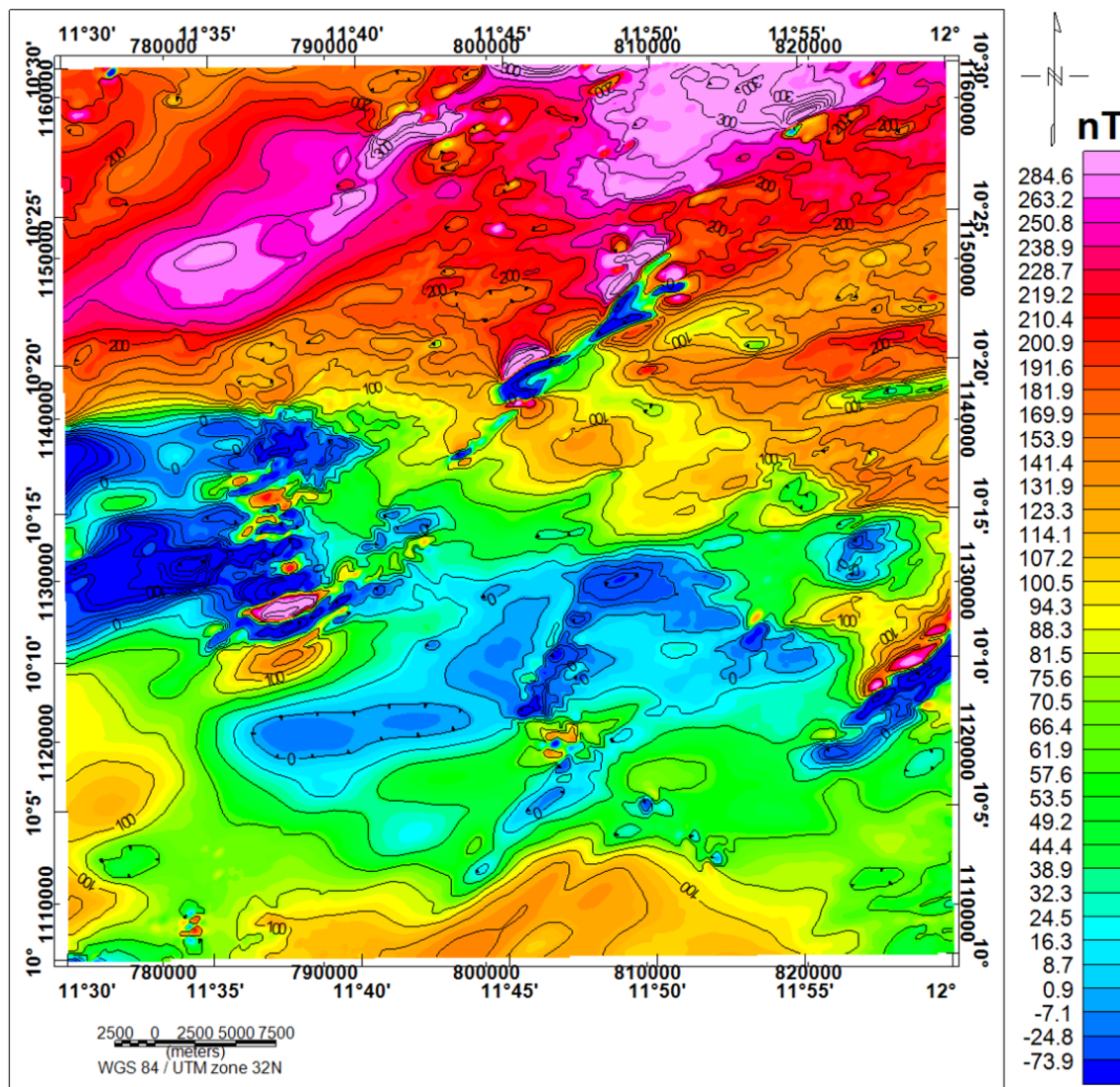


Fig. 2 Total anomaly field (TAF) map of the study area

was subtracted from the RTE map to obtain the residual map (Fig. 3b). This residual map was upward continued to a height of 200 m to remove responses from near surface cultural features. The upward continued residual map (Fig. 4a) was divided into nine overlapping blocks, which were subsequently subjected to spectral analysis. The results (magnetic source depths) obtained from the analysis of the radially averaged power spectrum of each block were compiled to produce the average depth map of the magnetic source layer in the study area. Horizontal Gradient Magnitude (HGM), First Vertical Derivative (FVD), and Analytical Signal (AS) source edge mapping techniques were applied on the filtered residual data to delineate the magnetic source boundaries. Euler Deconvolution (ED) method was also used to determine the geometry, location, and depth to the magnetic sources. More also, Source Parameter Imaging (SPI) technique was used to

determine depth to the magnetic source, and it was also used as constraint in 2D forward modelling. The radiometric data which comprise both the equivalent uranium and thorium maps (majorly used for uranium exploration) were displayed, and various ratios of these maps which include eU/eTh , eU^2/eTh , and $eU-(eTh/3.5)$ (which have different geological meanings) were calculated using the Oasis Montaj Software. The geologic, aeromagnetic, and radiometric maps were correlated, and 2D forward modelling of some suspected profiles across the study area was carried out using the GM-SYSTM module of the Oasis Montaj software to determine the variation in the geometry, depth, horizontal position, and magnitude of magnetization of the source body. Thereafter, environments and lineaments favourable for uranium deposit were deduced and interpreted accordingly.

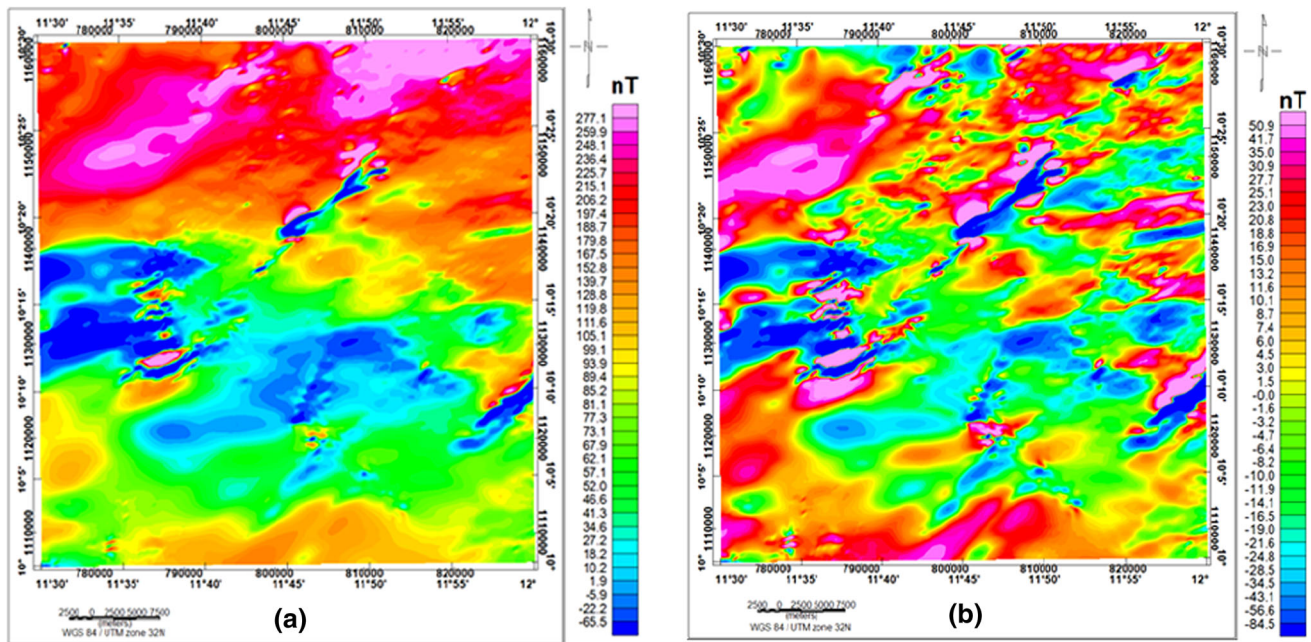


Fig. 3 **a** Reduction to the equator map of the TAF map; **b** residual map of the study area (obtained) from the removal of the regional field

Horizontal gradient of potential field anomalies is steepest approximately over edges of tabular sources (Dobrin and Savit 1988). The maxima of horizontal gradient are located at the edges of the tabular body and this can assist when inspecting for magnetization contrasts. HGM are used by some interpreters for mapping body outlines. The magnitude of the horizontal gradient of the RTP, RTE, or pseudogravity transformation of a gridded magnetic field data is given by

$$H(x, y) = \left[\left(\frac{\partial M}{\partial x} \right)^2 + \left(\frac{\partial M}{\partial y} \right)^2 \right]^{\frac{1}{2}}$$

From the equation above, $\partial M / \partial x$ and $\partial M / \partial y$ are the field gradients in the x (East) and y (North) directions, respectively.

Vertical derivative enhances shallow features at the expense of anomalies caused by deeper sources. When vertical derivative is applied to magnetic data, it sharpens the edges of the magnetic sources. The equation of first derivative can be written as

$$VD = \frac{\partial M}{\partial z}$$

In the equation above, VD is vertical derivative, and $\partial M / \partial z$ is the magnetic field in z direction.

Analytical signal shows an anomaly over a causative body which is independent of the directions of magnetization of the body, but on the location of the body itself. It has lower sensitivity to inclination of geomagnetic field which makes it effective for the transformation of the shape

of magnetic anomaly from any magnetic inclination to one positive body-centred anomaly (Nabighian 1972). The amplitude of analytical signal can be derived from three orthogonal gradients of the total magnetic field according to Roest et al. (1992)

$$A(x, y) = \left[\left(\frac{\partial M}{\partial x} \right)^2 + \left(\frac{\partial M}{\partial y} \right)^2 + \left(\frac{\partial M}{\partial z} \right)^2 \right]^{\frac{1}{2}}$$

where $A(x, y)$ is the amplitude of the analytical signal at (x, y) and M is the observed magnetic anomaly at (x, y) . Analytical signal, which peaks over the edges of source bodies, helps to reveal and highlight discontinuity using Hilbert transformation and Fourier transformation of the source field (Nabighian 1984).

Most processing algorithms proposed for the interpretation of magnetic data either estimate the depth or locate boundaries. However, Euler deconvolution is both a boundary finder and a depth estimator (Reid et al. 1990). It extracts information from grids using the homogeneity relation shown by Thompson (1982). This relation can be written in the form:

$$(x - x_0) \frac{\partial T}{\partial x} + (y - y_0) \frac{\partial T}{\partial y} + (z - z_0) \frac{\partial T}{\partial z} = N(B - T),$$

where (x_0, y_0, z_0) is the position of a magnetic source, whose total field T is detected at (x, y, z) ; B is the regional field value; and N is the degree of homogeneity interpreted as structural index (SI) (Thompson 1982), which is a measure of the rate of change with distance of a field, and this structural index is chosen based on the prior

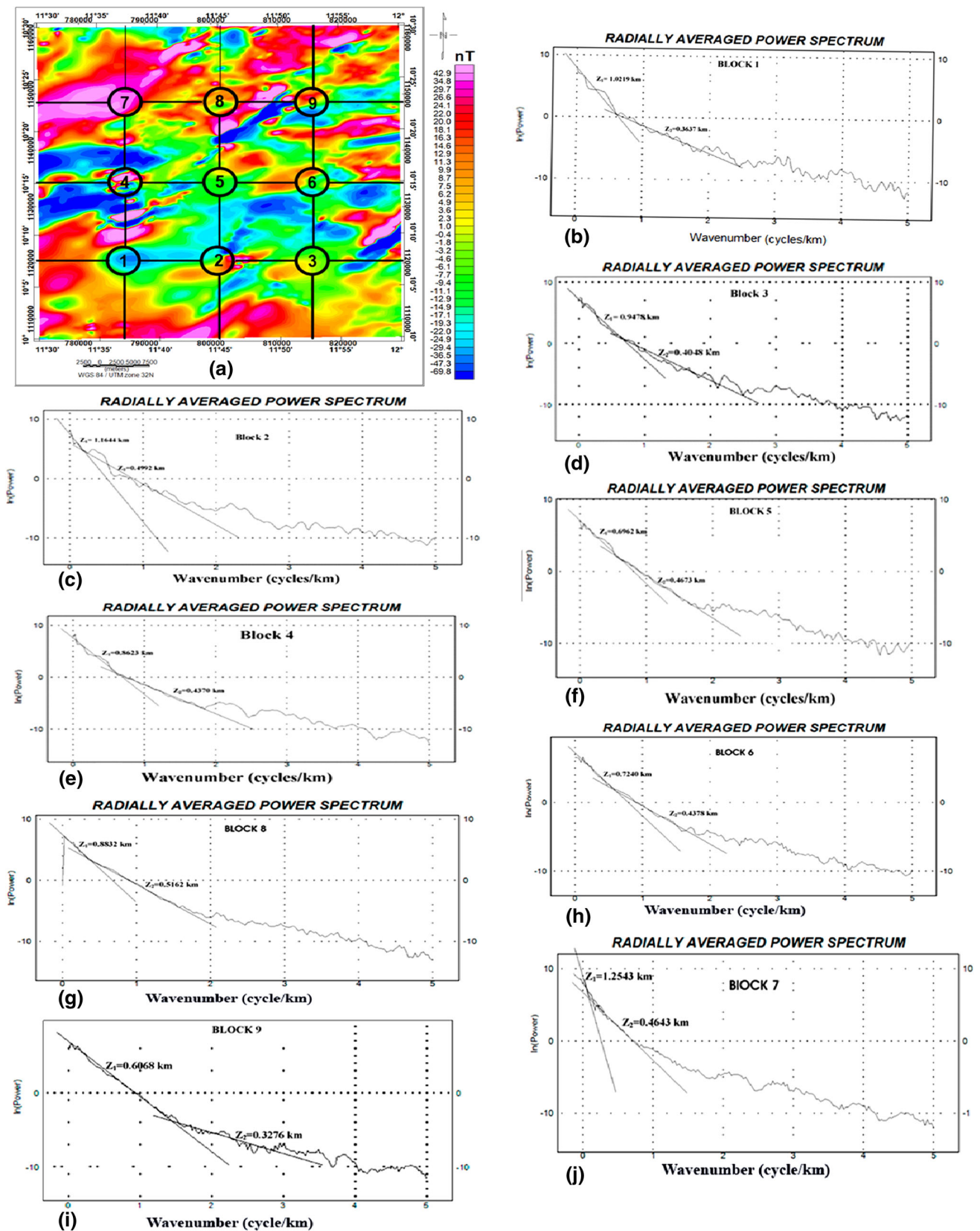


Fig. 4 a 200 m upward continuation map of the residual map—the super imposed numbers indicate the centre of the overlapping blocks; b–j radially averaged power spectrum of blocks 1–9

knowledge of the source geometry. SI varies from zero to three for different bodies ($N = 0$ for contacts, 1 for sill/dyke/fault, 2 for pipe/horizontal bodies, and 3 for spherical bodies, respectively) (Reid et al. 1990).

Source parameter imaging (SPI) is one of the methods used for the determination of depth to the magnetic basement that is beneath a sedimentary cover. This method sources its parameters from gridded data and uses an extension of complex analytical signal to estimate the magnetic source depth. The technique (sometimes referred to as the local wavenumber method) is a profile or grid-based method that estimates the magnetic source depth, dip, and susceptibility contrast of some source geometries (Thurston and Smith 1997; Thurston et al. 1999, 2000; Nwosu 2014).

Results and discussion

Qualitative interpretation of aeromagnetic maps

Qualitative interpretation of aeromagnetic data involves visual inspection of the map for recognition of zones with different magnetic characteristics, shapes, and trends. The study area, which covers both basement complex and sedimentary terrain, showed anomalies of various magnetic characteristics. This is as a result of the differences in the sizes, depths, and magnetic susceptibilities of the underlying rocks.

The basement complex zone of the study area is magnetically perturbed than the sedimentary zone because of the high sedimentary cover on the basement rocks. The TAF map (Fig. 2) shows high and low magnetic anomalies of various wavelengths. Most of the anomalies trend in the NE–SW direction, while others trend in the E–W and NW–SE directions. The magnetic intensity value of the study area varies from -74 to 285 nT. The upper region contains high magnetic intensities (114 – 284 nT), the central part is dominated by low magnetic intensities (-24 – 123 nT), while the magnetic intensities of the southern part are moderate (53 – 114 nT). The low magnetic intensity value observed within the magnetic high in the northern flank suggests the presence of deep-seated fault zone which trends in the same direction as the observed anomaly. The adjacent magnetic high and low anomalies at latitude $10^{\circ}10'$ (Fig. 2) of the southeastern part of the study area correspond to the Burashika group (Bongna hills lava and agglomerate and Jamboram hill porphyry) on the geological map.

Computation of residual

The residual and filtered residual maps are presented in Figs. 3b and 4a. The magnetic intensity of the filtered map

ranges between -70 and 43 nT. The E–W trending low amplitude anomalies observed at the western flank of the study area show the presence of rocks of high magnetic susceptibility in the area. Some intercalations of E–W and ENE–WSW trending magnetic highs, which are of shorter wavelengths, into the magnetic lows in the area indicate the presence of smaller and less magnetic rock bodies over or in between the rocks giving the low magnetic anomaly signature. The high amplitude anomalies observed at the northwestern and southern parts of this map may be due to the presence of low magnetic rocks (e.g., shale, sand, sandstone, mudstone, and limestone) present in the study area. In the lower part of the northeastern region of the map, a prominent low magnetic intensity value, which is tabular in shape and trends in the ENE–WSW direction, was observed in between magnetic highs; this anomaly is likely to be from a dyke-like structure, fault, or fracture. From the central part to the northeastern part of the study area, an elongated structure trending NE–SW which has been featuring in both the TAF map and filtered residual map is likely to be major fault/fracture hosting magnetic minerals, whose response results in the significant low anomaly amplitude in between the relatively high amplitude anomalies in the area.

Quantitative interpretation of aeromagnetic data basement analysis

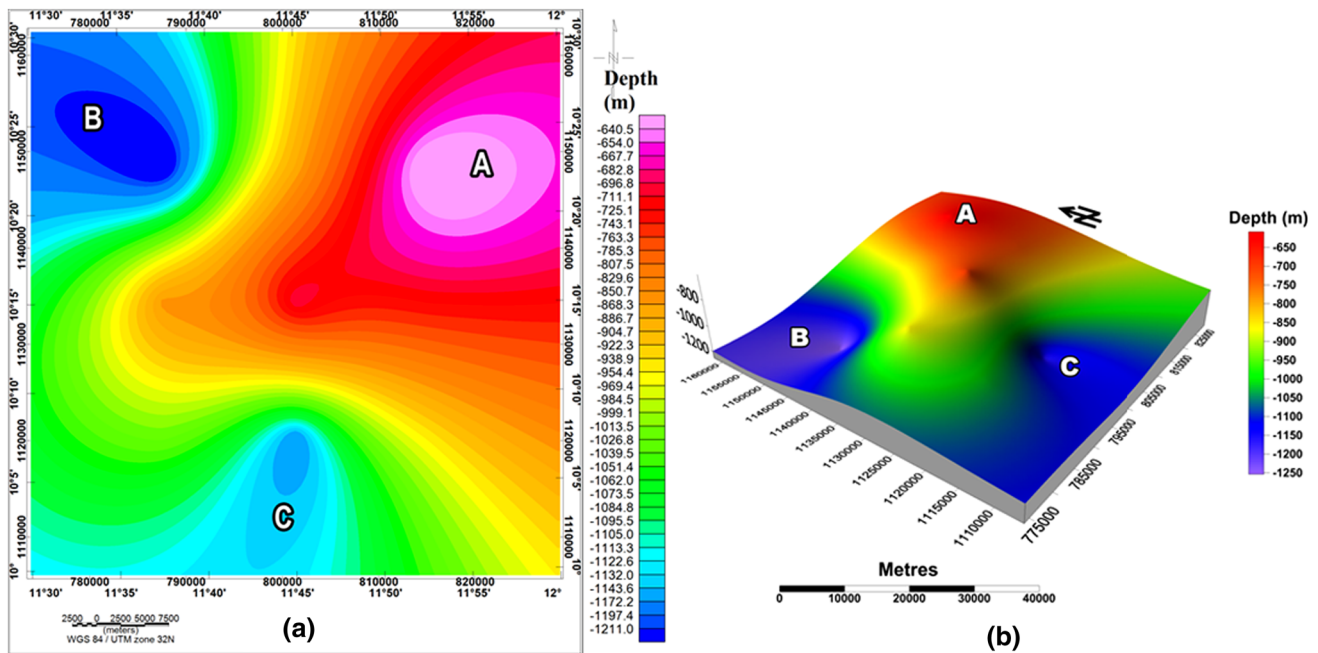
Magnetic basement average depth determination using spectral analysis

Figure 4 shows the subdivision of the filtered residual map into nine overlapping blocks and the radially averaged power spectrum of these nine blocks. In these plots, the log of energy reduces with increasing wavenumber. Since the effects from all physical sources (geology) contribute to any measurement taken in potential field, the energy spectrum clearly shows the ensemble of sources that contributed to the energy from low to high wavenumbers. In this study, the lower wavenumber sources which are the deep-seated sources are the sources of interest, and Table 1 shows the average depths estimated from each block.

The result obtained from the average power spectrum of these blocks, z_1 , in Table 1 was used to generate the 2D and 3D depth maps (Fig. 5a, b). The 2D map shows the sedimentary thicknesses of the study area, while the 3D map shows the basement morphology of the area. On the 2D map (Fig. 5a), the hot colours (red and pink) correspond to shallow depths, while the cool colours (e.g., blue) correspond to deep depths. The basement topography map (Fig. 5b) shows that depths to the magnetic basement range from 650 to 1250 m below the surface. The elevated

Table 1 Estimated depths from radially averaged power spectrum of blocks 1–9

Blocks	1	2	3	4	5	6	7	8	9
Depth Z_1 (km)	1.0219	1.1644	0.9478	0.8623	0.6962	0.7240	1.2543	0.8832	0.6068

**Fig. 5** **a** Depth to the basement (*sedimentary thickness*) map of the study area; **b** basement morphology map of the study area inferred from spectral analysis

portion of the map (labelled A) corresponds to the basement complex terrain that was observed on the geological map of the study area (Fig. 1), while the relatively deep regions (labelled B and C) mapped in the northwestern and southern parts of the study area correspond to the sedimentary terrains. Moderate depths were observed at the western flank.

Depth estimation using source parameter image (SPI)

The SPI map for the study area is shown in Fig. 6. The white portions on the map signify areas, where the derivative used for the estimation of the local wavenumber is so small that the SPI structural index cannot be estimated reliably. As shown on the SPI map, the depths to the magnetic basement vary from 150 to 1941 m. Some deep zones (>800 m) were observed in various parts of the map. The deep zones are more pronounced in the northwestern and southwestern parts of the study area, while those that are less pronounced (i.e., deep zones of very small width extent) were mapped in few parts of the upper diagonal of study area. The northeastern, central, and southeastern parts are dominated by shallow depths (<400 m) to the basement.

The SPI map correlates well with the spectral depth map (Fig. 5a, b). The northwestern and southwestern portions of the study area were also seen as depression or low-lying surface, while the northeastern, central, eastern, and southeastern portions are elevated. The difference in depth ranges obtained from the spectral method and the SPI is as a result of the average depths calculated from the spectral windows. The SPI generally gives a more localized estimation of depths than the power spectral and, therefore, shows a depth map of higher resolution. The results from both methods correlate with what was observed on the geological map. Areas with shallow depths correlate with basement complex terrain, whereas the high depth values correlate with sedimentary terrains.

Lineament mapping

Horizontal gradient magnitude (HGM) and analytical signal (AS) maps

As HGM peaks over the source edges, so does AS, but the shape of the analytic signal is independent on the direction of magnetization and local magnetic field. HGM map reveals that more structural complexities which include the

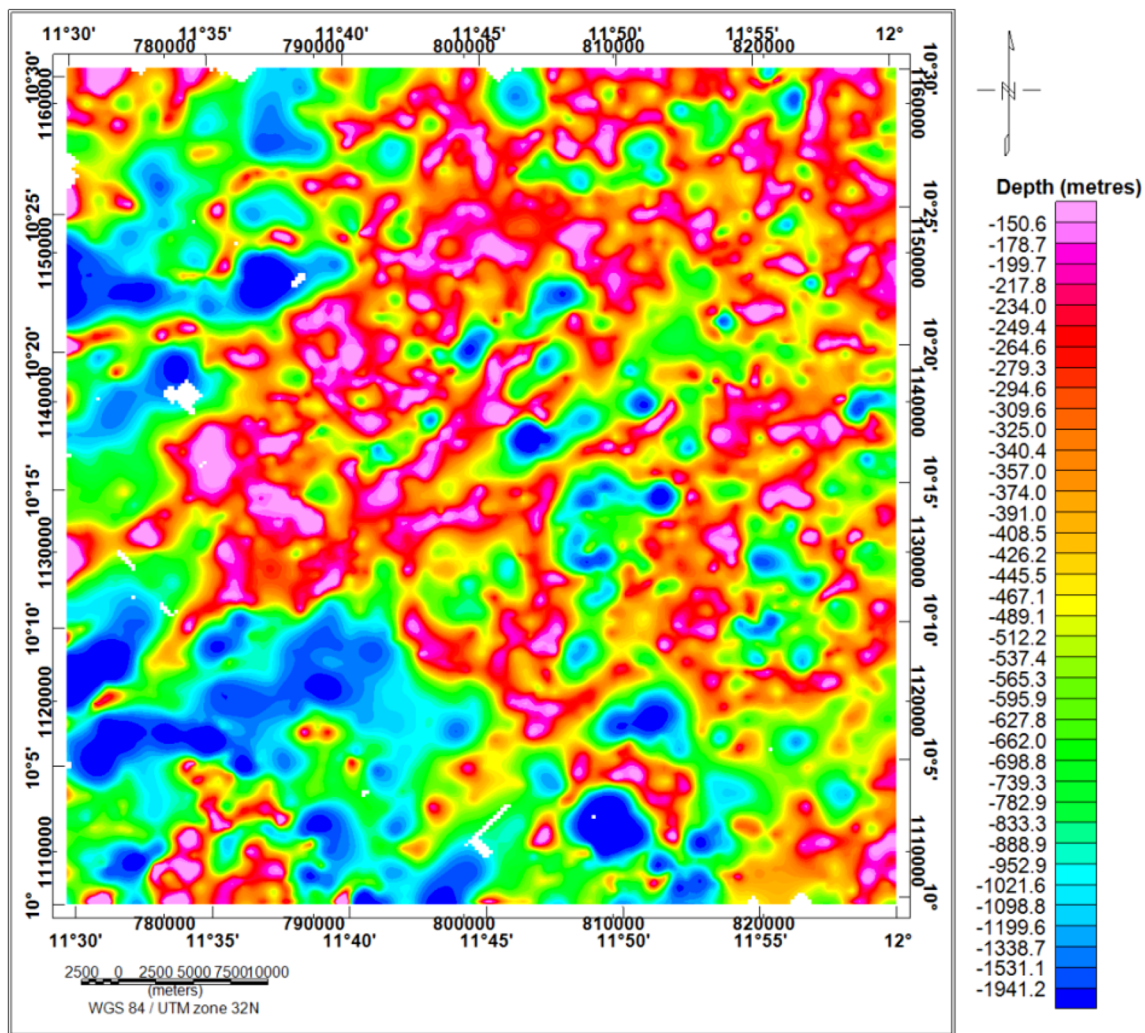


Fig. 6 Map showing the depth of magnetic source from source parameter imaging (SPI)

lithological contacts of various geological bodies than AS map and contacts produced in HGM maps, according to Philips (2000), are assumed to be dislocated in the down-dip direction for dipping contact sources. Figure 7 shows the locations of both HGM and AS maxima, respectively. From the maps, the maxima show contacts that trend mostly in the ENE–WSW, NE–SW, E–W, and NW–SE directions; among which, the ENE–WSW trends predominate.

Interpretation of 3D Euler deconvolution

According to Reid et al. (1990), magnetic contact has structural index of zero; however, real faults are typically complex structures, and the use of slightly higher indices is often appropriate. Therefore, to distinguish faults/fractures from lithological contacts in the study area, structural index of 1 was adopted. Figure 8 shows the Euler solution plot for structural index of 1. The depths were grouped every

500 m, and the result shows that faults/fractures existing between the depths of 500 and 1000 m dominate the study area. The result also shows prominent NE–SW, ENE–WSW, E–W, and NW–SE trending structures. A critical visual inspection of the faulting pattern indicated by the NE–SW trending alignments of many Euler solutions shows that the study area has been affected by an NE–SW trending regional fault system, whose history could be traced to the Pan African Orogeny. The Euler solutions show that the structures in the northwestern and southwestern portions of the study area exist at relatively deep depths than those in other parts. Linear clustering of different depth solutions indicates variation in depths along the fault zones. Many structures whose depths are greater than 1000 m featured in the northwestern and southwestern portions. Shallow solutions were observed from the central region to the northeastern part of the study area. These solutions, which are less than 1000 m in depth and trend in the NE–SW direction, also fall on the basement complex

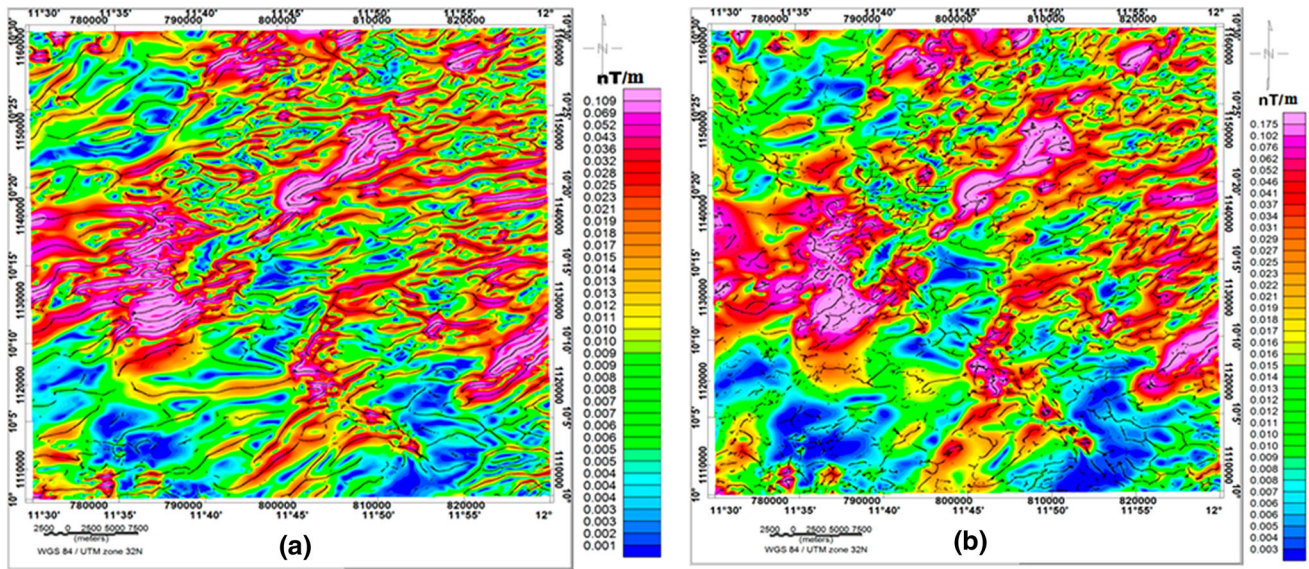


Fig. 7 a Peaks overlain on the HGM map; b peaks overlain on the AS map

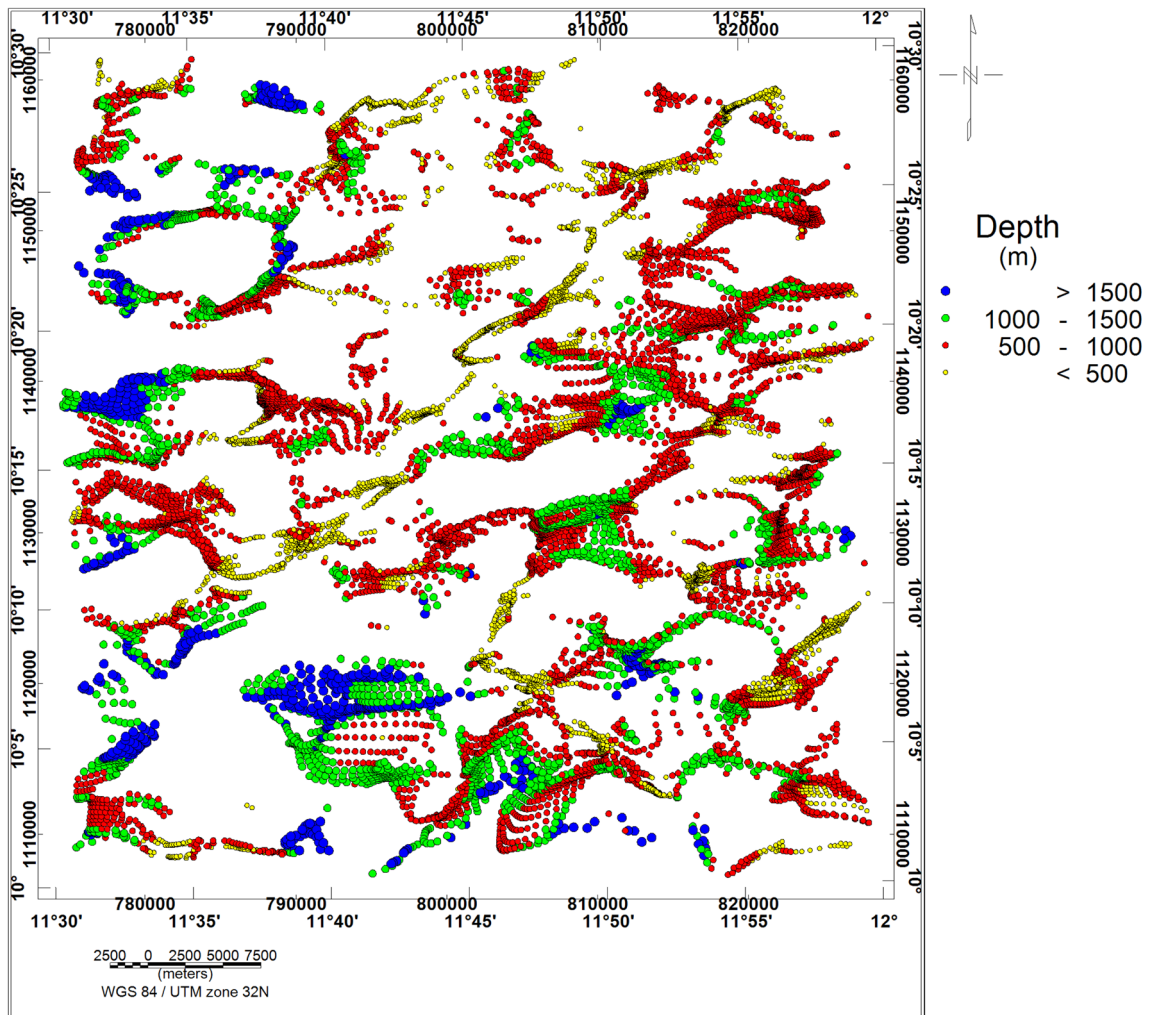


Fig. 8 Euler solution map for a structural index (N) of 1

terrain of the study area. These structures could be faults on or within the basement.

Composite map

The composite map (Fig. 9) was produced from the superposition of HGM maxima (red), ASA peaks (pink), ED solutions (yellow), and the First vertical Derivative (FVD) image of the filtered RTE map. The FVD image forms the background, while other maps were overlain. The integration of several methods for detecting source edges served as a reliable factor of confidence in mapping the geological structures. Superposition of HGM maxima and AS peaks helped in determining the actual location and the dip direction of the structures. According to Philips (2000) and Ndougsa-Mbarga et al. (2012), AS contact map shows the true contact location, while areas where the

HGM contacts are slightly parallel or offset from analytical signal located contacts signify the down-dip direction; however, when both overlay each other, the contact is said to be purely vertically dipping. The ED solutions obtained from using structural index of one were used to differentiate possible fault locations from lithological contacts. The FVD of the magnetic anomalies was carried out to sharpen the locations of the structures, and also aid in tracing other contact locations, extensions, and continuation that were not fully detected by the HGM and AS.

Inferred structural map of the study area

The structures delineated from the composite map were compiled to produce the structural map for the study area (Fig. 10). The structural map generally illustrates that the basement rocks are bounded by many contacts and faults

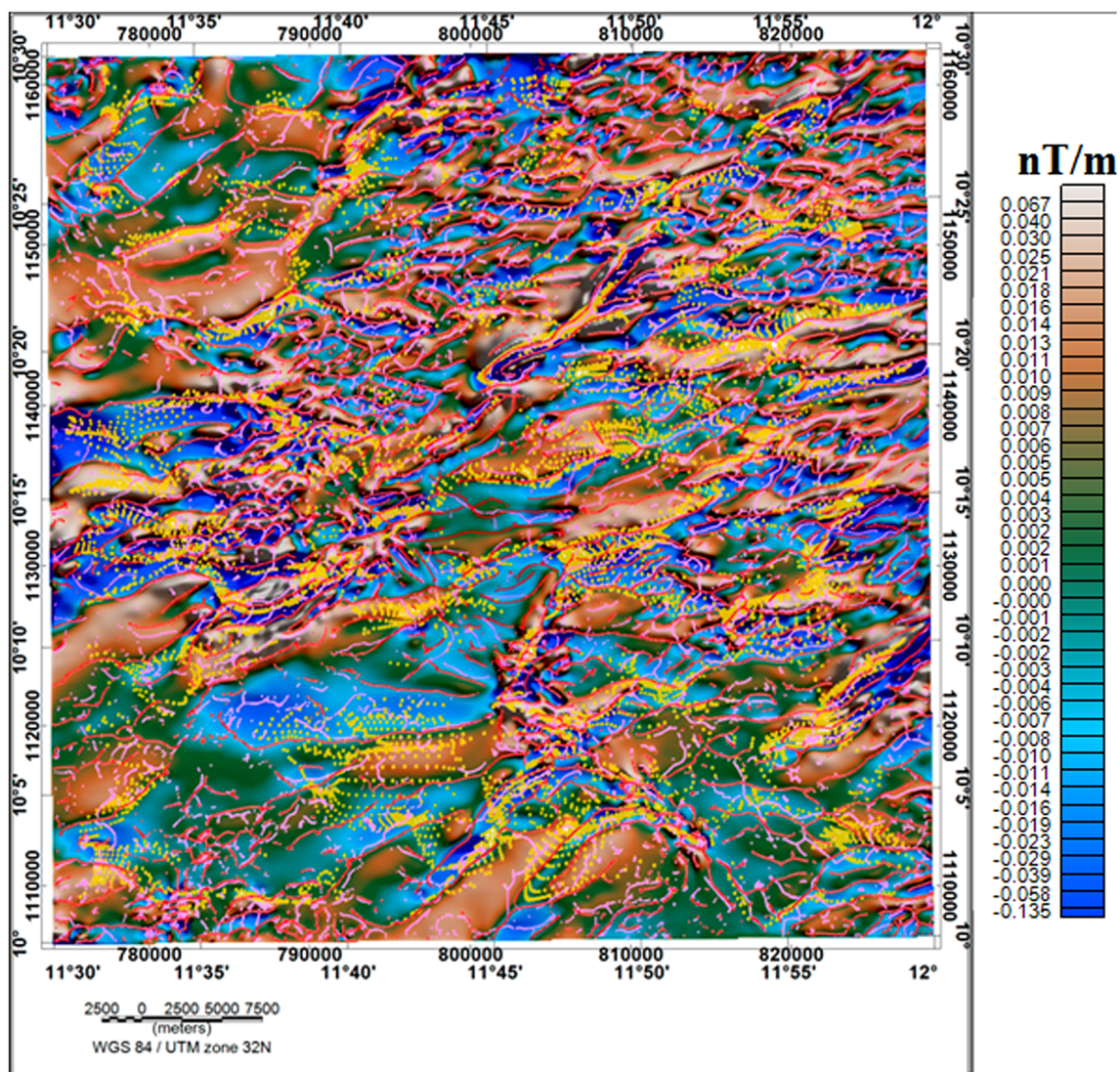


Fig. 9 Composite map of the estimated contact locations from HGM (red), AS (pink), and ED (yellow) overlain on FVD of the RTE map

that trend and dip in various directions. The black and red lines in the map, respectively, depict the inferred contact and fault locations. The short lines perpendicular to the strikes of the inferred faults indicate the dip directions. The faults without dip direction are considered vertical. The geological structures in the study area trend in the ENE–WSW, NE–SW, E–W, WNW–ESE, and NW–SE directions. These structures are more concentrated in the basement complex part of the study area than the sedimentary terrain. This is as a result of the closeness of the basement to the surface; the magnetic contours in cretaceous rocks are normally smooth with small variations which reflect the

basement rocks than the near surface features, while igneous and metamorphic rocks dominated areas normally exhibit complex magnetic variation (Telford et al. 1990).

The orientations (azimuth directions) of the lineaments on the structural map were measured and plotted on a rose diagram. The azimuth-frequency (rose) diagram (Fig. 11) shows that the geological structures in the study area majorly trend in the ENE–WSW and NE–SW directions. Few azimuthal frequencies were recorded for structural lineaments that trend in the E–W, NNE–SSW, WNW–ESE, and NW–SE directions. The NNE–SSW/N–S trends, which are very prominent Northeastern Nigeria, are related

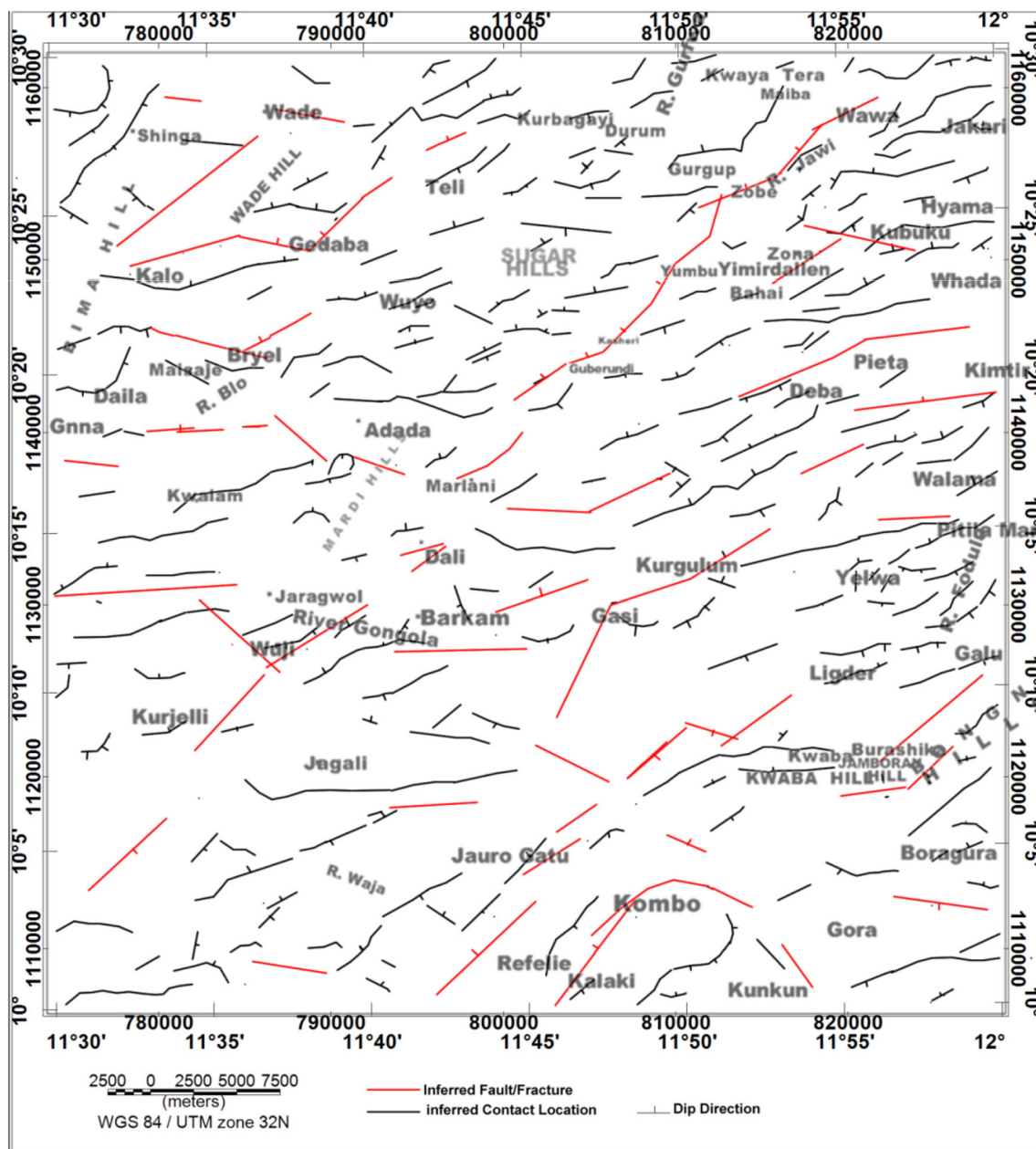


Fig. 10 Inferred structural map of the study area

to the late reactivation of Pan-African basement complex (Suh et al. 1998), while the E–W trends according Obiora (2009) are said to be pre-Pan African (over 800 Ma). The dip direction, as observed on the structural map, varies for different lithological contacts with dominant ones dipping in the NNW, SSE, NW, and SE directions, while others dip vertically, northeasterly, or southwesterly.

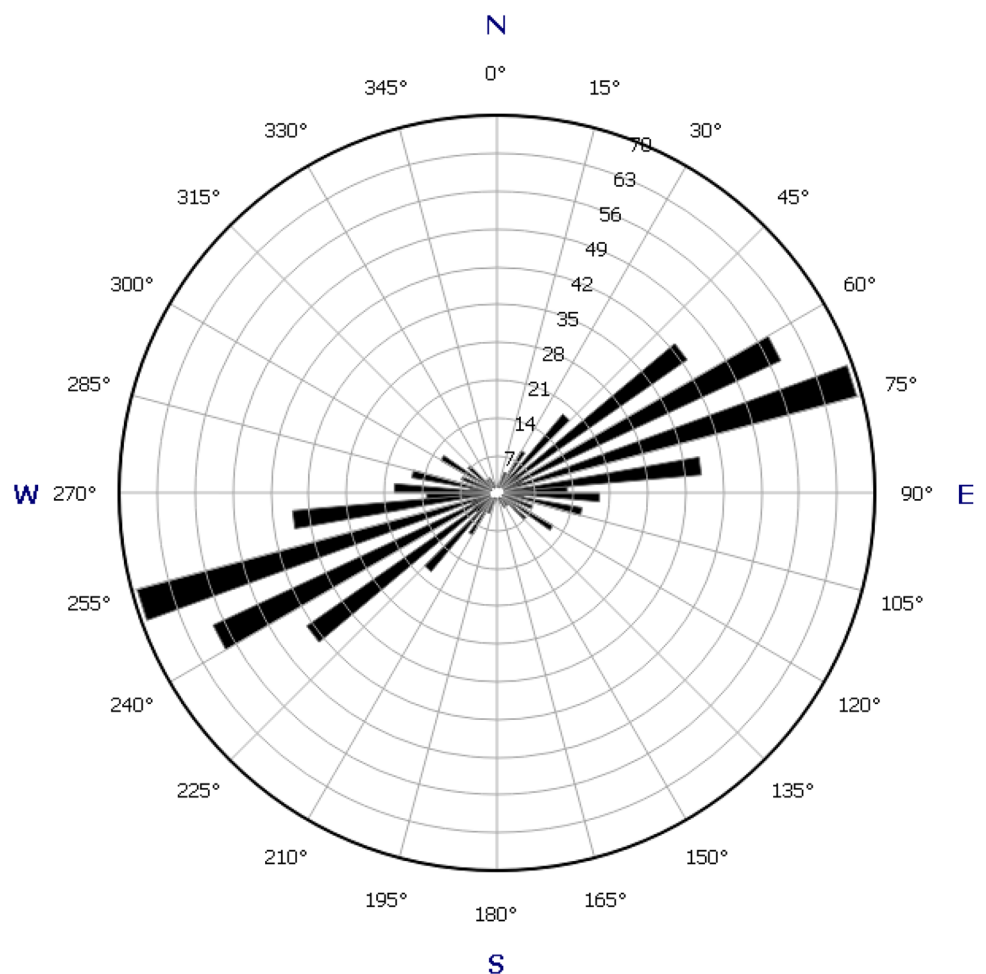
Radiometric interpretation

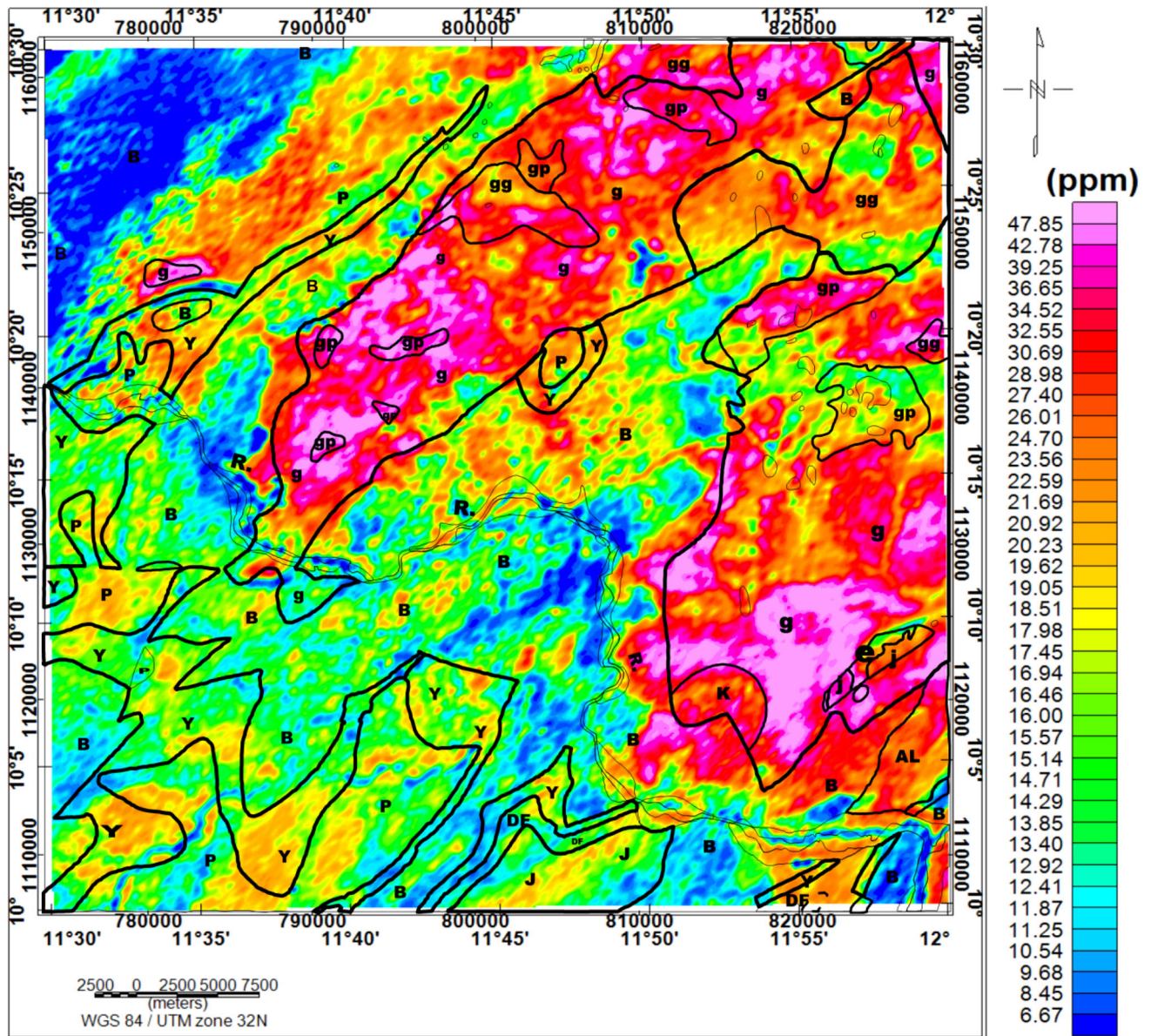
Equivalent Thorium (eTh) surface distribution map

Figure 12 shows the eTh distribution map of the study area overlain by the geological map. The geological map was superimposed to relate the observed eTh concentration with geology of the study area. The eTh distribution map has eTh concentration ranging from 6.67 to 47.85 ppm. For the purpose of this interpretation, the eTh concentration in the study area will be relatively grouped as high (>29 ppm), moderately high (21–29 ppm), moderately low (14–21 ppm), and low (<14 ppm).

The superposition of the geological map on the eTh surface distribution map has shown the significant relevance of radiometric data in geological mapping. The Bima sandstones at the northwestern flank of the study area are characterized by low eTh concentration, while moderately low-to-moderately high concentrations were observed at the neighbouring Pindiga formation. The sediments in the western and southern regions generally give low-to-moderately low eTh signature; these regions span the Bima, Yolde, Pindiga, and Jessu formations. The granitic rocks, forming the basement complex terrain of the study area, generally show strong signatures of thorium concentration. The NE–SW and E–W trending anomalous zones of high eTh content in the northern region are dominated by coarse porphyritic granite, biotite/muscovite granite, and anatectic migmatite, whereas the nearby Yolde, Pindiga, and Bima formations show relatively low concentration. In addition, the granitic rock in the northwestern region gives a distinct high thorium count from the bounding sediments of Pindiga, Yolde, and Bima formations which show low-to-moderately high eTh concentrations. The nearly circular high eTh concentration anomaly observed in the western

Fig. 11 Azimuth-frequency (*rose*) diagram of the inferred structural contact location





- | | | |
|----------------------------|---|--------------------------------------|
| AL Alluvium | Y Yolde Formation | K Kwaba Hill granite |
| J Jessu Formation | B Bima Sandstone | GP Coarse porphyritic granite |
| DF Dukul Formation | e Bongna Hills lavas and agglomerate | g Biotite/Muscovite Granite |
| P Pindiga Formation | J Jamboram Hill porphyry | gg Anatectic migmatite |
| R. River Gongola | | |

Fig. 12 Superposition of geological map on eTh concentration map

and southeastern regions is also dominated by granitic rocks. The Jamboram and Kwaba hills have moderately high-to-high concentrations, while the major part of the Bongna hill shows relatively low eTh concentration. Low eTh counts were recorded in most parts of the riverine areas.

Equivalent Uranium (eU) surface distribution map

In radiometrics, estimates of uranium concentration are usually reported as equivalent uranium, because these estimates are always based on the assumption of equilibrium conditions. Figure 13 shows the eU concentration map and geological map of the study area superimposed. The map shows various anomalous signatures with total eU concentrations varying between 0.5 and 6.8 ppm. The eU concentrations can be relatively grouped as high (>4.63), moderately high (3.66–4.63), moderately low (2.64–3.66), and low (<2.64). Most of the granitic bodies in the study area are associated with high eU signature, while the outer zone of the granitic rocks displays moderately low-to-moderately high counts. The anatectic-migmatite inlier which was intruded by the granitic rocks also has high uranium concentration. The Bima formation at the extreme of the northwestern flank of the study area shows a characteristic of low uranium concentration; however, very few intercalations of high signatures were recorded within it. The biotite/muscovite granitic inlier in this area also shows high uranium concentration. The Bima sandstone between the Yolde formation and the granitic body in the northwestern region gives relatively moderate-to-high count, while the Pindiga formation and the Yolde formation show low-to-high uranium concentration. From the western region down to the southern region, the Bima, Yolde, Jessu, Dukul, and Pindiga Formations are characterized by moderately low-to-moderately high uranium concentration.

As observed on the eTh and eU concentration maps, the river channel in the study area gives low values for eU and eTh concentrations. However, this does not mean that it does not contain radioactive material, but it is as a result of water being a strong absorber of radiation (Darnley 1975).

Ratio maps

Ratio maps are maps generated from meaningful arithmetical combination of two radioelement grids. These maps assist in the reduction of the effects of environmental factors (such as vegetation, soil moisture, topography, and weather condition) on the recorded radiometric data. In this study, three ratio maps [eU^2/eTh , eU/eTh , and $eU-(eTh/3.5)$] were adopted.

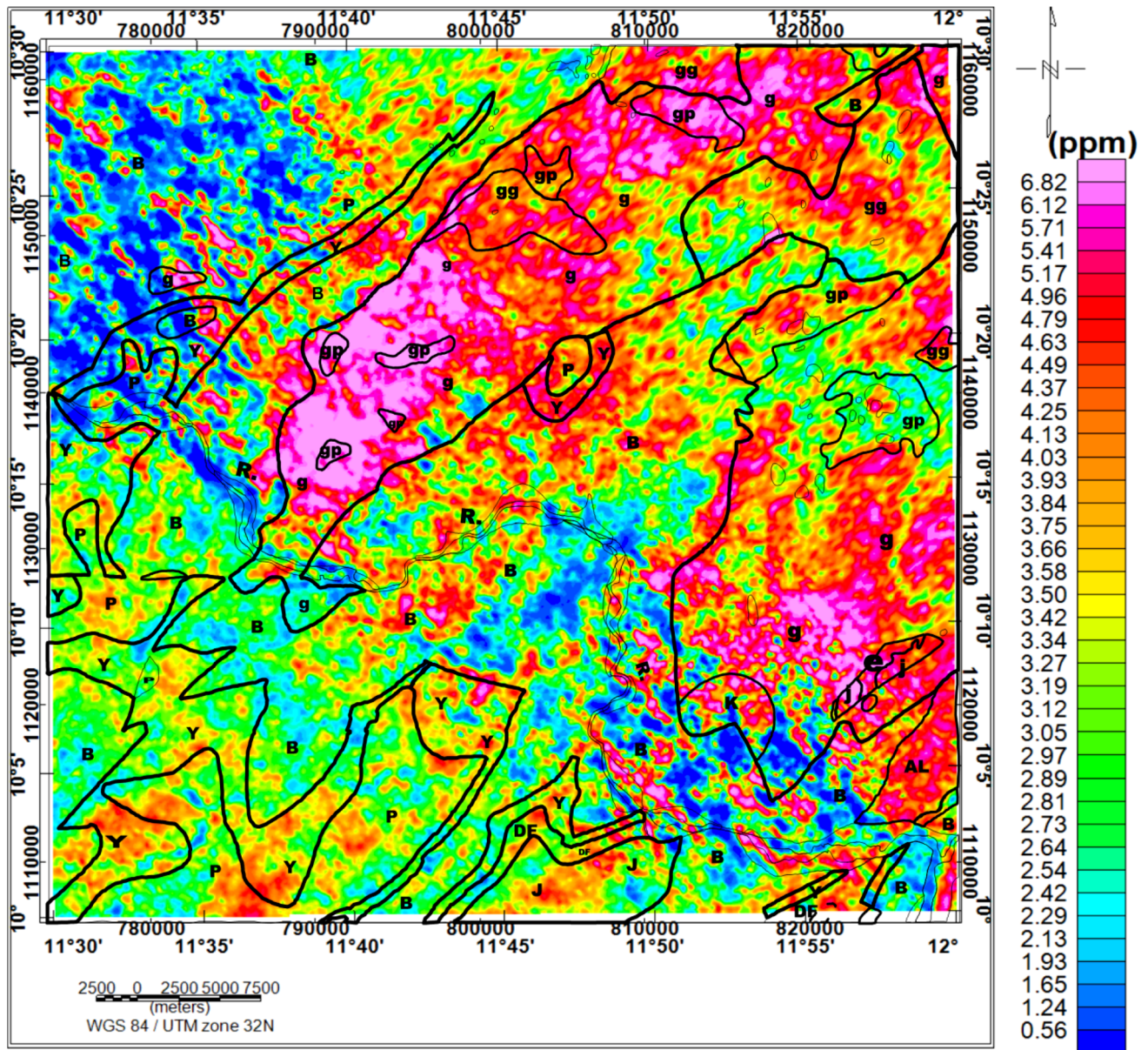
eU^2/eTh Map

The eU^2/eTh map was obtained by squaring the eU map and then dividing the resulted map by eTh map. The eU^2/eTh ratio map assists in the amplification of areas with high eU concentration which was decreased by damping effect of media (e.g., water). This ratio map transforms the eU measurement towards the ideal case in which the bedrock is not covered by soil or water (Lauri and Turunen 2015).

The eU^2/eTh map of the study area is presented in Fig. 14. On this map, various anomalous zones which were not shown in the eU concentration map were observed; however, some high counts in the eU concentration map were also suppressed. The values of the eU^2/eTh map range between 0.042 and 1.65 ppm. The granitic bodies in the study area still show high values, though less prominent than on the eU concentration maps. However, the Bima formations in various parts of the study area show more concentration than those on eU map. The Bongna hills lava and agglomerate at southeastern region still retain their high concentration. The formations at western, southwestern, and southern flank of the study area also retain their moderate concentration. The alluvial deposits at the southeastern part of the study area show significant eU concentration.

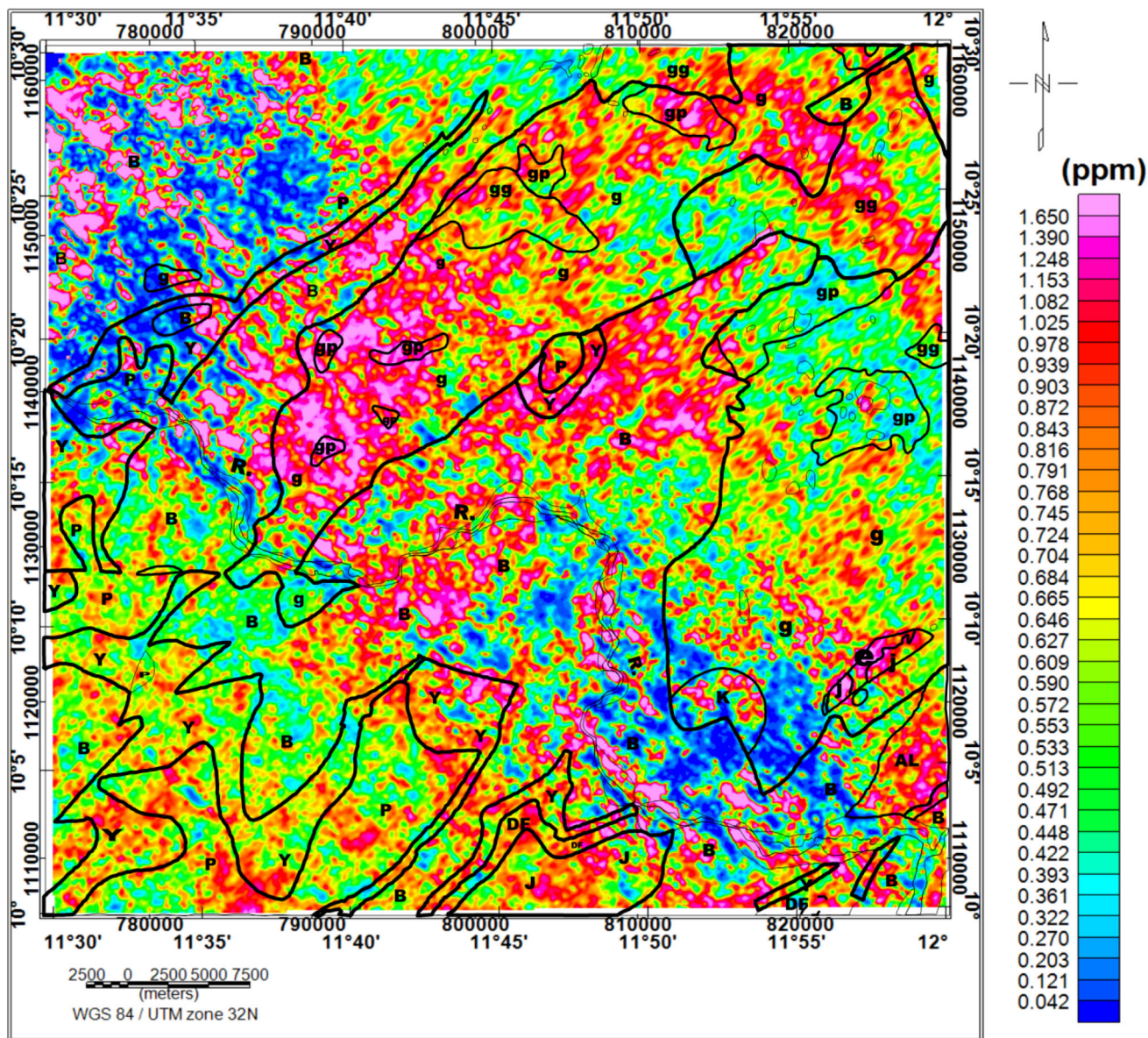
eU/eTh map

The eU/eTh ratio, which is important in uranium exploration, depends mainly on the mobile elements (i.e., uranium), and it also determines uranium enrichment areas (Gaafar and Aboelkhair 2014). According to Clark et al. (1966), the eU/eTh ratio for granitic rock is about 0.33; the enrichment area is above 0.33 in granites, while leaching out of uranium will be indicated by its decrease to less than 0.3 (Gaafar and Aboelkhair 2014). From the eU/eTh ratio map (Fig. 15), most of the granitic rocks in the study area have relatively low values compared to the surrounding lithological formations such as Bima, Yolde, and Pindiga. This shows that the granitic bodies in the study area are likely to be richer in thorium than uranium, and in addition, the ratio values suggest that uranium is leaching out from these bodies. In the northern part of the study area, the Bima formations at the opposite sides of the NE–SW trending granitic body show very high (>0.33) eU/eTh ratio. This shows that uranium ore is likely to have been deposited in the Bima sandstones. The Bongna hill also shows high ratios, while the Pindiga, Yolde, Bima, Dukul, and Jessu formations located at the western, southwestern, and some parts of the southeastern portions of the study area show intercalations of eU/eTh ratio anomalies ranging from moderate to high. It was also observed on the eU/eTh map that some parts of the Bima formation close to the



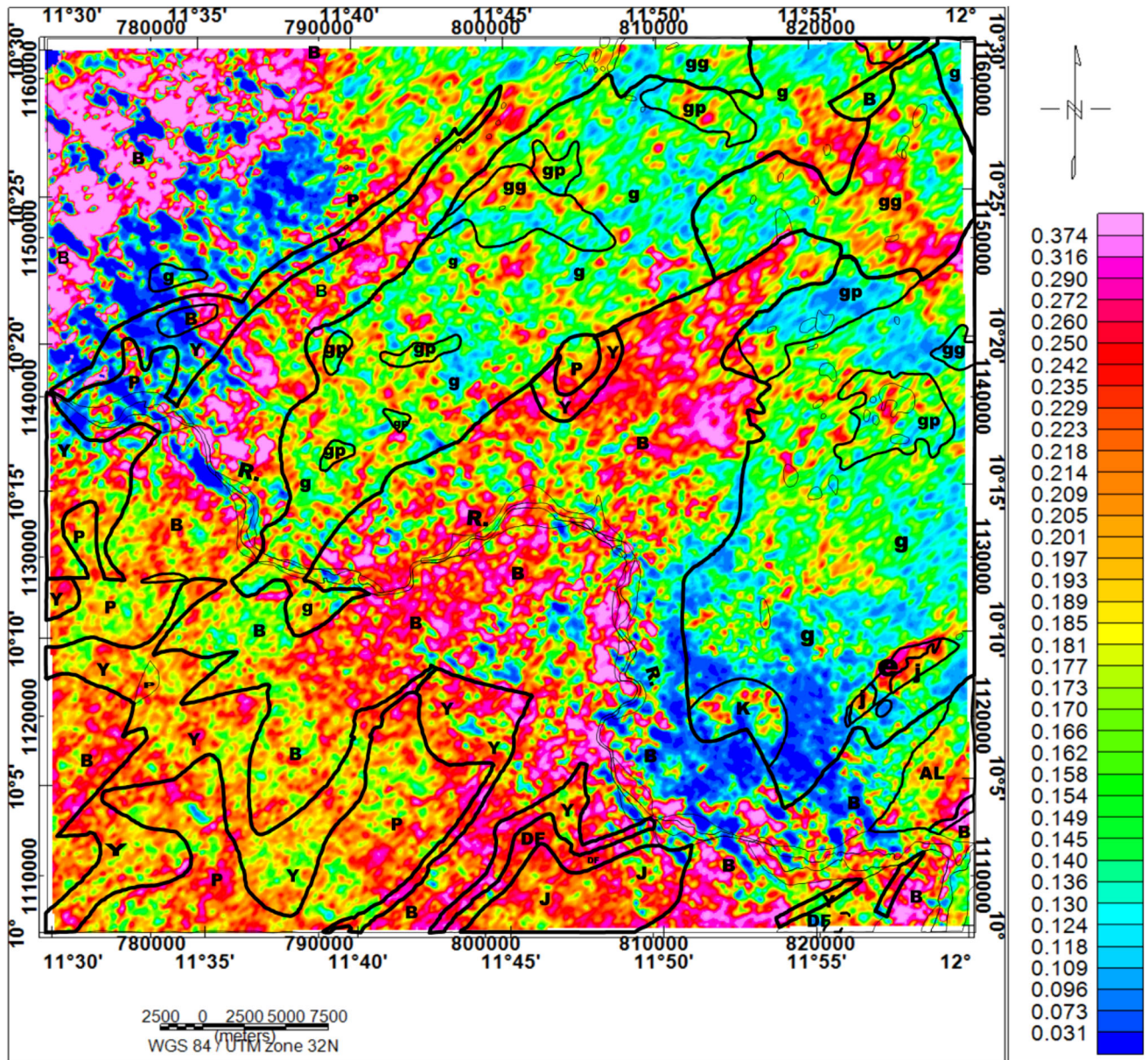
- | | | |
|----------------------------|---|--------------------------------------|
| AL Alluvium | Y Yolde Formation | K Kwaba Hill granite |
| J Jessu Formation | B Bima Sandstone | gp Coarse porphyritic granite |
| DF Dukul Formation | e Bongna Hills lavas and agglomerate | g Biotite/Muscovite Granite |
| P Pindiga Formation | J Jamboram Hill porphyry | gg Anatectic migmatite |
| R. River Gongola | | |

Fig. 13 Superposition of geological map on eU concentration map



- | | | |
|----------------------------|---|--------------------------------------|
| AL Alluvium | Y Yolde Formation | K Kwaba Hill granite |
| J Jessu Formation | B Bima Sandstone | gp Coarse porphyritic granite |
| DF Dukul Formation | e Bongna Hills lavas and agglomerate | g Biotite/Muscovite Granite |
| P Pindiga Formation | j Jamboram Hill porphyry | gg Anatectic migmatite |
| R. River Gongola | | |

Fig. 14 Superposition of geological map on eU^2/eTh concentration map



- | | | |
|----------------------------|---|--------------------------------------|
| AL Alluvium | Y Yolde Formation | K Kwaba Hill granite |
| J Jessu Formation | B Bima Sandstone | gp Coarse porphyritic granite |
| DF Dukul Formation | e Bongna Hills lavas and agglomerate | g Biotite/Muscovite Granite |
| P Pindiga Formation | j Jamboram Hill porphyry | 99 Anatectic migmatite |
| R. River Gongola | | |

Fig. 15 Superposition of geological map on eU/eTh concentration map

riverine areas at the southeastern flank of the study area show high ratio. The uranium enrichment of the sandstone (Bima sandstone) might have resulted from the precipitation of soluble uranium deposits flowing along the river channel.

eU–(eTh/3.5) map

Uranium is a mobile element which can be liberated from the source, transported in aqueous solutions and deposited in various environments due to redox changes, absorption, precipitation, or metasomatism or due to a combination of some of these processes (Ruzicka 1975). This kind of deposition occurs under various pressure and temperature (P–T) conditions. Uranium redistribution or remobilization in this area can be estimated by dividing the eTh content by 3.5 (the eTh/eU ratio in granitic rocks) and subtracting the result from the eU content (Clark et al. 1966; Cambon 1994; Gaafar and Aboelkhair 2014). The resulting map, which is useful in defining the trends of uranium migration, shows the hypothetical uranium distribution; the negative contour areas connote the leaching area, while the positive, deposition (Gaafar and Aboelkhair 2014). The direction of the uranium mobilization can be traced with directions trending from the negative anomalies to the high positive ones (Gaafar and Aboelkhair 2014).

Figure 16 shows the eU–(eTh/3.5) distribution map of the study area. The labels A, B, C, and F on the distribution map are uranium rich Bima formations, while D and E are the migmatite and Bongna hill uranium rich rocks. Directional arrows D1, D2, D3, and D4 show the hypothetical directions from leaching to deposition. D1 shows the direction arrow for leaching uranium from the NE–SW trending granitic rock into B and C. Also from the map, direction D2 shows that the granitic rock in the northwestern part of study area is leaching, and it is being deposited into A. The continued leaching of the NE–SW trending granitic body through B might have also contributed to the uranium deposition in A. The granitic rock spanning the eastern and the upper part of the southeastern region is leaching in various directions (D3, D4, D5, and D6). D3 shows that the uranium particles leaching out from the granitic rock have also contributed to the deposits in C. D4 and D5 show the directions of uranium leaching from the granitic rock into F and other formations in the lower part of the southwestern region. Zone D in the northeastern part of the study area shows the likelihood of uranium rich basement rock, whose surrounding rock is leaching out. The eU–(eTh/3.5) map of the study area has prominently shown that the uranium ore leaching from the granitic rocks is mostly deposited in the Bima formations, and these deposits (A, B, C, F, and E) trend in the NE–SW direction, while D trends in the NW–SE direction.

Superposition of the inferred structural map on eU/eTh map

The superposition of the inferred structural map on eU/eTh map assists in delineating structural features that are rich in uranium. The superposition map for the study area is presented in Fig. 17. The high eU/eTh ratio areas in this study were grouped into eight zones, which were labelled: J, K, L, M, N, O, P, and Q. The possible areas of uranium deposition indicated on the eU – (eTh/3.5) distribution map (Fig. 16) were also taken into account when marking the uranium-enriched zones (i.e., zones J–Q) in the study area. It was observed on the map that the zones consist of many structural features that are dominantly trending in the NE–SW directions. Among these structural features are inferred faults, also dominantly trending in the NE–SW direction. Zone J, comprising Wade and Shinga districts, is dominated by NE–SW trending structural features. Other notable structures in the zone trend in the NW–SE and E–W directions. Three structure spanning several kilometres were prominent in this zone. One of these structures is a fault that has a high potential of hosting uranium deposits in its vein.

Majority of the structural trends at Zone K, consisting of Wuyo, Teli, Gedaba, and Bryel town, are in NE–SW direction; however, two structural faults trending in the NW–SE and E–W directions are also present. Zone M, whose deposition trends in the NW–SE direction (Fig. 17), comprises Gasi, Dali, and Barkan settlement; this zone contains majorly NE–SW structural features, but minor NW–SE structural features also exist. Zone N covers Boragara settlement; this area also comprises some alluvium deposits that are rich in uranium with faulted zone trending in E–W direction, while other structural features in the area trend in NW–SE direction. Zone L, comprising Zona, Yumbu, Yimirdallen, and Bahai settlements, has been reported by several authors (Suh et al. 1998; Oshin and Rahaman 1986) to be rich in uranium. Most structures in the zone trend in the NE–SW direction, except one, which trends in the NW–SE direction. Zones O and P, which are from the Burashika group, are made up of diverse suite of extrusive lavas and agglomerate to form the Bongna hills. These zones are characterized by two structures, a fault and contact zone, trending in NE–SW; these fault and contact zones are likely to contain high uranium deposits. Zone Q, which trends in the NW–SE direction and covers Whada, Wawa, Jakari, Hyama, and Kubuku settlements, is also dominated by NW–SE and NE–SW structural features; however, some NE–SW features also exist in the area.

From the map (Fig. 17), it was observed that the dominant structures that are rich in uranium trend in NE–SW direction, while the directions of leaching (Fig. 16), which

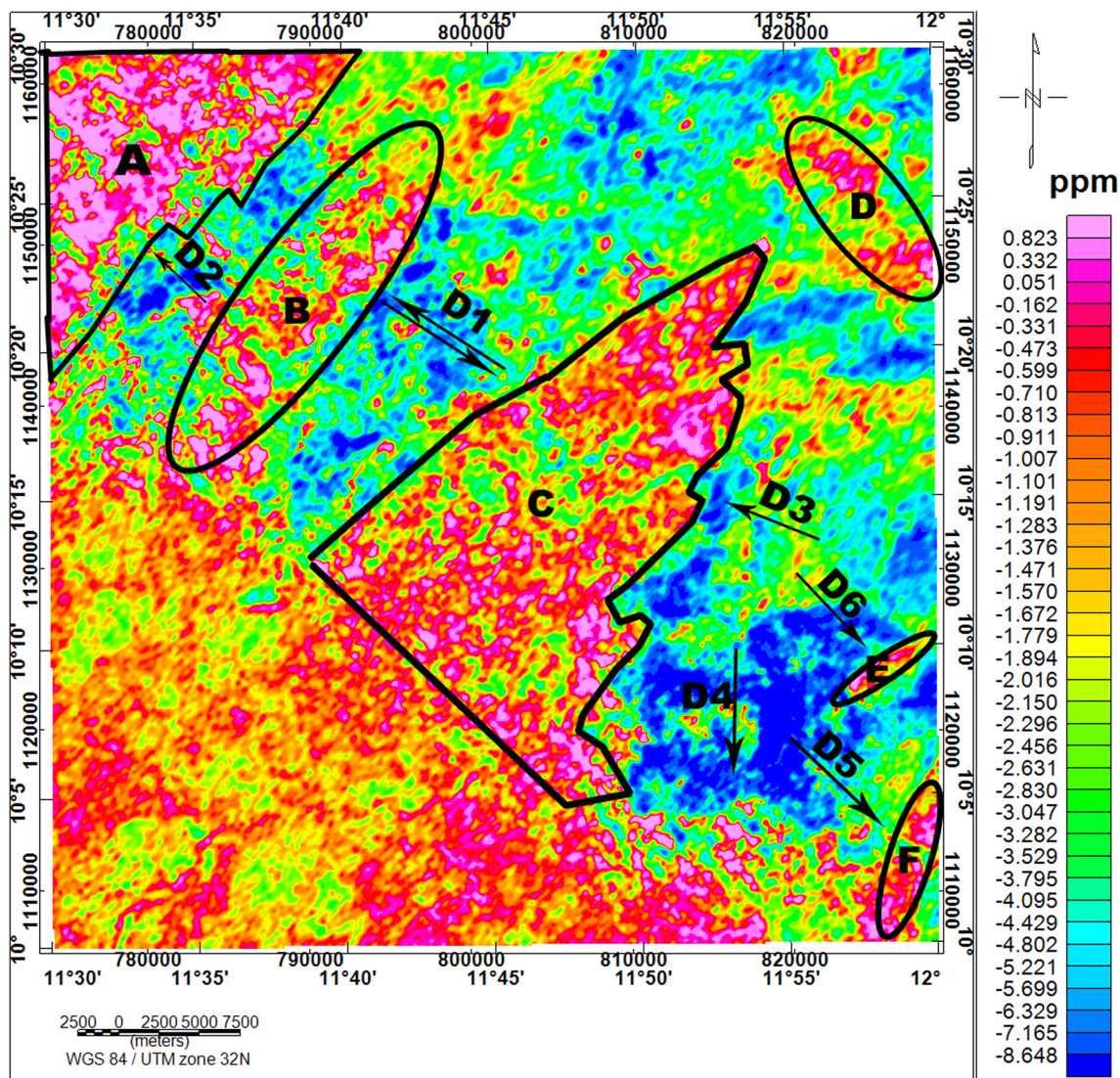


Fig. 16 eU-(eTh/3.5) map with the directional *arrows* showing the hypothetical trend of uranium migration

is also the paleocurrent direction for sediments in the area according to Haruna et al. (2012), are towards NW and SE. The perpendicular nature of the structural feature to the leaching direction has made this dominant structural trend to be more favourable for uranium deposition. Some of the NW–SE trending structures in the study area have been reported by Suh et al. (1998) to be rich in uranium.

Magnetic modelling of some selected uranium rich areas

Magnetic modelling of two profiles taken across some uranium rich zones (Fig. 18a) were carried out to provide 2D images of the subsurface that more accurately represent the topography, magnetic property, and structural geometry of the basement along the profiles. The profiles, labelled PP' and TT' in Fig. 18b, were taken in the NW–SE

direction. The result of the SPI analysis (Fig. 6) was used as depth constraint, and the resulting models along these profiles, PP' and TT', are presented in Fig. 18c, d.

As shown in Fig. 18c, d, profiles PP' and TT' were modelled as 29 basement blocks (R1–R29) and 21 basement blocks (R1–R21), respectively. The magnetic susceptibilities of the modelled blocks range from ~ 0.0001 to ~ 0.007 and ~ 0.002 to ~ 0.005 cgs across both profiles. The high number of visible basement blocks was as a result of the high-resolution aeromagnetic data used. Most of the contacts (boundaries) between these magnetic blocks were modelled to be approximately vertically dipping.

On PP' profile, contacts between blocks R15 and R16, and blocks R25 and R26 show magnetic anomaly that is more typical of a fault. Variation in the basement topography was also observed, with the sedimentary thicknesses of the entire area undulating between 35 and 1125 m on the

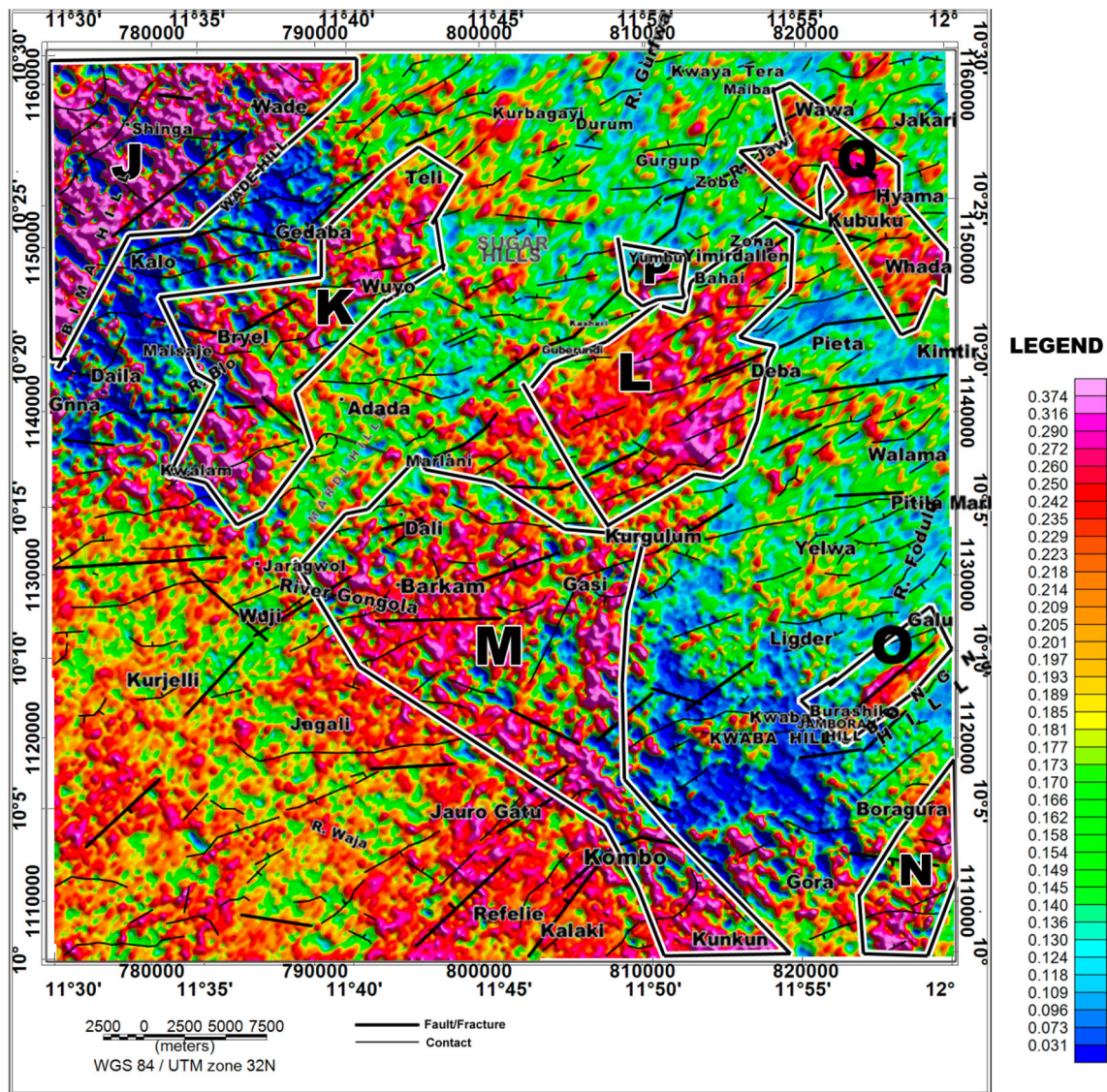


Fig. 17 Superposition of inferred structural map on eU/eTh map with selected zones with high concentration

magnetic basement. The uranium rich areas on the profile were labelled A, B, C, and D. At D, the interpreted fault between R25 and R26 is characterized by high uranium concentration on the eU/eTh ratio map (Fig. 15) and the eU-(eTh/3.5) distribution map (Fig. 16). This fault is, therefore, likely to be vein hosting uranium deposits. The areas marked B and C have relatively thick overburden with magnetic basement having susceptibilities ranging between ~ 0.004 and ~ 0.007 cgs. However, the basement rock below A is characterized by lower susceptibility of ~ 0.001 cgs. Each of these observed points (B, C, and D) shows a basin basement structure that is bounded on both sides by ridges. These ridges are likely to be the sources of the sediments deposited in this basin like structure.

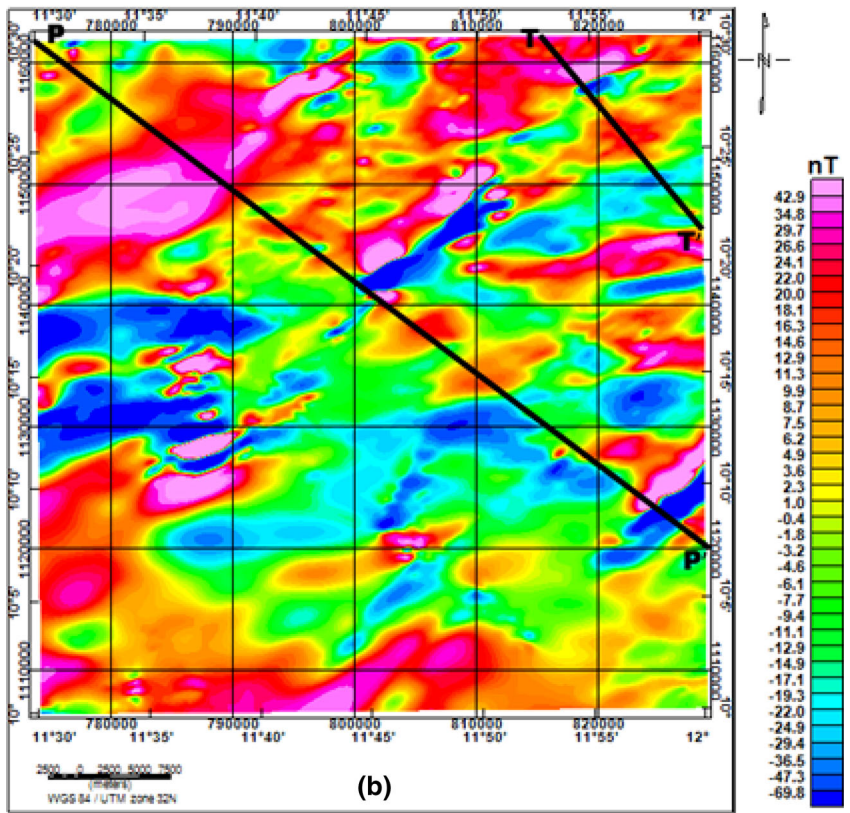
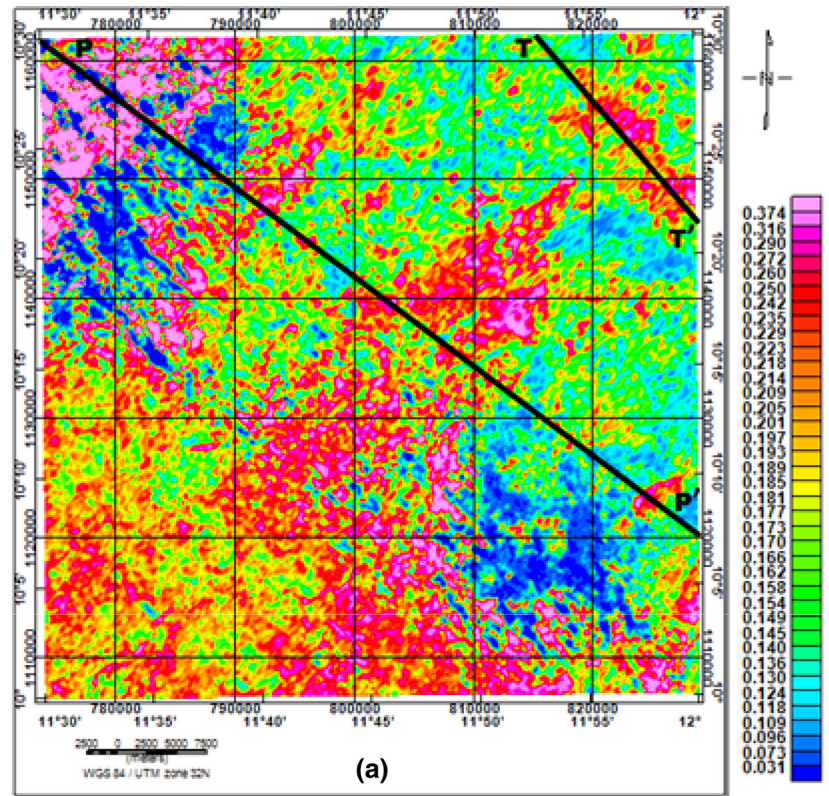
On TT' map, the uranium enrichment area covers blocks R7–R19. The modelled overburden thicknesses of this area

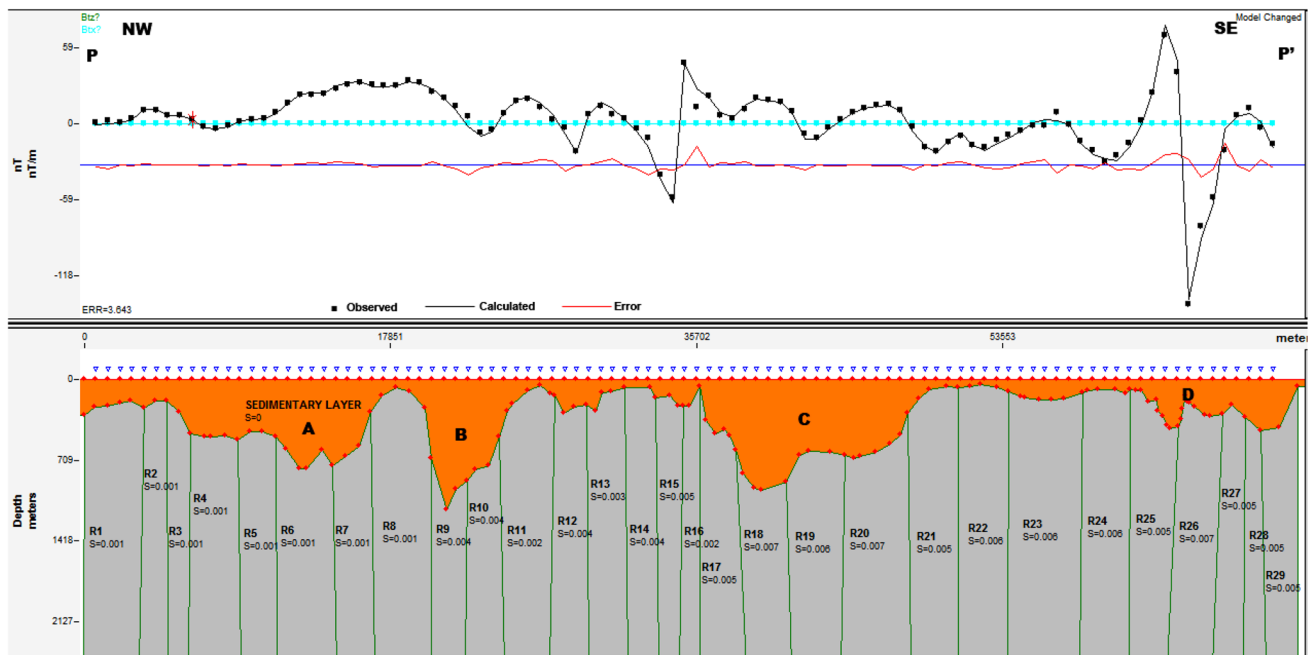
range between 13 m and 749 m. Contact between blocks R6 and R7 shows the magnetic signature of a geological structure which is likely to be a dyke or vein. The inferred structural map (Fig. 10) also shows that the location of this contact is a faulted zone. The trend of the contact is perpendicular to the trend of the high eU/eTh ratio anomaly observed in the region. This structure is, therefore, likely to contain uranium ore deposits.

Discussion

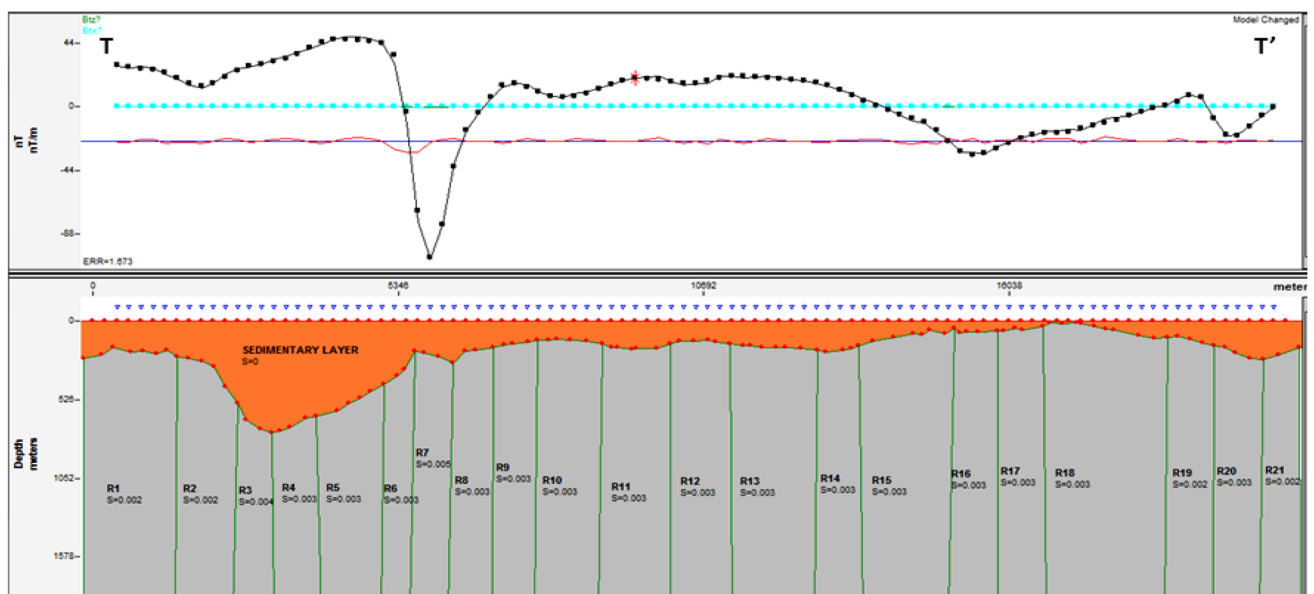
The study area, being a transitional zone, encompasses both the basement complex and sedimentary terrain. The result from the eU and eTh maps shows that the granitic bodies in the study area are rich in uranium and thorium

Fig. 18 **a** Profiles taken across the uranium rich zones. **b** Profiles' locations on filtered RTE map. **c** Magnetic model along profile P–P'. **d** Magnetic model along profile T–T'





(c)



(d)

Fig. 18 continued

than cretaceous rocks in the area. However, uranium which is the major interest in this study cannot be single handedly interpreted based on eU and eTh maps, because the source geometry clearly affects the absolute count rate, but has no effect on relative count rates; therefore, the use of ratio maps showing relative count rates was employed. The eU^2/eTh map reveals other uranium enrichment areas that were not exposed by the eU map which may be as a result of vegetation or damping effect. On the eU^2/eTh map, granitic

bodies, the Bima formation, and some other alluvium deposits were revealed. However, the eU^2/eTh map did not reveal areas suitable for uranium exploration, and this led to the use of eU/eTh ratio map which shows more defined uranium enrichment area. The eU/eTh map reveals that the granitic bodies are not extremely rich in uranium compared to Bima formation, Bongna hill lavas and agglomerate, and the anatectic migmatite at the northeastern region of the study area. The Burashika group (Bongna hill) at the

southeastern flank, anatectic migmatite at the northeastern region and most of the Bima formations in the study area show high eU/eTh concentration ratio of about 0.374. However, other sedimentary formations such as Yolde, Pindiga, Jessu, Dukul, and even the Bima formation at the southwestern region of the study area show moderate uranium concentration. These formations (Yolde, Pindiga, Jessu, and Dukul) are, therefore, not geologically ascertained for uranium deposition.

The possible trends of uranium distribution in the study area were shown on the eU – (eTh/3.5) map (Fig. 16). The map hypothetically reveals the leaching rocks and the direction of remobilization of uranium ore, with its source shown to be from the granitic bodies in the study area. The deposition observed in the region according to the eU – (eTh/3.5) map is secondary deposition (epigenetical remobilization of uranium ore). In addition to what was observed in the eU – (eTh/3.5) map, the result from magnetic basement depth analysis using SPI and forward modelling techniques shows basement highs at both sides of the uranium rich formations, while the locations of these uranium rich formations show pull-apart sub-basin structures. The basement morphological map, obtained from the radially averaged power spectral, shows horst and graben structures in the basement complex and sedimentary terrain, respectively.

The Bima (sandstone) formation was observed as the uranium richest sedimentary formation in the study area. This sandstone formation (Bima), being the most outcropping formation of the Upper Benue (Suh et al. 1998), has been reported by Carter et al. (1963) and Guiraud (1990) to contain three (3) lithological units known as lower Bima (B₁), middle Bima (B₂), and upper Bima (B₃). B₁, representing alluvium fan deposit, contains coarse-grained sandstone with matrix of scanty-muddy-to-sandy matrix; B₂, whose deposits were from high braided river deposits, comprises coarse-grained feldspathic sandstone with thin bands of clay, shale, and scanty calcareous sandstone, while B₃, whose sequence deposited under fluvial to deltaic environment, consists of well-sorted, medium-to-fine-grained feldspathic sandstone. Furthermore, the loose cementation and fine-to-medium-grained properties of Bima formation enabled the permeability of the uranium rich groundwater (since uranium is soluble in water) into the formation, and the calcareous (organic debris of animals) sandstones present in this formation served as the reducing agent for the precipitation of uranium. This type of deposition is also found in Canada (British Columbia), Western United States (Jack Pile mine, Lucky Mack mine), East Germany (Koenigstein), Gabon, Niger Republic, and South Africa (Karoo Basin) (Bell 1996; Ruzicka 1975, 1992). However, this region, which has been subjected to regional uplift and effects from various volcanic activities, also

shows likely abundant tectonic traps for deposition of uranium ore. It is a known fact that geological structures play a vital role in the formation, migration, and deposition of minerals in an area. The results from the structural mapping of the study area show that the basement in the study area is dissected, at various depths, by many structures that trend and dip in various directions. The dominant trends of the structures are ENE–WSW and NE–SW, while the minor structural trends are E–W, NNE–SSW, WNW–ESE, and NW–SE. The structures dip vertically, northeasterly, southwesterly, northwesterly, and southeasterly. The major ones, which dip northwesterly and southeasterly, trail in the same direction as the paleocurrent directions (Haruna et al. 2012), which is the direction of depositions of sediments in the study area. The basement faults in the study area dominantly exist between the depths of 500 and 1000 m. The NE–SW trending faults, which could have been created or reactivated during the reactivation of the Pan African basement, are perpendicular to the direction of uranium deposition in the study area and thus could have served as a trap for the migrating uranium. These NE–SW structural features show the highest uranium rich structural trends and were observed in both the sedimentary and basement complex uranium rich terrains. Uranium deposition in the sedimentary terrain of the study area is likely to be a sandstone type of deposition, while uranium depositions in the faults/fracture veins of the basement complex terrain might have also been formed as a result of the occurrence of volcanic activities in the area. These volcanic activities might not only have provided the thermal energy fluid containing dissolved uranium ore, but might have also served as a reducing agent for the precipitation of uranium ore.

The HRAD and radiometric data analyses, and the geological settings of the study area show that the Bima sandstone formation serves as a reservoir for uranium mineralization bearing solutions. The fault, fracture, and contact zones in the sedimentary units show the tendency of providing favourable post depositional zones for uranium concentration. Wade, Zona, Shinga, Bima Hill, Wuyo, Teli, Bryel, Dali, Barkan, Gasi, Kunkun, Boragara, and Deba localities have shown high affinity for uranium depositions in the sedimentary unit of the study area. Whada, Gberundi, and Kubuku localities in the basement complex unit also show high affinity with uranium depositions. In addition, the Burashika fault around Bongna hills lava and agglomerate at Kawaba and Galu regions, and Wawa zones show possible uranium rich veins. Zona and Wawa areas, which have also been reported by Suh and Dada (1998) and Oshin and Rahaman (1986) to be rich in uranium and favourable for uranium deposition, were also found to have high uranium concentration. However, uranium depositions in the study area (rift-related basin) might

be low-grade due to multiple tectonic reactivation and re-precipitation of the ore (Haruna et al. 2012).

Conclusions

Results from the structural analysis of the aeromagnetic data showed that the study area is dissected by many structures that trend ENE–WSW, NE–SW, E–W, NNE–SSW, WNW–ESE, and NW–SE; among which the ENE–WSW and NE–SW trends dominate. These structures dip vertically, northeasterly, southwesterly, northwesterly, and southeasterly. The basement faults in the study area dominantly exist between the depths of 500 and 1000 m. The northwesterly and southeasterly dipping faults dip in the same direction as the paleocurrent direction (direction of depositions of sediments) and trend in a direction perpendicular to the direction of uranium deposition in the study area. These faults could, therefore, serve as potential traps for uranium deposition in the study area.

The result of this study has shown that the uranium ores were remobilized epigenetically from the granitic rocks and were re-deposited into sedimentary rocks (Bima sandstone formation). The depth to the basement was estimated to be between 150 and 1941 m below the flight line. The areas showing vein-type deposition were found in the Burashika Group (Bongna Hills) and Wawa area. The anatectic migmatite in the northeastern region and the uranium rich Bima formations in the study area show both fault/fracture and contact types of depositions. The structures in these identified formations are highly favourable for uranium mineralization in the study area.

The study, therefore, concluded that the studied area is dissected by several linear structures, among which the ENE–WSW and NE–SW trending structures dominate, and that the deposits of uranium ore in the studied area are likely to be found in: the Bima sandstones of Wade, Shinga, Bima Hill, Wuyo, Teli, Bryel, Dali, Barkan, Gasi, Kunkun, Boragara, Deba, and Gberundi localities; the anatectic migmatite at Kubuku, Whada, and Hyama; and the Bongna hills and agglomerates around Burashika, Kawaba, and Galu. However, these areas which are likely to be mineralized zones of uranium deposition are needed to be probed further for exploration purposes.

Compliance with ethical standards

Conflict of interest There is no conflict of interest in this research.

References

- Anudu GK, Stephenson RA, Macdonald DM (2014) Using high resolution aeromagnetic data to recognise and map intra-sedimentary volcanic rocks and geological structures across the Cretaceous middle Benue Trough, Nigeria. *Elsevier J Afr Earth Sci* 99:625–636
- Bell RT (1996) Sandstone uranium. *Geology Survey of Canada, Geology of Canada*, no 8, pp 212–219
- Benkhelil J (1986) Geological map of part of the Upper Benue Valley; Explanatory Note. Elf Nigeria Ltd, p 4–16
- Bowden P, Bennett JN, Kinnaird JA, Whitley JE, Abaa SI, Hadzigeorgiou-Stavrakis PK (1981) Uranium in the Niger-Nigeria younger granite province. *Mineral Mag* 44:379–389
- Cambon AH (1994) Uranium deposits in granitic rocks. In: Notes on the national training course on uranium geology and exploration. IAEA and NMA, Cairo, Egypt, pp 8–20
- Carter JD, Barber DFM, Tait EA (1963) The geology of parts of Adamawa, Bauchi and Bornu Provinces in Northeastern Nigeria. *Bulletin of Geological Survey, Niamey*, p 30
- Clark SP, Peterman ZE, Heier KS (1966) Abundance of uranium, thorium and potassium. In Clarke SP Jr. (Ed), *Handbook of physical constants*. Geological Society of America. *Memoir* 97, Section 24, p 521–554
- Darnley AG (1975) Geophysics in uranium exploration. *Geological Survey of Canada, Uranium Exploration*, Ottawa, pp 21–31
- Dentith M (2011) Magnetic methods, airborne. In: Gupta HS (ed) *Encyclopedia of solid earth geophysics*, vol 1. Springer, Dordrecht, pp 761–766
- Dobrin MB, Savit CH (1988) *Introduction to geophysical prospecting*, 4th edn. McGraw-Hill Books, New York, pp 633–725
- Foote RS, Humphrey NB (1976) Airborne radiometric techniques and applications to Uranium exploration, *Exploration for Uranium Ore (IAEA-SM 208/47)*. IAEA, Vienna
- Funtua II, Okujeni CD (1996) Element distribution patterns in the uranium occurrence at Mika, northeastern Nigeria. *Chem Erde* 56:245–260
- Gaafar I, Aboelkhair H (2014) Analysis of geological and geophysical datasets for radioelement exploration in KabAmiri area, central eastern desert. *Egypt. Open Geol J* 8(Suppl 1: M3):34–53
- Guiraud M (1990) Tectono-sedimentary framework of the early Cretaceous continental Bima Formation (Upper Benue Trough, Northeastern Nigeria). *J Afr Earth Sci* 10:341–353
- Haruna IV, Ahmed HA, Ahmed AS (2012) Geology and tectonosedimentary disposition of the Bima sandstone of the Upper Benue Trough (Nigeria): implications for sandstone-hosted Uranium deposits. *J Geol Mining Res* 4(7):168–173
- Lauri LS, Turunen P (2015) Airborne radiometric data as a uranium exploration tool case studies from Southern Lapland. *Geophysical Signatures of Mineral Deposit types in Finland*, Geological Survey of Finland, Special Paper 58, pp 107–116
- Maurin JC, Lancelot JR (1990) Structural setting and U-Pb dating of uranium mineralization from the north-eastern part of Nigeria (Upper Benue Region). *J Afr Earth Sci* 10:421–433
- Nabighian MN (1972) The analytic signal of two dimensional magnetic bodies with polygonal crosssection: its properties and use for automated anomaly interpretation. *Geophysics* 37
- Nabighian MN (1984) Toward a three-dimensional automatic interpretation of potential field data via generalised Hilbert transforms: fundamental relations. *Geophysics* 49:780–789
- Ndougsa-Mbarga T, Feumoe ANS, Manguelle-Dicoum E, Fairhead JD (2012) Aeromagnetic data interpretation to locate buried faults in South East Cameroon. *Geophysica* 48(1–2):49–63
- Nwajide CS (2013) *Geology of Nigeria's sedimentary basins*. CSS Bookshop Limited, First Published, ISBN 978-978-8401-67-4, pp 27–110
- Nwosu OB (2014) Determination of magnetic basement depth over parts of middle Benue Trough by Source Parameter Imaging (SPI) technique using HRAM. *Int J Sci Technol Res* 3(1):262–271

- Obaje NG (2009) Geology and mineral resources of Nigeria. Springer, Berlin, pp 2, 49–65
- Obiora SC (2009) Field measurements in descriptions of igneous and metamorphic rocks. In: Lambert-Aikhionbare DO, Olayinka AI (eds) Proceedings of field mapping standardisation workshop, Ibadan University Press, Ibadan, pp 105–125
- Odebode MO (2010) A handout on the Geology of the Benue and Anambra Basin, Nigeria (unpublished work)
- Oshin IO, Rahaman MA (1986) Uranium favourability study in Nigeria. *J Afr Earth Sci* 5(2):167–175
- Philips JD (2000) Locating magnetic contacts: a comparison of the horizontal gradient, analytic signal, and local wavenumber methods: Calgary. In: 70th Meeting, society of exploration geophysicists, expanded abstracts with biographies, 2000 Technical Program, vol 1, pp 402–405
- Reid AB, Allsop JM, Granser H, Millet AJ, Somerton IW (1990) Magnetic interpretation in three dimensions using Euler deconvolution. *Geophysics* 55:80–91
- Roest W, Verhoef J, Pilkington M (1992) Magnetic interpretation using 3-D analytical signal. *Geophysics* 57:116–125
- Ruzicka V (1975) New sources of uranium? Types of uranium deposits presently unknown in Canada. *Geological Survey of Canada, Uranium Exploration* 75, pp 13–47
- Ruzicka V (1992) Types of uranium deposits in the former U.S.S.R.; *Colorado School of Mines Quarterly Review* 92(1):19–27
- Sambo AS (2008) Matching electricity supply with demand in Nigeria. In: Paper presented at the “National Workshop on the Participation of State Governments in the Power Sector: Matching Supply with Demand”, 29 July 2008, LadiKwali Hall, Sherato Hotel and Towers, Abuja
- Saunders DF, Potts MJ (1976) Interpretation and application of high sensitivity airborne gamma ray spectrometer data; in *Exploration for Uranium Ore Deposits. Proc. Series, IAEA, Vienna*, pp 107–125
- Suh CE, Dada SS (1998) Mesostructural and microstructural evidences for a two stage tectono-metallogenic model for the uranium deposit at Mika, northeastern Nigeria: a research note. *Nonrenew Resour* 7(1):75–83
- Suh CE, Dada SS, Ajayi TR, Matheis G (1998) Integrated structural and mineral alteration study of the Zona uranium anomaly, northeast Nigeria. *J Afr Earth Sci* 27(1):129–140
- Tauchid M (1993) Nuclear raw Materials: developing resources through technical cooperation. *Int Atom Energy Agency Bull* 35:14–17
- Telford WM, Geldart LP, Sheriff RE (1990) *Applied geophysics*, 2nd edn. Cambridge University Press, Cambridge, pp 62–123, 611–636
- Thompson DT (1982) EULDPH: a new technique for making computer-assisted depth estimates from magnetic data. *Geophysics* 47:31–37
- Thurston JB, Smith RS (1997) Automatic conversion of magnetic data to depth, dip, and susceptibility contrast using the SPI method. *Geophysics* 62:807–813
- Thurston JB, Guillon C, Smith R (1999) Model independent depth estimation with the SPITM method. In: 69th Annual International Meeting, SEG, Expanded Abstracts, pp 403–406
- Thurston JB, Smith RS, Guillon JC (2000) A multi-model method for depth estimation from magnetic data. *Geophysics* 67:555–561

Key preprocessing technology and its application for CBM AVO analysis

Zhiwei Liu¹  · Guoshuai Si² · Xinping Chen³ · Qing Wang⁴ · Shiguang Deng¹

Received: 16 February 2017 / Accepted: 7 September 2017 / Published online: 21 September 2017
© Institute of Geophysics, Polish Academy of Sciences & Polish Academy of Sciences 2017

Abstract The hazards of amplitude versus offset (AVO) technique mostly applied in seismic explorations for predicting coalbed methane (CBM) content mainly derive from multi-stage amplitude modifications during seismic signal preprocessing. The modifications are undoubtedly necessitated by improving high signal-to-noise ratio (SNR) and high resolution, and achieve high fidelity to some extent; and nevertheless lead to an unfavorable possibility to implement CBM AVO analysis. Similar to sandstone reservoir with gas, AVO analysis preprocessing for CBM reservoir strictly abides by a relative amplitude preserved (RAP) principle and particularly emphasizes on preserving the evanescent class IV AVO anomaly. As for those indispensable dealings with linear noise attenuations, near-surface variety compensations and time/depth spatial imaging, the key technologies adapted to CBM AVO preprocessing should use radial trace (RT) filter, refined surface-consistent amplitude compensation (SCAC), and RAP Kirchhoff prestack time migration (PSTM). The theoretical analysis and one real 3D example in this paper demonstrate that three key technologies compliant to RAP principle in CBM AVO preprocessing can preserve the class IV AVO

anomaly and benefit an operation of CBM AVO analysis and an improvement of CBM evaluation.

Keywords CBM AVO analysis · Relative amplitude preserved · Radial trace filter · Surface-consistent amplitude compensation · Kirchhoff prestack time migration

Introduction

The AVO (amplitude versus offset) technique mainly assesses and takes advantage of trends in seismic reflection amplitude with variety of distances between shots and receivers. AVO analysis allows geophysicists to better assess reservoir rock properties, including porosity, density, lithology and fluid content (Gochioco 2002; Hong and Bancroft 2006; Peng et al. 2006). To further reduce coal-mining hazards and efficiently exploit coalbed methane (CBM) resource as a type of green fuel, the seismic AVO technique for a traditional sandstone gas' identification has been increasingly brought into the CBM reservoir's prediction (Andrew and Taylor 2016). Based on many analyzes conducted on well data as well as theoretical AVO modeling, it has been shown that the geophysical AVO response in CBM reservoir is completely different from conventional sandstone bearing gas (Zuber 1998). The CBM AVO anomaly belonging to Class IV in the AVO classification table presents that seismic reflection amplitudes (absolute value) at a roof and floor of coal beds gradually decreases with increasing source–receiver distance (offset) (Antonio Ramos and Thomas 1997, Peng et al. 2006, Wu et al. 2016). Some related theory prove that seismic AVO technique can be completely extended to an enriching region of CBM if the class IV AVO anomaly

✉ Zhiwei Liu
zwliu007@sina.com

¹ Chinese Academy of Geological Sciences, Beijing 100037, People's Republic of China

² Research Institute, BGP Inc, CNPC, Zhuozhou 072751, People's Republic of China

³ Geomodulus Co. Ltd, Beijing 102208, People's Republic of China

⁴ Institute of Geology and Geophysics, Chinese Academy of Sciences, Beijing 100029, People's Republic of China

comes into processor's attention (Chen et al. 2014). In a few productions, a series of favorable and unfavorable factors on CBM AVO analysis have recently been detailedly discussed (Peng et al. 2006). However, many cases from coalfield companies around the world have been shown that it is risky to apply AVO technique for CBM reservoir and the risk mainly derives from how to preserve the Class IV AVO abnormal amplitudes during seismic preprocessing (Hu et al. 2002).

As we know, there are some factors in seismic exploration, such as earth filter systems, seismic acquisition conditions, environmental noises, etc., that affect the amplitude of seismic reflections. The first factor will usually lead to a spherical spreading, stratigraphic energy absorption, a thin interbed tuning, some anisotropy and geological structure characters. The second often possesses a kind of surface-consistent property, such as the source and receiver's conditions, the lateral variety of near-surface weathered layer, and so on. The last one includes different types of noises, for example, ground-roll wave, linear subrefraction wave, random noise, source-caused noises and secondary interference noises. Since kinds of coalbeds are not in accord with a precise horizontal model, dip moveout (DMO) used in seismic processing as one type of prestack partial migration methods for diffraction wave imaging and stacking velocity refining is traditionally applied to AVO preprocessing of seismic data. However, DMO cannot be rigorously abided with a relative amplitude preserved (RAP) principle and hardly achieve subsurface reflection points truly homing. Therefore, it is a prevailing trend that the prestack time migration (PSTM) for CBM AVO preprocessing takes place of DMO and subtly avoids more amplitude contaminations aroused by a spherical diffusion and precisely restores the complex geological structure. Compared with other migration algorithms, Kirchhoff PSTM has been confidently considered as the key technology for CBM AVO preprocessing due to widely adapting to a lateral velocity variety and complex acquisition systems, and providing a more accurate root-mean-square (RMS) velocity model and more RAPer common reflection point (CRP) gathers. Then, multiple wave attenuating, frequency bandwidth extending, tuning deconvolution, source wavelet consistent processing directed against the first factor are basically similar to the thin interbed's preprocessing, which application can be found in many references (Gochioco 1991; Liu and Wang 2013). As for CBM AVO preprocessing, some near-surface amplitude corrections and non-reflection wave's suppressions should be inserted before the crucial PSTM preprocessing. Except for much of artificial and environmental anomalies, seismic noises mainly include the linear interferences strongly existing near to the target events, such as ground-roll wave and secondary refractions. These linear noises' attenuating and excluding based on transform

domain filtering can partly induce reflection amplitudes' distortions and low frequency missing, while the method on the radial trace (RT) transform can protect reflection amplitudes so well that RT filter has been confidently considered as the key technology of CBM AVO preprocessing. Surface-consistent amplitude compensation (SCAC) has been seen as one of effective approaches to eliminating near-surface weathering changes about seismic velocity and strata density (Liu et al. 2013). More rigorously, SCAC compensating coefficients in sources and receivers may be sequentially decomposed into long wavelength (high frequency) and short wavelength (low frequency) contents. Low frequency represents the difference of source explosive charges, numbers of combined wells, receiver types, and high frequency reflects the change of the near-surface geological conditions. Therefore, SCAC based on the separating frequencies will become the key technology of CBM AVO analysis preprocessing.

In this article, we will detailedly discuss amplitude-preserved Kirchhoff PSTM, linear noise suppression using RT filter and refined SCAC based on high/low frequency separating which are as the key technologies for CBM AVO analysis preprocessing. Finally, we will comprehensively analyze the applications of these technologies.

The key technology of CBM AVO preprocessing

Amounts of coalfield seismic data and CBM AVO forward modelings discover that seismic reflection response on a roof and floor of coalbed in seismic prestack gathers attributes to class IV AVO anomaly (Jason et al. 2007, Chen et al. 2013, 2014). When an incidence angle is less than or equal to 45° , reflection coefficients from the coalbed roof decrease along with the increasing angle, behaving as a negative gradient and a positive intercept, and the coefficients from the coalbed floor decrease too, as a positive gradient and a negative intercept (Chen et al. 2013). Based on the relationships between offsets associated with incidence angles and reflection amplitudes with reflection coefficients, seismic reflection amplitudes from the roof and floor of coalbed are gradually decreasing along with the offsets increasing (Rutherford and Williams 1989). Considering the CBM AVO anomaly, reflection amplitudes in seismic preprocessing should be enough protected during the former discussed linear noise attenuating, SCAC and PSTM closely related to amplitude modifications.

Radial trace filter

Henley and Lamont have applied the radial trace transform (RTT), first introduced by Claerbout in 1975, to multiple reflections' excluding in 1999, and widely deployed to

attenuating coherent noises (Henley 2003). The filter designs based on the RTT have been further developed because of its simplicity and operability. First, let us review the mathematical principle of RTT and reassess its RAP ability of RT filter. The RTT can achieve a type of transform from time-offset (T - X) domain to radial-trace (T' - V) domain in a seismic ensemble, where T' represents new time scale and the V points to linear velocity, defined as

$$T' = T - T_0 \quad (1)$$

$$V = (X - X_0)/(T - T_0), \quad (2)$$

(T_0, X_0) defined as original point of transform. Along with a certain velocity direction, the RTT will put samples from different offsets in an ensemble onto a velocity trace marked as a lateral axis, meanwhile keeping the same time scale unchanging. After scanning ranges of velocity with an interval, the RTT converts a sector area of time-offset domain into a rectangular zone of time-velocity ensemble. As shown in Fig. 1a, b, some linear noises in one time-offset ensemble become concentrated on/near to many velocity lines (trace) and frequency dispersing a little in radial-trace ensemble, while those reflection hyperbolas widely intersperse among the velocity traces.

As it is shown in Fig. 1, the new time scale and regular offsets make RTT preferably adapted to 3D's linear noise conversion when offset is nonlinearly varying with an increasing crossline interval. If the velocity interval is small enough, early linear noise will be densely sampled and present divergent frequencies, while reflection amplitudes do not almost be changing. Therefore, this transformation from sector to rectangle can cause a stretch of early samples and produce a spatial alias, and the alias is just a transform response of linear noise. If we simply extract the space alias (amplitude and frequency) by low-pass filter, inversely transform it into time-offset domain as a noise model, and then apply adaptive filtering based on model subtraction method, the objective reflection can be fully protected and the expected linear noises be attenuated. Compared with other 2D transforms, such as Tau-P and F-K, in which an intersecting area between linear noises and valid reflections is always larger than in RTT, just shown in Fig. 1c, d. So, the RT filtering can decrease the possibility to modify reflection amplitudes and become fit for the CBM AVO analysis preprocessing.

(2) SCAC based on a frequency separating

Amplitude corrections as one of key flows in AVO preprocessing sequences include Earth spherical spread

compensating (SSC) and surface-consistent amplitude compensating (SCAC) which, respectively, come to achieve a temporal and spatial correction. As regards the SSC, Ostrander's research has discovered that the zero offset compensating instead of nonzero offset will lead to an under-compensating because of absorption effect of large offsets (Ostrander 1984). Additionally, RAP PSTM algorithm has been carefully considered on the influence of spherical spreading (Liu et al. 2013). Therefore, it is unnecessary for CBM AVO analysis preprocessing to apply the SSC flow before the SCAC. The SCAC aims to eliminate some surface-consistent variations associated with sources and receivers caused by near-surface geological settings and seismic acquisition system, and this flow has been always preferred as the necessary step for a conventional AVO analysis preprocessing (Liu and Wang 2013). The SCAC is mostly appropriate to CBM AVO analysis preprocessing as well, and furthermore, the only consideration is how to deal with the Class IV AVO anomaly.

Some aspects on compensating operators' computing and applying in SCAC need to be considered about a target window, a statistic amplitude-type, and a decomposing domain (Liu et al. 2013). The target window determines the compensating depth, on surface or sub-surface, and both amplitude statistics are likely to be contaminated by seismic noises. On fact of shallower target of coalbeds, SCAC's target window should put first-break wave aside and include target coalbeds. A statistic amplitude-type is popularly classified into root-mean-square (RMS) and average absolute (AA) types, and RMS amplitude generally suffers more effect of boundary and influence of exceptional spikes. The operating sequences of SCAC executed on different domains (source, receiver, offset and so on) will finally lead to a different precision and error. How to reduce the non-uniqueness of solution and set up the reasonable constraint is the key point to implement the refined SCAC in CBM AVO analysis preprocessing.

The SCAC's operators in source domain present on a low and high frequency characteristic (long wavelength (LW) and short wavelength (SW)). The LW components mainly point to the difference between explosive charges and hole depths in acquisition, and the SW components imply the near-surface geological circumstance changing. The operators in the receiver domain are similar to those in the source domain. The factors in common middle point (CMP) domain and common offset (CO) domain represent not only the near-surface conditions changing, but also the anomaly of subsurface target reservoir, which is a particularity for CBM AVO analysis preprocessing. Thus, to refine SCAC and protect Class IV AVO anomaly to an extreme extent, SCAC's LW and SW components in CMP

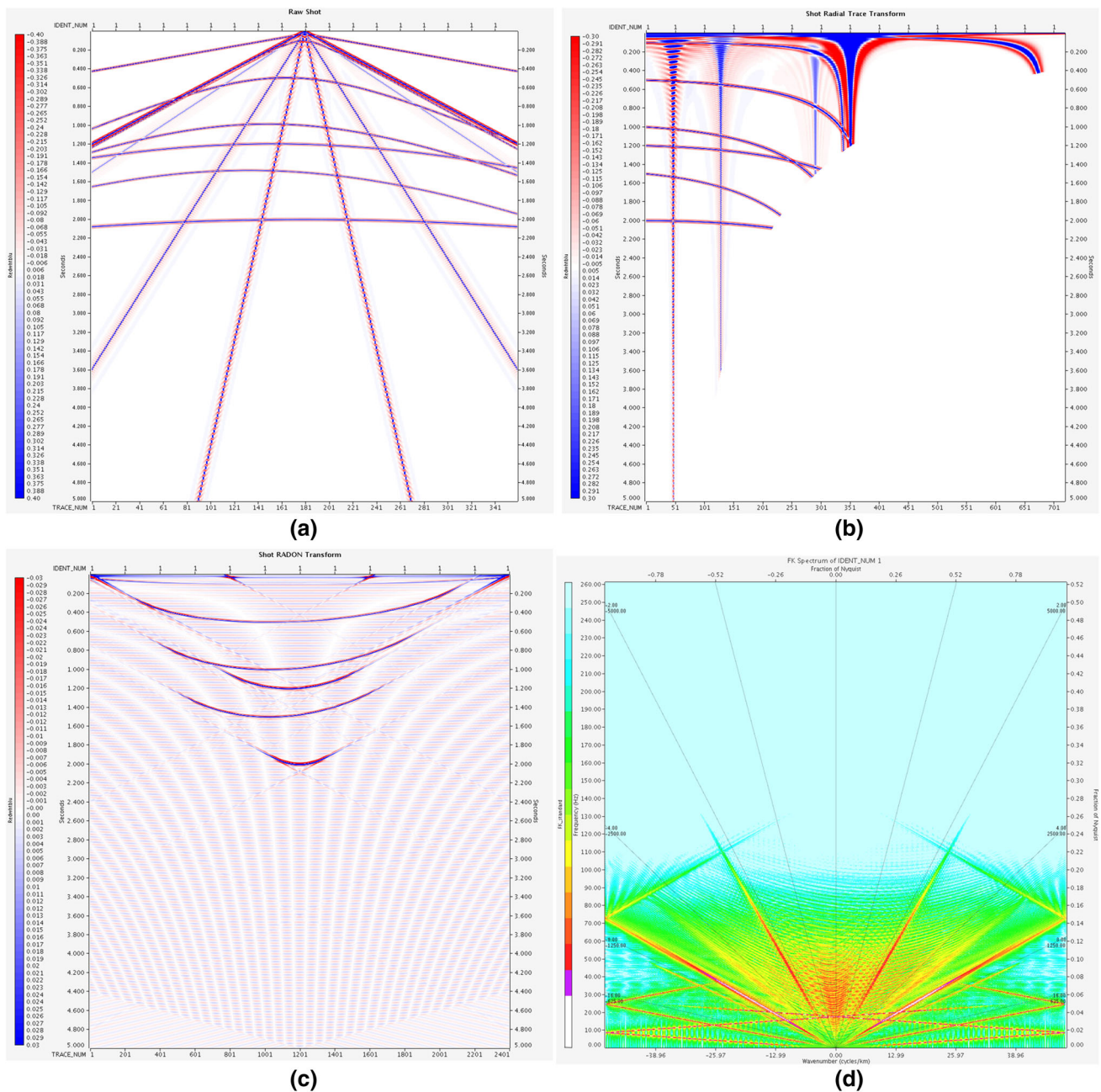


Fig. 1 Presentation of a model shot in different domains. **a** T-X domain, **b** radial domain, **c** Tau-P domain, **d** F-K domain

domain should be recomputed and extracted after SCAC in source and receiver domains. This means that LW component represent true AVO anomaly.

The distribution on a sample time between amplitudes and offsets of a moveout CMP gather from a real CBM deposition zone shows in Fig. 2a. The amplitudes' jump implies both imbalance of source–receiver's amplitude and CBM AVO anomaly in subsurface reservoir.

According to the Shuey formula (Shuey 1985), amplitudes' variation with offsets in CMP domain has been approximately expressed as:

$$Amp(x) = A_0 + A_1x + A_2x^2 + A_3x^3 + \dots \quad (3)$$

The multinomial coefficients (A_0, A_1, A_2, \dots) as a multivariable function of time and velocity can be solved by means of fitting these amplitudes in a CMP gather, then these fitting amplitudes as LW component (Red circles in Fig. 2b) and those scale factors as SW component (Green

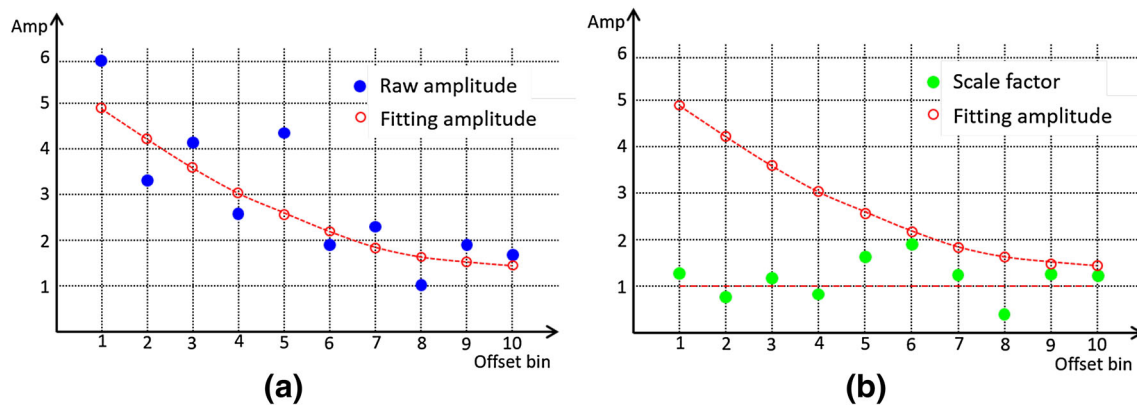


Fig. 2 High–low frequency amplitudes decomposition of a CMP gather. **a** Amplitude fitting; **b** high-low frequency separating

points in Fig. 2b) can be gained. Considering on influence of the Fresnel zone and lower fold zone, it is necessary to smooth a span of CMPs.

Because a diameter of the Fresnel zone is determined by two-way travel time, primary frequency of seismic data and RMS velocity, a more CMPs need to be smoothed when CBM targets lie in a deeper depth. The red circles in Fig. 2b show that CBM AVO anomaly belong to Class IV.

RAP PSTM

Under the condition of horizontal geological structure, there are many successful cases in CBM AVO preprocessing included normal moveout (NMO) and DMO on CMP gathers. As we know, the NMO has been seen as an origin of stretch inducing an amplitude interpolation of some far-offset traces. DMO or prestack partial migration can partly achieve the diffracted waves imaging and eliminate an influence of strata's dip angles, but it is not completely a standard RAP processing because of identification of multiple reflection waves and velocity preconditions (Charles et al. 1996).

A standard AVO analysis equation has been derived on base of such a local horizontal model that a CRP from PSTM is more objective to execute CBM AVO analysis than a CMP, especially under non-horizontal geological conditions (Charles et al. 1996).

Except for the tilt reflection, the PSTM preprocessing for those curve reflectors, such as anticline and syncline folds, could correct the abnormal amplitudes from the wave impedance interface and remove an effect of curvature. Considering on a curve interface and a horizontal interface with normal incidence plane waves, the reflection amplitude ratio CE defined as:

$$CE=1/\sqrt{1+A^{-1}z} \quad (4)$$

Here Z is the reflector depth, and A is the reflector curvature, a negative indicating syncline, a positive

indicating anticline. When a bunch of plane waves are getting to the interfaces with normal incidence, reflection amplitude varies with CE. Based on Huygens principle, reflection amplitudes from a curve interface like a syncline are larger than from the flat interface, and the amplitudes from a curve interface like an anticline are smaller than from the flat interface. The physical interpretation about the phenomenon is that the syncline has a capacity to focus reflected energy, while the anticline just scatters reflected energy.

Considering on one curve interface and one horizontal interface with a point source wave, the reflection amplitude ratio CE is defined as:

$$CE=1/\sqrt{1+A^{-1}z/\cos^2\theta}, \quad (5)$$

Here θ is an incidence angle. When a point source wave is propagating onto the interfaces, reflection amplitude more complicatedly varies with CE.

The PSTM's algorithms generally include Kirchhoff integral, finite difference and Fourier transform based on the wave equation, and RAP method of every type is not the same. The RAP point in the Fourier transform PSTM is to obtain the stable phase function of migration operator. When the operator spatially shifts the phase, reflection energy moves a DMO distance along with the source–receiver line; when the operator temporally shifts the phase, this represents the DMO function and RAP characteristics varies with cross-line offsets and velocity in inline and crossline. The finite difference PSTM is presently similar to the Fourier transform, meanwhile some high-precision full wave equation migration (FWEM) can complete true amplitude migration and its theory and applications are relatively few in CBM AVO preprocessing. The RAP consideration of Kirchhoff integral PSTM is to acquire true amplitude weight function, which used to compensate the geometric diffusion during the diffraction stacking. The methods getting true amplitude weight function mainly depend on Green's function quantities, Beylkin

determinant and paraxial ray trace which, respectively, has a different RAP characteristic for a certain geological structure (Zhang 2006). As for a horizontal reflector, a simple and steady weight function on velocity, frequency and dip can be easily obtained to meet a RAP requirement; otherwise, AVO analysis error will be increasing if true amplitude weight function is not used as for a complex reflector.

Among three types, Kirchhoff integral PSTM based on true amplitude weight function relatively has a RAP advantage in CBM AVO analysis preprocessing. First, simple weight function is used to maintain an amplitude fidelity. Second, a relatively accurate RMS or interval velocity is provided for CBM AVO analysis. Therefore, the Kirchhoff PSTM is the key technology of CBM AVO analysis preprocessing.

Application

3D seismic survey involved in this paper is designed to CBM developing and gas drainage in coalfield. The survey's geographic landform belongs to a kind of rivated plain with some NW–SE hills in the north-central and some denuded intervals in the south. An elevation fall from hill to interval reaches to about 270 m, and there are more sandstones outcropping on top of these hills. Such poor geological conditions, as well as the presence of farmhouses and rivers that should be avoided during acquisition, make the 3D seismic acquisition geometry not uniform. The acquisition parameters are detailedly listed in Table 1. About the geological setting, the main structure of study area is one wide and gentle NW–SE orientated anticline with 320° axis, and its NE limb is steeper than its SW limb. A thrust fault NW striking and NE dipping lies in the anticline's axis, and a normal fault NE striking and NW dipping lies in the west. Many coalbeds lie in about 800 m underground and CBM content of coalbed is approximately 6.65 m³/t. The overlying Cenozoic strata have an uncomfortable contact with the underlying coalbeds, which are

outcropped superficially in some places. The coalbed #ER₁ almost exists in the whole area, 7 m thick on the average, and its roof stratum is mainly sandy mudstone and mudstone and the floor belongs to limestone. The coalbed's roof and proof as a fair acoustic impedance boundary can produce a few set of strong reflection events.

Seismic AVO analysis on study area aims to an estimation of CBM content and guides a follow-up production. Based on the fact of general geological structure, the special AVO anomaly, and the complex acquisition system, CBM AVO analysis preprocessing focuses on taking into account SNR and fidelity of CMP gathers, and RAP PSTM (CRP gathers). Except for 3D tomographic inversion statics, surface-consistent zone anomaly processing (ZAP), multichannel deconvolution and reflection residual statics, three key technologies applied to CBM AVO preprocessing include radial trace filter eliminating linear noises, refined SCAC compensating reflection amplitudes, and RAP PSTM imaging and outputting RAP CRP gathers.

The frequency analysis on some typical shots shows that a valid frequency bandwidth is 8–70 Hz, and the dominant frequency is about 35 Hz. Seismic noise mainly includes ground-roll waves, linear refraction noises and burst spikes, shown in Fig. 3a, which are almost submerging partial reflection waves. The ground-roll wave's velocity is basically less than 1000 m/s, and its frequency is distributing on range of 0–15 Hz. Secondary refraction's velocity is generally less than 2000 m/s. Some abnormal amplitudes like a spike possess low frequency less than 10 Hz and high frequency more than 50 Hz attributes and randomly spread all over a shot record.

The linear noises less than 2000 m/s velocity can be mostly attenuated by radial trace filter, which cannot only protect reflection amplitudes in full spectrum but also not introduce a spatial aliasing, as shown in Fig. 3b. We can see in Fig. 3c that the noise model does not contain reflection waves, and non-linear noises in near offset traces can be suppressed effectively.

To correct amplitude changes caused by a source-vibrating charge mass, a receiver coupling, and a subsurface

Table 1 Seismic geometry system of the study area

Geometry pattern	8L × 8S	Samples	2000*1 ms
Lateral grid	10 m	Vertical grid	10 m
Receiver line interval	40 m	Full folds area	13.52 km ²
Receiver interval	20 m	Swath number	36 swaths
Source line interval	60 m	Physical points	12,880
Source interval	20 m	Lateral fold number	4
Receiver lines	8	Vertical fold number	6
Single line receiver number	36 traces	Full fold number	24
Vertical minimum offset	20 m	Lateral minimum offset	10 m
Vertical maximum offset	720 m	Lateral maximum offset	210 m

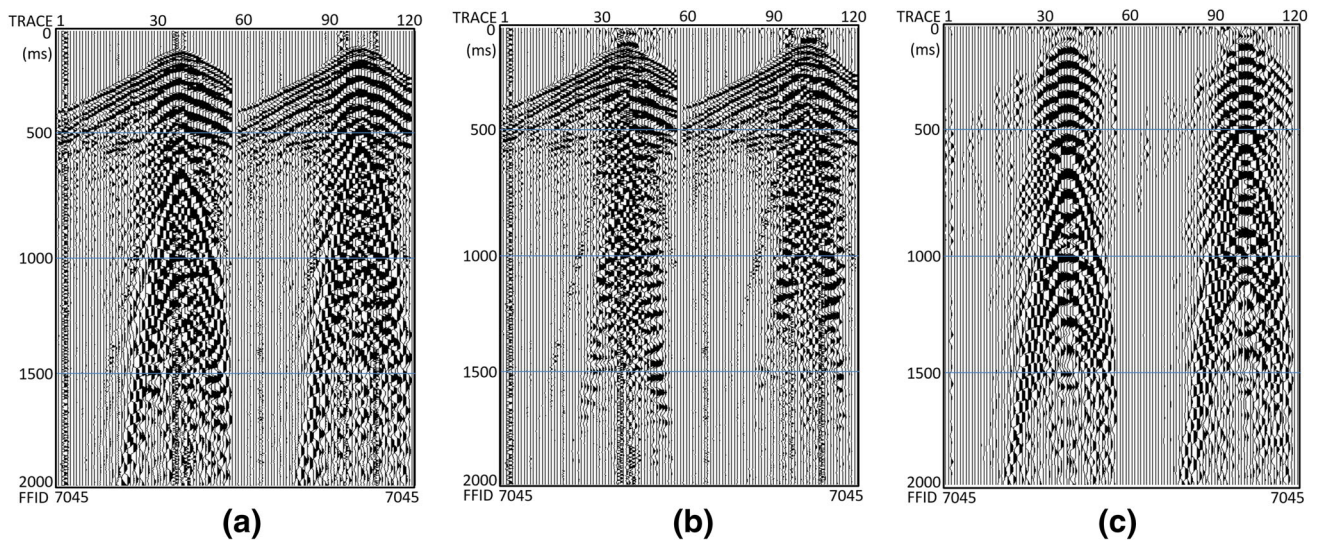


Fig. 3 A shot before and after RT filter, and filtered noises. **a** Raw shot, **b** shot after RT filter, **c** extracted noise from raw shot

weathering, CBM AVO analysis preprocessing repeatedly executes SCAC flow and SCAC operators be sequentially applied to the source domain, receiver domain, CMP domain and CO domain. As shown in Fig. 4a, b, the processes in source and receiver domains can almost eliminate valid reflection amplitude's lateral variations. The operators in CMP domain are generally smaller than in source or receiver domain, and those larger values represent the low-velocity zone in weathering layer. After above compensating in three domains, we basically have reason to believe that the non-geological amplitudes' unbalance can be removed. Next, the CMP gathers will be followed up an inverse Q filter and surface-consistent deconvolution (SCDC) for frequency bandwidth extending and spectrum balancing. On amplitudes' compensating in CO domain, the LW and SW contents of the operators are derived from

a few neighboring CMP points and only SW contents can be carefully applied because of LW contents associated with CBM AVO characteristics. Figure 5a, b shows that there are little differences of AVO Gradient attribute attracting from CRP gathers before and after amplitudes' compensating in CO domain and the dotted areas point to a different CBM content and trend. Actual drilling information shows that the CBM content in south area is richer than in north area. Therefore, the SCAC technology based on a frequency separating can be used to preserve CBM AVO abnormal. Additionally, when applying this technology, an optimal window should be more than 1000 ms and at least include objective layers for statistical analysis.

This CBM AVO preprocessing mainly considers about the RAP and SNR qualities of CMP gathers before PSTM and the controlling of diffraction weight function during

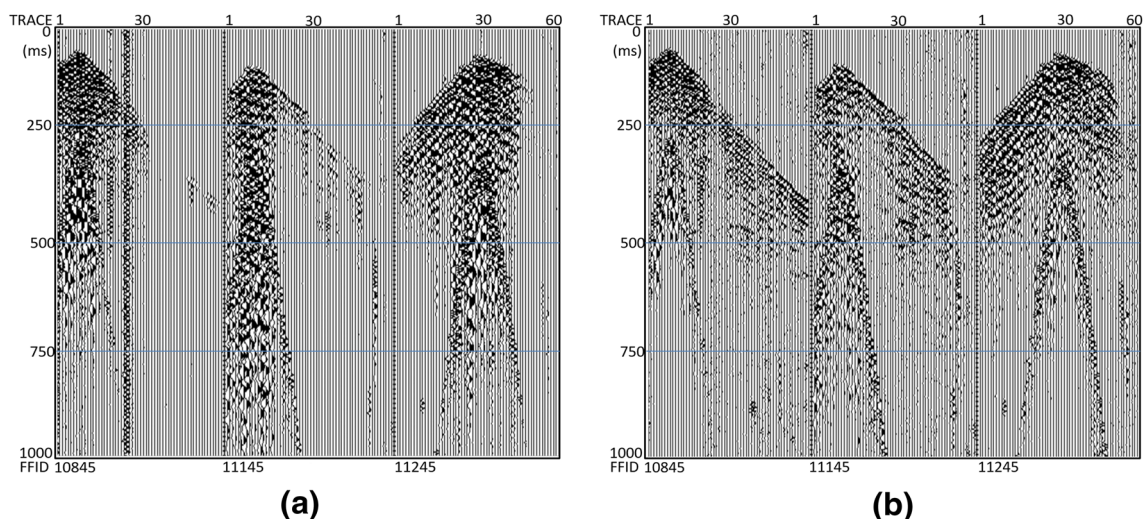


Fig. 4 A shot before and after SCAC applied in source and receiver domains. **a** Raw shot, **b** shot after compensated

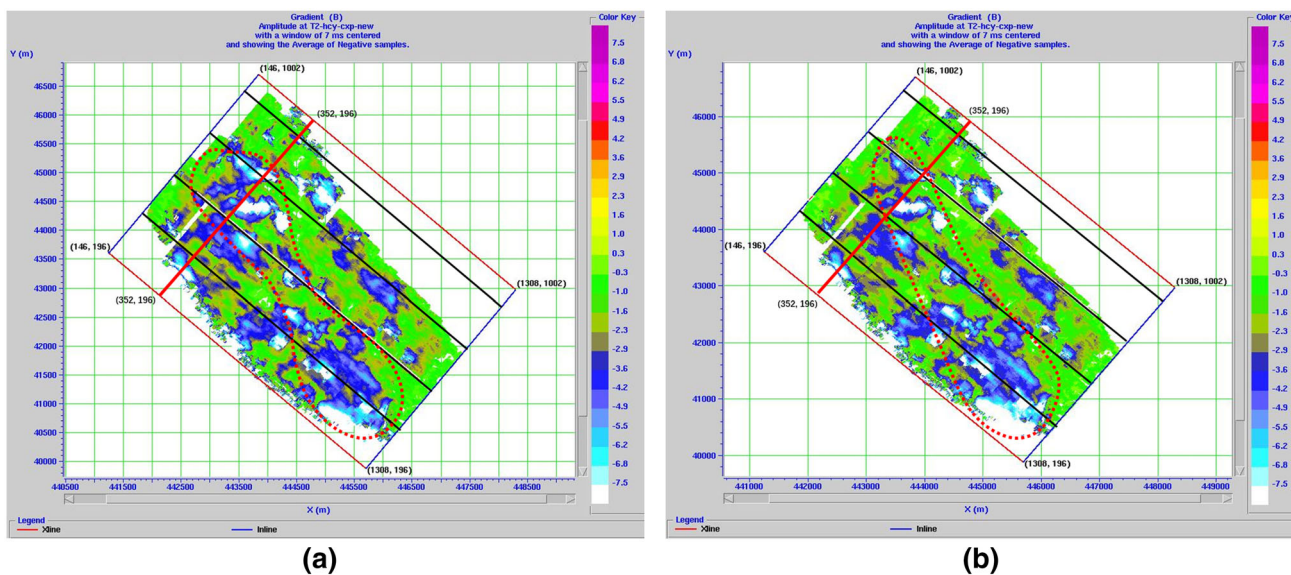


Fig. 5 An AVO gradient attribute attracting from CRP gathers. Before (a) and after (b) SCAC applied in CO domain

RAP Kirchhoff PSTM. The irregular seismic acquisition gives rise to uniform CMP coverage, as shown in Fig. 6a, and the non-uniformity will inevitably lead to a massive migrating arc like some inverse diffractions in RAP Kirchhoff PSTM. On the one hand, it is very necessary to apply a trace interpolating to CO gathers in a frequency domain (F-XY) or a high-precision Radon domain for the offset's uniform distribution. On the other hand, RAP Kirchhoff PSTM algorithm in theory was considered on the weighting factor for non-horizontal folds, and this dealing with irregular geometry can bring more accurate wave field imaging at subsurface than interpolation method. The CMP's coverage distribution is shown in Fig. 6a, b after a partly regularized offset processing shows that the offset distribution is more regular and relatively smooth besides the zone including some villages and rivers.

Granted, the migration aperture, the calculating travel time and the anti-alias filter in RAP Kirchhoff PSTM have

a considerable influence on the CBM AVO anomaly, and the key parameters' selections are almost similar to AVO preprocessing in conventional sandstone bearing gas and need to be optimally determined by tests.

The contrast on AVO gradient and intercept attributes between DMO stacking section and PSTM section in No. 352 Inline is displayed in Fig. 7a, b, and the corresponding CMPs and CRPs across No. 510 Xline are shown in Fig. 7c, d. Obviously, we see that DMO stacking cannot accurately image reflection points, especially for those dipping stratum, and the imaging deviation reaches to 15 ms, shown by green arrows in Fig. 7c, d. The red and pink arrows point out the position and varying trends of CBM AVO abnormal. At the same time, the gradient and intercept attributes combined with seismic waveforms are vertically displayed in Fig. 7a, b and CBM AVO abnormal can be seen at 500 ms where CBM was enriched, as marked by red dotted circles in Fig. 7b. The plane map of

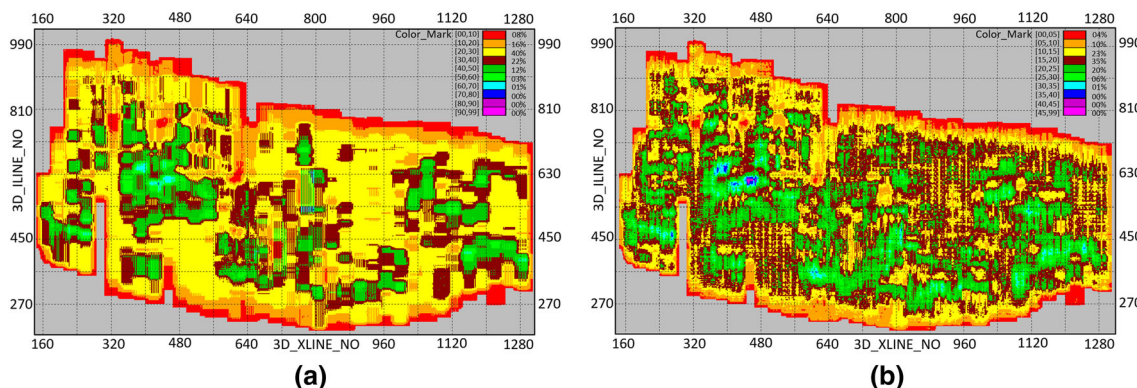


Fig. 6 A fold distribution before (a) and after (b) a regularized offset processing

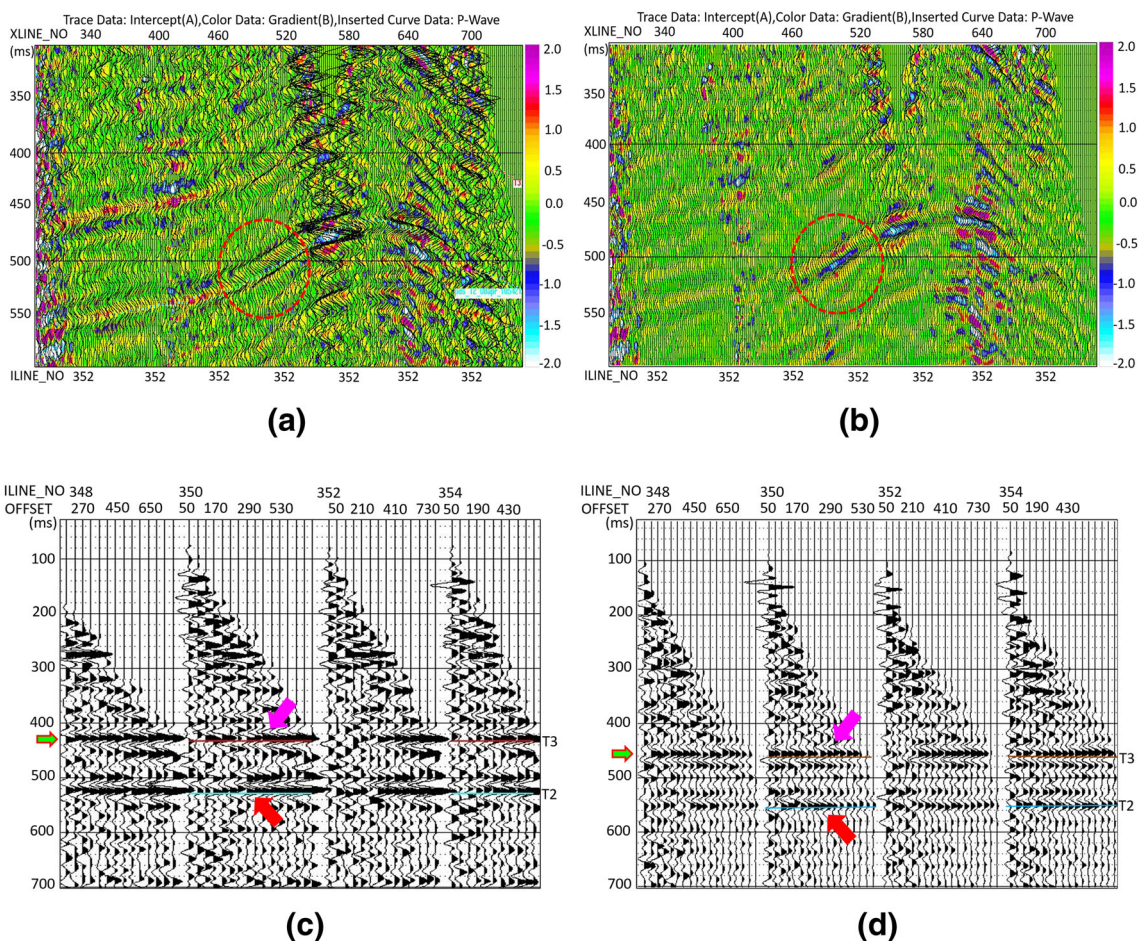


Fig. 7 An AVO section’s and 4 gathers’ comparison after DMO or PSTM. **a** Inline #352 AVO attributes section after DMO, **b** Inline #352 AVO attributes section after PSTM, **c** Inline #(348-354) CMPs in Xline #510 after DMO, **d** Inline #(348-354) CRPs in Xline #510 after PSTM

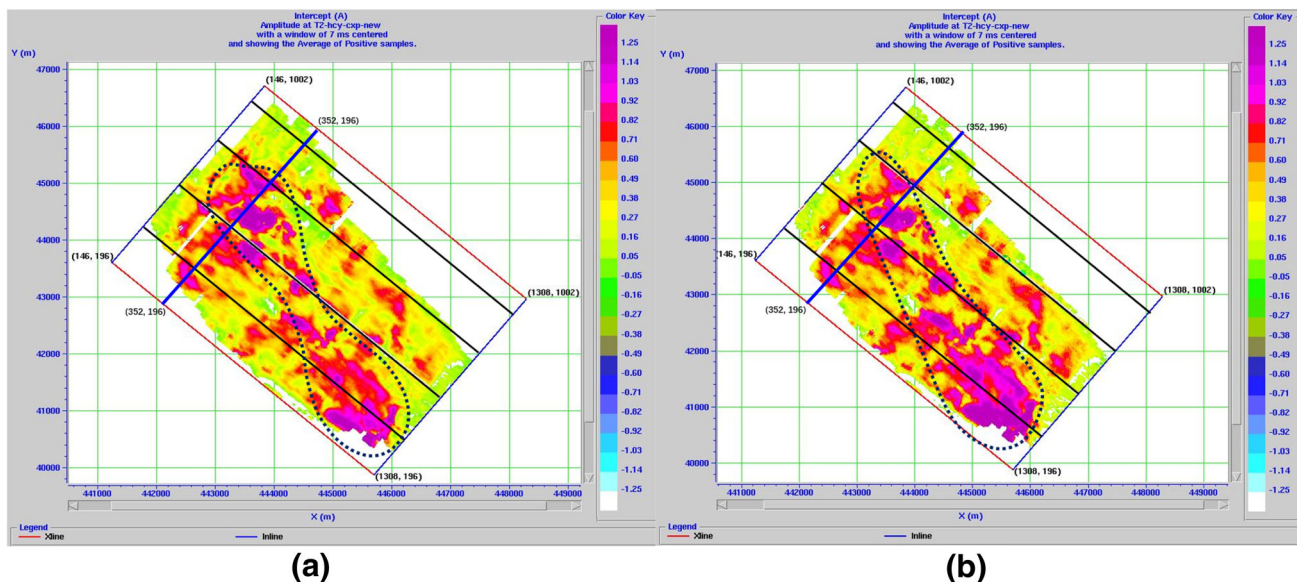


Fig. 8 An AVO intercept attribute attracting after DMO (a) and after PSTM (b)

AVO intercept attributes along with T2 interface refers to Fig. 8a, b, paying attention to the difference of black dotted area. So, the RAP Kirchhoff PSTM is proved to be behaving more reliably than DMO stacking in CBM AVO analysis preprocessing.

The authors try to set up a geophysical simulation verifying CBM AVO characteristics and attribute of AVO gradient and intercept in the study area, as shown in Fig. 9. As is seen in Fig. 9b, c, the roof reflection of coalbed in a CRP corresponds to a negative phase, and the seismic amplitude decreases along with an increasing offset and shows a strong negative intercept anomaly. Meanwhile, the floor reflection corresponds to a positive phase, and its amplitude decreases with an increasing offset too and shows a strong positive intercept. According to the coalbed velocity's change in the well log (a) (Time: 536–544 ms, Depth: 825–837 m), the CBM AVO gradient attribute just corresponds to the PSTM section near to Inline527/Xline360 in the Fig. 9c, e. Overall, three key technologies of CBM AVO analysis preprocessing discussed in this paper are appropriate, and they can meet the geological requirements.

The CBM AVO analysis preprocessing belongs to the category of lithological processing and focuses on the IV class AVO anomaly preserved. In general, QC of the seismic noise's attenuation, the amplitude's compensation, a wavelet deconvolution, multiple reflection residual static correction, an offset regularization, a prestack trace interpolation and a RAP PSTM are closely related to reflection

amplitudes' changing. Based on an integrated analysis of seismic amplitude, frequency and phase on raw gathers, CBM CRP gathers and stacking sections have been obtained by means of radial trace filter, refined SCAC and RAP PSTM, and been reasonably suitable for AVO analysis. Compared with CMP gathers and DMO stacking sections, the AVO gradient and intercept sections in CRPs and PSTM sections can be more accurately and reliably used to identify CBM anomalies.

Conclusions

CBM AVO analysis preprocessing should be assigned to the category of seismic lithological processing, and RAP as a basic principle should be paid more attention to reflection amplitude preservation associated to Class IV AVO anomalies. Its goal is to carefully remove the amplitude changes introduced by non-geological factors, meticulously restore and keep the index relationship between seismic amplitudes and reflection coefficients.

Based on the theory analysis and a real 3D application above, RAP Kirchhoff PSTM is proved an inevitable imaging technology for CBM AVO analysis preprocessing, and radial trace filtering and SCAC based on a frequency separating are the key technologies in RAP Kirchhoff PSTM for prestack gather preconditioning. The three technologies depend on each other in CBM AVO analysis preprocessing and possess the maximum retained

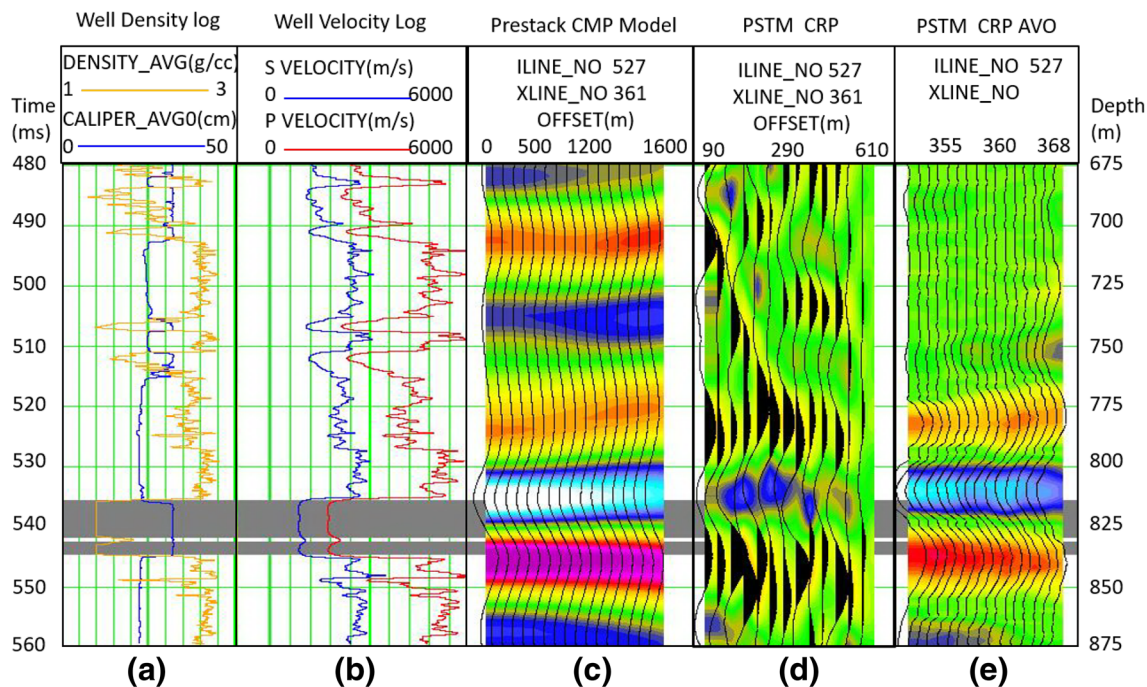


Fig. 9 A CRP gather, model gather and AVO sections referred to a well. **a** Density log; **b** velocity log, **c** modeling, **d** CRPs, **e** AVO attribute

IV class AVO anomalies. Undoubtedly, some regular preprocessing technologies such as statics, deconvolution, inverse Q filtering, and velocity analysis will have a fundamental role on CBM AVO analysis preprocessing.

Considering about a complex 3D seismic exploration and some shallow targets in CBM zone, we suggest that CBM AVO analysis preprocessing need to improve the prestack gathers' regularizing level for the uniformity of preprocessing data before PSTM.

Acknowledgements We thank the INDEPTH team members in Chinese Academy of Geological Sciences, Wang Yanchun team in China University of Geosciences (Beijing), technical staff from Pingdingshan Coal Group, Liu Jianhong from BGP Geophysical Research Institute, Duan Wensheng from Tarim Oilfield Company Geophysical Institute and Liu Junjie from CGG Geophysical Company (Beijing) for their guide and seismic processing recommends.

References

- Antonio Ramos CB, Thomas LD (1997) 3D AVO analysis and modeling applied to fracture detection in coalbed methane reservoirs. *Geophysics* 62(6):1683–1695. doi:[10.1190/1.1444268](https://doi.org/10.1190/1.1444268)
- Andrew A, Taylor R (2016) Valuable lessons from acquiring 3D seismic for coal-seam gas. *Lead Edge* 35(1):58–63. doi:[10.1190/tle35010058.1](https://doi.org/10.1190/tle35010058.1)
- Charles CM, Timothy HK, Arthur BW (1996) The impact of migration on AVO. *Geophysics* 61(6):1603–1615. doi:[10.1190/1.1444079](https://doi.org/10.1190/1.1444079)
- Chen XP, Huo QM, Lin JD et al (2013) The inverse correlations between methane content and elastic parameters of coal-bed methane reservoirs. *Geophysics* 78(4):D237–D248. doi:[10.1190/geo2012-0352.1](https://doi.org/10.1190/geo2012-0352.1)
- Chen XP, Huo QM, Lin JD et al (2014) Theory of CBM AVO, Part 1: characteristics of anomaly. *Geophysics* 79(2):1–11. doi:[10.1190/geo2013-0195.1](https://doi.org/10.1190/geo2013-0195.1)
- Gochioco LM (1991) Tuning effect and interference reflections from thin beds and coal seams. *Geophysics* 56(8):1288–1295. doi:[10.1190/1.1443151](https://doi.org/10.1190/1.1443151)
- Gochioco LM (2002) Recently role of geophysics in U.S. coal and CBM development. *Lead Edge* 21(5):452–455. doi:[10.1190/1.1885502](https://doi.org/10.1190/1.1885502)
- Henley DC (2003) Coherent noise attenuation in the radial trace domain. *Geophysics* 68(4):1408–1416. doi:[10.1190/1.1598134](https://doi.org/10.1190/1.1598134)
- Hong F, Bancroft JC (2006) AVO principles, processing and inversion. CREWES Research Report-Volume 18:1–19
- Hu XG, Shang XM, Shi LG et al (2002) AVO processing technique based on prestack time migration data. *Geophysical prospecting for petroleum (in Chinese)* 41(3):343–346
- Jason MC, Lawton Don C, Lu HX, Hall Kevin (2007) Time-lapse AVO modeling for enhanced coalbed methane production. SEG technical program expanded abstracts 2007:274–278. doi:[10.1190/1.2792425](https://doi.org/10.1190/1.2792425)
- Liu ZW, Wang YC (2013) A joint high-resolution processing method and its application for thin inter-beds. *Petroleum Sci* 10(2):195–204. doi:[10.1007/s12182-013-0267-4](https://doi.org/10.1007/s12182-013-0267-4)
- Liu ZW, Wang YC, Zhao HX et al (2013) High-resolution processing methods of thin inter-beds imaging. *Chinese J Geophys (in Chinese)* 56(4):1350–1359. doi:[10.6038/cjg20130429](https://doi.org/10.6038/cjg20130429)
- Ostrander WJ (1984) Plane-wave reflection coefficient for gas sands at non-normal angles of incidence. *Geophysics* 49(10):1637–1648. doi:[10.1190/1.1441571](https://doi.org/10.1190/1.1441571)
- Peng SP, Chen HJ, Yang RZ et al (2006) Factors facilitating or limiting the use of AVO for coalbed methane. *Geophysics* 71(4):C49–C56. doi:[10.1190/1.2217137](https://doi.org/10.1190/1.2217137)
- Rutherford SR, Williams RH (1989) Amplitude-versus-offset variation in gas sands. *Geophysics* 54(6):680–688. doi:[10.1190/1.1442696](https://doi.org/10.1190/1.1442696)
- Shuey RT (1985) a simplification of the Zoeppritz equations. *Geophysics* 50(4):609–614. doi:[10.1190/1.1441936](https://doi.org/10.1190/1.1441936)
- Wu HB, Dong SH et al (2016) Brittleness index calculation and evaluation for CBM reservoirs based on AVO simultaneous inversion. *J Appl Geophys* 134:191–198. doi:[10.1016/j.jappgeo.2016.09.010](https://doi.org/10.1016/j.jappgeo.2016.09.010)
- Zhang Y (2006) the theory of true amplitude one-way wave equation migration. *Chinese J. Geophysics (in Chinese)* 49(5):1410–1430. doi:[10.1002/cjg2.951](https://doi.org/10.1002/cjg2.951)
- Zuber Michael D (1998) Production characteristics and reservoir analysis of coalbed methane reservoirs. *Int J Coal Geol* 38(1–2):27–45. doi:[10.1016/S0166-5162\(98\)00031-7](https://doi.org/10.1016/S0166-5162(98)00031-7)

Fluid identification based on P-wave anisotropy dispersion gradient inversion for fractured reservoirs

J. W. Zhang^{1,2} · H. D. Huang^{1,2} · B. H. Zhu^{1,2} · W. Liao³

Received: 23 April 2017 / Accepted: 19 September 2017 / Published online: 22 September 2017
© Institute of Geophysics, Polish Academy of Sciences & Polish Academy of Sciences 2017

Abstract Fluid identification in fractured reservoirs is a challenging issue and has drawn increasing attentions. As aligned fractures in subsurface formations can induce anisotropy, we must choose parameters independent with azimuths to characterize fractures and fluid effects such as anisotropy parameters for fractured reservoirs. Anisotropy is often frequency dependent due to wave-induced fluid flow between pores and fractures. This property is conducive for identifying fluid type using azimuthal seismic data in fractured reservoirs. Through the numerical simulation based on Chapman model, we choose the P-wave anisotropy parameter dispersion gradient (PADG) as the new fluid factor. PADG is dependent both on average fracture radius and fluid type but independent on azimuths. When the aligned fractures in the reservoir are meter-scaled, gas-bearing layer could be accurately identified using PADG attribute. The reflection coefficient formula for horizontal transverse isotropy media by Rüger is reformulated and simplified according to frequency and the target function for inverting PADG based on frequency-

dependent amplitude versus azimuth is derived. A spectral decomposition method combining Orthogonal Matching Pursuit and Wigner–Ville distribution is used to prepare the frequency-division data. Through application to synthetic data and real seismic data, the results suggest that the method is useful for gas identification in reservoirs with meter-scaled fractures using high-qualified seismic data.

Keywords P-wave anisotropy · Frequency dependence · AVAZ · Fluid identification · Spectral decomposition

Introduction

Naturally fractured reservoirs have attracted increasing attention in oil and gas explorations. Analysis and understanding of the distribution law of fracture development are important in exploration and development of fractured reservoirs, since mesoscopic fracture distributions and development degrees control the enrichment of underground oil and gas. Meanwhile, fluid identification in fractured reservoirs has been one of the hot spots of the present researches.

Anisotropy, which is induced by aligned fractures, is a useful attribute for the detection and characterization of fractures. As a consequence of overlying strata compaction and tectonic stress, horizontal or low angle fractures usually disappear, while high angle and near vertical fractures remain. Theoretically, layers with vertical or near vertical aligned fractures could be simplified as transversely isotropic media with a horizontal symmetry axis, namely, horizontal transverse isotropy (HTI) media. Therefore, the basis for prediction of fractured reservoirs is the propagation theory of seismic waves in anisotropic media, especially in HTI media, which has attracted considerable

✉ H. D. Huang
webhhd@163.com

J. W. Zhang
zhangjinwei.1987@163.com

¹ Unconventional Natural Gas Research Institute, State Key Laboratory of Petroleum Resources and Prospecting, China University of Petroleum, No.18, Fuxue Road, Changping District, Beijing, China

² State Key Laboratory of Petroleum Resources and Prospecting, CNPC Key Lab of Geophysical Exploration, China University of Petroleum, No.18, Fuxue Road, Changping District, Beijing, China

³ Xinjiang Oilfield Branch Company, PetroChina Company Limited, Karamay, China

interests in recent years. Fracture-induced anisotropy has notable effects on seismic wave propagation. As fractures in subsurface media are more developed, the azimuth differences of seismic waves are more remarkable. The azimuthal differences between seismic channels can be characterized through a series of seismic attributes, such as amplitude, velocity, travel time, attenuation, and so on. Many conventional seismic techniques that use longitude wave data are available to estimate seismic anisotropy. Detections of azimuthal variations of normal moveout velocities and reflection amplitudes are the most widely adopted methods for characterizing and predicting fractures. Daley and Hron (1977) derived the formula of reflection and transmission coefficients for longitude wave and transition wave in vertical transverse isotropy (VTI) media. Banik (1987) proposed a P-wave reflection coefficient expressed by weak anisotropic parameters on the interface between two transverse isotropy (TI) media with small velocity differences. Schoenberg and Protazio (1992) applied the Zoeppritz equation to anisotropic media and calculated the relationship between reflection coefficient and azimuthal angles. Based on the studies by Banik (1987) and Thomsen (1995), Rüger (1997) derived a more precise approximation expression of longitudinal wave reflection coefficient which could fit relatively larger incident angles. Václav and Ivan (1998) confirmed that P-wave reflection coefficient of weak anisotropic media was close to the accurate value. Macbeth and Lynn (2000) studied the azimuthal changes characteristics of P-wave amplitude associated with fluid.

Fluid recognition using seismic data is commonly relied on the inversion of those abnormal features related to fluid which are called fluid factors. The efficiency of fluid recognition mainly depends on two aspects: the sensitivity of fluid factors and the reliability of seismic inversion. For isotropic media, elastic parameters and combination of AVO (amplitude versus offset) attributes are common fluid factors (Huang et al. 2012). Smith and Gidlow (1987) first proposed the concept of fluid factor and detected gas-bearing layer using weighted stack method; Fatti (1994) used the difference between P-wave impedance and S-wave impedance to detect gas-bearing layers; Goodway et al. (1997) adopted parameters such as $\lambda\rho$, $\mu\rho$, and λ/μ as fluid factors, and achieved preferable effects; Gray (2002) directly extracted λ and μ by improving the Goodway's method. Russell et al. (2011) studied the Gassmann fluid term, which could be used to recognize fluid in deep reservoirs. For fractured anisotropic reservoirs, we must choose parameters independent with azimuths to construct fluid factors, such as fracture excess compliance (Chen et al. 2017). Such conventional fluid factors have achieved good results in practical applications, but they ignore the influence of seismic dispersion and attenuation, resulting in low precision and low accuracy.

According to Chapman et al. (2006), velocity dispersion and attenuation greatly affect the AVA (Amplitude Versus Angle) and AVAZ (Amplitude Versus incident Angle and Azimuth) analysis of seismic data for fractured reservoirs. The influence is more considerable when large offset data are available. The reflection coefficient on the interface between the overburden layer and fractured layer is frequency dependent, and is closely related to fracture parameters (e.g., fracture density, fracture size, and fracture aperture) and fluid properties (e.g., bulk modulus and viscosity). The frequency-dependent reflection coefficient contains more information about the reservoir in comparison with the frequency-independent reflection coefficient. Frequency-dependent amplitude versus offset (FAVO) in isotropic media has been studied in-depth. Wilson (2010) proposed a method for calculating dispersion property based on the Smith–Gidlow approximation, and constructed the FAVO inversion frame on the basis of petrophysical theory, spectral decomposition, and amplitude versus offset (AVO) analysis. Wu et al. (2012) applied FAVO to field data using Wigner–Ville distribution, and estimated gas saturation using FAVO analysis (2014). Zhang et al. (2011) derived a frequency-dependent reflection coefficient approximation based on dispersion degree and gradient of longitudinal wave. Cheng and Xu (2012) constructed a series of FAVO attributes to recognize fluid. Zhang et al. (2014) studied the application of dispersion attribute for Gassmann fluid term in fluid identification.

Studies for FAVO in anisotropy media, especially the anisotropy parameters variation with frequency, however, are relatively scarce. Due to wave-induced fluid flow taking place within seismic frequency band, the seismic wave propagation, as well as the anisotropy is frequency dependent, which is conducive for fluid identification. The special theory of squirt flow of Chapman (2003) took mesoscopic fluid flow into account and could explain the dispersion and attenuation of seismic waves reasonably. In this paper, we first analyze the frequency-dependent characteristics of HTI media based on Chapman's model, and then present a new attribute P-wave anisotropy parameter dispersion gradient (PADG) as the fluid indicator to detect gas in fractured reservoirs. We have analyzed the sensitivity of PADG on fluid type, and discuss its restrictions and adaption capacity. Based on the relationship between PADG and Rüger's reflection coefficient formula in anisotropy media, the inversion scheme to obtain the PADG attribute using the azimuthal P-wave seismic data after spectral decomposition is established. We use a spectral composition method combining the Orthogonal Matching Pursuit and Wigner–Ville distribution to prepare the frequency-division seismic data. Finally, we apply the method to synthetic seismogram and field data and the results demonstrate its potential for gas identification for reservoirs with meter-scaled fractures.

Methodology

Selection of fluid factor

Squirt-flow model can characterize the dispersion and attenuation due to wave-induced fluid flow in porous media. Squirt flow (Mavko and Jizba 1991) is caused by pressure gradients at the microscopic or mesoscopic scale and in the direction potentially different from that of the wave propagation. Chapman et al. (2002) present a poroelastic model based on squirt-flow theory and calculated the frequency-dependent modulus, considering the fluid exchange between pores and microcracks and between microcracks of different orientations. Then, Chapman (2003) extended the microscale squirt-flow model to a mesoscopic scale by adding a set of aligned mesoscale fractures in porous background media and analyzed frequency-dependent anisotropy caused by fluid flow between fractures, pores, and microcracks.

In Chapman's mesoscopic squirt-flow model, the radii of the microcracks and the pores are identified with the grain size, whereas the fracture radius is much greater than the grain size but smaller than the wavelength of the seismic waves. Microcracks and pores are interconnected and connected to at most one fracture. Fractures are not connected with other fractures. The random isotropic distribution of microcracks and pores and aligned fractures make the model for fractured porous media possess hexagonal symmetry, and when the fractures are vertical, the model will be HTI media. One of the crucial parameter is the characteristic frequency in "squirt-flow" theory. The model concerns two scales of fluid flow, so there are two timescales (reciprocal of characteristic frequency) τ_m and τ_f , corresponding to microcracks and fractures. The relationship between the two timescales is

$$\tau_f = \frac{a_f}{\zeta} \tau_m, \quad (1)$$

where a_f is the radius of fracture and ζ is the grain size. The frequency-dependent anisotropic elastic tensor is expressed as

$$C = C^0 - \varphi_p C^1 - \varepsilon_c C^2 - \varepsilon_f C^3, \quad (2)$$

where C^0 is the isotropic elastic tensor for the background medium; C^1 , C^2 , and C^3 are the corrections to the stiffness tensor of pores, microcracks, and fractures, respectively. φ_p is the porosity; ε_c is microcrack density and ε_f is the density of the aligned fractures. C^1 , C^2 , and C^3 in complex expression containing attenuation information are functions of the Lamé parameters (λ and μ), fluid properties, fracture length, time-scale parameters, and frequency. The Chapman model is restricted to low porosity case originally. For the cases of high porosity calculation, the stiffness tensor

with the grain moduli λ and μ can result in substantial errors (Al-Harrasi et al. 2011). Chapman et al. (2003) proposed a modified parameterization method which overcomes the restriction to low porosity. They suggested using the velocities V_p^0 and V_s^0 of the unfractured porous rock to calculate λ^0 and μ^0 first as

$$\lambda^0 = (V_p^0)^2 \rho - 2\mu^0, \quad (3)$$

$$\mu^0 = (V_s^0)^2 \rho, \quad (4)$$

where ρ is the density of the saturated rock. The isotropic tensor C^0 needs to be expressed by the measured isotropic velocities at a certain frequency f_0 with the correction from pores and cracks. The new Lamé parameters are defined as

$$A = \lambda^0 + \Phi_{c,p}(\lambda^0, \mu^0, f_0), \quad (5)$$

$$T = \mu^0 + \Phi_{c,p}(\lambda^0, \mu^0, f_0), \quad (6)$$

where $\Phi_{c,p}$ is the correction function due to the microcracks and pores. Thus, Eq. 2 becomes

$$C(f) = C^0(A, T) - \Phi_p C^1(\lambda^0, \mu^0, f) - \varepsilon_c C^2(\lambda^0, \mu^0, f) - \varepsilon_f C^3(\lambda^0, \mu^0, f), \quad (7)$$

where f denotes the frequency. The detailed parameterization process is available in the literature (Chapman 2003).

To single out the fluid identification factor, we first performed a numerical simulation to evaluate the frequency dependence of P-wave-related attributes and their fluid sensitivities. The reference velocities of "unfractured rock" (saturated with brine water, a 10% porosity) are $V_p^0 = 4000$ m/s, $V_s^0 = 2500$ m/s, respectively. The fracture density which only influences the degree of anisotropy is set to be 0.05. The average fracture radius is 1 m. The microcrack density is zero for simplicity. In the squirt-flow model, there is a transition zone, where maximum velocity dispersion and attenuation occurs. The central frequency of this transition zone for an unfractured rock is often referred to as the mineral scale "squirt-flow frequency", ω_m (angular frequency), with the associated relaxation timescale, $\tau_m = \omega_m^{-1}$. τ_m is usually evaluated from laboratory experiments, but it is found to be proportional to the viscosity of the saturating fluid, and inversely proportional to the permeability of the host rock. Here, the timescale is assumed to be $\tau_m = 4.75 \times 10^{-5}$ s for water saturation and $\tau_m = 9.5 \times 10^{-7}$ s for gas saturation (Al-Harrasi 2011). τ_f is calculated through Eq. 1 (ζ is assumed to be 200 μ m).

After the frequency-dependent stiffness tensor of the complex media including pores and aligned fractures is derived through the Chapman model, the P-wave anisotropic parameter ε and ε dispersion gradient (PADG) are expressed as

$$\varepsilon = \frac{C_{11} - C_{33}}{2C_{33}}, \tag{8}$$

$$\text{PADG} = \frac{\partial \varepsilon}{\partial f}. \tag{9}$$

The P-wave velocity at normal incidence in HTI media is computed as

$$V_p = \sqrt{C_{33}/\rho}. \tag{10}$$

C_{11} and C_{33} are the coefficients of the stiffness tensor obtained by Eq. 7. ρ is the density of the saturated rock. As the stiffness tensor derived from Chapman model is complex and frequency dependent, the P-wave velocity from Eq. 10 is also a complex value. The real-phase velocity and inverse quality factor can be calculated as

$$v_p = \left[\text{Re} \left(\frac{1}{V_p} \right) \right]^{-1}, \tag{11}$$

$$Q_p^{-1} = \frac{\text{Im}(V_p)}{\text{Re}(V_p)}. \tag{12}$$

Figure 1 illustrates the predicted dependence of P-wave velocity (Fig. 1a) and Q_p^{-1} (Fig. 1b) on frequency for water and gas saturation (normal incidence). As real seismic data normally lack the low-frequency information, the frequency band considered in the model is set to 10–100 Hz. We can see that there are obvious differences for the P-wave velocities at gas and water saturation cases, as shown in Fig. 1a. The velocity for gas saturation is slightly frequency dependent, increasing from 3555 to 3575 m/s, while the velocity for water saturation is almost unchanged, so that the transition zone for gas is located in the frequency band we choose. Furthermore, the velocity dispersion gradients for both gas and water saturation are displayed in Fig. 2. The velocity dispersion gradient curve shows the distinction between gas and water more clearly. The velocity dispersion gradient for gas is nonlinear by presenting an initial increase and then a decreasing trend.

Fig. 1 Variation of velocity (a) and inverse quality factor (b) with frequency for gas and water saturation situation

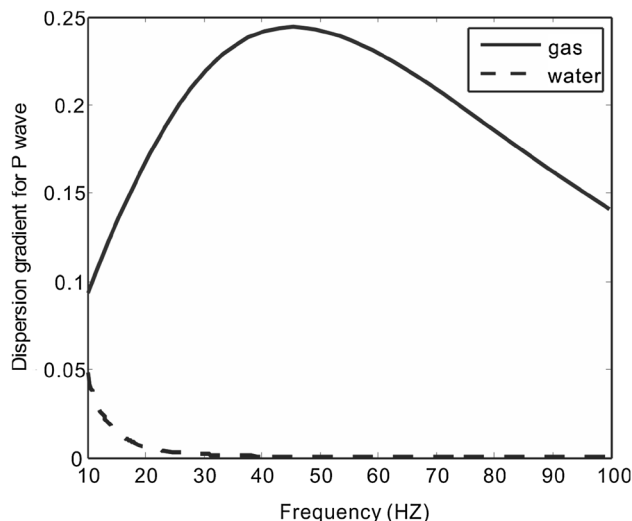
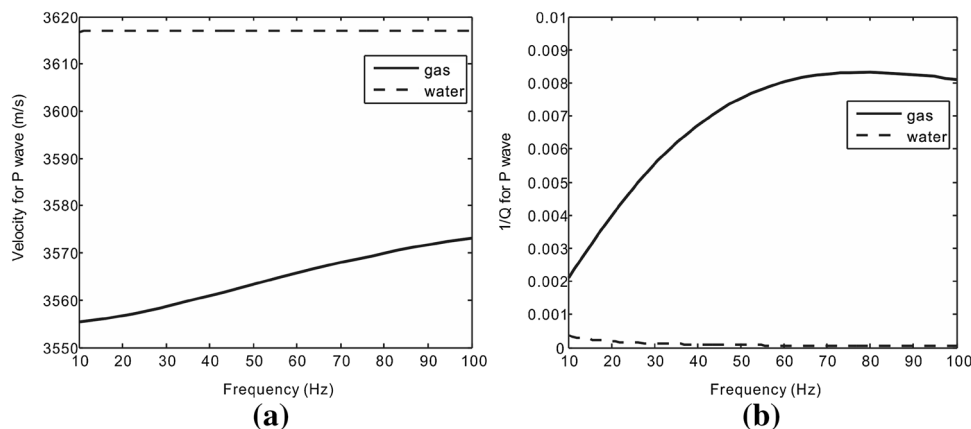


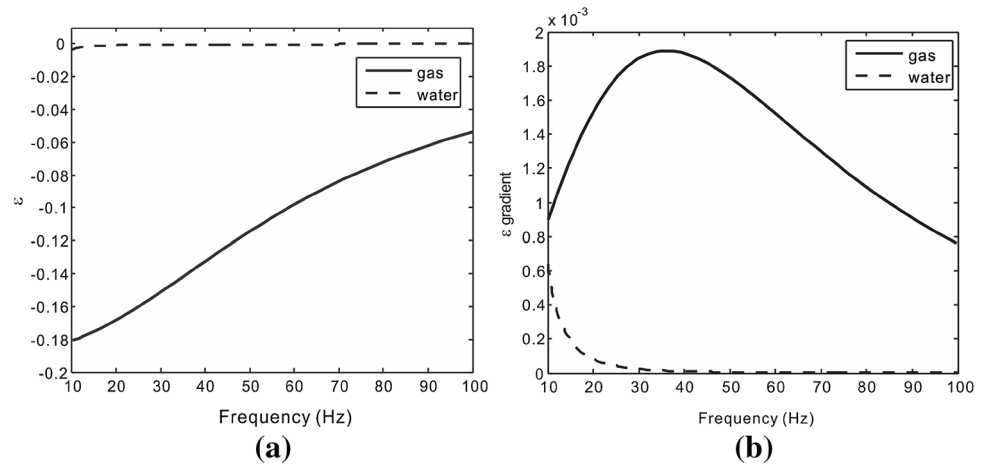
Fig. 2 Variation of P-wave velocity dispersion gradient with frequency

However, for the case of water saturation, the velocity dispersion gradient quickly drops to 0 in the frequency band 10–100 Hz. The velocity dispersion gradient shows a similar pattern with P-wave attenuation, as shown in Fig. 1b. The P-wave anisotropic parameter ε is expected to show an analogous feature with P-wave velocity. Figure 3 shows variations of ε (Fig. 3a) and PADG (Fig. 3b) dependent on frequency. Notably, the high value of PADG indicates the occurrence of gas. Therefore, we finalize the PADG as the fluid factor for gas detection in fractured reservoirs.

Frequency-dependent AVAZ inversion for PADG

Schoenberg and Protazio (1992) gave explicit solutions for the plane-wave reflection and transmission problem using submatrices of the Zoeppritz equation coefficient matrix. For weakly anisotropic media, simple analytical formulas can be used to compute AVAZ responses at the interface of

Fig. 3 Variation of ε (a) and ε dispersion gradient (PADG) (b) with frequency



anisotropic media that can be either VTI, HTI, or orthorhombic. The P-wave reflection coefficient for weakly anisotropic VTI media as limited by small impedance contrast was derived by Thomsen (1993) and corrected by Rüger (1997). For HTI media, Chen (1995) and Rüger (1997, 1998) derived the P-wave reflection coefficient in the symmetry planes for reflections at the interface of two HTI media, which has become one of the most common equations to calculate the AVAZ response and could be written as

$$R_{PP}^{HTI}(\theta, \varphi) = \frac{1}{2} \frac{\Delta Z}{Z} + \frac{1}{2} \left\{ \frac{\Delta \alpha}{\bar{\alpha}} - \left(\frac{2\bar{\beta}}{\bar{\alpha}} \right)^2 \frac{\Delta G}{G} + \left[\Delta \delta^{(v)} + 2 \left(\frac{2\bar{\beta}}{\bar{\alpha}} \right)^2 \Delta \gamma \right] \cos^2 \varphi \right\} \sin^2 \theta + \frac{1}{2} \left\{ \frac{\Delta \alpha}{\bar{\alpha}} + \Delta \varepsilon^{(v)} \cos^4 \varphi + \Delta \delta^{(v)} \sin^2 \varphi \cos^2 \varphi \right\} \sin^2 \theta \tan^2 \theta \quad (13)$$

where θ is incident angle and φ is azimuthal angle; α and β are the velocities of longitude wave and shear wave propagating in the isotropic plane, respectively; Z is P-wave impedance; and $G = \rho \beta^2$ is the tangential modulus with ρ for density. The symbol Δ denotes the contrast across an interface. Bar over a symbol denotes an average calculation. $\varepsilon^{(v)}$, $\delta^{(v)}$ and γ are the anisotropy coefficients for HTI media proposed by Tsvankin (1997) based on the Thomsen’s result (1995) for VTI media.

From Eq. 13, the reflection coefficient R_{PP}^{HTI} can be divided into two parts: the isotropic part R_{PP}^{iso} (14) dependent on incident angle θ and the anisotropic part R_{PP}^{ani} (15) dependent both on θ and azimuthal angle φ :

$$R_{PP}^{iso} = \frac{1}{2} \frac{\Delta Z}{Z} + \frac{1}{2} \left\{ \frac{\Delta \alpha}{\bar{\alpha}} - \left(\frac{2\bar{\beta}}{\bar{\alpha}} \right)^2 \frac{\Delta G}{G} \right\} \sin^2 \theta + \frac{1}{2} \frac{\Delta \alpha}{\bar{\alpha}} \sin^2 \theta \tan^2 \theta \quad (14)$$

$$R_{PP}^{ani} = \left(\frac{2\bar{\beta}}{\bar{\alpha}} \right)^2 \Delta \gamma \cos^2 \varphi \sin^2 \theta + \frac{1}{2} \left\{ \Delta \varepsilon^{(v)} \cos^4 \varphi + \Delta \delta^{(v)} \sin^2 \varphi \cos^2 \varphi \right\} \sin^2 \theta \tan^2 \theta. \quad (15)$$

To simplify the reflection coefficient expression, a subtraction operation between two reflection coefficients at two orthogonal azimuths φ and $\varphi + \pi/2$ is done. To distinguish the elastic parameters difference between two layers from the reflection coefficient difference, $\delta R_{PP}(\theta, \varphi)$ is used to denote the difference of the reflection coefficients of two azimuths. After subtraction, we obtain

$$\delta R_{PP}(\theta, \varphi) = R(\theta, \varphi)_{PP} - R(\theta, \varphi + \pi/2)_{PP} = \frac{1}{2} \left[2 \Delta \gamma \left(\frac{2\bar{\beta}}{\bar{\alpha}} \right)^2 + \Delta \delta^{(v)} \right] \cos 2\varphi \sin^2 \theta + \frac{1}{2} \Delta \varepsilon^{(v)} \cos 2\varphi \sin^2 \theta \tan^2 \theta. \quad (16)$$

Equation 16 can be written as

$$\delta R_{PP}(\theta, \varphi) = a(\theta, \varphi) \Delta \gamma + b(\theta, \varphi) \Delta \delta^{(v)} + c(\theta, \varphi) \Delta \varepsilon^{(v)}, \quad (17)$$

where

$$a(\theta, \varphi) = \left(\frac{2\bar{\beta}}{\bar{\alpha}} \right)^2 \cos 2\varphi \sin^2 \theta \\ b(\theta, \varphi) = \frac{1}{2} \cos 2\varphi \sin^2 \theta \\ c(\theta, \varphi) = \frac{1}{2} \cos 2\varphi \sin^2 \theta \tan^2 \theta. \quad (18)$$

There are only three Thomsen style anisotropy parameters and velocity ratio remaining as the longitude wave impedance and tangential modulus have been eliminated. Under certain circumstances, the velocity ratio is often known from well-logging data. Therefore, there are only

three unknown quantities in Eq. 17. As mentioned previously, the anisotropy parameters are frequency dependent, and δR_{PP} is considered to vary with frequency in the dispersive media:

$$\delta R_{PP}(\theta, \varphi, f) = a(\theta, \varphi)\Delta\gamma(f) + b(\theta, \varphi)\Delta\delta^{(v)}(f) + c(\theta, \varphi)\Delta\varepsilon^{(v)}(f), \tag{19}$$

where f represents frequency.

Expand Eq. 19 as a first-order Taylor series around a reference frequency f_0 :

$$\begin{aligned} \delta R_{PP}(\theta, \varphi, f) &= a(\theta, \varphi)\Delta\gamma(f_0) + (f - f_0)a(\theta, \varphi)I_a \\ &+ b(\theta, \varphi)\Delta\delta^{(v)}(f_0) + (f - f_0)b(\theta, \varphi)I_b \\ &+ c(\theta, \varphi)\Delta\varepsilon^{(v)}(f_0) + (f - f_0)c(\theta, \varphi)I_c, \end{aligned} \tag{20}$$

where I_a , I_b , and I_c are the derivatives of the anisotropy parameter contrasts with respect to frequency:

$$I_a = \frac{d\Delta\gamma}{df}, \quad I_b = \frac{d\Delta\delta^{(v)}}{df}, \quad I_c = \frac{d\Delta\varepsilon^{(v)}}{df}. \tag{21}$$

A continuation of rewriting Eq. 20 yields

$$\begin{aligned} \delta R_{PP}(\theta, \varphi, f) - \delta R_{PP}(\theta, \varphi, f_0) &= (f - f_0)a(\theta, \varphi)I_a \\ &+ (f - f_0)b(\theta, \varphi)I_b + (f - f_0)c(\theta, \varphi)I_c, \end{aligned} \tag{22}$$

where $\delta R_{PP}(\theta, \varphi, f_0) = a(\theta, \varphi)\Delta\gamma(f_0) + b(\theta, \varphi)\Delta\delta^{(v)}(f_0) + c(\theta, \varphi)\Delta\varepsilon^{(v)}(f_0)$.

To emphasize the azimuthal variation of seismic waves, we keep the incident angle as a fixed value. Accordingly, Eq. 20 with regard to different frequency and azimuthal angle has the form of

$$\begin{aligned} \Delta\delta R_{PP}(\varphi_i, f_j) &= (f_j - f_0)a(\varphi_i)I_a \\ &+ (f_j - f_0)b(\varphi_i)I_b + (f_j - f_0)c(\varphi_i)I_c, \end{aligned} \tag{23}$$

where $\Delta\delta R_{PP}(\varphi_i, f_j) = \delta R_{PP}(\varphi_i, f_j) - \delta R_{PP}(\varphi_i, f_0)$.

Equation 23 can be expressed in matrix form as $d = \mathbf{G}m$. d denotes the data. \mathbf{G} is the kernel function. m is the unknown parameters. For the simple circumstance of two layers, two frequencies and three sets of azimuths, the specific form of Eq. 23 is

$$\begin{bmatrix} \Delta\delta R_1^1 \\ \Delta\delta R_2^1 \\ \Delta\delta R_3^1 \\ \Delta\delta R_1^2 \\ \Delta\delta R_2^2 \\ \Delta\delta R_3^2 \end{bmatrix} = \begin{bmatrix} (f_1 - f_0)a(\varphi_1) & (f_1 - f_0)b(\varphi_1) & (f_1 - f_0)c(\varphi_1) \\ (f_1 - f_0)a(\varphi_2) & (f_1 - f_0)b(\varphi_2) & (f_1 - f_0)c(\varphi_2) \\ (f_1 - f_0)a(\varphi_3) & (f_1 - f_0)b(\varphi_3) & (f_1 - f_0)c(\varphi_3) \\ (f_2 - f_0)a(\varphi_1) & (f_2 - f_0)b(\varphi_1) & (f_2 - f_0)c(\varphi_1) \\ (f_2 - f_0)a(\varphi_2) & (f_2 - f_0)b(\varphi_2) & (f_2 - f_0)c(\varphi_2) \\ (f_2 - f_0)a(\varphi_3) & (f_2 - f_0)b(\varphi_3) & (f_2 - f_0)c(\varphi_3) \end{bmatrix} \begin{bmatrix} I_a \\ I_b \\ I_c \end{bmatrix}. \tag{24}$$

The seismic records can be expressed by convolution of wavelets and reflection coefficients: $D = w * R + e$, where D represents seismic amplitude, w represents wavelet, R represents reflection coefficient, and e

represents the noise term. Therefore, Eq. 24 in a well-known inverse problem form is

$$\Delta\delta d = \mathbf{G}'m, \tag{25}$$

where $\Delta\delta d$ is the seismic data difference; $\mathbf{G}' = \mathbf{W}\mathbf{A}$, where \mathbf{W} is wavelet matrix that is introduced to simplify calculation, and \mathbf{A} is the matrix related to azimuthal angles. An extension of Eq. 24 up to n sample points, q azimuths, and k frequencies is

$$\begin{bmatrix} \Delta\delta d_1^1 \\ \Delta\delta d_2^1 \\ \vdots \\ \Delta\delta d_q^1 \\ \Delta\delta d_1^2 \\ \vdots \\ \Delta\delta d_q^2 \\ \vdots \\ \Delta\delta d_1^k \\ \vdots \\ \Delta\delta d_q^k \end{bmatrix} = \begin{bmatrix} \mathbf{W}^1\mathbf{A}_1^1 & \mathbf{W}^1\mathbf{B}_1^1 & \mathbf{W}^1\mathbf{C}_1^1 \\ \mathbf{W}^1\mathbf{A}_2^1 & \mathbf{W}^1\mathbf{B}_2^1 & \mathbf{W}^1\mathbf{C}_2^1 \\ \vdots & \vdots & \vdots \\ \mathbf{W}^1\mathbf{A}_q^1 & \mathbf{W}^1\mathbf{B}_q^1 & \mathbf{W}^1\mathbf{C}_q^1 \\ \mathbf{W}^2\mathbf{A}_1^2 & \mathbf{W}^2\mathbf{B}_1^2 & \mathbf{W}^2\mathbf{C}_1^2 \\ \vdots & \vdots & \vdots \\ \mathbf{W}^2\mathbf{A}_q^2 & \mathbf{W}^2\mathbf{B}_q^2 & \mathbf{W}^2\mathbf{C}_q^2 \\ \vdots & \vdots & \vdots \\ \mathbf{W}^k\mathbf{A}_1^k & \mathbf{W}^k\mathbf{B}_1^k & \mathbf{W}^k\mathbf{C}_1^k \\ \vdots & \vdots & \vdots \\ \mathbf{W}^k\mathbf{A}_q^k & \mathbf{W}^k\mathbf{B}_q^k & \mathbf{W}^k\mathbf{C}_q^k \end{bmatrix} \begin{bmatrix} I_a \\ I_b \\ I_c \end{bmatrix}. \tag{26}$$

In Eq. 26, $\Delta\delta d_{i(i=1,2,\dots,q;j=1,2,\dots,k)}^j$ represents the column vector of length n for the i th azimuth, j th frequency; $\mathbf{W}_{(j=1,2,\dots,k)}^j$ is the wavelet matrix corresponding with the j th frequency; \mathbf{A}_i^j , \mathbf{B}_i^j , and \mathbf{C}_i^j are the diagonal matrixes related to different azimuthal angles. \mathbf{I}_a , \mathbf{I}_b , and \mathbf{I}_c are the frequency dispersion gradient vectors of three anisotropic parameters to be inverted, respectively. Above all, Eq. 26 is a linear system of equations on \mathbf{I}_a , \mathbf{I}_b , and \mathbf{I}_c , under the circumstance of known α/β . We can solve the equations through the damped least squares method. The unknown $\mathbf{m} = [\mathbf{I}_a, \mathbf{I}_b, \mathbf{I}_c]^T$ was derived by

$$\mathbf{m} = \left[\mathbf{G}'^T\mathbf{G}' + \sigma\mathbf{I} \right] \mathbf{G}'^T \delta d, \tag{27}$$

where \mathbf{G}'^T is the transpose matrix of \mathbf{G}' , σ is the damping factor, and \mathbf{I} is the identity matrix. \mathbf{I}_c is the P-wave anisotropy dispersion gradient (PADG) that we focus on treated as the new fluid indicator.

Spectral decomposition

Application of spectral decomposition techniques allows frequency-dependent behavior to be detected from seismic data. Reflections from hydrocarbon-saturated zones can be anomalous in this regard (Castagna et al. 2003). For non-stationary signals, such as seismic record, spectral decomposition techniques transform the signal from the time domain to the frequency domain through time–frequency analysis methods. There are a variety of spectral decomposition techniques, such as the short time Fourier transform (STFT), continuous wavelet transform (CWT), generalized S transformation (GST), Wigner Ville

distribution (WVD), and matching pursuit decomposition (MPD). These different techniques have been studied and used for different applications, including layer thickness determination (Partyka et al. 1999), stratigraphic visualization (Marfurt and Kirlin 2001), as well as direct hydrocarbon detection. In this paper, we combined the MPD and WVD methods for adaption to azimuthal seismic data.

Both CWT and GST use the idea of window function, belonging to linear algorithms, so that the resolution is restricted by the uncertainty principle. In other words, time and frequency resolution is a pair of contradictions. However, MPD algorithm overcomes the window function restriction by precisely characterizing the signal according to both time and frequency domains. Mallat and Zhang (1993) proposed the idea of sparse decomposition using over-complete dictionary, and introduced the MPD algorithm. MPD is excellent for analyzing spectrum characteristics of signals due to the superiority of sparse representation. As a type of greedy iteration algorithm, MPD decomposes the seismic record into a series of wavelets. MPD selects an optimal fit wavelet m_{γ_n} from the wavelet dictionary by matching time–frequency features in each matching process. After N times matching, the seismic signal $s(t)$ could be expressed with N wavelets and the residual as

$$s(t) = \sum_{n=1}^N a_n m_{\gamma_n} + R^{(N)}f, \tag{28}$$

where n is the number of matching; a_n is the amplitude of the n th wavelet m_{γ_n} ; and $R^{(n)}f$ mean the residual after n matchings and $R^{(0)}f = s(t)$. We adopted Morlet wavelet (29) to construct the redundant dictionary due to its high time and frequency resolution:

$$m(t) = \exp\left(-4 \ln 2 \frac{f^2(t - \tau)^2}{\sigma^2}\right) \exp[i(2\pi f(t - \tau) + \phi)]. \tag{29}$$

In the Morlet wavelet function, there are four parameters: τ standing for time delay, f standing for dominant frequency, σ standing for the attenuative coefficient, and ϕ standing for phase. Thus, the Morlet wavelet can be described by the parameter set $\gamma = \{\tau, f, \sigma, \phi\}$. The creation of the wavelet set is controlled by three parameters, which are the main frequency, phase and attenuation factor, with fixed range and fine division. Thus, the wavelet set is called complete wavelets.

If the vertical projection of the signal (residual) in selected atoms is non-orthogonal, it will make each matching result suboptimal, rather than optimal. Therefore, extra iterations are needed for convergence. Orthogonal

matching pursuit (OMP) can effectively solve the problem using an orthogonal processing on all selected atoms in each step of decomposition for a faster convergence. The difference between OMP and MP is that the residual after each matching in OMP is orthogonal to each atom selected before

$$\langle R^{(N)}f, m_{\gamma_n} \rangle = 0, \quad n = 1, 2, \dots, N. \tag{30}$$

The symbol $\langle \cdot \rangle$ means the inner product operation.

Wigner Villa distribution (WVD) is an effective non-linear time spectral decomposition method, but there are cross-term interferences in the analysis of composite signals that consist of multiple frequency components. However, the WVD maintains a high resolution in the time and frequency domains simultaneously for Morlet wavelet:

$$W_{m_{\gamma_n}}(t, f) = \frac{1}{2\pi} \int_{-\infty}^{\infty} m_{\gamma_n}\left(t + \frac{\tau}{2}\right) \cdot m_{\gamma_n}\left(t - \frac{\tau}{2}\right) \cdot \exp(-i2\pi f\tau) d\tau \tag{31}$$

where $W_{m_{\gamma_n}}(t, f)$ is the time–frequency spectrum. Finally, the time–frequency spectrum of seismic signal can be calculated by Eqs. 29 and 31:

$$Af(t, f) = \sum_{n=0}^{N-1} \frac{a_n}{\|m_{\gamma_n}\|} \sqrt{W_{m_{\gamma_n}}(t, f)}. \tag{32}$$

Synthetic data example

A three-layer numerical model is constructed to test the theory. The model includes an upper isotropic elastic layer with P-wave velocity of 2743 m/s, S-wave velocity of 1394 m/s, a density of 2060 kg/m³, a middle dispersive layer that consists of three parts: two water saturated sandstone layers on two sides, a gas-saturated layer in the middle, and a lower layer with parameters which are as the same as those of the upper layer. The parameters for the dispersive layer are consistent with those introduced in section “[Selection of fluid factor](#)”. The density is 2600 kg/m³ under water saturation, and 2540 kg/m³ under gas saturation.

The velocities and anisotropy parameters of the dispersive layer are calculated after the effective stiffness tensor is derived for each frequency (20, 30, 40, and 50 Hz). Then, the synthetic azimuthal gathers for different frequencies are computed using the reflection coefficient Eq. 13 with the corresponding Ricker wavelets as the explosive sources. The incident angle is fixed to 22.5°, and three pairs of azimuthal angles with 90° displacement are chosen to generate azimuthal gathers. Figure 4 displays typical synthetic gathers of two azimuths. To test the robustness of our methods, two kinds of noises have been

added to the whole synthetic data, the correlated noises (Fig. 4a) and uncorrelated noises (Fig. 4b). The correlated noise is a sine wave with a frequency of 50 Hz and the uncorrelated noise is a Gauss random noise. The signal-to-noise ratio (SNR) for both cases is 20. Since we need to do a subtraction operation between two seismic volumes, the correlated noises will be eliminated. Therefore, we will mainly consider the influence of random noises. The amplitudes for the gas saturation case are apparently less than those for water saturation, as the difference between the synthetic data of two azimuths (Fig. 5a). As a consequence, the strong event unfortunately hides the amplitude variation induced by anisotropy. To address this issue, we replace the absolute difference with relative difference (shown in Fig. 5). The relative difference between azimuthal gathers could prominently reveal the manifestation of seismic anisotropy (Fig. 5b). Finally, the inverted attribute PADG shown in Fig. 6a exhibits significant difference

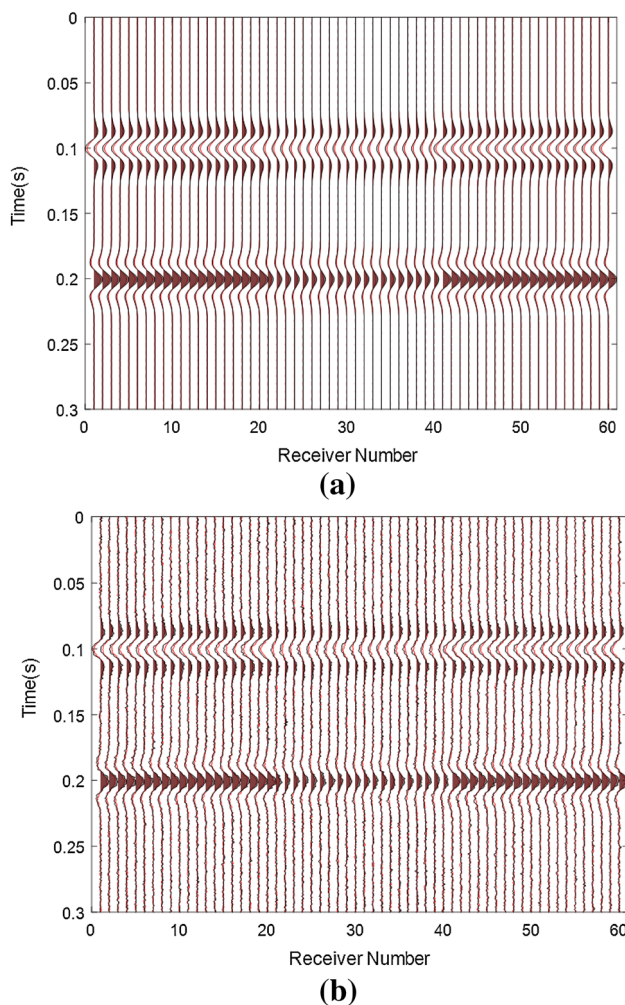


Fig. 4 Synthetic gathers: **a** with a 50 Hz sin wave noise and **b** with Gauss random noise (black line: the azimuthal angle is 27°; red line: the azimuthal angle is 117°)

for gas and water. We also show the inversion results for cases SNR is 10 (Fig. 6b) and SNR is 30 (Fig. 6c). We can see that the noise has a great influence on the inversion results. When the SNR is low, we cannot efficiently distinguish gas and water sections just like Fig. 6b, but when the SNR is high, the PADG attribute can clearly indicate the gas section.

Field data application

Real seismic data are derived from a fractured porous reservoir which is a typical carbonate fractured vuggy reservoir characterized by marls, limestones, and dolomites. The fractures existing widely in the area result in strong anisotropy. The imaging logging of well A shows that high angle and near vertical fractures develop in this reservoir (Fig. 7). The lengths of fractures are in the range of 0.4–5 m and the average fracture radius is about 0.8 m which is adaptive for our method. Therefore, we apply the method to the seismic data for gas detection. The inversion based on Eq. 20 requires information about fracture strikes φ_f . The azimuthal angle φ in Eq. 13 is actually the combination of survey line azimuth φ_s and fracture strike φ_f : $\varphi = \varphi_s - \varphi_f + \pi/2$. The fracture strike angles are derived from frequency-independent AVAZ inversion. Figure 8 shows the rose diagram of fracture strikes. The fractures mainly develop along two mutually perpendicular directions 30° and 120° (0° indicates the direction of the North).

Pre-stack seismic data of eight azimuthal angles are available for this area. Figure 7 shows the processed profiles of four pairs of mutually orthogonal survey lines. We can see that the amplitudes of same seismic survey line for different azimuth are nearly the same for basic shape (Fig. 9a). Furthermore, we extract the same seismic trace (Fig. 9b) and select the sample points (Fig. 9c) at the same time for these eight azimuthal gathers. Although the phases seem alike, the amplitudes are apparently discrepant when specific to the sample points.

Seismic data resolution and signal-to-noise ratio have great influences on the structural interpretation, reservoir inversion, and other geophysical methods. The spectrum analysis provides a basis for favorable data, such as the dominant frequency and bandwidth of the seismic data for subsequent seismic data interpretation and stacking velocity inversion. The amplitude spectra of two arbitrary traces from two mutually perpendicular azimuthal data (5° and 95°) are analyzed with fast Fourier transform. As shown in Fig. 10, the dominant frequency is 28 Hz, and the bandwidth is approximately 5–65 Hz. Thus, the overall quality of seismic data with high folds in the study area meets the needs of fine seismic inversion and interpretation. Therefore, we stipulate the reference frequency as 28 Hz and

Fig. 5 Strong event unfortunately hides the amplitude variation induced by anisotropy in the absolute gather difference (a) and the relative gather difference (b) prominently reveals the manifestation of seismic anisotropy

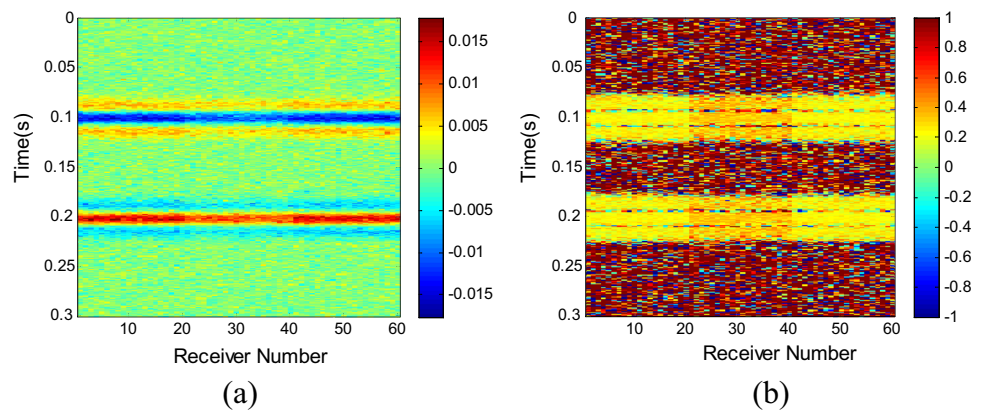
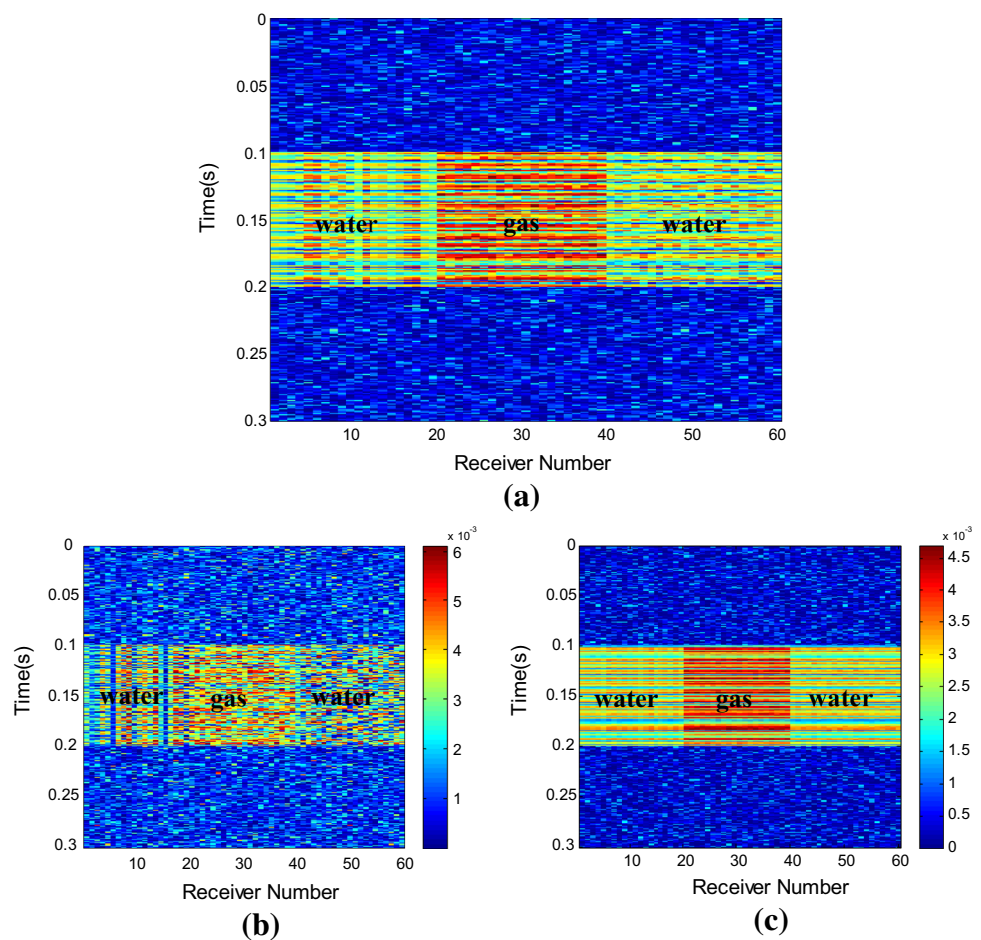


Fig. 6 Estimated PADG attribute: a SNR is 20; b SNR is 10; and c SNR is 30



define 20, 30, and 40 Hz as the set of frequencies for the frequency-division data.

Figures 11 and 12 show the frequency-division sections of the same survey line from two orthogonal azimuths, namely, 20, 30, and 40 Hz, respectively. As shown, the energy becomes weak when the frequency reaches 40 Hz, especially in the deep layers. Therefore, the wavelet matrix derived from the frequency-division data is needed to balance the spectra. The amplitude anisotropy results in an

amplitude spectrum difference for different azimuthal seismic data, which provides a good foundation for the analysis of anisotropic parameters characteristics. Finally, the inversion workflow is performed on the data. The inverted PADG attribute is shown in Fig. 13. The results are consistent with the well-logging interpretation results (the red patch represents gas-bearing layer and the green patch represents water bearing layer). The strong magnitude of PADG at approximately 1900 ms implies the

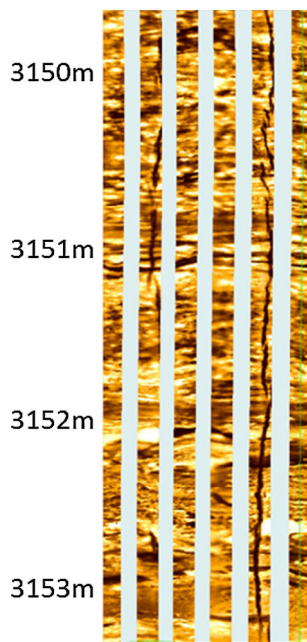


Fig. 7 Imaging logging of well A

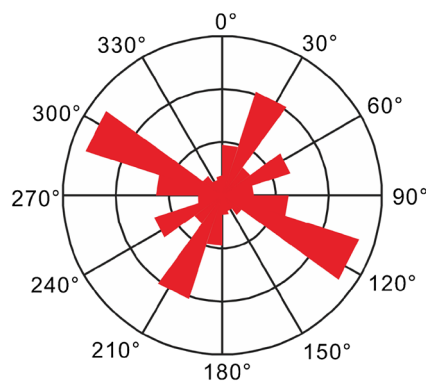


Fig. 8 Rose diagram of fractures

occurrence of gas, while the PADG for water bearing layer at 1750 ms is rather low.

Discussion

Model parameter selection

We have presented a new attribute PADG to identify fluid in fractured reservoirs from frequency-dependent AVAZ inversion. In fact, we take advantage of the sensitivity of the characteristic frequency or transition band to fluid type. The microscale characteristic frequency usually lies between the sonic and ultrasonic frequency ranges, which cannot explain the attenuation in seismic frequency band. The squirt flow between mesoscopic fractures and pores

proposed by Chapman (2003) makes the characteristic frequency drop into seismic frequency band. Unfortunately, the mesoscopic characteristic frequency is controlled by both fluid type and fracture size, so as the PADG attribute. If the fracture radius keeps unchanged, the characteristic frequency is highest for gas saturation. When the fractures are meter-sized, the characteristic frequency for gas saturation is just located in seismic frequency band, generating a strong dispersion and attenuation while that for oil or water is very low, meaning that the attenuation is close to 0 in seismic frequency band. Therefore, the method has a high accuracy for gas detection for reservoirs with meter-scaled fractures. For larger fractures, the method is not suitable as the transition band becomes low enough beyond the seismic band. For smaller fractures, the PADG attribute becomes remarkable for oil or water saturation in seismic frequency band; that is to say, we can use PADG to identify oil or water when fracture radius is small, for example, millimeter scaled.

The mesoscopic relaxation time is associated with the microscale relaxation time; however, the relaxation time (characteristic frequency) for field rocks is difficult to estimate, so there is some uncertainty in our results. We use τ_m from published laboratory data, since we do not have measurements of τ_m for the field rocks. Chapman (2001) deduced $\tau_m = 2 \times 10^{-5}s$ for brine-saturated sandstone and $\tau_m = 4 \times 10^{-7}s$ for gas-saturated sandstone. Chapman et al. (2003) obtained $\tau_m = 7.7 \times 10^{-7}s$ for gas-saturated sandstone. Al-Harrasi (2011) used $\tau_m = 9.5 \times 10^{-7}s$ for gas-saturated carbonatite, which is adopted in this paper. According to these published data, the microscale relaxation timescales for different rocks are different but in the same order. Therefore, the uncertainty of τ_m does influence the characteristic frequency, but the transition band hardly changes. Precise τ_m from experiments on the field rock sample will provide more convincing and exact fluid recognition results.

For the issue of patchy fluid or the calibration of degree of saturation, the difficult point is the measurement of τ_m and construction of effective fluid. We must consider the dynamic viscosity of the patchy fluid as the fluid shows viscoelastic characteristics. The future work will address these issues.

Weak contrast approximation

The objective function to invert the PADG is derived based on the Rüger equation, which is reformed into a frequency-dependent form. Almost all the approximate formulas based on the Zoeppritz equation are adaptive to the cases of weak contrast approximation. The weak contrast approximation can be expressed as

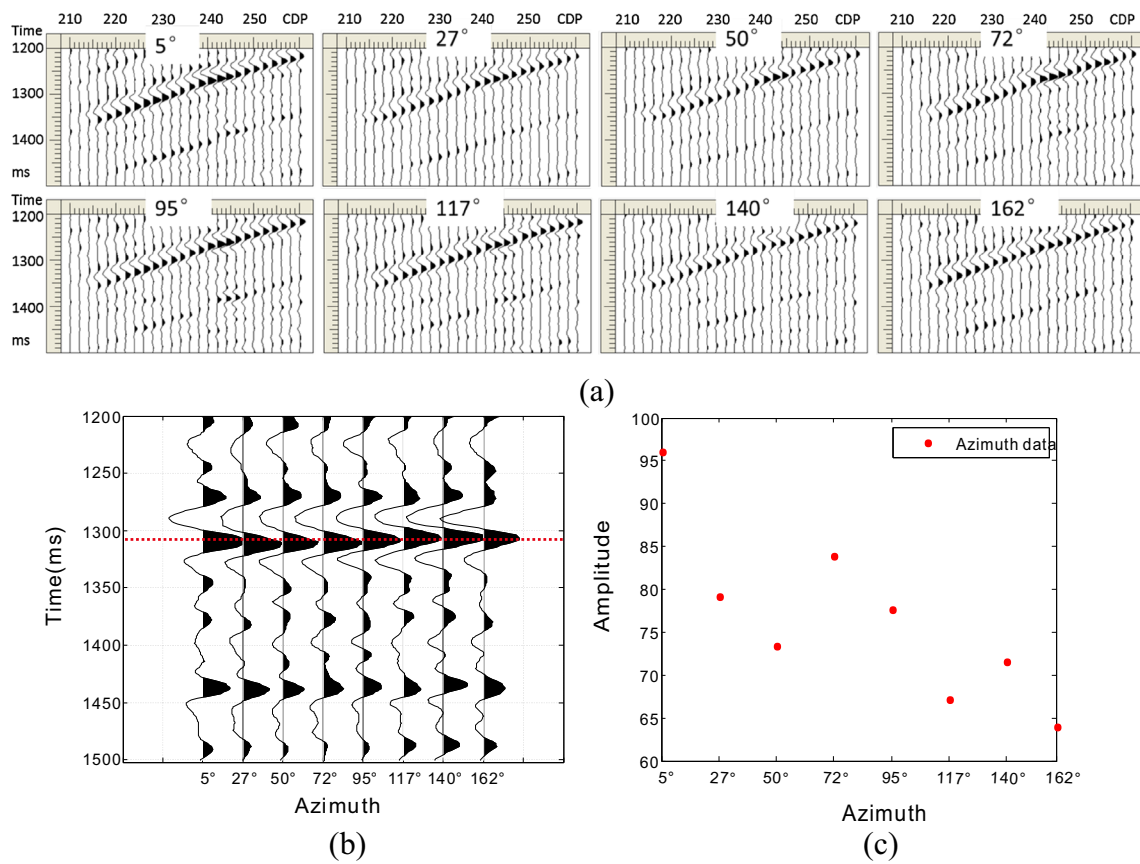
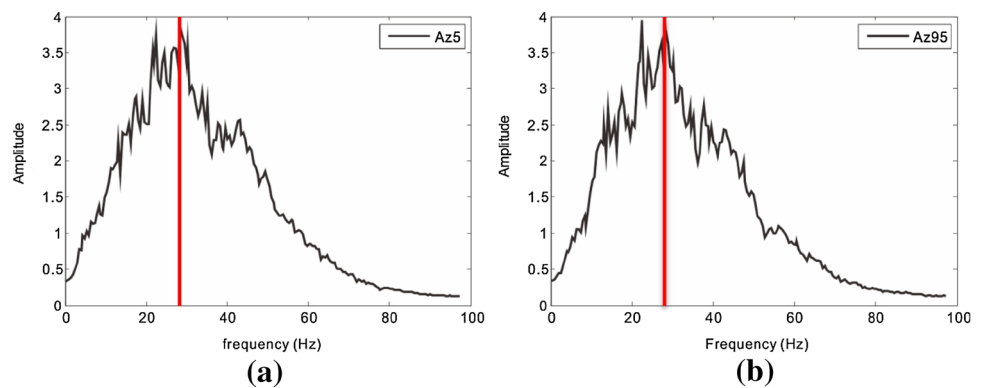


Fig. 9 a Seismic profiles for different azimuths; b seismic azimuthal traces; and c amplitude of the same sample point for different azimuths

Fig. 10 Amplitude spectra of the same survey line for azimuths 5° (a) and 95° (b)



$$\frac{\Delta X}{\bar{X}} < 1, \tag{33}$$

where X is the parameter of layer medium which can be velocity, density, and anisotropic parameters, ΔX is the parameter contrast between two layers, and \bar{X} is the average value of the parameters of two layers. The weak contrast approximation is adaptive for most cases. In the case of dispersion and attenuation, $\Delta X/\bar{X}$ will be frequency dependent. Taking the parameters introduced in section

“Frequency-dependent AVAZ inversion for PADG”; for example, we calculate $\Delta v_p/\bar{v}_p$ variation with frequency. As shown in Fig. 14, $\Delta v_p/\bar{v}_p$ increases with frequency, but is still less than 1. Thus, on most geological conditions, the weak contrast approximation is feasible, and Rüger equation is suitable for the dispersive cases. Furthermore, the anisotropy is weak and the contrast across the interface is also weak in many practical cases. Therefore, our method is doable both in theory and in application.

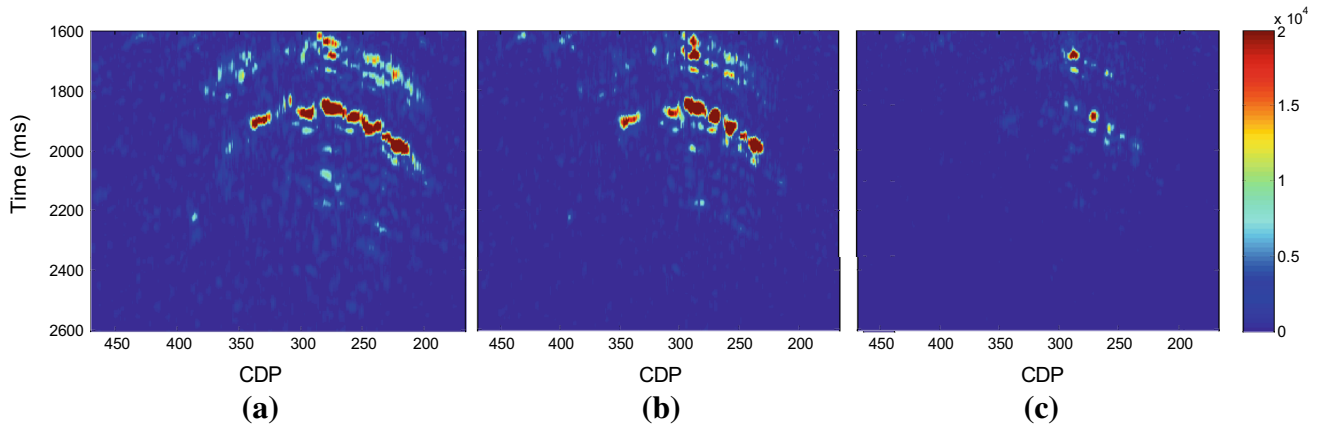


Fig. 11 Frequency-division sections: **a** 20 Hz; **b** 30 Hz; and **c** 40 Hz (the azimuthal angle is 5°)

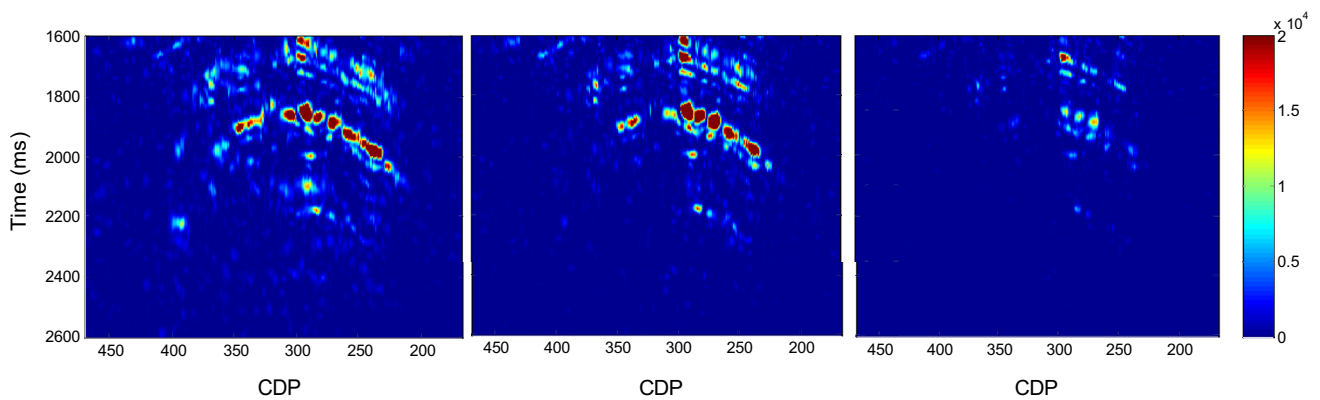


Fig. 12 Frequency-division sections: **a** 20 Hz; **b** 30 Hz; and **c** 40 Hz (the azimuthal angle is 95°)

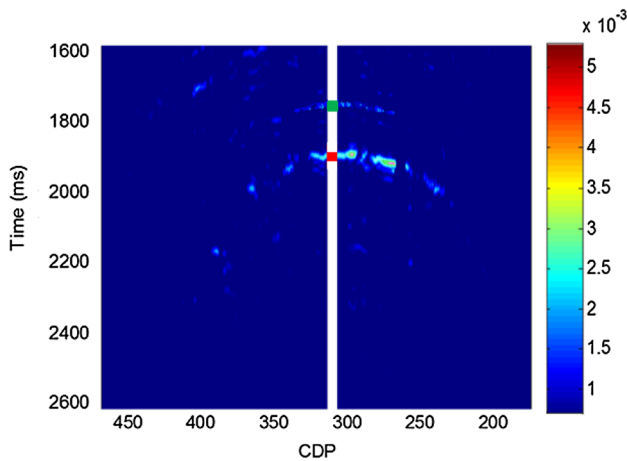


Fig. 13 Estimated PADG attribute

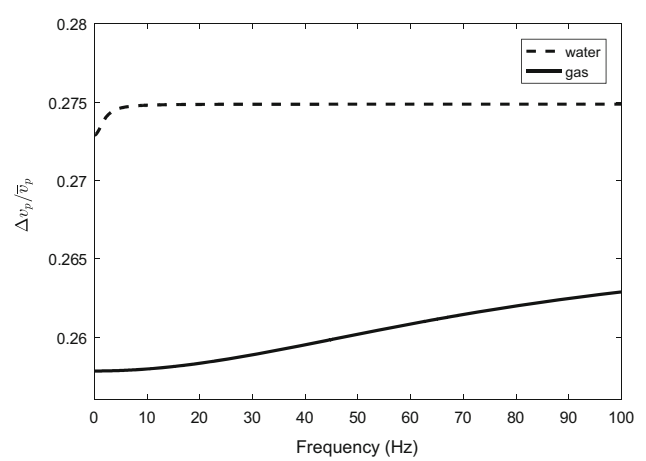


Fig. 14 $\Delta v_p/v_p$ variation with frequency

Conclusions

Fluid-related dispersion and attenuation makes a significant difference on amplitude versus offset and azimuth and give rise to a frequency dependence of reflection coefficients. Furthermore, frequency-dependent anisotropy is sensitive

to the fluid type. Through the numerical simulation based on Chapman model, we analyze the frequency dependence of phase velocity, attenuation, and P-wave anisotropic parameter, and choose P-wave anisotropy parameter dispersion gradient (PADG) as the fluid factor. When the aligned fractures in the reservoir are meter-scaled, gas-

bearing layer could be accurately identified using PADG attribute. The multi-azimuthal seismic data allow us to analyze the anisotropic characteristic for the fractured reservoirs. In this paper, the target function of inverting PADG using frequency-dependent AVAZ is derived by rewriting the reflection coefficient equation in HTI media. A method combining a high-resolution spectral decomposition technique and least squares inversion is performed to the synthetic data and real data from a fractured reservoir. The results of the synthetic data with noises show that our method needs high-qualified seismic data. When the seismic data are contaminated by noises seriously, the identification results could be unreliable. When seismic data are with high SNR, the results demonstrate that our method is potentially useful for gas detection in reservoirs with meter-scaled fractures.

References

- Al-Harrasi OH, Kendall JM, Chapman M (2011) Fracture characterization using frequency-dependent shear wave anisotropy analysis of microseismic data [J]. *Geophys J Int* 185(2):1059–1070
- Banik NC (1987) An effective anisotropy parameter in transversely isotropic media [J]. *Geophysics* 52(12):1654–1664
- Castagna JP, Sun S, Siegfried RW (2003) Instantaneous spectral analysis: detection of low-frequency shadows associated with hydrocarbons. *Lead Edge* 22(2):120–127
- Chapman M (2001) Modelling the wide-band laboratory response of rock samples to fluid pressure changes. Ph.D. thesis, University of Edinburgh
- Chapman M (2003) Frequency-dependent anisotropy due to meso-scale fractures in the presence of equant porosity. *Geophys Prospect* 51(5):369–379
- Chapman M, Zatsepin S, Crampin S (2002) Derivation of a microstructural poroelastic model [J]. *Geophys J Int* 151(2):427–451
- Chapman M, Maultzsch S, Liu E et al (2003) The effect of fluid saturation in an anisotropic multi-scale equant porosity model [J]. *J Appl Geophys* 54(3–4):191–202
- Chapman M, Liu E, Li XY (2006) The influence of fluid-sensitive dispersion and attenuation on AVO analysis. *Geophys J Int* 167(1):89–105
- Chen W (1995) AVO in azimuthally anisotropic media: fracture detection using P-wave data and a seismic study of naturally fractured tight gas reservoirs. Ph.D. dissertation, Stanford University
- Chen H, Zhang G, Ji Y et al (2017) Azimuthal seismic amplitude difference inversion for fracture weakness [J]. *Pure Appl Geophys* 174:279
- Cheng BJ, Xu TJ (2012) Research and application of frequency dependent AVO analysis for gas recognition [J]. *Chin J Geophys Chin Edn* 55(2):608–613
- Daley PF, Hron F (1977) Reflection and transmission coefficients for transversely isotropic media [J]. *Bull Seismol Soc Am* 67(3):661–675
- Fatti JL (1994) Detection of gas in sandstone reservoirs using AVO analysis: a 3-D seismic case history using the Geostack technique [J]. *Geophysics* 59(5):1362–1376
- Goodway W, Chen T, Downton J (1997) Improved AVO fluid detection and lithology discrimination using Lamé petrophysical parameters; “ $\lambda\rho$ ”, “ $\mu\rho$ ”, & “ λ/μ fluid stack”, from P and S inversions [J]. In: SEG technical program expanded abstracts, pp 183–186
- Gray FD (2002) Elastic inversion for lamé parameters [J]. In: SEG technical program expanded abstracts, pp 697–700
- Huang HD, Wang JB, Guo F (2012) Application of sensitive parameters analysis in fluid recognition based on pre-stack inversion [J]. *Geophys Geochem Explor* 36(6):941–946
- Macbeth C, Lynn HB (2000) Applied seismic anisotropy: theory background and field studies [C]. Society of Exploration Geophysicists, Tulsa, pp 682–685
- Mallat S, Zhang Z (1993) Matching pursuit with time–frequency dictionaries [J]. *IEEE Trans Signal Process* 41(12):3397–3415
- Marfurt KJ, Kirlin RL (2001) Narrow-band spectral analysis and thin-bed tuning [J]. *Geophysics* 66(4):1274–1283
- Mavko G, Jizba D (1991) Estimating grain-scale fluid effects on velocity dispersion in rocks [J]. *Geophysics* 56(12):1940–1949
- Partyka GJ, Gridley J, Lopez J (1999) Interpretational applications of spectral decomposition in reservoir characterization. *Lead Edge* 18(3):173–184
- Rüger A (1997) P-wave reflection coefficients for transversely isotropic models with vertical and horizontal axis of symmetry [J]. *Geophysics* 62(3):713–722
- Rüger A (1998) Variation of P-wave reflectivity with offset and azimuth in anisotropic media [J]. *Geophysics* 63:935–947
- Russell BH, Gray D, Hampson DP (2011) Linearized AVO and poroelasticity [J]. *Geophysics* 76(3):C19–C29
- Schoenberg M, Protazio J (1992) “Zoeppritz” rationalized, and generalized to anisotropic media [J]. *J Seism Explor* 1(2):125–144
- Smith GC, Gidlow PM (1987) Weighted stacking for rock property estimation and detection of gas [J]. *Geophys Prospect* 35(9):993–1014
- Thomsen L (1993) Weak anisotropic reflections. In: Castagna J, Backus M (eds) *Offset-dependent reflectivity—theory and practice of AVO analysis*. Society of Exploration Geophysicists, Tulsa, pp 103–114
- Thomsen L (1995) Elastic anisotropy due to aligned cracks in porous rocks. *Geophys Prospect* 43(6):805–829
- Tsvankin I (1997) Reflection moveout and parameter estimation for horizontal transverse isotropy [J]. *Geophysics* 62(2):614–629
- Václav V, Ivan P (1998) PP-wave reflection coefficients in weakly anisotropic elastic media [J]. *Geophysics* 63(6):2129–2141
- Wilson A (2010) *Theory and methods of frequency-dependent AVO Inversion*. University of Edinburgh, Edinburgh
- Wu X, Chapman M, Li XY (2012) Frequency-dependent AVO attribute: theory and example [J]. *First Break* 30:67–72
- Wu X, Chapman M, Li XY et al (2014) Quantitative gas saturation estimation by frequency-dependent amplitude-versus-offset analysis [J]. *Geophys Prospect* 62(6):1224–1237
- Zhang SX, Yin XY, Zhang GZ (2011) Dispersion-dependent attribute and application in hydrocarbon detection [J]. *J Geophys Eng* 8(4):498–507
- Zhang Z, Yin XY, Hao QY (2014) Frequency dependent fluid identification method based on AVO inversion. *Chin J Geophys Chin Edn* 57(12):4171–4184